BORESKOV INSTITUTE OF CATALYSIS

ZINFER R. ISMAGILOV

SELECTED PAPERS

VOLUME 3

NOVOSIBIRSK
2010

Ismagilov Z.R.

A book of selected papers: volume 3. – Novosibirsk: BIC SB RAS, 2010.

This three-volume book comprises selected papers written by Professor Z.R. Ismagilov and his colleagues at the Boreskov Institute of Catalysis SB RAS and published over the last 35 years. Various papers included in the book are grouped thematically and presented in 10 chapters:

1. Mechanistic studies of complete oxidation reactions. Scientific basis for catalytic combustion of fuels.
2. Development of advanced catalysts and technologies for environmental protection.
3. Mechanistic studies of heterogeneous-homogeneous oxidation reactions over solid catalysts.
4. Development of scientific basis for the production of monolith supports and catalysts. Establishment of the first national production facility.
5. Catalytic methods for conversion of sulfur compounds: direct oxidation of hydrogen sulfide, raw oil hydrofining, catalytic synthesis of thiophene. Creation of a industrial plant for direct oxidation of hydrogen sulfide.
6. Preparation of nanostructured zeolite catalysts. Copper-containing linear structures and molybdenum-containing catalysts for methane dehydroaromatization.
7. Catalytic synthesis of carbon nanofibers (CNF). Their structure, properties and application for fuel cells.
8. Design and testing of catalytic microreactors.
9. Synthesis and study of supports and catalysts. Oxygen-permeable perovskite membranes.
10. Nanostructured titanium dioxide for medicine and biology.

CONTENT OF VOLUME 3

CHAPTER 7

Catalytic synthesis of carbon nanofibers (CNF). Their structure, properties and application for fuel cells..

CHAPTER 8

Design and testing of catalytic microreactors

4. Determination of the Tolman length in the improved Derjaguin-Broekhoff-de Boer theory for capillary condensation of ethanol in mesoporous thin films by ellipsometric porosimetry
5. Design of Pt-Sn catalysts on mesoporous titania films for microreactor application.
6. Control of the thickness of mesoporous titania films for application in multiphase catalytic microreactors

CHAPTER 9

Synthesis and study of supports and catalysts. Oxygen-permeable perovskite membranes.

1. Исследование катализаторов и реакций каталитического окисления. III. Формирование текстуры псевдобемитов при грануляции жидкостным методом сферических носителей для катализаторов КГТ
2. Study of Structural and Mechanical Properties of Granulated Alumina Supports Using X-Ray Microprobes
3. Improvement of the Hydrocarbon-Ammonia Granulation Method for Production of Spherical Alumina with Variable Properties Adsorption-Contact Method of Drying of Thermolabile Materials
4. Interrelation between structural and mechanical characteristics of spherical alumina granules and the initial hydroxide properties
5. Production of spherical granules of alumina with controlled porous structure
6. Исследование катализаторов и реакций каталитического сжигания. X. Особенности создания прочных носителей для катализаторов кипящего слоя с применением жидкостного формования
7. Synthesis of mechanically strong and thermally stable spherical alumina catalyst supports for the process of methane dimerization in a fluidized bed
8. Porous structure of alumina ceramic supports for gas separation membranes. I.Preparation and study of the extrusion masses
9. Porous structure of alumina ceramic support for gas separation membranes. II. Study of porous structure of ceramic composition
10. Synthesis of a mechanically strong and thermally stable alumina support for catalysts used in combustion processes
11. Исследование реакций и катализаторов сжигания топлив. XVII. Влияние лантана и церия на структурно-механические свойства оксида алюминия
12. Porous alumina as a support for catalysts and membranes. Preparation and

study

13. Metal foam supported perovskite catalysts
14. New technology for production of spherical alumina supports for fluidized bed combustion
15. Application of plasma spraying in the preparation of metal-supported catalysts
16. Исследование реакций и катализаторов сжигания топлив. XIX. Термостабильность оксида алюминия, содержащего одновременно добавки лантана и кремния
17. Исследование реакций и катализаторов сжигания топлив. XX. Термостабильность и другие свойства системы CeO_2–MgO–Al_2O_3
18. A catalytic heat-exchanging tubular reactor for combining of high temperature exothermic and endothermic reactions
19. Исследование реакций и катализаторов сжигания топлив. XXI. Синтез и исследование модифицированных Mn–Al–O катализаторов для высокотемпературного окисления
20. Study of Supported Catalysts Synthesized by the Use of Plasma Technique
21. EXAFS Study of Nb Doped Sr(Co/Fe)O_{3-x} Perovskites
22. High-temperature catalysts with a synergetic effect of Pd and manganese oxides
23. Oxygen diffusion in nanostructured perovskites
24. Properties of Nb-doped SrCo0.8Fe0.2O3-d perovskites in oxidizing and reducing environments

CHAPTER 10

Nanostructured titanium dioxide for medicine and biology

1. Synthesis and stabilization of nano-sized titanium dioxide
2. An Examination of the Ability of Titanium Dioxide Nanoparticles and Its Conjugates with Oligonucleotides to Penetrate into Eucariotis Cells
3. Interaction of Titanium Dioxide Nanoparticles with Influenza Virus

CHAPTER 7
Catalytic synthesis of carbon nanofibers (CNF).
Their structure, properties and application for fuel cells.

Eurasian ChemTech Journal 2 (2000) 237-244

Microdesign of nickel-cooper alloy catalysts for production of new carbon materials

T.V.Reshetenko, L.B.Avdeeva, Z.R.Ismagilov*, A.L.Chuvilin, V.A.Likholobov

Boreskov Institute of Catalysis, Pr. Akad. Lavrentieva, 5, Novosibirsk, 630090, Russia

Abstract

The reaction of methane decomposition was investigated on the Ni-Cu-Al_2O_3 alloy catalysts at 625-675°C at a gas pressure of 1 bar to produce catalytic filamentous carbon (CFC) with a simultaneous formation of hydrogen. Using Ni-Cu alloy catalysts (8-15 wt.% Cu) at 625°C permits a CFC yield of 525 g/g_{cat} (700 g/g_{Ni}). According to the X-ray powder diffraction (XRD) and transmission electron microscopy (TEM) studies of Ni-Cu-Al_2O_3 catalysts, morphology of catalysts begins to change during 10 minutes after CH_4 decomposition by formation of "octopus" CFC structures. It should be noted, that copper additives substantially increase the thermal stability of Ni and modify the textural and structural properties of CFC.

Introduction

Fibrous carbon materials which can be obtained by decomposition of hydrocarbons on 3d-metal catalysts (Ni, Co, Fe) are of prime interest today [1-6].

Hydrocarbon decomposition, under certain conditions, may result in formation of filamentous carbon which does not poison the catalyst for a long time. It was shown [2] that Ni-Al_2O_3 catalysts with a high nickel content (60-90 wt.%) have such properties. These catalysts are active for 16 hours on methane decomposition at 550°C, the maximum carbon deposition is to 100 g/g_{cat}. The mechanism of catalytic CFC growth is still unclear, but the conventional model includes the below stages: decomposition of CH_4 on Ni (100) and (110) planes involving the formation of surface carbon; carbon diffusion through a Ni particle and graphite precipitation on the Ni (111) planes [7]. The structure and activity of Ni-Al_2O_3 catalysts, modified with copper, were studied on the CH_4 decomposition at 500-600°C [2,8,9]. In the presence of Ni-Cu catalysts, the yield of CFC is 200 g/g_{cat} and higher, and the methane conversion is about 10-15% at 550°C.

The interaction between C_2H_4, C_2H_2, CH_4 and the Ni-Cu catalysts was investigated in [6]. Ni-Cu catalysts react with ethylene and acetylene at 600°C, and methane decomposes at temperatures above 900 °C. Cracking of the unsaturated hydrocarbons, CFC formation and catalytic particle transformations under the effect of reaction conditions were studied by TEM method.

The reaction of CH_4 decomposition on the coprecipitated Ni-Cu catalysts (2, 15 wt. % Cu) at 500 and 600°C was investigated in [8]. The kinetics of the reaction was studied by the weight method. For this purpose a catalyst sample with an optimal molecular ratio of Ni^{2+}:Al^{3+}:Cu^{2+}=75:23:2 was chosen. The lifetime of the catalyst is 7.5 hours and the amount of the formed carbon is 80 mg/mg_{cat} at 500°C. An increase in temperature of CH_4 decomposition reduces the catalyst activity. According to the TEM studies of carbon formed on the above sample, one carbon filament grows from one catalytic particle, the later being located on its top. Diameter of a filament depends on the size of a catalyst particle and ranges from 10 to 60 nm. To explain catalytic properties of the nickel-copper alloy, the authors assumed that the copper introduction decreases the reduction temperature of NiO, because filling of d-orbitals of Ni with Cu electrons affects formation of the Ni-Cu alloy.

In [9], Ni-Cu-MgO catalysts were investigated on the CH_4 decomposition at 525-600°C. These catalysts were obtained by mechanical activation of the metal oxide and hydroxide powders. The kinetics of CFC formation was studied in the reactor using a Mac-Ben balance. CFC was investigated by HRTEM and XRD. The mechanism of methane decomposition and CFC deposition on the catalyst crystallites

*corresponding author. E-mail: zri@catalysis.nsk.su

was discussed.

It was found [2] that the copper additives increase stability of the Ni-Al_2O_3 catalyst and influence the microstructure of CFC. The CFC, produced by methane decomposition on the Ni-Al_2O_3 catalyst, is formed by graphite-like layers packed at 45° to the filament axis. The "octopus"-type carbon, formed on the Ni-Cu-Al_2O_3 catalyst, consists of several filaments growing from one particle, the graphite layers in filaments are oriented perpendicular to their axis [9-11]. The Ni-Cu-Al_2O_3 catalysts were developed to produce large amounts of filamentous carbon at low temperatures (500-600°C). This CFC was recently suggested to be a novel carbon support and an adsorbent [12-14]. Despite of numerous publications devoted to the study of Ni-Cu catalytic systems on the hydrocarbon cracking, the role of copper remains unknown.

The main objective of this publication is a detailed investigation of thermal stability and efficiency of Ni-Cu-Al_2O_3 catalysts on methane decomposition at 625-675°C. The copper content was varied within a wide range of concentrations (8 wt. % to 45 wt. %). To study structure and activity of the prepared catalysts, we used their reduced forms. Effect of copper on the textural and microstructure properties of CFC was studied by XRD, TEM and adsorption methods.

Experimental

Using aqueous solutions of salts $Ni(NO_3)_2 \cdot 6H_2O$, $Cu(NO_3)_2 \cdot 3H_2O$, $Al(NO_3)_3 \cdot 9H_2O$ and NaOH as a precipitate, we prepared the catalysts by a procedure described in detail elsewhere [1]. The samples were carefully washed with distilled water, dried at 110°C, and calcined in a flow of N_2 at 350°C for 3 hours. The catalysts were reduced in a flow of pure hydrogen at 550°C for 3 hours. To minimize pyrophoric behavior of the reduced catalysts, the samples were in situ passivated in ethanol and dried at room temperature. This procedure did not influence the properties of the catalysts. Catalytic activity of the reduced samples (100 mg) was measured in a vibrating flow quartz reactor 30 $см^3$ in volume. Methane was supplied at a rate of 3 to 12 l/h.

Concentration of methane was measured by gas chromatography and methane conversion was calculated. To determine carbon deposition, the sample was weighted after the reaction, which was performed to the complete catalyst deactivation.

The samples of catalysts and CFC were investigated by TEM, XRD, and adsorption methods. The XRD studies were performed in a Siemens URD-63 diffractometer using CuK_α radiation and a graphite crystal monochromator. Crystallite sizes were calculated from the line width following the Scherrer equation. TEM pictures were obtained on a JEM-100CX. The adsorption measurements were carried out using an ASAP-2400 to provide adsorption of N_2 at -196°C.

Results

Catalyst properties

We have prepared a number of catalysts where Cu concentration was 8, 15, 25, 35, and 45 wt.%. XRD data in Table 1 show that the catalysts are represented by a Ni-Cu alloy in all cases. As the Cu:Ni ratio increases, the lattice parameter also increases, which result in formation of two phases of nickel-

Table 1

X-ray powder diffraction characterization of the reduced Ni-Cu-Al_2O_3.

Sample	Ni:Cu:Al_2O_3, wt. %	Lattice parameter Ni (d), Å	D_{111} Ni, nm	Phase composition
82Ni8Cu	82:8:10	3.5276	10	$Ni_{0.98}Cu_{0.02}$
75Ni15Cu	75:15:10	3.5341	13	$Ni_{0.98}Cu_{0.11}$
65Ni25Cu	65:25:10	3.5618	13	$Ni_{0.59}Cu_{0.41}$
		3.6187	12	Cu
55Ni35Cu	55:35:10	3.6022	20	$Ni_{0.15}Cu_{0.85}$
		3.5335	10	$Ni_{0.9}Cu_{0.1}$
45Ni45Cu	45:45:10	3.6012	20	$Ni_{0.16}Cu_{0.84}$
		3.5358	10	$Ni_{0.87}Cu_{0.13}$

copper alloys [10]. In contrast to the Ni-Al_2O_3 system [1], the spinel phase was not observed in the diffraction pattern of Ni-Cu catalysts. The presence of the copper phase was identified for the sample with a high Cu content.

Figure 1 shows particle size distributions of the reduced catalysts determined by TEM. A rather narrow particle size distribution (10-30 nm) is observed for the Ni-Cu system. The maximum distribution is observed in the range 20-25 nm for the samples of 15 and 25 wt.% Cu and in the range 15-20 nm for the sample of 45 wt.% Cu.

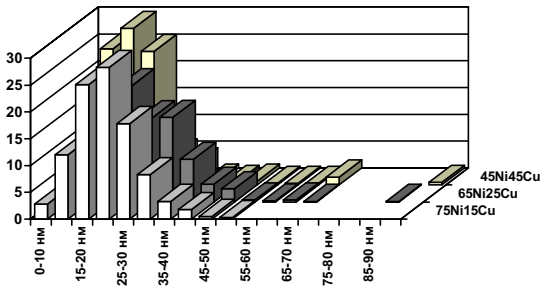

Fig. 1. Distribution of particle sizes of the reduced catalysts obtained by TEM.

Catalytic activity of Ni-Cu systems

Decomposition of methane on the Ni-Cu catalysts was studied at 625-675°C (Table 2). To compare catalytic properties of different samples, we used the below parameters: CH_4 conversion, carbon accumulation to complete deactivation of the catalysts (the so called carbon capacity G_c, calculated as gram of carbon per 1 gram catalyst) and lifetime of catalysts.

The data show that about 30% CH_4 is converted at 625°C on the 90Ni-Al_2O_3 catalyst. Note that the sample loses its activity during 2 hours. By introducing 8 wt.% Cu to the catalyst composition one reduces methane conversion to 22%, and increases the catalyst lifetime to 60 hours. If Cu concentration increases by more than 8 wt.% at 625°C, the activity, carbon capacity and lifetime of the catalysts decrease at a time.

An increase in the reaction temperature to 675°C (Table 2) provides a decrease in the activity of the 90Ni-Al_2O_3 catalyst. For 82Ni8Cu the methane conversion is 35%, but high activity holds only for 9 hours. If copper (15 wt.%) is introduced, the methane conversion decreases to 27 %, and the lifetime of the above catalyst increases to 27 hours. A further increase in the copper concentration provides a decrease in the catalyst activity and stability. Figure 2 shows methane conversion versus reaction time for the 75Ni15Cu catalyst at 625-675°C. It should be noted that carbon capacity of the samples with a copper content higher than 15 wt. % does not depend on temperature.

Therefore, thermal stability of Ni-Cu-Al_2O_3

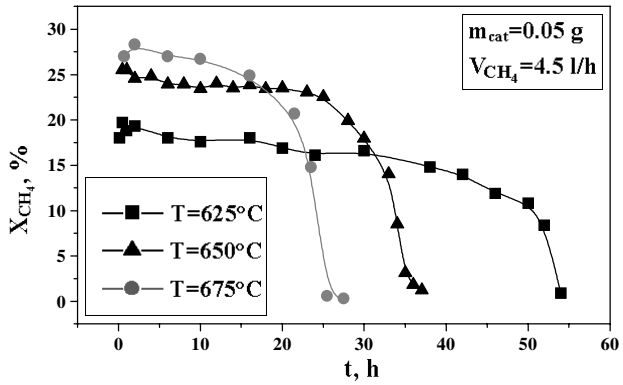

Fig. 1. Distribution of particle sizes of the reduced catalysts obtained by TEM.

Table 2

Catalytic properties of coprecipitated Ni-Cu alumina catalysts (methane conversion (x, %), carbon capacity (G, g_c/g_{cat}) and lifetime of catalyst (t, h); sample weight 0.05 g, gas flow 4.5 l/h).

Sample	625°C			650°C			675°C		
	x, %	G, g_c/g_{cat}	t, h	x, %	G, g_c/g_{cat}	t, h	x, %	G, g_c/g_{cat}	t, h
82Ni8Cu	22	515	61.5	22	169	15.5	35	150	9
75Ni15Cu	18	525	54	18	400	37	27	404	27.5
65Ni25Cu	15	291	35.5	15	309	32	26	293	20
55Ni35Cu	13	205	31	13	207	26	20	222	19.5
45Ni45Cu	10	118	23	10	115	13.5	17	126	12
90Ni Al_2O_3	31	22.4	2.5	34	11.2	2.5	7.0	8.0	5.0

catalysts strongly depends on the quantity of the added copper. The 82Ni8Cu catalyst is more stable and active at 625°C, whereas 75Ni15Cu and 65Ni25Cu catalysts are stable at 675°C.

Variation of some kinetic parameters on methane decomposition

A 65Ni25Cu sample was used to study some kinetic parameters. Methane conversion was studied in a temperature range of 550 - 700°C (Fig. 3). The conversion of methane was below a thermodynamically possible level, which was found from the condition that carbon was generated as a graphite phase [15,16].

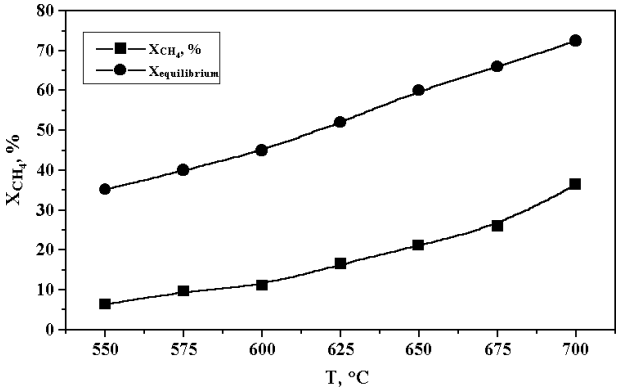

Fig. 2. Methane conversion as a function of time on the 75Ni15Cu catalyst.

Dependence between methane conversion and initial residence time τ was investigated. The residence time was set by changing the gas flow rate at a constant catalyst loading and in some cases by changing the catalyst loading at a constant gas flow rate. The experiments were performed at 650°C for 2 hours using the 65Ni25Cu catalyst (Fig. 4). Methane conversion grows from 15 % (τ = 0.01 s) to 24% (τ = 0.06 s). If the residence time further increases, methane conversion varies insignificantly. The data indicate that the kinetic conditions of methane decomposition retain to τ = 0.03 s.

In order to determine the reaction order, we have studied the dependence between the initial rate of methane decomposition and the initial concentration of hydrocarbon at 675°C (Fig. 5). For this purpose two mixtures of methane in helium (25 and 50 vol.% CH_4) were used. Figure 5 shows that the initial rate of methane decomposition grows proportionally to the initial methane concentration in the presence of all catalysts. This indicates the first reaction order with

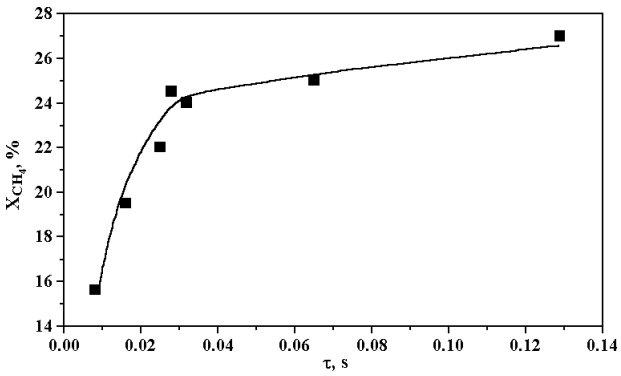

Fig. 4 Methane conversion as a function of residence time (m_{cat} = 0.1 g, V_{CH_4} = 9 l/h, time of reaction 2 hours).

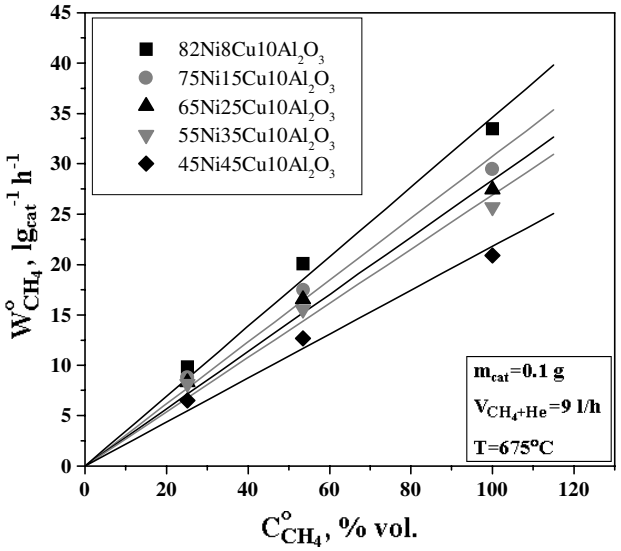

Fig. 5. Plot of the experimental initial rates of methane decomposition on the Ni-Cu-Al_2O_3 catalysts in CH_4+He gas mixtures at 675°C versus the initial concentration of methane.

respect to methane for all samples, which allows us to assume that copper additives do not affect the mechanism of methane decomposition.

Structural and textural properties of catalytic filamentous carbon.

Figure 6 shows TEM pictures of the active catalyst particles of 82Ni8Cu and 75Ni15Cu samples and CFC.

Two types of catalytic particles and correspondingly two types of CFC are observed for the 82Ni8Cu sample:

1. The particles 40-50 nm in size are pear shaped. These particles are typical for nickel-aluminum catalysts. Structure and morphology of CFC are similar to those CFC formed on the Ni-Al_2O_3, that is one

a b

Fig. 6. TEM pictures of the samples: 82Ni8Cu (a), 75Ni15Cu (b) after 2 hours of methane decomposition at 650°C.

carbon filament grows from one catalytic particle, and the graphite planes in filaments are coaxially arranged as cones. It should be noted the angle between graphite planes and the filament axis varies from 45° to 75°. Average diameter of the carbon filament and the catalyst particle is identical. The amount of the given particles forms about 65% of the total number.

2. The catalyst particles 70-100 nm in size are of octahedral shape. In this case, several filaments of CFC grow from one particle to form the so-called "octopus" structure [11]. The diameter of the growing filaments is less than the size of the "mother" particle. Graphite layers in the filaments are stacked perpendicular to their axis. The amount of octahedral particles is about 35%.

Thus, the microstructure of the catalytic filamentary carbon, formed on the 82Ni8Cu sample, is inhomogeneous.

For the catalysts containing more than 15% Cu the particles of the first type do not form. In this case, "octopus" carbon is predominantly observed, the diameter of fibers ranges from 50 to 150 nm. According to the TEM pictures (Fig. 6b), fibers 100-120 nm in size consist of several thin filaments 50 nm in diameter.

Interplanar distance d_{002} and the average size of the coherent scattering area directed perpendicular to the graphite plane (002) (L_c) of CFC were determined from XRD data. According to Table 3, the CFC structural parameters depend on the temperature of CH_4 decomposition. An increase in the reaction temperature results in a decrease in the magnitude of interplanar distance d_{002} to 3.389 Å, which is close to d_{002} = 3.354 Å of graphite. In addition, an increase in the average size of CFC coherent scattering area occurs because of a rise in the reaction temperature. Thus, the degree of CFC graphitization increases as temperature rises to 675°C.

Textural properties of CFC, formed on the catalysts containing 15-45 wt.% Cu at 625-675°C, were determined by nitrogen adsorption at −196°C (see Table 3). It should be noted that introduction of copper essentially influences the CFC texture, which is exhibited in an increase of the BET surface area and pore volume as compared to CFC formed on the Ni-Al_2O_3 catalyst [17]. The highest value of carbon surface area is obtained on the 45Ni45Cu catalyst at 625°C. If reaction temperature further increases to 675°C, the surface area of the formed CFC decreases. Hence the modification of catalysts with copper provides a deposition of CFC whose microstructure and texture differ from that of CFC formed on the 90Ni-Al_2O_3.

Discussion

The experimental results show that the reaction temperature and catalyst composition mainly affect the process of methane decomposition. By introducing copper into Ni-Al_2O_3, one can increase thermal stability of the catalysts, which is evidenced by an increase in the carbon capacity of Ni-Cu catalysts at temperatures above 600°C.

Figure 2 shows methane conversion versus reaction time on the 75Ni15Cu catalyst at a temperature range of 625-675°C. One clearly sees that the reaction consist of: (i) a period with a constant methane conversion, (ii) a period of the catalyst deactivation. In contrast to 90Ni-Al_2O_3 catalyst, an induction period is not observed for the Ni-Cu-Al_2O_3 catalyst [2].

Table 3
Textural and structural CFC properties.

Sample	Temperature, °C	S_{BET}, m^2/g	V_{pore}, cm^3/g	D_{pore}, Å	d_{002}, Å	L_c, Å
75Ni15Cu	625	232.5	0.4175	71.8	3.411	74
	650	202.9	0.4200	82.8	3.389	78
	675	179.1	0.3928	87.7	3.393	85
65Ni25Cu	625	260.7	0.4047	62.1	3.401	69
	650	229.8	0.3948	68.7	3.389	74
	675	210.4	0.4266	81.1	3.388	81
45Ni45Cu	625	285.9	0.4314	60.4	3.414	68
	650	250.9	0.4372	69.7	3.409	80
	675	236.9	0.4241	71.6	3.393	74
90Ni-Al_2O_3	550	105	0.25	100	3.43	60

However formation of the active catalyst particles during a rather short reaction time can be postulated, because the TEM studies show that the size of catalyst particles increases from 20 nm to 50 nm during 10 minutes of methane decomposition at 625°C.

As is known, the cooper addition to the Ni-Al_2O_3 catalyst at the stages of catalysts preparation and preliminary treatment resulted in the formation of a nickel-copper alloy and in enrichment of surface particles with copper [18]. Copper additives prevent formation of the nickel-aluminum spinels and decrease the reduction temperature for NiO [1,2]. Besides, copper additives change the crystallographic state of the nickel catalysts on the hydrocarbon decomposition [2,6,8,9,11]. These facts are important for explanation of the changes in properties of the Ni-Cu-Al_2O_3 catalyst.

According to the mechanism accepted in the literature, the activation and decomposition of methane occur on the (100) and (110) planes of nickel. A cluster or an ensemble of seven Ni atoms participates in this process [19]. Graphite is precipitated on the Ni (111) planes [7]. Copper introduced into the catalyst changes the shape of the active particle formed under the reaction medium effect as compared to Ni catalysts (Fig. 7). So, the active particle has several (111) planes where carbon deposition can take place, which will increase the carbon capacity of the catalyst. Integrity of the Ni (111) plane where carbon grows due to enrichment of the catalyst particle surface with Cu may be destructed to provide growth of several thin filaments from one plane [2,9]. There are also several (100) and (110) planes where methane molecules are activated. As a result, the number of planes suitable for the methane decomposition and carbon precipitation on the Ni-Cu-Al_2O_3 surface increases.

The enrichment of Ni (111) plane with Cu is likely to influence nucleation of the graphite-like carbon phase and to decrease the rate of CFC growth [2, 20]. After formation of the graphite-like carbon phase which carries a particle from the fusion "zone", sintering of the reduced catalyst particles is terminated [2]. It was found that the presence of copper in the catalysts decreases the initial rate of filamentous carbon formation to 11.6 $g_C \cdot s/g_{cat} \cdot h$ (16.6 $g_C \cdot s/g_{cat} \cdot h$ for Ni-Al_2O_3) at 625°C. Thus a decrease in the rate of the graphite-like carbon phase formation leads to the fact that the size of the active centers on the Ni-Cu-Al_2O_3 catalysts exceeds that on the Ni-Al_2O_3 catalysts.

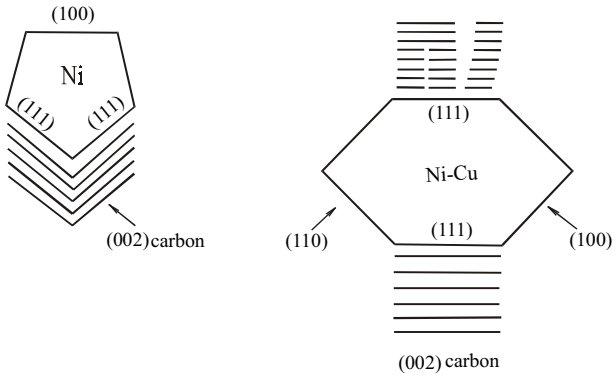

Fig. 7. Structure of the reaction active centers for the Ni-Al_2O_3 (left) and Ni-Cu-Al_2O_3 (right) catalysts.

$Ni-Al_2O_3$ catalyst are deactivated by destruction of the catalyst active centers with a growing carbon filament and Ni penetrating deep into the filament, because of the intercalation and erosion [2,9]. Adding Cu, both the shape of the active center and the microstructure of the growing filament are modified. In this case, graphite layers are deposited parallel to (111) planes of the crystal catalyst particles, which apparently reduces the rate of the active center destruction and increases the amount of the formed carbon as compared to $Ni-Al_2O_3$.

Changes in the CFC microstructure are caused by modification of the surface composition of the active catalyst center. It is assumed [19] that Ni catalyst particles 50 nm in size are most favorable for growth of carbon filaments as regards thermodynamics. According to TEM studies, the diameter of some carbon fibers, formed during 2 hours of methane decomposition, is as much as 100-150 nm (Fig. 6 b). The fibers consist of several thin filaments 40-60 nm in diameter. We propose that Ni atom clusters about 50 nm in size, occurring on the (111) alloy plane, builds a center for CFC growth. On these clusters, the carbon filaments intergrow to form a fiber 100-150 nm in diameter, that reduces the excess surface energy of the graphite layers.

Thus, the carbon capacity and thermal stability of $Ni-Cu-Al_2O_3$ catalysts depend on the nature and shape of the reaction active center which may be either pear or octahedral shaped upon Cu introduction. Modifying the particle shape, one increases the number of (100) and (110) planes where methane is decomposed, and (111) planes where carbon is deposited, which in turn, provide an increase in the carbon capacity of the catalysts. The introduction of copper permits one to create catalysts exhibiting thermal stability and high activity at 625-675°C. Thus, copper in the $Ni-Al_2O_3$ catalysts possesses structure-forming properties, and acts as a stabilizing component, which results in an increase the lifetime of catalysts.

Conclusion

The introduction of Cu in $Ni-Al_2O_3$ catalysts provides modification of state of the active particle in the reduced form, which results in changes in rates of methane decomposition and precipitation of carbon, and prevents sintering of particles at temperatures above 625°C. The presence of Cu affects the mechanism of formation of the CFC filament structure. The change in crystallographic orientation of the catalyst particles reduces the rate of the active center destruction through the capture of Ni atoms by the CFC layers. As a result, the thermal stability and carbon capacity (which can reach 525 g/g_{cat}) increase. The modification of Ni catalysts with Cu additives provides wide-range changes in the textural and microstructural properties of catalytic filamentous carbon.

Acknowledgements

The research described in this publication was made possible in part by Award No. REC-008 from the U.S. Civilian Research and Development Foundation for the Independent States of the Former Soviet Union (CDRF) and project № 959 from the International Science and Technology Center. We are grateful to Dr. V.A. Ushakov for the XRD measurements and Professor V. B. Fenelonov for the adsorption data.

References

1. Shaikhutdinov, Sh. K., Avdeeva, L. B., Goncharova, O. V., Kochubey, D. I., Novgorodov, B. N., Plyasova, L. M., Appl. Catal. A, 126: 125 (1995).
2. Avdeeva, L. B., Goncharova, O. V., Kochubey, D. I., Zaikovskii, V. I., Plyasova, L. M., Novgorodov, B. N.,. Shaikhutdinov, Sh. K., Appl. Catal. A, 141: 117 (1996).
3. Avdeeva, L. B., Kochubey, D. I., Shaikhutdinov, Sh. K., Appl. Catal. A, 177: 43 (1999).
4. Avdeeva, L. B., Likholobov, V. A., The patent of Russian Federation № 2146648 (2000).
5. Park, C., Baker, R.T.K., J. Catal. 179: 361 (1998).
6. Kim, M. S., Rodriguez, N. M., Baker, R. T. K., J. Catal. 131: 60 (1991).
7. Yang, R.T., Chen, J.P., J. Catal. 115: 52 (1989).
8. Li, Y., Chen, J., Chang, L., Qin, Y., J. Catal. 178: 76 (1998).
9. Chesnokov, V. V., Zaikovskii, V. I., Buyanov, R. A., Molchanov, V. V., Plyasova, L. M., Catal. Tod. 24: 265 (1995).
10. Van Stiphout, P. C. M., Stobbe, D.E., Scheur, F. Th. V. D., Geus, J. W., Appl. Catal. 40: 219 (1988).
11. Bernardo, C. A., Alstrup, I., Rostrup-Nielsen, J. R., J. Catal. 96: 517 (1985).
12. Shaikhutdinov, Sh. K., Avdeeva, L. B., Novgorodov, B. N., Zaikovskii, V. I., Kochubey, D. I., Catal. Lett. 47: 35 (1997).

13. N. M. Rodriguez, M. S. Kim, M.S. Downs, R. T. K. Baker, in Carbon Fiber Filaments and Composites, ed. J.L. Figuieredo, C.A. Bernardo, R.T.K. Baker and K.J. Huttinger, Kluwer Acad. Publ. Dordct, Boston/London, 1990, p. 541.
14. Dandekar, A., Baker, R. T. K., Vannice, M. A., J. Catal. 183: 131 (1999).
15. J. E. Germain. Catalytic conversion of hydrocarbon. Academic press London and New York, 1969.
16. Rostrup-Nielsen, J.R., J. Catal. 27: 343 (1972).
17. Fenelonov, V. B., Derevyankin, A. Yu., Okkel, L. G., Avdeeva, L. B., Zaikovskii, V. I., Moroz, E. M., Salanov. A. N., Rudina, M. A., Likholobov, V. A., Shaikhutdinov, Sh. K., Carbon, 35: 1129 (1997).
18. Ponec, V., Adv. Catal. 32: 149 (1983).
19. Trimm, D. L., Appl. Catal. 5: 263 (1983).
20. Rodriguez, N. M., Kim, M. S., Baker, R. T. K., J. Catal. 140: 16 (1993).

Received 8 November 2000.

ELSEVIER

Applied Catalysis A: General 228 (2002) 53–63

APPLIED CATALYSIS A: GENERAL

www.elsevier.com/locate/apcata

Iron-containing catalysts of methane decomposition: accumulation of filamentous carbon

Lyudmila B. Avdeeva*, Tatyana V. Reshetenko, Zinfer R. Ismagilov, Vladimir A. Likholobov

Boreskov Institute of Catalysis, Pr. Akad. Lavrentieva 5, Novosibirsk 630090, Russia

Received 25 July 2001; received in revised form 1 November 2001; accepted 2 November 2001

Abstract

Iron-containing catalysts were tested in methane decomposition reaction at moderate temperature and pressure 1 bar in order to evaluate their catalytic properties and produce catalytic filamentous carbon (CFC). Catalyst preparation method and composition of the catalysts were found to influence their properties. The best performance was found with coprecipitated Fe-Co-Al_2O_3 catalysts, where carbon capacity has achieved 52.4 g/g_{cat}. TEM investigations have shown that carbon nanotubes were formed. © 2002 Elsevier Science B.V. All rights reserved.

Keywords: Fe-Al_2O_3 catalysts; Bimetallic Fe-Co catalysts; Methane decomposition; Filamentous carbon; Carbon nanotubes

1. Introduction

At present, many catalysts of methane transformation have been widely investigated because of their importance in the utilization of natural gas [1]. Numerous studies of Ni, Fe, Co catalysts in CO disproportionation, steam reforming, hydrocarbon decomposition have shown that formation of filamentous carbon with graphitic structure occurred [2–13]. Recently we have established, that methane decomposition over 3d (Ni, Ni-Cu, Co) metal is a promising route to utilize methane into useful inexpensive products: hydrogen and catalytic filamentous carbon (CFC) [11–14]. It was shown, that Ni and Co catalysts exhibit essential efficiency in CFC accumulation and methane conversion is close to equilibrium at temperatures 500–550 °C. We found that a large amounts of filamentous carbon can be produced using coprecipitated catalysts: 90 wt.% Ni-Al_2O_3 yields 100 g/g_{cat}, while 75 wt.% Co-Al_2O_3 −60 g/g_{cat}. CFC is usually formed as the granules of chaotically interlaced filaments or fibers. One carbon filament grows from one catalytic particle, the latter being located on its top. Carbon filament consists from graphitic planes which are coaxially arranged as cones. Average diameter of the carbon filament for Ni-based CFC is 50 nm, for Co-based −20 nm. The nature of catalyst influences the microstructure of filament, that becomes apparent in the angle between graphitic planes and the filament axis, which varies from 45° for Ni catalyst [12] to 15° for Co catalyst [13].

However, in contrast with nickel, the carbon fibers produced on Co catalysts also have graphitic planes becoming rather parallel to fiber axis with hollow core forming multiwall carbon nanotubes (MWNTs). The core diameter is 5–10 nm. Thus, despite the lower carbon accumulation, Co catalysts produce

* Corresponding author. Fax: +7-3832-343056.
E-mail address: avdeeva@catalysis.nsk.su (L.B. Avdeeva).

PII: S0926-860X(01)00959-0

other type of carbon fibers with hollow-like core morphology.

The methane decomposition over iron-containing catalysts was investigated at temperatures 800–900 °C with the purpose of deriving hydrogen [15]. However, the developed iron catalysts were soon deactivated at carbon yield in 30%. During this process iron carbide was produced, which cannot find practical application.

The method of obtaining carbon fibers on the suspension of Fe particles with size of 12 nm in $CH_4 + H_2$ stream at 1100 °C is developed in [16–18]. After some seconds, the long fibers of thermal carbon are produced, having application as an isolation material, sealant, etc. Basis for the growth of such thermal carbon fibers is filamentous carbon, so the attempts were undertaken to stop methane decomposition at the stage of filamentous carbon formation. The works concerning methane decomposition over iron-containing catalysts at temperatures lower than 700 °C are unknown.

The main purpose of the given work is development of the long-living iron-containing catalysts of methane decomposition and carbon accumulation at moderate temperatures. In this paper, we investigate the activity of coprecipitated Fe-Al_2O_3 and Fe-Co-Al_2O_3 catalysts, structure and texture of the formed CFC.

2. Experimental part

Fe-Al_2O_3 and Fe-Co-Al_2O_3 catalysts were prepared by different methods: coprecipitation using aqueous solution of the mixture of salts, impregnation of the supports, precipitation of the support suspension with salts solution. The coprecipitated samples were carefully washed with distilled water, dried at 110 °C, and calcined in a flow of air at 450 °C for 3 h. The catalysts were reduced in a flow of pure hydrogen at 580 °C for 5 h, then the samples were in situ passivated in ethanol and dried at room temperature.

Catalytic activity of the reduced samples was measured in a vibrating flow quartz reactor 30 cm^3 in volume. Methane was supplied at a rate of 45 l/g_{cat} h. Concentration of methane was measured by gas chromatography, and methane conversion was calculated. To determine the amount of carbon deposited, sample was weighted after the reaction, which was performed until complete catalyst deactivation.

The samples of catalysts and CFC were investigated by TEM, XRD and adsorption methods. The XRD studies were performed in a Siemens URD-63 diffractometer using Cu Kα radiation and a graphite crystal monochromator. Crystallite sizes were calculated from the line width following the Scherrer equation. TEM and HRTEM pictures were obtained with JEM-100CX and JEM-2010 microscopes, respectively. The adsorption measurements were carried out using an ASAP-2400 apparatus to provide adsorption of N_2 at 77 K.

3. Results

In order to compare the carbon formation efficiency of prepared catalysts, we use the following parameters of a methane decomposition reaction: methane conversion, carbon accumulation until complete deactivation of the catalysts (the so-called carbon capacity *G*, calculated as gram of carbon per gram of catalyst) and lifetime of catalysts.

3.1. Method of catalyst preparation

Table 1 demonstrates the effect of catalyst preparation method on the catalytic properties of the Fe catalysts tested in methane decomposition at 625 °C. Earlier we have shown, that for high-loading catalysts the method of coprecipitation from aqueous solution of the salts is more favorable [12,13]. Moreover, studying the Ni-Al_2O_3 and Co-Al_2O_3 we have found, that the best catalytic performance was observed with the catalysts prepared using sodium hydroxide as a precipitant.

In contrast to Ni and Co catalysts, from Table 1 one can see that the greatest carbon capacity of Fe-Al_2O_3 catalysts is observed for samples prepared by coprecipitation using aqueous solution of ammonia as a precipitant. The further studies were realized with catalysts prepared by this method.

3.2. Effect of the catalyst composition and temperature

Since the maximum carbon capacity during methane decomposition was observed for catalysts with the high metal loading (90 wt.% Ni and 60–75

Table 1
Catalytic properties of Fe-based catalysts for methane decomposition, demonstrating the influence of preparation methods[a]

Catalysts	Preparation	X_{CH_4} (%)	Lifetime (h)	G (g/g_{cat})
25 wt.% Fe-Al_2O_3	Impregnation of a support by $Fe(NO_3)_3$ solution, calcined at 200 °C for 3 h, reduced at 500 °C for 3 h	–	2	1.1
25 wt.% Fe-SiO_2	Impregnation of a support by $Fe(NO_3)_3$ solution, calcined at 200 °C for 3 h, reduced at 500 °C for 3 h	–	2	0.7
32 wt.% Fe-Al_2O_3	Impregnation of a support by $Fe(NO_3)_3$ solution, calcined at 200 °C for 3 h, reduced at 500 °C for 3 h	–	2	0
25 wt.% Fe-Al_2O_3	Precipitation of support suspension with $Fe(NO_3)_3$ solution (precipitant NH_4OH), calcined at 400 °C for 3 h, reduced at 580 °C for 3 h	–	2	0.5
50 wt.% Fe-Al_2O_3	Precipitation of support suspension with $Fe(NO_3)_3$ solution (precipitant NH_4OH), calcined at 400 °C for 3 h, reduced at 580 °C for 3 h	–	2	1
50 wt.% Fe-Al_2O_3	Precipitation of support suspension with $Fe(NO_3)_3$ solution (precipitant NH_4HCO_3), calcined at 400 °C for 3 h, reduced at 580 °C for 3 h	–	7	4.5
50 wt.% Fe-Al_2O_3	Coprecipitation aqueous solution of salts with NH_4OH as precipitant, calcined at 450 °C for 3 h, reduced at 580 °C for 5 h	4	23	26.5
50 wt.% Fe-Al_2O_3	Coprecipitation aqueous solution of salts with NaOH as precipitant, calcined at 450 °C for 3 h, reduced at 580 °C for 5 h	6	6	3.3
50 wt.% Fe-Al_2O_3	Coprecipitation aqueous solution of salts with Na_2CO_3 as precipitant, calcined at 450 °C for 3 h, reduced at 580 °C for 5 h	4	6	2.3

[a] T = 625 °C, methane space velocity = 45 l/g_{cat} h, P_{CH_4} = 1 bar, X_{CH_4} = methane conversion during 1 h.

wt.% Co), the iron content in coprecipitated Fe-Al_2O_3 catalysts has been varied from 20 to 90 wt.%. The obtained values of carbon capacity are plotted in Fig. 1 as a function of nominal bulk Fe concentration. Data show that carbon capacity reaches maximum (20–28 g/g_{cat}) on the catalysts with 50–80 wt.% Fe. It is known, that Co additives (5–10 wt.%) render activating influence on iron catalysts [19], therefore, we have investigated the influence of Co on Fe-Al_2O_3 catalysts of methane decomposition at 625 °C. Table 2 shows that introduction of Co in small amounts (3–10 wt.%) results in the magnification of carbon yields 2–3 times. So, carbon capacity on the catalyst 50Fe-6Co-Al_2O_3 achieves 52.4 g/g_{cat}. Apparently, the presence of Co increases number of the carbon growth centers on Fe-Al_2O_3 catalyst.

Table 2
Catalytic properties of Fe-Co-Al_2O_3 catalysts in the methane decomposition[a]

Catalysts	Fe:Co:Al_2O_3 (wt.%)	Lifetime (h)	X_{CH_4} (%)	G (g/g_{cat})
90Fe-Al_2O_3	90:–:10	7	5.2	5.5
85Fe-5Co-Al_2O_3	85:5:10	16.5	7.9	16
50Fe-Al_2O_3	50:–:50	23	4	26.5
50Fe-6Co-Al_2O_3	50:6:44	40	8	52.4

[a] T = 625 °C, methane space velocity = 45 l/g_{cat} h, P_{CH_4} = 1 bar.

The studies of temperature dependence of methane decomposition over 85Fe-5Co-Al_2O_3 catalyst have shown, that carbon capacity reaches its maximum at 625–650 °C (Table 3). Fig. 2 shows methane conversion versus reaction time for the iron-containing catalysts at 625 °C.

3.3. Structure of catalysts

We performed XRD and TEM study of the reduced and post-reacted 50Fe-Al_2O_3 and 85Fe-5Co-Al_2O_3

Table 3
Temperature dependence of catalytic properties of 85Fe-5Co-Al_2O_3 catalyst[a]

T (°C)	X_{CH_4} (%)	Lifetime (h)	G (g/g_{cat})
600	5.1	8.5	6.7
625	7.9	16.5	16
650	12.9	13	15
675	10.9	8	13.2

[a] Methane space velocity = 45 l/g_{cat} h, P_{CH_4} = 1 bar.

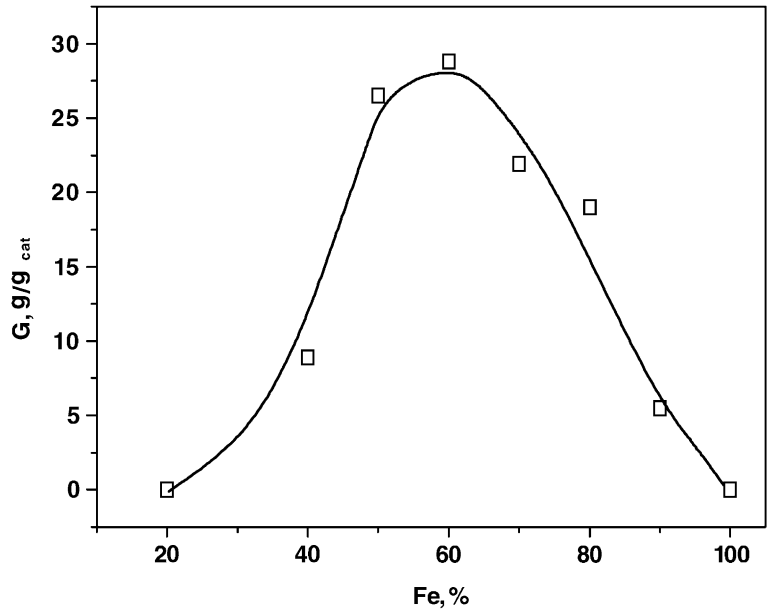

Fig. 1. The relationship between carbon capacity and metal loading in the coprecipitated Fe-Al_2O_3 catalysts, prepared using NH_4OH as precipitant, in the methane decomposition reaction at 625 °C, $P_{CH_4} = 1$ bar, methane space velocity = 45 l/g_{cat} h.

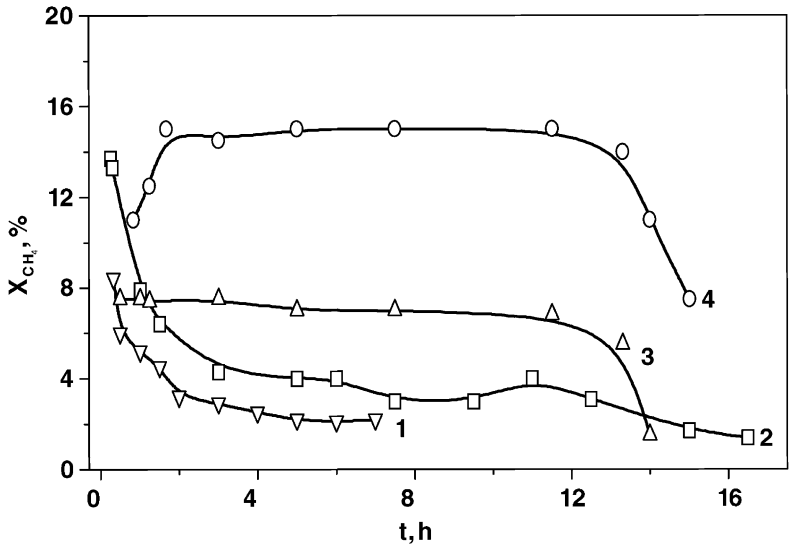

Fig. 2. The global kinetics of methane decomposition over: curve 1—90Fe-Al_2O_3 ($T = 625$ °C), curve 2—85Fe5Co-Al_2O_3 ($T = 625$ °C), curve 3—75Co-Al_2O_3 ($T = 500$ °C), curve 4—90Ni-Al_2O_3 ($T = 550$ °C).

Table 4
X-ray diffraction data for the 50Fe-Al_2O_3 and 85Fe-5Co-Al_2O_3 catalysts

Sample	Phase	L_c^{graph}(nm)	d_{002}^{graph} (nm)
50Fe-Al_2O_3 reduced in 1 bar H_2 at 580 °C [20]	α-Fe	–	–
50Fe-Al_2O_3 post-reacted in 1 bar CH_4 at 625 °C [20]	α-Fe, graphite	∼6	0.343
85Fe-5Co-Al_2O_3 reduced in 1 bar H_2 at 580 °C	α-Fe, Co_3O_4 (or Co-Al-O spinel)	–	–
85Fe-5Co-Al_2O_3 post-reacted in 1 bar CH_4 at 625 °C	α-Fe, graphite	6.5	0.343

catalysts. It is known, that iron can exhibit several crystal structures. α-Fe having a body centered cubic lattice with symmetry *Im3m* exists at the temperatures below 769 °C. α-Fe has ferromagnetic properties. It was established that a bulk $\alpha \rightarrow \beta$ phase transition occurs at 769 °C. β-Fe has the same symmetry as α-Fe, but already exhibits paramagnetic properties. γ-Fe is formed at the temperatures above 917 °C, and has face centered cubic lattice with *Fm3m* symmetry. Since we work at the temperatures below 700 °C, we should expect formation of only α-Fe, that is confirmed by XRD.

XRD data (Table 4) of reduced catalysts show presence of α-Fe phase in both above-mentioned samples. The traces of Co_3O_4 (or Co-Al-O spinels) are observed in the latter one. The α-Fe phase is also present in post-reacted samples.

3.4. Morphology and texture of carbon

TEM images of CFC, formed upon methane decomposition over 50Fe-Al_2O_3 and 85Fe-5Co-Al_2O_3 catalysts, are presented in Fig. 3. The formed carbon has filamentary morphology and represents carbon nanotubes, consisting from the turbostratic carbon layers, which are parallel to the fiber axis and look as cylinders with growing diameters enclosed in each other. The turbostratic nature of the formed carbon is confirmed by XRD data (Table 4), indicating that the interplanar distance d_{002} is equal to 0.343 nm, i.e. a little higher than in a perfect graphite (d_{002} = 0.335 nm), and also by HRTEM data (Figs. 3b and 4a). The diameter of carbon nanotubes is 10–30 nm, and corresponds to the active iron crystallite size.

The analysis of TEM data allows to pick out two types of filamentous carbon.

I. Nanotubes, consisting from 7 to 15 graphitic cylindrical layers, with outer diameter (o.d.) ranging between 25 and 30 nm and inner channel of 10 nm (Fig. 3b).
II. Carbon fibers, which have internal caps formed by linkage of the inner carbon layers are observed. All of the internal caps are oriented perpendicularly to the fiber axis and along one direction only for the given fibers. Carbon fibers are observed predominantly in CFC (50Fe-Al_2O_3) and to a lesser extent in CFC (85Fe-5Co-Al_2O_3).

Nanotubes (type I) are formed mainly upon methane decomposition over 85Fe-5Co-Al_2O_3, however, their yield does not exceed 20 g/g_{cat} The carbon capacity is increased up to 52.4 g/g_{cat} with a diminution of the iron contents in the catalyst down to 50 wt.% (catalyst 50Fe-6Co-Al_2O_3), however, in this case carbon fibers (type II) are formed.

Textural properties of the tubular formed carbon were determined by nitrogen adsorption at 77 K (see Table 5). The magnitude of specific surface area (S_{BET})

Table 5
Textural CFC properties

Sample	S_{BET} (m^2/g)	V_{pore} (cm^3/g)	V_{micro} (cm^3/g)	D_{pore} (Å)
CFC(85Fe-5Co-Al_2O_3)	103.1	0.4417	0.0046	171
CFC(80Fe-10Co-Al_2O_3)	118.2	0.3737	0.0057	126
CFC(70Fe-20Co-Al_2O_3)	123.2	0.5581	0.0052	181
CFC(50Fe-Al_2O_3)	151.5	0.5006	0.0068	132
CFC(50Fe-6Co-Al_2O_3)	155	0.5582	0.0101	144

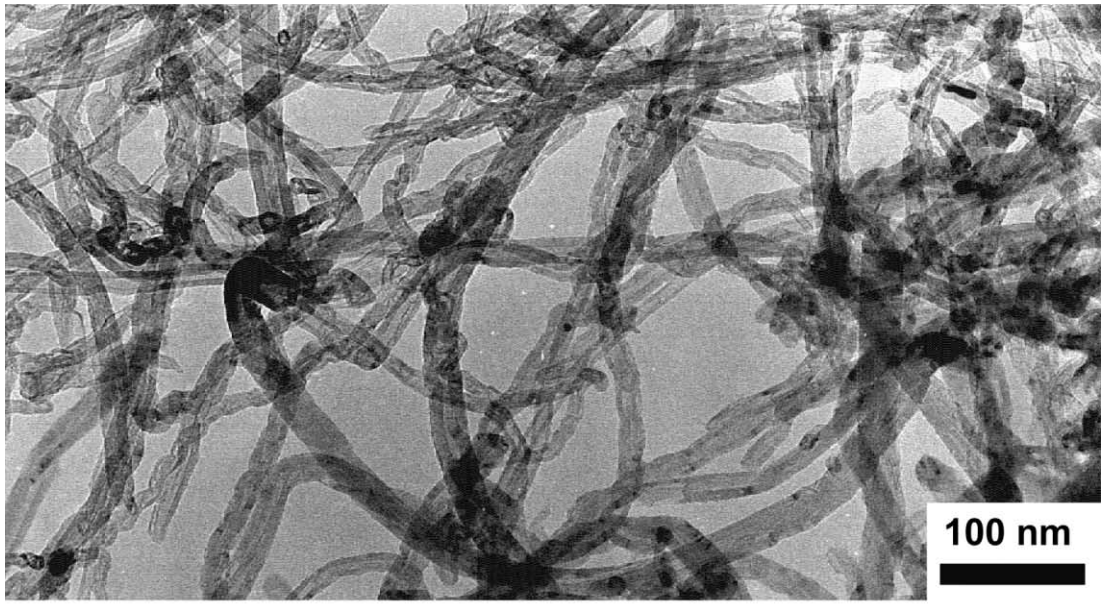

(a)

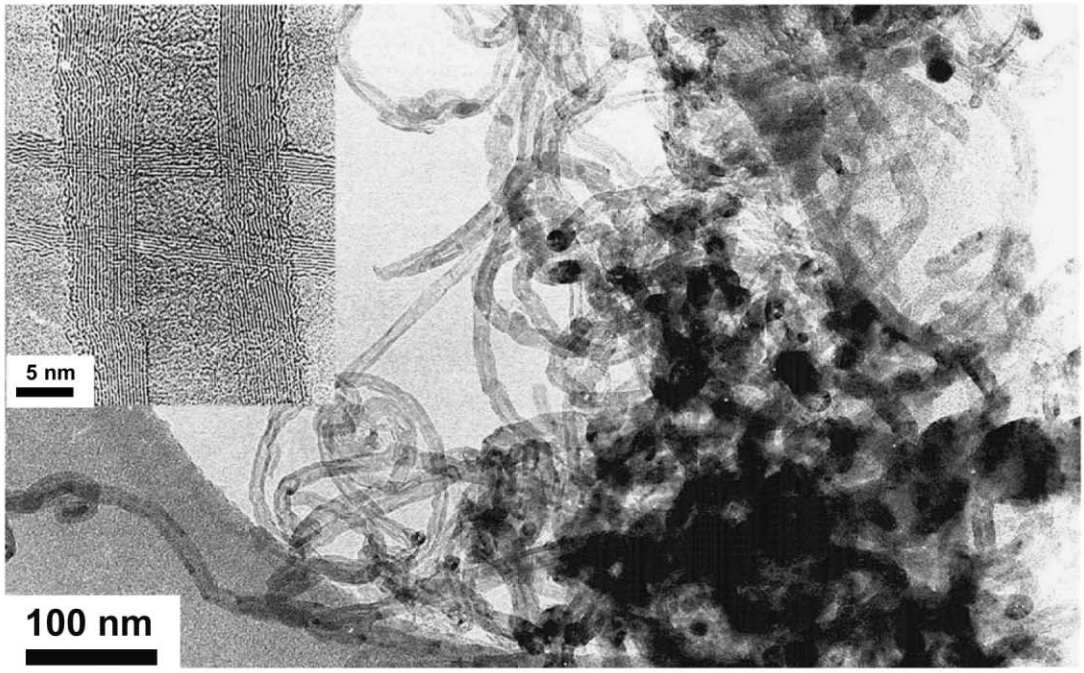

(b)

Fig. 3. TEM photographs of the catalysts: (a) 50Fe-Al_2O_3, (b) 85Fe-5Co-Al_2O_3 after methane decomposition at 625 °C, showing formation of the carbon nanotubes.

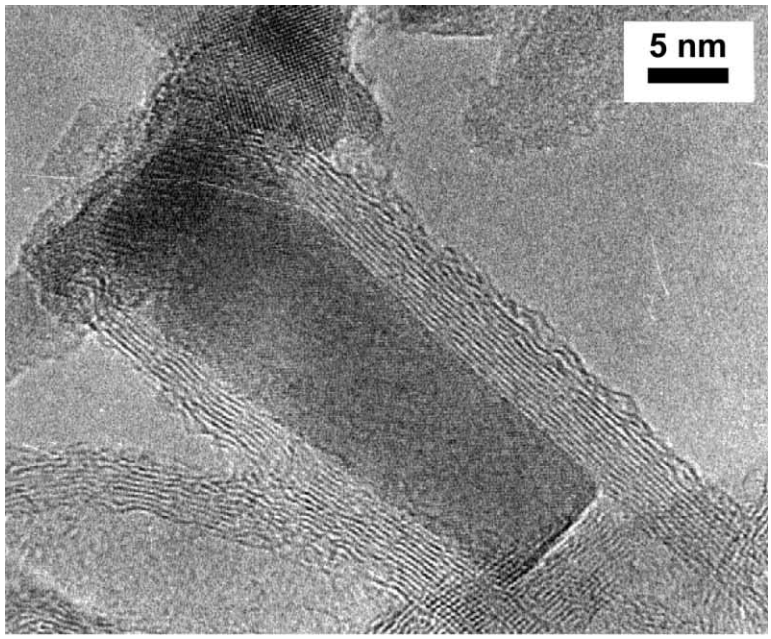

(a)

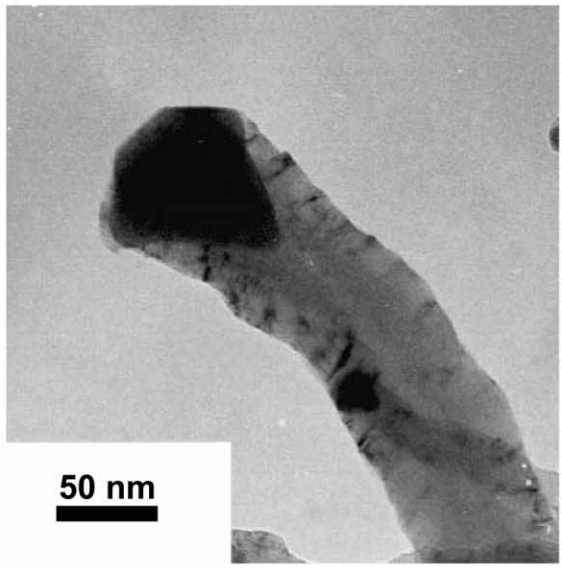

(b)

Fig. 4. High resolution TEM images of the catalysts: (a) 85Fe-5Co-Al_2O_3 catalyst particle after 50 min in the methane decomposition reaction at 625 °C, (b) 90Ni-Al_2O_3 catalyst particle after 50 min in the methane decomposition reaction at 550 °C [12], (c) 75Co-Al_2O_3 catalyst particle after 50 min in the methane decomposition reaction at 500 °C [13].

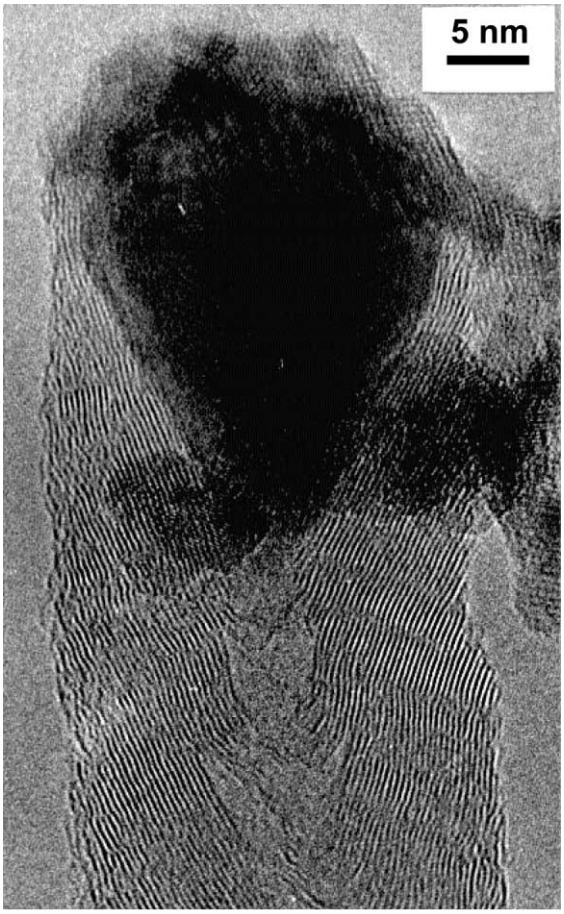

(c)

Fig. 4. (*Continued*).

varies in the range of 100–150 m^2/g. The tubular CFC is more friable on the packing with a bulk density of 0.2 g/cm^3, pore volume of 0.5 cm^3/g and average pore diameter of 15 nm.

4. Discussion

It is known, that carbon deposition deactivates the catalyst in hydrocarbon decomposition reactions at high temperatures. However, hydrocarbon decomposition under certain conditions, may result in the formation of filamentous carbon which does not poison the catalyst for a long time [4,5]. It was shown, that Ni-Al_2O_3 catalysts with a high nickel content (60–90 wt.%) have such properties [11,12]. Later we created 60–75 wt.% Co-Al_2O_3 catalysts of methane decomposition at 500 °C [13]. Data presented above, show that it is possible to create long-living iron catalysts of methane decomposition if the conditions of filamentous carbon growth are ensured.

The properties of iron-containing catalysts are found to be similar to the properties of Co-containing catalysts, and depend on the preparation method, amounts of the metal and temperature regimes. Among the investigated catalysts, the best properties are exhibited by coprecipitated Fe-Al_2O_3 using aqueous solution of NH_4OH as a precipitant and containing not less than 50 wt.% of Fe (Table 1).

XRD and EXAFS [20] measurements of the reduced Fe-Al_2O_3 samples have shown, that there is α-Fe phase existing in the active catalysts with a particle size varying in the range of 10–30 nm. It should be noted, that Fe crystallite size detected by the TEM method on the tips of filamentous carbon (20 nm) is close to that observed by XRD (Fig. 4a).

We have found, that the maximum growth of filamentous carbon on Fe-Al_2O_3 catalysts occurs at 625 °C. However, the carbon capacity of pure iron catalysts was small, that can be explained by the low contents of iron metal, which is a center of carbon deposition. It was established, that some cobalt (5 wt.%) has a beneficial influence on iron for nitrogen adsorption, synthesis of ammonia and isotope exchange $^{14}N_2$–$^{15}N_2$ [19]. We have shown, that introduction of the small amounts of cobalt (3–10 wt.%) in Fe-Al_2O_3 catalysts at the stage of coprecipitation increases CFC yields 2–3 times (Table 2). In work [21], it was shown, that introduction of Co at the stage of Fe and Al hydroxides formation results in the decrease of reducing temperature of iron oxides. Indeed, the known iron Fischer–Tropsch catalysts and catalysts for ammonia synthesis are reduced at the temperatures below 600 °C. We have found, that the most effective Fe-Al_2O_3 catalysts of methane decomposition are formed after reduction at the temperature of 580 °C, with subsequent passivation at room temperature in ethanol.

Taylor et. al. [19] assume, that the small amounts of Co affect the crystallization of iron such that a greater proportion of the surface area exists as (1 1 1) faces, which are particularly active in the synthesis of ammonia and adsorption of N_2 [22], and these faces are

necessary for the deposition of graphitic carbon upon hydrocarbon decomposition.

The typical global kinetics of the methane decomposition over Fe-Al_2O_3 is illustrated in Fig. 2 (curves 1, 2). For comparison, we also insert in the plot data obtained for Ni-Al_2O_3 [12] and Co-Al_2O_3 [13] catalysts (the data are represented for temperatures at which we observed the maximum carbon capacity). There is no induction period for Fe-Al_2O_3 catalysts, which is characteristic for Ni-Al_2O_3. Previously, we have assigned this to the sintering of carbon-saturated Ni particles from 17 to 50 nm within the first minutes of reaction [12]. The Fe-Al_2O_3 (Fe-Co-Al_2O_3) active particle size is 20 nm, which is comparable with the size of Co active particles, and seems to be large enough for filamentous carbon growth [13].

Though methane conversion on 75Co-Al_2O_3 catalyst was 1.5 times lower, than on Ni-Al_2O_3 catalyst (at the expense of different temperature of methane decomposition), the lifetimes of these catalysts were close, but the carbon yield on Co catalyst is 2 times lower. The initial methane conversion on Fe-Al_2O_3 (Fig. 2, curve 1) is comparable with Co-Al_2O_3, but it sharply drops within 2 h of the reaction. Such catalytic behavior can be explained in terms of the microstructure of growing carbon filaments and the mechanism of deactivation. General scheme of the carbon filaments growth has been discussed quite intensively and seems to be identical for Ni, Co, Fe. The evolution of the catalyst morphology in the reactor was described in detail in the works [12,13]. Fig. 4a–c demonstrate the active centers of methane decomposition catalysts. Conventional model of methane decomposition includes the following stages: decomposition of CH_4 on the metal (1 0 0) and (1 1 0) planes involving the formation of surface carbon; carbon diffusion through a metal particle, and graphite precipitation on the metal (1 1 1) planes [10]. The microstructure and catalyst carbon capacity depend on the nature, structure and size of the carbon growth metal center. Thus, stable carbon growth centers on Ni-Al_2O_3 catalysts are Ni crystallites with a size of 50 nm, on which carbon is deposited as graphitic layers, located under an angle of 45° to filament axis (Fig. 4b) [12]. The CFC growth centers on Co catalysts have the drop-shaped form with a size of 20 nm, and graphitic layers are placed on them under an angle of 15° to axis and form carbon fibers of hollow-like core structures (Fig. 4c) [13].

As it was found in this work, upon methane decomposition on the iron-containing catalyst at 625 °C, the carbon growth centers are well faceted and generate carbon filaments, such as true nanotubes and hollow carbon fibers (Fig. 4a).

From the literature, it is known, that carbon nanotubes, representing large scientific and practical interest, are obtained upon acetylene decomposition on 2.5% Fe-SiO_2 catalyst at 700 °C [23–25]. The carbon yields reach 184% [23]. The o.d. of nanotubes is 20 nm, and inner −8 nm. For the first time nanotubes were obtained by us from methane on the catalyst 85Fe-5Co-Al_2O_3 at the temperature of 625 °C, with the yield of 2000% [26]. The fibers represent MWNTs with an external diameter of 25–30 nm, and internal channel width of 10 nm (Fig. 4a). The nanotubes consist from enclosed to each other graphitic "cylinders" with growing diameters, while interlayer distance is 0.34 nm. The number of such "cylinders" in the nanotubes reaches 8–14. The carbon materials obtained as nanotubes are rather friable (the bulk density is 0.2 g/cm^3) and do not contain amorphous carbon (that determined by annealing in CO_2 at 650 °C). The quality of received carbon nanotubes is worsened with a diminution of iron content in the catalyst. A fair amount of curved and spiral nanotubes is formed. The decrease of inner channel diameter, the formation of internal caps and nanotubes having "leguminous pod" structure (Fig. 3a) are observed. Thus, it was found, that carbon fibers of hollow-like core structure, in which turbostratic layers are placed under an angle of 0–15° to the growth axis, are formed on Co particles [13], Fe particles or their alloys [20,26] having the size 20–30 nm upon the methane decomposition at moderate temperatures.

It is necessary to note, that diminution of the declination angle of graphitic layers in fibers results in modification of the deactivation mechanism for cobalt- and iron-containing methane decomposition catalysts. Deactivation of catalysts in general occurs due to the encapsulation of metal active center by formed graphitic layers consisting of "cylinders" enclosed into each other. The "cylinders" tend to be closed as "cap" (or internal caps inside the filament) on the free growing tops. Fastest deactivation caused by such encapsulation (self-closing graphitic "cylinders") is observed for iron-containing catalysts of methane decomposition (Fig. 2), is defined, apparently, by the

mechanism of carbon deposition on Fe particles [3].

Thus, it is established, that carbon capacity of the high-loading metal catalysts of methane decomposition decreases in a row: Ni > Co ≫ Fe.

This correlates with affinity of carbon and metal [27]. The enthalpy of surface carbide formation is −117 kJ/mol for Fe, −50 kJ/mol for Co, 4 kJ/mol for Ni. Apparently, only the decomposition of unstable "virtual" metal carbide-like phases results in the formation of filamentous carbon. The formation of stable carbides at high temperatures (600 °C for Ni and Co, 800 °C for Fe) leads to fast deactivation of the metal catalysts. Deactivation at moderate temperature depends on the microstructure of growing carbon filament: the larger is the inclination angle of graphite layers to a filament axis, the more stable is catalyst of methane decomposition (as it was shown by us for Ni-Cu-Al_2O_3 catalysts [12,14]).

5. Conclusions

Fe-Al_2O_3 and Fe-Co-Al_2O_3 catalysts have sufficient efficiency in filamentous carbon formation and in a methane decomposition at moderate temperature (625 °C). It have been established, that the properties of iron-containing catalysts depend on a preparation method. The best method is a coprecipitation of components from a mixture of solutions of nitrates of iron, cobalt and aluminium by a solution of ammonia. Carbon capacity of Fe-Al_2O_3 catalysts is increased in the presence of Co and reaches 52.4 g/g_{cat}. TEM data have shown, that the carbon nanotubes are observed upon methane decomposition on the 85Fe-5Co-Al_2O_3 catalyst. Application of the developed catalysts allows to obtain CFC with a new microstructure (carbon nanotubes), having advanced specific surface area.

Acknowledgements

The research described in this publication was made possible in part by Award no. REC-008 from the US Civilian Research and Development Foundation for the Independent States of the Former Soviet Union (CDRF). We are grateful to Dr. V.A. Ushakov for the XRD measurements, Professor V.B. Fenelonov for the adsorption data, Dr. V.I. Zaikovskii, Dr. A.L. Chuvilin and Dr. G.N. Kryukova for the TEM measurements.

References

[1] L. Guczi, R.A. Van Santen, K.V. Sarma, Catal. Rev. Sci. Eng. 38 (1996) 249.
[2] M. Audier, A. Oberlin, M. Oberlin, M. Coulon, L. Bonnetain, Carbon 19 (1981) 217.
[3] L. Bonnetain, P. Gadelle, M. Audier, in: J.L. Figuieredo, C.A. Bernardo, R.T.K. Baker, K.J. Huttinger (Eds.), Carbon Fiber Filaments and Composites, Kluwer Academic Publishers, Dordrecht, MA, 1990, p. 507.
[4] N.M. Rodriguez, M.S. Kim, M.S. Downs, R.T.K. Baker, in: J.L. Figuieredo, C.A. Bernardo, R.T.K. Baker, K.J. Huttinger (Eds.), Carbon Fiber Filaments and Composites, Kluwer Academic Publishers, Dordrecht, MA, 1990, p. 541.
[5] C.A. Bernardo, I. Alstrup, J.R. Rostrup-Nielsen, J. Catal. 96 (1985) 517.
[6] P.C.M. Van Stiphout, D.E. Stobbe, F.Th.V.D. Scheur, J.W. Geus, Appl. Catal. 40 (1988) 219.
[7] P.K. De Bokx, A.J.H.M. Kock, E. Boellaard, W. Klop, J.W. Geus, J. Catal. 96 (1985) 454.
[8] N.M. Rodriguez, M.S. Kim, F. Fortin, I. Mochida, R.T.K. Baker, Appl. Catal. A 148 (1997) 265.
[9] C. Park, R.T.K. Baker, J. Catal. 179 (1998) 361.
[10] R.T. Yang, J.P. Chen, J. Catal. 115 (1989) 52.
[11] Sh.K. Shaikhutdinov, L.B. Avdeeva, O.V. Goncharova, D.I. Kochubey, B.N. Novgorodov, L.M. Plyasova, Appl. Catal. A 126 (1995) 125.
[12] L.B. Avdeeva, O.V. Goncharova, D.I. Kochubey, V.I. Zaikovskii, L.M. Plyasova, B.N. Novgorodov, Sh.K. Shaikhutdinov, Appl. Catal. A 141 (1996) 117.
[13] L.B. Avdeeva, D.I. Kochubey, Sh.K. Shaikhutdinov, Appl. Catal. A 177 (1999) 43.
[14] T.V. Reshetenko, L.B. Avdeeva, Z.R. Ismagilov, A.L. Chuvilin, V.A. Likholobov, Eur. Chem. Tech. J. 2 (2000) 237.
[15] V.V. Veselov, T.A. Levanyuk, P.S. Pilinenko, N.T. Meshenko, in: V.V. Veselov (Ed.), Scientific Basics of Hydrocarbon Catalytic Conversion, Kiev, Naukova dumka, 1977, p. 84 (in Russian).
[16] G. Tibbetts, M. Devour, E. Rodda, Carbon 25 (1987) 357.
[17] F. Benissad, P. Gadelle, M. Coulon, L. Bonnetain, Carbon 26 (1988) 61.
[18] A. Oberlin, M. Endo, T. Koyama, J. Cryst. Growth 32 (1976) 335.
[19] D.W. Taylor, P.J. Smith, D.A. Dowden, G. Kemball, D.A. Whan, Appl. Catal. 3 (1982) 161.
[20] L.B. Avdeeva, V.I. Zaikovskii, D.I. Kochubey, Sh.K. Shaikhutdinov, in: Proceedings of the 4st European Congress on Catalysis (Eurpocat-IV), Rimini, Italy, 1999, p. 559.
[21] R. Brown, M.E. Cooper, D.A. Whan, Appl. Catal. 3 (1982) 177.

[22] F. Zaera, A.J. Gellman, G.A. Somorjai, Acc. Chem. Res. 19 (1986) 24.
[23] K. Hernadi, A. Fonseca, J.B. Nagy, B. Bernaerts, A.A. Lucas, Carbon 34 (1996) 1249.
[24] M. Jose-Yacaman, M. Miki-Yoshida, L. Rendon, Appl. Phys. Lett. 62 (1993) 657.
[25] W.Z. Li, S.S. Xie, L.X. Qian, B.H. Chang, B.S. Zou, W.Y. Zhou, R.A. Zhao, G. Wang, Science 274 (1996) 1701.
[26] L.B. Avdeeva, V.A. Likholobov, The Patent of Russian Federation, No. 2146648 (2000).
[27] E. Shustorovich, Adv. Catal. 37 (1990) 101.

Promoted Iron Catalysts of Low-Temperature Methane Decomposition

T. V. RESHETENKO[1], L. B. AVDEEVA[1], Z. R. ISMAGILOV[1], V. A. USHAKOV[1], A. L. CHUVILIN[1] and Yu. T. PAVLYUKHIN[2]

[1]*G. K. Boreskov Institute of Catalysis, Siberian Branch of the Russian Academy of Sciences, Pr. Akademika Lavrentyeva 5, Novosibirsk 630090 (Russia)*

E-mail: ZRI@catalysis.nsk.su

[2]*Institute of Solid State Chemistry and Mechanochemistry, Siberian Branch of the Russian Academy of Sciences, Ul. Kutateladze 18, Novosibirsk 630128 (Russia)*

Abstract

Iron-containing catalysts promoted by nickel or cobalt were tested in methane decomposition reaction at low temperature (600–650 °C) and pressure 1 bar in order to study their catalytic properties and to produce catalytic filamentous carbon (CFC). Catalyst preparation method and composition of the catalysts were found to influence their properties. It was found, that introduction of cobalt or nickel in small amount (3–10 % mass) results in the magnification of carbon yields 2–3 times in comparison with Fe-Al_2O_3. Investigations of Fe-Co-Al_2O_3 and Fe-Ni-Al_2O_3 catalysts genesis were performed by Mössbauer spectroscopy, XRD, TEM. It is established that Co or Ni additives render activating influence on Fe catalysts which become apparent in decrease of the methane decomposition temperature and the formation of multiwall carbon nanotubes (MWNTs).

INTRODUCTION

The increase of CO_2 concentration (a major greenhouse effect gas) in the atmosphere due to the use of fossil fuels such as petroleum, natural gas and coal leads to change in the planet's climate, so we have to develop a new energy production systems which decrease the CO_2 emission. From this point of view H_2 is a clean fuel that emits no CO_2 when it is burned or used in H_2–O_2 fuel cells. At present, many catalysts of methane transformation have been widely investigated because of their importance in the utilization of natural gas and production of H_2 [1]. Numerous studies of Ni, Fe, Co catalysts in steam reforming, hydrocarbon decomposition have shown that formation of filamentous carbon with graphitic structure – catalytic filamentous carbon (CFC) occurred [2–13]. Realistic way to produce hydrogen considers decomposition of methane, the main component of natural gas, into carbon and hydrogen without CO_2 emission. The hydrogen is used as a clean energy (or a fuel for fuel-cells) and the carbon should be used for synthesis of useful chemicals through synthesis-gas production by water gas reaction. The carbon can be also used as the functional material such as composites, electrodes, catalyst supports, adsorbents *etc.*

It was shown, that Ni and Co catalysts exhibit essential efficiency in CFC accumulation and methane conversion is close to equilibrium at temperatures 500–550 °C. We found that a large amounts of filamentous carbon can be produced using coprecipitated catalysts: the 90 % mass Ni-Al_2O_3 yields 110 g/g_{Ni}, 75 % mass Co-Al_2O_3 – 60 g/g_{Co}. The CFC is usually formed as the granules of chaotically interlaced filaments or fibers. One carbon filament grows from one catalytic particle, the latter being located on its top. Carbon filament consists from graphitic planes which are coaxially arranged as cones. Average diameter of the carbon filament for Ni-based CFC is 50 nm, for Co-based – 20 nm. The nature of catalyst influences the microstructure of filament, that becomes apparent in the angle between graph-

itic planes and the filament axis, which varies from 45° for Ni catalyst [10] to 15° for Co catalyst [11]. The copper addition into Ni catalyst changes the crystallographic orientation of the catalyst particles and as a consequence changes microstructural and textural properties of formed CFC. As a result, the thermal stability and carbon capacity (which can reach 700 g/g_{Ni}) of Ni-Cu increase [12]. Earlier the methane decomposition over iron-contained catalysts was investigated at temperatures above 800 °C with the purpose of deriving hydrogen [14] or carbon fibers [15]. However the developed iron catalysts were soon deactivated. Recently it was shown that CFCs were formed at methane decomposition over 85 % mass Fe-SiO_2 catalyst at temperature not lower than 680 °C [16]. It has been established that Co additives render activating influence on Fe catalysts which become apparent in decrease of the methane decomposition temperature and the formation of multiwall carbon nanotubes (MWNTs) [17, 18].

The main purpose of the given work is development of the long-living promoted by Ni and Co iron-containing catalysts of methane decomposition and carbon accumulation at low temperatures. In this paper we investigate the activity of coprecipitated Fe-Al_2O_3, Fe-Ni-Al_2O_3 and Fe-Co-Al_2O_3 catalysts, as well as the structure and texture of the formed CFC.

EXPERIMENTAL

Fe-Al_2O_3, Fe-Ni-Al_2O_3 and Fe-Co-Al_2O_3 catalysts were prepared by a coprecipitation method from a solution of metal nitrates using different precipitants. The coprecipitated samples were carefully washed with distilled water, dried at 110 °C, and calcined in a flow of air at 450 °C for 3 h. The catalysts were reduced in a flow of pure hydrogen at 580 °C for 5 h, then the samples were in situ passivated in ethanol and dried at room temperature.

Catalytic activity of the reduced samples was measured in a vibrating flow quartz reactor 30 cm^3 in volume. Methane was supplied at a rate of 45 $l/(g_{cat}\ h)$. Concentration of methane was measured by gas chromatography, and methane conversion was calculated. To determine the amount of carbon deposited, sample was weighted after the reaction, which was performed until complete catalyst deactivation.

The samples of catalysts and CFC were investigated by TEM, Mössbauer spectroscopy, XRD and adsorption methods. The XRD studies were performed in a Siemens URD-63 diffractometer using CuK_α radiation and a graphite crystal monochromator. Crystallite sizes were calculated from the line width of diffraction peaks (110) for α-Fe, (440) for Fe-Co-Al spinel and (002) for graphite following the Scherrer equation. Mössbauer spectra were obtained by using constant-acceleration NZ-640 (Hungary) spectrometer with a ^{57}Co in Rh source. Isomer shifts were reported relative to α-Fe at room temperature. TEM and HRTEM pictures were obtained with JEM-100CX and JEM-2010 microscopes respectively. The adsorption measurements were carried out using an ASAP-2400 apparatus to provide adsorption of N_2 at 77 K.

RESULTS AND DISCUSSION

In order to compare the carbon formation efficiency of prepared catalysts, we use the following parameters of the methane decomposition reaction: methane conversion, carbon accumulation until complete deactivation of the catalysts (the so-called carbon capacity *G*, calculated as gram of carbon per gram of a catalyst) and lifetime of the catalysts.

Effect of catalyst preparation method

Earlier we have shown, that for high-loading catalysts the method of coprecipitation from aqueous solution of the salts is more favorable. Moreover, studying the Ni-Al_2O_3 and Co-Al_2O_3 systems we have found, that the best catalytic performance was observed with the catalysts prepared using sodium hydroxide as a precipitant [10, 11]. In order to study an effect of the preparation method for Fe catalysts we vary a precipitant (NH_4OH, NH_4HCO_3, NaOH, Na_2CO_3) which, in principle, can lead to the different Fe precursors. Data are summarized in Table 1.

In contrast to Ni and Co catalysts, from Table 1 one can see that the greatest carbon ca-

TABLE 1

Catalytic properties of Fe-based catalysts for methane decomposition, demonstrating the influence of preparation methods (T = 625 °C, methane space velocity 45 l/(g_{cat} h), P_{CH4}= 1 bar, X_{CH4} – methane conversion during 1 h)

Catalysts	Precipitant	X_{CH4}, %	Lifetime, h	G, g/g_{cat}	Co or Ni, % mass (chemical analysis)
50 Fe-Al_2O_3	NH_4OH	4	23	26.5	–
50 Fe-Al_2O_3	NaOH	6	6	3.3	–
50 Fe-Al_2O_3	Na_2CO_3	4	6	2.3	–
90 Fe-Al_2O_3	NH_4OH	5.2	7	5.5	–
85Fe-5Co-Al_2O_3	NH_4OH	8	16.5	16.0	4.86
85Fe-5Co-Al_2O_3	NH_4HCO_3	7.7	16	16.0	4.89
85Fe-5Ni-Al_2O_3	NH_4OH	10	16.5	13.5	–
85Fe-5Ni-Al_2O_3	NH_4HCO_3	6	16	12.9	3.66
85Fe-10Ni-Al_2O_3	NH_4OH	10.3	15	17.6	3.03
85Fe-10Ni-Al_2O_3	NH_4HCO_3	7	16	14.9	6.63
85Fe-10Ni-Al_2O_3	NaOH	10	11	11.9	8.22
85Fe-10Ni-Al_2O_3	Na_2CO_3	8	9	7.2	5.82

pacity of Fe-Al_2O_3 and Fe-Co-Al_2O_3 catalysts is observed for samples prepared by coprecipitation using aqueous solution of ammonia as a precipitant. In case of the Fe-Ni-Al_2O_3 catalysts ammoniac complexes of nickel are formed at coprecipitation by NH_4OH that results in incomplete precipitation of the components. We concluded that the best method of Fe-Ni-Al_2O_3 catalysts preparation is coprecipitation by NH_4HCO_3 solution and our studies were realized with catalysts prepared by the appropriate method.

Effect of the catalyst composition and temperature

Since the maximum carbon capacity during methane decomposition was observed for catalysts with the high metal loading (90 % mass Ni and 60–75 % mass Co), the iron content in coprecipitated Fe-Al_2O_3 catalysts has been varied from 20 to 90 % mass. The obtained values of carbon capacity are plotted in Fig. 1, *a* as a function of nominal bulk Fe concentration. Data show that carbon capacity reaches maximum (20–28 g/g_{cat}) on the catalysts with 50–80 % mass Fe. It is known, that Co or Ni additives (5–10 % mass) render activating influence on iron catalysts [19], therefore we have investi-

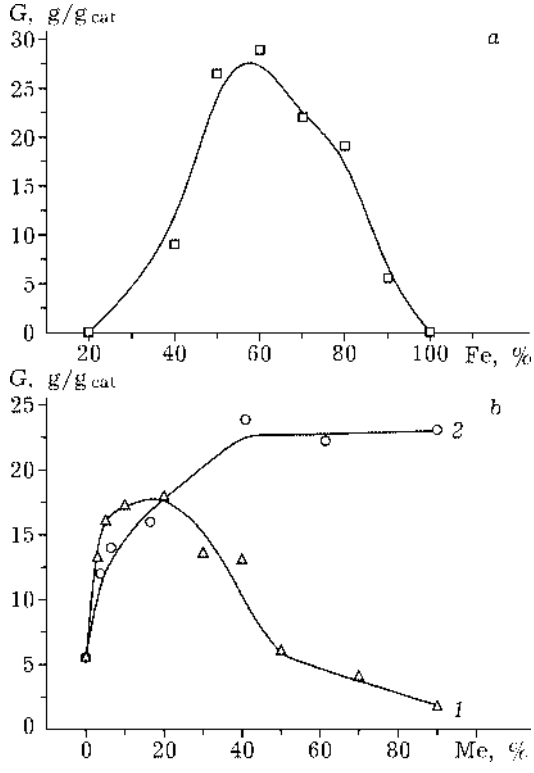

Fig. 1. The relationship between carbon capacity and metal loading in the coprecipitated Fe-Al_2O_3 catalysts, prepared using NH_4OH as precipitant (*a*) and second metal content in the Fe-Me-10 % mass Al_2O_3 (*b*): *a* – methane decomposition reaction at 625 °C, P_{CH4} = 1 bar, methane space velocity = 45 l/(g_{cat} h); *b* – Me = Co (*1*) or Ni (*2*).

TABLE 2

Catalytic properties of Fe-containing catalysts in the methane decomposition (T = 625 °C, methane space velocity 45 l/(g_{cat} h), P_{CH4}= 1 bar)

Catalysts	Fe : Me : Al_2O_3, % mass	Co or Ni, % mass (chemical analysis)	Lifetime, h	X_{CH4}, %	G, g/g_{cat}
90Fe-Al_2O_3	90 : – : 10	–	7	5.2	5.5
85Fe-5Co-Al_2O_3	85 : 5 : 10	4.86	16.5	7.9	16
60Fe-30Co-Al_2O_3	60 : 30 : 10	–	15	7.3	12.4
50Fe-Al_2O_3	50 : – : 50	–	23	4	26.5
50Fe-6Co-Al_2O_3	50 : 6 : 44	4.0	40	8	52.4
85Fe-5Ni-Al_2O_3	85 : 5 : 10	3.66	16	6	12.9
80Fe-10Ni-Al_2O_3	80 : 10 : 10	6.5	16	7	14.9
20Fe-70Ni-Al_2O_3	20 : 70 : 10	61.4	4	33.9	22.3
90Ni-Al_2O_3	0 : 90 : 10	–	4	34.8	23.1
85Co-Al_2O_3	0 : 85 : 15	–	2	2	1.7

gated the influence of Co and Ni on Fe-Al_2O_3 catalysts of methane decomposition at 625 °C. Table 2 and Fig. 1, *b* show that introduction of Co or Ni in small amounts (3–10 % mass) results in the magnification of carbon yields 2–3 times. So, carbon capacity on the catalyst 50Fe-6Co-Al_2O_3 achieves 52.4 g/g_{cat}. An increase of nickel amount up to 45 % mass and above in the series of catalysts leads to the formation of catalysts with properties close to the properties of 90 % mass Ni-Al_2O_3. Apparently, the presence of Co or Ni increases the number of the carbon growth centers of the Fe-Al_2O_3 catalyst. The studies of temperature dependence of methane decomposition over 85Fe-5Co-Al_2O_3 catalyst have shown, that carbon capacity reaches its maximum at 625–650 °C (Table 3). The methane conversion at 650 °C reaches ≈ 13 %. Fig. 2 shows methane conversion *versus* reaction time for the Fe-containing catalysts at 625 °C.

TABLE 3

Temperature dependence of catalytic properties of 85Fe-5Co-Al_2O_3 catalyst (methane space velocity 45 l/(g_{cat} h), P_{CH4}= 1 bar)

T, °C	X_{CH4}, %	Lifetime, h	G, g/g_{cat}
550	3.0	13	5.1
600	5.1	8.5	6.7
625	8.0	16.5	16
650	12.9	13	15
675	10.9	8	13.2

Structure of catalysts

We performed XRD, Mössbauer spectroscopy and TEM studies of the calcined and fresh reduced Fe-Al_2O_3 and Fe-Co-Al_2O_3 catalysts, as well as of samples after their exposition to reaction mixture.

According to the XRD data calcined samples of Fe-Al_2O_3 and Fe-Co-Al_2O_3 are X-ray amorphous that testifies to formation of highly dispersed phase. The Mössbauer spectrum of the calcined 85Fe-5Co-Al_2O_3 catalyst represents a composition of a quadrupole doublet and six-line pattern (Table 4). The spectrum,

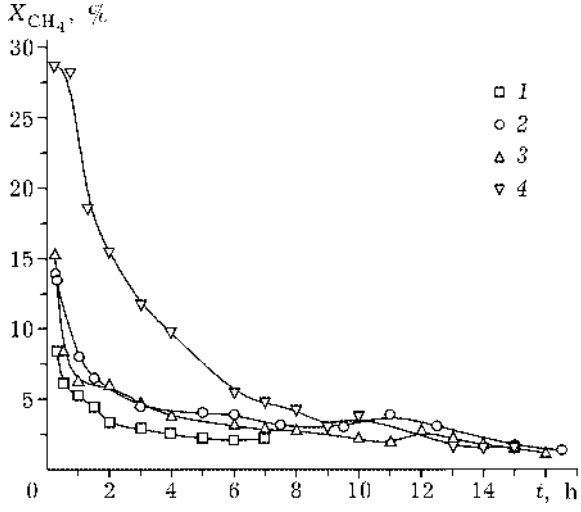

Fig. 2. The global kinetics of methane decomposition on the Fe-Al_2O_3, Fe-Co-Al_2O_3 and Fe-Ni-Al_2O_3 catalysts at 625 °C: *1* – 90Fe-Al_2O_3; *2* – 85Fe-5Co-Al_2O_3; *3* – 85Fe-5Ni-Al_2O_3; *4* – 45Fe-45Ni-Al_2O_3.

TABLE 4

Mössbauer parameter for 85Fe-5Co-Al_2O_3 catalyst (δ is isomer shift, ε is quadrupole splitting, *H* is magnetic field)

Sample	Spectrum	Phase	δ, mm/s	ε, mm/s	*H*, T	Rel area
85Fe-5Co-Al_2O_3 calcined in air	Doublet	Superparamagnetic Fe_2O_3	0.34±0.01	0.86±0.02		0.92
at 450 °C	Six-line pattern	Fe_2O_3	0.39±0.03	−0.12±0.02	51.2±0.07	0.08
85Fe-5Co-Al_2O_3 reduced in H_2 at 580 °C	The same	Fe-Co	0.01±0.01	0.00±0.02	34.2±0.02	1.00
85Fe-5Co-Al_2O_3	»	Fe-Co	−0.01±0.01	0.01±0.01	34.5±0.02	0.77
after 20 min in CH_4 decomposition at 625 °C	»	Fe_3C	0.20±0.03	0.01±0.03	20.6±0.05	0.23
85Fe-5Co-Al_2O_3	»	Fe-Co	0.03±0.01	0.00±0.01	34.7±0.02	0.94
post reacted in CH_4 at 625 °C	»	Fe_3C	0.20±0.04	0.01±0.04	20.5±0.08	0.06

according to the determined parameters, is characteristic for Fe^{3+}, located in a high-spin state and octahedral surrounding of oxygen anions. Accounting for the chemical nature of the precursor and method of preparation of a Fe−Co oxide system it may be assumed that following the proposed method of synthesis the iron oxide is obtained. The presence of the quadrupole doublet and large value of ε indicate that it is in highly dispersed, superparamagnetic condition, and the particle size is not more than 80 Å. The similar parameters of the spectra were observed for highly dispersed Fe_2O_3 in the work [20]. The six-line pattern (see Table 4) corresponds to the admixture of the Fe_2O_3 with a rather large size of particles. The fraction of this state is estimated as about 8 % based on the area under the lines.

It is known, that iron can exhibit several crystal structures. α-Fe having a body centered cubic lattice with symmetry *Im3m* exists at the temperatures below 769 °C. α-Fe has ferromagnetic properties. It was established that a bulk α→β phase transition occurs at 769 °C. β-Fe has the same symmetry as α-Fe, but already exhibits paramagnetic properties. γ-Fe is formed at the temperatures above 917 °C, and has face centered cubic lattice with *Fm3m* symmetry. Since we work at the temperatures below 700 °C, we should expect formation of only α-Fe, that is confirmed by XRD.

XRD data (Table 5) of reduced catalysts show presence of α-Fe phase in the samples. The traces of Fe-Co-Al spinels are observed for the catalysts containing 10 % mass Al_2O_3. The Mössbauer spectrum of the reduced 85Fe-5Co-Al_2O_3 sample shows a six-line pattern characteristic of Fe-Co alloy plus a central doublet which can be attributed to the traces of superparamagnetic Fe_2O_3. The reduced catalyst represents an alloy Fe-Co. The value of magnetic field exceeds the magnetic field for pure iron and corresponds to the alloy Fe-Co with 5 % mass of Co (see Table 4). According to the TEM data average particle size of the 85Fe-5Co-Al_2O_3, 60Fe-30Co-Al_2O_3, 50Fe-6Co-

TABLE 5

X-ray diffraction and TEM data for the reduced Fe-Al_2O_3 and Fe-Co-Al_2O_3 catalysts

Sample	*d*, Å	Phase	Particle size (TEM), nm
90Fe-Al_2O_3	2.867	α-Fe, Fe-Al spinel (traces)	35−55
50Fe-Al_2O_3	2.867, 8.242	α-Fe, Fe-Al spinel	30−40
85Fe-5Co-Al_2O_3	2.866	α-Fe, Fe-Co-Al spinel (traces)	25−35
60Fe-30Co-Al_2O_3	2.863	α-Fe, Fe-Co-Al spinel (traces)	25−35
50Fe-6Co-Al_2O_3	2.865, 8.261	α-Fe, Fe-Co-Al spinel	25−35

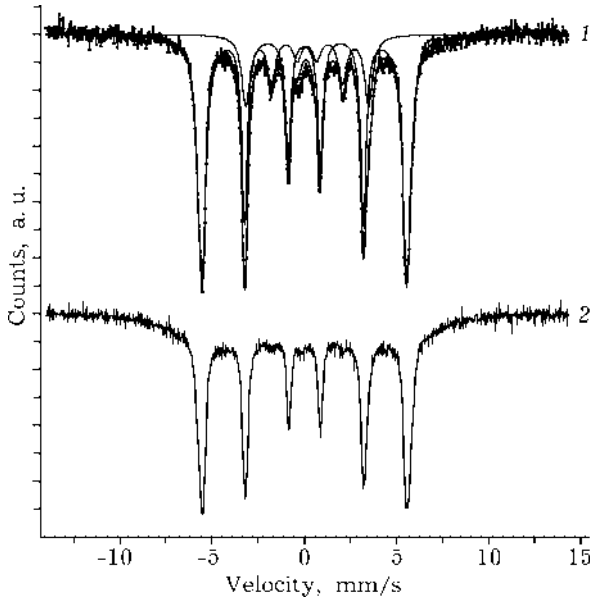

Fig. 3. Mössbauer spectra of 85Fe-5Co-Al_2O_3 catalyst: *1* – after 20 min in methane decomposition reaction at 625 °C; *2* – after 50 min in methane decomposition reaction at 625 °C.

Al_2O_3 samples is 25–35 nm, for the 90Fe-Al_2O_3 – 35–55 nm, in case of the 50Fe-Al_2O_3 – 30–40 nm.

The Mössbauer spectrum of the catalysts after 20 min in methane decomposition reaction (Fig. 3, curve *1*) and after complete deactivation at 625 °C consist of superposition two sextets which can be attributed to Fe–Co alloy and Fe_3C. It should be noted that the amount of observed Fe_3C in the deactivated catalyst is essentially less than in the sample after 20 min in methane decomposition. XRD data show also formation of Fe_3C phase.

In the case of the 85Fe-5Co-Al_2O_3 sample after 50 min exposition to reaction mixture the Mössbauer spectrum with complicated structure is observed (see Fig. 3, curve *2*). There is a "sagging" of the spectrum central part. Probably the formation of metastable [Fe-C] has resulted in appearance of such kind of the spectrum.

Morphology and texture of carbon

TEM images of CFC, formed upon low-temperature methane decomposition over 50Fe-Al_2O_3, 85Fe-5Co-Al_2O_3 and 70Fe-20Ni-Al_2O_3 catalysts, are presented in Fig. 4. The formed carbon has filamentary morphology and represents carbon nanotubes, consisting from the turbostratic carbon layers, which are parallel to the fiber axis and look as cylinders with growing diameters enclosed in each other. The turbostratic nature of the formed carbon is confirmed by XRD data (Table 6), indicating that the interplanar distance d_{002} is equal to

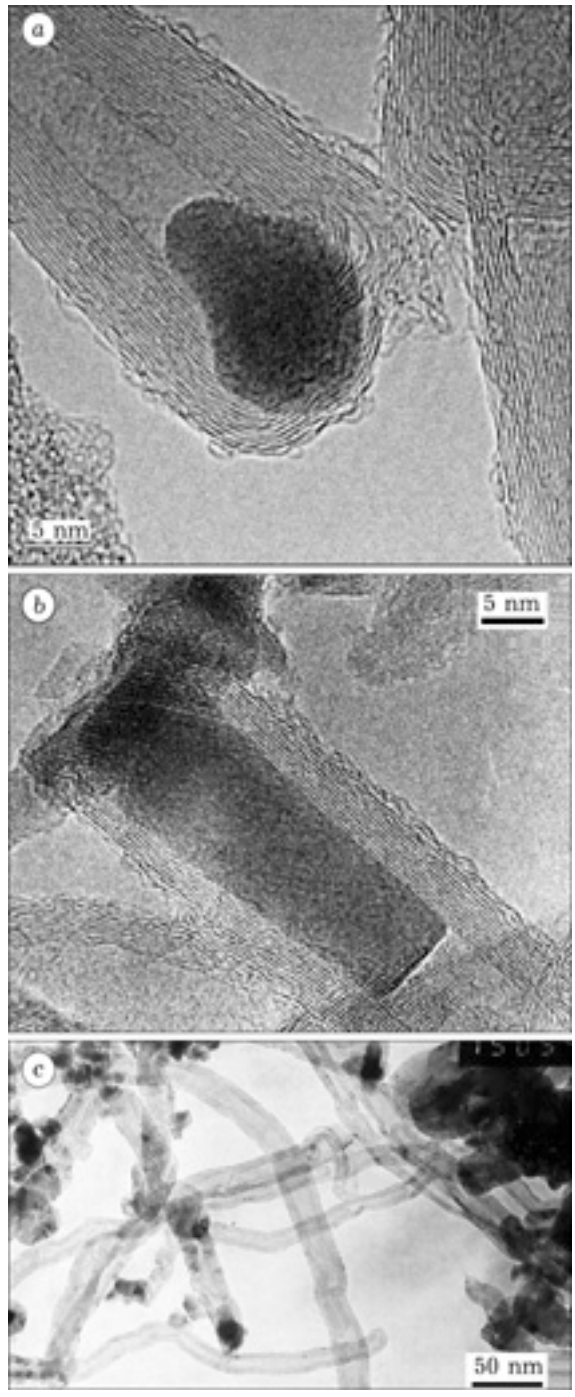

Fig. 4. TEM photographs of the catalysts: *a* – 50Fe-Al_2O_3, *b* – 85Fe-5Co-Al_2O_3, *c* – 70Fe-20Ni-Al_2O_3 after 50 min in methane decomposition at 625 °C, showing formation of the carbon nanotubes.

TABLE 6

Textural and structural properties of CFC formed in the methane decomposition at 625 °C

Sample	S_{BET}, m^2/g	V_{pore}, cm^3/g	V_{μ}, cm^3/g	D_{pore}, Å	d_{002}, nm	L_c, nm
85Fe-5Co-Al_2O_3	103.1	0.4417	0.0046	171	0.342	6.5
80Fe-10Co-Al_2O_3	118.2	0.3737	0.0057	126	–	–
60Fe-30Co-Al_2O_3	136.0	0.4744	0.0047	149	0.340	11.0
50Fe-Al_2O_3	151.5	0.5006	0.0068	132	0.343	8.7
50Fe-6Co-Al_2O_3	155	0.5582	0.0101	144	0.342	8.2
80Fe-10Ni-Al_2O_3	139.1	0.4871	0.0070	140	–	–
70Fe-20Ni-Al_2O_3	121.1	0.5481	0.0073	188.6	–	–

0.343 nm, *i. e.* a little higher than in a perfect graphite (d_{002} = 0.335 nm), and also by HRTEM data (see Fig. 4, *a, b*). The diameter of carbon nanotubes varies at the range of 30–50 nm.

The analysis of TEM data allows to pick out two types of filamentous carbon. Type I is nanotubes, consisting from 7–15 graphitic cylindrical layers, with outer diameter ranging between 25–30 nm and inner channel of 10 nm (see Fig. 4, *b*). Type II is carbon fibers, which have internal caps formed by linkage of the inner carbon layers are observed. All of the internal caps are oriented perpendicularly to the fiber axis and along one direction only for the given fibers. Carbon fibers are observed predominantly in CFC (50Fe-Al_2O_3) and to a lesser extent in CFC (85Fe-5Co-Al_2O_3).

Nanotubes (type I) are formed mainly upon methane decomposition over 85Fe-5Co-Al_2O_3, however their yield does not exceed 20 g/g_{cat}. The carbon capacity is increased up to 52.4 g/g_{cat} with a diminution of the iron contents in the catalyst down to 50 % mass (catalyst 50Fe-6Co-Al_2O_3), however in this case carbon fibers (type II) are formed.

An increase of the Ni content in the Fe–Ni catalysts up to 70 % mass formation of CFC characteristic for CFC (90 % mass Ni-Al_2O_3) is observed. The catalytic particles have cubooctahedral shape, the carbon filament consists from graphitic planes which are coaxially arranged as cones at the angle 45° [10].

Textural properties of the tubular formed carbon were determined by nitrogen adsorption at 77 K (see Table 6). The magnitude of specific surface area (S_{BET}) varies in the range of 100–150 m^2/g. The tubular CFC is more friable on the packing with a bulk density of 0.2 g/cm^3, pore volume of 0.5 cm^3/g and average pore diameter of 15 nm. Interplanar distance d_{002} and the average size of the coherent scattering area directed perpendicular to the graphite plane (002) (L_c) of CFC were determined from XRD data and represented in Table 6.

The nature of iron-containing catalyst promotion

It is known, that carbon deposition deactivates the catalyst in hydrocarbon decomposition reactions at high temperatures. However hydrocarbon decomposition under certain conditions, may result in the formation of filamentous carbon which does not poison the catalyst for a long time. Data presented above, show that it is possible to create long-living iron catalysts of methane decomposition if the conditions of filamentous carbon growth are ensured.

The properties of Fe-containing catalysts are found to be similar to the properties of Co-containing catalysts, and depend on the preparation method, amounts of the metal and temperature regimes [11]. Among the investigated catalysts, the best properties are exhibited by coprecipitated Fe-Al_2O_3 using aqueous solution of NH_4OH as a precipitant and containing not less than 50 % mass of Fe (see Table 1). Brown *et al.* [21] had established, that introduction of Co at the stage of Fe and Al hydroxides formation results in the decrease of reducing temperature of iron oxides. Indeed, the known iron Fischer–Tropsch catalysts and catalysts for ammonia synthesis are reduced at the temperatures below 600 °C. We have found, that the most effective Fe-Al_2O_3

catalysts of methane decomposition are formed after reduction at the temperature of 580 °C, with subsequent passivation at room temperature in ethanol.

We have determined, that the maximum growth of filamentous carbon on Fe-Al_2O_3 catalysts occurs at 625 °C. Thus, the temperature at which iron-containing catalysts show considerable efficiency in CFC deposition is much below than it was found in the works [15, 16]. It is known that the high-loaded metal catalysts have the greatest activity in low-temperature methane decomposition and CFC formation. However, the carbon capacity of pure iron catalysts was small, that can be explained by the low contents of iron metal, which is a center of carbon deposition, and the maximum carbon yield is observed for the sample with 50–80 % mass Fe. Apparently the increase of high-to-reduce oxide admixture (Al_2O_3) in the catalyst results in the formation of the iron particles having appropriate size (≈25–35 nm) to growth of carbon filament.

We have shown, that introduction of the small amounts of cobalt (3–10 % mass) in Fe-Al_2O_3 catalysts at the stage of coprecipitation increases CFC yields 2–3 times (see Table 2, Fig. 1, *b*). The carbon capacities presented in Fig. 1, *b* show that iron is less active than Fe-Co or Fe-Ni alloys. But the curves of the carbon capacity dependence for Fe-Co and Fe-Ni on the second metal loading (Co, Ni) differ from each other. The carbon capacity dependence for Fe-Co has a brightly expressed maximum at 10–20 % mass Co, while for Fe-Ni extremum is not observed. There is, however, a significant decrease in the carbon yield for Fe-Co catalysts with increase of the Co content. This catalytic behavior is connected to the fact that pure cobalt is active in methane decomposition reaction at 500 °C, and inactive at 625 °C due to sintering of catalytic particles. Our results show that an increase in the Ni content of the Fe-Ni catalysts from 5 to 40 % mass is accompanied by an increase in the amount of deposited carbon from 12 to 22 g/g_{cat}. Further addition of Ni appeared to exert very little impact on the carbon yield and catalyst properties become similar to that exhibited by 90 % mass Ni-Al_2O_3 under the same condition, that is expressed in the increase of methane conversion and the modification of the CFC characteristics. The Fe-Co catalysts containing 5–10 % mass of Co are some effective in nanotube formation than Fe-Ni alloys, *i. e.* the promotion influence of the small amount of Co is more expressed than in case of Ni.

Taylor *et. al.* [19] had established that some cobalt (5 % mass) or nickel (5–15 % mass) has a beneficial influence on iron for nitrogen adsorption, synthesis of ammonia and isotope exchange $^{14}N_2$–$^{15}N_2$. They assumed [19], that the small amounts of Co or Ni affect the crystallisation of iron such that a greater proportion of the surface area exists as (111) faces, which are particularly active in the synthesis of ammonia and adsorption of N_2 [22], and these faces are necessary for the deposition of graphitic carbon upon hydrocarbon decomposition.

The typical global kinetics of the methane decomposition over Fe-Al_2O_3 is illustrated in Fig. 2. There is no induction period for Fe-Al_2O_3 catalysts, which is characteristic for Ni-Al_2O_3. Previously we have assigned the induction period to the sintering of carbon-saturated Ni particles from 17 to 50 nm within the first minutes of reaction [10]. The Fe-Al_2O_3 (Fe-Co-Al_2O_3) active particle size is 20–35 nm, which seems to be large enough for filamentous carbon growth. Based from the kinetics of methane conversion, it is possible to explain gradual fall of catalyst activity due to a covering of the active centers by constantly generating carbon nanotubes, so-called encapsulation of the active centers.

Fig. 4, *a*–*c* demonstrate the active centers of iron-containing catalysts of methane decomposition. On the basis of the TEM data it can be assumed that the formation of graphite phase at initial stage of methane decomposition reaction leads to generation of faceted catalyst crystallites – the carbon nanotube growth centers apparently only at addition of the second metal (Co or Ni). Conventional model of methane decomposition includes the following stages: decomposition of CH_4 on the metal (100) and (110) planes involving the formation of surface carbon; carbon diffusion through a metal particle, and graphite precipitation on the metal (111) planes [8].

The Co addition is likely to cause the formation of catalyst particles with allocation of

(100) planes where methane decomposition occurs, and planes (111) where carbon deposition can take place. Due to the certain orientation of the catalyst particle when the plane (100) is located perpendicularly to the carbon fiber growth direction the formation of carbon nanotubes with hollow internal channel is provided. Thus iron catalyst promotion by Co or Ni changes the shape of the active particles and the mechanism of the carbon deposition.

CONCLUSION

Fe-Al_2O_3, Fe-Co-Al_2O_3 and Fe-Ni-Al_2O_3 catalysts have sufficient efficiency in filamentous carbon formation and in a methane decomposition at moderate temperature (625 °C). It have been established, that the properties of Fe-containing catalysts depend on a preparation method. The best method is a coprecipitation of components from solutions of appropriate metal nitrates by a solution of ammonia (Fe-Co-Al_2O_3) or ammonia bicarbonate (Fe-Ni-Al_2O_3). Carbon capacity of Fe-Al_2O_3 catalysts is increased in the presence of Co or Ni and reaches 52.4 g/g_{cat} (104 g/g_{Fe}). TEM data have shown, that the carbon nanotubes are observed upon methane decomposition on the Fe-Co(Ni)-Al_2O_3 catalyst. Application of the developed catalysts allows to obtain CFC with a new microstructure (carbon nanotubes), which now have scientific and practical interest.

Acknowledgements

We are grateful to Prof. V. B. Fenelonov for the adsorption data. The research described in this publication was made possible in part by Award No. REC−008 from the U. S. Civilian Research and Development Foundation for the Independent States of the Former Soviet Union (CRDF) and NWO−2001.

REFERENCES

1 L. Guczi, R. A. Van Santen, K. V. Sarma, *Catal. Rev.-Sci. Eng.*, 38 (1996) 249.
2 L. Bonnetain, P. Gadelle, M. Audier, in J. L. Figueiredo, C. A. Bernardo, R. T. K. Baker and K. J. Huttinger (Eds.), Carbon Fiber Filaments and Composites, Kluwer Acad. Publ. Dordct, Boston/London, 1990, p. 507.
3 N. M. Rodriguez, M. S. Kim, M. S. Downs, R. T. K. Baker, in J. L. Figuieredo, C. A. Bernardo, R. T. K. Baker and K. J. Huttinger (Eds.), Carbon Fiber Filaments and Composites, Kluwer Acad. Publ. Dordct, Boston/London, 1990, p. 541.
4 C. A. Bernardo, I. Alstrup, J. R. Rostrup-Nielsen, *J. Catal.*, 96 (1985) 517.
5 P. K. De Bokx, A. J. H. M. Kock, E. Boellaard *et al.*, *Ibid.*, 96 (1985) 454.
6 C. Park, R. T. K. Baker, *Ibid.*, 179 (1998) 361.
7 K. P. de Jong, J. W. Geus, *Catal. Rev.-Sci. Eng.*, 42 (2000) 481.
8 R. T. Yang, J. P. Chen, *J. Catal.*, 115 (1989) 52.
9 Sh. K. Shaikhutdinov, L. B. Avdeeva, O. V. Goncharova *et al., Appl. Catal. A*, 126 (1995) 125.
10 L. B. Avdeeva, O. V. Goncharova, D. I. Kochubey *et al.*, *Ibid.*, 141 (1996) 117.
11 L. B. Avdeeva, D. I. Kochubey, Sh. K. Shaikhutdinov, *Ibid.*, 177 (1999) 43.
12 T. V. Reshetenko, L. B. Avdeeva, Z. R. Ismagilov *et al.*, *Eurasian ChemTech J.*, 2 (2000) 237.
13 V. V. Chesnokov, R. A. Buyanov, *Russ. Chem. Rev.*, 69 (2000) 623.
14 V. V. Veselov, T. A. Levanyuk, P. S. Pilinenko, N. T. Meshenko, in V. V. Veselov (Ed.), Scientific Basics of Hydrocarbon Catalytic Conversion, Kiev, Naukova dumka, 1977, p. 84 (in Russian).
15 G. Tibbetts, M. Devour, E. Rodda, Carbon, 25 (1987) 357.
16 M. A. Ermakova, D. Yu. Ermakov, A. L. Chuvilin, G. G. Kuvshinov, *J. Catal.*, 201 (2001) 183.
17 L. B. Avdeeva, V. A. Likholobov, Pat. 2146648 Russia, 2000.
18 L. B. Avdeeva, T. V. Reshetenko, Z. R. Ismagilov, V. A. Likholobov, *Appl. Catal. A*, 228 (2002) 53.
19 D. W. Taylor, P. J. Smith, D. A. Dowden et al., *Appl. Catal.*, 3 (1982) 161.
20 J. W. Niemanisverdriet, A. M. van der Kraan, W. N. Deglass, M. A. Vannice, *J. Phys. Chem.*, 89 (1985) 67.
21 R. Brown, M. E. Cooper, D. A. Whan, *Appl. Catal.*, 3 (1982) 177.
22 F. Zaera, A. J. Gellman, G. A. Somorjai, *Acc. Chem. Res.*, 19 (1986) 24.

PERGAMON

Carbon 41 (2003) 1605–1615

CARBON

Catalytic filamentous carbon
Structural and textural properties

T.V. Reshetenko[a], L.B. Avdeeva[a,*], Z.R. Ismagilov[a], V.V. Pushkarev[b], S.V. Cherepanova[a], A.L. Chuvilin[a], V.A. Likholobov[a]

[a]*Boreskov Institute of Catalysis, Siberian Branch of the Russian Academy of Sciences, Pr. Akad. Lavrentieva 5, Novosibirsk 630090, Russia*

[b]*Department of Chemical and Petroleum Engineering, University of Pittsburgh, 1249 Benedum Hall, Pittsburgh, PA 15260, USA*

Received 25 January 2003; accepted 3 March 2003

Abstract

Catalytic filamentous carbon (CFC) synthesized by the decomposition of methane over iron subgroup metal catalysts (Ni, Co, Fe or their alloys) is a new family of mesoporous carbon materials possessing the unique structural and textural properties. Microstructural properties of CFC (arrangement of the graphite planes in filaments) are shown to depend on the nature of catalyst for methane decomposition. These properties widely vary for different catalysts: the angle between graphite planes and the filament axis can be 0° (Fe–Co–Al_2O_3), 15° (Co–Al_2O_3), 45° (Ni–Al_2O_3), 90° (Ni–Cu–Al_2O_3). The textural properties of CFC depend both on the catalyst nature and the conditions of methane decomposition (T, °C). The micropore volume in CFC is very low, 0.001–0.022 $cm^3\,g^{-1}$ at the total pore volume of 0.26–0.59 $cm^3\,g^{-1}$. Nevertheless, the BET surface area may reach 318 $m^2\,g^{-1}$. Results of the TEM (HRTEM), XRD, Raman spectroscopic, SEM and adsorption studies of the structural and textural properties of CFC are discussed.

Keywords: A. Carbon filaments; B. Chemical vapor deposition; C. Raman spectroscopy, Transmission electron microscopy; D. Texture

1. Introduction

During the past decades carbon materials have attracted ever increasing interest of scientists and technologists. The family of catalytic filamentous carbon (CFC) encompasses novel materials produced by the decomposition of carbon-containing gases over 3d-metal catalysts [1–29]. CFC was the subject of numerous studies (see, for example, the works by Baker [4–12], Rostrup-Nielsen [13,14], Geus [15–17], Avdeeva [22–26]) due to its unique structure and properties. At present, this kind of carbon is suggested to be used for the structural reinforcement applications [1], as a catalyst support [30–33] and adsorbent [25,34,35].

Various carbon-containing gases (CH_4, C_2H_4, C_2H_2, CO) can be used as feedstock for the production of CFC, while metals of the iron subgroup and their alloys are traditionally used as the catalysts for hydrocarbon decomposition. Our earlier studies have been focused on the investigation of high-loaded Ni–Al_2O_3, Ni–Cu–Al_2O_3, Co–Al_2O_3 and Fe-containing co-precipitated catalysts for methane decomposition at the temperatures of 500–675 °C [22–24,36]. These long-living catalysts allow carbon to be produced in large amounts.

The structural and textural properties of CFC depend on the catalyst composition, gaseous precursor, temperature, etc. Decomposition of methane usually produces CFC in the form of granules built-up of the chaotically interlaced filaments. Carbon filaments ca. 50 nm in diameter, which are grown on the Ni–Al_2O_3 catalysts at 550 °C, consist of graphitic planes which are arranged as coaxial cones, with the angle α between graphitic layers and filament axis being 45° [14,17,22]. Formation of the so-called 'octopus' carbon is observed during methane decomposition over Ni–Cu–Al_2O_3 catalysts at 550 °C and above, when several filaments grow from the one metal particle, and graphite layers are stacked perpendicular to the filament axis (α = 90°) [13,22,27]. The CFC formed on Co–Al_2O_3, Fe–Al_2O_3, Fe–Co–Al_2O_3, Fe–Ni–Al_2O_3 catalysts is 'classical' filamentous carbon (one carbon filament is originated

*Corresponding author. Fax: +7-383-234-3056.
E-mail address: avdeeva@catalysis.nsk.su (L.B. Avdeeva).

0008-6223/03/$ – see front matter
doi:10.1016/S0008-6223(03)00115-5

from one catalyst particle). The Co-based CFC formed at 500 °C is similar to the Ni-based CFC, but the angle between graphitic planes and the filament axis is 15° [23]. For the same catalyst, elevation of the reaction temperature up to 600 °C leads to the another type of carbon filaments with hollow-like core morphology. Also, the multiwall carbon nanotubes (MWNTs) of 30 nm size are formed upon the methane decomposition at 625 °C over the Fe-containing catalysts [24,36]. Hence, the nature of catalyst used for the methane decomposition has the principal effect on carbon filament structure, including the textural features of CFC.

CFC samples synthesized by the pyrolysis of unsaturated hydrocarbons (alkenes and alkynes) are powder materials. Their structural and textural properties are shown to be quite different from the properties of CFC formed upon the methane decomposition [37,38].

In the present work we continued the studies of CFC produced by methane decomposition over the 3d-metal catalysts; our purpose has been to investigate the structural and textural properties of CFC using various experimental tools.

2. Experimental

CFC samples were synthesized by the catalytic methane decomposition at 500–675 °C, as described elsewhere [22–24]. Catalysts were prepared by the co-precipitation technique using aqueous solutions of the metal nitrates. Sodium hydroxide was used as a precipitant for preparation of Ni–Al_2O_3 (90 wt% Ni), Ni–Cu–Al_2O_3 (82 wt% Ni, 8 wt% Cu) and Co–Al_2O_3 (75 wt% Co) catalysts, and ammonia—for Fe–Co–Al_2O_3 (85 wt% Fe, 5 wt% Co) catalyst. The co-precipitated catalysts were carefully washed with distilled water and dried at 110 °C. The Ni–Al_2O_3, Ni–Cu–Al_2O_3 and Co–Al_2O_3 were calcined in a flow of N_2 at 350 °C for 2 h, and the Fe–Co–Al_2O_3—in a flow of air at 450 °C also for 2 h. Three of the catalysts were reduced in a flow of H_2 (99.9% purity) at 550 °C (Ni–Al_2O_3, Ni–Cu–Al_2O_3) and 580 °C (Fe–Co–Al_2O_3) for 5 h, then in situ passivated in ethanol and dried at room temperature. Then, for the synthesis of CFC samples, these catalysts were placed (~0.1 g each) into the flow quartz reactor (~30 cm^3 in volume) with vibro-fluidized catalyst bed, the methane was supplied and the reactor was heated up to the required temperature. The fourth catalyst Co–Al_2O_3 (~0.1 g) was placed directly into such reactor with vibro-fluidized catalyst bed and reduced in H_2 flow at 500 °C for 3 h. Subsequently, H_2 was substituted by methane and the reactor was heated further up. Undiluted methane ($p=1$ bar, 99.99% purity) was supplied into reactor at the rate of 45–90 $l\,h^{-1}\cdot g_{cat}^{-1}$. Concentration of methane was measured by gas chromatography, and methane conversion was calculated. Carbon deposition was measured by weighting the samples after reaction, which was performed until complete catalyst deactivation.

The transmission electron microscopy (TEM) and its high resolution mode (HRTEM), scanning electron microscopy (SEM), X-ray diffraction (XRD), Raman spectroscopy and adsorption techniques were used in this work.

XRD studies were performed at the URD-63 diffractometer, using Cu Kα radiation. The average size of coherently scattering domains (CSD) along the normal to graphite layers, L_c, was determined from the integral width H_{002} of reflection 002 by the Sherrer equation:

$$L_c = \frac{\lambda}{\cos(\theta_{002})\, H_{002}} \quad (1)$$

where λ is the wavelength, θ_{002} is the diffraction angle.

The average size of CSD in the layer plane, L_a, was determined from the full width at the half-maximum H_{11} of diffusion peak 11. The Sherrer formula, including correction coefficient $K=1.75$ obtained by Warren [39] for the asymmetric diffusion peaks *hk* characteristic of turbostratic (that is, disordered) structures, was also used for the calculations:

$$L_a = \frac{K\lambda}{\cos(\theta_{11})\, H_{11}} \quad (2)$$

The interlayer distance d_{002} was determined from the position of reflection 002, corrected for the background and the Lorenz factor.

TEM and HRTEM pictures were taken using the JEM-100CX and JEM-2010 microscopes, respectively. SEM studies were performed with a TESLA-BS-350 microscope at the resolution of 5–10 nm.

The Raman spectra were acquired using a Renishaw System 2000 confocal Raman spectrometer, equipped with a Leica DMLM microscope and a 514.5 nm Ar^+ ion laser as the excitation source. The low laser power of 10 mW was used to prevent the sample damage. An objective with magnification up to 20 times was used to focus the unpolarized laser beam onto the sample surface, and to collect the back-scattered light. The spectra were recorded in the air atmosphere at room temperature. A carbon sample of ca. 10 mg weight was layered on a surface of thin microscope slide, and the slide was mounted into the microscope. For each spectrum, ten scans were collected in the 100–4000 cm^{-1} region, with the resolution of 4 cm^{-1}. Deconvolution of the spectrum into constituent bands was done using Grams/32, version 4.14 software.

Adsorption measurements were carried out using an ASAP-2400 instrument (Micromeritics) with the adsorption of N_2 at 77 K. The adsorption isotherms were used to calculate the surface area A_{BET}, total pore volume V_S and pore size distribution (PSD). V_S values were determined at $P/P_0=0.98$, which corresponds to the pores with effective diameter up to 100 nm. PSD was calculated based on the desorption branches of adsorption isotherms by the de

Boer–Broekhoff approach [40], using the model of non-crossed cylindrical pores. The mesopore surface area A_α and micropore volume V_μ were determined by the comparative approach (version of Sing's α_S method [41]). In addition, PSD was also measured using the mercury porosimetry (MP) with a PoreSiser-9300 instrument (Micromeritics).

The pycnometric density (ρ) was determined with respect to He at room temperature using an AutoPycnometer-1320 instrument (Micromeritics). The bulk density (Δ) was measured by weighing granules in a cylinder with diameter six times larger than the granule diameter. The apparent density (δ) was measured by MP.

3. Results and discussion

3.1. Synthesis of CFC

The present study was focused on the characterization of properties of CFC formed by the decomposition of methane over high-loaded metal catalysts. It was established that the variations in catalyst nature result in the changes of CFC microstructural properties, namely in the angle α between carbon filament axis and constituent graphite planes. Table 1 shows the optimal conditions (catalyst, temperature) providing the maximal yield of CFC. The reaction was conducted until complete catalyst deactivation. The performance of catalysts was compared using the following parameters: methane conversion (x, %), carbon accumulation until complete deactivation of the catalyst (the so-called carbon capacity, calculated as gram of carbon per gram of catalyst, G, g g_{cat}^{-1}) and catalyst lifetime (t, h).

3.2. Microstructural properties of CFC

The TEM (HRTEM), SEM, XRD, Raman spectroscopy and adsorption methods are, perhaps, the most effective for investigating the structure of carbon materials. The necessity for structural information throughout the filaments makes TEM (HRTEM) an important tool for analyzing the complex microstructure of CFC.

Figs. 1–5 show the TEM (HRTEM) micrographs of five different CFC types obtained in this work, that we assigned as: CFC-I, II, III; CFC (Co) and CFC (Fe–Co).

In the case of CFC-I (see Fig. 1a,b), Ni–Al_2O_3 catalyst produces the 'classical' filamentous carbon. One carbon filament grows from one catalytic particle, while the latter is located on the tip of filament. The filament diameter corresponds to the size of cube-octahedral particle (40–50 nm), and it is built up by the graphite planes, arranged as cones put one into another. The graphite planes make the angle of 45° with the filament axis [22].

CFC-II (see Fig. 2a,b) is formed upon methane decomposition on the Ni–Cu–Al_2O_3 catalyst. It is non-homogeneous by microstructure, and the two types of carbon filaments can be classified [22,42,43]. Type I is identical to CFC-I, except that angle α tends to increase within the range between 45° and 90°. The content of this CFC type is ca. 65%. Type II is the 'octopus' carbon: several filaments are originating from one catalyst particle of the quasi-octahedral shape. The particle size is larger than the filament diameter, and reaches 50–100 nm, while the graphite planes are stacked perpendicular to the filament axis. In turn, content of this CFC type is ca. 35%. Hence, CFC-II is a mixture of CFC-I and CFC-III (see below).

CFC-III (see Fig. 3a,b) is the pure 'octopus' carbon. According to the TEM images, filaments of 100–120 nm

Table 1
Effects of the catalyst composition and temperature on the production of CFC (α = angle between graphite layers and filament axis)

Sample	Catalyst	Me_1:Me_2:Al_2O_3 (wt%)	T (°C)	G (g g_{cat}^{-1})	x (%)	t (h)	α (°)
CFC-I [22]	90Ni–Al_2O_3	90:0:10	550	100	15	14	45
CFC-II [22,42]	82Ni–8Cu–Al_2O_3	82:8:10	550	165	9	38	45–75,
			575	220	14	38	90
			625	515	22	61.5	
			650	169	30	15.5	
			675	150	35	9	
CFC-III [22,42]	57Ni–23Cu–Al_2O_3	57:23:20	550	84	5.5	32	90
			575	212	9	77	
			625	291	15	35.5	
			650	309	21	32	
			675	294	25	20	
CFC (Co) [23]	75Co–Al_2O_3	75:0:25	500	45	8.5	14	15
			600	13	$20^{1\ h}$	4.5	0
CFC (Fe–Co) [24]	85Fe–5Co–Al_2O_3	85:5:10	625	16	$8^{1\ h}$	16.5	0

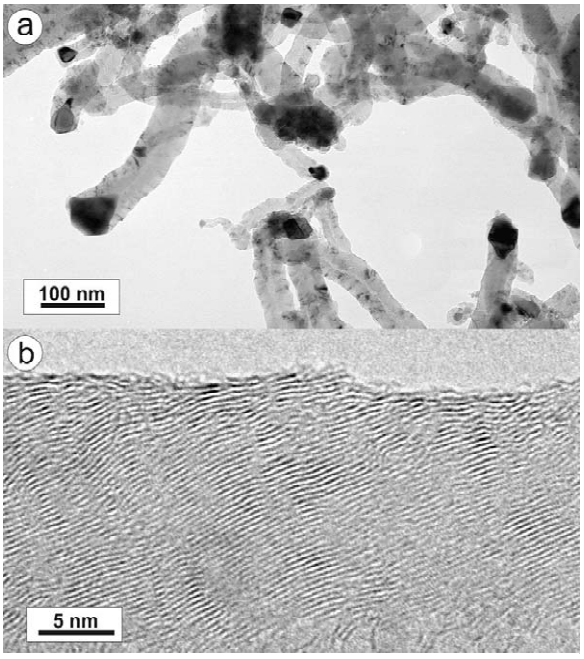

Fig. 1. TEM (a) and HRTEM (b) photographs of the CFC-I.

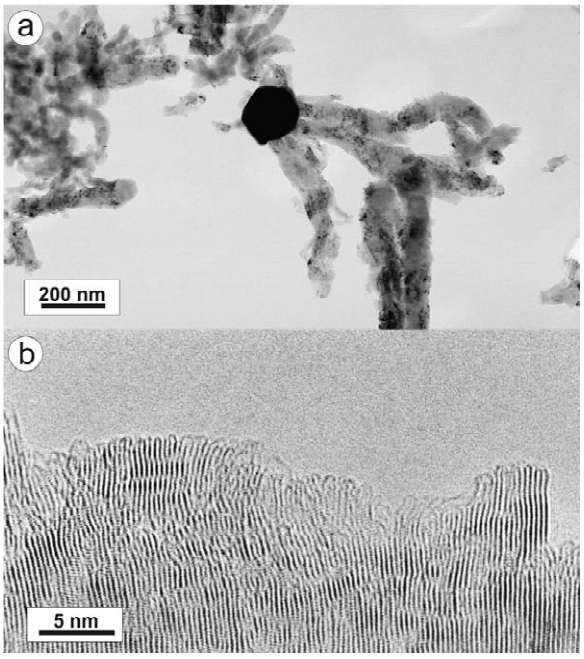

Fig. 3. TEM (a) and HRTEM (b) photographs of the CFC-III.

in overall diameter consist of several thin 40–50 nm filaments.

Fig. 4a is a TEM image of CFC (Co) formed on the $Co–Al_2O_3$ catalyst, which reacted for 50 min at 500 °C. In contrast to CFC-I produced by the $Ni–Al_2O_3$ catalyst, a

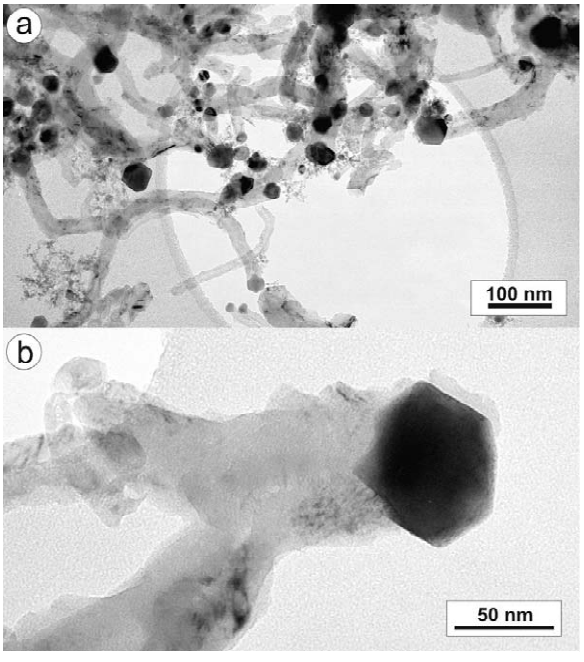

Fig. 2. (a, b) TEM photographs of the CFC-II.

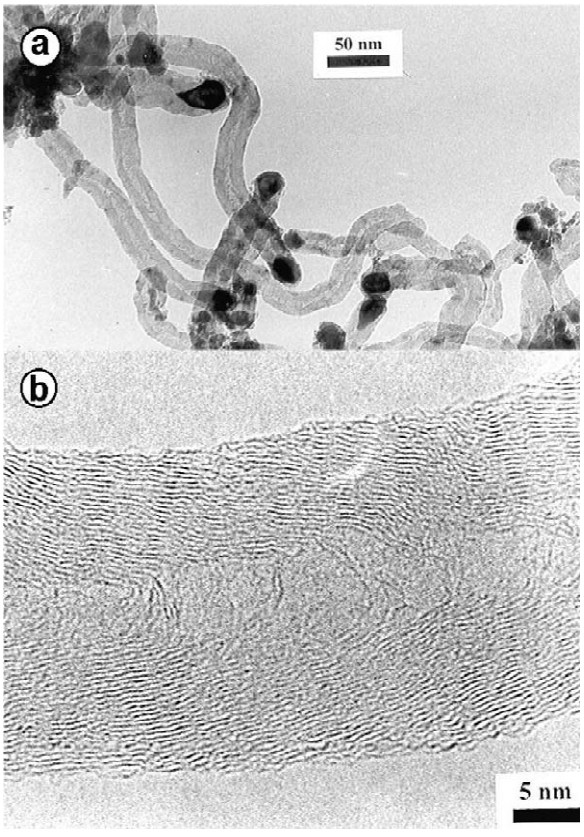

Fig. 4. TEM (a) and HRTEM (b) images of the CFC (Co).

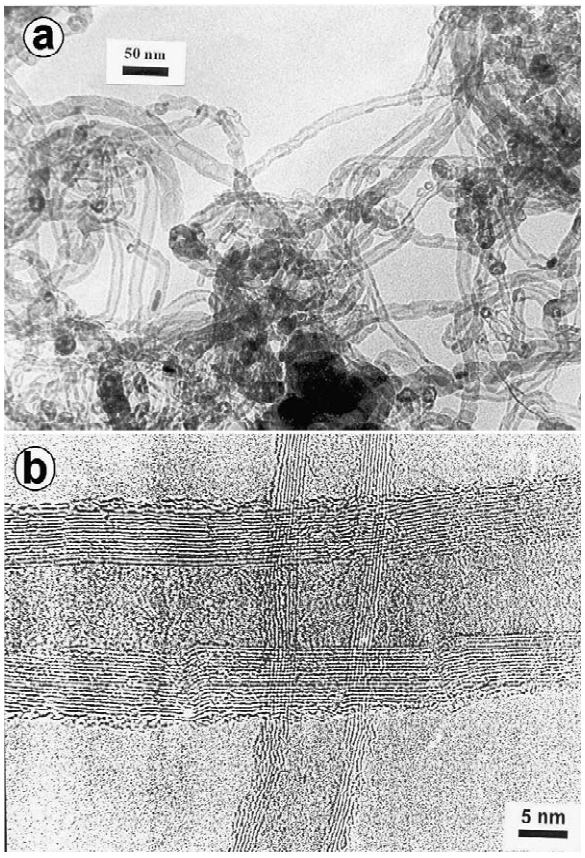

Fig. 5. TEM (a) and HRTEM (b) photographs of the CFC (Fe–Co).

hollow core is clearly seen along filament axis. This structure is resolved by the HRTEM image shown in Fig. 4b, which demonstrates graphite layers stacked at small angle (~15°) to filament axis [23]. Upon the elevation of reaction temperature up to 600 °C, the stacking angle decreases and the basal graphite planes are becoming almost parallel to the filament axis.

TEM images of CFC (Fe–Co), which was formed upon methane decomposition over Fe–Co–Al_2O_3 catalyst at 625 °C are presented in Fig. 5a. The filamentary morphology based on multiwall carbon nanotubes (MWNTs) is also characteristic for this type of carbon, which consists of turbostratic layers shaped as cylinders of increasing diameter, and enclosed one into another in parallel to the filament axis. The analysis of HRTEM data (see Fig. 5b) allows the two types of MWNTs to be distinguished:

(I) Nanotubes consisting of 7–15 graphitic cylindrical layers, with outer diameter ranging between 25 and 30 nm and inner channel of ~10 nm size.
(II) Carbon fibers with internal partitions formed by the linkage of inner carbon layers. All the internal partitions are oriented perpendicular to the filament axis along one direction. They are thin and comprise about 2–7 monolayers [24,36].

HRTEM images (see Figs. 1, 3–5) show the highly graphitic structure of CFC samples. Moreover, one can see defects in the CFC structure. The apparent long range modulation of the layer contrast, seen in the bulk of filament, seems to indicate that the adjacent graphite crystallites are twisted a little around the commonly directed *c*-axis, parallel to the filament axis (misoriented graphite blocks). Graphite edges are not opened and do not form any slit pores with diameter ~0.343 nm, as could be expected for graphite single crystal facets. Generally, the nearest or next-nearest layers are linked to produce the surface seen as nano-caps or closed-layer structures. This leads to the appearance of steps and terraces, formed by the fragments of basal graphite layers. In principle, it is well known [44] that the surface enthalpies for graphite are 0.16 J m^{-2} for basal planes and 6.3 J m^{-2} for edge planes. The linkage of surface edges should be thermodynamically favorable. Only a small part of the filament surface is represented by open edges of the graphitic layers [25,26,45].

The maximal carbon yields are attained at the following temperatures: 550 °C for CFC-I ($G=100$ g g_{cat}^{-1}), 625 °C for CFC-II ($G=515$ g g_{cat}^{-1}) and CFC-III ($G=291$ g g_{cat}^{-1}), 500 °C for CFC (Co) ($G=45$ g g_{cat}^{-1}) and 625 °C for CFC (Fe–Co) ($G=16$ g g_{cat}^{-1}).

The obtained data make it evident that the chemical nature of catalyst and, less often, the conditions of methane decomposition (temperature) are the key factors affecting the microstructural properties of CFC. Changes in the catalyst composition allow the structural properties of CFC to be varied over wide range, with the graphite plane constituents of carbon filaments arranged by a normal to ($\alpha=90°$ for Ni–Cu–Al_2O_3 catalyst) or along ($\alpha=0°$ for Fe–Co–Al_2O_3 catalyst) the filament axis.

3.3. XRD studies of CFC

The quasi-graphitic nature of CFC is supported not only by the HRTEM data, but also by the results of XRD and Raman spectroscopic studies.

XRD studies reveal the turbostratic structure of all CFC samples. This kind of carbon is built up by graphite networks stacked in random manner with one another. Calculations of the diffraction patterns in terms of the random stacking networks model [46] showed only 00*l*-type reflections and asymmetric diffusion *hk*-type maxima, which are characteristic of turbostratic carbon. Reflections assigned to the metal catalyst components (nickel, iron and cobalt) were also observed in the XRD patterns.

XRD patterns of the CFC samples are only different in the widths and positions of 00*l*-type reflections, i.e. there

Table 2
XRD characterization of CFC

Sample	T (°C)	d_{002} (nm)	L_c (nm)	L_a (nm)
CFC-I	550	0.343	4.3	6.2
CFC-III	625	0.341	5.2	9.5
CFC (Co)	500	0.344	3.3	4.4
CFC (Fe–Co)	625	0.342	5.5	8.5

are only qualitative differences. Interplanar distance d_{002} and average CSD (crystallite) sizes along the *a*- and *c*-axis of carbon (L_a, L_c) are presented in Table 2. The d_{002} ranges between 0.341 and 0.344 nm, that is higher than for ideal graphite (0.335 nm). The average values of L_c and L_a are 3–5.5 and 4–9.5 nm, respectively.

Thus, XRD characterization indicates that CFC is the typical turbostratic carbon with a high d_{002} and low L_a, L_c values [47], i.e. CFC filaments consist of mutually disoriented domains with the graphite-like structure. No correlation was established between these parameters (d_{002}, L_a, L_c) and CFC microstructure.

3.4. Raman spectroscopic studies of CFC

Raman spectroscopy is an effective method to study properties of the different carbon materials, including CFC and carbon nanotubes [37,48–51]. It is known that carbon can form two crystalline structures: diamond and graphite, and a wide range of disordered forms. The Raman spectrum of face-centered cubic lattice of diamond is quite simple. The Raman-active phonon of diamond is a single, triply degenerate zone-centered vibrational mode, which is characteristic of the C–C single bonds between sp^3-carbon atoms in its cubic structure. This is the only Raman-active mode, and the first order band appears at 1332 cm^{-1} as a sharp peak [52]. The Raman spectrum of graphite is more complicated. In the case of hexagonal crystal graphite, it consists of the main first order E_{2g2}-band at 1582 cm^{-1} with weaker bands at 42 cm^{-1} (E_{2g1}) and 2724 cm^{-1} [52,53]. The band at 1582 cm^{-1}, the so-called G-mode, is assigned to the in-plane displacement of carbon atoms in the hexagonal sheets. When disorder is introduced into the graphite structure, the existing bands broaden and additional bands are found at about 1357 cm^{-1} (the so-called D-mode), 1620 cm^{-1} (D′-mode), 2450 cm^{-1}, and 3250 cm^{-1} (2D-mode), which have been assigned to the non-zone-centered phonons [54,55]. The band at 1357 cm^{-1} corresponds to second maximum in the graphite vibrational density of states near the M-point of Brillouin zone boundary, which becomes active in small graphite crystallites when the lack of long range translational symmetry leads to the breakdown of *k*-momentum conservation rule [53,56]. In the rather small or disordered crystals with very little three-dimensional order, the G- and D′-bands merge into a single broader feature. The band at 1550–1450 cm^{-1} belongs to amorphous carbon, saturated with the sp^2 and sp^3 hybrid carbon–carbon bonds [50,57].

The integral intensity ratio I_D/I_G is inversely proportional to the microcrystalline planar size L_a, which corresponds to the in-plane dimension of single microcrystalline CSD in graphite. Both the band positions and bandwidths of G- and D-modes are sensitive to L_a, and the downshifting of the G-band position has been correlated with the presence of bond-angle disorder. The D- and G-modes were also found to be sensitive to the type of carbon bonding, i.e. sp^2 or sp^3 hybridization. Information on the sp^2/sp^3-bonded fraction of carbon can be obtained from the band position of D- and G-modes, and from the integral intensity of D-band [57].

Recently it was shown that the following relationship holds for a wide array of sp^2-bonded carbons over the range $2.5 < L_a < 300$ nm for laser wavelengths of 488 and 514.5 nm [51,53]:

$$\frac{I_D}{I_G} = \frac{4.4\ \text{nm}}{L_a} \tag{3}$$

Raman spectra of the CFC samples are shown in Fig. 6. All the spectra have a group of similar bands at 1350 cm^{-1} (D-mode), 1580 cm^{-1} (G-mode) with a shoulder at 1615 cm^{-1} (D′-mode), and a strong band at 2710 cm^{-1} (2D-mode). The graphitic nature of CFC can be deduced from the observation of D- and G-bands. The appearance and width of 2D-band give an indication of the 'ordered' nature of CFC. The results of spectra deconvolution are shown in Table 3. Based on these data, the CFC samples

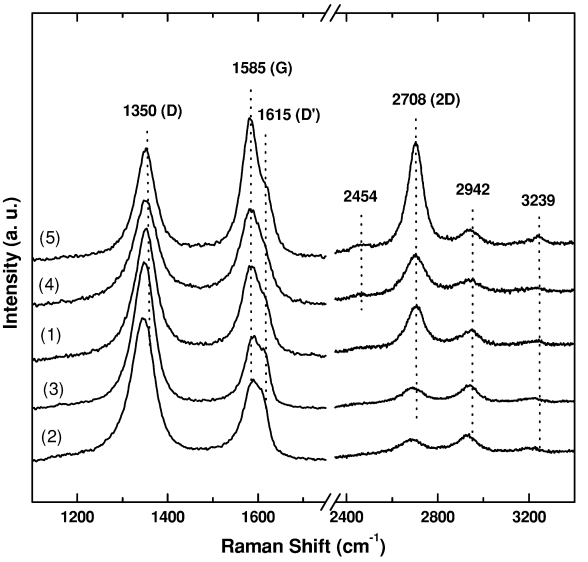

Fig. 6. Raman-spectra of the catalytic filamentous carbons with different structure: (1) CFC-I, (2) CFC-III (625°), (3) CFC-III (675 °C), (4) CFC (Co), (5) CFC (Fe–Co).

Table 3
Raman spectroscopic parameters obtained for CFC

Sample	Peak position (cm^{-1})	Bandwidth ($\omega_{1/2}$, cm^{-1})	Intensity (a.u.)	I_D/I_G	L_a^{Raman} (nm)	L_a^{XRD} (nm)
CFC-I	1351	60	193791	1.9	~2.5	6.2
	1508	105	9693			
	1582	47	102853			
	2702	95	101309			
CFC(Co)	1351	71	179565	1.4	3.1	4.4
	1512	131	18478			
	1584	55	127666			
	2701	111	110368			
CFC-III	1345	63	221372	3.2	<2.5	9.5
(625 °C)	1552	111	14409			
	1584	42	70045			
	2684	126	43589			
CFC-III	1347	56	216784	3.1	<2.5	10
(675 °C)	1551	98	8730			
	1586	38	68985			
	2688	128	51814			
CFC (Fe–Co)	1351	54	146930	0.95	4.6	8.5
	1472	73	5402			
	1582	44	154481			
	2702	81	206314			

can be classified into three types by the ordering of graphite structures formed: (i) CFC-III (625 °C) and CFC-III (675 °C); (ii) CFC-I, CFC (Co); and (iii) CFC (Fe–Co).

The first type of samples features the highest disordering of graphite structure. The 3 cm^{-1} upshifting of E_{2g}-band (G-mode) frequency means that the crystallite size is less than 2.5 nm. The I_D/I_G intensity ratio is 3.1. The average crystallite size is estimated by formula (3) as 1.4 nm. The 4 cm^{-1} downshifting of D-band maximum and its apparent asymmetry indicate the presence of diamond-like ordering domains in the carbon. The amount of amorphous phase can be estimated from the intensity of band at 1550 cm^{-1}. Comparison of intensities of the bands for two samples of this type allows to make the conclusion about a higher content of amorphous phase in the sample CFC-III (625 °C).

The second type of samples is characterized by the intermediate defectness of graphite structure. The I_D/I_G intensity ratios are 1.9 (CFC-I) and 1.4 CFC (Co), and the average crystallite sizes are 2.5 and 3.1 nm, respectively. Analysis of the intensities of bands of amorphous phase in CFC-I and CFC (Co) indicates, that the content of this phase is lower than for the first type of samples.

For CFC (Fe–Co), which represents the third type of samples, the I_D/I_G ratio is 0.95 (<1), which indicates a higher graphitization degree compared to the first and second types of samples. Moreover, the 2D-band is narrower and more intensive than for the previous samples. Formula (3) gives the average crystallite size L_a of 4.6 nm. The amorphous phase is present in a considerably lower content than in the rest of samples.

Data in Table 3 show a remarkable divergence in the values for L_a^{XRD} and L_a^{Raman}. It has been demonstrated before, that for disordered carbon materials the average Raman crystallite size is lower than the XRD size [48,58]; this divergence is more considerable in the case of highly disordered carbon compounds at $I_D/I_G>2$, when formula (3) predicts $L_a<2$ nm. Notice, that Raman spectroscopy is more sensitive than XRD with respect to the intrinsic defects of graphite lattice, such as 'missing atom' and 'missing plane', which cause symmetry breakdown of the whole crystal.

Formula (3) assumes, that graphite becomes uniformly nanocrystalline. However, for a system with mixed grain sizes, with volume fraction X_i and dimensions L_{ai}, the effective L_a is given by the formula:

$$\frac{1}{L_{a,\mathrm{eff}}} = \sum_i^N X_i \frac{1}{L_{a,i}} \quad (4)$$

Thus, we can explain why the XRD dimensions are larger than the Raman ones: formula (3) will underestimate L_a due to the dominant effect of small crystallites [48,58].

The obtained data show, that CFC is structured as the turbostratic carbon with amorphous inclusions. The minimal contribution of inclusions is characteristic of the CFC (Fe–Co), along with the maximal value of $L_a^{Raman}=4.6$ nm.

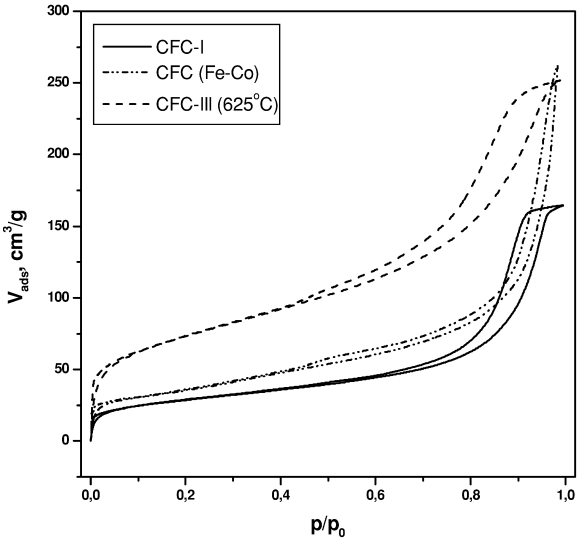

Fig. 7. The isotherms of N_2 adsorption at 77 K of CFC samples.

3.5. Textural properties of CFC

The typical isotherms of N_2 adsorption on CFC at 77 K are shown in Fig. 7. All these are H3-type isotherms, according to the IUPAC classification [41]. PSD curves obtained from the N_2 adsorption isotherms are shown in Fig. 8. The curves have two maxima centered at $d_1 = 3–4$ nm (region I, pore volume V_1) and $d_2 = 10–30$ nm (region II, pore volume V_2). In addition, a wide, low intensity peak at $d_3 > 100$ nm (region III, pore volume V_3) was detected by the MP measurements.

The data show, that formation of the CFC granules is accompanied by the 170–1810 times increase in the sample volume (f_v values) or, correspondingly, by 7–10 times increase in the granule size. The apparent, bulk and pycnometric densities are shown in Table 4.

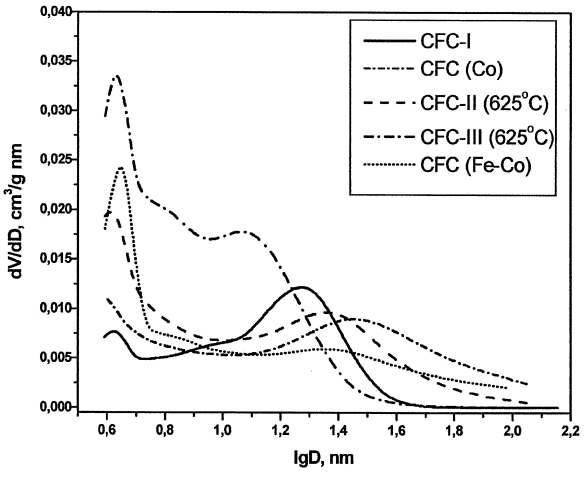

Fig. 8. Pore size distribution of CFCs.

As it follows from above, the external surface structure of carbon filaments is considerably different from the bulk structure. The external surface is covered by nano-caps and closed-layer structures, forming a system of pores of 3–4 nm in size [25,26]. Pores of 10–30 nm in size are formed as the interstices between interlaced filaments. The porosity ε_Σ is 0.77 and 0.87 for CFC (Co) and CFC (Fe–Co) samples, respectively, that is considerably higher than ε_Σ of CFC-I, II, III samples (see Table 4). The high V_3 values of 1.021 and 2.725 $cm^3\ g^{-1}$ were established for CFC (Co) and CFC (Fe–Co), respectively.

The SEM micrographs of CFC-I, CFC-III and CFC (Fe–Co) samples illustrate the texture of large pores (see Fig. 9). Taking these micrographs into consideration, the estimated filament diameter is 50–80 nm, with the pore size of 0.3–0.5 μm for CFC-I, III and up to 1 μm for CFC (Fe–Co). Notice, that the filaments are more loosely packed in CFC (Fe–Co) than in CFC-I,III.

The data on BET surface area, mesopore surface area, micropore volume and total pore volume are summarized in Table 5. The temperature dependence of textural properties of CFC-III is illustrated in Table 6. BET surface area varies over a wide range between 102 and 318 $m^2\ g^{-1}$, depending on the conditions of methane decomposition and CFC structure. The micropore volume is small in all of the samples, 0.007–0.022 $cm^3\ g^{-1}$ at the total pore volume of 0.26–0.59 $cm^3\ g^{-1}$. Hence, CFC is a mesoporous material with pores of 9.9–20 nm in average size and a large surface area. Elevation of the methane decomposition temperature results in the decrease of surface area from 268.1 to 177.6 $m^2\ g^{-1}$, and the decrease of total pore volume upon the increase of average pore size. It seems like the carbon surface is predominantly mesoporous. Minor part of the surface (~5%) is covered by the slit-like micropores of ca. 0.34 nm size [25,45].

4. Conclusions

The results of thorough studies of catalytic filamentous carbon (CFC) samples produced by the catalytic decomposition of methane were discussed. It is shown, that the catalyst nature considerably affects the structural and textural properties of CFC, which can be widely varied. CFC is a typical turbostratic carbon, as confirmed by the X-ray diffraction (XRD) and Raman spectroscopic data. The interplanar distance d_{002} ranges between 0.344 and 0.341 nm; the sizes of coherently scattering domains are: along the *a*-axis (L_a) 4–9.5 nm (XRD) or 2–4.6 nm (Raman spectroscopy), and along the *c*-axis (L_c) 3–5.5 nm.

Depending on the catalyst formulation used for methane decomposition, the microstructure of CFC can vary as

Table 4
Parameters of porous structure of CFC

Sample	G ($g\ g_{cat}^{-1}$)	Δ ($g\ cm^{-3}$)	δ ($g\ cm^{-3}$)	ρ ($g\ cm^{-3}$)	V_1 ($cm^3\ g^{-1}$)	V_2 ($cm^3\ g^{-1}$)	V_3, $cm^3\ g^{-1}$	ε_Σ	f_v
CFC-I	100	0.76	1.41	2.17	0.036	0.201	0.011	0.35	266
CFC-II (625 °C)	515	0.57	1.05	2.19	0.058	0.327	0.110	0.52	1810
CFC-III (625 °C)	291	0.62	1.12	2.19	0.124	0.199	0.116	0.49	971
CFC (Co)	45	0.34	0.49	2.15	0.039	0.529	1.021	0.77	271
CFC (Fe–Co)	16	0.20	0.28	2.13	0.058	0.321	2.725	0.87	170

where: G is the carbon capacity ($g\ g_{cat}^{-1}$);

Δ, δ and ρ are the bulk, apparent and pycnometric densities, respectively ($g\ cm^{-3}$): $\Sigma V_i = \frac{1}{\delta} - \frac{1}{\rho}$, $\delta = \frac{1}{\Sigma V_i + \frac{1}{\rho}}$; V_1 and V_2 are volumes of pores with effective diameters of $d_1 < 10$ nm and $10 \leq d_2 \leq 100$ nm effective diameters, respectively ($cm^3\ g^{-1}$).

V_3 is the volume of pores of $100 \leq d_3 \leq 1000$ nm determined by MP ($cm^3\ g^{-1}$).

ε_Σ is the total porosity of CFC granules determined as $\varepsilon_\Sigma = \frac{\rho \Sigma V_i}{1 + \Sigma V_i}$.

$f_v = (1 + G)\frac{\Delta_0}{\Delta}$ is the volume expansion coefficient equal to the ratio of the volume of carbon granule to that of the original granule of catalysts, where Δ_0 and Δ are the bulk densities of the catalyst and CFC, respectively ($\Delta_0 \sim 2.0\ g\ cm^{-3}$).

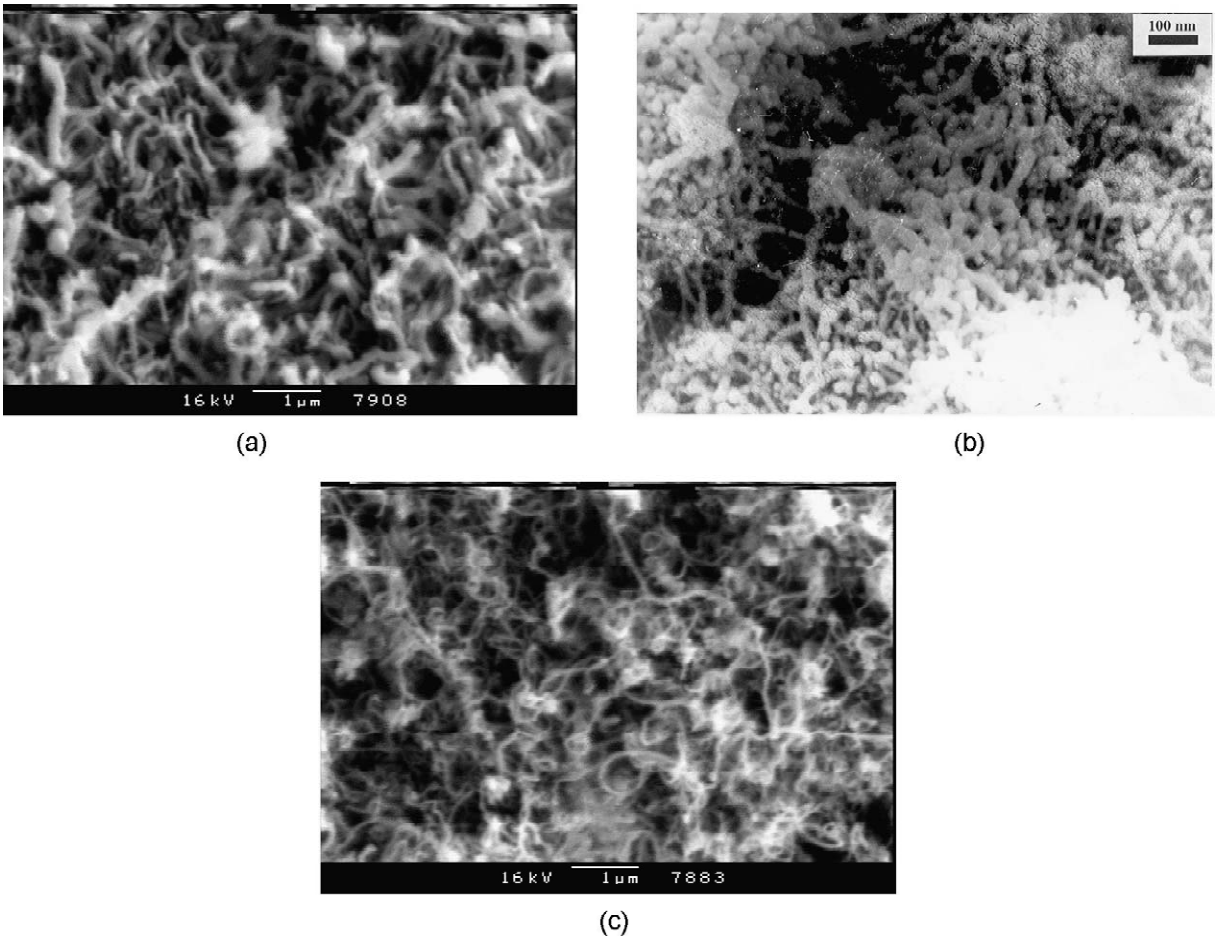

Fig. 9. SEM images of (a) CFC-I, (b) CFC-III, (c) CFC (Fe–Co).

Table 5
Texture parameters calculated from adsorption isotherms of N_2 at 77 K of CFC with different microstructure

Sample	BET surface (A_{BET}, $m^2 g^{-1}$)	Mesopore surface (A_α, $m^2 g^{-1}$)	Micropore volume (V_μ, $cm^3 g^{-1}$)	Total pore volume (V_S, $cm^3 g^{-1}$)	Average pore diameter (D^{BET}, nm)
CFC-I	102.4	86.9	0.007	0.255	9.9
CFC-II (625 °C)	180.0	157.6	0.010	0.428	9.5
CFC-III (625 °C)	262.7	231.2	0.014	0.391	5.9
CFC (Co)	116.4	116.4	0.001	0.585	20.1
CFC (Fe–Co)	125.5	112.4	0.008	0.406	12.9

Table 6
Temperature dependence of the CFC-III texture properties

T (°C)	BET surface (A_{BET}, $m^2 g^{-1}$)	Mesopore surface (A_α, $m^2 g^{-1}$)	Micropore volume (V_μ, $cm^3 g^{-1}$)	Total pore volume (V_S, $cm^3 g^{-1}$)	Average pore diameter (D^{BET}, nm)
575	318.4	268.1	0.022	0.464	5.8
625	262.7	231.2	0.014	0.391	5.9
650	229.8	213.4	0.007	0.395	6.9
675	195.4	177.6	0.008	0.383	7.8

follows (α is the angle between filament axis and graphite planes):

1. Multiwall carbon nanotubes ($\alpha = 0°$, Fe–Co–Al_2O_3 (85 wt% Fe, 5 wt% Co));
2. 'Fishbone' structure ($\alpha = 15°$, Co–Al_2O_3 (75 wt% Co); $\alpha = 45°$, Ni–Al_2O_3 (90 wt% Ni));
3. 'Octopus' carbon ($\alpha = 90°$, Ni–Cu–Al_2O_3 (82 wt% Ni, 8 wt% Cu)).

The specific surface area reaches 318 $m^2 g^{-1}$ in the case of CFC-III (Ni–Cu–Al_2O_3 (57 wt% Ni, 23 wt% Cu) at 575 °C). Hence, CFC is a new family of mesoporous carbon materials with structural and textural properties varied over the wide range.

Acknowledgements

We are grateful to Dr A.N. Salanov for the SEM measurements; Dr V.I. Zaikovskii and Dr G.N. Kryukova for the TEM (HRTEM) measurements, Professor V.B. Fenelonov and T.Ya. Efimenko for the adsorption data, Dr S.V. Tsybulya for the discussion of XRD data. The research described in this publication was partially supported by Award No. REC-008 from the US Civilian Research and Development Foundation for the Independent States of the Former Soviet Union (CRDF), and by the Netherlands Organization for Scientific Research (NWO) in the year of 2001.

References

[1] Robertson SD. Nature 1969;221(5185):1044–6.
[2] Robertson SD. Carbon 1972;10(2):221–9.
[3] Baird T, Fryer JR, Grant B. Nature 1971;233(5318):329–30.
[4] Rodriguez NM, Kim MS, Downs MS, Baker RTK. In: Figuieredo JL, Bernardo CA, Baker RTK, Hüttinger KJ, editors, Carbon fiber filaments and composites, Dordrecht: Kluwer, 1989, pp. 541–58.
[5] Kim MS, Rodriguez NM, Baker RTK. J Catal 1992;134(1):253–68.
[6] Baker RTK, Waite RJ. J Catal 1975;37(1):101–5.
[7] Baker RTK. Carbon 1989;27(3):315–23.
[8] Krishnankutty N, Park C, Rodriguez NM, Baker RTK. Catal Today 1997;37(3):295–307.
[9] Rodriguez NM, Kim MS, Fortin F, Mochida I, Baker RTK. Appl Catal A 1997;148(2):265–82.
[10] Park C, Baker RTK. J Catal 1998;179(2):361–74.
[11] Rodriguez NM, Kim MS, Baker RTK. J Catal 1993;140(1):16–29.
[12] Rodriguez NM, Chamber A, Baker RTK. Langmuir 1995;11(10):3862–6.
[13] Tavares MT, Bernardo CA, Alstrup I, Rosrtup-Nielsen JR. J Catal 1986;100(2):545–8.
[14] Bernardo CA, Alstrup I, Rosrtup-Nielsen JR. J Catal 1985;96(2):517–34.
[15] de Bokx PK, Kock AJHM, Boellaard E, Klop W, Geus JW. J Catal 1985;96(2):454–67.
[16] Kock AJHM, de Bokx KP, Boellaard E, Klop W, Geus JW. J Catal 1985;96(2):468–80.
[17] Boellaard E, de Bokx PK, Kock AJHM, Geus JW. J Catal 1985;96(2):481–90.
[18] Figuieredo JL, Bernardo CA. In: Figuieredo JL, Bernardo CA, Baker RTK, Hüttinger KJ, editors, Carbon fiber fila-

ments and composites, Dordrecht: Kluwer, 1989, pp. 441–57.
[19] Tibbetts GG. In: Figuieredo JL, Bernardo CA, Baker RTK, Hüttinger KJ, editors, Carbon fiber filaments and composites, Dordrecht: Kluwer, 1989, pp. 525–40.
[20] Auder M, Coulon M, Oberlin A. Carbon 1980;18(1):73–6.
[21] Bonnetain L, Gadelle P, Audier M. In: Figuieredo JL, Bernardo CA, Baker RTK, Hüttinger KJ, editors, Carbon fiber filaments and composites, Dordrecht: Kluwer, 1989, pp. 507–24.
[22] Avdeeva LB, Goncharova OV, Kochubey DI, Zaikovskii VI, Plyasova LM, Novgorodov BN, Shaikhutdinov SK. Appl Catal A 1996;141(1–2):117–29.
[23] Avdeeva LB, Kochubey DI, Shaikhutdinov SK. Appl Catal A 1999;177(1):43–51.
[24] Avdeeva LB, Reshetenko TV, Ismagilov ZR, Likholobov VA. Appl Catal A 2002;228(1–2):53–63.
[25] Fenelonov VB, Derevyankin AY, Okkel LG, Avdeeva LB, Zaikovskii VI, Moroz EM, Salanov AN, Rudina NA, Likholobov VA, Shaikhutdinov SK. Carbon 1997;35(8):1129–40.
[26] Shaikhutdinov SK, Zaikovskii VI, Avdeeva LB. Appl Catal A 1996;148(1):123–33.
[27] Chesnokov VV, Buyanov RA. Russ Chem Rev 2000;69(7):623–38.
[28] Ermakova MA, Ermakov DY, Chuvilin AL, Kuvshinov GG. J Catal 2001;201(2):183–97.
[29] Kuvshinov GG, Mogilnikh YI, Kuvshinov DG, Yermakov DY, Yermakova MA, Salanov AN, Rudina NA. Carbon 1999;37(8):1239–46.
[30] Shaikhutdinov SK, Avdeeva LB, Novgorodov BN, Zaikovskii VI, Kochubey DI. Catal Lett 1997;47(1):35–42.
[31] Timofeeva MN, Matrosova MM, Reshetenko TV, Avdeeva LB, Paukshtis EA, Budneva AA, Chuvilin AL, Likholobov VA. Russ Chem Bull 2002;51(2):243–8.
[32] Dandekar A, Baker RTK, Vannice MA. J Catal 1999;183(1):131–54.
[33] Kovalenko GA, Kuznetsova EV, Mogilnikh YI, Andreeva IS, Kuvshinov DG, Rudina NA. Carbon 2001;39(7):1033–43.
[34] Likholobov VA, Fenelonov VB, Okkel LG, Goncharova OV, Avdeeva LB, Zaikovskii VI, Kuvshinov GG, Semikolenov VA, Duplyakin VK, Baklanova ON, Plaksin GN. React Kinet Catal Lett 1995;54(2):381–411.
[35] Park C, Engel ES, Crowe A, Gilbert TR, Rodriguez NM. Langmuir 2000;16:8050–6.
[36] Reshetenko TV, Avdeeva LB, Ismagilov ZR, Chuvilin AL, Pavlyukhin YT. Promoted iron catalysts of low-temperature methane decomposition. In: Extended Abstracts of the Russian–Dutch Workshop on Catalysis for Sustainable Development, Novosibirsk. Russia, Boreskov Institute of Catalysis Siberian Branch of the Russian Academy of Sciences, 2002, pp. 328–41.
[37] Otsuka K, Kobayashi S, Takenaka S. Appl Catal A 2001;210(1–2):371–9.
[38] de Jong KP, Geus JW. Catal Rev Sci Eng 2000;42(4):481–510.
[39] Warren BE. Phys Rev 1941;59:693–793.
[40] Broekhoff JCP, de Boer JH. J Catal 1968;10:368–78.
[41] Gregg SJ, Sing KSV. Adsorption, surface area and porosity, 2nd ed. London: Academic Press, 1982.
[42] Reshetenko TV, Avdeeva LB, Ismagilov ZR, Chuvilin AL, Likholobov VA. Eurasian Chem Tech J 2000;2(3–4):237–44.
[43] Reshetenko TV, Avdeeva LB, Ismagilov ZR, Chuvilin AL, Ushakov VA. Appl Catal A 2003: in press.
[44] Abrahamson J. Carbon 1973;11:337–47.
[45] Fenelonov VB, Likholobov VA, Derevyankin AY, Mel'gunov MS. Catal Today 1998;42(3):341–5.
[46] Cherepanova SV, Tsybulya SV. J Mol Catal A 2000;158(1):263–366.
[47] Warren BE. J Chem Phys 1934;2:554–64.
[48] Cuesta A, Dhamelincourt P, Laureyns J, Martinez-Alonso A, Tascon JMD. J Mater Chem 1998;8:2875–9.
[49] Escribano R, Sloan JJ, Siddique N, Sze N, Dudev T. Vibrat Spectrom 2001;26:179–86.
[50] Jawhari T, Roid A, Casado J. Carbon 1995;33(11):1561–5.
[51] Knight DS, White WB. J Mater Res 1989;4:385–95.
[52] Nakamoto K. Infrared and raman spectra of inorganic and coordination compounds. New York: Wiley, 1997.
[53] Tunistra F, Koenig JL. J Chem Phys 1970;53(3):1126–30.
[54] Matthews MJ, Pimenta MA, Dresselhaus G, Dresselhaus MS, Endo M. Phys Rev B 1999;59(10):6585–8.
[55] Wang Y, Almeyer DC, McCreery RL. Chem Mater 1990;2:557–63.
[56] Nemanich RG, Solin SA. Phys Rev B 1979;20(2):392–401.
[57] Robins L, Farabaugh E, Feldman A. J Mater Res 1990;5:2456–66.
[58] Ferrari AC, Robertson J. Phys Rev B 2000;61(20):14095–107.

Available online at www.sciencedirect.com
SCIENCE DIRECT®
Applied Catalysis A: General 247 (2003) 51–63
APPLIED CATALYSIS A: GENERAL
www.elsevier.com/locate/apcata

Carbon capacious Ni-Cu-Al_2O_3 catalysts for high-temperature methane decomposition

Tatyana V. Reshetenko, Lyudmila B. Avdeeva*, Zinfer R. Ismagilov, Andrey L. Chuvilin, Vladimir A. Ushakov

Boreskov Institute of Catalysis, Pr. Akad. Lavrentieva 5, Novosibirsk 630090, Russia

Received 15 August 2002; received in revised form 19 December 2002; accepted 9 January 2003

Abstract

Steady and efficient decomposition of methane can be achieved at 625–675 °C over copper-promoted (8–15 wt.% of copper) nickel catalysts prepared from a Feitknecht compound precursor. Such catalysts permit one to increase the yield of catalytic filamentous carbon (CFC) and control both microstructural and textural properties of CFC by varying the copper concentration in the catalyst. The maximal conversion of methane into hydrogen and carbon reaches 40% at 675 °C at the carbon capacity not lower than 700 g/g_{Ni} under optimal conditions. The BET surface area of the CFC is 285.9 m^2/g. The influence of promotion of nickel-containing catalysts with copper on the catalytic activity is discussed.

Keywords: Ni-Cu alloy; Methane decomposition; Catalytic filamentous carbon

1. Introduction

Catalytic processing of hydrocarbon is always accompanied by the catalyst deactivation. As is known, the main reasons for deactivation of metal catalysts are: sintering of the dispersed active component [1], poisoning of catalyst with sulfur-containing compounds involved in the feedstock [2], and carbon formation [3–5]. Among the known facts is deactivation of nickel-containing catalysts for steam and carbon dioxide reforming of methane as well as hydrocarbon decomposition due to carbon deposition. The catalyst stability can be improved by choosing a proper support and adding of promoters to the active component [6,7].

High-loaded nickel-containing catalysts are traditionally used for methane decomposition into hydrogen and carbon [8–11]. Their stable operation is determined by formation of carbon in the form of filaments with nickel particles on their tips, which does not deactivate the catalyst for a long time. However, these catalysts can operate at temperatures not higher than 600 °C. Thus, for catalyst 90Ni-Al_2O_3, the maximal amount of carbon deposits is 145 g/g_{cat} at 550 °C [8], and <20 g/g_{cat} at 625 °C [12]. On the other hand, the process of methane decomposition performed at temperatures above 600 °C attracts considerable interest today, because the methane conversion is much higher at these temperatures.

The application of alloys as catalysts opens up interesting possibilities, because their properties can be more or less smoothly modified by varying their composition. Moreover, the introduction of a second metal to a catalytic system may provide significant changes

* Corresponding author. Fax: +7-3832-343056.
E-mail address: avdeeva@catalysis.nsk.su (L.B. Avdeeva).

0926-860X/03/$ – see front matter
doi:10.1016/S0926-860X(03)00080-2

in the catalyst activity and selectivity as compared with those of individual metals.

For example, addition of copper to nickel catalysts or their passivation with sulfur-containing compounds (H_2S) suppress both sintering of the active component and carbon formation on the methane steam reforming at 500–600 °C [7,13]. Adding gold to nickel catalysts for steam methane reforming, one can prevent formation of carbon deposits [14].

According to a number of publications [7,8,12, 15–17] the Ni-Cu catalysts for hydrocarbon decomposition are more stable than Ni-Al_2O_3 catalysts under conditions of carbon segregation. For example, when Ni:Cu = 7:3 the catalyst lifetime is 60 h and the carbon yield attains 250 g/g_{cat} on the methane decomposition at 575 °C [18]. Li et al. have reported [19] the possibility of hydrogen production by decomposing a $CH_4 + N_2$ mixture over Ni-Cu alloy at 600 °C, the carbon is 585 g/g_{Ni}. Unfortunately, the properties of the formed carbon were not investigated.

At present there is a number of works devoted to the studies of Ni-Cu alloy catalysts for the reactions of hydrogenation of aromatic and aliphatic compounds, dehydrogenation of cyclohexane to benzene, steam reforming [7,8,20,21]. Since the selectivity of such catalysts differs from that of Ni catalysts, they attract considerable interest of the researches. However the mechanism of nickel promotion with copper is still not completely understood and the relation between catalytic activity and composition or any other physical property of the Ni-Cu alloy has not been found.

The application of Ni-Cu alloy catalysts in the methane decomposition permits one to control properties and yields of the produced hydrogen and carbon materials. Thus, catalytic filamentous carbon (CFC) belongs to a new family of mesoporous carbon materials that hold interest as catalyst supports and sorbents [22]. Unfortunately, the influence of composition of Ni-Cu alloy catalysts on the CFC properties has not been thoroughly investigated.

The present work is devoted to detailed studies of the activity and stability of Ni-Cu alloy catalysts for methane decomposition at temperatures above 600 °C as well as the influence of copper additives on the textural and structural properties of formed CFC.

2. Experimental

It was prepared by a number of catalysts with Cu concentration of 8, 15, 25, 35, and 45 wt.%. Catalysts were prepared by the procedure described in detail elsewhere [23] using aqueous solutions of salts $Ni(NO_3)_2{\cdot}6H_2O$, $Cu(NO_3)_2{\cdot}3H_2O$, $Al(NO_3)_3{\cdot}9H_2O$, and NaOH as a precipitate. The samples were thoroughly washed with distilled water, dried at 110 °C, and calcined in a flow of N_2 at 350 °C for 3 h. The catalysts were reduced in a pure hydrogen (99.9% purity) flow at 550 °C for 3 h. To minimize pyrophoric behavior of the reduced catalysts, the samples were in situ passivated in ethanol and dried at room temperature. This procedure does not influence the properties of the catalysts. The concentration of sodium in the reduced samples is lower than 0.005%.

Catalytic activity of the reduced samples (100 mg) was measured in a fluidized catalyst bed reactor 30 cm^3 in volume. Methane (P_{CH_4} = 1 bar, 99.99% purity) was supplied at 90 l/g_{cat} h. Concentration of methane was measured by gas chromatography and methane conversion was calculated. He (99.9% purity) was used as carrier gas. To determine carbon deposition, the catalyst sample was weighted before and after the reaction, which proceeded until the complete catalyst deactivation.

The samples of catalysts and CFC were investigated by TEM, XRD, and adsorption methods. The XRD studies were performed in a HZG-4 diffractometer using Cu Kα radiation. Crystallite sizes were calculated from the line width following the Scherrer equation. TEM pictures were obtained on a JEM-100CX. The adsorption measurements were carried out using an ASAP-2400 to provide adsorption of N_2 at 77 K.

3. Results

3.1. Catalyst properties

The compounds resulting from the above mentioned preparation procedure and used as precursors for the Ni-Cu-Al_2O_3 catalysts are so-called the Feitknecht compound (FC). They are similar to a natural ionic clays with a layered structure, which also called hydrotacite-like compounds [11,24]. They are formed by brucite-like layers containing octahedral

coordinated bivalent and trivalent cations and interlayer anions and water. The cations are uniformly distributed in the brucite-like layer. FC form layer structures with a strong bonding within the layer, a weak interlayer bonding and often imperfect stacking of the layers. Hexagonally packed layer of M^{2+} is enclosed between two hexagonal layers of anions and water. The latter form a close-packed structure. Due to the difficulty of solid phase diffusion of metal ions, this precursor results in the well-mixed oxides after calcination. On the reduction, well-mixed oxides form a paracrystalline metal phase in which irreducible domains like Al_2O_3 exist.

XRD data of the catalysts calcined at 350 °C show that only NiO exists in 82Ni-8Cu-Al_2O_3 and 75Ni-15Cu-Al_2O_3 samples. The rest of the catalysts exhibit the presence of NiO and CuO phases.

XRD data (Table 1) show that the catalysts are represented by a Ni-Cu alloy after reduction in all cases. The reduced catalysts have only one alloy phase, when the copper content is less than 15 wt.%. As the Cu:Ni ratio increases, the lattice parameter also increases, and the catalysts with copper content more than 25 wt.% have two metal phases: Cu-rich alloy and Ni-rich alloy [7,25]. The presence of the copper phase was identified for the sample containing 25 wt.% Cu. The alloy composition is determined based on the lattice constant data. The coherent scattering area D^{XRD} determined from the widths of the diffraction peaks and the particle size of the reduced catalysts determined by TEM are shown in Table 1. In contrast to the Ni-Al_2O_3 system, the spinel phase was not observed in the diffraction pattern of Ni-Cu-Al_2O_3 catalysts [8].

3.2. Catalytic activity of Ni-Cu system

Table 2 summarizes some kinetic data on the methane decomposition at 625–675 °C over Ni-Cu-Al_2O_3 catalysts. The reactions were carried out until complete deactivation of the catalysts. In order to compare the activity of prepared catalysts, we use the following parameters of the methane decomposition reaction: methane conversion (x%), carbon accumulation until complete deactivation of the catalysts (the so-called carbon capacity G, calculated as gram of carbon per gram of catalyst, g/g_{cat}) and lifetime of catalysts (t in hours).

Table 2 suggests that Ni-Cu-Al_2O_3 catalysts provide the lower methane conversion at 625 °C compared to 90Ni-Al_2O_3. At the same time, the lifetime of the latter is no more than 2 h against 60 h for the 82Ni-8Cu-Al_2O_3 catalyst. For the 90Ni-Al_2O_3, a temperature increase to 675 °C results in the sharp decrease in the methane conversion (to 7%) and in rapid drop in the catalytic activity, which is probably caused by deactivation of the active component. As regards the Ni-Cu systems, the conversion of methane increases as the temperature rises above 625 °C. The methane conversion is about 40% over 53Ni-27Cu-20Al_2O_3 catalyst at 675 °C. The conversion of methane is below a thermodynamically possible level, but the carbon yield is 298 g/g_{cat} (562 g/g_{Ni}).

The curves of the time course of the reaction are shown in Fig. 1. Three stages are resolved for 82Ni-8Cu-Al_2O_3 sample: (1) the induction period, when methane conversion (x) increases, (2) the steady state, when x value is constant, (3) deactivation stage, when x falls to zero. The catalytic behavior of

Table 1
X-ray powder diffraction and TEM characterization of the reduced Ni-Cu-Al_2O_3

Sample	Ni:Cu:Al_2O_3 (wt.%)	Lattice parameter Ni-Cu alloy (Å)	D^{XRD} (nm)	Phase composition	D^{TEM} (nm)
90Ni-Al_2O_3 [23]	90:0:10	3.523	13	Ni + Ni-Al spinel	15–17
82Ni-8Cu-Al_2O_3	82:8:10	3.528	10	$Ni_{0.98}Cu_{0.02}$	–
75Ni-15Cu-Al_2O_3	75:15:10	3.534	13	$Ni_{0.89}Cu_{0.11}$	20–25
65Ni-25Cu-Al_2O_3	65:25:10	3.562	13	$Ni_{0.59}Cu_{0.41}$	20–25
		3.619	12	Cu	
55Ni-35Cu-Al_2O_3	55:35:10	3.602	20	$Ni_{0.15}Cu_{0.85}$	–
		3.534	10	$Ni_{0.9}Cu_{0.1}$	
45Ni-45Cu-Al_2O_3	45:45:10	3.6012	20	$Ni_{0.16}Cu_{0.84}$	15–20
		3.5358	10	$Ni_{0.87}Cu_{0.13}$	

Table 2
Catalytic properties of coprecipitated Ni-Cu-Al_2O_3 catalysts

Sample	625 °C			650 °C			675 °C		
	x (%)	G (g/g_{cat})	t (h)	x (%)	G (g/g_{cat})	t (h)	x (%)	G (g/g_{cat})	t (h)
90Ni-Al_2O_3	31	22.4	2.0	34	11.2	2.5	7.0	8.0	5.0
82Ni-8Cu-Al_2O_3	22	515	61.5	29	169	15.5	35	150	9
75Ni-15Cu-Al_2O_3	18	525	54	23	400	37	27	404	27.5
65Ni-25Cu-Al_2O_3	15	291	35.5	20	309	32	26	293	20
55Ni-35Cu-Al_2O_3	13	205	31	17	207	26	20	222	19.5
45Ni-45Cu-Al_2O_3	10	118	23	15	115	13.5	17	126	12

Methane space velocity = 90 l/g_{cat} h, P_{CH_4} = 1 bar.

82Ni-8Cu-Al_2O_3 is similar to that of 90Ni-Al_2O_3. Previously we have attributed the induction period to the increasing of the carbon-saturated catalyst particles from 17–20 to 50 nm within the first minute of reaction and forming active centers for carbon growth [8]. There is no induction period for catalyst samples containing more than 15 wt.% of copper. However, the formation of the active catalysts particles during a rather short reaction time can be postulated from the TEM data, which show that the catalyst particles are three–four times increased in size during 10–20 min of methane decomposition at 625 °C (Table 3). XRD and TEM data of the catalysts after the reaction of methane decomposition are summarized in Table 3. The catalyst samples were cooled and unloaded from the reactor before the studies. As follows from the XRD data, the lattice constant and coherent scattering region increase as the reaction proceeds for 2 h at 625 °C, formation of Ni_3C was not detected; the catalyst particles grow to 45–60 nm after 10–20 min of the reaction (TEM data).

Fig. 2 shows dependence between the carbon capacity and copper content in the catalysts at different temperatures. These all are extremal curves, the position of maximum is shifted towards high copper concentration with temperature elevation. The maximal carbon yield was 240 g/g_{cat} over catalyst containing 3 wt.% of copper at 550 °C [8], and the carbon capacity is 515 g/g_{cat} (628 g/g_{Ni}) and 525 g/g_{cat} (700 g/g_{Ni}), respectively, over catalysts 82Ni-8Cu-Al_2O_3 and 75Ni-15Cu-Al_2O_3, as the temperature increased to 625 °C. The maximal carbon yield over sample 75Ni-15Cu-Al_2O_3 is 400 g/g_{cat} (530 g/g_{Ni}) at 650 and 675 °C. Note that if the catalyst contains more than 25 wt.% of copper, the carbon capacity does not depend on temperature at 625–675 °C.

Table 3
XRD and TEM data of the Ni-Cu-Al_2O_3 catalysts after the decomposition of methane

Sample	Lattice parameter Ni-Cu alloy (Å)	D^{XRD} (nm)	D^{TEM} (nm)
82Ni-8Cu-Al_2O_3	3.591	17	45–70
75Ni-15Cu-Al_2O_3	3.604	27	–
65Ni-25Cu-Al_2O_3	3.602	21	45–70
55Ni-35Cu-Al_2O_3	3.606	21	–
45Ni-45Cu-Al_2O_3	3.602	21	60–80

XRD patterns are recorded for catalysts after 2 h of methane decomposition at 625 °C, TEM data for the catalysts after the 10–20 min reaction at 625 °C.

In Fig. 3, the Arrhenius plots of the Ni-Cu alloy catalysts are represented, where W_{CH_4} is the average reaction rate for 2 h divided by the catalyst weight. The effective activation energies $E_{a,\,eff}$ are: 65.5 (82Ni-8Cu-Al_2O_3), 65.1 (75Ni-15Cu-Al_2O_3), 77.7 (65Ni-25Cu-Al_2O_3), 74.8 (55Ni-35Cu-Al_2O_3), 75.2 kJ/mol (45Ni-45Cu-Al_2O_3). It should be noted that the values of effective activation energy obtained for the Ni-Cu-Al_2O_3 catalysts exceed that of 90Ni-Al_2O_3 (~46 kJ/mol) [18].

It is rather difficult of impossible to derive information about the mechanism of the reaction from the value of effective activation energy, which is usually determined from the Arrhenius plot of the overall methane decomposition rate. However, it is well known that the dissociative adsorption of CH_4 is the rate-determining step of methane decomposition [26–28].

In order to determine the reaction order, we have studied the dependence between the initial rate of methane decomposition and the initial concentration of hydrocarbon at 675 °C (Fig. 4). For this purpose, two mixtures of methane in helium (25 and 50 vol.%

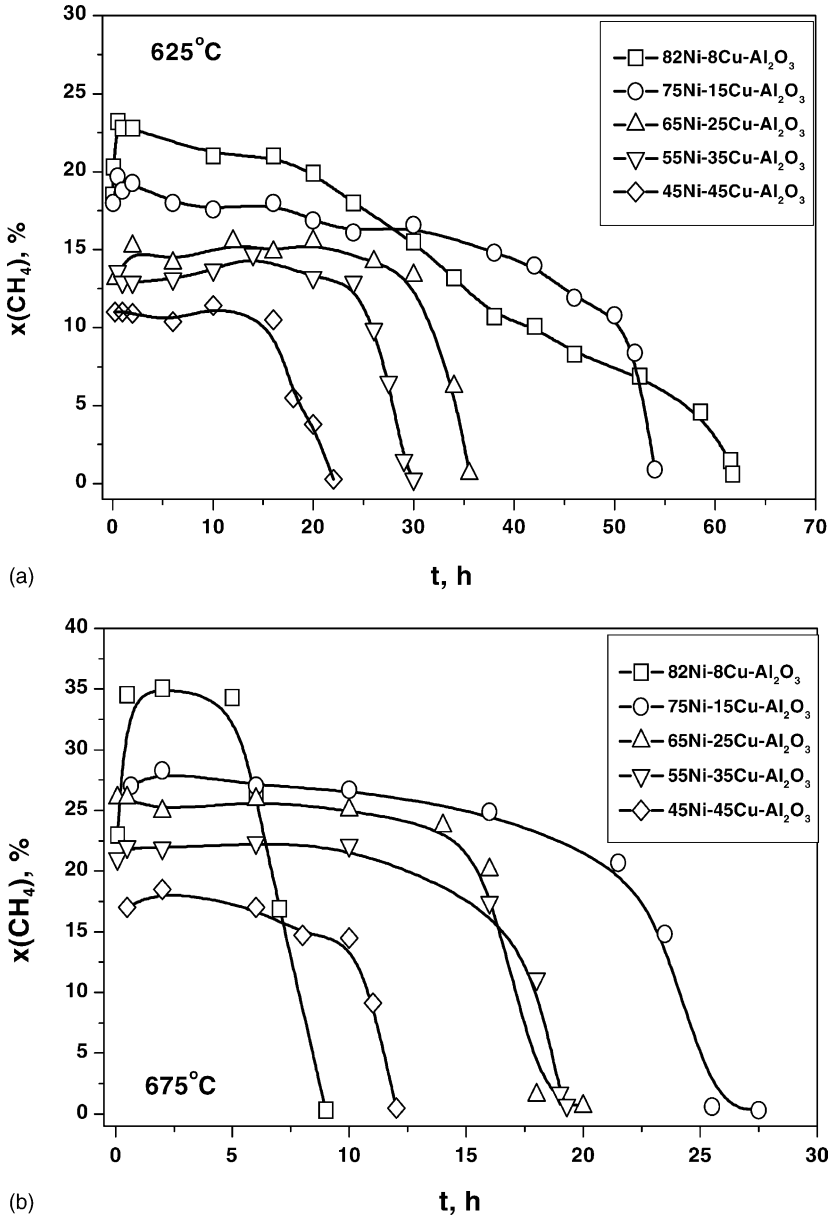

Fig. 1. Methane conversion as a function of time on the Ni-Cu-Al_2O_3 catalysts: (a) 625 °C and (b) 675 °C.

CH_4) have been used. The initial rate of methane decomposition is proportional to the initial methane concentration in the presence of all the catalysts (Fig. 4) that indicates the first reaction order with respect to methane. Therefore one can assume that the copper additives do not affect the mechanism of methane decomposition.

3.3. The nature of catalytic active centers and structural and textural properties of CFC

Fig. 5 shows TEM pictures of the active catalyst particles of 90Ni-Al_2O_3, 82Ni-8Cu-Al_2O_3 and 75Ni-15Cu-Al_2O_3 as well as CFC.

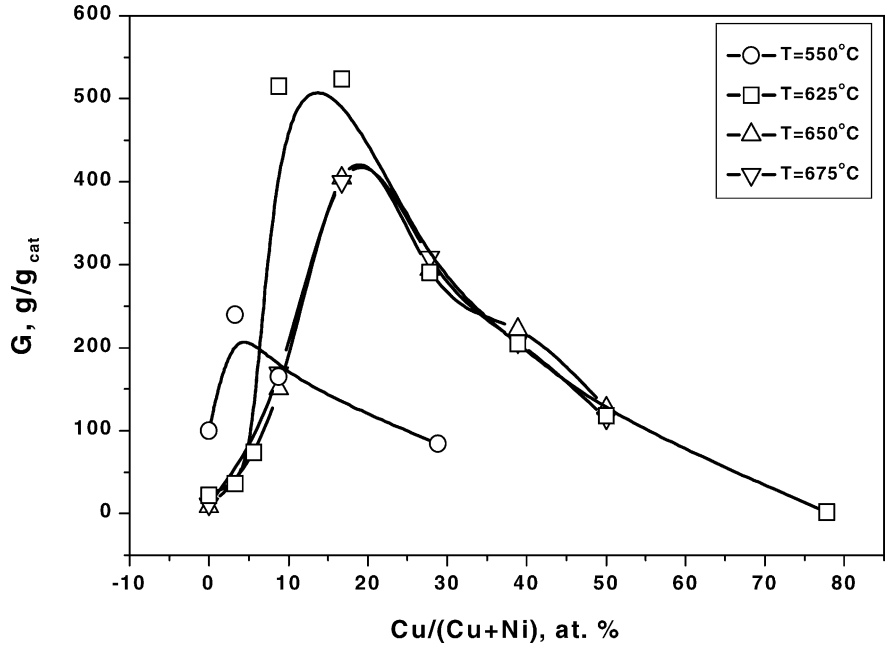

Fig. 2. The dependence between catalyst carbon capacity and copper content at different temperatures of methane decomposition.

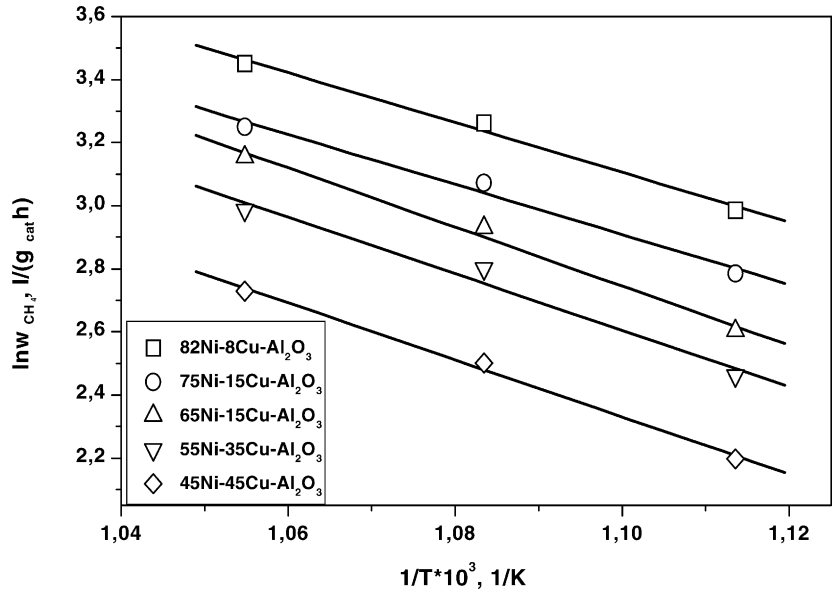

Fig. 3. Arrhenius plot for the investigated catalysts.

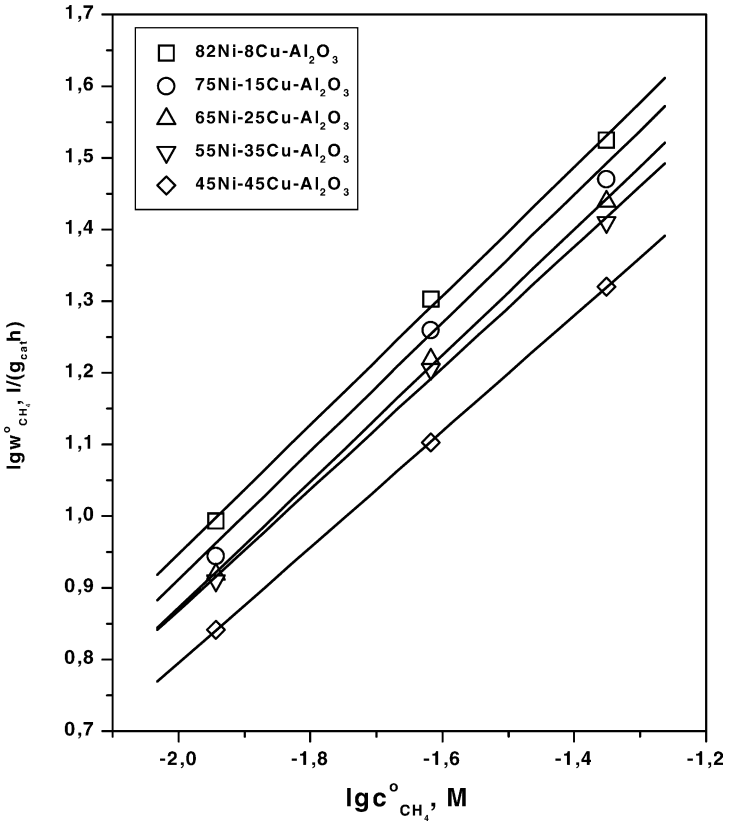

Fig. 4. Plot of the experimental initial rates of methane decomposition on the Ni-Cu-Al_2O_3 catalysts in $CH_4 + He$ gas mixture at 675 °C vs. the initial concentration of methane.

Cuboctahedral Ni particles 50 nm in size are formed in the case of 90Ni-Al_2O_3 (Fig. 5a). One particle gives rise to one carbon filament. Each carbon filament is built-up by coaxial cone-shaped layers of graphite, the inclination angle between the filament axis and graphite layers is 45°.

Two types of catalytic particles and correspondingly two types of CFC are observed for the 82Ni-8Cu-Al_2O_3 sample:

1. Pear-shaped particles 40–50 nm in size. These particles are typical for nickel-aluminum catalysts. The structure and morphology of CFC are similar to those CFC formed on the Ni-Al_2O_3, i.e. one carbon filament grows from one catalytic particle, and the graphite planes in filaments are arranged as coaxially cones. However, the angle between graphite planes and the filament axis varies from 45 to 75°. The average diameter of the carbon filament and the catalyst particle are identical (40–50 nm). The amount of the given particles is about 65% of the total number (Fig. 5b).
2. Quasi-octahedral particles 70–100 nm in size (Fig. 5c). In this case, several filaments grow from one particle to form the so-called "octopus" structure [7,29]. The diameter of the growing filaments is less than the size of the "mother" particle. The graphite layers in the filaments are stacked perpendicular to their axis. The amount of octahedral particles is about 35%. Thus, the microstructure of the catalytic filamentous carbon, formed on the 82Ni-8Cu-Al_2O_3 sample, is inhomogeneous.

The first type particles do not form over the catalysts containing more than 15 wt.% Cu. The "octopus"-type carbon is predominantly observed, the diameter of

fibers ranges from 40 to 150 nm. According to the TEM pictures (Fig. 5d and e), the fibers 100–120 nm in size consist of several thin filaments 40–50 nm in diameter.

Interplanar distance d_{002} and the average coherent scattering region directed perpendicular to the graphite plane (0 0 2) (L_c) of CFC are determined from XRD data. As Table 4 suggests, the structural parameters of CFC depend on the temperature of CH_4 decomposition. An increase in the reaction temperature results in the decrease of d_{002} from 3.414 to 3.389 Å, which is close to that of perfect graphite ($d_{002} = 3.354$ Å). In addition, the average size of CFC coherent scattering region increases as the reaction temperature elevates.

Textural properties of CFC formed on the Ni-Cu-Al_2O_3 catalysts at 625–675 °C are studied using nitrogen adsorption at 77 K (see Table 4). It should be noted that introduction of copper essentially influences

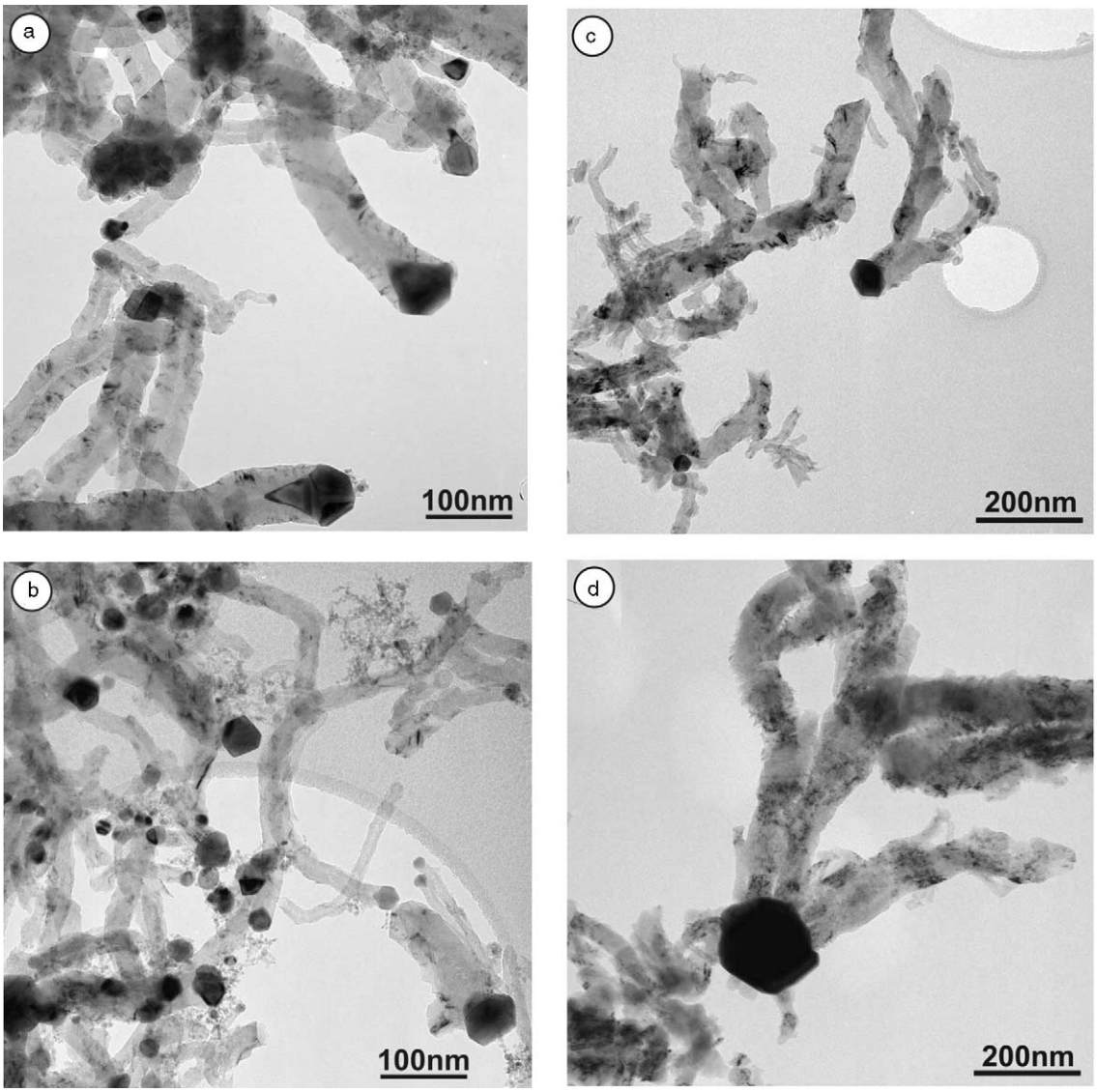

Fig. 5. TEM pictures of the samples: (a) 90Ni-Al_2O_3; (b) and (c) 82Ni-8Cu-Al_2O_3; (d) and (e) 75Ni-15Cu-Al_2O_3 after 2 h of methane decomposition at 650 °C.

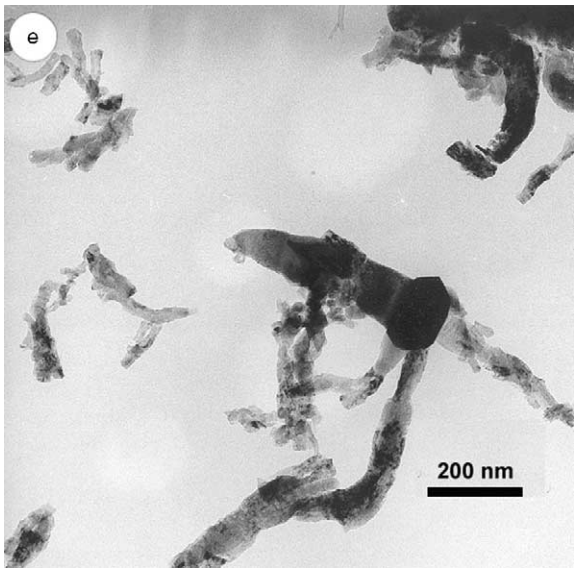

Fig. 5. (*Continued*).

the CFC texture, which is exhibited in an increase of the BET surface area and pore volume as compared to CFC formed on the 90Ni-Al_2O_3 catalyst [30]. The highest surface area of carbon (285.9 m^2/g) is obtained on the 45Ni-45Cu-Al_2O_3 catalyst at 625 °C. If reaction temperature further increases to 675 °C, the surface area of the formed CFC decreases. Hence the modification of catalysts with copper provides a formation of CFC whose microstructure and texture differ from that of CFC formed on the 90Ni-Al_2O_3.

4. Discussion

The primary role of copper additives is to improve carbon capacity of the Ni-Al_2O_3 catalysts when the temperatures of methane decomposition is above 600 °C. The additives provides both the increase of carbon capacity and modification of the growing CFC structure, which is probably associated with a change in the crystallographic orientation and size of the catalytic particles.

The addition of copper (8 wt.%) to the high-loaded nickel-containing catalyst results, as mentioned above, in formation of the active catalytic particles and carbon filaments of two types (Fig. 5). As the angle between graphite planes in filament and the filament axis increases to 75°, the carbon yield increases to 515 g/g_{cat} at 625 °C (Fig. 5b and c). The active particles in 82Ni-8Cu-Al_2O_3 are intermediate between those in Ni-Al_2O_3 and Ni-Cu-Al_2O_3 (at the copper content is not lower than 15 wt.%).

Table 4
Textural and structural CFC properties

Sample	T (°C)	S_{BET} (m^2/g)	V_{pore} (cm^3/g)	D_{pore} (Å)	d_{002} (Å)	L_c (nm)
CFC (90Ni-Al_2O_3)	550	105	0.25	100	3.43	6.0
CFC (82Ni-8Cu-Al_2O_3)	625	180	0.428	95	3.414	6.6
	650	139	0.372	107	3.409	9.0
	675	130	0.301	93	3.393	8.8
CFC (75Ni-15Cu-Al_2O_3)	625	233	0.418	72	3.411	7.4
	650	203	0.420	83	3.389	7.8
	675	179	0.393	88	3.393	8.5
CFC (65Ni-25Cu-Al_2O_3)	625	261	0.405	62	3.401	6.9
	650	230	0.395	69	3.389	7.4
	675	210	0.427	81	3.388	8.1
CFC (55Ni-35Cu-Al_2O_3)	625	277	0.406	59	3.414	6.8
	650	247	0.449	73	3.414	7.0
	675	211	0.408	77	3.393	7.5
CFC (45Ni-45Cu-Al_2O_3)	625	286	0.431	60	3.414	6.8
	650	251	0.437	70	3.409	8.0
	675	237	0.424	72	3.393	7.4

When the concentration of Cu is higher than 15 wt.% the active catalytic particles are quasi-octahedral (not pear-shaped as in case of 90Ni-Al_2O_3). In this case, the "octopus"-type carbon is formed (Fig. 5d and e). The "octopus"-type carbon also forms over the sulfur-passivated nickel catalysts, when the sulfur coverage corresponds to ca. 70% of the saturation coverage [7]. As for sulfur case, formation of the "octopus"-type carbon could indicate a change in the carbon nucleation at the copper concentration is above 15 wt.%, which is caused by a decrease in the carbon dissolution in nickel [7,11,13,31].

The commonly accepted model of methane decomposition and carbon growth over nickel catalysts includes the stages of activation and decomposition of methane on (1 0 0) and (1 1 0) metal surface planes, carbon dissolution and diffusion through the particle, carbon segregation in the form of graphite-like phase on (1 1 1) nickel planes due to crystallographic matching of (1 1 1) nickel surface to (0 0 2) graphite planes [31–34]. This is exactly the mechanism of formation of catalytic active cuboctahedral nickel particles at the initial stage of the reaction.

In the case of Ni-Cu alloy we have observed another catalytic active particles (Fig. 5d and e). They have several (1 1 1) planes where carbon segregation can take place, that contributes to an increase in the carbon capacity of the catalyst. Integrity of the Ni(1 1 1) plane where carbon grows due to enrichment of the catalyst particle surface with Cu may be destroyed to provide growth of several thin filaments from one plane [7,8,15]. There is a number of (1 0 0) and (1 1 0) planes where methane molecules are activated. As a result, the number of planes suitable for the methane decomposition and carbon precipitation on the Ni-Cu-Al_2O_3 surface increases.

The catalytic properties of Ni-Cu catalyst are explained in literature in terms of two mechanism: an ensemble (geometric) effect and ligand (electronic) effect [20,35,36]. For the Ni-Cu alloy, the ensemble effect implies the formation of nickel atom ensembles of a certain size on the surface of the active particle due to copper surface segregation. The ligand effect relates to the modification of electronic properties of Ni-Cu alloy in comparison with individual metals [21,36–38].

In the case of Ni-Cu catalysts for methane decomposition, the ensemble effect should prevail. This assumption is supported by the following facts. First, the reaction of methane decomposition is structurally sensitive, as the process of methane decomposition and carbon segregation proceed on different surface planes of the catalytic active particle, and the rate of carbon formation depends on the catalyst particle size [39]. Second, the process of copper segregation on the alloy particle surface is characteristic for the Ni-Cu system [40]. Since the surface energy of copper and nickel are 1.85 and 2.45 J/m^2 [25], respectively, it is expected that the copper surface concentration will exceed that in the bulk.

The process of Cu segregation on the reduced Ni-Cu-Al_2O_3 catalyst surface was observed by Auger spectroscopy [23]. Moreover the reduction of the Ni-Cu-Al_2O_3 samples significantly increases the intensity of Auger aluminum peak [23]. A comparison of data obtained for the Ni-Al_2O_3 and Ni-Cu-Al_2O_3 catalysts shows that an increase of the surface alumina in the Ni-Cu sample could be connected with the absence of Ni-Al spinel phase. It is known, that Cu^{2+} ions are stabilized by a square plane coordination which differs from the octahedral one for Ni^{2+}. So, the layer structure of the precipitate found after coprecipitation for the Ni-Al_2O_3 system (Feitknecht compound) [24] can be partially fragmented or distorted by copper ions. Therefore, the introduction of copper could prevent the formation of spinel or its growth in the samples subjected to calcination. In turn Al_2O_3 behave as a texture promoter that prevents sintering of the active component during the catalyst reduction [23].

It should be noted that the faceted particles form under the reaction medium, so the influence of methane and formed carbon can not be excluded from consideration, because the nature of gas that contacts with the alloy surface can significantly affect the surface composition. Thus, if gas interacts sufficiently strongly and selectively with one of the alloy (Ni) component, the surface tends to be enriched in that particular component (Ni) even if the other component (Cu) is the predominant surface species in an inert atmosphere [17,41].

An increase of the effective activation energy of methane decomposition over Ni-Cu-Al_2O_3 can be attributed to the ligand effect of alloying. The ligand effect (leading to the alteration of bond strength) is also assisted by the ensemble effect, since a significant difference in the catalytic behavior of Ni-Al_2O_3 and

Ni-Cu-Al_2O_3 can not be elucidated by the ensemble effect alone.

Based on the obtained results and literature data, we can make some assumptions concerning the copper influence on the properties of nickel-containing catalysts for methane decomposition.

TEM data allow one to conclude that the copper introduction leads to formation of the active catalytic particles whose crystallographic orientation differs from that of 90Ni-Al_2O_3: the angle between (1 1 1) planes of particles increases and the particle shape changes from cuboctahedral to quasi-octahedral. The copper promotion results in a slight decrease in methane conversion and in the rate of carbon deposition ($W_{90Ni\text{-}Al_2O_3} = 11.2\,g_c/(g_{cat}\,h)$, $W_{82Ni\text{-}8Cu\text{-}Al_2O_3} = 8.4\,g_c/(g_{cat}\,h)$) at 625 °C. The fact that the catalyst carbon capacity is in 10 times and more increased, that allows one to suggest a considerable decrease in the catalyst deactivation rate. The catalyst deactivation is the undesirable reactionary way, which is directly connected with the shape and size of catalyst particle.

Since the ensemble of nickel atoms (~11 nm), providing the adsorption and dissociation of methane, is smaller than the ensemble required for nucleation and stable growth of graphite phase (50 nm) [4,39,42], copper mainly affects the carbon deposition, because several carbon filaments grow from one active site. It is likely that the Cu-enrichment of Ni(1 1 1) plane influences the nucleation of the graphite-like phase due to decrease in the carbon dissolution in nickel and rate of the CFC growth [7,17].

In general, the catalysts of hydrocarbon decomposition are deactivated due to the encapsulation of the metal active center by formed graphite layers or destruction of the catalytic particle. The deactivation of Ni-Al_2O_3 catalysts has been shown before to results from destruction of the catalytic active particle by deposited graphite layers of carbon filament and penetration of nickel atoms deep into the filament due to the so-called intercalation or erosion [8]. This process constantly proceeds during the whole catalyst operation. “Disappearance” of the catalytic particles from the filament tip is often observed in TEM images of deactivated nickel catalysts. TEM studies of evolution of Ni-Al_2O_3 catalysts reveal a decrease in the particle volume on the side of (1 1 1) planes that contact with (0 0 2) facets of graphite. Thus, the nickel particle decreases in length along (1 0 0) direction. During the catalytic formation of carbon filaments, the metal undergoes dispersing and is predominantly consumed for formation of the solid nickel graphite solution. As the nickel particle reaches 1–5 nm, the process of methane decomposition and carbon filament growth arrest themselves. For Ni-Cu, the perpendicular arrangement of graphite planes (0 0 2) and the filament axis diminishes the fast fragmentation of nickel particles by carbon filament. Fig. 1a and b suggest that the catalyst lifetime depends on their composition and reaction temperature, so the deactivation proceeds at different rates.

The fact that D^{XRD} of Ni-Cu-Al_2O_3 is lower than TEM size of catalytic particles (Table 3) suggests the existence of polycrystalline alloy catalytic particles. If so, one can assume that the diffusion of carbon atoms preferably proceeds on the surface of crystallites forming the catalyst particle (not through the particle bulk) as was supposed in [7,13,31]. Hence, the surface diffusion of carbon atoms will apparently results in the more slight fragmentation and destruction of the particles.

The maximum on the curve of carbon capacity versus alloy composition probably indicate the stable carbon growth on the ensemble with a certain composition that can be attributed to suppression of self poisoning effects (as deactivation) due to the destruction of the catalyst particle (Fig. 2).

The carbon capacity of Ni-Cu-Al_2O_3 catalysts depends on the nature and shape of the catalytic active center (either cuboctahedral or quasi-octahedral) depending on copper content. Modifying the particle shape, one increases the number of (1 0 0) and (1 1 0) planes for methane decomposition, and (1 1 1) planes for carbon segregation, which in turn, provide an increase in the carbon capacity of the catalysts and decrease of the deactivation rate. Copper in the Ni-Al_2O_3 catalysts possesses structure-forming properties, and acts as a stabilizing component, which results in an increase the catalysts lifetime.

5. Conclusion

Copper additives are shown to improve the carbon capacity of the Ni-Al_2O_3 catalysts for methane decomposition, which leads to the increase of their

lifetime and efficiency of the Ni-Cu-Al_2O_3 catalysts at 625–675 °C. The lifetime of nickel-containing catalysts is closely associated with their deactivation mechanism, which depends on the crystallographic orientation of the active center.

Introducing copper into the catalyst, the active center changes its habitus from cuboctahedral up to quasi-octahedral at an increase in the number of (1 1 1) the alloy planes available for carbon segregation. According to the TEM data, the promotion of the active center with copper increases the angle between the graphite planes and the filament axis of formed carbon from 45 to 90°. The mutual orientation of (1 1 1) alloy planes and (0 0 2) graphite planes is assumed to prevent rapid catalyst deactivation due to destruction of the catalytic particle by growing carbon filament. Two types of CFC are formed depending on the catalyst composition and structure of the active catalytic center.

Ni-Cu alloy systems are promising catalysts for the methane decomposition yielding hydrogen and CFC, since the methane conversion is 40% at 675 °C and CFC yield reaches 525 g/g_{cat} (700 g/g_{Ni}) under optimal conditions.

In this paper, the textural and microstructural properties of formed CFC, depending on the composition of the Ni-Cu alloy catalysts and the conditions of methane decomposition, are investigated in detail for the first time. Modifying the nickel catalysts with Cu additives is shown to provide wide-range changes in the properties of catalytic filamentous carbon. The specific surface area of CFC can reach 285.9 m^2/g.

Acknowledgements

We are grateful to Prof. V.B. Fenelonov for the adsorption data. The research described in this publication was made possible in part by Award No. REC-008 from the US Civilian Research and Development Foundation for the Independent States of the Former Soviet Union (CRDF) and NWO-2001.

References

[1] A.A. Slinkin, Itogi nauki i tekhniki, Kinet. katal. 10 (1982) 5 (in Russian).
[2] D.L. Trimm, in: J.L. Figueiredo (Ed.), Progress in Catalyst Deactivation, NATO Series A Applies Sciences No. 54, Nijholf (Martinus), London, 1982, p. 3.
[3] R.A. Buyanov, Coke Formation on Catalysts, Nauka, Novosibirsk, 1983 (in Russian).
[4] J.R. Rostrup-Nielsen, J. Catal. 33 (1974) 184.
[5] R.T.K. Baker, Carbon 27 (1989) 315.
[6] O.V. Krylov, Russ. Zh. Chem. 44 (2000) 19 (in Russian).
[7] C.A. Bernardo, I. Alstrup, J.R. Rostrup-Nielsen, J. Catal. 96 (1985) 517.
[8] L.B. Avdeeva, O.V. Goncharova, D.I. Kochubey, V.I. Zaikovskii, L.M. Plyasova, B.N. Novgorodov, Sh.K. Shaikhutdinov, Appl. Catal. A 141 (1996) 117.
[9] V.V. Chesnokov, R.A. Buyanov, Russ. Chem. Rev. 69 (2000) 623.
[10] M.A. Ermakova, D.Yu. Ermakov, G.G. Kuvshinov, L.M. Plyasova, J. Catal. 187 (1999) 77.
[11] Y. Li, J. Chen, L. Chang, Y. Qin, J. Catal. 178 (1998) 76.
[12] T.V. Reshetenko, L.B. Avdeeva, Z.R. Ismagilov, A.L. Chuvilin, V.A. Likholobov, Eurasian Chem. Tech. J. 2 (2000) 237.
[13] D.L. Trimm, Catal. Today 37 (1997) 233.
[14] F. Besenbacher, I. Chorkendorff, B.S. Clausen, B. Hammer, A.M. Molenbroek, J.K. Norskov, I. Stensgaard, Science 279 (1998) 1913.
[15] V.V. Chesnokov, V.I. Zaikovskii, R.A. Buyanov, V.V. Molchanov, L.M. Plyasova, Kinet. Katal. 35 (1994) 146.
[16] J.R. Rostrup-Nielsen, I. Alstrup, Catal. Today 53 (1999) 311.
[17] N.M. Rodriquez, M.S. Kim, R.T.K. Baker, J. Catal. 140 (1993) 16.
[18] L.B. Avdeeva, unpublished.
[19] Y. Li, J. Chen, Y. Qin, L. Chang, Energy Fuels 14 (2000) 1188.
[20] J.H. Sinfelt, J.L. Carter, D.J.C. Yates, J. Catal. 24 (1972) 283.
[21] K.C. Khulbe, R.S. Mann, Catal. Rev. Sci. Eng. 24 (1982) 311.
[22] Sh.K. Shaikhutdinov, L.B. Avdeeva, B.N. Novgorodov, V.I. Zaikovskii, D.I. Kochubey, Catal. Lett. 47 (1997) 35.
[23] Sh.K. Shaikhutdinov, L.B. Avdeeva, O.V. Goncharova, D.I. Kochubey, B.N. Novgorodov, L.M. Plyasova, Appl. Catal. A 126 (1995) 125.
[24] F. Cavani, F. Trifiro, A. Vaccari, Catal. Today 11 (1991) 173.
[25] P.C.M. Van Stiphout, D.E. Stobbe, F.Th.V.D. Scheur, J.W. Geus, Appl. Catal. 40 (1988) 219.
[26] I. Alstrup, M.T. Tavares, J. Catal. 139 (1993) 513.
[27] G.G. Kuvshinov, Yu.I. Mogilnykh, D.G. Kuvshinov, Catal. Today 42 (1998) 357.
[28] J.W. Snoek, G.F. Froment, M. Fowles, J. Catal. 169 (1997) 250.
[29] M.T. Tavares, C.A. Bernardo, I. Alstrup, J.R. Rostrup-Nielsen, J. Catal. 100 (1986) 545.
[30] V.B. Fenelonov, A.Yu. Derevyankin, L.G. Okkel, L.B. Avdeeva, V.I. Zaikovskii, E.M. Moroz, A.N. Salanov, M.A. Rudina, V.A. Likholobov, Sh.K. Shaikhutdinov, Carbon 35 (1997) 1129.
[31] I. Alstrup, J. Catal. 109 (1988) 241.

[32] R.T. Yang, J.P. Chen, J. Catal. 115 (1989) 52.
[33] F.C. Schouten, E.W. Kaleveld, G.A. Bootsma, Surf. Sci. 63 (1977) 460.
[34] F.C. Schouten, O.L. Gijzeman, G.A. Bootsma, Surf. Sci. 87 (1979) 1.
[35] A. Roberti, V. Ponec, W.M.H. Sachtler, J. Catal. 28 (1973) 381.
[36] V. Ponec, Appl. Catal. A 222 (2001) 31.
[37] N.D. Lang, H. Ehreneich, Phys. Rev. 168 (1968) 605.
[38] J.R. Anderson, Structure of Metallic Catalysts, Academic Press, London, 1975.
[39] J.R. Rostrup-Nielsen, J. Catal. 31 (1973) 173.
[40] T.S. Cale, J.T. Richardson, J. Catal. 79 (1983) 378.
[41] J.H. Sinfelt, Bimetallic Catalysts, Discoveries, Concepts and Applications, Wiley, New York, 1983, p. 25.
[42] A. Frennet, Catal. Rev. Sci. Eng. 10 (1974) 1.

Eurasian ChemTech Journal 5 (2003) 19-27

Adsorption Methods of Hydrogen and Methane Storage for the Fuel Cell Application

Z.R. Ismagilov[1*], V.B. Fenelonov[1], A.V. Krechetova[1], A.Yu. Derevyankin[1], L.B. Avdeeva[1], T.V. Reshetenko[1], Ch.N. Barnakov[2], A.P. Kozlov[2], S.K. Seit-Ablaeva[3], V.V. Chesnokov[1], V.N. Parmon[1]

[1]Boreskov Institute of Catalysis SB RAS, Novosibirsk,
[2]Institute of Carbon and Chemistry of Carbon SB RAS, Kemerovo,
[3]Kemerovo Technological Institute of Food Industry

Abstract

Adsorption of H_2 and CH_4 was performed at a pressure of to 100 atm on the samples of catalytic filamentous carbon (CFC) and supermicroporous active carbon (SAC) with a surface area ca. 3000 m^2/g. It is shown that H_2 is better sorbed on the CFC than on the SAC, while the opposite is observed for the CH_4 adsorption. The high values of H_2 sorption on the CFC (to 25-35 mg H_2/g carbon) with a surface area of 100-300 m^2/g is explained by hydrogen intercalation between the graphite-like CFC layers. Thus, it is worthwhile investigating the possibility of hydrogen and methane storage on the carbon porous materials.

Introduction

At the moment, a huge attention is devoted to the problem of switching the vehicles to the fuel cell (**FC**) powered electric engines, which generate the electric energy by means of the electrochemical oxidation of hydrogen by oxygen from the air [1-4]. Such switching allows both to solve the environmental problems and to sharply increase the engine efficiency, which in the case of **FC** is not limited by the Carnot cycle [1]. However, the **FC** introduction is strongly slowed down by the problems of hydrogen storage or its generation from the suitable sources on board of the vehicle [2-9]. Fueling the automobile with compressed or liquid hydrogen or other gas is additionally complicated by the necessity to create the new infrastructure of fuel dispensing instead of the existing gasoline pump stations. Due to these reasons, many leaders of this direction are considering as the main source of hydrogen the liquid fuel, mostly methanol, despite the complexity of the on-board hydrogen production [2-4]. But all the carbon from the carbon-containing fuel is eventually emitted as CO_2, which decreases the environmental compatibility of such **FC**. Therefore, solving the task of on-board hydrogen storage is still important.

*corresponding author. E-mail: zri@catalysis.nsk.su

In 1998-1999, the Journal of Physical Chemistry has published two works of Rodriguez et al. [8,9], which attracted specific attention to the carbon fibers, obtained upon catalyzed decomposition of carbon-containing gases and their mixtures over Ni, Fe, Co and their alloys. The authors of [8] reported the exotic values of H_2 adsorption upon the exposure of such fibers to H_2 at 120 atm and 25°C. The values of *reversible desorption* when the pressure was lowered to atmospheric without any heating were reaching 1.5-2.0 g H_2/g carbon, which corresponds to the sorption of 10-12 H_2 molecules per one carbon atom. In the second communication [9], are presented somewhat more modest values of reversible sorption – up to 4 molecules H_2/atom C, which still exceeds twice the H/C atomic ratio in CH_4 and corresponds to the sorption of 0.4 g H_2/g C. But these values have not been confirmed by other authors and were subject to the strict critics [7,10-14].

The carbon fibers used in [8,9] have a long history [15,16], and were studied many times from the different viewpoints, see, for example, [17-23]. In the literature they are called graphite nanofibers (GNF) [8,9], carbon nanofibers (CNF) [10,23], vapor-grown carbon fibers (VGCF) [7], carbon nano-

tubes (CNT) [24] etc. But by the mechanism of formation and structure such fibers are significantly different from, for example, carbon fibers obtained from polymers or coke chemical pitch, which can also have nanosizes and be graphitized. They are even more different from the popular single-walled nanotubes (SWNT). Therefore, in order to avoid confusion, we prefer to call them *catalytic filamentous carbon* (CFC) [21,22], implying under CFC the fibers which are formed as a result of catalytic decomposition of a precursor hydrocarbon on the active face of catalyst metal nanoparticle, diffusion of the carbon through this particle and its yield on the face, which is coherent to the graphite structure [22].

In the Boreskov Institute of Catalysis were conducted the detailed studies of molecular and supramolecular structure (texture) of CFC, obtained via the methane decomposition over Ni and Ni-Cu catalysts at 823-848 K, see, for example, [21,22,25,26]. It was shown, that the graphite planes (graphenes) stacking arrangement near the surface of studied CFC is substantially different from their stacking in the bulk of filament, because graphenes on the surface tend to be parallel to the filament axis. According to the data of high resolution transmission electron microscopy (HRTEM) and scanning tunnelling microscopy (STM) [21,22], the surface of CFC having the herringbone bulk structure (further – type **I**) is covered by the steps and terraces formed from the graphenes. In its turn, the surface of CFC having the plateled bulk structure (further – type **II**) is covered by the curved "closed layers" or "caps". It is interesting to note, that the filamentss with herringbone bulk structure, formed over the Ni catalysts, have the "fish-skin"-like coverage, while CFC with plateled bulk structure and characteristic macroscopic octopus morphology, obtained over the Ni-Cu catalysts, are covered by the numerous "suckers" [22]. Such surface structure of the filaments is governed not by the special conditions of their synthesis, but by the general thermodynamic tendency to minimize the surface energy. Indeed, according to Abramson [27] the surface enthalpy of the open edge planes is almost 40 times higher in comparison with that of the basal plane of graphite (*ca.* 6.1 and 0.155 Jm^{-2}, respectively [27]). Such screening of the open edge planes occurs spontaneously and is confirmed by the numerical calculations using the molecular dynamics methods [28].

This is the reason why the surface structure of the filaments must be different from their bulk structure and tentatively (as it was shown experimentally) only a small part of the filament external surface could be represented by the open graphene edges. According to [22], the surface not covered by graphenes constitutes only 2÷7% of the total external surface of the filaments. This part of the surface can be envisaged as a deck of playing cards with non-aligned edges. The spaces between the next-neighbor graphene layers with different length are forming the slit-like micropores, which have the uniform size *ca.* 0.34 nm. This size was experimentally measured by the new gas-chromatographic molecular probe method, using the halogenated benzene derivatives as the molecular probes [26]. The total volume of such micropores is extremely small, its measurements by means of the adsorption of nitrogen at 77 K or of benzene and heptane at 298 K give the values of about ~0.01 ml/g or $2\div6\bullet10^{-5}$ ml/m^2 of the external surface of filaments of the type **I** or **II** [22]. According to the secondary ion mass spectrometry (SIMS) data, the depth of defect zone, corresponding to the length of micropores, expanded for 1÷2 nm into the bulk of filaments [25]. At the same time, the external surface of filaments, calculated after the filling of micropores, reaches ~100 m^2/g for the type **I** and ~300 m^2/g for the type **II** [22].

Rodriguez et al. [8,9] explain the anomalously high values of H_2 sorption in such filaments by its intercalation in the molecular form between the graphene layers, which are held together by the weak van der Waals bonds. In the authors opinion, that the key moment of such intercalation is in the fact, that "kinetic" diameter of the hydrogen molecule (0.289 nm) has a value slightly smaller than that of the interlayer spacing in graphite and turbostrate graphite-like materials (0.335÷0.350 nm). The authors suppose, that as a result of nonrigidity such system can expand to accommodate hydrogen in multilayer configuration [8]. However, though the size of intercalated component is important, it is by far not the determining parameter of intercalation [29,30]. The most important is electron exchange between the "guest" (intercalate) and "host" (carbon), where carbon can be both the donor and the acceptor of electrons [29]. Thus, for example, the large complex PtF_6^- is intercalated easily enough (in this case, graphite is the acceptor), and the relatively large cations of cesium and rubidium are intercalated substantially easier than the small ions of lithium and sodium with lower electronegativity [29]. In the graphite/hydrogen system, the difference in electronegativities is

small, and therefore the possibility of hydrogen intercalation into the graphite and graphite-like systems is under discussion. Still, the defective structure and the mosaic pattern of carbon filaments allow to make various assumptions, though the possibility of *multilayer* intercalation of hydrogen seems to be even more doubtful.

Given in the literature data on the H_2 sorption on CFC at the ambient temperature are rather controversial, which can be caused by the structural features of CFC, methods of the sample pre-treatment, and also incorrect measurements due to the existence of small leakage, mistakes in the calculation of reversible sorption values, etc. Such controversies also remain upon the studies of CFC, obtained and pre-treated in the regimes, recommended by Rodriguez et al. [8,9]. For instance, according to Gupta and Strivastava, the CFC prepared from ethylene at ~600°C over the Cu/Ni catalysts have the hydrogen storage capacity of 10÷15 wt.% at the pressure of ~90 atm [31] (however, it should be noted that these CFC could contain a rather significant amount of Ni, which was used as a catalyst; therefore part of the sorption can be assigned to the formation of hydride NiH_3). On the other hand, according to Poirier et al. [14], the CFC produced from acetylene or ethylene over the Ni or Cu/Ni catalysts at the same hydrogen pressure demonstrated the storage capacity of only ~0.7 wt.%. It is remarkable, that upon the same hydrogen pressure of 10.5 MPa the identical capacity was shown by supermicroporous AX-21 [14]. The latter one has the surface area *ca.* 3000 m^2/g and possesses, in the opinion of Dubinin [32], a very highly developed micropore volume (~1.5 ml/g). The CFC with the same hydrogen storage capacity had the surface area value of *ca.* 290 m^2/g and, apparently, was the analogue of CFC, studied in [22], which were obtained over the Cu/Ni catalysts of the same composition and had the identical value of surface area. But in this case the huge difference in the specific adsorption values, referred to the surface area, can be regarded as a proof of intercalation effect in CFC, studied in [14].

The objective of this work is to examine the presence of hydrogen intercalation in CFC at the ambient temperature and increased pressures. In order to do this, we had previously conducted comparative studies of the hydrogen adsorption at the ambient temperature on some samples of CFC with different textural characteristics, synthesized in the Boreskov Institute of Catalysis. The same conditions were used to study the sorption of hydrogen on a number of microporous carbon sorbents with the amorphous structure, synthesized from the oil coke in the Institute of Carbon and Carbon Chemistry. The choice of the latter ones as a reference materials is conditioned by the fact, that all of them are obtained from the same precursor, have the amorphous structure with the texture varied in a wide range, and the samples with the maximum value of surface area (~3000 m^2/g) are the analogues of AX-21 (Amoco) or AX-31M (Anderson Development Co.) [33], which have been thoroughly studied in many works, for example, [14, 32-36]. As an additional reference in the same conditions was studied the adsorption of methane, which is also considered as a potentially perspective type of fuel for the hydrogen generation [2,3], and its sorption has been investigated in many works [32-38].

Experimental

The extensive series of CFC samples were prepared via the decomposition of methane, ethylene, divinyl and hydrogen mixtures over the selected supported metal catalysts at the temperatures between 500 and 600°C. Further are discussed the results, obtained using the typical representatives of this series, which illustrate the diversity of properties of the obtained CFC. The composition of metal component of the catalysts employed is given in the name of each sample. The catalyst composition, hydrocarbons used as the CFC precursors and the synthesis temperature are listed in Table 1, which also includes the main textural characteristics of CFC. The procedures of catalyst preparation and characteristics of the CFC are described more thoroughly in the previous publications [20-22].

The microporous carbons for the reference series were prepared from the oil coke using the different regimes of thermochemical activation. Their synthesis and properties will be described in more detail in a separate communication.

The standard textural characteristics of all the carbon materials were determined by the nitrogen adsorption isotherms at 77 K, which have been measured using the instrument ASAP-2400 Micrometrics. These characteristics included the values of surface area A_{BET}, the volume of micropores $\mathbf{V}_\mu$, the total area of meso- and macropores $\mathbf{A}_\alpha$ remaining after the filling of micropores, the total volume of micro- and mesopores (with characteristic sizes up to ~100 nm) $\mathbf{V}_\Sigma$. The A_{BET} was determined by the

Table 1

Conditions of synthesis of the typical CFC and their main textural characteristics

No	Conditions of CFC synthesis			CFC textural characteristics		
	Catalyst	Hydrocarbon	T, °C	A_{BET}, m^2/g	V_Σ, cm^3/g	V_μ, cm^3/g
1	70 wt.% Ni + 30 wt.% Cu	ethylene	600	243.6	0.19	0.041
2	82 wt.% Ni + 8 wt.% Cu/Al_2O_3	methane	550	203.9	0.55	0.012
3	85 wt.% Fe/Al_2O_3	methane	625	103.1	0.44	0.005
4	90 wt.% Ni/MgO	methane	550	88.4	0.15	0.006
5	Fe:Ni:Cu = 12:7:1	ethylene	600	133.7	0.15	0.026
6	Ni-100-1	divinyl	550	139	-	0.002
7	Ni-100-2	divinyl	550	366	-	0.010
8	Ni-100-3	divinyl	500	250	-	-

standard procedure [39] for the BET method. The $\mathbf{V}_\mu$ and $\mathbf{A}_\alpha$ were calculated using the comparative method [36] (modification of the more known α_S-method by Sing [39]), the related calculations routine is considered in detail in [41]. The $\mathbf{V}_\Sigma$ was determined by the limiting value of nitrogen adsorption at the relative pressure of $P/P_0 = 0.98$ [39].

The adsorption of hydrogen and methane was measured in the statical volumetric high pressure setup, the scheme of which is shown in Fig. 1. The setup is made of stainless steel and includes electric solenoid high pressure valves, the ampoule-adsorber for the sample with volume of $\mathbf{V}_0$, reference volume $\mathbf{V}_R$ between the valves 1 and 2, electric pressure gauge; it is connected with the cylinders containing helium and hydrogen or methane, vacuum pump, the line of atmospheric air admission, and also with the system of measurement of the amount of gas evolving during the desorption.

The volume of ampoule $\mathbf{V}_0$, reference volume $\mathbf{V}_R$

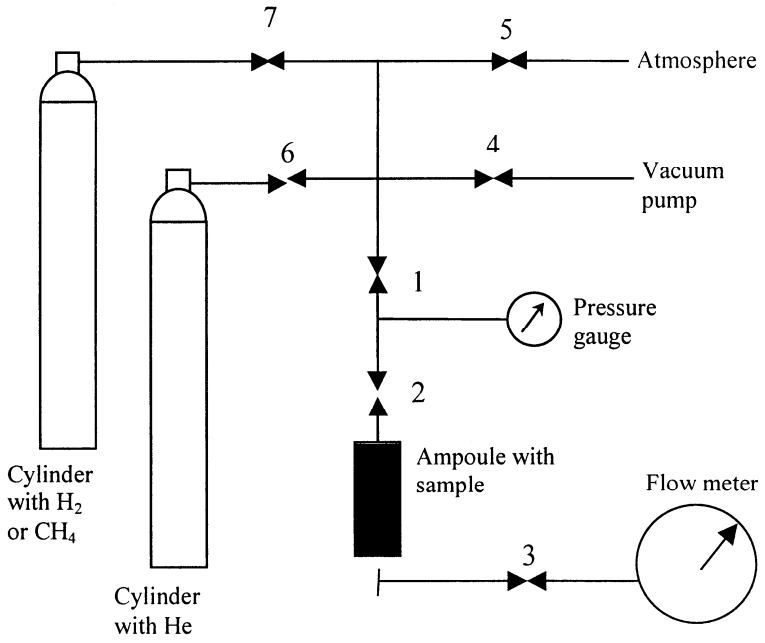

Fig. 1. Scheme of the laboratory setup for the measurement of hydrogen and methane sorption at the pressures up to 100-200 atm.

and the free volume of ampoule V_{0A}, remaining after the loading of sample, were determined via the calibration by He, which was considered as a non-sorbing gas. Two ampoules were used, with the V_0 volumes of 6.15 cm^3 and 15.10 cm^3, respectively, and V_R = 18.57 cm^3. In order to measure the sorption of hydrogen or methane, the system was first evacuated, then a dose of adsorbate at the pressure of P_1 was introduced into the reference volume V_R, after which the valve 1 was opened and the equilibrium pressure P_2 was established within 0.5-3 hours. The moment of equilibrium pressure establishment was registered by the termination of pressure change by more than 1% within 0.5 hour. The equilibrium value of sorption a_e at the pressure P_2 was calculated from the balance equation

$$P_1V_R/RT = P_2(V_R + V_{0A})/RT + a_em \quad (1)$$

where **R** – universal gas constant, **T** – absolute temperature, **m** – adsorbent loading. Activation (pretreatment) of the samples was conducted at 300°C under vacuum in a separate unit, after which the sample was weighted and loaded into the ampoule. The measurements were performed in the P_1 pressure range up to 100÷120 atm using either the regime of stepwise P_1 values increase, or the desorption by means of lowering the pressure to atmospheric and measuring the amount of evolved gas.

All the measurements were conducted upon the maximum filling of ampoule volume by the adsorbent in the form of powder or fraction of 2÷3 mm, which corresponded to the loadings of several grams.

Results and Discussion

Summary of the main results of studying the reference microporous samples of active carbon is presented in Table 2: here are given the main textural characteristics and the sorption values of hydrogen (pressure 70-90 atm) and methane (pressure 30-40 atm) at the ambient temperature.

The surface area of studied reference samples was varied in the range of 400÷3400 m^2/g, the micropore volume – in the range of 0.2÷1.12 cm^3/g. Among them most interesting are the samples with surface area over 3000 m^2/g, for which the area of mesopores, remaining after the micropores are filled, constituted 5-7% of the total surface area, and 60÷70% of the total pore volume belonged to the micropores. Presented rough estimate of the average micropore size as $H = 2V_\mu/\Delta A$, where $\Delta A = A_{BET} - A_\alpha$, gives the values of **H** ~0.70÷0.75 nm. Evaluation using the DR equations of the theory of micropore volume filling [42-44] gives the values of **H** ~1.0÷1.1 nm.

The values of total surface area and volume of micropores for the samples AC-1, AC-2 and AC-3 are very close to those values, which are usually given in literature for the supermicroporous AX-21 (same as Amoco PX-21, later known as Anderson AX-21 and now made by Kansai under license from Amoco and marketed as Maxsorb [33]). Cook et al. [33] have recently made the survey of works, where this unique adsorbent is used for the methane storage. According to this survey, the typical value of total surface area, measured in different works, is ~2800÷3200 m^2/g, and the micropore volume ~1.1÷1.2 cm^3/g. Therefore, one can expect, that porous structure of the samples with surface area above 3000 m^2/g, presented in Table 2, is similar to the structure of AX-21. This is also confirmed by the close values of hydrogen and methane sorption on these samples and AX-21. For instance, according to the survey [33],

Table 2

Results of study of the reference microporous samples of active carbon

Sample	Surface area, m^2/g		Micropore size H*, nm	Pore volume, cm^3/g		Adsorption, mg/g	
	BET method, A_{BET}	Mesopores, A_α		Micropores, V_μ	Total, V_Σ	H_2	CH_4
AC-1	3195.7	168.1	0.74	1.12	1.62	6.0	158
AC-2	3349.3	256.4	0.71	1.10	1.84	8.0	107
AC-3	3100.6	143.7	0.73	1.08	1.55	6.6	128
AC-4	864.0	132.6	1.07	0.39	0.44	5.4	6.0
AC-5	1404.2	238.7	1.11	0.65	0.81	4.5	7.8
AC-6	449.7	13.3	0.96	0.21	0.23	7.0	5.2

* The size of micropores **H** was evaluated using the relationship $H = 2V_\mu/\Delta A$ where $\Delta A = A_{BET} - A_\alpha$, which corresponds to the slit shape pores [39].

the data of different authors show, that the values of CH_4 sorption at 3.4 MPa and 298 K vary in the range of 130÷160 mg/g, which matches well the data listed in Table 2. According to [14], in the conditions studied by us AX-21 sorbs ~7 mg H_2/g, and the similar values are obtained if the data are extrapolated [34]. These values are also corresponding to those listed in Table 2. In the whole, these results confirm the substantial reliability of the measurement methods used by us.

Now let us consider the results of hydrogen sorption study in the same conditions on the CFC samples. In this case, the sorption of methane did not exceed 1-2 mg/g, that is it was close to the measurement accuracy, and therefore these data are not shown. Summary of the main results of hydrogen adsorption measurements is presented in Table 3.

From Table 3 it can be seen, that on the different samples H_2 sorption varies in a wide range – from 3-6 mg/g to 35 mg/g. The obtained limiting values of H_2 sorption are much lower than those presented in the works of Rodriguez et al. [8,9] and Gupta et al. [31], but are much higher than obtained in the works [7,10-14]. Note that these results disprove the opinion of Tibbetts et al. about the impossibility of achieving the values of adsorption over 10 mg/g on the carbon materials without deep cooling [7]. Our measurements of H_2 sorption on CFC and AC, employed as the references, are conducted in the identical conditions. The data for references are in good agreement with the results of other authors, which supports the reliability of results obtained for CFC.
From the comparison of data in Tables 2 and 3 it follows, that adsorption of H_2 on the samples CFC 1,5,6,7, which have the surface area in the range of 130-360 m^2/g, is 3-5 times greater than on the samples of supermicroporous active carbon AC, which have the surface area over 3000 m^2/g (see Table 2). This effect can not be explained by the adsorption in the micropores of CFC, the volume of which is negligibly small. We assume, that here the only possible explanation is associated with the intercalation effect.

Dresselhaus et al. [45,46] carried out solely geometrical estimates of the limiting hydrogen sorption on the surface of graphite basal face. We will use the similar approach in order to calculate the limiting intercalation capabilities of molecular hydrogen. According to the modern concepts of the structure of intercalated graphite compounds [29], the intercalate **G** ("guest") is located precisely in the "hollows" between the carbon atoms of the neighboring layers, that is in the centers of opposite hexagons C_6 with vertexes at the carbon atoms. This provides maximum interaction between the intercalate and carbon, but requires the displacement of graphene layers with the transition from sequence **ABABAB** to **AGAGA**. Fig. 2 gives the examples of some configurations, which can be formed in the basal plane. The densiest structure of the $\mathbf{GC_2}$ type is shown, where one "guest" molecule accounts for the two carbon atoms (Fig. 2 b,c), as well as the loose structure of the $\mathbf{GC_6}$ type, where one "guest" molecule accounts for the six carbon atoms (Fig. 2 d,e). Also the structures of $\mathbf{GC_3}$, $\mathbf{GC_4}$, etc. types are possible [29]. The type of structure formed depends on the geometric relationships between the sizes of H_2 molecule and hexagon, and the interactions of **GG** and **AGA** types.

Into the hexagon with the edge size of 0.1415 nm,

Table 3
Adsorption of hydrogen at the ambient temperature and pressure of 70-90 atm

No	Sample	H_2 adsorption, mg/g	H_2 desorption, mg/g
1	CFC (70 wt.% Ni + 30 wt.% Cu)	20.0	20.0
2	CFC (82 wt.% Ni + 8 wt.% Cu/Al_2O_3)	2.1	-
3	CFC (85 wt.% Fe/Al_2O_3)	8.0	-
4	CFC (90 wt.% Ni/MgO)	2.7	2.7
5	CFC (Fe12Ni7Cu1)	24.5	24.5
6	CFC (Ni-100-1)	26.1	-
7	CFC (Ni-100-2)	35.4	27.5
8	CFC (Ni-100-3)	4.3	4.3

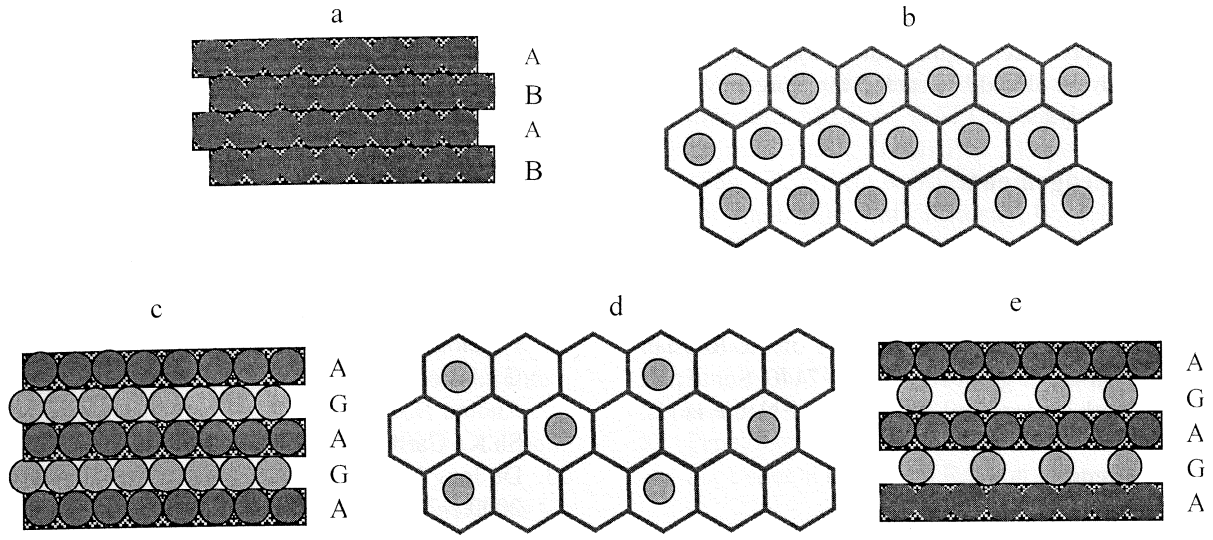

Fig. 2. Models of the molecular hydrogen placement upon intercalation: **a** – initial graphite structure, **b** and **c** – intercalated structure of the GC_2 type, **d** and **e** – intercalated structure of the GC_6 type; **b** and **d** – view in the basal plane, **c** and **e** – view in the direction normal to the basal plane.

equal to the distance between carbon atoms in graphene, can be inscribed the circle with the diameter 0.245 nm. In the calculations of Dresselhaus et al. [45,46] is used the "kinetic" diameter of H_2, equal 0.29 nm. This size corresponds to the Lennard-Jones diameter, which value, according to the different estimates, can vary in the range of 0.291-0.287 nm [47,48]. Such model molecule does not fit into the hexagon C_6 and allows to obtain only the loose packing of the GC_6 type (see Fig. 2 d,e) with the calculated sorption capacity of 28 mg H_2/g C. Exactly this sorption value is given in [45,46]. In addition, the authors of [45,46] evaluated the maximal sorption of H_2 for the situation, when the placement of hydrogen molecules on the surface of graphite basal planes is not correlated with the location of carbon atoms. For the random dense packing of the molecular hydrogen with effective diameter of 0.29 nm, the maximal sorption value obtained was 42.7 mg H_2/g C.

However, in reality the hydrogen molecule is not a sphere, but a *configuration of two spheres*. The minimum and maximum van der Waals dimensions of this molecule are, respectively, 0.24 and 0.31 nm [47-50], and according to [51] its characteristic van der Waals diameter is 0.240 nm. Packing of the molecules with diameter of 0.24 nm allows formation of the GC_2 type structure, shown in Fig. 2 b,c, to which corresponds the atomic ratio H/C (which also is the limiting sorption value) of 83.9 mg/g. This value exceeds, for example, the stoichiometric capacity of MgH_2 and looks substantial for the usage of such carbon sorbents in the systems of hydrogen storage for the **FC** powered vehicle engines [52].

Therefore, the experimental values of hydrogen sorption on CFC, obtained in the present work, are within the margins admissible if the intercalation exists. Upon all the other conditions being the same, the extent of usage of the limiting intercalation capabilities should significantly depend on the features of molecular and supramolecular structure of the particular carbon material. These features determine the key, in our opinion, intercalation conditions: lability and electronic properties. The importance of individual electronic properties is caused by the fact, that intercalation is associated with electron exchange interaction between the "guest" and the "host" (see [29,52] for more details). The lability of structure, providing the structural transformations necessary for intercalation, is determined, in its turn, by the extent of binding the neighboring graphenes via the covalent bond bridges, by the sizes and packing defectiveness of graphene aggregates [52]. Exactly these features can explain the difference in sorption properties of the studied CFC of different origin.

In order to explain the anomalously high values of hydrogen sorption, which are reported in the works [8,9,31], from our viewpoint it is necessary to admit the possibility of existence of multilayer intercalation of hydrogen – these problems are discussed in more detail in [52]. But, in any case, intercalation of

hydrogen into CFC at the ambient temperature and increased pressures requires more systematic studies, which are already started in the Boreskov Institute of Catalysis.

Acknowledgements

The authors are grateful for financial supply of the Russian Fund of Fundamental Investigations, Grants No 00-03-32431 and works within the framework of leading scientific schools of the Russian Federation under grant No 00-15-97440. Some part of this work is supported by NWO, The Netherlands.

References

1. Carrette L., Friedrich K.A., Stimming U., Fuell Cells, 2001, 1, 5.
2. Brown L.F., Int. J. Hydrogen Energy, 2001, 26, 381.
3. Pettersson L.J., Westerholm R., Int. J. Hydrogen Energy, 2001, 26, 243.
4. Progress Report for Fuel Cell Power Systems, U.S. Department of Energy, Washington, DC, October 2000.
5. Hynek S., Fuller W., Bentley J., Int. J. Hydrogen Energy, 1997, 22, 601.
6. Cheng H.-M., Yang Q.-H., Liu C., Carbon, 2001, 39, 1447.
7. Tibbetts G.G., Meisner G.P., Olk C.H., Carbon, 2001, 39, 2291.
8. Chambers A., Park C., Baker R. T.K., Rodriguez N.M., J. Phys. Chem. B, 1998 102 4253.
9. Park C., Anderson P.E., Chambers A., Tan C.D., Hidalgo R., Rodriguez N.M., J. Phys. Chem. B, 1999, 102, 10572.
10. Wang Q., Johnson, J.K., J. Phys. Chem. B, 1999, 103, 277; J. Chem. Phys., 1999, 110, 577.
11. Ahn C.C., Ye Y., Ratnakumar B.P., Witham C., Bowman R.C., Fultz B., Appl. Phys. Lett., 1998, 73, 3378.
12. Pinkerton F.E., Wicke B.G., Olk C.H., Tibbetts G.G., Meisner G.P., Meyer M.S., Herbst J.F., J. Phys. Chem. B, 2000, 104, 9460.
13. Yang R.T., Carbon, 2000, 38, 623.
14. Poirier E., Chahine R., Bose T.K., Int. J. Hydrogen Energy, 2001, 26, 831.
15. Hughes T.V., Chambers C.R., U.S. Patent 405480, 1989.
16. Schultzenberger P.L., C. R. Acad. Sci., Paris, 1990, 111, 174.
17. Kim M.S., Rodriguez N.M., Baker R.T.K., J. Catal., 1991, 131, 60.
18. Tibbets G.G., Devour M.G., Rodda E.I., Carbon, 1987, 25, 367.
19. Rostrup-Mielson J.R., Trimm D.L., J. Catal., 1977, 48, 155.
20. Zaikovskii V.I., Chesnokov V.V., Buyanov R.A., Appl. Catal. A, 1988, 38, 41
21. Shaikhutdinov Sh.K., Zaikovskii V.I., Avdeeva L.B., Appl. Catal. A, 1996, 148, 123.
22. Fenelonov V.B., Derevyankin A.Yu., Okkel L. G., Avdeeva L.B., Zaikovskii V.I., Salanov A.N., Rudina N.A., Likholobov V.A., Shaikhutdinov Sh.K., Carbon, 1997, 35, 1129.
23. De Jong K.P., Geus J.W., Catal. Rev. Sci. Eng., 2000, 42, 481.
24. Fasle Kibria A.K.M., Mo Y.H., Park K.S., Nahm K.S., Yun M.H., Int. J. Hydrogen Energy, 2001, 26, 823.
25. Ivanov V.P., Fenelonov V.B., Avdeeva L.B., Goncharova O.V., React. Kinet. Catal. Lett., 1994, 53, 197.
26. Fenelonov V.B., Melgunov M.S., Baronskaya N. A., React. Kinet. Catal. Lett., 1998, 63, 305.
27. Abramson J., Carbon, 1973, 11, 337.
28. Vorpagel E.R., Lavin J.G., Carbon, 1992, 30, 1033.
29. Okino F., Touhara H., in: Comprehensive Supermolecular Chemistry, Atwood S.L., MacNicol D. D., Davies S. E. D., Vogtle F., Lehn S.-M. (Eds.), Pergamon Press, New York, 1996, vol. 7, p. 25.
30. Zabel H, Solin S.A. (Eds.), Graphite Intercalation Compounds I (II), Springer Ser. Mater. Sci. 14 (18), Springer, Berlin, 1990 (1992).
31. Gupta B.K., Strivastava, Int. J. Hydrogen Energy, 2000, 25, 825; 2001, 26, 857.
32. Dubinin M.M., Kadlec O., Kataeva L.N., Onysaitis B.A., Russ. Chem. Bull., 1988, 5, 977.
33. Cook T.L., Komodromos C., Quinn D.F., Ragan S, in: Carbon Materials for Advanced Technologies, Burchell T.D. (Ed.), Pergamon Press, Amsterdam, 1999, p. 269.
34. Bénard P., Chahine R., Langmuir, 2001, 17, 1950; Int. J. Hydrogen Energy, 2001, 26, 849.
35. Zhou L, Zhou Y., Li M., Chen P., Wang Y, Langmuir, 2000, 16, 5955.
36. Sircar S., Golden T.C., Rao M.B., Carbon, 1996, 34, 1.
37. Chen X.S., McEnaney B., Mays T.J., Alcaniz-Monge J., Carbon, 1997, 35, 1251.

38. Milewska-Duda J., Duda J., NodzeHski A., Lakatos J., Langmuir, 2000, 16, 5458.
39. Gregg S.J., Sing K.S. W., Adsorption, Surface Area and Porosity, 2nd ed., Academic Press, London, 1982.
40. Karnaukhov A.P., Fenelonov V.B., Gavrilov V. Yu., Pure & Appl. Chem., 1989, 61, 1913.
41. Fenelonov V.B., Romannikov V.N., Derevyankin A.Yu., Micropor. Mesopor. Mater., 1999, 28, 57.
42. Dubinin M.M. Carbon, 1981, 19, 321; 1982, 20, 195; 1983, 21, 359; 1985, 23, 373.
43. Dubinin M.M., Stoeckli H.F., J. Colloid. Interface Sci., 1980, 75, 34.
44. Bansal R.C., Donnet J.-B., Active Carbon, Marcel Dekker, New York, 1988.
45. Brown S.D. M., Dresselhaus G., Dresselhaus M. S., MRS Symp. Proc., 1998, 497, 157.
46. Dresselhaus M.S., Williams K.A., Eklund P.C., MRS Bull., 1999, 24, 45.
47. Girschfelder I.O., Kertis K.F., Berd R.B., Molecular theory of gases and liquids, Inostrannaya literatura, Moscow, 1961 (in Russian).
48. Zefirov Yu.V., Zorkii P.M., Uspekhi khimii, 1989, 68, 713 (in Russian).
49. Pauling L., General Chemistry, W. H. Freeman, San Francisco, 1970.
50. Nekrasov B.V., Fundamentals of general chemistry, vol. 1, Moscow, Khimiya, 1973, 595 p. (in Russian).
51. Emsley J., The Elements, Clarendon Press, Oxford, 1991.
52. Fenelonov V.B., Derevyankin A.Yu., Parmon V. N., Uspekhi khimii (in Russian), in press.

Received 24 September 2002.

Available online at www.sciencedirect.com
SCIENCE DIRECT
Catalysis Today 102–103 (2005) 58–66
CATALYSIS TODAY
www.elsevier.com/locate/cattod

Development of active catalysts for low Pt loading cathodes of PEMFC by surface tailoring of nanocarbon materials

Z.R. Ismagilov [a,*], M.A. Kerzhentsev [a], N.V. Shikina [a], A.S. Lisitsyn [a], L.B. Okhlopkova [a], Ch.N. Barnakov [b], Masao Sakashita [c], Takashi Iijima [d], Kenichiro Tadokoro [d]

[a] *Boreskov Institute of Catalysis, Prospekt Akademika Lavrentieva 5, Novosibirsk 630090, Russia*
[b] *Institute of Coal and Coal Chemistry, Kemerovo 650616, Russia*
[c] *JATIS, Sogo-kojimachi No. 3 Building, 1-6 Kojimachi, Chiyoda-ku, Tokyo 102-0086, Japan*
[d] *Nippon Steel Corporation, 20-1 Shintomi, Futtsu, Chiba 293-8511, Japan*

Available online 22 April 2005

Abstract

The use of novel nanocarbon supports—carbon nanofibers (CNF) and amorphous supermicroporous carbons (ASC) for synthesis of platinum cathode catalysts for proton exchange membrane fuel cells (PEMFC) was investigated. Different types of CNF—with ''parallel'' and ''deck of cards'' arrangement of graphitic planes and samples of ASC originating from different organic precursors were synthesized and characterized by XRD, electron microscopy and adsorption methods. Platinum catalysts for PEMFC cathodes on different structural types of CNF and one sample of ASC were synthesized and characterized by XRD, electron microscopy, CO adsorption and by studying characteristics of conventional membrane electrode assembly (MEA) cell with a low Pt loading level of 0.02–0.09 mg/cm^2. The MEA testing showed that the Pt cathode catalysts on CNF exhibit inferior performance in comparison with a catalyst on conventional carbon black support Pt/Vulcan XC-72R. The cathode catalyst prepared on ASC support exhibits considerably better output in MEA, compared with Pt/Vulcan XC-72R even at a lower Pt loading.

Keywords: Nanocarbon; PEMFC; Carbon nanofiber; CNF; Cathode; Catalyst; Platinum; Low loading; Supermicroporous carbon

1. Introduction

To achieve uniform and highly dispersed Pt loadings, the proton exchange membrane fuel cell (PEMFC) cathode catalysts are usually supported on carbon supports with a high surface area—over 75 m^2/g. Common supports are carbon blacks with a high degree of graphitic character: Vulcan XC-72R, Black Pearls BP 2000, Ketjen Black, etc. The support material must provide a high electric conductivity and high and uniform catalyst dispersion, give good reactant gas access to the catalyst and have good corrosion resistance. On the whole, the conventional carbon black supports satisfy these requirements [1].

Recent publications show that, in order to increase the efficiency of cathode catalysts, novel non-conventional materials are proposed as supports for Pt. The examples are supports produced from aerogel nanocarbon [2], nanofibers of organic pigments [3], carbonized micro-cellular polymer materials [4].

The use of novel supports allow increase of catalyst activity, decrease of electrode thickness and reduction of Pt content in cathode to values of ca. 0.1 mg/cm^2, thus increasing the electrode efficiency and minimizing its cost.

The cost-effective use of PEMFC is possible if the content of Pt in PEMFC, primarily in cathode, is substantially reduced. The target is to achieve Pt loading in cathode 0.02 mg/cm^2.

The Pt content in cathode can be reduced by increasing the catalyst activity, which can be accomplished by surface tailoring of carbon support material resulting in high and uniform concentration of supported Pt particles with a size of 2–3 nm, preferably ca. 2 nm. Using such active cathode catalysts, smaller thickness of cathode can be attained. Thus,

* Corresponding author. Tel.: +7 3832 341219; fax: +7 3832 397352.
E-mail address: ZRI@catalysis.nsk.su (Z.R. Ismagilov).

0920-5861/$ – see front matter © 2005 Published by Elsevier B.V.
doi:10.1016/j.cattod.2005.02.007

the approach for preparation of low Pt loading cathodes consists in the use of active catalysts on new carbon supports, so that the electrocatalyst layer can be made very thin—ca. 1 μm and the Pt content per electrode area can be decreased by an order of magnitude to values 0.02–0.05 mg/cm^2. The decrease of the electrode thickness is beneficial also because it increases fuel cell efficiency by easier oxygen diffusion into the electrode and easier water removal.

The dispersion of platinum, catalytic activity and efficiency of platinum electrocatalysts presumably depends on the structure of the carbon support. Conventional supports—carbon blacks have predominantly basal graphite planes on their surface, resulting in weak interaction with supported platinum. This leads to the formation of relatively large globular platinum particles, subject to sintering (increase in particle size). We propose to use carbon nanofibers (CNF) as supports for platinum cathode catalysts, because these materials have different structure—namely, regular arrangement of graphite planes with their edges forming the outer surface of the fibers. These edges may serve as suitable sites for the stabilization of small platinum particles. In addition regular arrangement of such sites can provide more uniform distribution of platinum particles on the surface.

During the past decades, CNF have attracted ever-increasing interest of scientists and technologists. The family of CNF encompasses novel materials produced by the decomposition of hydrocarbons over 3d-metal catalysts [5–16]. Catalytically grown CNF was the subject of numerous studies (see, for example, the works by Baker and co-workers [5–7], Rosrtup-Nielsen and co-workers [8,9], Geus and co-workers [10–13] and our publications [14–17]) due to its unique structure and properties. This kind of carbon is suggested to be used for the structural reinforcement applications [18], adsorbent [19] and as a catalyst support [20–27].

The use of CNF as catalyst support in comparison with conventional supports (activated carbon, alumina) was shown to result in an increase of activity and selectivity of the catalysts in hydrogenation reactions [21–27]. The more detailed study of the performance of Ni catalysts supported on CNF of different structures in hydrogenation of alkenes and dienes showed that the catalyst activity and selectivity are extremely sensitive to the support structure [27].

Thus, the attraction of CNFs follows from possibility of purposeful synthesis and peculiarities of their structure. Three types of CNF different by structure are well known: with graphene planes arranged perpendicular to the filament axis (deck of cards morphology), at an angle of 45° to the axis (herringbone morphology) or parallel to the axis, forming multi-wall nanotubes (Fig. 1).

Various carbon-containing gases (CH_4, C_2H_4, C_2H_2, CO) can be used as feedstock for the production of CNF, while metals of the iron subgroup and their alloys are traditionally used as the catalysts for hydrocarbon decomposition.

Another type of nanocarbon materials different from carbon blacks—amorphous supermicroporous carbon

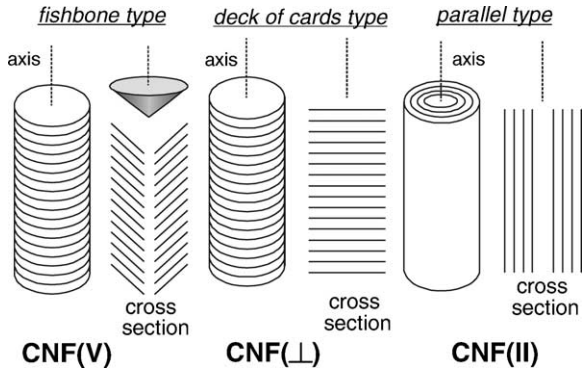

Fig. 1. Schematic representation of three types of CNF [13].

(ASC) [28] is an attractive material for cathode catalyst support because it has a very high specific surface area—up to 3300 m^2/g and large specific volume of micropores (i.e. pores with a diameter less that 2 nm)—from 1 to 1.6 cm^3/g. These micropores can contribute to stabilization of small Pt particles.

Thus, in this paper, we present data on synthesis of prospective catalysts for cathodes of PEM fuel cells on novel carbon materials: CNF and ASC, their characterization and MEA performance results.

2. Experimental

2.1. Synthesis of CNF

Decomposition of methane to produce CNF was carried out in a vibro-fluidized bed reactor that makes it possible to conduct the reaction under isoconcentration and isothermal conditions, prevent agglomeration of the carbonized catalyst and synthesize uniformly structured CNF [14–17]. The catalyst (∼0.1 g) was placed into the reactor (∼30 cm^3 in volume), the methane was supplied and the reactor was heated up to the required temperature—625 °C. Undiluted methane (p = 1 bar, 99.99% purity) was supplied into reactor at the rate of 45–90 l/(h g catalyst). Concentration of methane was measured by gas chromatography, and methane conversion was calculated. Carbon deposition was measured by weighting the samples after reaction, which was performed until complete catalyst deactivation. The catalysts 62% Fe–8% Ni–30% Al_2O_3 and 62% Fe–8% Ni–30% Al_2O_3 were used for growing CNF(||) and the catalysts 65% Ni–25% Cu–10% Al_2O_3 for preparation of CNF(⊥) [14–17].

2.2. Synthesis of ASC

Supermicroporous amorphous carbons were synthesized by mixing an organic precursor: oil coke, hydroquinone, etc. with concentrated sulfuric acid and potassium (or sodium) nitrites followed by thermal treatment at 700–800 °C in a reductive or inert medium.

The typical synthetic procedure is performed as follows. The initial carbonaceous precursor is ground to particle size 0.1–0.2 mm. A 5.5 g of the ground material is mixed with 90 ml of concentrated sulfuric acid under stirring and cooling with ice. Sodium nitrite in amount 36 mol/kg of the precursor (13.5 g) is added to the mixture gradually under stirring and the mixture is heated until foam formation and evolution of nitrogen oxides stop. Then, the mixture is diluted by water and evaporated to one-third of its initial volume. After cooling the precipitate is separated and washed to attain neutral pH of washing water. The product obtained is mixed with concentrated solution of 23 g of sodium hydroxide (107 mol/kg precursor). The mixture is heated to evaporate water and form a melt. After the end of the gas evolution, the melt is subjected to carbonization at 700 °C for 10 min. The obtained material is washed with water, then with 0.5 M H_2SO_4, then again with water until neutral medium. The washed product is dried at 105–115 °C. The typical yields of the obtained supermicroporous carbons are 20–30%.

2.3. Preparation of Pt cathode catalysts

For catalysts preparation, H_2PtCl_6 was used as the starting Pt compound, with following alkaline hydrolysis and Pt reduction.

The catalyst preparation procedure includes the following stages:

- Acid washing of the support from particles of metals—catalysts for CNF synthesis.
- Support drying.
- Preparation of solutions.
- Preparation of aqueous suspension of CNF.
- Adsorption of Pt precursor via alkaline hydrolysis.
- Pt reduction.
- Spectrophotometric control for completeness of the Pt deposition.
- Filtration and washing of the precipitate from Cl^- ions.
- Drying.

The catalyst preparation was made with variation of the Pt loading on the support (5, 10 and 30 wt.% of Pt in the final samples), alkaline agent (NaOH or Na_2CO_3), reducer (sodium formate or hydrogen), and other conditions (duration of the adsorption of H_2PtCl_6, temperature and duration of the hydrolysis and reduction, etc.). The CNF supports used for preparation of catalysts to be further tested in MEA were ground and jet-milled to size of 30–40 nm. The support ASC-1 was prepared following special procedure to produce particles of required size. Vulcan XC-72R was purchased from Cabot Corp. It had particle size 30 nm, BET area 254 m^2/g.

2.4. Characterization of carbon supports and cathode catalysts

Samples of carbon supports were investigated by XRD, TEM, HRTEM and adsorption methods. The catalysts were investigated by XRD, TEM and HRTEM. Pt dispersion was measured by XRD and CO adsorption method.

The XRD studies were performed in a HZG-4 diffractometer using Cu Kα radiation. Crystallite sizes were calculated from the line width following the Scherrer equation, TEM pictures were obtained in a JEM-100 CX. Studies by high-resolution electron microscopy were performed with HRTEM JOEL 2010, magnification up to 3,116,000×. The adsorption measurements were carried out using an ASAP-2400 to provide adsorption of N_2 at 77 K.Metal dispersion was probed by express method with CO chemisorption in a conventional flow system with a thermal conductivity detector and hydrogen as a support gas. Assuming CO adsorption on surface Pt in proportion one molecule per atom, the Pt dispersion was calculated by the formula: $D = CO_{ads}$ (moles)/Pt (moles). The average particle size was estimated using the formula: d (nm) = 1.08/D [29].

2.5. Preparation of membrane electrode assemblies and MEA operating conditions

Cathodes of membrane electrode assemblies were prepared by spraying a slurry consisting of the catalyst (30% Pt on carbon support), Nafion solution, hydrophobic powders, water and ethanol onto a Nafion-112 membrane of 50 μm thickness with effective cross-section of 25 mm × 25 mm and subsequent removing of solvents by heating to 150 °C. The content of Pt in cathode between about 0.02 and 0.09 mg/cm^2 was varied by amount of slurry loading. The anode in the MEA tests was a conventional 30 wt.%

Table 1
XRD characterization of CFC samples

Sample	T (°C)	d_{002} (nm)	L_c (nm)	L_a (nm)
CNF(⊥)	625	0.341	5.2	9.5
CNF(||)	625	0.342	5.5	8.5

Table 2
Textural characteristics of CNF samples

Sample	BET surface (A_{BET}, m^2/g)	Mesopore surface (A_{ME}, m^2/g)	Micropore volume (V_μ, cm^3/g)	Total pore volume (V_S, cm^3/g)	Average pore diameter (D^{BET}, nm)
CNF(⊥)	260	231.2	0.014	0.400	6.2
CNF(||)	150	112.4	0.01	0.406	17.5

Table 3
Textural characteristics of ASC samples

No.	Type ASC	Precursor	A_{BET} (m^2/g)	A_{ME} (m^2/g)	V_S (cm^3/g)	V_μ (cm^3/g)
1	ASC-1	Oil coke	3331.0	182.0	1.84	1.56
2	Ph	Phenol	2240.1	369.0	1.53	0.98
3	OQ	Oxyquinoline	2548.2	313.3	1.59	1.21
4	HQ	Hydroquinone	2453.2	111.3	1.36	1.22
5	ONA1K	*o*-Nitroaniline K^+	1673.7	55.9	0.87	0.79
6	ONA2K	*o*-Nitroacetonilide K^+	1691.8	30.7	0.85	0.80
7	ONA1	*o*-Nitroaniline Na^+	1920.6	242.0	1.34	1.05
8	ONA2	*o*-Nitroaniline Na^+	2559.0	392.3	1.74	1.25
9	ONA3	*o*-Nitroaniline Na^+	2508.0	156.7	1.51	1.31
10	HQ1	Hydroquinone K^+	2697.4	104.6	1.50	1.38
11	HQ2	Hydroquinone K^+	2835.0	171.9	1.70	1.50
12	HQ3	Hydroquinone K^+	2764.8	172.0	1.64	1.43
13	DNPh	2,4-Dinitrophenol	632.4	55.8	0.36	0.26
14	DNA	2,4-Dinitroaniline	1148.3	24.8	0.57	0.52
15	BA	Barbituric acid Na^+	500.0	81.0	0.38	0.19
16	BA	Barbituric acid K^+	1400.0	610.0	1.47	0.41
17	BQDO1	*n*-Quinondioxime:*n*-hydroquinone (1:2)	2470.0	304.0	1.64	1.27
18	BQDO2	*n*-Quinondioxime:*n*-hydroquinone (1:2)	2620.0	824.0	2.14	1.07
19	BQDO3	*n*-Quinondioxime:*n*-hydroquinone (1:2)	2770.0	499.0	1.92	1.29
20	QE-10	Quinolic ether	2360.0	95.0	1.25	1.10

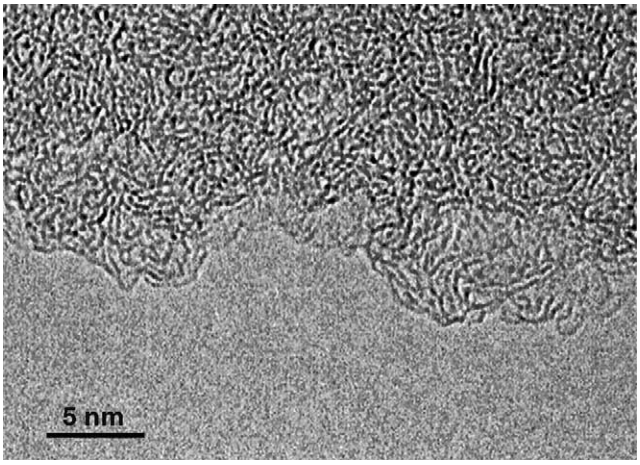

Fig. 2. HRTEM image of ASC-1 sample prepared from oil coke.

Pt/Ketjen Black of 0.05 mg Pt/cm^2 in all measurements. A hydrophobic porous carbon paper (Electrochem Inc. EC-TP1) serving as a gas distributor and current collector was applied to the electrodes. The MEAs were assembled in a standard graphite cell frame. The tests were performed under the following conditions: cell temperature 80 °C, pressures of H_2 of relative humidity of 100% at 85 °C and O_2 of relative humidity 100% at 75 °C were 0.1 MPa.

3. Results and discussion

3.1. Characterization of CNF and ASC

The XRD patterns of the CNF samples are only different in the widths and positions of (0 0 *l*)-type reflections, i.e.

Table 4
Metal dispersion in the catalysts prepared on CNF

No.	Catalyst code[a]	Catalyst used for CNF preparation	Pt loading (wt.%)	Characterization methods		
				Dispersion CO/Pt (%)	Particle size from CO/Pt (*D*, Å)	XRD
1	5C(⊥)F	65Ni25Cu	5	46	23	Carbon phase; Pt with *D* = 23 Å
2	10C(⊥)F	65Ni25Cu	10	35	31	Carbon phase; Pt with *D* = 43 Å
3	30C(⊥)F	65Ni25Cu	30	20	54	Carbon phase; Pt with *D* = 44 Å
4	5C(‖)F	62Fe8Ni	5	34	32	Carbon phase; Pt with *D* = 31 Å
5	10C(⊥)H	65Ni25Cu	10	53	20	Carbon phase; Pt with *D* = 21 Å
5a	10C(⊥)F	65Ni25Cu	10	40	27	Carbon phase; Pt with *D* = 29 Å
6	5C(⊥)H	75Ni15Cu	5	64	17	Carbon phase; Pt with *D* = 17 Å
6a	5C(⊥)F	75Ni15Cu	5	46	23	Carbon phase; Pt with *D* = 24 Å
7	10(⊥)H	75Ni15Cu	10	51	21	Carbon phase; Pt with *D* = 21 Å
7a	10C(⊥)F	75Ni15Cu	10	33	33	Carbon phase; Pt with *D* = 25 Å

[a] In the catalyst code, the first figure designates Pt content in the catalyst, the sign after C refers to CNF structure, index F means Pt reduction by formate, and H refers to Pt reduction by hydrogen.

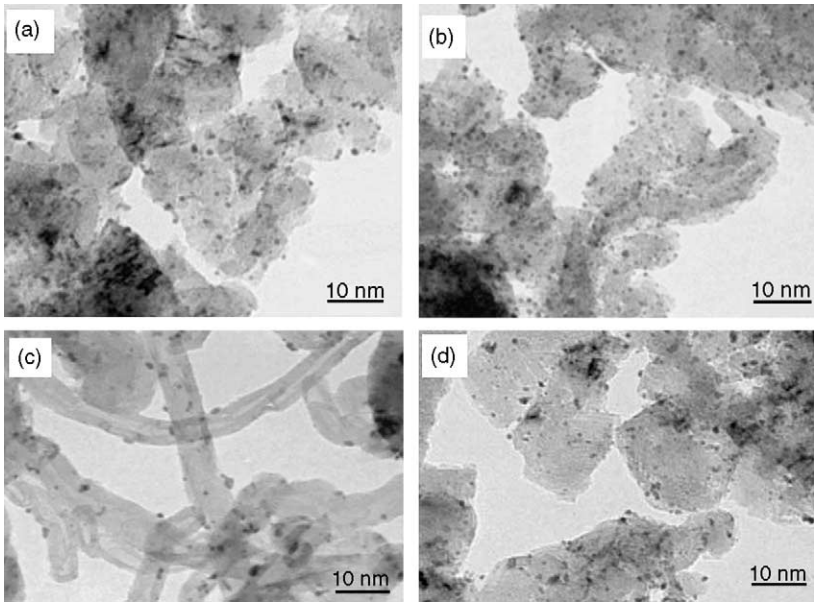

Fig. 3. TEM pictures of Pt catalyst samples: (a) 5C(⊥)F; (b) 10C(⊥)H; (c) 5C(||)F; (d) 10C(⊥)F.

there are only qualitative differences. Interplanar distance d_{002} and average CSD (crystallite) sizes along the *a*- and *c*-axis of carbon (L_a, L_c) are presented in Table 1. The d_{002} ranges between 0.341 and 0.342 nm, that is higher than for ideal graphite (0.335 nm). The average values of L_c and L_a are 5.2–5.5 and 8.5–9.5 nm, respectively.

Table 5
Characteristics of catalysts prepared for MEA test

Catalyst	Pt content (%)	D_{Pt} (nm)	
		XRD	TEM
30% Pt/CNF(⊥)	33.2	4.4	3–5
30% Pt/CNF(||)	31.9	4.1	3–5
30% Pt/ASC-1	30.0	3.2	3–4
30% Pt/XC-72R	36.4	4.7	3–5

Thus, XRD characterization indicates that CNF is the typical turbostratic carbon with a high d_{002} and low L_a and L_c values [30], i.e. CNF filaments consist of mutually disoriented domains with the graphite-like structure.

The data on BET surface area, mesopore surface area, micropore volume and total pore volume are summarized in Table 2. BET surface area is over 100 m^2/g. The micropore volume is small in both samples, ~0.01 cm^3/g at the total pore volume of 0.4 cm^3/g. Hence, CNF samples are mesoporous materials with pores of 6–18 nm in average size and a large surface area—over 100 m^2/g.

The preparation of amorphous supermicroporous carbon was performed from various initial precursors. The used precursors and textural properties of the obtained materials are shown in Table 3. These are typical microporous

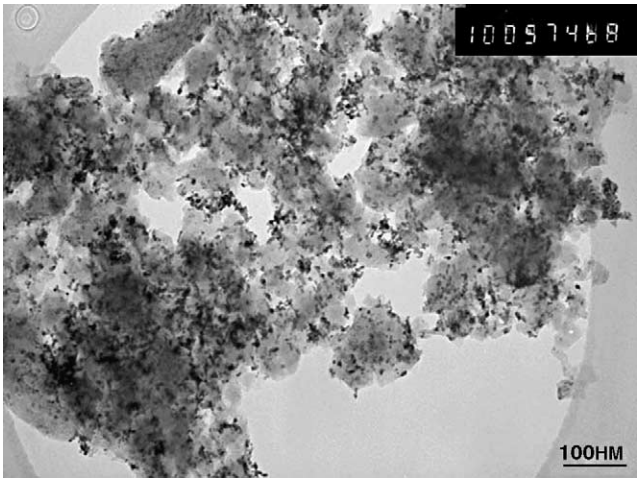

Fig. 4. TEM image of 30% Pt/CNF(⊥).

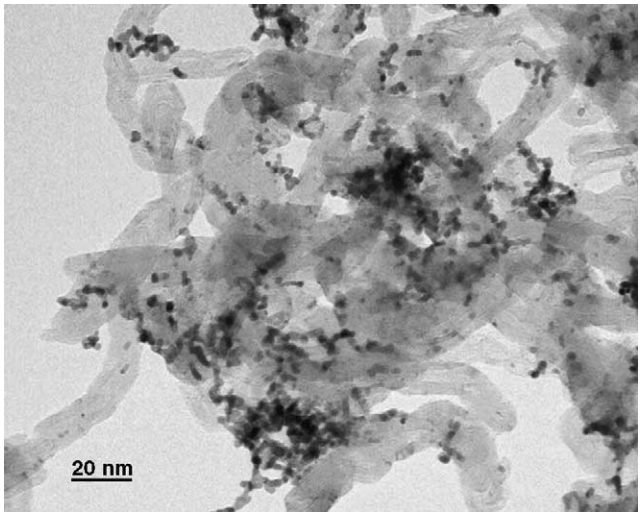

Fig. 5. TEM image of 30% Pt/CNF(||).

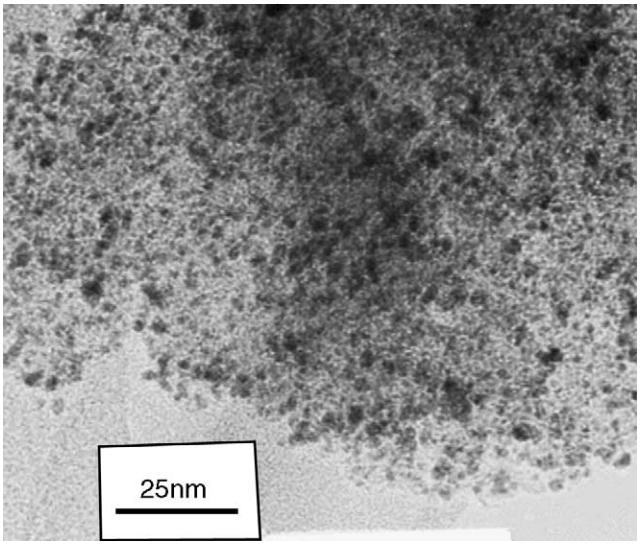

Fig. 6. TEM image of 30% Pt/ASC-1.

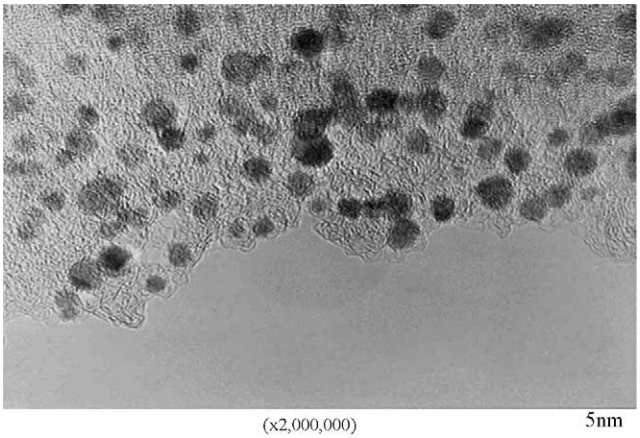

Fig. 7. HRTEM image of 30% Pt/ASC-1.

materials with high surface area exceeding 2000 m^2/g and large volume of micropores—over 1 g/cm^3. The micropore volume is over 80% of the total pore volume, with average pore size close to 2 nm.

The HRTEM studies on the example of ASC-1 formed from oil coke (Fig. 2) show that the material contains fragments with fully disordered cellular structure which are built up by graphite-like layers (graphenes) of monoatomic thickness (ca. 0.3 nm). There are cells of subnanometer characteristic size corresponding to micropores between the bent graphene layers.

Of the samples prepared, the sample ASC-1 was chosen for further studies as a support for Pt cathode catalyst of PEMFC because it has the largest micropore volume and surface area, and secondly it can be produced in a form of small uniform particles—ca. 40 nm, which can be used directly for electrocatalyst preparation without the stages of material grinding and jet-milling.

3.2. Characterization of Pt cathode catalysts

Catalysts supported on the CNF were prepared as described above using one of the basic techniques for

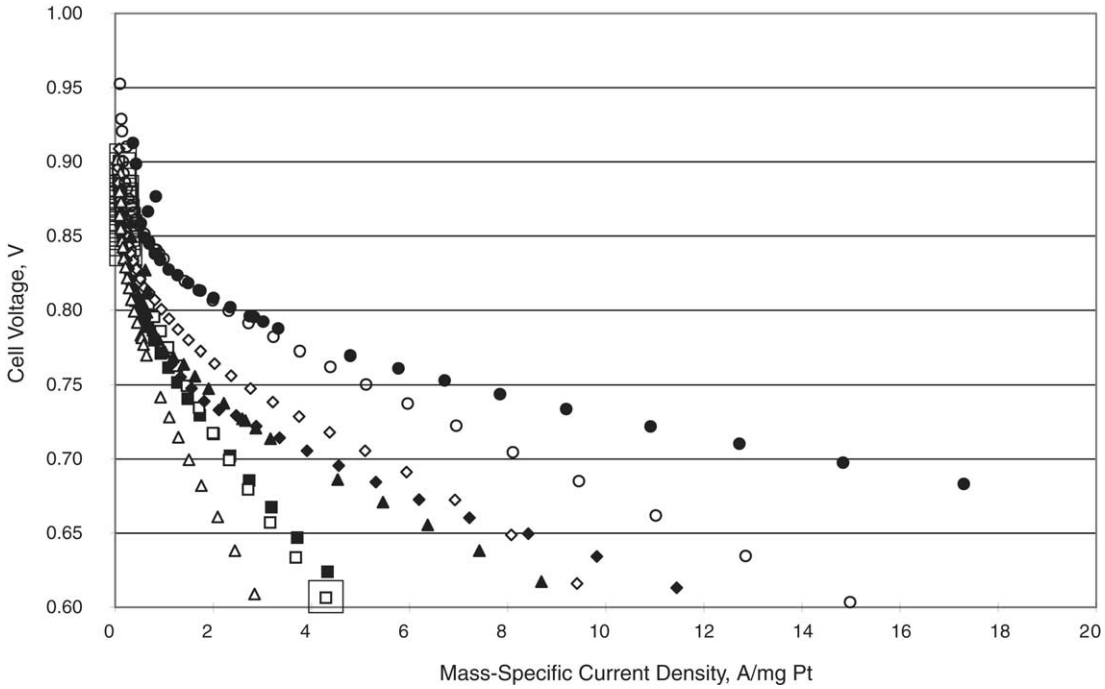

Fig. 8. Voltage vs. mass-specific current density in for MEA with Pt cathodes with low Pt loading and a conventional anode with 30 wt.% Pt/Ketjen Black of 0.05 mg Pt/cm^2. Vulcan XC-72R: (◆) 0.0380 mg Pt/cm^2; (◇) 0.0628 mg Pt/cm^2. Amorphous carbon ASC-1: (●) 0.0175 mg Pt/cm^2; (○) 0.0592 mg Pt/cm^2. CNF(||): (■) 0.0400 mg Pt/cm^2; (□) 0.0639 mg Pt/cm^2. CNF(⊥): (▲) 0.0185 mg Pt/cm^2; (△) 0.0914 mg Pt/cm^2.

preparation of catalysts with noble metals on carbon supports [31]. Several catalysts have been prepared to estimate applicability of this technique to different types of CNF at different Pt loadings on the support.

The used catalyst preparation technique provides rather high dispersion for the supported platinum at a large Pt loading (see data for catalysts 2, 5 and 7 with 10 wt.% of Pt and sample 3 with 30 wt.% of Pt in Table 4) and allow the dispersion to be controlled by variation of the preparation conditions (compare dispersions in the pairs of catalysts 5 and 5a, 6 and 6a, and 7 and 7a, which were prepared on the same support and have the same metal loading). Generally, reduction by hydrogen results in higher Pt dispersion in comparison with liquid phase reduction by formate ion.

There is very good correspondence between average size of Pt particles obtained by CO adsorption measurement and XRD.

The micrographs of some Pt catalysts on CNF of different types are shown in Fig. 3. TEM pictures of Pt on support C(⊥) show pieces of broken filaments (the breaking of filaments took place upon jet-milling) with Pt fine particles supported on carbon. The comparison of the TEM images of the catalysts of the same composition, but prepared by different techniques (10C(⊥)H and 10C(⊥)F) shows that reduction by hydrogen leads to higher dispersion and more uniform Pt distribution as compared to liquid phase reduction by formate ion—in agreement with data obtained by CO adsorption and XRD.

Sample 5C(||)F retains initial carbon structure as multi-wall nanotubes with long unbroken filaments, even after jet-milling of the support, and Pt particles are bonded to the external surface of the filaments. The Pt particles size is close to that of the sample 10C(⊥)F and 5C(⊥)F, but larger than that in the sample 10C(⊥)H.

For MEA tests we used 30% Pt/CNF(⊥) and 30% Pt/CNF(||) and for comparison the catalyst on conventional support 30% Pt/Vulcan XC-72R synthesized by the same method. The catalyst 30% Pt/ASC-1 was synthesized in Nippon Steel Corporation using proprietary technique. The catalyst characteristics are given in the Table 5.

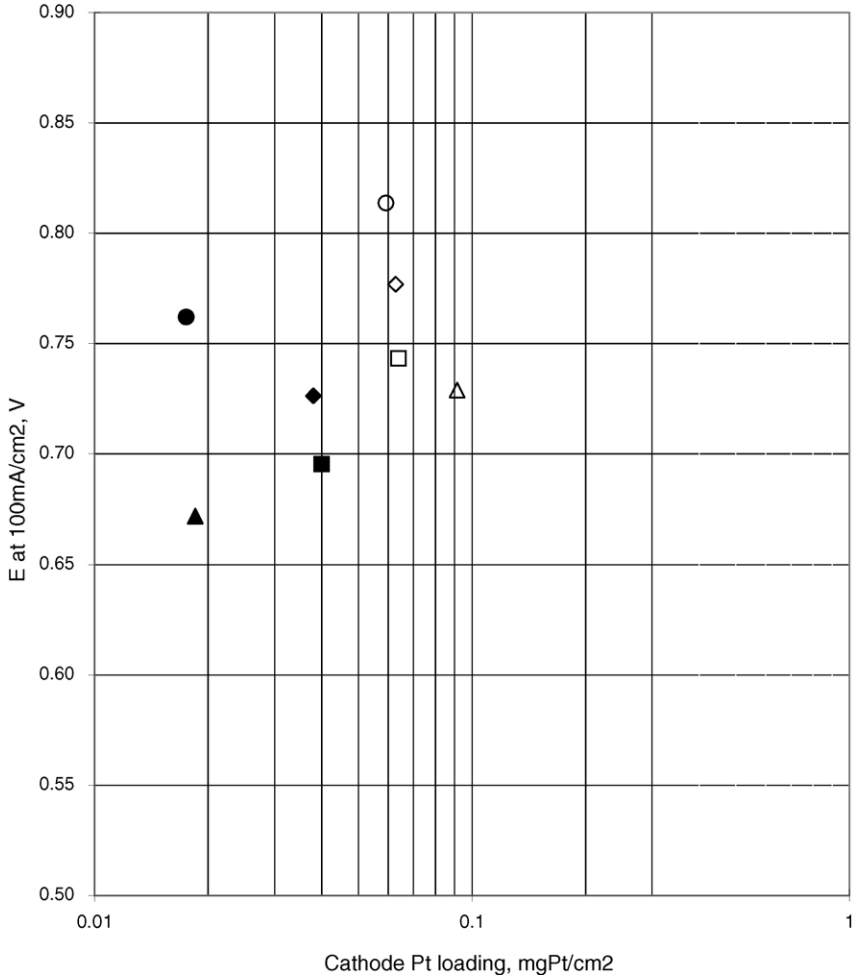

Fig. 9. Voltage at current density of 100 mA/cm^2 of geometric electrode area vs. Pt loading in cathodes for MEAs with low Pt loading cathodes and a conventional anode of 0.05 mg Pt/cm^2 with 30 wt.% Pt/Ketjen Black. Vulcan XC-72R: (◆) 0.0380 mg Pt/cm^2; (◇) 0.0628 mg Pt/cm^2. Amorphous carbon ASC-1: (●) 0.0175 mg Pt/cm^2; (○) 0.0592 mg Pt/cm^2, CNF(||): (■) 0.0400 mg Pt/cm^2; (□) 0.0639 mg Pt/cm^2. CNF(⊥): (▲) 0.0185 mg Pt/cm^2; (△) 0.0914 mg Pt/cm^2.

The micrographs of the catalysts are shown in Figs. 4–7. They demonstrate rather high Pt dispersion. In catalysts 30% Pt/CNF(⊥) and 30% Pt/CNF(||) major part of Pt particles have size of 3–5 nm, some of them are deposited individually and some compose chains or agglomerates consisting of several particles. Electron microscopy studies of 30% Pt/ASC-1 show smaller Pt particles and more uniform Pt distribution in comparison with sample Pt/CNF.

3.3. MEA tests of the catalysts

MEA testing of the Pt cathode catalysts prepared on novel supports were performed in comparison with the catalyst prepared on conventional support Vulcan XC-72R under identical conditions. The results of the tests are shown in Figs. 8 and 9.

Fig. 8 shows the dependence of the voltage of MEAs with different cathode catalysts and different Pt loadings versus mass-specific current density, i.e. current density divided by Pt surface density. It can be seen that the performance of cathodes with Pt/CNF catalysts adjusted to the same Pt loading is inferior to that of the cathodes prepared from the conventional Pt/Vulcan XC-72R catalyst or very close in case of the cathode prepared from Pt/CNF(⊥) with a Pt density of 0.0185 mg Pt/cm^2.

Fig. 9 shows the MEA performance characteristic defined as the MEA output voltage at a constant current density of 100 mA/cm^2, versus Pt loading in the cathode. It can be concluded that the novel catalyst 30% Pt/ASC-1 provides excellent MEA output with the voltage close to 0.8 V at very low platinum loadings 0.0175–0.0592 mg Pt/cm^2, considerably exceeding by the performance the other studied catalysts even at a lower Pt loading.

4. Conclusion

We have shown potential applicability of novel nanocarbon supports—carbon nanofibers and amorphous supermicroporous carbons for synthesis of active platinum cathode catalysts for proton exchange membrane fuel cells. Different types of CNF: with ''parallel'' and ''deck of cards'' arrangement of graphitic planes and samples of ASC from different precursors were synthesized and characterized by XRD, electron microscopy and adsorption methods. CNF samples studied are mesoporous materials with pores of 6–18 nm in average size and a large mesoporous surface area—over 100 m^2/g. The synthesized ASC samples are typical microporous materials with very high surface area exceeding 2000 m^2/g and large volume of micropores—over 1 g/cm^3. Platinum catalysts for PEMFC cathodes on different structural types of CNF and one sample of ASC were synthesized and characterized by TEM, XRD and CO adsorption. The used catalyst preparation technique provides rather high dispersion for the supported platinum at a large Pt loading. The catalysts were further characterized by studying characteristics of conventional MEA cell with a low Pt loading level of 0.02–0.09 mg/cm^2. The MEA test showed that the Pt cathode catalysts on CNF exhibit inferior or comparable performance adjusted to the same Pt loading in comparison with a catalyst on conventional carbon black support Pt/Vulcan XC-72R. On the contrary, the cathode catalyst prepared on the ASC-1 support provides excellent MEA output and exhibits better performance compared with the Pt/Vulcan XC-72R and other catalysts even at lower Pt loadings.

Thus, the application of novel supermicroporous materials as supports for catalysts for low Pt loading cathodes appears to be promising. Further research is now in progress on the improvement of Pt dispersion at high loadings on ASC-1, studies of catalysts on ASC supports prepared from different precursors and also on surface treatment of CNF supports for their adaptation as effective carbon supports for cathode catalysts.

Acknowledgements

To NEDO for support of the research in frame of project ''Development of active cathode catalysts with low Pt loading for PEFC by surface tailoring of carbon support materials'' under ''Proposal-Based International Joint Research Program on Energy and Environment''. To NWO for support on the research on CNF synthesis. To T.V. Reshetenko, L.B. Avdeeva and A.V. Shalagina for samples of CNF.

References

[1] T.R. Ralph, M.P. Hogarth, Platinum Met. Rev. 46 (2002) 3.
[2] H. Hara, Abstracts of the Third Annual Nanoenergy 2002—Production and Application of Nanostructured Materials for Energy Devices, Miami Beach, USA, 11–13 December 2002.
[3] M. Debe, A. Steinbach, K. Lewinski, G. Haugen, G. Vernstrom, R. Atanasoski, A. Hester, P. Turner, R. Ziegler, J. Larson, M. Hicks, P. Serim, Abstracts of the Fuel Cell Seminar 2003, Miami Beach, PA, 3–7 November 2003, p. 812.
[4] S. Ye, A.K. Vijh, L.H. Dao, J. Electroanal. Chem. 415 (1996) 115.
[5] M.S. Kim, N.M. Rodriguez, R.T.K. Baker, J. Catal. 134 (1992) 253.
[6] R.T.K. Baker, R.J. Waite, J. Catal. 37 (1975) 101.
[7] R.T.K. Baker, Carbon 27 (1989) 315.
[8] M.T. Tavares, C.A. Bernardo, I. Alstrup, J.R. Rosrtup-Nielsen, J. Catal. 100 (1986) 545.
[9] C.A. Bernardo, I. Alstrup, J.R. Rosrtup-Nielsen, J. Catal. 96 (1985) 517.
[10] P.K. de Bokx, A.J.H.M. Kock, E. Boellaard, W. Klop, J.W. Geus, J Catal. 96 (1985) 454.
[11] A.J.H.M. Kock, K.P. de Bokx, E. Boellaard, W. Klop, J.W. Geus, J. Catal. 96 (1985) 468.
[12] E. Boellaard, P.K. Bokx, A.J.H.M. Kock, J.W. Geus, J. Catal. 96 (1985) 481.
[13] K.P. De Jong, J.W. Geus, Catal. Rev. Sci. Eng. 42 (2000) 481.
[14] L.B. Avdeeva, T.V. Reshetenko, Z.R. Ismagilov, V.A. Likholobov, Appl. Catal. A 228 (2002) 53.

[15] T.V. Reshetenko, L.B. Avdeeva, Z.R. Ismagilov, V.V. Pushkarev, S.V. Cherepanova, A.L. Chuvilin, V.A. Likholobov, Carbon 41 (2003) 1605.
[16] T.V. Reshetenko, L.B. Avdeeva, Z.R. Ismagilov, V.A. Ushakov, A.L. Chuvilin, Yu.T. Pavlyukhin, Chem. Sustainable Dev. 11 (2003) 239.
[17] T.V. Reshetenko, L.B. Avdeeva, Z.R. Ismagilov, A.L. Chuvilin, V.A. Ushakov, Appl. Catal. A 247 (2003) 51.
[18] H.G. Tennet, US Patent 4,663,230 (1987).
[19] C. Park, E.S. Engel, A. Crowe, T.R. Gilbert, N.M. Rodriquez, Langmuir 16 (2000) 8050.
[20] A. Dandekar, R.T.K. Baker, M.A. Vannice, J. Catal. 183 (1999) 131.
[21] N.M. Rodriguez, M.-S. Kim, R.T.K. Baker, J. Phys. Chem. 98 (1994) 108.
[22] J.M. Planeix, N. Coustel, B. Coq, V. Brotons, P.S. Kumbar, R. Dutartre, P. Geneste, P. Bernier, P.M. Ajayan, J. Am. Chem. Soc. 116 (1994) 7935.
[23] C. Park, R.T.K. Baker, J. Phys. Chem. B 103 (1999) 2453.
[24] M.S. Hoogenraad, M.F. Onwezen, A.J. van Dillen, J.W. Geus, Stud. Surf. Sci. Catal. 101 (1996) 1331.
[25] M.S. Hoogenraad, R.A.G.M.M. van Leeuwarden, G.J.B. van Breda Vriesman, A. Broersma, A.J. van Dillen, J.W. Geus, Stud. Surf. Sci. Catal. 91 (1995) 263.
[26] B.L. Mojet, M.S. Hoogenraad, A.J. van Dillen, J.W. Geus, D.S. Koningsberger, J. Chem. Soc., Faraday Trans. 93 (1977) 4371.
[27] C. Park, R.T.K. Baker, J. Phys. Chem. B 102 (1998) 5168.
[28] C.N. Barnakov, S.K. Seit-Ablaeva, A.P. Kozlov, Yu.V. Rokosov, V.B. Fenelonov, V.N. Parmon, Russian Patent 2,206,394 (2003).
[29] J.R. Anderson, Structure of Metallic Catalysts, Academic Press, London, 1975.
[30] S.V. Cherepanova, S.V. Tsybulya, J. Mol. Catal. A 158 (2000) 263.
[31] L.B. Okhlopkova, A.S. Lisitsyn, N.I. Kuznetsova, V.A. Likholobov, React. Kinet. Catal. Lett. 52 (1994) 385.

Available online at www.sciencedirect.com
SCIENCE DIRECT®
Catalysis Today 102–103 (2005) 85–93
CATALYSIS TODAY
www.elsevier.com/locate/cattod

Development of methods of growing carbon nanofibers on silica glass fiber supports

Ismagilov Zinfer R. [a,*], Shikina Nadezhda V. [a], Kruchinin Vladimir N. [a], Rudina Nina A. [a], Ushakov Vladimir A. [a], Vasenin Nikolai T. [a], Veringa Hubert J. [b]

[a] *Boreskov Institute of Catalysis, Novosibirsk 630090, Russia*
[b] *ECN, P.O. Box 1, 1755 ZG Petten, The Netherlands*

Available online 24 March 2005

Abstract

Samples of carbon nanofibers (CNF) with different carbon contents (6.5–55 wt.%) are prepared by decomposition of CH_4 on Ni catalysts supported on silica glass fibers (SGF). The incipient wetness impregnation of support, introduction of the active component into alumina washcoat and ion-exchange methods were used to prepare Ni catalysts on SGF. On the optimal catalyst prepared on washcoated SGF, carbon forms as CNF of diameter 20–50 nm, and the carbon capacity is rather high—55 g_C/g_{Ni}. Diameter of the CNF corresponds to the size of catalyst particles of Ni metal, which have the cuboctahedral form typical for the formation of CNF with conical embedding of graphite layers with respect to the filament axis. The SGF with supported CNF is a mesoporous material with polydisperse pore distribution similar by structural and textural parameters to the granulated bulk CNF obtained in methane decomposition over high-loaded nickel-alumina catalysts.

The XRD, ESR and DTA methods were used for phase and structural analysis and demonstrated that CNF has a uniform graphite-like structure and does not include the amorphous phase.

Keywords: Structured supports; Carbon; Carbon nanofibers; CNF; Silica glass fiber; Methane decomposition

1. Introduction

Carbon nanofibers (CNF) can be produced as powder or granules via the decomposition of hydrocarbons, in particular methane, over catalysts composed of iron group metals [1–3] and oxides Al_2O_3, SiO_2, etc. For practical application, it is of interest to grow carbon filaments on the organized geometrical surface of structured materials [4,5], for instance, on honeycomb monoliths, reticulated foam materials, porous composite ceramics, woven and non-woven ceramic fibers.

Of special interest are glass fibers, due to physico-chemical properties of glass fiber in metastable amorphous state [6] and a high total geometrical surface area of macrostructured fibrous materials composed of thin elementary fibers. Besides, glass fibers exhibit high strength, they can be easily transformed to required geometric shape, which enhances the integration of catalysts into reactors of various space geometry. These advantages of glass fiber materials can be enhanced for preparation of catalyst supports by depositing carbon nanofibers layer with developed mesoporous structure.

Carbon nanofibers can be grown by the catalytic decomposition of hydrocarbons over nanodispersed metal catalysts loaded on the surface, e.g., on glass fibers. We summarized the known methods of active metal catalyst loading onto glass fibers into four groups:

1. Capillary incipient wetness impregnation of glass fiber with solutions of precursors [7].
2. Introduction of the active component by the impregnation method into preliminary formed oxide layer on the surface of glass fibers [8,9].
3. Impregnation by the ion-exchange method [10].
4. Introduction of active metals into the raw mix for glass fiber production, followed by their supporting with conventional methods [11].

* Corresponding author. Tel.: +7 3832 341219; fax: +7 3832 397352.
E-mail address: zri@catalysis.nsk.su (I.Z. R.).

0920-5861/$ – see front matter © 2005 Published by Elsevier B.V.
doi:10.1016/j.cattod.2005.02.009

In the present work, methane decomposition catalysts were prepared by methods 1–3.

The effects of preparation procedure on the properties of Ni-containing catalysts and their activity in methane decomposition have been determined.

Time of operation until deactivation for each supported catalyst and morphology of CNF were studied.

Structural and textural properties of CNF grown on glass fibers coated with a catalyst of optimum composition were investigated.

2. Experimental

2.1. Support

Silica glass fibers (SGF) used in experiments consists of filaments with a diameter of 6–7 μm (Fig. 1). After removal of a lubricant, the glass fiber was leached in a 5.5% solution of nitric acid for 1 h at 90 °C, washed with water to obtain pH 5.5–7, dried and calcined at 300 °C in air. The properties of SGF after pretreatment are as follows: S_{BET}^{Ar} is 0.7 m^2/g, $S_{BET}^{N_2}$ is 0.3 m^2/g, V_{pore} is 0.00056 cm^3/g, amorphous phase in XRD.

2.2. Catalysts

The Ni-containing catalysts supported onto SGF were prepared by three methods. In all cases, an aqueous solution of nickel nitrate was used as the active component precursor.

According to method 1 (catalyst 1), the active component was introduced via the incipient wetness impregnation of SGF itself at room temperature. Then the samples were separated from the impregnating solution, dried at 70 °C, calcined at 350 °C in nitrogen, and reduced in a mixture of 10 vol.% H_2 + 90 vol.% N_2 at 550 °C for 3 h. The Ni content in the catalyst was 4.2–4.5 wt.%.

By method 2 (catalyst 2), the active component was fixed in the alumina layer (0.75 wt.% alumina with respect to SGF) formed on SGF from a solution of aluminum nitrate. After separation of the impregnating solution, the samples were heat treated in the regime similar to that of method 1. The Ni content in the catalyst was 2.2–2.4 wt.%.

According to method 3 (catalyst 3), samples of the support were boiled in a precursor solution for 1 h, then the samples were separated from the solution, washed with distilled water to remove Ni cations weakly bonded to the support and treated under the conditions similar to those of methods 1 and 2. The Ni content in the catalyst was 0.02 wt.%.

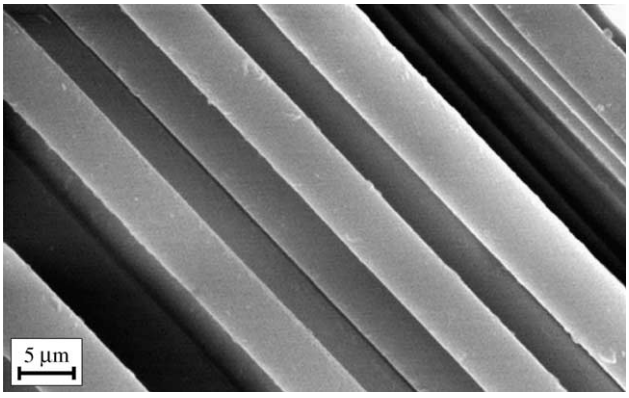

Fig. 1. The micrograph of SGF fibers.

2.3. Characterization

Chemical composition of the support and catalysts was determined by the method of atomic-emission spectroscopy with inductively confined plasma using a BLYRD spectrometer.

Carbon content in the samples was measured gravimetrically from the sample weight increment and weight loss after burning at 1000 °C. In some cases, thermogravimetric analysis (TGA) was used. TGA and DTA were performed in air at a heating rate 10°/min and a temperature range from 22 to 1000 °C with 100 mg samples.

Adsorption methods were used for characterization of the textural properties of support, catalysts and carbonized samples of glass fibers. The value of specific surface area was determined by the BET method from heat desorption of argon, S^{Ar}, and nitrogen adsorption at 77 K. Pore volume and pore size distribution were also determined from nitrogen adsorption at 77 K with an ASAP-2400 instrument. Effective pore diameter was found from the differential curve plotted with the data obtained by the Barrett–Joyner–Halenda method using the model of cylindrical pores. Average pore radius was calculated by the formula $4V/S_{BET}$.

Phase composition of support and catalysts, and size of the active component particles (coherent scattering region, c.s.r.) were determined by analyzing the diffraction patterns in the range of 2θ angles from 10 to 60° obtained with a HZG-4 diffractometer at monochromatic Cu Kα radiation. The structure of carbon nanofibers was characterized by d_{002} and c.s.r. in the directions perpendicular to the basal plane (L_c) and along it (L_a).

The degree of graphitization was determined according to [12] from the formula: $g = (0.344 - d_{002})/0.0086$.

Morphology of supports, catalysts and carbonized samples of glass fibers was studied by the SEM and TEM methods with microscope REM 100-U and a transmission electron microscope JEM-100CX. Samples for the TEM studies were pounded with a pestle, suspended in ethanol, then dispersed by ultrasound and fastened to copper nets.

The ESR studies of catalysts and carbon coating were performed with a Bruker ER 200D spectrometer (λ = 3 cm) at 77 and 300 K. Values of the ESR parameters were found by comparing with the position of the diphenylpicrylhydrazyl (DPPH) line.

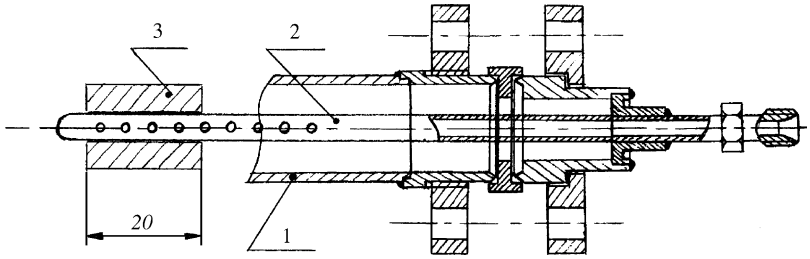

Fig. 2. The flow reactor: (1) reactor wall; (2) gas distributing tube; (3) catalyst on glass fiber support.

2.4. Methane decomposition and CNF growing

The methane decomposition reaction was performed in a horizontal flow reactor. The 20 mm tape of silica glass fiber containing supported Ni catalyst was rolled in a 20 mm diameter coil on a perforated metal tube operating as a gas distributor (see Fig. 2). The reaction mixture consisting of 25 vol.% natural gas (98% methane + trace amounts of ethane and propane) and 75 vol.% N_2 was fed into the reactor at a space velocity of 2500 h^{-1}. The reaction mixture (CH_4, N_2, H_2, hydrocarbons) was analyzed with GC. The experiments were performed at 550 °C until complete deactivation of a catalyst. Activity of catalysts in methane decomposition was characterized by methane conversion (X_{CH_4}), catalyst lifetime (time of its operation until a complete deactivation, τ_{cat}) and carbon capacity (G_C).

Methane conversion was calculated by the formula [13]:

$$X_{CH_4} = \frac{(C_0 - C)}{C_0(1 + C)} 100\%$$

where C_0 is the mole fraction of methane in the initial reaction mixture; C is the mole fraction of methane in the reaction products.

Carbon capacity of the catalysts was determined as the ratio of carbon weight in the carbonized catalyst sample to the weight of Ni in the catalyst.

3. Results and discussion

To reveal the degree of reduction of the active component and the size of its particles in catalysts prepared by different methods, structural and textural properties of the catalysts were studied using the ESR, XRD, nitrogen adsorption and scanning microscopy methods.

ESR studies of catalysts were performed after their reduction in hydrogen. ESR spectra are observed only for catalysts 1 and 2. The observed spectra have broad lines, exceeding 2000 Gs at room temperature, and show a further broadening at the temperature of liquid nitrogen. All these observations clearly indicate that the spectra correspond to ferromagnetic (superparamagnetic) particles of nickel metal Ni^0. Catalyst 3 has no ESR signals spectra both at room temperature and at 77 K, which evidences that nickel atoms are in a different electron state as compared to the first two catalysts.

The XRD data are presented in Table 1 and in Fig. 3. Before the reduction stage, the diffraction pattern of catalysts 1 and 2 is characterized by a mixture of two phases: X-ray amorphous phase of support and nickel oxide phase represented by the 2θ reflexes at 37.5 and 43.5°. The size of the nickel oxide particles determined from the coherent scattering region is 14 nm in catalyst 1 and 7 nm in catalyst 2. After heat treatment in H_2, the reflexes corresponding to NiO phase disappear from the diffraction pattern, and the 2θ maxima are observed at 44.5 and 52°, which are typical of the Ni metal phase with the particle size 20 and 16 nm, respectively, for catalysts 1 and 2. The size of Ni particles determined from the c.s.r. is an averaged characteristic. In catalyst 1, the reflexes corresponding to nickel metal phase have the profile (a broad base passing to a narrow peak) typical of polydisperse size distribution of Ni particles, which indicates that the catalyst comprises metal particles considerably differing in size.

In catalyst 2, a uniform size distribution of Ni particles is observed. Diffraction pattern of catalyst 3 sample after its calcining at 350 °C in nitrogen before the reduction stage and after heat treatment at 550 °C in hydrogen flow is identical to the diffraction pattern of amorphous glass fiber support represented by an extended hallo in the 2θ range of 22–23°. This result is obvious considering very low (0.02 wt.%) Ni content.

Catalysts 1 and 2 after heat treatment in N_2 have close values of textural parameters: the total pore volume, specific

Table 1
XRD data for Ni catalysts on glass fiber support

Catalyst type	Ni content (wt.%)	Heat treatment in N_2 (350 °C)		Heat treatment in H_2 (550 °C)	
		Phase	c.s.r. (nm)	Phase	c.s.r. (nm)
1	4.5	NiO, amorphous phase	14	Ni amorphous phase	20
2	2.2	NiO, amorphous phase	7	Ni amorphous phase	16
3	0.02	Amorphous phase	–	Amorphous phase	–

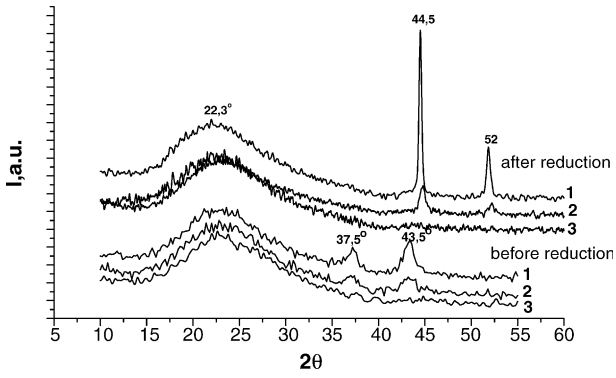

Fig. 3. XRD patterns of catalysts 1, 2 and 3 before and after the reaction.

surface area and effective pore radius (Table 2). After reduction at 550 °C, transformation of NiO to Ni occurs, and the specific surface area and pore volume decrease. This effect is more pronounced for catalyst 1. The decrease of the surface area is 10-fold while the measured particle size decreases only by a factor of 1.4 can be explained by the presence in this catalyst of large Ni particles in addition to smaller particles with an average size of 20 nm. Indeed, the determination of particle size over 50 nm cannot be performed by c.s.r. method used, and their presence in the catalyst sample may cause the observed sharp decrease of the SSA and pore volume values.

The presence of the alumina washcoating layer in catalyst 2 favors the stabilization of its textural parameters.

Textural properties of catalyst 3 are virtually similar to the properties of glass fiber ($S_{BET} = 0.3$ m^2/g, $V_{pore} = 0.00056$ cm^3/g).

Fig. 4 displays the electron micrographs demonstrating surface morphology of catalysts 1 (Fig. 4(1a)) and 2 (Fig. 4(2a)). In catalyst 1, the active component forms as coarse crystallites distributed over the external surface of glass fibers. One may expect a weak interaction between the active component and support. In catalyst 2, particles of the Ni active component are bonded rather strongly to alumina supported onto the surface of glass fibers.

It is known that alumina is a textural promoter in methane decomposition catalysts, on the one hand, providing the dispersity of catalytic particles (15 nm for Ni-Al catalyst) necessary for the carbon capacious state, and on the other hand, preventing the particles merging [14]. Table 3 presents the data on the initial degree of methane conversion, carbon capacity and lifetime of the catalysts prepared by various methods. It can be seen from these data that the catalysts exhibit considerably different activity in methane decomposition. At the initial moment, similar and rather high degrees of methane conversion (35–38%) on catalysts 1 and 2 are observed. High initial activity of these catalysts may be due to the presence of high-dispersed Ni particles (according to the XRD data) with an optimum size for the reaction. Methane decomposition does not occur on catalyst 3 obtained by the ion-exchange method due to the lack of Ni metal particles (according to the ESR data) on which the growth of carbon nanofibers occurs.

Table 2
Textural characteristics of catalysts obtained by methods 1 and 2

Catalyst	Heat treatment	$D^{ef.}_{pore}$ (nm)	D_{pore} average (nm)	S_{BET} (m^2/g)		V_{pore} (cm^3/g)
				Ar	N_2	
1	In N_2, 350 °C	3.5	5.2	8.1	7.9	0.01
2	In N_2, 350 °C	3.5	6.4	6.7	5.8	0.01
1	In H_2, 550 °C	9.5	16.7	0.9	0.62	0.0026
2	In H_2, 550 °C	3.5	9.6	4.4	3.4	0.0082

Fig. 5 shows the dependence of methane conversion on the reaction time. Catalyst 1 deactivates quite rapidly; 30 min after the reaction onset its activity drops sharply, and the reaction ceases in 3 h. Two periods of steady operation are observed on catalyst 2 (their total time is 120 min), the reaction proceeding with high methane conversion, then a gradual deactivation of the catalyst starts. The catalysts differ not only in their lifetime but also in the amount of carbon formed.

In catalyst 1, a weak interaction of the active component with the support, on the one hand, facilitates the detachment of metal particles from the support surface causing growth of carbon filaments unattached to the support; on the other hand, it favors the enlargement of Ni particles up to 400 nm (Fig. 4(1b)) during the reaction. The enlargement of Ni particles to this size may result in their partial peeling from the surface of glass fiber or incapsulation by carbon deposits, causing fast deactivation of the catalyst. Fig. 4(1b) displays the micrograph of carbonized sample of catalyst 1 after 30 min operation. Along with carbon filaments of thickness 25–70 nm, this sample contains 200–500 nm metal particles incapsulated by carbon. The active component of catalyst 2, uniformly distributed in the secondary washcoating alumina layer, is composed of particles ∼16 nm in size, which are enlarged to the size about 50 nm during methane decomposition (Fig. 4(2b)). Probably, this is the optimal size, providing a longer catalyst operation as compared to catalyst 1.

Morphology of catalysts affects also the macrotextural properties of the formed CNF. Even at the initial period of the reaction (30 min after the onset) at a low CNF content ($C_{CNF} \sim 10\%$), carbon filaments forming on catalyst 1 virtually ‘‘hang’’ in the space between the glass fibers (Fig. 4(1c)). In the case of catalyst 2, the washcoat holds carbon fibers on its surface, preventing their detachment into the interfibrillar space (Fig. 4(2c), $C_{CNF} \sim 10\%$). This effect is most pronounced at high carbon contents in the samples. Fig. 4(1d) presents the micrograph of catalyst 1 sample containing 15 wt.% CNF, which shows that carbon filaments are arranged separately from glass fibers. For catalyst 2, the detectable carbon coating detachment from the fiber surface occurs only at a rather high carbon content. This is demonstrated in Fig. 4(2d) for the sample with 24 wt.% CNF content.

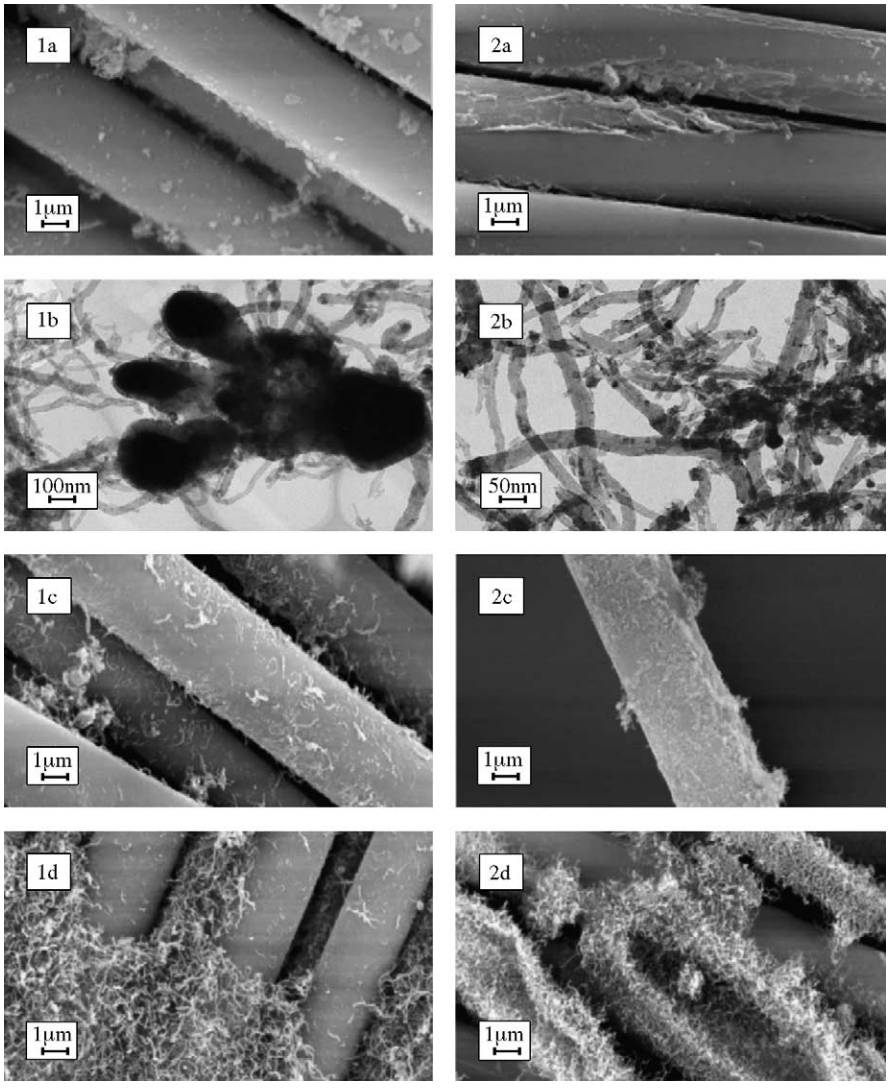

Fig. 4. The micrographs of catalysts 1 and 2 before and after the reaction: (1a) catalyst 1; (1b) CNF/cat. 1 (TEM); (1c) 10% CNF/cat. 1; (1d) 15% CNF/cat. 1; (2a) catalyst 2; (2b) CNF/cat. 2 (TEM); (2c) 10% CNF/cat. 2; (2d) 24% CNF/cat. 2.

4. Properties of CNF

The samples of CNF on catalyst 2 were taken for further physico-chemical studies. Depending on the reaction time, the samples contain different amounts of CNF (Table 4).

4.1. XRD

The size of Ni particles, determined from the coherent scattering region, changed from 16 nm for the initial catalyst

Table 3
Methane conversion, lifetime and carbon capacity of catalysts prepared by different methods

Catalyst	Ni (wt.%)	$X^0_{CH_4}$ (%)	τ_{cat} (h)	G_C (gC/gNi)
1	4.5	35	3	8.3
2	2.2	38	5.7	55
3	0.02	0	0	0

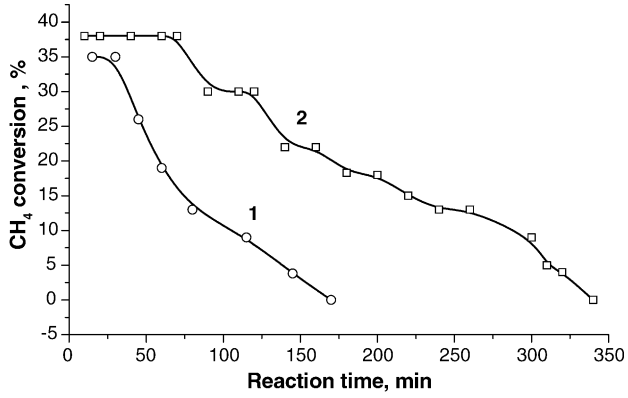

Fig. 5. The dependencies of methane conversion on the reaction time and preparation procedure (methods 1 and 2).

Table 4
List of samples prepared on catalyst 2

Sample code	CNF content (wt.%)	Reaction time (min)
2.1	6.5	15
2.2	10	25
2.3	24	60
2.4	55	350

to 20 nm after 15 min (sample 2.1), 35 nm after 25 min (sample 2.2) and 40 nm after 60 min (sample 2.3) of the reaction. The Ni metal phase is not detected in sample 2.4, since dilution of the sample with carbon decreases the nickel concentration by a factor of 2, making it lower than the sensitivity of the method. Carbon phase is detected in the samples with carbon content exceeding 10 wt.%. Diffraction pattern of sample 2.3 shows the maxima corresponding to three phases: X-ray amorphous phase of support at 22.3°; Ni metal phase at 44.5 and 52°, size 40 nm; and carbon phase with the maximum at 26°. Characteristics of the carbon structure ordering were determined only for the sample with the CNF concentration of 55 wt.%. Diffraction pattern of sample 2.4 corresponds to a nearly pure carbon phase, which is characterized by a local ordering in the structure of adjacent layers, parameter $L_c = 3.9$ nm, and by a local ordering within each layer, parameter $L_a = 6.9$ nm, which is much smaller than the diameter of filament. Interlayer distance d_{002} is 0.343 nm, and degree of graphitization (g) calculated from this parameter is 0.116. These parameters are close to those found for the turbostratic structure of granulated CNF synthesized under similar conditions ($L_c = 4.3$ nm; $L_a = 6.2$ nm; $d_{002} = 0.343$ nm) [15].

4.2. TEM

Fig. 6 displays the micrograph of carbonized fiber sample taken 1 h after the reaction onset (sample 2.3). Morphology of the carbon phase is presented by filaments 20–50 nm thick, corresponding to the size of metal particles. Ni metal particles have the cuboctahedral form typical for the

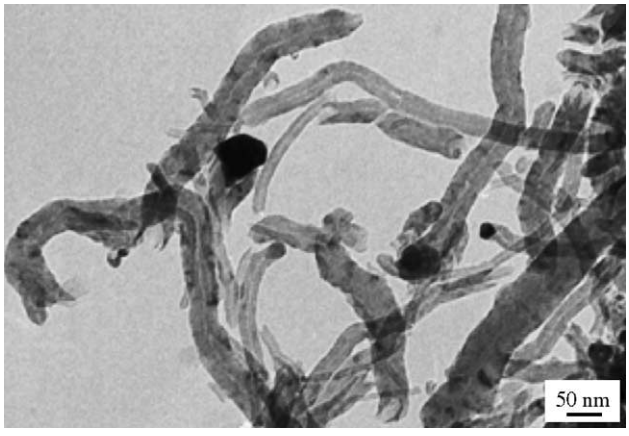

Fig. 6. Carbon nanofibers with Ni particles.

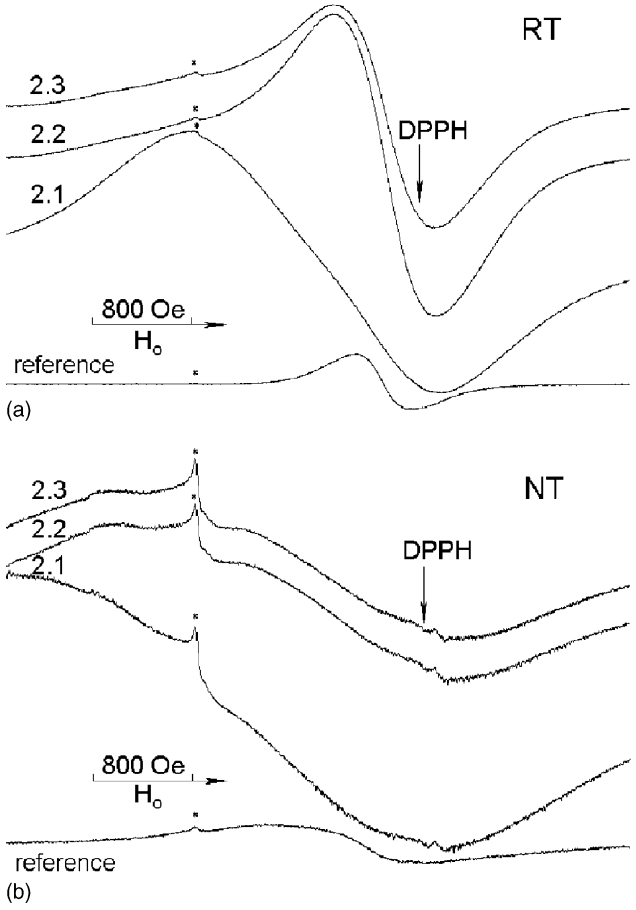

Fig. 7. ESR spectra of the samples with different CNF content: 2.1–6.5%, 2.2–10%, 2.3–24%, ref. – granulated CNF (a) at room temperature; (b) at 77 K.

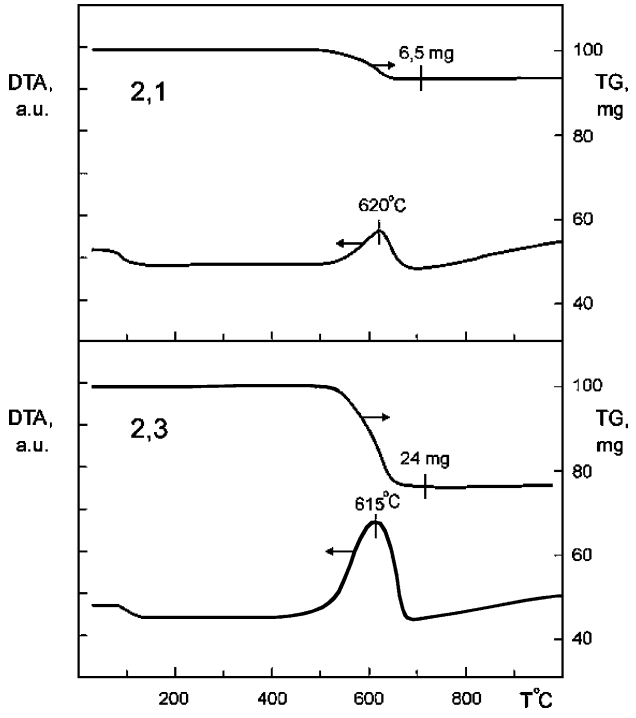

Fig. 8. DTA and TG curves of the samples: 2.1–6.5% CNF; 2.3–24% CNF.

Table 5
Textural properties of CNF on SGF after methane decomposition at different reaction times

Sample code	Reaction time (min)	CNF (wt.%)	$D_{pore}^{ef.}$ (nm)	$D_{pore}^{average}$ (nm)	V_{pore} (cm^3/g)	S_{BET} (m^2/g)	Size distribution of pore volume	
							(nm)	(%)
2.1	15	6.5	3.6	4.64	0.01	4.8	3.0–7.0	50
							7.0–12.0	7.5
							12.0–17.5	5
							>17.5	37.5
2.3	60	24	3.6	7.43	0.035	19	3.0–7.0	17
							7.0–12.0	14
							12.0–17.5	14
							>17.5	55
2.4	350	55	3.6; 12.0	10.64	0.138	51.7	3.0–7.0	10
							7.0–12.0	12
							12.0–17.5	18
							>17.5	60

formation of CNF with conical arrangement of graphite layers with respect to the filament axis [15].

4.3. ESR

XRD data showed that CNF that forms during CH_4 decomposition in the samples under study has a graphite-like structure. The experimentally obtained value $d_{002\ carbon} = 0.343$ nm exceeds the interplanar distance for ideal graphite ($d_{002\ graphite} = 0.335$ nm). It means that the structure of the formed carbon has only a local ordering and does not exclude the presence of the graphite structure defects. Presumably, different steps of the reaction yield carbon with different degree of structural ordering. It is not improbable that samples comprise a small amount of amorphous carbon (as coke). Coke is known to contain a large amount of paramagnetic sites, so the ESR method was used to study the samples after methane decomposition at different reaction times. Samples 2.1, 2.2 and 2.3 were used in these experiments. The samples contain ~2 wt.% Ni. Granulated CNF prepared on 90% Ni–Al_2O_3 and containing 0.18% Ni was used as the reference sample. ESR spectra were taken at room temperature (Fig. 7a) and at the temperature of liquid nitrogen (Fig. 7b). Spectral lines of samples are very broad (the width of the narrowest line is ~800 Gs) and cannot be assigned to the ESR spectra of coke, which has the g-factor equal to $g_e = 2.0023$ and the line width of 1–7 Gs. The ESR spectrum of granulated CNF differs from the above spectra only in a lower intensity of the lines. All the lines observed can be assigned to the ESR spectra of Ni^0 ferromagnetic particles. It was assumed that ferromagnetic nickel particles affect the paramagnetic pattern of coke and cause the line broadening. To exclude the effect of Ni, the samples were washed by boiling in a 3 M solution of hydrochloric acid, followed by repeated washing with distilled water to remove Cl^- ions. Ni content in the samples decreased approximately by a factor of 7. ESR spectra of the washed samples showed a much lower intensity of the lines, but no ESR spectra of coke were observed.

The effect of oxygen is well known from the literature on ESR studies of coke [16]. This effect is represented by broadening of the ESR spectra of coke at adsorption of small amounts of molecular oxygen. So, air was pumped out from the ampoules with samples at 250 °C to pressure 10^{-2} Torr. After removal of oxygen, ESR spectra did not change. The obtained data indicate that the ESR spectra of coke are absent in the samples studied irrespective of the degree of magnetism of nickel particles and the presence of oxygen. Therefore, it can be assumed that the formed CNF in the samples studied are of graphite-like structure, containing degenerated electron gas (the occurrence of electron conduction). It is known that in this case, electron gas is connected with localized paramagnetic sites of the graphite-like structure by exchange interaction, which leads to considerable broadening of ESR spectra of these sites.

4.4. TGA and DTA

Carbon species of different nature burn out at different temperatures, so the samples of CNF on glass fibers (2.1 and 2.3) obtained after 15 and 60 min of methane decomposition were studied by DGA and DTA. An exoeffect is observed at 615–620 °C in the DTA curves of samples 2.1 and 2.3

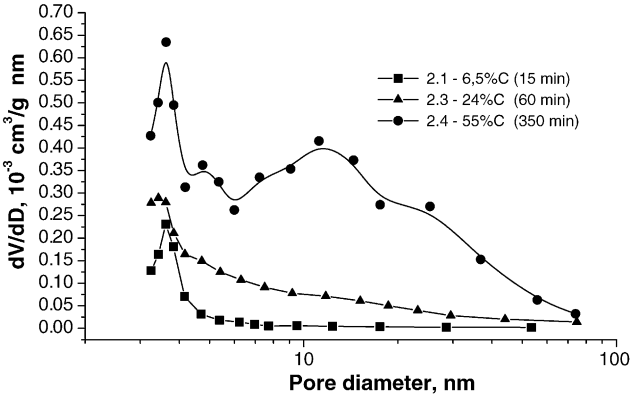

Fig. 9. Pore size distribution for the samples with different CNF content.

Table 6
Effect of treatment of CNF on SGF in neutral and acid media

Treatment conditions	Ni content in the initial sample (wt.%)	Ni content in the washed sample (wt.%)	Washing degree (%)	C content in the initial sample (wt.%)	C content in the washed sample (wt.%)	Carbon losses (%)
1) In H_2O at 100 °C for 10 h	2.3	Not determined	Not determined	23.3	22.9	1.7
2) In 3 M HCl at 100 °C for 10 h	2.3	0.3	87	23.3	21.8	6.4
3) In H_2SO_4 at 20 °C for 150 h	2.3	0.1	95.6	23.3	20.5	12.0

(Fig. 8). The absence of other peaks is an indirect evidence of the uniform composition of CNF. TGA was used for the determination of CNF content in samples.

4.5. Textural properties

Nitrogen adsorption isotherms at 77 K, obtained at measuring the textural properties CNF grown on SGF, form the capillary-condensation hysteresis loop, which is assigned to the H-3 type according to the IUPAC classification. The H-3 type loop is typical for mesoporous materials with predominating slit-like pores. Textural properties of CNF on SGF depend on the diameter of formed carbon filaments and their orientation in space relative to each other and to glass fibers. As the reaction proceeds, the size of Ni particles changes, and so does the thickness of carbon filaments. Thus, one may expect the textural parameters of the forming carbon phase to change with increasing reaction time. Textural properties of the samples with different CNF content obtained in 10 min, 1 and 6 h after the reaction onset are presented in Table 5. Fig. 9 shows the differential pore size distribution.

An observed increase in the total pore volume and specific surface area of the samples with increasing reaction time is obviously caused by the increased amount of mesoporous carbon phase.

Differential curves of the pore size distribution (Fig. 9) show the maximum at 3.6 nm for all samples. As the reaction time increases, broadening of the forming pores occurs. Filaments of different thickness can entangle or grow into the interfibrillar space, ultimately forming the porous structure with polydisperse pore distribution.

From the values of V_{pore} and S_{BET} for CNF and the same values for the initial catalyst, the pore volume and specific surface area of the carbon phase can be calculated: V_{pore} = 0.245 cm^3/g; S_{BET} = 94 m^2/g (sample 2.4). These values are close to those obtained for bulk CNF synthesized under similar conditions over the 90% Ni 10% Al_2O_3 catalyst (V_{pore} = 0.22 cm^3/g; S_{BET} = 109 m^2/g; D_{pore} = 10.8 nm) [15].

4.6. Stability of CNF on SGF

Samples of carbonized catalysts on glass fibers contain nickel particles. To prepare catalysts on carbon support or to modify functional groups on the carbon surface, the samples are treated with mineral acids for removing the metal particles. In such cases, of great importance is the stability of carbon coating to losses caused by the action of aggressive media under hydrothermal conditions. Results of treatment of carbonized samples under various conditions are presented in Table 6. It is seen that practically no carbon is removed if the treatment is performed in neutral medium. Boiling in a diluted hydrochloric acid or long treatment by concentrated sulfuric acid results in minor carbon losses, which may be caused by partial dissolution of the glass fiber components and peeling of carbon filaments weakly bonded to the surface.

5. Conclusion

Samples of CNF with different carbon content (6.5–55 wt.%) were prepared by decomposition of CH_4 on supported Ni catalysts. The influence of the preparation method of Ni catalysts on their properties and activities in methane decomposition was studied. The alumina coating in catalyst 2 was shown to stabilize its textural parameters and lead to the formation of the active component state with an optimum size of Ni particles providing a high carbon capacity of the catalyst.

The X-ray diffraction analysis showed that the obtained CNF has a graphite-like structure with the following parameters: d_{002} = 0.343 nm, L_c = 3.9 nm and L_a = 6.9 nm. The ESR and DTA methods demonstrated that the CNF has a uniform structure and does not include the amorphous phase. According to the ESR data, carbon has a graphite-like structure with electron conduction.

Carbon forms as filaments of diameter 20–50 nm. The diameter of the filaments corresponds to the size of catalytic particles of Ni metal, which has the cuboctahedral form typical for the formation of CNF with conical embedding of graphite layers with respect to the filament axis.

According to the nitrogen adsorption data, CNF is a mesoporous material with polydisperse pore distribution. It was revealed that the values of structural and textural parameters of CNF grown on glass fiber supports are close to those of granulated CNF obtained in methane decomposition over high-loaded nickel-alumina catalysts.

References

[1] J.R. Rostrup-Nielsen, D.L. Trimm, J. Catal. 48 (1977) 155.
[2] K.P. De Jong, J.W. Geus, Catal. Rev. 42 (4) (2000) 481.

[3] L.B. Avdeeva, T.V. Reshetenko, Z.R. Ismagilov, V.A. Likholobov, Appl. Catal. A 228 (2002) 53.
[4] C. Pham-Huu, N. Keller, L.J. Charbonniere, R. Ziessel, M.J. Ledoux, Chem. Commun. (2000) 1871.
[5] Th. Vergunst, F. Kapteijn, J.A. Moulijn, Carbon 40 (2002) 1891.
[6] V.V. Barelko, P.I. Khalzov, S.M. Baturin, et al., RU Patent 2081898 (1994).
[7] I. Yuranov, L. Kiwi-Minsker, M. Slin ko, E. Kurkina, E.D. Tolstunova, A. Renken, Chem. Eng. Sci. 55 (2000) 2827.
[8] V. Höller, I. Yuranov, L. Kiwi-Minsker, A. Renken, Catal. Today 69 (2001) 175.
[9] F. Reinone, L. Kivi-Minsker, D.A. Bulushev, Ph.A. Buffat, A. Renken, Appl. Catal. A 244 (2003) 251.
[10] V.V. Barelko, B.S. Balzhinimaev, C.P. Kildyashev, et al., US Patent 0082088 (2003).
[11] V.V. Barelko, P.I. Khalzov, V.N. Zvyagin, et al., RU Patent 2069584 (1994).
[12] J. Mering, J.J. Maire, Chem. Phys. 57 (1960) 803.
[13] K. Hedden, S. Ruch, Chem. Eng. Technol. 39 (1967) 1017.
[14] O.V. Goncharova, L.B. Avdeeva, V.B. Fenelonov, et al. Kinet. Catal. 36 (1995) 268.
[15] T.V. Reshetenko, L.B. Avdeeva, Z.R. Ismagilov, et al. Carbon 41 (2003) 1605.
[16] A.A. Shklyaev, V.F. Anufrievko, L.M. Vasilieva, DAN SSSR 200 (No. 5) (1971) 1165.

Углеродные материалы в химической технологии

УДК 546.261-161

Особенности свойств аморфного углеродного материала как носителя электродных катализаторов для топливных элементов

Ч. Н. Барнаков, А. П. Козлов, С. К. Сеит-Аблаева, А. И. Романенко, Н. Т. Васенин, В. Ф. Ануфриенко, З. Р. Исмагилов, В. Н. Пармон

ЧИНГИЗ НИКОЛАЕВИЧ БАРНАКОВ — кандидат химических наук, старший научный сотрудник лаборатории химии и химической технологии угля Института угля и углехимии СО РАН (ИУУ СО РАН). Область научных интересов: новые углеродные и композиционные материалы.

АЛЕКСЕЙ ПЕТРОВИЧ КОЗЛОВ — кандидат химических наук, научный сотрудник лаборатории химии и химической технологии угля ИУУ СО РАН. Область научных интересов: структура и свойства углеродных материалов.

650099 Кемерово, пр. Советский, 18, ИУУ СО РАН, тел. (3842)36-81-88, E-mail han@kemnet.ru

СВЕТЛАНА КАЮМОВНА СЕИТ-АБЛАЕВА — кандидат химических наук, доцент кафедры органической химии Кемеровского технологического института пищевой промышленности. Область научных интересов: окислительные превращения липидов.

АНАТОЛИЙ ИВАНОВИЧ РОМАНЕНКО — доктор физико-математических наук, ведущий научный сотрудник лаборатории физики низких температур отдела термодинамических исследований Института неорганической химии СО РАН. Область научных интересов: материаловедение, углеродные наноструктуры, сверхпроводимость.

630090 Новосибирск, пр. Акад. Лаврентьева, 3, ИНХ СО РАН, E-mail air@che.nsk.su

НИКОЛАЙ ТИМОФЕЕВИЧ ВАСЕНИН — младший научный сотрудник лаборатории экологического катализа Института катализа им. Г.К. Борескова СО РАН (ИК СО РАН). Область научных интересов: ЭПР, магнетизм. E-mail vasenin@catalysis.nsk.su

ВЛАДИМИР ФЕОДОСЬЕВИЧ АНУФРИЕНКО — доктор химических наук, ведущий научный сотрудник лаборатории каталитических методов преобразования солнечной энергии ИК СО РАН. Область научных интересов: физические методы в катализе, магнетизм.

ЗИНФЕР РИШАТОВИЧ ИСМАГИЛОВ — доктор химических наук, заведующий лабораторией экологического катализа ИК СО РАН. Область научных интересов: гетерогенный катализ, промышленная экология. E-mail zri@catalysis.ru

ВАЛЕНТИН НИКОЛАЕВИЧ ПАРМОН — академик, директор ИК СО РАН. Область научных интересов: физическая химия, химическая физика, катализ и фотокатализ, химическая кинетика в конденсированных фазах, радиоспектроскопия. E-mail parmon@catalysis.ru

630090 Новосибирск, пр. Акад. Лаврентьева, 5, ИК им. Г.К. Борескова СО РАН

Характеристика аморфного углеродного материала (АУМ) только по элементному составу и данным, полученным на основе анализа изотерм адсорбции азота, не является достаточной. Показано, что в процессе образования АУМ, в частности из ароматических предшественников с различными функциональными группами в условиях термокаталитического синтеза при различных времени и температуре карбонизации, образуется углеродный материал, обладающий как одномерной, так и трехмерной проводимостью.

Одномерная проводимость, возможно, связана с образованием карбина, как промежуточной стадии образования АУМ при температурах порядка 700 °С, либо при температуре 900 °С и небольшом (до 15 минут) времени карбонизации. Предполагается, что одномерная проводимость может влиять на выходную мощность топливного элемента, если АУМ используется в качестве носителя катализатора катодной мембраны.

Ранее методами электронной спектроскопии высокого разрешения (HRTEM) и дифракции электронов было показано [1], что аморфный углеродный материал, в отличие от активированного угля, волокнистых углеродных материалов и наноуглерода, состоит из структуры, сформированной графитоподобными слоя-

ми (графенами) моноатомной толщины (порядка 0,3 нм). Аналогичные результаты получены и при рентгенографических исследованиях образцов, приготовленных из ароматических соединений. Когда толщина поверхностного слоя приближается к молекулярным размерам, наночастица будет более рыхлой по сравнению с объемной конденсированной фазой, причем вся наночастица будет неоднородной [2]. Эта неоднородность дает разнообразие свойств углеродного материала, что может проявляться как в различных парамагнитных свойствах углеродного материала, так и в разной его проводимости.

В таблице представлены характеристики образцов АУМ, полученных из ароматических соединений с различными функциональными группами методом термокаталитического синтеза (карбонизация при 700—800 °С в присутствии щелочи — гидроксида натрия или калия, либо их эквимолярной смеси) [1, 3]. Элементный анализ образцов, выполненный по стандарту ISO 625-75 на приборе CarloErba с CHN анализатором, показал наличие углерода (89—90%(масс.)), водорода (0,5—0,6%(масс.)) и кислорода (остальное). Азот и сера не были обнаружены. Удельная поверхность по БЭТ, объем и поверхность микропор полученных образцов АУМ определяли на установке ASAP-2400 (Micromeritics) по адсорбции азота при 77 K. Перед измерениями проводили предварительную тренировку образцов при 300 °С и остаточном давлении менее 0,001 мм рт.ст. до прекращения газовыделения. После тренировки до измерения изотермы адсорбции контакт с атмосферой был исключен. Изотермы адсорбции азота записывали в диапазоне относительных давлений от 0,005 до 0,995 и проводили их стандартную обработку с расчетом суммарной поверхности методом БЭТ, объема микропор с размером до 2 нм и поверхности мезопор, остающейся после заполнения микропор. Полученные образцы АУМ можно представить, подобно изомерам, как гомологический ряд одного состава с разной структурой поверхности [2]. Одной из характерных особенностей этого гомологического ряда АУМ является наличие более 80% микропор.

Полученные образцы АУМ были испытаны в качестве носителей платиновых катализаторов для катодов топливных элементов с протонообменной мембраной. Лучшие показатели по выходной мощности топливного элемента получены на АУМ-1 — образце из нефтяного кокса [4]. Для этого образца АУМ характерна большая интенсивность спектра ЭПР, достигающая 10^{20} спин/г.

Для сравнения в качестве носителей были использованы углеродные нановолокнистые (УНВ) материалы различного строения и стандартный носитель Vulcan XC-72R. Результаты тестирования показали [4], что при плотности тока 100 мА/см^2 и содержании платины от 0,02 до 0,09 мг/см^2 катодный катализатор на основе УНВ, независимо от структуры носителя, имеет более низкие вольтамперные характеристики по

Таблица

Характеристики поверхности образцов АУМ

№	Предшественник образца	Удельная поверхность, м^2/г		Удельный объем, см^3/г	
		общая	микропор	всех пор	микропор
1	Нефтяной кокс	3331	3149	1,84	1,56
2	Фенол	2240	1871	1,53	0,98
3	8-Оксихинолин	2548	2235	1,59	1,21
4	Гидрохинон	2453	2342	1,36	1,22
5	*о*-Нитроанилин K^+	1674	1618	0,87	0,79
6	*о*-Нитроацетонилид K^+	1692	1661	0,85	0,80
7	*о*-Нитроанилин Na^+	1921	1679	1,34	1,05
8	*о*-Нитроанилин Na^+	2559	2167	1,74	1,25
9	*о*-Нитроанилин Na^+	2508	2351	1,51	1,31
10	Гидрохинон K^+	2697	2592	1,50	1,38
11	Гидрохинон K^+	2835	2663	1,70	1,50
12	Гидрохинон K^+	2765	2593	1,64	1,43
13	2,4-Динитроанилин	1148	1123	0,57	0,52
14	Барбитуровая кислота K^+	1400	790	1,47	0,41
15	*п*-Хинондиоксим *п*-гидрохинон (1:2)	2470	2166	1,64	1,27
16	*п*-Хинондиоксим *п*-гидрохинон (1:2)	2620	1796	2,14	1,07
17	*п*-Хинондиоксим *п*-гидрохинон (1:2)	2770	2271	1,92	1,29
18	Хиноловый эфир	2360	2265	1,25	1,10

сравнению с катализатором на основе традиционного Vulcan XC-72R при такой же концентрации платины (0,04—0,06 мг/см^2). И наоборот, катализатор, где в качестве основы выступает АУМ-1 имеет более высокие показатели вольтамперной характеристики, в том числе и при низком содержании платины (0,02—0,06 мг/см^2) в образце.

Для изучения спектров ЭПР нами специально по методике [1] из ароматических соединений, представленных в таблице, были синтезированы три образца, отличающиеся только удельной поверхностью. Образец № 1 — с удельной поверхностью 1800 м^2/г был получен в результате карбонизации в течение 30 мин при температуре 900 °С. Образец № 2 с удельной поверхностью 2200 м^2/г получен в результате карбонизации в течение 15 мин при 700 °С. Образец № 3 — с удельной поверхностью 2900 м^2/г, получен в результате карбонизации в течение 15 минут при 900 °С.

На рис. 1 показаны спектры ЭПР образцов, которые снимали на спектрометре Brucker 200 D при 77 и 273 К (λ = 3 см) после предварительного вакуумирования при 200 °С. Для образца № 1 каких-либо сигналов в спектре ЭПР не было обнаружено. Этот результат согласуется с давно известными фактами [5], что после карбонизации углеродного сырья или угля при температурах выше 700 °С спектры ЭПР локализованных электронов не наблюдаются, вероятно, из-за уширения спектров электронным газом образующихся графитовых структур.

Для вакуумированных образцов № 2 и № 3 наблюдаются симметричные спектры ЭПР $g = g_e$ (рис. 1). Ширина линий в спектре образца № 2 при комнатной температуре — 15 Гс, при температуре жидкого азота — 10 Гс. Образец № 3 имеет линии шириной 34 Гс (293 К) и 24 Гс (77 К). Отметим, что для углеродных систем (угли, коксы) ширина линий ЭПР заметно меньше (< 10 Гс). Для обоих образцов интегральная интенсивность спектров очень высокая и достигает $10^{19} \div 10^{20}$ спин/г. Обнаружено, что для спектров этих двух образцов не выполняется закон Кюри: при понижении температуры измерений интегральная интенсивность не только не возрастает, а заметно уменьшается. Это уменьшение проявляется для образца № 3 в существенно большей степени (в 4 раза), чем для образца № 2 (в полтора раза).

Анализ обнаруженной особенности спектров ЭПР позволяет предположить, что исчезновение спектров, вероятно, связано с некоторой локализацией электронного газа при понижении температуры вокруг дефектов структуры, на которых локализуются наблюдаемые неспаренные электроны (модель *C-S* релаксации [6], где *C* — локализованные электроны, *S* — электронный газ). Результаты измерения проводимости подтверждают это предположение.

Температурная зависимость проводимости измерялась четырехконтактным методом в интервале температур 4,2—300 К. Исследуемые образцы в виде порошка запрессовывались в ампулу. Контакты к ампуле подводились серебряной проволокой диаметром 0,1 мм и для лучшего контакта образца с проволокой порошок в ампуле поджимали.

Температурные зависимости электропроводности образцов № 1—3 (рис. 2, 3) существенно различаются. Достаточно низкая концентрация носителей тока в АУМ ведет к подавлению металлической проводимости и к локализации электронов проводимости в ограниченной области пространства. В этом случае наблюдается прыжковая проводимость носителей тока между этими областями локализации. При понижении температуры обычная прыжковая проводимость между ближайшими центрами локализации сменяется прыжковой проводимостью с переменной длиной прыжка (ППППДП) и описывается обобщенным законом Мотта [7]:

$$\sigma_{\text{ППППДП}}(T) = \sigma_0 \cdot \exp(-B/T)^{1/(d+1)} \qquad (1)$$

где d — размерность пространства при движении носителей тока, $B = [16a^3/k_{\text{Б}}N(E_F)]$, a — обратная величина длины, на которой спадает амплитуда атомной волновой функции (обычно $1/a \sim 8 \div 10$ Å), $N(E_F)$ — плотность состояний на поверхности Ферми, σ_0 — постоянная.

Для образца № 1 во всем исследованном интервале температур проводимость описывается зависимостью

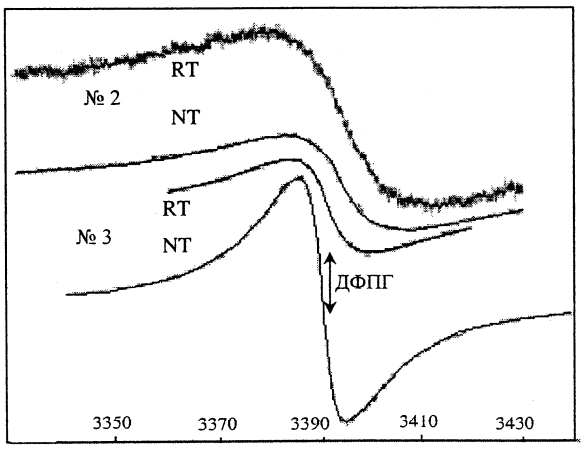

Рис. 1. Спектры ЭПР образцов № 2 и № 3 при комнатной температуре (*RT*) и температуре жидкого азота (*NT*)

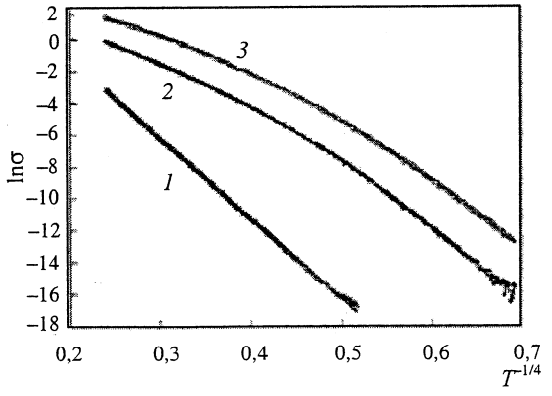

Рис. 2. Зависимость логарифма электропроводности от температуры в степени −1/4.

Цифры на кривых соответствуют номеру образца АУМ в тексте статьи

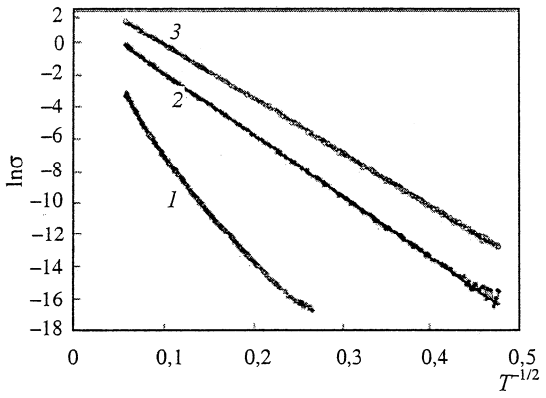

Рис. 3. Зависимость логарифма электропроводности от температуры в степени −1/2.

Цифры на кривых соответствуют номеру образца АУМ в тексте статьи

(2), соответствующей закону Мотта для трехмерного* случая, когда $d = 3$ (рис. 2).

$$\sigma(T) = \sigma_0 \cdot \exp(-T_0/T)^{1/4} \qquad (2)$$

Оценка величины B из данных рис. 2 для образца № 1 (линия 1) дает $B \sim 6{,}7 \cdot 10^6$ K. Оценка плотности состояний на поверхности Ферми $N(E_F)$ из этого значения параметра B (в предположении $1/a \sim 8 \div 10$ Å) дает $N(E_F) \sim 2 \cdot 10^{19}$ см$^{-3}$эВ$^{-1}$, что типично для дефектных графитов. Другими словами, для образца № 1 наблюдается обычный трехмерный закон Мотта, типичный для неупорядоченных проводников с малой концентрацией носителей тока, которые локализованы в ограниченной области пространства (дефектный графит). Тогда уширение спектров ЭПР локализованных электронов углерода объясняется эффектом «узкого горла» в модели *C-S* релаксации (T_{SL} очень короткое) за счет электронного газа *S* графитовых структур [7—9].

Для образцов № 2 и № 3 во всем исследованном интервале температур проводимость описывается зависимостью, соответствующей закону Мотта для одномерного случая, когда $d = 1$ (рис. 3).

$$\sigma(T) = \sigma_0 \cdot \exp(-T_0/T)^{1/2} \qquad (3)$$

Следует отметить, что закон Мотта для одномерного** случая уже наблюдался в углеродных структурах с карбиновыми цепочками [10—12], что сопровождается σ-подобной температурной зависимостью на рис. 3.

В связи с обнаружением одномерных структур для образцов № 2 и № 3 становится ясно, что зависимость $1/T_{SL}$ от температуры в этом случае будет существенно более ослаблена по сравнению со случаем трехмерных структур [6]. Это приведет к более слабой зависимости ширины сигнала ЭПР от температуры для образцов № 2 и № 3, по сравнению со случаем трехмерных структур. Заметно большее значение *H* для образца № 3 по сравнению с образцом № 2, вероятно, связано с большей концентрацией носителей для образца № 3. Это объясняет более слабую температурную зависимость интегральной интенсивности спектра ЭПР образца № 2, поскольку в таком случае структурное равновесие $C \leftrightarrow S$ сдвинуто вправо (типа химического обмена) и в целом для этой системы реализуется что-то типа парамагнетизма Паули, что приводит к слабой зависимости интегральной интенсивности спектра ЭПР от температуры.

Результаты работы позволяют сделать вывод о том, что характеристика АУМ только по элементному составу и характеристикам, полученным на основе анализа изотерм адсорбции азота, будет не полной. В процессе образования АУМ из ароматических предшественников с различными функциональными группами в условиях термокаталитического синтеза при различных времени и температуре карбонизации образуется углеродный материал, обладающий как одномерной, так и трехмерной проводимостью. Одномерная проводимость, по-видимому, связана с образованием карбина, как промежуточной стадии образования АУМ при низких температурах (700 °C), либо при температуре 900 °C и небольшом (до 15 минут) времени карбонизации. При равном содержании платины в катоде (0,02—0,09 мг/см^2) и размере частиц платины 2—4 нм выходная мощность топливного элемента, который использует в качестве носителя катализатора АУМ-1, оказалась выше, чем при использовании углеродных нановолокнистых материалов различного строения и стандартного носителя Vulcan XC-72R, по-видимому, из-за одномерной проводимости аморфного углеродного материала, к которой оказались чувствительны реакции на катоде.

* Трехмерная проводимость — свойство вещества, когда носители тока делокализованы во всех направлениях. В идеальном графите имеет место квазидвумерная проводимость — преимущественно вдоль слоя. В поперечном направлении проводимость тоже имеет место (из-за наличия ван-дер-вальсовых связей между слоями). Но эта проводимость более чем на четыре порядка меньше.

** Одномерная проводимость реализуется в случае наличия делокализации носителей тока только в одном направлении. В двух других направлениях носители тока двигаться не могут. Обычно это одномерные цепочки атомов или молекул. В случае карбина — вдоль оси карбина.

ЛИТЕРАТУРА

1. *Барнаков Ч.Н., Козлов А.П., Сеит-Аблаева С.К. и др.* Нефтехимия, 2004, № 6, с. 436—439.
2. *Русанов А.И.* Ж. общей химии, 2002, № 4, с. 532—549.
3. *Барнаков Ч.Н., Сеит-Аблаева С.К., Козлов А.П. и др.* Патент РФ № 2206394, 2003.
4. *Ismagilov Z.R., Kerzhentsev M.A., Shikina N.V. e. a.* Catal. Today, 2005, v. 102—103, p. 58—66.
5. Равилов Р. Г. Дисс.... канд. физ.-мат. наук..Новосибирск, 1980.
6. *Шкляев А.А., Ануфриенко В.Ф., Васильева Л.М.* Доклады АН СССР, 1971, т. 200, № 5, с. 1165.
7. *Hasegawa H.* Progr. Theor. Phys., 1959, v. 21, № 4, p. 483—500.
8. *Hirst L.L., Schafer W.* Phys. Rev., B, 1973, v. 8, № 1, p. 64.
9. *Gossard A.C., Heugar A.J., Wernick J.H.* J. Appl. Phys., 1967, v. 38, № 1, p. 12—51.
10. *Демишев С.В., Пронин А.А., Глушков В.В. и др.* Письма в ЖЭТФ, 2003, № 8, с. 984—993.
11. *Shenderova O.A., Zhirnov V.V., Brenner D.W.* Crit. Revs Solid State Mat. Sci., 2002, v. 27(3/4), p. 227—356.
12. *Сладков А.М.* Карбины — третья аллотропная форма углерода. Отв. редактор Ю.Н. Бубнов. М.: Наука, 2003, 151 с.

ISSN 0023-1584, Kinetics and Catalysis, 2007, Vol. 48, No. 4, pp. 581–588. © MAIK "Nauka/Interperiodica" (Russia), 2007.
Original Russian Text © Z.R. Ismagilov, A.E. Shalagina, O.Yu. Pod''yacheva, Ch.N. Barnakov, A.P. Kozlov, R.I. Kvon, I.Z. Ismagilov, M.A. Kerzhentsev, 2007, published in Kinetika i Kataliz, 2007, Vol. 48, No. 4, pp. 621–628.

CARBON IN CATALYSIS

Synthesis of Nitrogen-Containing Carbon Materials for Solid Polymer Fuel Cell Cathodes

Z. R. Ismagilov[a], A. E. Shalagina[a], O. Yu. Pod''yacheva[a], Ch. N. Barnakov[b], A. P. Kozlov[b], R. I. Kvon[a], I. Z. Ismagilov[a], and M. A. Kerzhentsev[a]

[a] *Boreskov Institute of Catalysis, Siberian Branch, Russian Academy of Sciences, Novosibirsk, 630090 Russia*
[b] *Institute of Carbon and Carbon Chemistry, Siberian Branch, Russian Academy of Sciences, Kemerovo, 650099 Russia*
e-mail: zri@catalysis.ru

Received December 5, 2006

Abstract—The following nitrogen-containing supports with various nitrogen contents and structure and texture properties were synthesized: carbon nanofibers (N-CNFs) and amorphous microporous carbon materials (N-AMCMs). It was found that the above characteristics can be regulated by varying synthesis conditions: precursor compositions and reaction temperature and time. Mesoporous nitrogen-containing CNFs with a specific surface area of 30–350 m^2/g and a pore volume of 0.10–0.83 cm^3/g were formed by the catalytic decomposition of a mixture of ethylene with ammonia at 450–675°C. Microporous materials (N-AMCMs) with a specific surface area of 472–3436 m^2/g and a micropore volume of 0.22–1.88 cm^3/g were prepared by the carbonization of nitrogen-containing organic compounds at 700–900°C. An increase in the carbonization temperature and reaction time resulted in an increase in the specific surface area and microporosity of N-AMCMs, whereas lower temperatures of 450–550°C and reaction times of 1–3 h were optimal for the preparation of N-CNFs with a developed texture. It was found that milder synthesis conditions and higher nitrogen contents of precursors were required for obtaining high nitrogen concentrations in both N-CNFs and N-AMCMs. The synthetic method developed allowed us to prepare carbon supports with nitrogen contents to 8 wt %.

DOI: 10.1134/S0023158407040179

INTRODUCTION

Platinum and platinum alloys supported on carbon materials are in current use as electrocatalysts in solid polymer fuel cell cathodes [1, 2]. The efficiency of these catalysts essentially depends on the specific surface area, pore structure, electric conductivity, and other characteristics of the carbon support [3, 4]. Carbon nanofibers (CNFs) have attracted considerable attention from the standpoint of the target-oriented synthesis of an optimum support for electrocatalysts [3–8]. CNFs are formed in the decomposition of carbon-containing compounds on iron subgroup metals; these are mesoporous materials with a specific surface area of 100–300 m^2/g. It is well known [9–14] that the structure and texture properties of CNFs depend on synthesis conditions such as the composition of the catalyst, the nature of the carbon precursor, and the temperature of the process. CNFs of a certain structure and morphology can be prepared by controlling the above parameters. It was found experimentally that the use of CNFs increased the activity and stability of platinum catalysts in electrode processes and increased the platinum efficiency, as compared with commercial carbon supports [3, 5–8].

The previously developed amorphous microporous carbon materials (AMCMs) with a high specific surface area (to 3300 m^2/g) and a considerable micropore volume (to 2 cm^3/g) [15–17] belong to another type of carbon supports that can be successfully used for the manufacture of highly active electrocatalysts. Previously [8, 18], we found that AMCMs can be efficiently used as the supports of platinum catalysts based on the stabilization of highly dispersed platinum particles in micropores.

Nitrogen-containing CNFs and AMCMs (N-CNFs and N-AMCMs, respectively) are promising materials for use as the supports of cathode catalysts. The presence of specific adsorption sites on the surface of nitrogen-containing materials results in a more uniform distribution of the active component and a high dispersion and high specific surface area of Pt particles [6, 9, 19]. In addition, an increased electric conductivity of N-CNFs, as compared with that of unmodified materials [20, 21], also facilitates high electrocatalytic activity.

The attractiveness of nitrogen-containing supports is due to the necessity of synthesizing new electrocatalysts with reduced noble metal concentrations and with the replacement of noble metals by Fe and Co compounds, in particular, based on Fe and Co complexes with ligands like phthalocyanines (N_4–M complexes, where M = Fe or Co) [22–28]. These metal chelates adsorbed on a carbon support after appropriate thermal treatment are active in the reaction of oxygen reduction in an acidic medium, and nitrogen-containing func-

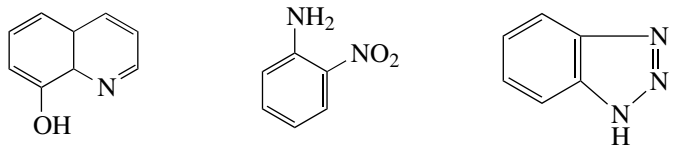

8-hydroxyquinoline *ortho*-nitroaniline 1,2,3-benzotriazole

Fig. 1. Nitrogen-containing organic precursors of N-AMCMs.

tional groups on the support surface can serve as transition metal adsorption and stabilization sites [29]. The activity of these catalysts increases with nitrogen concentration on the surface of the carbon material. As found using X-ray photoelectron spectroscopy (XPS) [29, 30], nitrogen atoms should occur in a pyridinic state in order to form an active site. Therefore, the electronic state of nitrogen atoms on the surface of a carbon support and the possibility of regulating this state by a controllable synthesis are of considerable importance.

The aim of this work was to synthesize carbon materials structurally modified with nitrogen atoms, to study the physical chemistry of formation of nitrogen-containing carbon materials, to optimize conditions for the preparation of materials with high specific surface areas and high nitrogen contents, and to determine the state distribution of nitrogen atoms depending on synthesis conditions.

Table 1. Effect of the chemical composition of the catalyst on the yield of N-CNFs (G), the nitrogen content of the material (N), and the specific surface area (S_{BET})

Catalyst	T, °C	G, g_C/g_{Cat}	N, wt %	S_{BET}, m^2/g
90Ni-Al_2O_3	550	11.6	0.47	158
82Ni-8Cu-Al_2O_3		11.5	0.90	206
65Ni-25Cu-Al_2O_3		12.4	1.58	282
45Ni-45Cu-Al_2O_3		11.2	0.74	280
72Co-3Mo-Al_2O_3	600	14.3	0.65	223
75Co-Al_2O_3		12.2	0.68	205
65Ni-25Cu-Al_2O_3		13.1	1.07	231
85Fe-5Co-Al_2O_3	625	0.5	–	–
62Fe-8Co-Al_2O_3		1.1	2.00	117
65Ni-25Cu-Al_2O_3		14.5	0.96	244

Note: Reaction conditions: decomposition of a mixture of 75% C_2H_4 and 25% NH_3 for 1 h.

EXPERIMENTAL

Synthesis of Nitrogen-Containing Carbon Materials

The N-CNFs were prepared by the decomposition of a mixture of C_2H_4 and NH_3 on the high-percentage metal catalysts[1]: 90Ni–Al_2O_3, 82Ni–8Cu–Al_2O_3, 65Ni–25Cu–Al_2O_3, 45Ni–45Cu–Al_2O_3, 85Fe–5Co–Al_2O_3, 62Fe–8Co–Al_2O_3, 75Co–Al_2O_3, and 72Co–3Mo–Al_2O_3. These catalysts were prepared by the coprecipitation of an active component and a support from a nitrate salt solution in accordance with published procedures [11, 31]. The mixtures of C_2H_4 and NH_3 with ammonia concentrations of 25, 50, and 75 vol % were used for the synthesis of the N-CNFs. The decomposition reaction was performed in a flow setup with a quartz vibrofluidized-bed reactor at 450–675°C and a pressure of 1 bar for 0.25–20 h. The catalyst load was 0.1 g; the flow rate of the reaction mixture was 2.25 l/h. The yield of carbon (G, g_C/g_{Cat}) was calculated as the weight ratio between the resulting carbon and the initial catalyst.

The N-AMCMs were prepared from nitrogen-containing organic precursors, which were either individual substances (8-hydroxyquinoline, *ortho*-nitroaniline, and 1,2,3-benzotriazole) or their equimolar mixtures (Fig. 1). The use of the equimolar mixtures of various nitrogen-containing organic compounds allowed us to obtain N-AMCMs with high nitrogen contents and high specific surface areas. To prepare N-AMCMs, the precursors were mixed with a concentrated aqueous solution of NaOH in a NaOH-to-precursor ratio of 1 : 3. The melt of an organic precursor with the alkali, which was obtained by the evaporation of water, was subjected to thermal treatment (carbonization) at 700–900°C for 20–80 min in a reducing atmosphere formed by carbonization gases or in an inert atmosphere. The carbonization product was washed with an aqueous solution of hydrochloric acid and then with water to a neutral reaction. The residue was dried at 105–115°C to constant weight.

[1] Henceforth, the number before the symbol of an element refers to the weight concentration in the catalyst with the balance aluminum oxide.

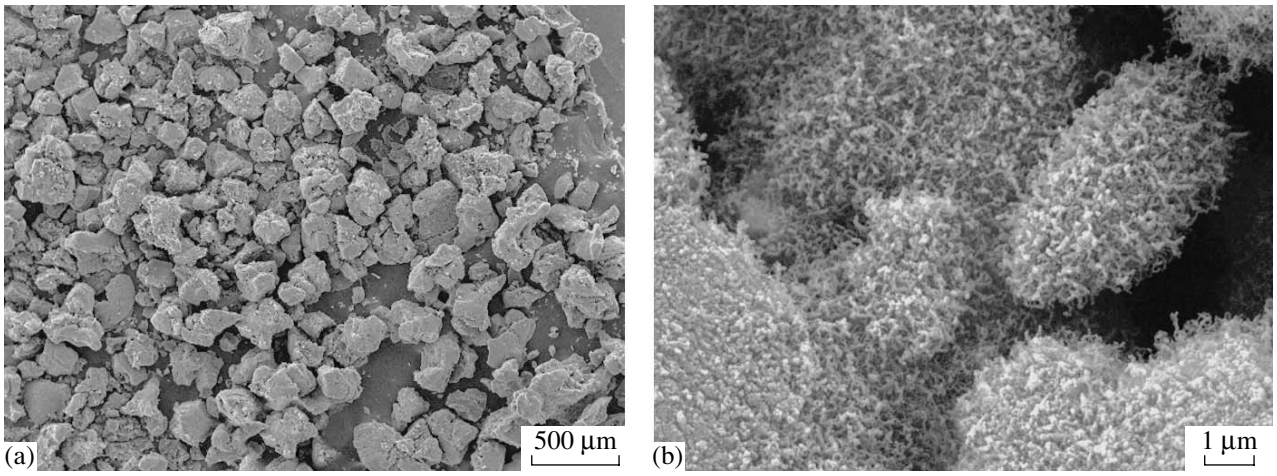

Fig. 2. SEM micrographs of the surfaces of N-CNF samples prepared by the decomposition of a 50% C_2H_4–50% NH_3 mixture on the 65Ni–25Cu–Al_2O_3 catalyst at 550°C.

Physicochemical Characterization Techniques

The phase composition and structure properties of carbon materials were studied using ex situ X-ray diffraction (XRD) analysis. The X-ray diffraction patterns were measured on an HZG-4 diffractometer with monochromated CuK_α irradiation.

The structure and morphology of N-CNFs and N-AMCMs were studied using transmission electron microscopy (TEM). The samples were supported onto a holey carbon film on a copper grid. The TEM images were obtained on a JEM-2010 transmission electron microscope with a lattice resolution of 1.4 Å and an accelerating voltage of 200 kV. The surface morphology of N-CNFs was studied using scanning electron microscopy (SEM) on a JSM-6460 microscope at an accelerating voltage of 20 kV.

The texture characteristics of carbon materials were determined using the low-temperature adsorption of nitrogen at 77 K on an ASAP-2400 automated instrument. The specific surface area was calculated from the BET equation.

The nitrogen contents of carbon samples were determined using elemental analysis on a Carlo Erba Model 1106 automatic elemental analyzer.

The surface composition and the electronic states of nitrogen and carbon atoms in N-CNFs and N-AMCMs were studied using XPS. The measurements were performed on a VG ESCALAB HP photoelectron spectrometer with the use of AlK_α irradiation; the spectrometer was calibrated using the following lines: Au4*f*(7/2) = 84.0 eV, Ag3*d*(5/2) = 368.3 eV, and Cu2*p*(3/2) = 932.7 eV. The residual gas pressure in the measurements was no higher than 3×10^{-8} mbar.

RESULTS AND DISCUSSION

Synthesis and Properties of N-CNFs

It is well known that the amount of carbon formed in the decomposition of hydrocarbons is proportional to the metal content of the initial catalyst [11, 12, 32]. Therefore, it is reasonable to use high-percentage metal catalysts with metal concentrations of 70–90 wt % in order to prepare a carbon material in a high yield. Data given in Table 1 indicate that iron-containing catalysts exhibited low activity in the decomposition of a mixture of C_2H_4 and NH_3, whereas the 90Ni–Al_2O_3, 82Ni–8Cu–Al_2O_3, 65Ni–25Cu–Al_2O_3, 45Ni–45Cu–Al_2O_3, 75Co–Al_2O_3, and 72Co–3Mo–Al_2O_3 catalysts exhibited similar activity in terms of the yield of a carbon product and resulted in the formation of 11–14 g_C/g_{Cat}

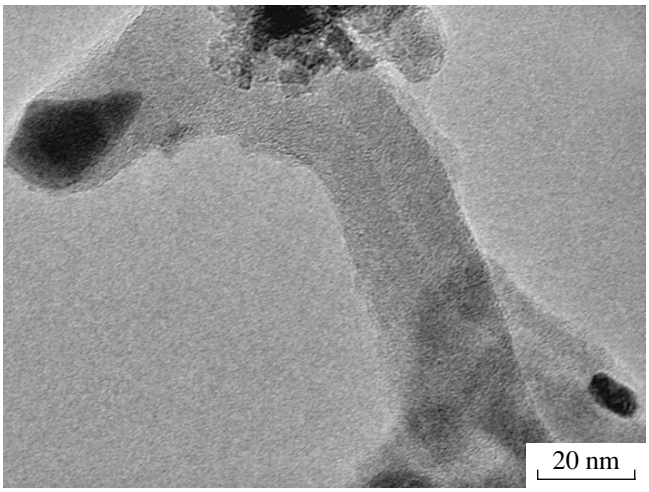

Fig. 3. TEM micrograph of an N-CNF sample prepared by the decomposition of a C_2H_4–NH_3 mixture on the 65Ni–25Cu–Al_2O_3 catalyst: the internal structure of carbon fiber.

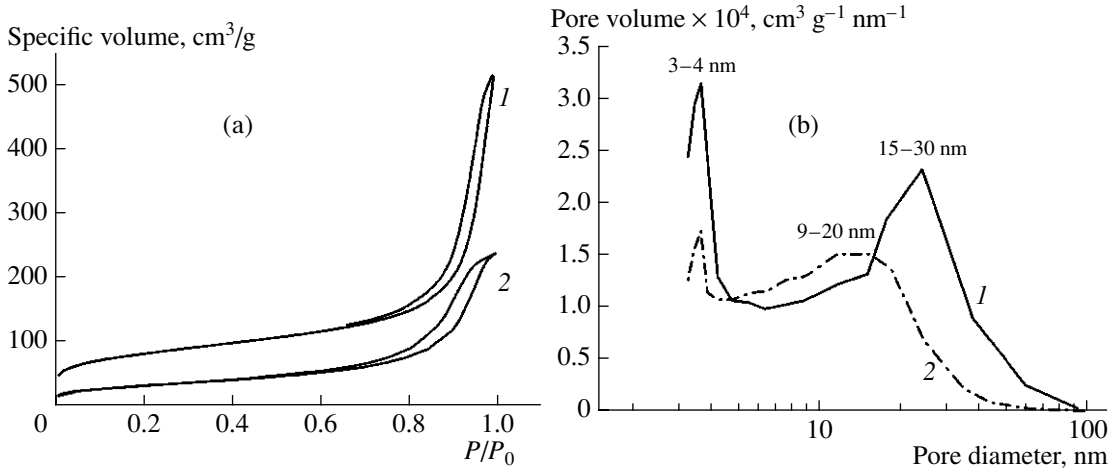

Fig. 4. (a) Sorption isotherms of N_2 at 77 K and (b) pore size distributions for N-CNF samples synthesized from a gas mixture of 50% C_2H_4 and 50% NH_3 for (*1*) 1 and (*2*) 20 h.

upon the decomposition of a 75% C_2H_4–25% NH_3 mixture for 1 h at 550–600°C. The maximum nitrogen content of N-CNFs and the maximum specific surface area were obtained with the use of the 65Ni–25Cu–Al_2O_3 catalyst. Therefore, this catalyst was chosen in order to perform a more detailed study of the formation of N-CNFs from a mixture of C_2H_4 and NH_3.

According to SEM data (Fig. 2a), a carbon material prepared by the decomposition of a mixture of C_2H_4 and NH_3 on the 65Ni–25Cu–Al_2O_3 catalyst consisting of granules of size 150–350 μm. As can be seen in high-resolution SEM micrographs (Fig. 2b), the surface of granules exhibited a fibrous morphology. Moreover, large pores about several micrometers in size were observed. It is likely that each granule was a combination of several agglomerates; in turn, these agglomerates were formed by chaotically interwoven CNFs.

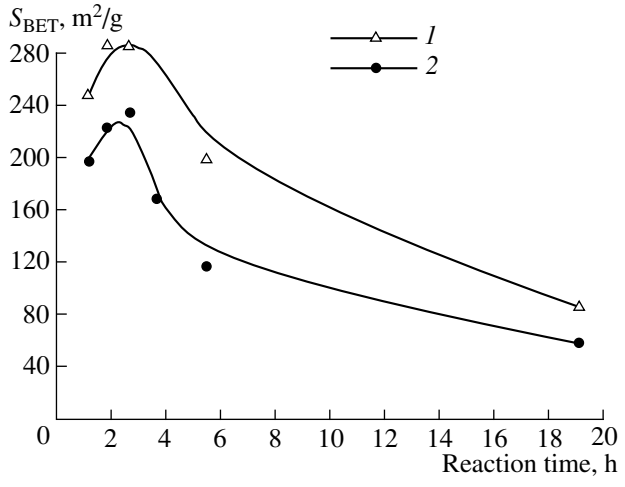

Fig. 5. Dependence of the specific surface area of CNFs on the composition of the initial reaction mixture: (*1*) 75% C_2H_4 and 25% NH_3 or (*2*) 100% C_2H_4. T = 550°C.

According to TEM data, CNFs are helical with a coaxial conical packing of graphite layers (Fig. 3); the fiber diameter is 25–100 nm. The XRD analysis of N-CNFs demonstrated that this material is graphite-like. The interplanar spacing varied within the range 0.343–0.347 nm depending on synthesis conditions. These values are higher than the interplanar spacing of ideal graphite (0.335 nm) [33]; this suggests the turbostratic structure of N-CNFs. With the use of XRD analysis, it was found that the size of coherent scattering regions of N-CNFs lies in the range 3.2–7.0 nm and is comparable with the size of coherent scattering regions for unmodified CNFs (3.3–9.5 nm) [14].

According to data on the low-temperature adsorption of N_2, the N-CNFs are mainly mesoporous materials, as evidenced by the type H1 capillary condensation hysteresis according to the IUPAC classification [34] (Fig. 4a). The BET average pore size was 5–19 nm. The specific surface area (S_{BET}) depended on CNF synthesis conditions and varied from 30 to 350 m^2/g. The pore size distribution curves had two maxima in the regions of 3–4 and 10–30 nm (Fig. 4b). Fenelonov et al. [35, 36] believed that pores of size 3–4 nm resulted from the formation of curved graphene structures on the closure of edge graphite planes at the fiber surface, whereas large pores of size 10–30 nm were spaces formed by the interweaving of fibers in the course of fiber growth. As the N-CNF synthesis time was increased, a distribution maximum in the region of large pores shifted toward smaller sizes. At the same time, the total pore volume decreased by a factor of 2 from 0.34–0.82 to 0.02–0.37 cm^3/g depending on the process temperature. It was found that the time dependence of S_{BET} exhibited a maximum in the region of 1–3 h at all of the reaction temperatures examined; in this case, lower synthesis

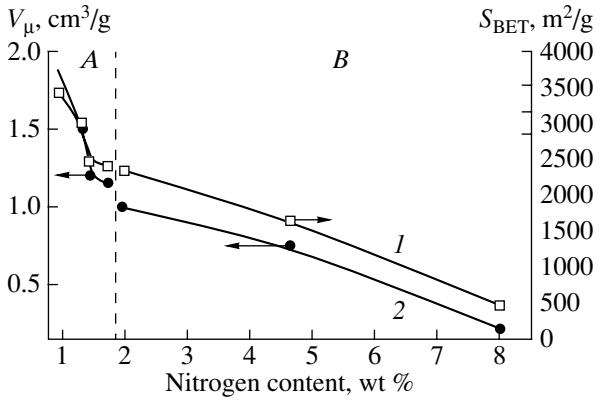

Fig. 6. Dependence of (*1*) specific surface area and (*2*) micropore volume on the nitrogen content of N-AMCM samples prepared with the use of (*A*) 8-hydroxyquinoline with benzotriazole or (*B*) *ortho*-nitroaniline with benzotriazole as precursors.

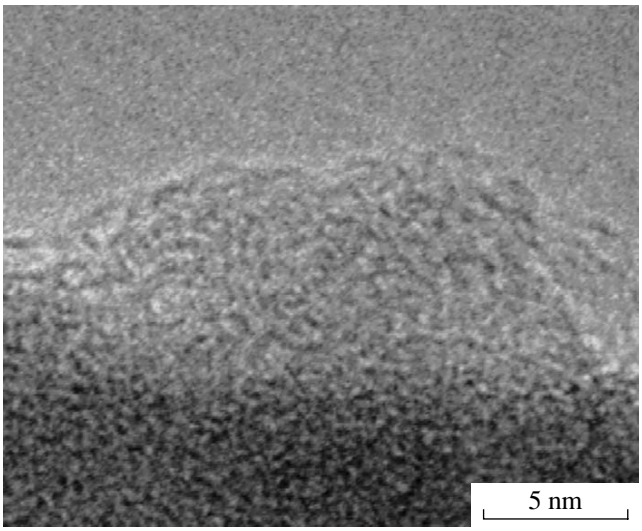

Fig. 7. TEM micrograph of an N-AMCM sample prepared from a mixture of *ortho*-nitroaniline and 8-hydroxyquinoline at 700°C (Table 3, sample no. 9).

temperatures were favorable for the production of higher specific surface areas. The dependence of S_{BET} on reaction time was also analogous for CNFs formed from 100% C_2H_4 (Fig. 5). Data shown in Fig. 5 indicate that the value of S_{BET} increased by a factor of 1.2–1.8 on the addition of ammonia to ethylene; in this case, the total pore volume increased by a factor of 1.1–1.6 and the micropore volume increased by a factor of 2.6–5.7 depending on reaction time.

A study of the effect of synthesis conditions on the nitrogen content of N-CNFs demonstrated that an increase in the reaction temperature from 550 to 675°C and an increase in the reaction time from 1 to 20 h resulted in a decrease in the nitrogen content of N-CNFs, whereas the nitrogen content of N-CNFs increased from 1.27 to 7.00 wt % as the concentration of ammonia in the reaction mixture was increased from 25 to 75 vol % (Table 2).

Synthesis and Properties of N-AMCMs

In the development of a preparation procedure for high-surface-area N-AMCMs with high nitrogen contents, we found that an increase in the alkali-to-precursor ratio, as well as an increase in the temperature and time of carbonization, resulted in an increase in the specific surface area and micropore volume of the resulting materials (Table 3). However, the severe conditions of carbonization resulted in a decrease in the nitrogen content of N-AMCMs to 1–2 wt % (sample nos. 3–7 and 9 in Table 3). It can be seen in Table 3 that milder carbonization conditions (700°C, a carbonization time of <40 min, and an alkali-to-precursor ratio of <2) were required for preparing N-AMCMs with a high nitrogen content. Under these conditions, we managed to obtain N-AMCMs with a nitrogen content of 4–8 wt % and a specific surface area of 472–1643 m^2/g. Based on the experimental data, we found a correlation between texture characteristics and nitrogen concentration in N-AMCMs: an increase in the texture parameters

Table 2. Effect of synthetic conditions on the properties of N-CNFs

Precursor	T, °C	Time, h	N, wt %	Texture			
				S_{BET}, m^2/g	S_μ^*, m^2/g	V_{pore}, cm^3/g	V_μ^*, cm^3/g
75% C_2H_4/25% NH_3	550	1	1.58	282	33	0.51	0.02
75% C_2H_4/25% NH_3	675	1	1.27	199	0	0.31	0
50% C_2H_4/50% NH_3	550	1	3.13	287	32	0.82	0.02
50% C_2H_4/50% NH_3	550	20	2.44	112	0	0.37	0
25% C_2H_4/75% NH_3	550	1	7.00	191	0	0.71	0

* Micropore characteristics.

Table 3. Effect of synthetic conditions on the properties of N-AMCMs

Sample no.	Precursor	NaOH/precursor, g/g	T, °C	Time, min	N, wt %	Texture			
						S_{BET}, m^2/g	S_μ, m^2/g	V_{pore}, cm^3/g	V_μ, cm^3/g
1	*ortho*-nitroaniline/1,2,3-benzotriazole	1.25	700	20	8.02	472	465	0.25	0.22
2		1.50	700	25	4.66	1643	1588	0.81	0.75
3		2.50	700	25	1.94	2352	1766	1.59	1.00
4	8-hydroxyquinoline/1,2,3-benzotriazole	1.75	700	45	1.74	2401	2242	1.31	1.14
5		2.00	900	25	1.42	2458	2418	1.24	1.20
6		2.50	700	80	0.92	3436	3183	2.16	1.88
7		3.00	700	30	1.47	3002	2536	1.97	1.50
8	*ortho*-nitroaniline/8-hydroxyquinoline	1.55	700	35	5.29	840	840	0.40	0.40
9		2.00	700	30	2.11	2559	2507	1.42	1.26

(S_{BET} and micropore volume) was accompanied by a decrease in the nitrogen content (Fig. 6). Nevertheless, the synthetic procedure developed allowed us to prepare N-AMCMs with a nitrogen content of 8 wt % and a sufficiently high specific surface area of 472 m^2/g.

Figure 7 shows the TEM micrograph of an N-AMCM sample with a nitrogen content of 2.11 wt % and S_{BET} = 2559 m^2/g. This sample was prepared by the carbonization of an equimolar mixture of *ortho*-nitroaniline and 8-hydroxyquinoline (Table 3, sample no. 9). According to TEM data, the structure of the N-AMCM consisted of curved graphite layers arranged at a distance of ~1 nm from each other, and it was identical to the structure of AMCMs free of bound nitrogen [15, 16].

State of Nitrogen in Carbon Materials

Based on an analysis of the XPS spectra of N-CNFs, we can conclude that at least two states of nitrogen with binding energies (BE) of 398.5 and 400.8 eV occurred in N-CNFs (Fig. 8). According to published data, a line with BE = 398.5 eV belongs to pyridinic nitrogen (N_{Py}) [37–39], whereas the N1*s* line with BE = 400.4–400.9 eV belongs to quaternary nitrogen (N_Q), that is, nitrogen atoms with a formal charge of +1, which replaced carbon atoms in the graphite plane and constituted an extended aromatic structure [38, 39]. The ratio between nitrogen species N_{Py}/N_Q in N-CNFs depended on the ammonia content of the starting mixture. As the concentration of ammonia in the reaction mixture was increased and, correspondingly, as the nitrogen content of N-CNFs increased, the fraction of pyridinic nitrogen

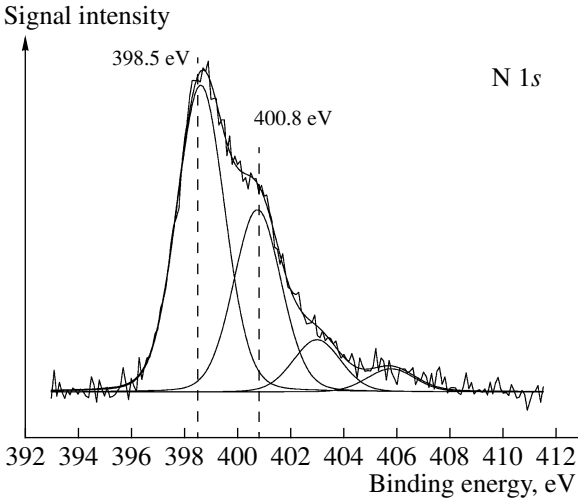

Fig. 8. XPS spectrum of N-CNF with a nitrogen content of 7.00 wt %.

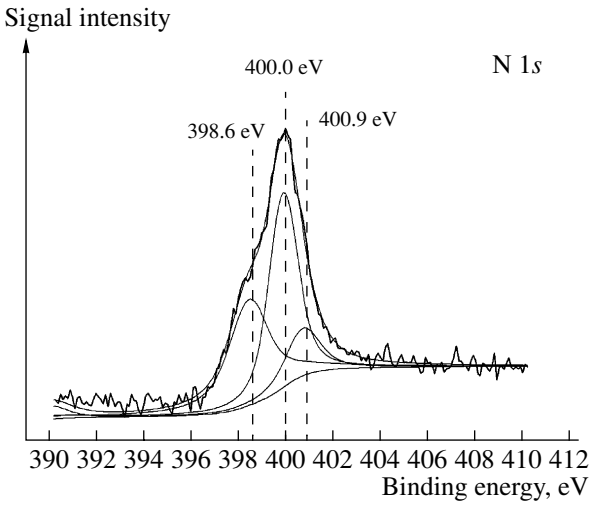

Fig. 9. XPS spectrum of an N-AMCM sample with a nitrogen content of 5.29 wt % (Table 3, sample no. 8).

increased. The N_{Py}/N_Q ratio increased from 1.1 at 1 wt % to 1.7 at 7 wt % nitrogen in N-CNFs.

Figure 9 shows the N 1*s* spectrum of an N-AMCM sample with a nitrogen content of 5.29 wt % (Table 3, sample no. 8). An analysis of the XPS spectra of N-AMCMs allowed us to detect three electronic states of nitrogen atoms with binding energies of 398.6, 400.0, and 400.9 eV. Two signals, a more intense signal at 398.6 eV and a less intense signal at 400.9 eV, were analogous to the N 1*s* signals in the spectra of N-CNFs (Fig. 9). According to published data, an additional peak at 400.0 eV can be attributed to nitrogen atoms as the constituents of amino [40, 41], nitrile [41], or nitroso groups [39] bound to the graphite framework of a carbon material.

CONCLUSIONS

The study of the formation of nitrogen-containing carbon supports by the catalytic decomposition of a C_2H_4/NH_3 mixture and the carbonization of nitrogen-containing organic precursors allowed us to find the following regularities: The catalytic synthesis resulted in the production of a mesoporous material formed by chaotically interwoven structured CNFs. The carbonization of organic compounds produced AMCMs with high specific surface areas (to 3436 m^2/g). The nitrogen content of these materials depended only on synthetic conditions. An increase in the process temperature and time resulted in a decrease in the nitrogen contents of N-CNFs and N-AMCMs. An increase in the nitrogen content of a precursor (the concentration of ammonia in a C_2H_4/NH_3 mixture or the number of nitrogen atoms in an organic compound) was accompanied by an increase in the nitrogen content of carbon materials. As a result, nitrogen-containing carbon supports with nitrogen contents to 8 wt % could be prepared.

We found that nitrogen atoms as the constituents of carbon materials can occur in various electronic states. The following two main nitrogen species as the constituents of N-CNFs were detected: pyridinic (398.5 eV) and quaternary nitrogen (400.8 eV). The electronic state distribution of nitrogen atoms depended on the total nitrogen content of N-CNFs; the contribution of the pyridinic component increased as the total nitrogen content was increased. An additional state of nitrogen atoms (400.0 eV), which could be interpreted as the nitrogen constituent of nitroso groups, was observed in the case of amorphous microporous materials.

The dependence of the texture properties of N-CNFs on synthetic conditions was directly opposite to that of N-AMCMs. Thus, milder process conditions (low temperatures and short-time synthesis) resulted in a larger surface area of N-CNFs. Higher carbonization temperatures and longer process times facilitated the formation of high-surface-area N-AMCMs with large micropore volumes.

Thus, the developed approaches to the synthesis of nitrogen-containing carbon supports can be used for the preparation of a wide range of carbon materials structurally modified with nitrogen. In this case, the properties of the materials synthesized depend on preparation conditions, and they can be varied over a wide range. This provides opportunities to perform the target-oriented synthesis of nitrogen-containing carbon supports for electrocatalysts with specified properties.

ACKNOWLEDGMENTS

We are grateful to O.G. Abrosimov and N.A. Rudina for the TEM and SEM studies of nitrogen-containing carbon materials, respectively, and to V.A. Ushakov for performing XRD analysis.

This work was supported by the Presidium of the Siberian Branch of the Russian Academy of Sciences (Complex Integration Project SB RAS 2006 no. 4.5), the Netherlands Organization for Scientific Research (NWO) and the Russian Foundation for Basic Research (NWO-RFBR grant no. 047.017.028), and INTAS (grant no. 05-1000005-7726).

REFERENCES

1. Gottesfeld, S. and Zawodzinski, T.A., *Adv. Electrochem. Sci. Eng.*, 1997, vol. 5, p. 195.
2. Gasteiger, H.A., Kocha, Sh.S., Sompalli, B., and Wagner, F.T., *Appl. Catal., B*, 2005, vol. 56, p. 9.
3. Thompson, S.D., Jordan, L.R., and Forsyth, M., *Electrochim. Acta*, 2001, vol. 46, p. 1657.
4. Ralph, T.R. and Hogarth, M.P., *Platinum Met. Rev.*, 2002, vol. 46, p. 3.
5. Bessel, C.A., Laubernds, K., Rodrigues, N.M., and Baker, R.T.K., *J. Phys. Chem. B*, 2001, vol. 105, no. 6, p. 1115.
6. Matsumoto, T., Komatsu, T., Nakano, H., Arai, K., Nagashima, Y., Yoo, E., Yamazaki, T., Kijima, M., Shimizu, H., Takasawa, Y., and Nakamura, J., *Catal. Today*, 2004, vol. 90, p. 277.
7. Gangeri, M. and Centi, G., La Malfa A., Perathoner S., Vieira R., Pham-Huu C., Ledoux M.J, *Catal. Today*, 2005, vols. 102–103, p. 50.
8. Ismagilov, Z.R., Kerzhentsev, M.A., Shikina, N.V., Lisitsyn, A.S., Okhlopkova, L.B., Barnakov, Ch.N., Sakashita, M., Iijima, T., and Tadokoro, K., *Catal. Today*, 2005, vols. 102–103, p. 58.
9. Serp, Ph., Corrias, M., and Kalck, Ph., *Appl. Catal., A*, 2003, vol. 253, p. 337.
10. De Jong, K.P. and Geus, J.W., *Catal. Rev. Sci. Eng.*, 2000, vol. 42, no. 4, p. 481.
11. Avdeeva, L.B., Reshetenko, T.V., Ismagilov, Z.R., and Likholobov, V.A., *Appl. Catal., A*, 2002, vol. 228, nos. 1–2, p. 53.
12. Avdeeva, L.B., Kochubey, D.I., and Shaikhutdinov, Sh.K., *Appl. Catal., A*, 1999, vol. 177, p. 43.
13. Shaikhutdinov, Sh.K., Zaikovskii, V.I., and Avdeeva, L.B., *Appl. Catal., A*, 1996, vol. 148, p. 123.

14. Reshetenko, T.V., Avdeeva, L.B., Ismagilov, Z.R., Pushkarev, V.V., Cherepanova, S.V., Chuvilin, A.L., and Likholobov, V.A., *Carbon*, 2003, vol. 41, p. 1605.
15. RF Patent 2 206 394, 2003.
16. Barnakov, Ch.N., Kozlov, A.P., Seit-Ablaeva, S.K., Fenelonov, V.B., Cherepanova, S.R., Ismagilov, Z.R., and Parmon, V.N., *Neftekhimiya*, 2004, no. 6, p. 436 [*Pet. Chem.* (Engl. Transl.), no. 6, p. 403].
17. Barnakov, Ch.N., Kozlov, A.P., Seit-Ablaeva, S.K., Romanenko, A.I., Vasenin, N.T., Anufrienko, V.F., Ismagilov, Z.R., and Parmon, V.N., *Ross. Khim. Zh.*, 2006, vol. 50, no. 1, p. 54.
18. Japanese Patent 2005135817, 2005.
19. Maiyalagan, T., Viswanathan, B., and Varadaraju, U.V., *Electrochem. Commun.*, 2005, vol. 7, p. 905.
20. Miyamoto, Y., Cohen, M.L., and Louie, S.G., *Solid State Commun.*, 1997, vol. 102, no. 8, p. 605.
21. Golberg, D., Dorozhkin, P.S., Bando, Y., Dong, Z.-C., Tang, C.C., Uemura, Y., Grobert, N., Reyes-Reyes, M., Terrones, H., and Terrones, M., *Appl. Phys. A*, 2003, vol. 76, p. 499.
22. Bron, M., Radnik, J., Fieber-Erdmann, M., Bogdanoff, P., and Fiechter, S., *J. Electroanal. Chem.*, 2002, vol. 535, p. 113.
23. Jasinski, R., *Nature*, 1964, vol. 201, p. 1212.
24. Jahnke, H., Schonborn, M., and Zimmermann, G., *Top. Curr. Chem.*, 1976, vol. 61, p. 133.
25. Van Veen, J.A.R., Colijn, H.A., and van Baar, J.F., *Electrochim. Acta*, 1988, vol. 33, p. 801.
26. Van Wingerden, B., van Veen, J.A.R., and Mensch, C.T.J., *J. Chem. Soc., Faraday Trans.*, 1988, vol. 84, p. 65.
27. Lalande, G., Côté, R., Tamizhmani, G., Guay, D., Dodelet, J.P., Dignard-Bailey, L., Weng, L.T., and Bertrand, P., *Electrochim. Acta*, 1995, vol. 40, p. 2635.
28. Tamizhmani, G., Dodelet, J.P., Guay, D., and Capuano, G., *J. Electrochem. Soc.*, 1994, vol. 141, p. 41.
29. Faubert, G., Cote, R., Dodelet, J.P., Lefevre, M., and Bertrand, P., *Electrochim. Acta*, 1999, vol. 44, p. 2589.
30. Wei, G., Wainright, J.S., and Savinell, R.F., *J. New Mater. Electrochem. Syst.*, 2000, vol. 3, p. 121.
31. Shaikhutdinov, Sh.K., Avdeeva, L.B., Goncharova, O.V., Kochubey, D.I., Novgorodov, B.N., and Plyasova, L.M., *Appl. Catal., A*, 1995, vol. 126, p. 125.
32. Reshetenko, T.V., Avdeeva, L.B., Ushakov, V.A., Moroz, E.M., Shmakov, A.N., Kriventsov, V.V., Kochubey, D.I., Pavlyukhin, Yu.T., Chuvilin, A.L., and Ismagilov, Z.R., *Appl. Catal., A*, 2004, vol. 270, p. 87.
33. Hishiyama, Y. and Nakamura, M., *Carbon*, 1995, vol. 33, no. 10, p. 1399.
34. Gregg, S.J. and Sing, K.S.W., *Adsorption, Surface Area, and Porosity*, London: Academic, 1967.
35. Fenelonov, V.B., Avdeeva, L.B., Zheivot, V.I., Okkel', L.G., Goncharova, O.V., and Pimneva, L.G., *Kinet. Katal.*, 1993, vol. 34, no. 3, p. 545.
36. Fenelonov, V.B., Derevyankin, A.Yu., Okkel, L.G., Avdeeva, L.B., Zaikovskii, V.I., Moroz, E.M., Salanov, A.N., Rudina, N.A., Likholobov, V.A., and Shaikhutdinov, Sh.K., *Carbon*, 1997, vol. 35, no. 8, p. 1129.
37. Kvon, R.I., Il'inich, G.N., Chuvilin, A.L., and Likholobov, V.A., *J. Mol. Catal. A*, 2000, vol. 158, p. 413.
38. Kim, T.-Y., Lee, K.-R., Eun, K.Y., and Oh, K.-H., *Chem. Phys. Lett.*, 2003, vol. 372, p. 603.
39. Pels, J.R., Kapteijn, F., Moulijn, J.A., Zhu, Q., and Thomas, K.M., *Carbon*, 1995, vol. 33, no. 11, p. 1641.
40. Seno, M., Tsuchiya, Sh., and Ogawa, Sh., *J. Am. Chem. Soc.*, 1977, vol. 99, no. 9, p. 3014.
41. Riedo, E., Comin, F., Chevrier, J., and Bonnot, A.M., *J. Appl. Phys.*, 2000, vol. 88, no. 7, p. 4365.

available at www.sciencedirect.com

ScienceDirect

journal homepage: www.elsevier.com/locate/carbon

Structure and electrical conductivity of nitrogen-doped carbon nanofibers

Zinfer R. Ismagilov[a], *Anastasia E. Shalagina*[a], *Olga Yu. Podyacheva*[a,*], *Arkady V. Ischenko*[a], *Lidiya S. Kibis*[a], *Andrey I. Boronin*[a], *Yury A. Chesalov*[a], *Dmitry I. Kochubey*[a], *Anatoly I. Romanenko*[b,c], *Olga B. Anikeeva*[b,c], *Timofey I. Buryakov*[b,c], *Evgeniy N. Tkachev*[b,c]

[a]*Boreskov Institute of Catalysis, Pr. Akad. Lavrentieva 5, Novosibirsk 630090, Russia*
[b]*Nikolaev Institute of Inorganic Chemistry, Pr. Akad. Lavrentieva 3, Novosibirsk 630090, Russia*
[c]*Novosibirsk State University, Pirogova St. 2, Novosibirsk 630090, Russia*

ARTICLE INFO

Article history:
Received 17 October 2008
Accepted 19 February 2009
Available online 24 March 2009

ABSTRACT

The effect of nitrogen concentration in carbon nanofibers (CNFs) on the structural and electrical properties of the carbon material was studied. CNFs with nitrogen concentration varied from 0 to 8.2 wt.% (N-CNFs) with "herringbone" structure were prepared by decomposition of ethylene and ethylene mixture with ammonia over 65Ni–25Cu–10Al_2O_3 (wt.%) catalyst at 823 K. Detailed investigation of the CNFs and N-CNFs by XPS, FTIR and Raman spectroscopy showed that the nitrogen introduction in carbon material distorts the graphite-like lattice and increases the structure defectiveness. Both effects become more significant as the nitrogen concentration in N-CNFs grows.

The electrical conductivity of N-CNFs with different nitrogen concentrations is caused by the competition of the nanofiber graphite-like structure disordering after introduction of nitrogen atoms and doping of an additional electron into the delocalized π-system of the graphite-like material. As a result, the maximum electrical conductivity among the samples studied was observed at nitrogen concentration in N-CNFs equal to 3.1 wt.%.

1. Introduction

Today selective synthesis of carbon nanofibers (CNFs) with desired structure ("herringbone", "deck of cards", nanotubes) and physicochemical properties is an important branch of nanotechnology with a wide range of possible practical applications of these materials [1–8]. CNFs are of great interest for development of components for nanoelectronics (field transistors, autoelectron emitters, diodes, supercapacitors) and for development of new composite materials, gas and bio sensors, sorbents, catalysts and catalyst supports. The conducting properties of CNFs that can be varied from metal to semiconductor depending on the structural parameters and doping with heteroatoms are very important for practical applications [9]. It is rather difficult to control the CNF structural characteristics, such as diameter, length, chirality, topological defects, etc., during synthesis. Therefore, significant attention has been paid lately to the investigation of methods for regulating the CNF properties by doping the graphite-like structure of the nanofibers with nitrogen atoms [10,5].

Nitrogen atoms substituting carbon atoms in the graphite matrix are electron donors and promote n-type conductivity. It was shown by tunneling microscopy that nitrogen-doped carbon nanotubes have metallic properties independent of

* *Corresponding author:* Fax: +7 383 3306219.
E-mail address: pod@catalysis.ru (O.Yu. Podyacheva).
0008-6223/$ - see front matter
doi:10.1016/j.carbon.2009.02.034

the structural parameters and are characterized by the presence of a donor state close to the Fermi level [11]. The increase of the localized density of states at the Fermi level results in larger emission currents at lower voltages [12–14]. Due to the metal-type conductivity and stable emission characteristics at low voltages, nitrogen-doped carbon nanotubes are promising materials for field emitters and conducting coatings and composites. Furthermore, the enhancement of the donor properties and electrical conductivity of CNFs after doping with nitrogen increases the activity of the carbon material in electron-transfer reactions [15] and electrocatalytic reduction of oxygen [16].

Doping with nitrogen has a significant effect on the structure of the carbon material. In most cases, multiwalled carbon nanotubes doped with nitrogen have a bamboo-like structure and contain regularly arranged compartments with a hollow channel [17]. Another characteristic property of nitrogen-doped materials is the formation of a more defective structure of the carbon layers. For example, the higher the N content, the less graphitic and linear the nanotubes and nanofibers become [17,18]. Using quantum chemical calculations it was shown that incorporation of nitrogen atoms into a graphite-like lattice promotes the formation of pentagons facilitating distortion of the graphite layer [19]. The EELS data revealed that the curvature of the graphite layer in nitrogen-doped nanotubes [20] and nano-onions [21] correlated with the nitrogen concentration in the layer. The structure of CN_x films prepared by magnetron spraying of a graphite target in the Ar/N_2 discharge was shown to be determined by the nitrogen concentration in the film ([N]) [22]. At [N] < 5 at.% the film had a graphite-like structure. Meanwhile, at [N] > 15 at.% a fullerene-like phase was formed. A transition region was observed at 5 at.% < [N] < 15 at.%.

Thus, summarizing the literature data we would like to conclude that the CNF doping with nitrogen makes it possible to modify both the structure of the carbon nanofiber and the electrophysical properties of these materials. However, the experimental data on the dependence of the conductivity of nitrogen-doped carbon materials on the nitrogen concentration in the structure are limited. It was reported that the conductivity of CN_x films depended not linearly on the nitrogen concentration reaching a maximum at [N] = 10.4 at.% and decreasing at higher nitrogen concentrations in the film [23]. The authors explained this effect by the formation of an insulating phase at high nitrogen concentration in the film. This result suggests that there could be an interrelation between the nitrogen concentration in the N-doped carbon material, the material structure and its electrical properties. If such relation is found, this would allow predicting and regulating the electrical properties of carbon materials.

In our previous paper we discussed the formation of nitrogen-doped CNFs with "herringbone" structure by decomposition of C_2H_4/NH_3 mixture over metal catalysts and determined optimum conditions for synthesis of N-CNFs with regulated nitrogen concentration, structural and textural characteristics [24]. In this paper we continue the investigation of the nitrogen effect on the CNF structure and study the electrical properties of N-CNFs.

2. Experimental

2.1. Synthesis of CNFs and N-CNFs

CNFs and N-CNFs were synthesized by decomposition of ethylene and ethylene/ammonia mixtures over 65Ni–25Cu–$10Al_2O_3$ (wt.%) catalyst at 823 K for 1 h [24]. Earlier we demonstrated that these synthesis conditions are optimal for the production of uniform material with nitrogen content up to 8.2 wt.% and maximum values of textural characteristics ($S_{BET} \sim 200–300\ m^2/g$, $V_{pore} \sim 0.6–0.9\ cm^3/g$) [24,25]. In this study we varied the ammonia concentration in reaction mixture from 0 to 75 vol.% to prepare N-CNFs with different nitrogen content and to investigate the effect of nitrogen on structure and electrical properties of the materials. The procedure of N-CNF synthesis was described in detail previously [24].

Synthesized CNFs and N-CNFs were subjected to treatment with hydrochloric acid to remove the catalyst particles. Then, the samples were washed with hot water to pH 5.5. The acid treatment did not affect the specific surface area and porosity of the carbon material.

The synthesis conditions, nitrogen content and textural characteristics of the synthesized CNFs and N-CNFs are summarized in Table 1.

2.2. Investigation of CNFs and N-CNFs by physicochemical methods

Nitrogen concentrations in N-CNFs were determined by elemental analysis using a Carlo Erba 1106 automatic elemental analyzer.

Textural properties of CNFs and N-CNFs were studied by low-temperature N_2 adsorption at 77 K using an ASAP-2400 automatic adsorption installation. Specific surface areas were calculated using the BET method.

Structure and morphology of carbon nanofibers were studied by transmission electron microscopy (TEM) using a JEOL JEM-2010 electron microscope operating at 200 kV with 1.4 Å lattice resolution. Samples for TEM studies were dispersed in ethanol and then placed onto holey carbon film deposited on a copper grid.

The electronic states of nitrogen and carbon atoms in CNFs and N-CNFs were studied by X-ray photoelectron spectroscopy (XPS). The experiments were carried out using ES-300 photoelectron spectrometer by KRATOS Analytical with MgKα X-ray source. The spectrometer was calibrated relatively Au4f and Cu2p lines with $E_b(Au4f_{7/2}) = 84.0$ eV and $E_b(Cu2p_{3/2}) = 932.7$ eV, respectively. The residual gas pressure in the analyzer chamber during the measurements did not exceed 3×10^{-8} mbar. Qualitative chemical composition of the surface was controlled using survey spectra in the range of 0–1100 eV with resolution corresponding to maximum sensitivity (analyzer pass energy 50 or 75 eV) and energy step 1 eV. For quantitative analysis of the chemical composition and for the determination of chemical state of elements the spectra were recorded in narrow ranges using precision mode with high accumulation time. In this case the analyzer pass energy was 20–25 eV and energy step 0.1 eV. The N1s and C1s spectra were

Table 1 – Synthesis conditions and properties of CNFs and N-CNFs.

Synthesis conditions	Properties[a]				
$[NH_3]$, vol.%	[N], wt.%	S_{BET}[b], m^2/g	V_{pore}[c], cm^3/g	V_{μ}[d], cm^3/g	D_{BET}[e], nm
0	0	230	0.60	0.016	10.2
25	1.7	275	0.78	0.023	11.4
50	3.1	290	0.87	0.021	12.0
75	8.2	195	0.87	0	17.8

a Parameters are presented for carbon materials after the acid treatment.
b Surface area determined by BET method.
c Pore volume.
d Volume of micropores.
e Average pore size.

fitted by approximation of the experimental curves with a combination of Gaussian and Lorenzian functions. The quantitative analysis of the surface composition of the carbon materials was based on calculations of the integral intensities of the corresponding lines in the XPS spectra taking into account atomic sensitivities for each element (ASF).

The FTIR spectra of CNFs and N-CNFs were recorded using BOMEM MB-102 FTIR spectrometer in 4000–250 cm^{-1} range with 4 cm^{-1} resolution. The samples were prepared by pressing pellets containing 0.5 mg of the studied sample and 500 mg of KBr.

The effect of nitrogen on the structure of the graphite layers was studied by Raman spectroscopy using Bruker RFS 100/S FT-Raman spectrometer. Nd-YAG laser line at 1064 nm with 100 mWt power was used for excitation.

The electrical properties of CNFs and N-CNFs were studied using an original procedure developed for measurement of temperature dependence of electric conductivity $\sigma(T)$ of powder-like samples by a four-contact method in the temperature range 4.2–293 K [26]. The samples were pressed into the glass cylinders. The contacts to the sample were made by 0.1 mm silver wires. In this article the comparison of electrical conductivity was made for the N-CNF samples with nitrogen content 0, 1.7, 3.1 and 8.2 wt.% of N in CNFs.

3. Results

3.1. TEM

According to the TEM data, carbon nanofibers prepared by catalytic decomposition of ethylene have helical-like morphology (Fig. 1a) and "herringbone" internal structure formed by turbostratic graphite-like layers oriented at 45–75° angle to the fiber axis (Fig. 1b). The fiber diameters range from 20 to 100 nm. The ammonia addition to the feed did not result in any evident changes of the CNF structure. Only the fiber diameters slightly decreased. When the ammonia concentration in the C_2H_4/NH_3 mixture was changed from 25 to 75 vol.%, the fiber diameters decreased from 20–50 nm to 10–30 nm. The TEM images show that the crystallinity of the N-CNF graphite layers is similar to that of CNFs without nitrogen (Fig. 1b and c).

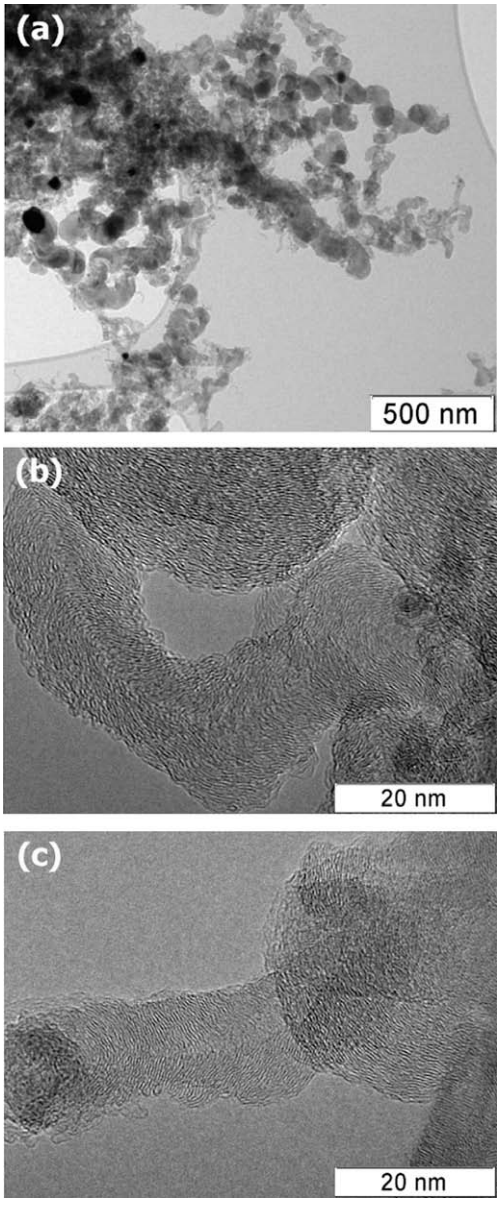

Fig. 1 – TEM images of CNF and N-CNF samples: (a, b) CNFs synthesized by catalytic decomposition of 100% ethylene, (c) N-CNFs with 3.1 wt.% N prepared from 50%C_2H_4/50%NH_3 mixture.

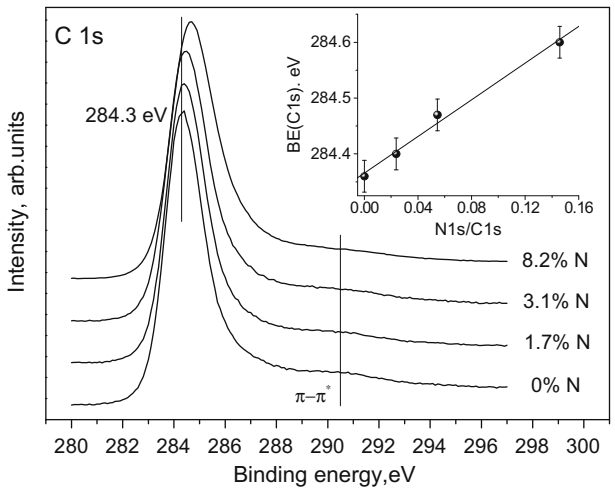

Fig. 2 – X-ray photoelectron C1s spectra of CNF and N-CNF samples with different nitrogen concentrations (wt.%). The dependence of the main C1s peak position on the ratio of the peak intensities N1s/C1s is shown on the inset.

3.2. XPS

Fig. 2 presents the C1s spectra of CNFs and N-CNFs with different nitrogen concentration. The position of the main C1s line at 284.3–284.6 eV proves that carbon is in the form of graphite [27]. This conclusion is additionally confirmed by the presence of a strong π–π^* "shake-up" satellite at 290–291 eV accompanying the photoionization process of 1s electron in conjugated π-system of graphite-like carbon [28]. The difference in the position of the main C1s peak and its "shake-up" satellite is about 6–7 eV that is typical for aromatic carbon systems.

The position of C1s peak at 284.3 eV for CNF sample without nitrogen matches the energy of the sp^2 C—C bond in C1s spectrum of highly-oriented pyrolytic graphite [29]. When the nitrogen concentration in the sample increases, the peak is slightly shifted to higher binding energies (BE) and the peak asymmetric broadening is appeared. The C1s BE in the sample with the highest nitrogen content 8.2 wt.% was 284.6 eV. The dependence of the C1s BE on the ratio of the peak intensities N1s/C1s is presented in the inset of Fig. 2. Note that the ratio of the N1s and C1s peaks characterizes the nitrogen concentration in N-CNFs. The shift of the C1s maximum by 0.1–0.3 eV agrees with the results of the XPS studies of nitrogenated nanotubes [29] and thin films [30]. It is explained by disordering of the graphite-like structure after introduction of nitrogen [31–33].

The N1s spectra of N-CNFs have a complex shape, Fig. 3a. They consist of partially resolved elastic peaks at ~400 eV and extended satellite structure at about 409 eV. For more precise identification of the nitrogen states the N1s peak was decomposed into three components (Fig. 3b). The peak at 398.7 eV is assigned in the literature to pyridine nitrogen. The N1s signal with BE at 400.5 eV is attributed to quaternary nitrogen, i.e. graphite-like nitrogen incorporated into the structure of extended aromatic system of the carbon nanofibers [27,34–36]. A weaker signal at 401.8 eV can be assigned to an oxygenated nitrogen groups, such as nitrosyls [37].

A wide satellite peak at 406–412 eV, most likely, is a "shake-up" satellite from both the pyridine and three-coordinated nitrogen. When only π–π^* transitions are considered for the satellite, the distance from the main peak to the satellite should be ~6–7 eV. In this case the splitting is ~8–9 eV that is significantly larger than for π–π^* transitions in carbon systems. The appearance of a wide satellite peak may be also related to participation of the unshared electron pair of the pyridine nitrogen atom in photoionization of N1s electron with excitation of an electron from the unshared pair to the vacant σ^* orbital. Such π–σ^* transition results in energy losses for the N1s photoelectron and shift of the peak by ~9–10 eV. Thus, a wide line at ~409 eV is appeared as a result of the overlapping of the satellite peaks formed due to the π–π^* transitions and π–σ^* transitions.

The increase of the nitrogen concentration in N-CNFs from 1.7 to 8.2 wt.% changes the ratio of the relative intensities of the elastic peaks. This fact indicates that relative intensities

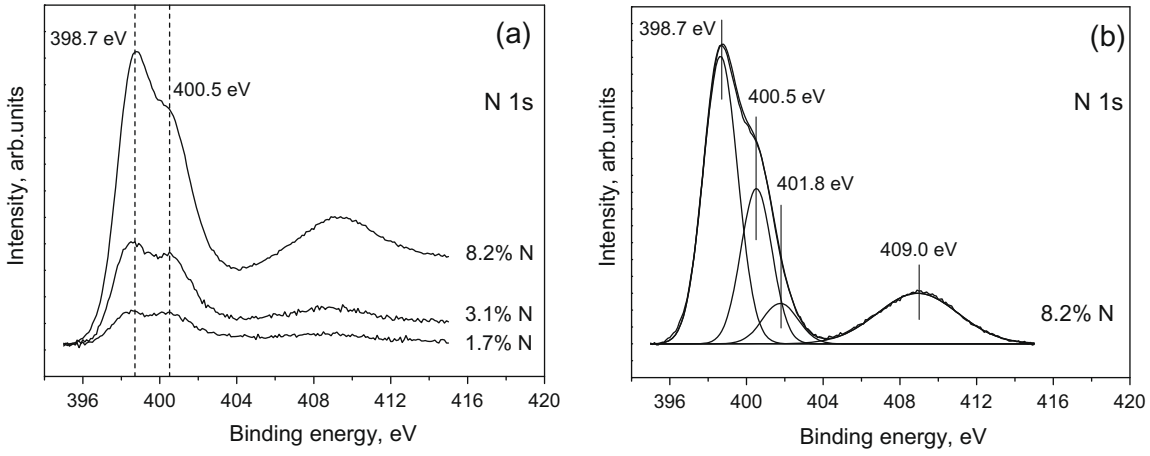

Fig. 3 – X-ray photoelectron N1s spectra of N-CNF samples: (a) effect of nitrogen concentration (wt.%) on distribution of N atoms among the electronic states; (b) fitting of N1s spectrum for N-CNF sample with the highest nitrogen concentration (8.2 wt.% N).

of the electronic states of nitrogen are changed. In particular, the contribution of the pyridine state grows (Fig. 3a).

3.3. FTIR Spectroscopy

The bands at 3420, 2915, 2850, 1630, 1585, 1220 and 880 cm^{-1} were observed in the FTIR spectrum of CNFs (Fig. 4). The bands at 3420 and 1630 cm^{-1} can be attributed to stretching and bending vibrations of water molecules. The bands at 2915–2850 cm^{-1} correspond to stretching vibrations of C—H groups. The band at ~1550 cm^{-1} and a band at about ~1220 cm^{-1} were observed in the FTIR spectra of carbon nanofibers synthesized by the catalytic method [38]. However, the band at ~1220 cm^{-1} was not observed in the spectrum of nanotubes prepared in an electric arch [39]. The complete vibrational representation of the structure of crystalline graphite has the following form [40]:

$$\Gamma = A_{2u} + 2B_{2g} + E_{1u} + 2E_{2g} \quad (1)$$

Modes A_{2u} (867 cm^{-1}) and E_{1u} (1588 cm^{-1}) are active in IR [40]. Therefore, we may conclude that the appearance of the band at ~1220 cm^{-1} in the spectra of carbon nanotubes [38] and nanofibers in our case as well can be related to the translational symmetry disturbance caused by the defectiveness of the graphite-like structure.

No new lines appeared in the FTIR spectra in nitrogenated samples. However, the bands related to the graphite-like structure were shifted (Fig. 4). The spectra of CNF and N-CNF samples with different nitrogen concentrations in the selected region 800–1800 cm^{-1} corresponding to vibrations of C—C bonds in the graphite-like structure are shown in Fig. 5.

When the nitrogen concentration in the nanofibers grows the bands are continuously shifted to higher frequencies from 1585 and 1220 cm^{-1} (0 wt.% N) to 1590 and 1261 cm^{-1} (8.2 wt.% N) respectively. Such changes in the FTIR spectra of carbon nanofibers with the increase of nitrogen content can be explained by the growing defectiveness of the graphite-like structure due to incorporation of nitrogen atoms into the carbon lattice.

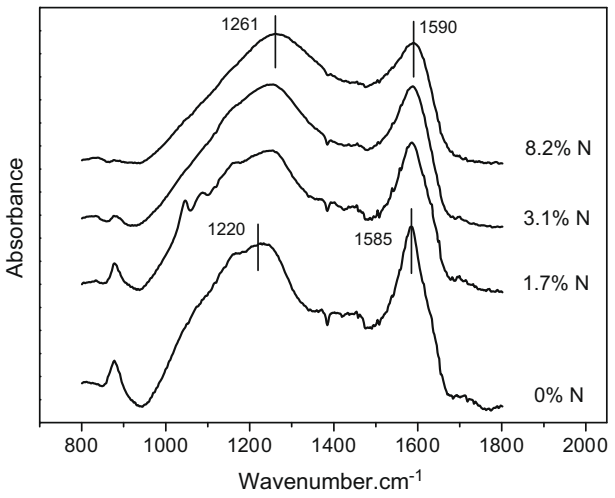

Fig. 5 – FTIR spectra of CNF and N-CNF samples with different nitrogen concentrations (wt.%) after baseline correction.

3.4. Raman spectroscopy

Two lines were observed in the Raman spectra of CNFs and N-CNFs at 1597–1599 cm^{-1} (G line) and 1288–1315 cm^{-1} (D line, Fig. 6). The G line corresponds to allowed vibrations of E_{2g} hexagonal graphite lattice (Eq. (1)) [40]. The presence of defects in the graphite structure results in broadening of the lines in the Raman spectra and appearance of an additional D line. It corresponds to the A_{1g} mode that is forbidden according to the selection rules in ideal graphite.

The analysis of the line positions, intensities and half-widths gives information about changes of the structural characteristics of the carbon material, namely graphite layer defectiveness, resulting from the increase of the nitrogen concentration in the nanofibers. A continuous increase of the vibration frequency corresponding to the D line and the half-widths of peaks D and G was observed with the increase of the nitrogen concentration in N-CNFs (Table 2, Fig. 6). The

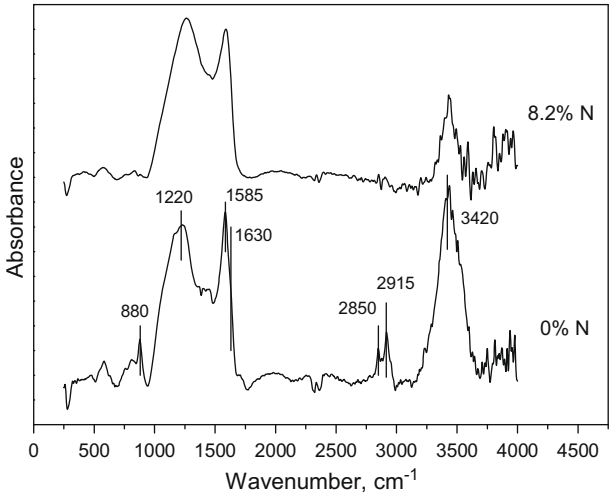

Fig. 4 – FTIR spectra of CNFs and N-CNFs with 8.2 wt.% N after baseline correction.

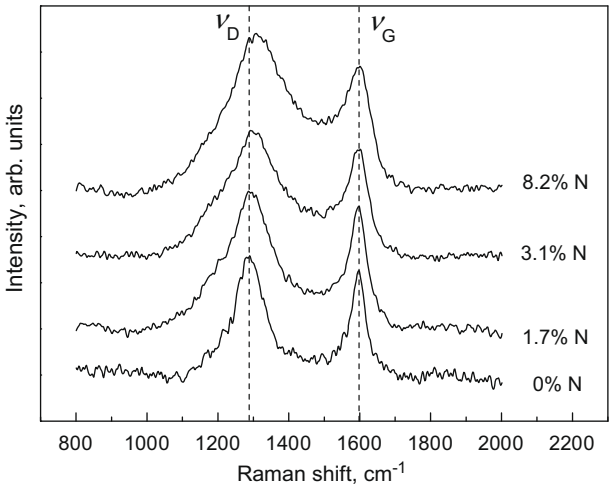

Fig. 6 – Raman spectra of CNF and N-CNF samples with different nitrogen concentrations (wt.%).

Table 2 – Parameters of the Raman spectra of CNF and N-CNF samples depending on the nitrogen concentration (wt.%).

Sample	[N], wt.%	D line		G line		I_D/I_G
		ν_D, cm^{-1}	$\omega_{1/2}$, cm^{-1}	ν_G, cm^{-1}	$\omega_{1/2}$, cm^{-1}	
CNF	0	1288	100	1598	54	2.2
N-CNF (1.7% N)	1.7	1295	147	1597	61	2.8
N-CNF (3.1% N)	3.1	1304	166	1597	62	3.3
N-CNF (8.2% N)	8.2	1315	210	1599	83	3.7

ν_D and ν_G – positions of lines D an G, correspondingly.
$\omega_{1/2}$ – line width at half-height.
I_D/I_G – ratio of integral intensities of lines D and G.

position of the G line did not depend on the nitrogen concentration. The increasing ratio of the integral intensities I_D/I_G indicates that the defectiveness of the graphite-like layers grows with increasing of nitrogen concentration in the materials. N-CNF sample with the highest nitrogen concentration 8.2 wt.% was the most defective.

3.5. *Electrical properties*

The dependencies of conductivity on temperature $\sigma(T)$ for CNF and N-CNF samples (1.7, 3.1 and 8.2 wt.% N) were studied in the temperature range $T = 4.2$–293 K. In temperature range 4.2–50 K the electrical conductivity can be described by two-dimensional variable range hopping conductivity with variable length of hops between localized states located in a narrow energy range close to the Fermi level. This is proven by the experimental observation of relation (2) (Mott's law) with $d = 2$ [41]. In this case the $\sigma(T)$ is linearized in $\ln(\sigma) - T^{-1/3}$ axes (Fig. 7).

$$\sigma(T) = \sigma_0 \cdot \exp[-(T_0/T)^{1/(d+1)}] \quad (2)$$

$$\text{Here } T_0 = \frac{\beta}{a_{loc}^d k_B N(E_F)} \quad (3)$$

β is a constant depending on the dimension, a_{loc} is a localization radius of electron wave function, d is the movement dimension of the current carriers, k_B is the Boltzmann constant, $N(E_F)$ is the density of states at the Fermi level.

The 2D variable range hopping mechanism could be explained by high anisotropy of movement of current carriers in these materials due to the formation of decks of graphite layers. Obviously, the current carries movement occurs across the graphite layers that have a tendency to form bonds with each other forming "nanocaps" or "closed-layer structures" [24].

At temperature $T > 50$ K more weak power dependence $\sigma \sim (T^x)$ typical for quasi-two-dimensional graphite is registered [42].

The localization radius of electron wave function a_{loc} we estimated from the data of magnetoresistivity $\rho(B) = 1/\sigma(B)$ at temperature 4.2 K taking into account the model of wave function shrinkage for the localized state in magnetic field [43]:

$$a_{loc} = (c^2\hbar^2 A/e^2 t_d)^{1/4}(T/T_0)^{3n/4} \quad (4)$$

Here c – velocity of light, $\hbar$ – Planck's constant, $t_d = 1/360$ – the constant, $n = 1/(1 + d)$, $A = \partial \ln\rho(B)/\partial B^2$ and it was determined from the slope of quadratic dependences $\ln\rho(B)$ at low field (Fig. 8).

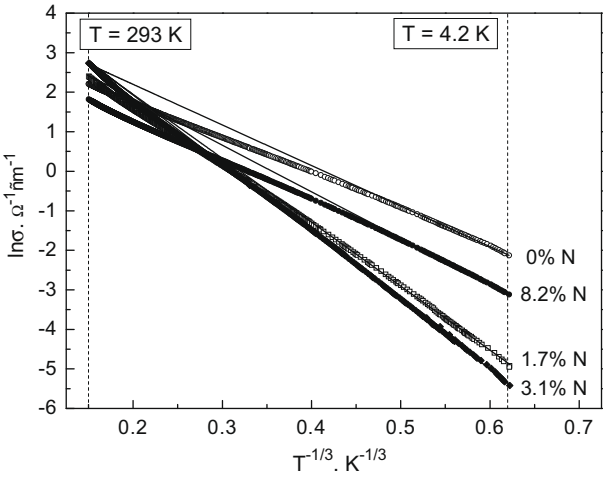

Fig. 7 – Temperature dependencies of conductivity of CNF and N-CNF samples with different nitrogen concentrations (wt.%). Solid lines correspond to approximation of the experimental data with Eq. (2) at 4.2 K < T < 10 K.

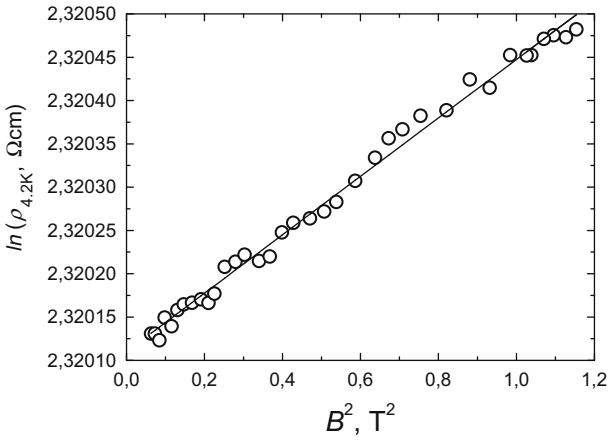

Fig. 8 – The typical magnetic field dependence of the resistivity logarithm $\ln\rho(B)$ (where $\rho(B) = 1/\sigma(B)$) measured at temperature 4.2 K for N-CNF sample with nitrogen content 8.2 wt.%. Solid line corresponds to approximation of the experimental data with $\ln\rho(B) = A \cdot B^2$

Table 3 – Effect of nitrogen concentration in carbon nanofibers on electrical properties of CNFs and N-CNFs.

Sample	[N], wt.%	$\sigma_{293\ K}$, $Om^{-1}\ cm^{-1}$	$\sigma_{4.2\ K}$, $Om^{-1}\ cm^{-1}$	a_{loc}, nm	$N(E_F)$, $eV^{-1}\ cm^{-3}$
CNFs	0	9.1	1.2×10^{-1}	6.7	2.5×10^{19}
N-CNFs (1.7% N)	1.7	11.0	7.3×10^{-3}	6.1	1.1×10^{19}
N-CNFs (3.1% N)	3.1	15.4	4.4×10^{-3}	5.5	0.9×10^{19}
N-CNFs (8.2% N)	8.2	6.1	4.3×10^{-2}	4.9	2.8×10^{19}

$\sigma_{293\ K}$ and $\sigma_{4.2\ K}$ – conductivity at ambient (293 K) and liquid helium (4.2 K) temperatures.
a_{loc} – localization radius of electron wave function.
$N(E_F)$ – density of localized states at the Fermi level.

Based on the temperature and magnetic field dependencies of the electrical conductivity and observed variable range hopping conductivity (Eq. (2)), we calculated the densities of localized states at the Fermi level $N(E_F)$ at helium temperature (4.2 K) by the use of Eq. (3). At this temperature $N(E_F)$ varied from 0.9×10^{19} to 2.8×10^{19} $eV^{-1}\ cm^{-3}$ (Table 3).

The nanofiber conductivity at the ambient temperature $\sigma_{293\ K}$ grows after introduction of just 1.7 wt.% N into CNFs and grows further when the nitrogen concentration increases to 3.1 wt.%. However, the material with the highest nitrogen concentration equal to 8.2 wt.% is characterized by lower conductivity at ambient temperature. It was shown earlier by XPS, FTIR and Raman spectroscopy that when nitrogen concentration rises the defectiveness of the graphite-like structure increases and N-CNF with nitrogen concentration 8.2 wt.% is the most defective. The latter leads to the decrease of the current carriers mobility in this sample. Apparently, there is an optimum nitrogen concentration among the samples studied in the graphite layer at which the effect of doping an additional electron to the delocalized π-system prevails over disordering of the graphite crystal lattice. Indeed, the XPS data indicate that quaternary nitrogen atoms are preferentially formed at nitrogen concentration in N-CNFs equal to 1.7 and 3.1 wt.%. At higher nitrogen concentration equal to 8.2 wt.% the fraction of the pyridine nitrogen form increases, leading to a corresponding increase of the fraction of localized electronic states in N-CNF system.

A reverse order of changes of N-CNF electrical conductivity with increasing nitrogen concentration was observed at the liquid helium temperature (4.2 K). In this case nitrogen-free CNF were characterized by the highest conductivity in comparison with the nitrogenated materials. The lowest conductivity was observed for the samples with nitrogen concentrations 1.7 and 3.1 wt.%. The conductivity of N-CNF with 8.2 wt.% N at helium temperature was slightly higher than 1.7–3.1 wt.% N-CNFs. This is related to higher $N(E_F)$ value, which leads to a slower decrease of conductivity with the temperature decrease (Eq. (2)).

To estimate the potential for practical application of the synthesized N-CNFs as conducting materials we compared the electrical conductivity of some carbon materials. The electrical conductivity of CNF and N-CNF samples $\sigma_{293\ K}$ = 6.1–15.4 $Om^{-1}\ cm^{-1}$ exceeded those of nitrogenated nanotubes synthesized by catalytic decomposition of acetonitrile at 1073 K ($\sigma_{293\ K}$ = 5.8 $Om^{-1}\ cm^{-1}$ [44]) and carbon with onion-like structure prepared by annealing of finely dispersed diamonds at 1903–2143 K ($\sigma_{293\ K}$ = 3.6–6 $Om^{-1}\ cm^{-1}$ [45]), and was comparable with that of soot ($S_{BET}\sim800\ m^2/g$, $\sigma_{293\ K}\sim15\ Om^{-1}\ cm^{-1}$ [42]).

4. Conclusions

The effect of doping carbon nanofibers with nitrogen atoms on the structural and electrical properties of CNFs was studied. It was shown that nanofibers with "herringbone" structure were formed after decomposition of pure ethylene and ethylene–ammonia mixture over 65%Ni–25%Cu–10%Al_2O_3 catalyst. Two main electronic states of nitrogen in N-CNFs, pyridine and quaternary, were observed by XPS. Detailed investigation of the CNFs and N-CNFs structure by XPS, FTIR and Raman spectroscopy revealed that the nitrogen introduction in CNFs distorted the graphite-like lattice and facilitated the structure defectiveness. Both effects become more significant as the nitrogen concentration in N-CNFs grows, the highest effects were registered for the sample with nitrogen content 8.2 wt.%.

The dependence of conductivity of N-CNFs at room temperature on the nitrogen content is non-monotone and has maximum of 15.4 $Om^{-1}\ cm^{-1}$ at N concentration 3.1 wt.% among the samples studied. Such dependence can be explained by a competition of two independent processes taking place during nitrogen incorporation into the graphite structure. On the one hand, it results in disordering of the graphite lattice. On the other hand, it gives an additional electron in the delocalized π-system. Consequently, the maximum conductivity of synthesized N-CNFs is observed at an intermediate nitrogen concentration that was equal to 3.1 wt.% in our case.

Acknowledgements

The study was supported in part by Presidium RAS (Integration Project 27.58), by Presidium SB RAS (Integration Project 88), by Russian Ministry of Education and Science (Grant RNP 2.1.1/410) and INTAS (Grant 05-1000005-7726).

REFERENCES

[1] Baker RTK. Catalytic growth of carbon filaments. Carbon 1989;27:315–23.
[2] De Jong KP, Geus JW. Carbon nanofibers: catalytic synthesis and applications. Catal Rev Sci Eng 2000;42(4):481–510.
[3] Alstrup I. A new model explaining carbon filament growth on nickel, iron, and Ni–Cu alloy catalysts. J Catal 1988;109:241–51.

[4] Serp Ph, Corrias M, Kalck Ph. Carbon nanotubes and nanofibers in catalysis. Appl Catal A 2003;253:337–58.
[5] Terrones M, Jorio A, Endo M, Rao AM, Kim YA, Hayashi T, et al. New direction in nanotube science. Mater Today 2004;7(10):30–45.
[6] Reshetenko TV, Avdeeva LB, Ismagilov ZR, Chuvilin AL, Ushakov VA. Carbon capacious Ni–Cu–Al_2O_3 catalysts for high-temperature methane decomposition. Appl Catal A 2003;247:51–63.
[7] Reshetenko TV, Avdeeva LB, Ismagilov ZR, Pushkarev VV, Cherepanova SV, Chuvilin AL, et al. Catalytic filamentous carbon. Structural and textural properties. Carbon 2003;41:1605–15.
[8] Reshetenko TV, Avdeeva LB, Ismagilov ZR, Chuvilin AL. Catalytic filamentous carbon as supports for nickel catalysts. Carbon 2004;42:143–8.
[9] Wildöer JWG, Venema LC, Rinzler AG, Smalley RE, Dekker C. Electronic structure of atomically resolved carbon nanotubes. Nature 1998;391:59–62.
[10] Ewels CP, Glerup M. Nitrogen doping in carbon nanotubes. J Nanosci Nanotech 2005;5:1345–63.
[11] Terrones M, Ajayan PM, Banhart F, Blase X, Carroll DL, Charlier JC, et al. N-doping and coalescence of carbon nanotubes: synthesis and electronic properties. Appl Phys A 2002;74:355–61.
[12] Zhang G, Duan W, Gu B. Effect of substitutional atoms in the tip on field-emission properties of capped carbon nanotubes. Appl Phys Lett 2002;80:2589–91.
[13] Sun H-L, Jia J-F, Zhong D, Shen Q-T, Sun M, Xue Q-K, et al. Scanning tunneling microscopy study of polymerized carbon nanobells: electronic effect and evidence of nitrogen incorporation. Phys Rev B 2002;66:085423-1–5.
[14] Srivastava SK, Vankar VD, Rao DVS, Kumar V. Enhanced field emission characteristics of nitrogen-doped carbon nanotube films grown by microwave plasma enhanced chemical vapor deposition process. Thin Solid Films 2006;515:1851–6.
[15] Strelko VV, Kuts VS, Thrower PA. On the mechanism of possible influence of heteroatoms of nitrogen, boron and phosphorus in a carbon matrix on the catalytic activity of carbons in electron transfer reactions. Carbon 2000;38:1499–524.
[16] Matter PH, Zhang L, Ozkan US. The role of nanostructure in nitrogen-containing carbon catalysts for the oxygen reduction reaction. J Catal 2006;239:83–96.
[17] Jang JW, Lee CE, Lyu SC, Lee TJ, Lee CJ. Structural study of nitrogen-doping effects in bamboo-shaped multiwalled carbon nanotubes. Appl Phys Lett 2004;84:2877–9.
[18] Terrones M, Redlich Ph, Grobert N, Trasobares S, Hsu W-K, Terrones H, et al. Carbon nitride nanocomposites: formation of aligned C_xN_y nanofibers. Adv Mater 1999;11(8):655–8.
[19] Sjöström H, Stafström S, Boman M, Sundgren J-E. Superhard and elastic carbon nitride thin films having fullerene like microstructure. Phys Rev Lett 1995;75:1336–9.
[20] Han W-Q, Kohler-Redlich Ph, Seeger T, Ernst F, Rühle M, Grobert N, et al. Aligned CN_x nanotubes by pyrolysis of ferrocene/C_{60} under NH_3 atmosphere. Appl Phys Lett 2000;77:1807–9.
[21] Czigány Z, Brunell IF, Neidhardt J, Hultman L, Suenaga K. Growth of fullerene-like carbon nitride thin solid films consisting of cross-linked nano-onions. Appl Phys Lett 2001;79:2639–41.
[22] Hellgren N, Johansson MP, Broitman E, Hultman L, Sundgren J-E. Role of nitrogen in the formation of hard and elastic CN_x thin films by reactive magnetron sputtering. Phys Rev B 1999;59:5162–9.
[23] Zhang W, Xia Y, Ju J, Wang L, Fang Z, Zhang M. Electrical conductivity of nitride carbon films with different nitrogen content. Solid State Commun 2003;126:163–6.
[24] Shalagina AE, Ismagilov ZR, Podyacheva OYu, Kvon RI, Ushakov VA. Synthesis of nitrogen-containing carbon nanofibers by catalytic decomposition of ethylene/ammonia mixture. Carbon 2007;45:1808–20.
[25] Ismagilov ZR, Shalagina AE, Pod"yacheva OYu, Barnakov ChN, Kozlov AP, Kvon RI, et al. Synthesis of nitrogen-containing carbon materials for solid polymer fuel cell cathodes. Kinet Catal 2007;48:581–8.
[26] Kuznetsov VL, Butenko YuV, Chuvilin AL, Romanenko AI, Okotrub AV. Electrical resistivity of graphitized ultra-disperse diamond and onion-like carbon. Chem Phys Lett 2001;336:397–404.
[27] Pels JR, Kapteijn F, Moulijn JA, Zhu Q, Thomas KM. Evolution of nitrogen functionalities in carbonaceous materials during pyrolysis. Carbon 1995;33:1641–53.
[28] Barr TL, Yin M. Concerted X-ray photoelectron spectroscopy study of the character of select carbonaceous materials. J Vac Sci Technol A 1992;10:2788–95.
[29] Maldonado S, Morin S, Stevenson KJ. Structure, composition, and chemical reactivity of carbon nanotubes by selective nitrogen doping. Carbon 2006;44:1429–37.
[30] Papakonstantinou P, Lemoine P. Influence of nitrogen on the structure and nanomechanical properties of pulsed laser deposited tetrahedral amorphous carbon. J Phys: Condens Matter 2001;13:2971–87.
[31] Zhao JP, Chen ZY, Yano T, Ooie T, Yoneda M, Sakakibara J. Core-level and valence-band characteristics of carbon nitride films with high nitrogen content. Appl Phys A 2001;73:97–101.
[32] Droppa R, Hammer P, Carvalho ACM, dos Santos MC, Alvarez F. Incorporation of nitrogen in carbon nanotubes. J Non-Cryst Solids 2002;299–302:874–9.
[33] Maldonado S, Stevenson KJ. Influence of nitrogen doping on oxygen reduction electrocatalysis at carbon nanofiber electrodes. J Phys Chem B 2005;109:4707–16.
[34] Kim T-Y, Lee K-R, Eun KY, Oh K-H. Carbon nanotube growth enhanced by nitrogen incorporation. Chem Phys Lett 2003;372:603–7.
[35] Ronning C, Feldermann H, Merk R, Hofsäss H, Reinke P, Thiele J-U. Carbon nitride deposited using energetic species: a review on XPS studies. Phys Rev B 1998;58:2207–15.
[36] Choi HC, Bae SY, Jang W-S, Park J, Song HJ, Shin H-J, et al. Release of N_2 from the carbon nanotubes via high-temperature annealing. J Phys Chem B 2005;109:1683–8.
[37] Kelemen SR, Gorbaty ML, Kwiatek PJ. Quantification of nitrogen forms in Argonne premium coals. Energy Fuels 1994;8:896–906.
[38] Shaffer MSP, Fan X, Windle AH. Dispersion and packing of carbon nanotubes. Carbon 1998;36:1603–12.
[39] Kastner J, Winter J, Kuzmany H. Raman spectroscopy of conjugated carbon systems: polymers, carbynes and fullerenes. Mater Sci Forum 1995;191:161–70.
[40] Nemanich RJ, Solin SA. First- and second-order Raman scattering from finite-size crystals of graphite. Phys Rev B 1979;20:392–401.
[41] Mott NF, Davis EA. Electron processes in noncrystalline materials. 2nd ed. Oxford: Clarendon Press; 1979.
[42] Romanenko AI, Okotrub AV, Kuznetsov VL, Obraztsov AN. Non-uniform electronic states in carbon nanostructures of different dimensionality and curvature of graphene layers forming them. Uspekhi Fizicheckh Nauk 2005;175:1000–4.
[43] Shklovskii BI, Efros AL. Electronic properties of doped semiconductors. Berlin: Springer; 1984.
[44] Kudashov AG, Okotrub AV, Yudanov NF, Romanenko AI, Bulusheva LG, Abrosimov OG. Gas-phase synthesis of nitrogenated carbon nanotubes and their electronic properties. Fizika tverdogo tela 2002;44:626–9.
[45] Zhmurikov EI, Romanenko AI, Anikeeva OB, Tecchio L. Quantum correction to conductivity of carbon–carbon composite based on ^{13}C isotope with increased density. Novosibirsk: Institute of Nuclear Physics; 2006.

Catalysis Today 147S (2009) S58–S65

Contents lists available at ScienceDirect

Catalysis Today

journal homepage: www.elsevier.com/locate/cattod

Preparation of carbonized rice husk monoliths and modification of the porous structure by SiO_2 leaching

Zinfer R. Ismagilov [a,*], Nadezhda V. Shikina [a], Irina P. Andrievskaya [a], Nina A. Rudina [a], Zulkhair A. Mansurov [b], Mukash M. Burkitbaev [b], Makhmut A. Biisenbaev [b], Arkhat A. Kurmanbekov [b]

[a] Boreskov Institute of Catalysis, 5, Pr. Akad. Lavrentieva, 630090, Novosibirsk, Russia
[b] Al-Faraby Kazakh National University, 71, al-Farabi av., 050038, Almaty, Kazakhstan

ARTICLE INFO

Article history:
Available online 5 August 2009

Keywords:
Honeycomb monoliths
Rice husk
Carbonization
Textural properties
Silica leaching

ABSTRACT

The possibility of preparing honeycomb monoliths from unconventional materials with high adsorption capacity, such as carbonized rice husk (CRH), was studied. Two schemes including modification of the porous structure by silica leaching were suggested for preparation of the monoliths: (1) preparation of CRH monoliths with the addition of Ca-montmorillonite (Ca-M) followed by leaching and (2) preliminary leaching of initial components followed by monolith extrusion. Chemical and textural properties of the materials were studied at each preparation step. The effect of temperature of rice husk (RH) pyrolysis and conditions of leaching treatment on the physico-chemical properties of CRH was investigated. By the data of nitrogen adsorption and SEM characterization, CRH has low specific surface area, pore volume less than 0.1 cm^3/g, and composed mainly of macropore channels 5–10 μm in diameter, micropores less than 17 Å in size, and a minor amount of mesopores. Treatment of the carbonized product with a 12% solution of potassium hydroxide at 80–100 °C leads to a 90–95% leaching of SiO_2 from the CRH composite and increases the specific surface area to 400 m^2/g and pore volume to 0.4 cm^3/g due to formation of mesoporous structure. The feasibility of CRH honeycomb monoliths preparation and applicability of silica leaching from the monolith material for modification of the porous structure are demonstrated. The resulting monoliths are characterized by specific surface area exceeding 300 m^2/g, pore volume 0.3 cm^3/g, and high mechanical strength.

1. Introduction

Honeycomb monoliths have some advantages over granulated and powder materials. Low-pressure drop and large geometric surface area per unit volume make them attractive for catalysis. Chemical composition of the monoliths, morphology of their components, porous structure and geometrical parameters determine their properties, mechanical strength, surface area, resistance to the action of water and various chemical agents, which in turn determine the functional properties of the monoliths in adsorption and catalytic processes [1–3]. When choosing adsorbents and catalyst supports, highly developed porous structure is a preferable property. A special niche in this field belongs to natural porous materials [4–16] including rice husk [5,6,13,14].

Rice husk, a by-product of rice milling industry, is a waste with the annual world production of ca. 545 million tons [14]. In the rice producing countries, rice husk is used as a fuel. However, this product is characterized by low caloric value, 13–15 MJ/kg [17], and high ash content. On the other hand, rice husk as a lignocellulose biomass is a valuable carbonaceous precursor that can be used to obtain a carbon material with special textural properties, high specific surface area and large pore volume [18–21].

Usually, these materials are represented by powders or granule pieces having wide particle size dispersion and low mechanical strength. One of the promising directions of their practical application is extrusion as monoliths with a regular honeycomb structure.

There are several approaches for preparation of carbon containing composite monoliths [22], by carbonization of carbon precursors on the surface of cordierite monolithic substrate, c.a. sucrose [23] and polyfurfuryl alcohol [24], or by growing of carbon nanofibers in porous structure of a substrate [25,26]. For direct extrusion of carbon monoliths, a large amount of binder should be added because of low plasticity of carbon materials. Natural clays, in particular montmorillonite $Ca_{0.2}(Al,Mg)_2Si_4O_{10}(OH)_2{\cdot}4H_2O$ (Ca-M), are commonly used as a binder [27–30]. On the one hand,

* Corresponding author. Tel.: +7 383 3306219; fax: +7 383 3306219.
E-mail address: zri@catalysis.ru (Z.R. Ismagilov).

0920-5861/$ – see front matter © 2009 Elsevier B.V. All rights reserved.
doi:10.1016/j.cattod.2009.07.043

binder increases the plasticity of carbonaceous molding composition and mechanical properties of monoliths. On the other hand, the increased mechanical strength of products has negative effect on their porous structure since a part of pores is plugged with a binder. To enhance the porosity of composite monolith substrate the chemical treatment of finished monoliths or their initial components with KOH and Na_2CO_3 solutions can be applied. This technique of alkaline treatment early was used for carbonized rice husk and a considerable development of the porous structure was achieved [18–21].

The alkaline treatment being applied for monolithic structure, will allow modifying the porous structure of monoliths due to formation of new pores upon removal of silica both from the carbon component of monolith and from montmorillonite that was used as a binder.

The goal of this work is to develop methods for honeycomb monoliths preparation from carbonized rice husk with the emphasis on control of textural characteristics and extension of functional properties on the basis of well-known methods [31,32] and our previous experience [27–30].

2. Experimental

2.1. Rice husk carbonization

The carbonization was carried out via RH pyrolysis in argon atmosphere at 400–800 °C for 60 min after attaining a desired temperature with a ramp rate 2.5 °C/min. For carbonization, 500 cm^3 of RH was placed in a steel reactor and heated in a muffle furnace.

2.2. Monoliths preparation

For monoliths preparation we used rice husk carbonized at 700 °C and Ca-montmorillonite. The CRH, initial or after the alkaline treatment, was grinded into powder with particle size of ca. 50–100 μm. Ca-M was dispersed in water under intense stirring with electric stirrer to obtain a homogeneous suspension. The suspension was poured into a flat vessel and allowed to stay open for several days until the clay swelled and a viscous mass with the moisture content 65–68% formed. The CRH powder and Ca-M suspension were blended in a Z-shape mixer for 15–30 min. The optimal content of CRH to Ca-M necessary to obtain a plastic mass is 60 and 40% respectively in terms of the calcined substance. Moisture content of the mass ready for molding is 45–50%. First the mass was consolidated and compacted by vacuum, then extruded through a die plate 10 mm in diameter using a pneumatic press with a vertical piston. This was followed by drying, which is an essential preparation step. Moisture transfer and shrinkage proceeding in a wet monolith have impact on the finished product shaping (bending, channels rupture, cracking) and mechanical strength. Thus, the formed monoliths were first seasoned for 3 days in cartons permeable to water vapor, then dried at 100 °C, and calcined at 700 °C in flowing Ar. The chosen calcination temperature provides the 100% water resistance of monoliths.

2.3. Chemical treatment with alkaline agents

The finished monoliths made of CRH were treated with a 12% solution of KOH or Na_2CO_3 at 80–100 °C for 3 h. The volume ratio of liquid and solid was 10:1. After treatment in the KOH solution, samples were washed out repeatedly with a large amount of distilled water to remove soluble compounds of Si. Then the monoliths were blown by air to remove moisture from the channels and dried at 100 °C for 2 h. The steps of alkaline treatment and washing with water were repeated up to four times. The same KOH treatment procedure was used for initial CRH and Ca-M when monoliths were prepared by using preliminarily treated components.The monolith samples were treated also by impregnation with a saturated Na_2CO_3 solution followed by drying at 100 °C and calcination at 700 °C in Ar. Then the sample was washed repeatedly with distilled water and dried at 100 °C for 2 h. The steps of treatment with sodium carbonate and washing with water were repeated four times.

2.4. Physical methods of investigation

The textural properties of CRH samples, Ca-M and monoliths were studied by low-temperature nitrogen adsorption with an ASAP-2400 analyzer (Micromeritics Instrument Corp., Norcross, GA, USA) after samples pretreatment at 150 °C. The nitrogen adsorption isotherms were determined at the liquid nitrogen temperature, 77 K, in the range of relative pressures from 0.005 to 0.991, which was followed by a standard processing by the Barret–Joyner–Halenda scheme to calculate the total surface area A_{BET}, total pore volume V_Σ and micropore volume V_μ. The pore volume available to water, V_{H_2O} (moisture capacity), of CRH samples, Ca-M and monoliths was determined by immersion of samples in water until complete saturation of pores with moisture, generally for 4 h. Then the weight amount of absorbed water referred to the weight of dry sample was calculated:

$$V_{H_2O} = (m_1 - m_0) : m_0,$$

where m_1 and m_0 are the weights of wet and dry samples, respectively.

Thermogravimetric analysis of CRH and CRH-based monoliths was made with a NETZSCH STA 449C instrument upon heating the 10 mg samples from room temperature to 1000 °C under air atmosphere at a ramp rate of 10°/min.

The XRD analysis of CRH, both initial and after the alkaline treatment, was made with a HZG-4C instrument (FRE/Berger Prazisionmechanik, Germany) using monochromated cobalt radiation in the 2θ angle range of 15–75°.

The morphology of CRH and monoliths was studied by scanning electron microscopy (SEM) using a JSM 6460LV microscope (JEOL, Japan) with accelerating voltage 25 kV.

Carbon content in the samples was determined with a VARIO ELEMENTAR III elemental analyzer. Silicon content was measured by X-ray fluorescence spectroscopy using a VRA-30 analyzer equipped with a Cr anode of X-ray tube and by means of a SPRUT-001 energy dispersive analyzer.

Mechanical crushing strength of monoliths was tested with an MP-9C device (Russia) by measuring the force required to destruct a monolith fragment with diameter 10 mm and length 10 mm between two parallel planes. Strength (P, kg/cm^2) was calculated by the formula:

$$P = \frac{p}{S} = \frac{p}{(\pi D^2/4)},$$

where p is the indicator reading, kg; S is the cross-section area of monolith, cm^2; D is the diameter of monolith, cm.

3. Results and discussion

3.1. Rice husk carbonization and alkaline activation

Table 1 lists the gravimetric data on the weight loss of rice husk versus carbonization temperature. One may see from the tabulated data that changes in the sample weight gradually become more pronounced as the temperature rises; Δm increases from 21.4% at carbonization temperature of 400 °C to 49.2% at 800 °C. Samples carbonized at different temperatures strongly differed in their

Table 1
Weight loss of rice husk versus carbonization temperature.

Samples	Δm(%)
RH-400	21.4
RH-450	23.7
RH-500	29.3
RH-550	32.6
RH-600	35.9
RH-650	42.7
RH-700	46.1
RH-750	47.5
RH-800	49.2

external appearance. In particular, samples carbonized at temperatures up to 600 °C were dark brown rather than black in color. Presumably, at temperatures lower than 600 °C only the partial carbonization occurred, whereas heavy tars and low-molecular carbonaceous compounds are evolved at higher temperatures. As the pyrolysis temperature increases, so does the content of carbon phase in the samples (see Fig. 1).

For monoliths preparation, we chose the RH sample obtained by carbonization at 700 °C, the temperature at which the monoliths will be calcined. The CRH sample contains 49 wt.% of carbon and 17 wt.% of Si, the rest being represented by N, H, O and traces of K, Ca, Fe, Zn, Ti, Al, Cl, S, P, Cu, Ni and Mn.

First we studied the morphological and textural properties of CRH and explored the possibility of modifying the porous structure by alkaline treatment.

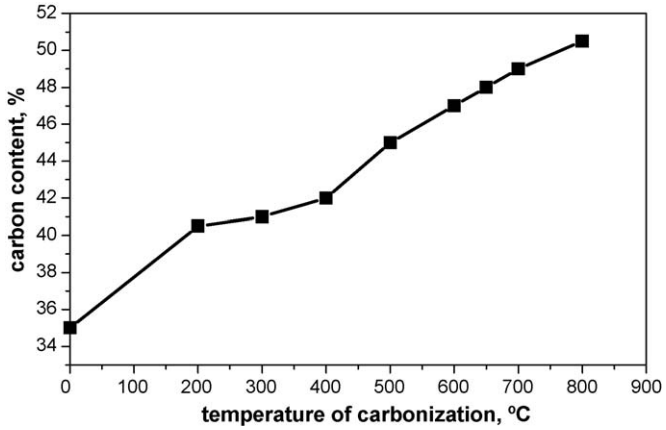

Fig. 1. Content of the carbon phase in carbonized rice husk versus the pyrolysis temperature.

The SEM images of RH sample carbonized at 700 °C are displayed in Fig. 2. Textural characteristics of the sample, BET specific surface area, pore volume available to water, volume of mesopores and micropores, and diameter of mesopores according to the nitrogen adsorption data are presented in Table 2.

One may see from the SEM images that macrostructural particles following the shape of rice husk form during carbonization. The particles are made of plate walls and virtually round channels of various size inside the plates (Fig. 2a). The

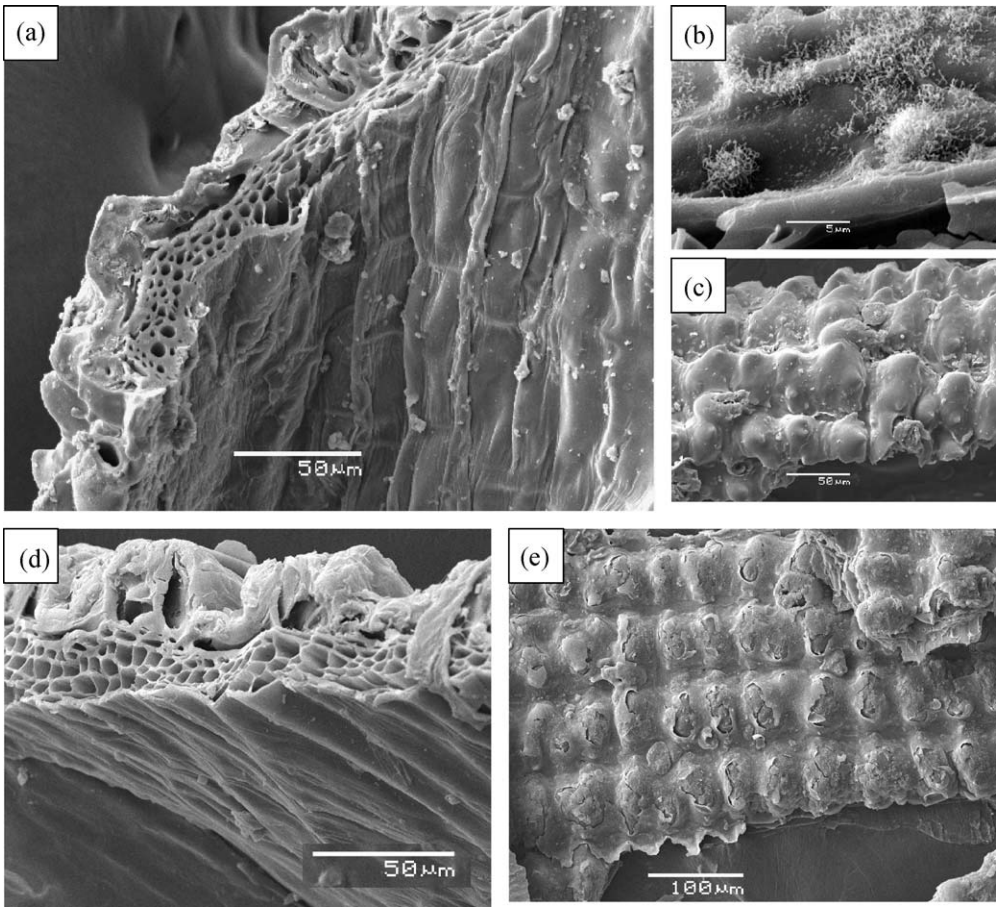

Fig. 2. SEM images of the rice husk carbonized at 700 °C: a—CRH cross-section showing the channel structure formed after removal of cellulose; b—carbon fibers on the CRH walls; c—the 'button-like' structure of CRH external surface; d and e—CRH after three operations of leaching with KOH solution.

Table 2
Dependence of textural properties of carbonized rice husk and monoliths prepared from it on a number of leaching operations and on the monolith preparation method.

No	Samples*	Number of operations leaching-alkaline agent	A_{BET} (m^2/g)	V_{H2O} (cm^3/g)	V_{Σ},/V_{μ} (cm^3/g)	Mesopore fraction (vol.%)	D_{pore} (nm)	P (kg/cm^2)
1	CRH-0	Before leaching	165	3.8	0.095/0.07	26	1.7	
2	CRH-1K	1-KOH	370	5.2	0.38/0.06	84	3.0	
3	CRH-3K	3-KOH	390	5.7	0.39/0.05	87	3.2	
4	CRH-4K	4-KOH	395	5.7	0.39/0.055	86	3.0	
Preparation of monoliths by scheme 1								
5	M1-0	Before leaching	120	0.44	0.09/0.04	56	2.3	60
6	M1-1 K	1-KOH	205	0.70	0.20/0.05	75	2.8	45
7	M1-2 K	2-KOH	260	0.76	0.26/0.046	82	2.9	40
8	M1-3 K	3-KOH	280	0.80	0.27/0.043	84	2.8	40
9	M1-4 K	4-KOH	350	0.85	0.32/0.05	84	2.7	29
10	M1-4 Na	4-Na_2CO_3	185	0.60	0.14/0.046	67	2.3	56
Preparation of monoliths by scheme 2								
11	M2-3 K	3-KOH leaching of initial components	306	0.89	0.28/0.042	85	2.7	23

*-samples designation: 1–4—CRH-lK, where CRH is carbonized rice husk; l—number of leaching operations; K-cation of an alkaline agent. 5–11—MN-lK, Na, where M is monolith; N—number of the scheme of monolith preparation; l—number of leaching operations; K, Na-cation of alkaline agent.

skeletal part of the particle is microporous; the nitrogen adsorption study revealed that ca. 75% of the porous space is occupied by micropores (see Table 2, sample 1). Morphology of the particle walls is uniform, dense, with local formation of carbon fibers on the surface (Fig. 2b). The presence of channels with diameter 5–10 μm in the CRH structure determines a remarkably high moisture capacity. External wall of the sample is structured by regular cambers (Fig. 2c), which are called button-like or bumps by the authors of [33]. According to the data reported in [33], the channels emerge from the rice husk pores upon removal of cellulose during pyrolysis, while the bumps form due to fast removal of volatile components from the particle surface.

Summing up the SEM and nitrogen adsorption data, one may conclude that the CRH sample comprises mainly the macropores of size 5–10 μm, micropores of size less than 17 Å, and a minor amount of mesopores.

The development of our method for alkaline treatment of CRH was based on the literature data. In [20,34] it was demonstrated that KOH is preferable for the preparation of carbon materials with high specific surface area and large pore volume, due to activation of the surface upon interaction of carbon with KOH by the reaction:

$$6KOH + 2C \rightarrow 2K + 3H_2 + 2K_2CO_3. \quad (1)$$

In the process, mainly the formation of microporous structure is facilitated.

In the case of silicone containing carbon composites the use of Na or K carbonates as alkaline agents [20,21] is another method to obtain mesoporous materials due to washing out from the matrix the water-soluble Na or K silicates forming by the reaction:

$$Me_2CO_3 + SiO_2 \rightarrow Me_2SiO_3 + CO_2, \quad (2)$$

where (Me = Na, K), and SiO_2 serves as a template for pore formation.

In reported methods of impregnation or mechanical mixing of carbon material with an alkaline agent the weight ratio of KOH and K_2CO_3 (Na_2CO_3) to carbon material is 4:1 and 3:1, respectively. The treatment is performed in inert atmosphere at 650–1000 °C.

Taking into account the role of mesoporous structure in functionalization of monoliths, most preferable for us is the procedure of leaching by Na or K carbonates. However, the application of procedure including impregnation of monoliths in an excess of concentrated Na_2CO_3 solution, drying, and calcination at 700 °C in Ar atmosphere resulted in cracking of the monolith and appearance of the Na_2CO_3 thermal decomposition products on the external surface of monolith structure. Evidently the porous space of monoliths is insufficient for introduction of the Na_2CO_3 amount necessary for leaching, so this procedure is not convenient for monolith samples.

We assumed that the use of more reactive KOH at temperatures far lower than those reported in the literature would allow us to modify the porous structure by SiO_2 leaching accompanied by the formation of mesopores. Thus, further alkaline treatment of CRH and CRH-based monoliths was carried out at 80–100 °C using a 12% solution of potassium hydroxide.

As shown in Table 2, the application of this procedure considerably enhances all the parameters of CRH porous structure. Even after a single leaching operation, the specific surface area increases more than 2-fold, and the total pore volume increases nearly 4-fold (Table 2, sample 2). It is essential that the development of porous structure occurs mainly due to mesopores formation (Fig. 3) caused by silica removal from the matrix, which is confirmed by the Si content analysis of alkaline solutions and wash water. Note that main changes in the porous structure occur in a first leaching operation, and repeated treatment with KOH virtually does not change the porous structure (Table 2, samples 2–4). A similar dynamics of Si washing out of the CRH matrix is observed: main decrease of silicon concentration in the sample occurs in the first leaching operation (Fig. 4, curve 1). After three operations of KOH treatment, washing with water and drying under the IR lamp, the Si content in CRH sample decreases from 17 to 1.6%, while the carbon content increases from 50 to 81%.

Note that leaching enhances also the CRH moisture capacity from 3.7 to 5.7 cm^3/g, probably due to increasing the diameter of channels (macropores). However, the SEM study of CRH sample after three leaching operations (Fig. 2d) can give only an assumptive answer to this question. There are some changes in the morphology of CRH walls: due to removal of silicon from the wall surface they become more loose and brittle (Fig. 2d and e) as compared to the initial sample.

The XRD characterization of CRH samples before and after leaching did not reveal any significant changes in the samples structure. XRD pattern of the initial sample (Fig. 5, curve 1) of carbonized rice husk shows the first maximum in the

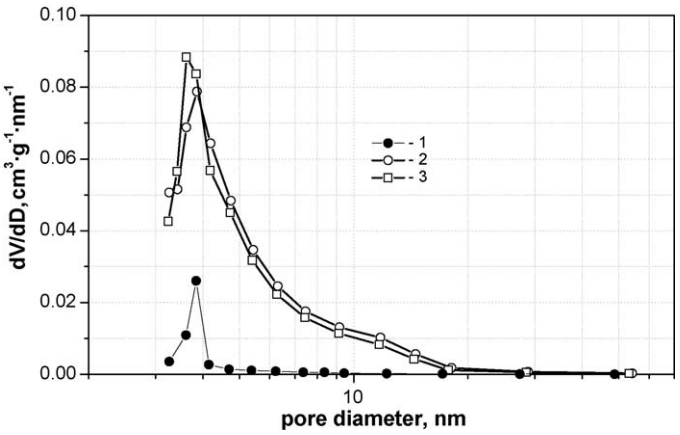

Fig. 3. Differential pore size distribution in CRH samples versus the number of leaching operations: 1—before leaching; 2—after single leaching; 3—after triple leaching.

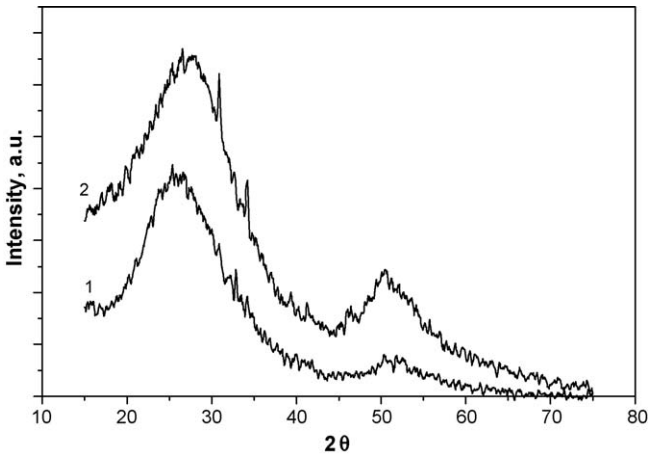

Fig. 5. Diffraction pattern of carbonized rice husk: 1—before leaching; 2—after triple leaching.

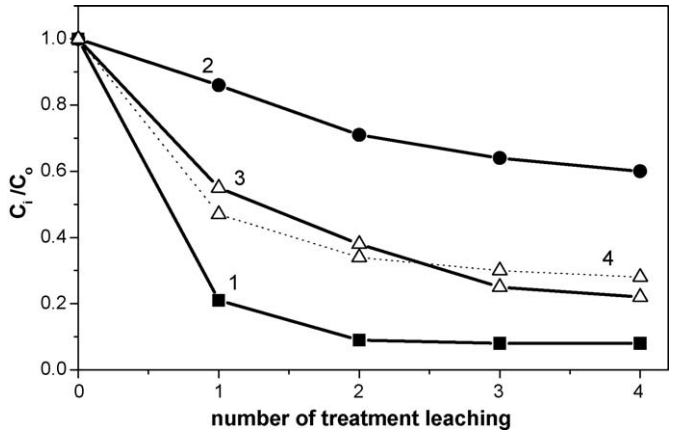

Fig. 4. The Si concentration versus the number of leaching operations in the samples: 1—CRH; 2—Ca-M; 3—experimental curve for CRH monolith (scheme 1); 4 (dots)—calculated curve for CRH monolith.

range of 18–35°, which is a superposition of the most intense maximum of amorphous SiO_2 ($2\theta = 22–26°$) and graphite-like material with interfacial distance $d/n = 3.86$ Å. After three leaching operations and SiO_2 removal from CRH, a maximum appears in the diffraction pattern (Fig. 5, curve 2), which virtually corresponds only to finely dispersed graphite-like carbon with $d/n = 3.81$ Å.

3.2. Monoliths preparation and alkaline treatment

Considering the effect of CRH to binder (Ca-M) ratio on plasticity of the molding material its composition was optimized and contains 60% of CRH and 40% of Ca-M in terms of the calcined substance. Our previous publications [27–30] showed that Ca-M provides good plasticity of the molding composition due to its ability to swell in the presence of water that penetrates into the interlayer space of this clay. On the other hand, Ca-M as a monolith component retains its ability to absorb water, whereas the monoliths should have high water resistance for their further application as catalyst supports or adsorbents. So the monoliths with montmorillonite clays were calcined at 700 °C, the temperature that provides irreversible joining of the interlayer space, which makes it possible to obtain products with high mechanical strength and water resistance.

We explored two schemes (Fig. 6) for preparation of monoliths with developed mesoporous structure from carbonized rice husk. By the first scheme, the monoliths were first produced from CRH and binder, dried, calcined, and only then

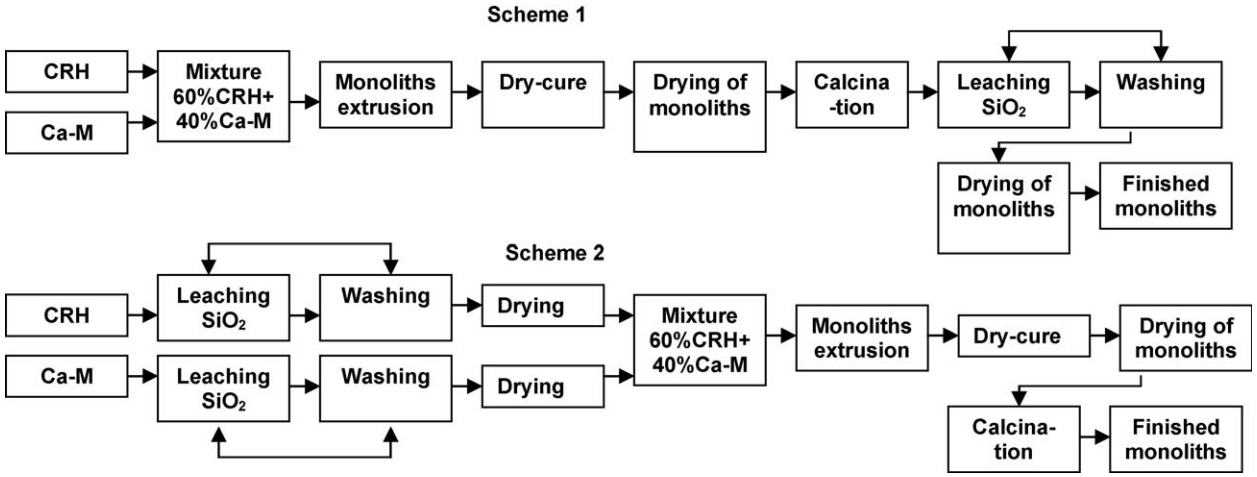

Fig. 6. Schemes of monoliths preparation including the step of leaching with KOH solution: 1—forming the monoliths from initial components followed by repeated treatment with KOH; 2—forming the monoliths from components pretreated with KOH.

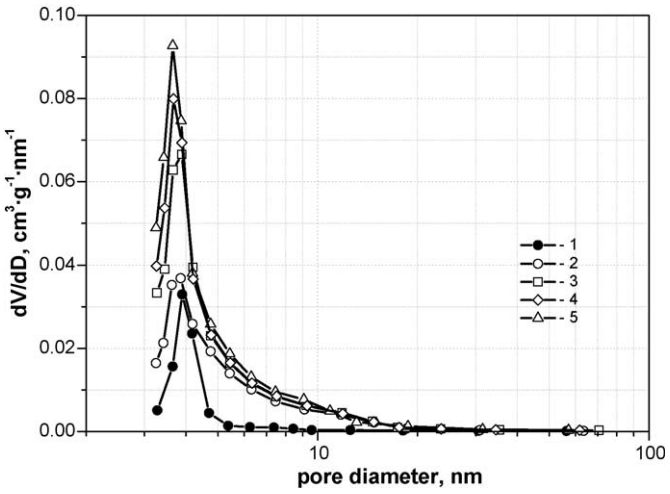

Fig. 7. Differential pore size distribution in CRH monolith samples prepared by scheme 1 versus the number of leaching operations: 1—before leaching; 2—after single leaching; 3—after double leaching; 4—after triple leaching; 5—after quadruple leaching.

treated repeatedly with KOH. Textural properties of the monoliths were tested after each treatment cycle (Table 2, samples 5–9). The KOH treatment enhances all the textural parameters of monoliths (pore volume available to water, volume of micropores and mesopores according to nitrogen adsorption, and BET specific surface area). Similar to the case of CRH itself, porous structure of monolith samples is developing mainly due to mesopores (Fig. 7); at that, in distinction to CRH material, parameters of the porous structure are enhanced gradually, increasing with each leaching cycle. A slower dynamics of SiO_2 removal from the monolith structure (Fig. 4) is related with the presence of Ca-montmorillonite, which contains bound silicon in alumosilicate composition. Experiments on SiO_2 leaching from monoliths by Na_2CO_3 solution revealed a lower efficiency of this alkaline agent as compared to KOH (Table 2, sample 10).

Fig. 8 shows a general view of CRH monolith. SEM images of cross-sections of monolith (Fig. 8b) and monolith material at high magnification (Fig. 8c) demonstrate that morphological properties of the material are determined by the morphology of monolith components, fragments of CRH and Ca-M. After silica leaching (the triple treatment with KOH), the sample morphology remains virtually the same by the SEM data (Fig. 8d), but becomes more defective due to SiO_2 removal from CRH and Ca-M. This is evidenced by a minor decrease in mechanical strength of monolith samples after each cycle of KOH treatment.

The monoliths preparation by scheme 2 (Fig. 6) includes preliminary triple treatment of CRH and Ca-M powders with KOH solution followed by washing with water after each leaching cycle, forming, drying, and heat treatment. The following steps are similar to the scheme 1: mixing, extrusion, seasoning, drying and calcinations. As a result, monoliths were produced having the porous structure parameters close to those of sample M1-3K which was prepared by scheme 1 and subjected to triple alkaline treatment (compare samples 8 and 11 from Table 2). These two samples produced by different schemes are characterized by close contents of carbon phase, which burning out is accompanied by exothermal effect in the range of 470–500 °C (TGA data, Fig. 9). However, sample M1-3K shows a much higher mechanical strength than sample M2-3K; it means that preliminary leaching of Ca-montmorillonite leads to loss its binding ability in the finished monolith.

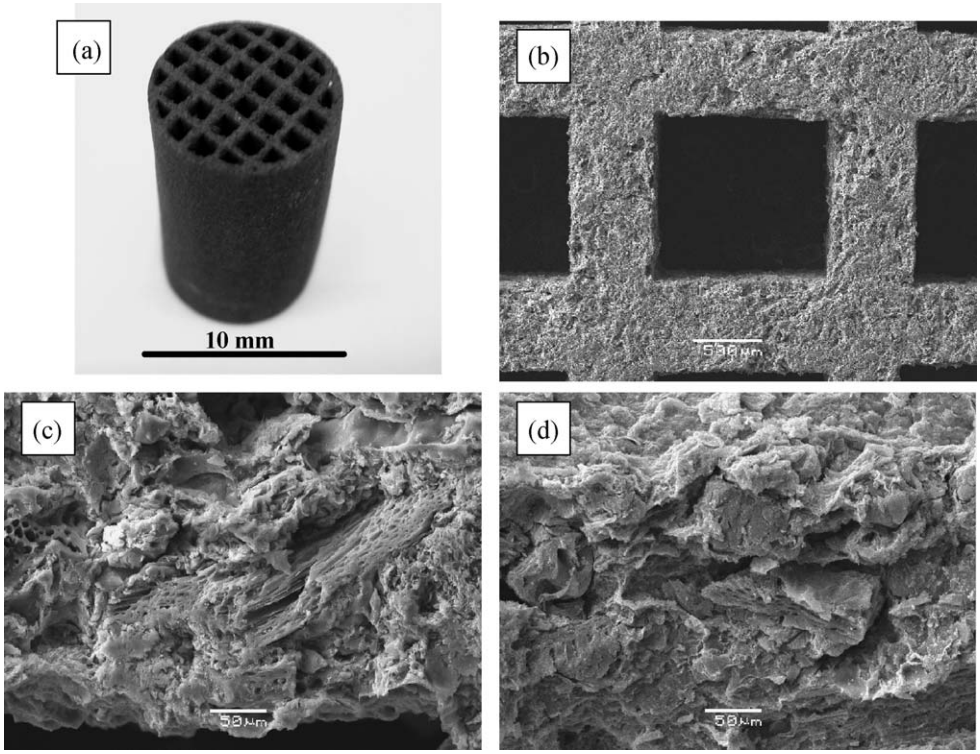

Fig. 8. CRH monoliths (scheme 1): a—external appearance of the monolith; b—SEM image of monolith partitions; c—SEM image of the monolith material before leaching; d—SEM image of the monolith material after triple leaching with KOH.

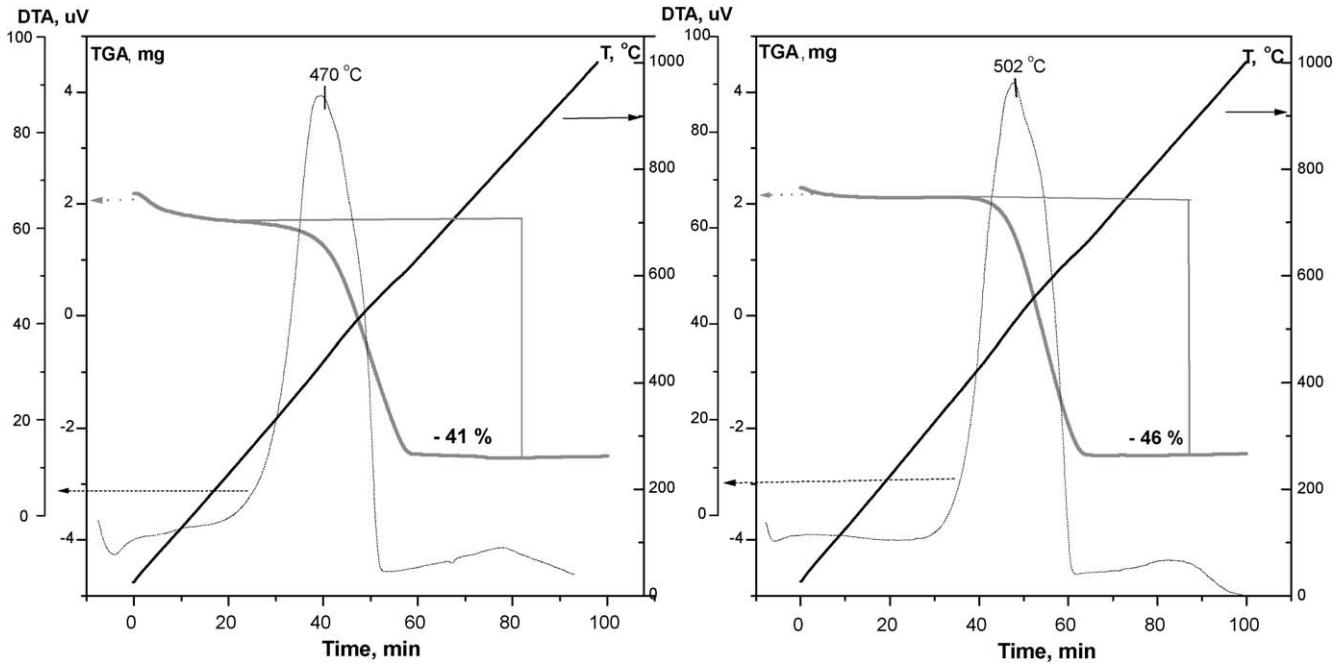

Fig. 9. TGA of CRH monolith samples: on the right—a monolith prepared by scheme 1 after triple leaching with KOH, weight loss due to carbon burn-out is 41 wt.%; on the left—a monolith prepared by scheme 2, weight loss due to carbon burn-out is 46 wt.%.

4. Conclusion

A method for preparation of monoliths from carbonized rice husk with developed mesoporous structure via modification of the porous structure by silica leaching has been developed. The effect of preparation procedure and treatment with alkaline agents, such as KOH and Na_2CO_3, on the chemical and textural properties of monolith samples was studied. Treating the monoliths with a 12% solution of KOH provides the development of mesoporous structure due to leaching out 70–75% of SiO_2 from the monolith material. After three cycles of KOH treatment and washing with water, the resulting monoliths have specific surface area of 280 m^2/g, pore volume determined from nitrogen adsorption as high as 0.3 cm^3/g, moisture capacity of 0.8 cm^3/g, and a rather high mechanical strength. These properties are appropriate for further use of the monoliths as catalyst supports and adsorbents.

Special interest was paid to CRH sample obtained by pyrolysis of rice husk at 700 °C in argon atmosphere. By the XRD data, the carbonized product is a finely dispersed graphite-like material containing X-ray amorphous silica. According to the SEM and nitrogen adsorption studies, CRH comprises mainly the macropores formed by 5–10 μm channels, micropores of size less than 17 Å, and a minor amount of mesopores. The channel structure of the macropores provides a high moisture capacity of CRH, ca. 4 cm^3/g. Treatment of the carbonized product with a 12% solution of potassium hydroxide leads to a 90–95% leaching of SiO_2 from the matrix material, increases the specific surface area from 167 to 400 m^2/g, and pore volume from 0.1 to 0.4 cm^3/g due to formation of mesoporous structure.

Acknowledgements

The authors are grateful to V.A. Ushakov for XRD analysis and interpretation, T.Ya. Efimenko for determination of textural properties, and G.S. Litvak for thermogravimetric measurements.

References

[1] V.N. Parmon, Z.R. Ismagilov, M.A. Kerzhentsev, in: J.M. Thomas, K.I. Zamaraev (Eds.), Catalysis for Energy Production. In Perspectives in Catalysis: Chemistry for 21st Century, Blackwell Scientific Publication, Oxford, 1992, p. 337.
[2] A. Cybulski, J.A. Moulijn, Catal. Rev. – Sci. Eng. 36 (2) (1994) 179.
[3] J.A. Moulijn, A. Cybulski, Structured catalysts and reactors, Marcel Dekker (1998).
[4] Z.R. Ismagilov, N.V. Shikina, S.A. Yashnik, S.R. Khayrulin, V.B. Koptenarmusov, A.A. Smislov, A.V. Polonik, Russian-International Conference of Catalytic Technologies of Environments Protection for the Industry and Transport, St. Petersburg, 11–14 December, (2007), p. 209.
[5] M.M. Yemuranov, V.A. Biisenbayev, Z.A. Mansurov, A.N. Sabitov, Zh.M. Basygaeraev, S.A. Ibragimova, M.K. Gil'manov, Izvestiya NAS RK 3 (375) (2006) 76.
[6] Z.A. Mansurov, in: R. Gross et al (Ed.), Nonoscale-Devices–Fundamentals and Applications, Springer, 2006, p. 355.
[7] P. Brown, I.A. Jefcoat, D. Parrish, S. Gil, E. Graham, Adv. Environ. Res. 4 (1) (2000) 19.
[8] A. Sukla, Y.-H. Zhang, P. Dubey, J.L. Margrave, S.S. Sukla, J. Hazard. Mater. 95 (2002) 137.
[9] K. Conrad, H.C.B. Hansen, Biores. Technol. 98 (2007) 89.
[10] N. Fiol, I. Villaesscusa, M. Martinez, N. Miralles, J. Poch, J. Serarols, Sep. Purif. Technol. 50 (2006) 132.
[11] B.M.W.P.K. Amarasinghe, R.A. Williams, Chem. Eng. J. 132 (1–3) (2007) 299.
[12] V.K. Gupta, I. Ali, J. Colloid Interf. Sci. 271 (2004) 321.
[13] T.C. Chuah, A. Jumasiah, I. Azni, S. Katayan, S.Y.T. Choong, Desalination 175 (2005) 305.
[14] Q. Feng, Q. Lin, F. Gong, S. Sugita, M. Shoya, J. Colloid Interf. Sci. 274 (2004) 1.
[15] Z.A. Mansurov, N.K. Zhylybaeva, P.S. Valieva, R.M. Mansurova, Chem. Sustainable Dev. 10 (2002) 321.
[16] F. Adam, J.H. Chua, J. Colloid Interf. Sci. 280 (2004) 55.
[17] E. Natarajan, A. Nordin, A.N. Rao, Biomass Bioenergy 14 (1998) 533.
[18] Y. Guo, S. Yang, K. Yu, J. Zhao, Z. Wang, H. Xu, Mater. Chem. Phys. 74 (3) (2002) 320.
[19] Y. Guo, K. Yu, Z. Wang, H. Xu, Carbon 41 (8) (2003) 1645.
[20] P.M. Yeletsky, V.A. Yakovlev, V.B. Fenelonov, V.N. Parmon, Kinet. Catal. 49 (2008) 708.
[21] P.M. Yeletsky, V.A. Yakovlev, M.S. Mel'gunov, V.N. Parmon, Micropor. Mesopor. Mater. 121 (2009) 34.
[22] K.M. de Lathouder, T. Marques Fló, F. Kapteijn, J.A. Moulijn, Catal. Today 105 (2005) 443.
[23] T. Valdés-Solís, G. Marbán, A.B. Fuertes, Micropor. Mesopor. Mater. 43 (2001) 113.
[24] Th. Vergunst, F. Kapteijn, J.A. Moulijn, Carbon 40 (2002) 1891.
[25] T.A. Nijhuis, A. Beers, T. Vergunst, I. Hoek, F. Kapteijn, J.A. Moulijn, Catal. Rev. 43 (2001) 345.
[26] K.P. de Jong, J.W. Geus, Catal. Rev. Sci. Eng. 42 (2000) 481.
[27] S.A. Yashnik, Z.R. Ismagilov, I.V. Koptyug, I.P. Andrievskaya, A.A. Matveev, J.A. Moulijn, Catal. Today 105 (3–4) (2005) 507.

[28] S.A. Yashnik, I.P. Andrievskaya, O.V. Pashke, Z.R. Ismagilov, J.A. Moulijn, Catal. Ind. 1 (2007) 35.
[29] Z.R. Ismagilov, S.A. Yashnik, A.A. Matveev, I.V. Koptyug, J.A. Moulijn, Catal. Today 105 (3–4) (2005) 484.
[30] Z.R. Ismagilov, R.A. Shkrabina, N.V. Shikina, 4th Conf. Scientific Based for Preparation and Technology of Catalysts, Sterlitamak, Russia, 29 August–1 September, (2000), p. 131.
[31] Z.R. Ismagilov, International Seminar on Monolith Honeycomb Supports and Catalysts, St. Petersburg, (1995), p. 9.
[32] R.M. Heck, R.J. Farrauto, Catalytic Air Pollution Control. Commercial Technology, VNR, New York, 1995, p. 206.
[33] A. Bharadwaj, Y. Wang, S. Sridhar, V.S. Arunachalam, Res. Commun. 87 (7) (2004) 981.
[34] M.A. Lillo-Rodenas, D. Cazorla-Amoros, A. Linares-Solano, Carbon 41 (2003) 267.

ISSN 0023-1584, Kinetics and Catalysis, 2010, Vol. 51, No. 2, pp. 312–317. © Pleiades Publishing, Ltd., 2010.
Original Russian Text © Ch.N. Barnakov, A.P. Kozlov, A.I. Romanenko, N.T. Vasenin, V.F. Anufrienko, Z.R. Ismagilov, 2010, published in Kinetika i Kataliz, 2010, Vol. 51, No. 2, pp. 330–335.

Synthesis and Properties of a Microporous Carbon Material As a Catalyst Support for Fuel Cells

Ch. N. Barnakov[a], A. P. Kozlov[a], A. I. Romanenko[b], N. T. Vasenin[c], V. F. Anufrienko[c], and Z. R. Ismagilov[c]

[a] *Institute of Carbon and Carbon Chemistry, Siberian Branch, Russian Academy of Sciences, Kemerovo, 650099 Russia*
[b] *Institute of Inorganic Chemistry, Siberian Branch, Russian Academy of Sciences, Novosibirsk, 630090 Russia*
[c] *Boreskov Institute of Catalysis, Siberian Branch, Russian Academy of Sciences, Novosibirsk, 630090 Russia*
e-mail: han@kemnet.ru

Received April 16, 2009

Abstract—It is stated that one-dimensional conductivity in amorphous microporous carbon material (AMCM) samples is associated with the considerable imperfection of graphene fragments in the carbon material rather than the presence of unshared electrons. It is likely that the graphene fragments are formed upon the carbonization of a carbon precursor accompanied by the partial or complete removal of precursor heteroatoms. It is hypothesized that the presence of localized unpaired electrons, which give EPR spectra, is due to the formation of local defects in carbene fragments. Thus, the effects of the value of conductivity and the concentration of unpaired electrons on the power output of a fuel cell cannot be distinguished based on the experimental data with the use of an AMCM as a catalyst support. The interaction of localized paramagnetic centers with electron gas can be interpreted in terms of the C–S relaxation model.

DOI: 10.1134/S0023158410020217

INTRODUCTION

Previously [1], we found that the power output of a fuel cell in which a new amorphous microporous carbon material (AMCM) was used as a catalyst support was higher than that with the use of a Vulcan XC-72R standard support or structurally different nanofibrous carbon materials at the same platinum content (0.02–0.09 mg/cm^2) of the cathode and a platinum particle size of 2–4 nm. The main difference of the AMCM from the Vulcan XC-72R support and nanofibrous carbon materials is that it exhibits one-dimensional hopping conduction and a high concentration (10^{19}–10^{20} spin/g) of unpaired electrons. In this case, Barnakov et al. [2] found that the Curie law was not obeyed for the EPR spectra of the above samples: as the measurement temperature was decreased, the integrated intensity noticeably decreased rather than increased. Barnakov et al. [2] hypothesized that processes occurring at the cathode of a fuel cell are sensitive to these properties of AMCMs. The question now arises of to what extent the above properties are characteristic of AMCM samples and in what cases they can appear in carbon cokes.

The EPR spectra of the free radicals of carbon materials (singlet lines without HFS with $\Delta H = 1$–10 G and $g = g_e$) were first recorded long ago [3]. As a rule, such EPR spectra are observed for coals, cokes, and pyrolysis products of organic compounds (sugar). The integrated intensity of these spectra usually obeys the Curie law, and the line width depends only slightly on the measurement temperature. After the detection of the EPR spectra of coals and cokes sensitive to adsorbed oxygen [4–6], it became clear that the appearance of electron gas upon pyrolysis has a considerable effect on the spectra. This effect is due to the exchange interaction of localized centers (C) with electron gas (S) (C–S relaxation). The physical principles of the C–S relaxation for systems with a degenerate three-dimensional electron gas have been adequately developed [7, 8]. The detection of a sharp broadening of the EPR spectra of Fe^{3+} ions in a matrix of V_2O_4 [9] provided a support for the C–S relaxation. The V_2O_4 oxide is well known as a system with the Mott dielectric–metal transition as the temperature is increased above 280 K. At this temperature, the EPR spectra of Fe^{3+} ions with localized electrons are dramatically broadened.

Unfortunately, the temperature dependence of the spin–lattice relaxation time τ_{SL} remained unknown in the case of coals and cokes. The effect of the C–S relaxation on the EPR spectra of carbon structures has been considered in detail [7]. In the description of this relaxation mechanism, the temperature dependence of the relaxation time τ_{SL}, where L is the lattice, is of paramount importance. There was good reason to believe that this relaxation time depends on the dimension of electron gas in the resulting carbon structure and the number of electrons in the electron gas responsible for its degeneracy. To solve all of these problems, it was necessary to measure the temperature

Synthesis conditions, specific surface areas, and conductivities (at 300 K) of AMCM samples

No.	Precursor	Carbonization temperature, °C	Carbonization time, min	Specific surface area, m^2/g	Conductivity, σ (300 K), $(\Omega/cm)^{-1}$
1*	Phenol and 1,2,3-benzotriazole	900	23	1800	0.06
2*	Phenol and 1,2,3-benzotriazole	700	15	2200	1.06
3*	Phenol and 1,2,3-benzotriazole	900	15	2900	4.95
4	*o*-Nitroaniline and 1,2,3-benzotriazole	700	20	470	0.0002
5	Sample no. 4	900	10	490	0.78
6	8-Hydroxyquinoline and 1,2,3-benzotriazole	700	80	3400	0.33
7	Sample no. 6	900	10	3300	3.32
8	PVC	700	25	2300	0.005
9	Pine nut shells	700	15	2075	1.62

* The synthesis and properties of these samples were described elsewhere [2, 10].

dependence of the conductivity of carbon structures depending on the synthesis methods. It has long been noted [3] that the EPR spectra were not observed if the pyrolysis temperature of coals or organic compounds (sugar) was increased above 700°C; this was likely due to the interaction of localized centers (C), which give EPR spectra, with the formed electron gas (S). The specific characteristics of the electron gas remained unclear.

The aim of this work was to study the electric conductivity and EPR spectra of AMCM samples, which can be used as catalyst supports for fuel cell cathodes.

EXPERIMENTAL

It is well known that the properties of a carbon material depend on its precursor and pyrolysis conditions. For this purpose, we synthesized carbon material samples from various precursors. The common feature of all of the synthesized samples was the occurrence of electric conductivity, although the temperature dependences were different. The AMCM samples were synthesized in accordance with patented procedures [10, 11]. The following organic compounds with various degrees of aromaticity and containing various functional groups were used as sample precursors: phenol, 1,2,3-benzotriazole, *o*-nitroaniline, and 8-hydroxyquinoline, as well as the synthetic and natural polymer materials—poly(vinyl chloride) (PVC) and Siberian pine nut shells. Preliminary communications concerning the studies of test samples have been published elsewhere [2, 12–14].

The table summarizes the main conditions of the synthesis of AMCM samples.

Sample no. 1 was prepared by the carbonization of a mixture of phenol and 1,2,3-benzotriazole in a molar ratio of 2 : 1. Sodium hydroxide was used as an alkali at an organic matter to alkali ratio of 1.76. The carbonization was performed in a closed crucible (in a carbonization gas atmosphere). After cooling, the sample was washed with water to a neutral reaction and dried in air at 110–120°C to constant weight.

Sample no. 2 was obtained under the same conditions as sample no. 1 except for the mixture carbonization temperature and time.

Sample no. 3 was prepared from the same components as sample no. 1, but the organic matter to alkali ratio was 5.0.

A mixture of *o*-nitroaniline and 1,2,3-benzotriazole in a molar ratio of 2 : 1 was used as a precursor for sample no. 4. Sodium hydroxide was used as an alkali in an organic matter to alkali ratio of 1.25. The subsequent treatment was the same as with sample no. 1.

Sample no. 5 was obtained by the repeated carbonization of sample no. 4 in a closed crucible. After the carbonization, the crucible was cooled in air to room temperature.

A mixture of 8-hydroxyquinoline and 1,2,3-benzotriazole in a molar ratio of 1 : 1 was used as a precursor for sample no. 6. Sodium hydroxide was used as an alkali in an organic matter to alkali ratio of 2.5. The sample was carbonized in a closed crucible, and the subsequent treatment was performed as specified for sample no. 1.

Sample no. 7 was prepared after the repeated carbonization of sample no. 6 in a closed crucible. After the carbonization, the crucible with the sample was cooled to room temperature, as with sample no. 5.

To synthesize sample no. 8, commercial S-7059M PVC was used; it was mixed with an aqueous equimolar mixture of potassium and sodium hydroxides in a weight ratio of 1 : 5. The mixture was evaporated and carbonized; the subsequent treatment was performed as specified for sample no. 1.

To synthesize sample no. 8, Siberian pine nut shells were used; they were mixed with a concentrated aqueous solution of potassium hydroxide in a weight ratio of 1 : 2. The mixture was evaporated and carbonized. Then, the sample was treated as specified for sample no. 1.

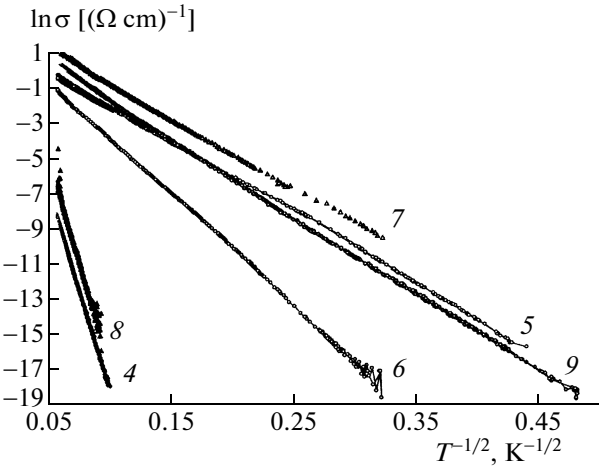

Fig. 1. The temperature dependence of the logarithm of the electric conductivity of AMCM sample nos. 4–9.

The texture characteristics of the resulting AMCM samples were determined on an ASAP-2400 instrument (Micromeritics) using the adsorption of nitrogen at 77 K after the pretreatment of the samples at 300°C away from atmospheric air at a residual pressure of <0.001 Torr until the termination of gas evolution. Then, nitrogen adsorption isotherms were measured at relative pressures from 0.005 to 0.995 and processed in accordance with a standard procedure to calculate the overall surface area (S_{sp}) using the BET method. The EPR spectra were measured on a Bruker ER-200 D spectrometer at 77 and 293 K ($\lambda = 3$ cm) after evacuation at 200°C. The temperature dependence of the conductivity of samples was measured using a four-contact method over the temperature range of 4.2–300 K. The samples as powders were pressed in ampoules. Silver wire 0.1 mm in diameter was used as a contact wire, and powder in the ampoule was pressed to contact the sample with the wire. Raman spectra were recorded on a DILOR OMARS 89 spectrometer with an LN/CCD-1100 PB multichannel detector (Princeton Instruments) and a holographic zero filter. The green line of an ILA-120 argon laser (Carl Zeiss) with a wavelength of 514.5 nm was used as the excitation line. The beam power was 200 mW. The spectra were recorded using an unfocused laser beam lest the power should not burn.

RESULTS AND DISCUSSION

The possibility of conductivity electron localization in a restricted structure region can result in the hopping conduction of current carriers between these localization regions. As the temperature is increased, ordinary hopping conduction between the nearest localization centers is changed by variable-range hopping conduction (VRHC) and described by the generalized Mott law [8]

$$\sigma_{VRHC}(T) = \sigma_0 \exp(-B/T)^{1/(d+1)},$$

where d is the dimension of current carrier migration, $B = [16\alpha^3/k_B N(E_F)]$, α is the reciprocal of the length at which the atomic wave function amplitude decays, $N(E_F)$ is the density of states on the Fermi surface, and σ_0 is a constant.

Figure 1 shows the temperature dependence of the electric conductivity of AMCM sample nos. 4–9. The temperature dependences of the electric conductivities of these samples are noticeably different. However, over the entire test temperature range, the conductivity is described by the relationship corresponding to the Mott law for a one-dimensional case ($d = 1$)

$$\sigma(T) = \sigma_0 \exp(-T_0/T)^{1/2},$$

where $T_0 = [16\alpha/k_B N(E_F) L_\parallel L_\perp^2]$ and $1/\alpha \sim 8$–10 Å [15].

Note that one-dimensional conductivity accompanied by the temperature dependence analogous to that shown in Fig. 1 was observed previously in carbon structures with carbyne chains [16–20]. As can be seen in Fig. 1, the one-dimensional conductivity depends on the nature of the initial carbonization products. Among the above samples, the AMCM sample prepared from Siberian pine nut shells exhibited one-dimensional conductivity over the broadest temperature range (4.2–300 K). The narrowest range (150–300 K) of the temperature dependence of conductivity was observed in the AMCM sample prepared from PVC at a carbonization temperature of 700°C. An increase in the carbonization temperature resulted in an increase in the initial one-dimensional conductivity (σ_0) of the carbon material. In this case, the time of carbonization at 900°C should be no longer than 10–15 min. If the time of carbonization is longer than 20 min, the one-dimensional conductivity of the carbon material changes to the three-dimensional one, which is described by the following relation corresponding to the Mott law for a three-dimensional case ($d = 3$):

$$\sigma(T) = \sigma_0 \exp(-T_0/T)^{1/4} \text{ [2, 14]}.$$

Previously [2, 12–14], we hypothesized that one-dimensional conductivity in our samples was associated with the presence of carbyne. To test this hypothesis, we measured the Raman spectra of sample nos. 7 and 9 with the use of a green laser. Unfortunately, we failed to detect the spectrum of carbyne. It is likely that the one-dimensional conductivity is due to the considerable imperfection of graphene particles in the carbon material, which is formed upon the removal of nitrogen in the course of the carbonization of a carbon precursor. In the cases when PVC or pine nut shells serve as a precursor, it is likely that the formation of defect graphene fragments results from the removal of chlorine or oxygen atoms, respectively.

The table summarizes data on changes in the conductivity (σ) of samples at 300 K. As noted previously,

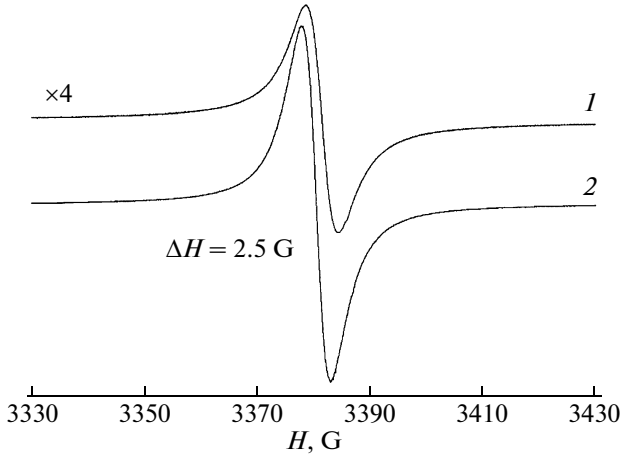

Fig. 2. EPR spectra of evacuated sample no. 4 at (*1*) 293 K room temperature and (*2*) 77 K liquid nitrogen temperature.

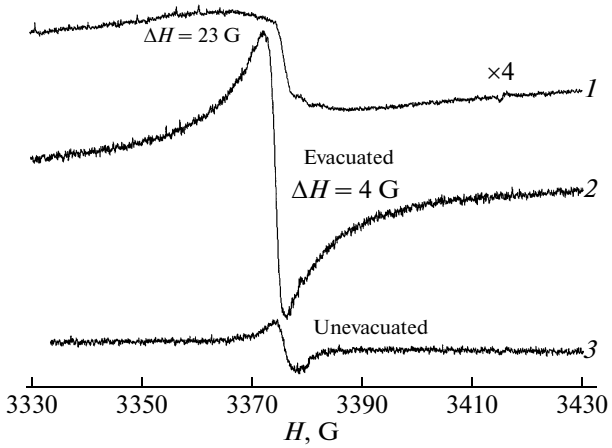

Fig. 3. EPR spectra of evacuated sample no. 6 at (*1*) room temperature, (*2*) liquid nitrogen temperature, and (*3*) unevacuated sample no. 6 at liquid nitrogen temperature.

sample no. 4 exhibited an EPR spectrum. As the initial one-dimensional conductivity (σ) increased, the EPR spectrum broadened, and sample no. 5 did not exhibit an EPR spectrum. Such a behavior was also observed in sample nos. 6 and 7, as well as nos. 2 and 3.

Previously [14], it was noted that sample no. 1 did not exhibit EPR spectra. In evacuated sample nos. 2 and 3, symmetrical EPR spectra with $g = g_e$ were observed. The integrated intensity of all of the EPR spectra was as high as 10^{19} spin/g. It was found that the spectra of these samples, which were shown in [14], as well as the spectra of sample nos. 4 and 6 (Figs. 2, 3) after evacuation, obeyed the Curie law typical of isolated or weakly interacting paramagnetic centers: as the measurement temperature was decreased, the integrated intensity not only did not increase, but it noticeably decreased. It was noted previously [12, 13] that the EPR spectra were broadened upon the repeated carbonization of these samples at 900°C for 10–15 min. It was found that the Curie law was also not obeyed in sample nos. 8 and 9 but in the opposite direction, as compared with sample nos. 2–4 and 6. For example, after the vacuum pumping of sample no. 8 (Fig. 4), a good EPR spectrum of coke with $\Delta H = 5.5$ G was observed, and this spectrum disappeared after opening the ampoule. Its temperature dependence did not obey the Curie law: as the temperature was decreased to 77 K, the intensity increased by a factor of ~15 rather than 4 according to the Curie law; that is, the Curie law violation was opposite to that in the above case of sample nos. 2–4 and 6. This was likely due to different natures of the starting materials.

The found special features of the temperature dependence of the EPR spectra can be understood using the C–S relaxation model [8, 16]. This model (see the scheme) takes into account the effect of the exchange interaction of electron gas (S) with localized centers (C) on the width of the EPR signal of the localized centers. From the narrow neck model ($\tau_{SC} < \tau_{SL}$) for the C–S relaxation, it follows [8, 16] that the width of the EPR spectrum of the localized center (C) is determined by the following expression:

$$\Delta H \approx \frac{\rho(E_F)kT}{N_C}\frac{1}{\tau_{SL}},$$

where $\rho(E_F)$ is the density of electronic states on the Fermi surface; N_C is the concentration of the localized centers (C); τ_{SL} is the spin–lattice relaxation time of electron gas (S); and k is Boltzmann's constant.

Note that the value of τ_{SL} for a three-dimensional electron gas strongly depends on temperature [8, 15, 16] ($1/\tau_{SL} \sim T^n$, where $n = 4$–7 for various models). Thus, in the case of a one-dimensional electron gas for sample no. 8, the EPR spectra of a portion of localized centers, which are strongly broadened at 300 K, dramatically narrow as the temperature is decreased; this is equivalent to a greater increase in the EPR signal intensity with decreasing temperature than that follows from the Curie law ($I \approx C/T$, where C is a constant).

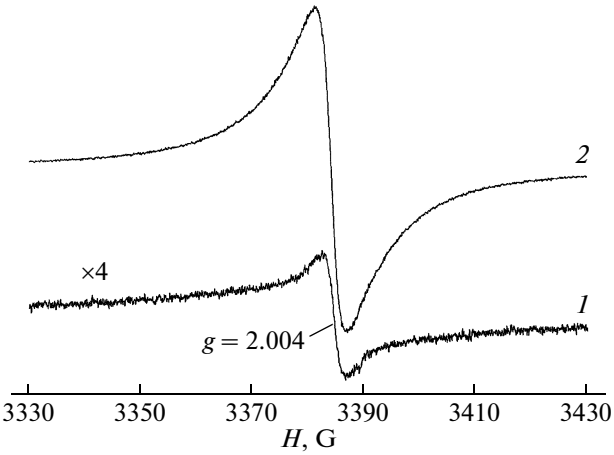

Fig. 4. EPR spectra of evacuated sample no. 8 at (*1*) room temperature and (*2*) liquid nitrogen temperature.

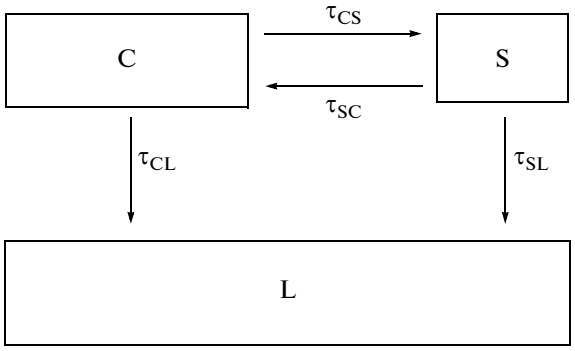

Schematic diagram of C–S relaxation: (C) are localized electrons, (S) is electron gas, L is the crystal lattice, and τ_{CS}, τ_{SC}, τ_{SL} are the relaxation times.

It is likely that, as the measurement temperature is decreased, the electron localization of electron gas on defects in sample no. 8 weakens the exchange interaction of localized centers (C) and electron gas (S). That is, in this case at a low temperature (77 K), the C–S relaxation model is completely excluded and the "pure" EPR spectrum of localized centers (C) is observed. The inverse relation between the EPR spectrum intensity and temperature, which was found in sample nos. 2–4 and 6, can also be understood. Physically, it is clear than the temperature dependence of the line width ΔH depends on the properties of electron gas. There is good reason to believe that the localization of a portion of electron gas near localized centers (C) occurs as the temperature is decreased; this results in a noticeable broadening of the EPR spectra of centers (C)—the disappearance of spectra as the temperature is decreased.

The found special features of the effect of the properties of electron gas on the EPR spectra of carbon structures should be studied in more detail.

CONCLUSIONS

We found that the one-dimensional conductivity of a carbon material is not necessarily associated with the presence of unshared electrons, but it is caused by the considerable imperfection of graphene fragments in the carbon material. In the case of a nitrogen-containing carbon material, this imperfection results from the partial or complete removal of nitrogen atoms in the course of carbonization. In the cases that PVC or pine nut shells serve as an AMCM precursor, it is likely that the imperfection of graphene fragments results from the removal of chlorine or oxygen atoms, respectively. It is believed that localized unpaired electrons, which give an EPR spectrum, are associated with the formation of local defects in the graphene fragments of AMCMs. The samples exhibit an EPR spectrum when the number of one-dimensional conductivity carriers is small. As the number of carriers increases with the retention of one-dimensional conductivity, the EPR spectrum broadens. The EPR spectrum can also broaden because of a change of the one-dimensional conductivity of the carbon material to the three-dimensional conductivity. Thus, based on the experimental results, we cannot distinguish between the effects of the conductivity and the concentration of unpaired electrons upon the change in the power output of a fuel cell, in which an AMCM is used as a catalyst support. The interaction of localized paramagnetic centers with electron gas can be explained in terms of the C–S relaxation model.

ACKNOWLEDGMENTS

This work was supported by the Presidium of the Siberian Branch of the Russian Academy of Sciences (Complex Integration Project SO RAN 2006 no. 4.5), the Russian Foundation for Basic Research (grant no. 07-03-96042), and the Ministry of Education and Science (grant no. RNP.2.1.1.1604).

We are grateful to N.N. Ovsyuk for recording the Raman spectra.

REFERENCES

1. Ismagilov, Z.R., Kerzhentsev, M.A., Shikina, N.V., Lisitsyn, A.S., Okhlopkova, L.B., Barnakov, Ch.N., Masao Sakashita, Takashi Iijima, and Kenichiro Tadokoro, *Catal. Today*, 2005, vols. 102–103, p. 58.
2. Barnakov, Ch.N., Kozlov, A.P., Seit-Ablaeva, S.K., Romanenko, A.I., Vasenin, N.T., Anufrienko, V.F., Ismagilov, Z.R., and Parmon, V.N., *Ross. Khim. Zh.*, 2006, vol. 50, no. 1, p. 54.
3. Ingram, D.J., *Spectroscopy at Radio and Microwave Frequencies*, London: Butterworths, 1955.
4. Sidorov, A.A and Anufrienko, V.F., *Kinet. Katal.*, 1966, vol. 7, p. 1060.
5. Vasil'ev, L.M. and Anufrienko, V.F., *Kinet. Katal.*, 1971, vol. 12, p. 1310.
6. Shklyaev, A.A., Anufrienko, V.F., and Vasil'eva, L.M., *Dokl. Akad. Nauk SSSR*, 1971, vol. 200, p. 1165.
7. Ravilov, R.G., *Cand. Sci. (Phys.–Math.) Dissertation*, Novosibirsk: Inst. of Catalysis, 1980.
8. Mott, N.F. and Davis, E.A., *Electron Processes in Non-crystalline Materials*, Oxford: Clarendon, 1979, 2nd ed.
9. Ioffe, V.A. and Andronenko, R.R., *Fiz. Tverd. Tela*, 1983, vol. 25, p. 2212.
10. RF Patent 2206394, 2003.
11. RF Patent 2307069, 2007.
12. Barnakov, Ch.N., Romanenko, A.I., Kozlov, A.P., Seit-Ablaeva, S.K., Vasenin, N.T., Anufrienko, V.F., and Ismagilov, Z.R., *"Catalysis: Fundamentals and Application," Proc. III Int. Conf.*, Novosibirsk, Russia, 2007.
13. Barnakov, Ch.N., Romanenko, A.I., Kozlov, A.P., Seit-Ablaeva, S.K., Vasenin, N.T., Anufrienko, V.F., and Ismagilov, Z.R., *Proc. Int. Carbon Conf.*, Seattle, Wash., 2007.

14. Kozlov, A.P., Barnakov, Ch.N., Romanenko, A.I., Anufrienko, V.F., Kerzhentsev, M.A., Ismagilov, Z.R., and Parmon, V.N., *Preprint of the 231st ACS National Meeting*, Atlanta, Ga., 2006, FUEL 0121.

15. Joo, J., Long, S.M., Pouget, J.P., Oh, E.J., MacDiarmid, A.G., and Epstein, A.J., *Phys. Rev. B: Condens. Matter*, 1998, vol. 57, p. 9567.

16. Hirst, I.I. and Schafer, W., *Phys. Rev. B: Condens. Matter*, 1973, vol. 8, p. 64.

17. Gossard, A.C., *J. Appl. Phys.*, 1967, vol. 38, no. 1, p. 12.

18. Demishev, S.V., Pronin, A.A., Glushkov, V.V., Sluchanko, N.E., Samarin, N.A., Kondrin, M.V., Lyapin, A.G., Brazhkin, V.V., Varfolomeeva, T.D., and Popova, S.V., *Pis'ma Zh. Eksp. Teor. Fiz.*, 2003, no. 8, p. 984.

19. Shenderova, O.A., Zhirnov, V.V., and Brenner, D.W., *Crit. Rev. Solid State Mater. Sci.*, 2002, vol. 27, nos. 3–4, p. 227.

20. Sladkov, A.M. *Karbiny – tret'ya allotropnaya forma ugleroda* (Carbynes: The Third Allotropic Form of Carbon), Moscow: Nauka, 2003, p. 151.

CHAPTER 8
Design and testing of catalytic microreactors.

Available online at www.sciencedirect.com
SCIENCE DIRECT
Catalysis Today 105 (2005) 516–528
CATALYSIS TODAY
www.elsevier.com/locate/cattod

Optimization of anodic oxidation and Cu–Cr oxide catalyst preparation on structured aluminum plates processed by electro discharge machining

I.Z. Ismagilov [a,b], R.P. Ekatpure [a], L.T. Tsykoza [b], E.V. Matus [b], E.V. Rebrov [a], M.H.J.M. de Croon [a], M.A. Kerzhentsev [b], J.C. Schouten [a,*]

[a] *Laboratory of Chemical Reactor Engineering, Eindhoven University of Technology, P.O. Box 513, 5600 MB Eindhoven, The Netherlands*
[b] *Laboratory of Environmental Catalysis, Boreskov Institute of Catalysis SB RAS, Prospekt Akademika Lavrentieva, 5, Novosibirsk 630090, Russia*

Abstract

This paper describes the optimization of three processes applied in fabrication of a microstructured reactor for complete oxidation of volatile organic compounds. The first process involves the optimization of the electro discharge machining (EDM) method to produce a set of microchannels with a high length to diameter ratio of 100, with a standard deviation from the average diameter below 0.2%, and with a surface roughness not higher than 2.0 μm. To satisfy these criteria, fabrication of microchannels must be carried out with two machining passes in the Al51st alloy. Then, the effect of several parameters on the anodization current efficiency with respect to oxide formation was studied. The best process conditions to get a 30 μm porous alumina layer in a 0.4 M oxalic acid electrolyte, were found to be a temperature of 1 °C, an anodic current density of 5 mA/cm^2, and 23 h oxidation time. At last, the resulting coatings were impregnated with an aqueous solution of copper dichromate followed by drying and calcination at 450 °C to produce active catalysts. The effect of a copper dichromate concentration, number of impregnation cycles (1 or 2), and different after-treatments on catalytic activity and stability in complete oxidation of n-butane were studied. The catalytic activity of the obtained coatings is superior to that of alumina supported pelletized catalysts even at much lower loadings of active metals.

Keywords: Microstructured reactor; Electro discharge machining; Anodic oxidation; Copper chromite; Catalytic combustion; VOC

1. Introduction

In general, a high and uniform accessibility of catalytic sites is of great importance to get a high activity and a high selectivity in any chemical process. The objective of the present work is to obtain a uniform accessibility of a particular catalyst that is distributed over a large volume in a microstructured reactor. To reach this goal, it is important to create a uniform reactant flow distribution across the microchannels in this reactor as well as to obtain a uniform pore size distribution of the catalyst support material. Furthermore, it is relevant to develop the proper structure of the catalyst and its support.

A non-uniformity in the diameter of microchannels, created at different stages of microrector fabrication, can disturb considerably the residence time distribution, thereby decreasing the reactor performance. One of the goals of this study is to examine the effect of different treatments on dimensional quality of the geometry during electro discharge machining (EDM) and anodic oxidation. EDM is a machining method in which a voltage is applied through a dielectric medium between the tool electrode and a workpiece, using electro-discharge generated when electrode and workpiece are positioned close to each other. Many researchers have used EDM to obtain microchannels in

* Corresponding author. Tel.: +31 40 247 2850; fax: +31 40 244 6653.
E-mail address: j.c.schouten@tue.nl (J.C. Schouten).

0920-5861/$ – see front matter © 2005 Elsevier B.V. All rights reserved.
doi:10.1016/j.cattod.2005.06.053

different metals. However, data relating to differences between different methods of EDM remain rare. Thus, we have focused in this study on the dimensional accuracy of methods of one, two and three machining passes applied to two different aluminum alloys. Aluminum based alloys were chosen as a substrate material because of their high thermal conductivity and high corrosion stability, as well as the possibility to form coatings of aluminum oxide. These coatings were reported to be effective catalyst supports [1–4]. They can be grown to a thickness of tens to hundreds of micrometers [2,3,5,6] and exhibit specific surface areas of 10–40 m^2/g [2–4].

Microreactors are typically built up from several dozens up to several thousands of individual channels. Therefore, the anodic oxidation procedure is repeated by application of a number of oxidation runs until a desired number of substrate plates is obtained. In a classical procedure, the aluminum substrate is placed in the solution of a weak organic acid, which is used as electrolyte. In an electrolysis cell, the aluminum cathodes are usually applied. However, uniform coating properties, such as layer thickness and pore structure, are difficult to obtain in a subsequent set of oxidation runs, because the properties of the electrolyte are changing in the course of the electrolysis process, due to dissolution of alloying elements. Refreshing the electrolyte after each oxidation run would lead to a large amount of waste, which is not attractive from a practical point of view. Decreasing the volume of the electrolysis cell creates substantial problems in temperature control, due to heat evolution in the process. Recently, a method for scale-up of anodic oxidation was proposed. The anode, carrying ten aluminum plates, was slowly rotated in the electrolyte. The plates were thus cycled between the top and the bottom of the vessel and the materials were treated under the same conditions despite the temperature gradients present [7]. In our study, we propose a different concept for scale-up of the oxidation procedure, in which the electrolyte is circulating vertically in a vessel with a fixed anode, and a heat-exchanger is incorporated to remove the heat effectively. It will be demonstrated that such design allows to oxidize a large number of aluminum substrates under near isothermal conditions.

The microreactors to be developed from this study are intended for kinetic studies and optimization of the catalytic combustion of volatile organic compounds. In particular, we wish to study combustion of unsymmetrical dimethylhydrazine; a component of rocket fuel. Alumina supported copper chromite ($CuCr_2O_4$) has been selected as a catalyst because this is one of the most active and stable catalysts for complete oxidation of nitrogen containing organic compounds [8]. The direct formation of copper chromite from corresponding oxides typically proceeds above 500 °C [9]. An alumina supported copper chromite catalyst was prepared by impregnation with a copper dichromate solution followed by calcinations in air at 600 °C [10]. However, copper chromite can be formed under milder conditions (425–540 °C) upon decomposition of copper chromate ($CuCrO_4$) and copper dichromate ($Cu_2Cr_2O_7$), [11,12]. In this study, an attempt was made to obtain copper chromite coatings in the temperature range considerably below the melting point of the aluminum substrate in order to avoid its thermal deformation. The experimental procedures of catalyst preparation were studied and optimized to provide the most active and uniform catalytic coatings. The performance of catalytic coatings was studied in butane oxidation, which was chosen as a model reaction.

2. Experimental

2.1. EDM micromachining

Two types of aluminum were used: A199.5 (1050A series) and A151st (AlMgSi1 alloy, 6082 series, alloying elements Si: 1.0 wt.%, Mg: 0.9 wt.%, Cr: 0.15 wt.%, Zn: 0.1 wt.%, Mn: 0.7 wt.%, Cu: 0.1 wt.%). Microchannel fabrication tests with one machining pass were conducted using a low sparking energy by applying 80 V voltage, and a maximum current of 8 A with 1.0 μs ON and OFF time pulse durations. When a method with two machining passes is applied, a different generator code is used in the second pass: a voltage of 120 V, and a maximum current of 8 A with 0.2 μs ON and OFF time pulse durations. A copper electrode with a diameter of 250 μm coated with a zinc layer of ca. 1 μm (SW25X) was used. The plate was always connected to the positive polarity and the electrode to the negative polarity. Demineralized water (15 μS) was used as a dielectric medium. Machined microfeatures were examined using an optical microscope and a scanning electron microscope (SEM). The method with one machining pass was applied to fabricate a set of plates for optimization of anodic oxidation. The plates had a thickness of 430 μm. In each plate, 45 semi-cylindrical microchannels with a diameter of 388 μm and a distance of 500 μm between their centerlines were produced.

2.2. Anodic oxidation

In anodic oxidation experiments, the Al51st alloy was used. Two geometries of Al51st plates are studied. Flat plates of 35 mm × 20 mm with a thickness of 1 mm were oxidized to optimize the catalyst deposition techniques (A-plates). Also microstructured plates of 40 mm × 26.6 mm with a thickness of 430 μm, produced as described in Section 2.1, were oxidized to study the changes in geometry during oxidation (M-plates). The plates were first degreased in acetone at room temperature followed by boiling in xylene for 1 h. After that, the plates were dried at 300 °C in air for 1 h, cooled down and weighed. Then, the plates were immersed into a 1.0 M NaOH solution at 50 °C for 15 s. Afterwards, the plates were washed twice with distilled water and fixed in a holder in a 1.1 L electrolysis vessel. Two

platinum foils of 40 mm × 50 mm positioned at a distance of 10 cm from both sides of the aluminum plate were used as cathodes. A 25 μm alumina layer was produced on A-plates under current control conditions with an anodic current density of 15 mA/cm^2, in an aqueous 1.1 M oxalic acid solution at 7.0 °C. The electrolyte was continuously stirred by a magnetic stirrer. The apparent density of alumina was estimated to be 2.0 g/cm^3 based on a volume of the alumina layer of 0.0407 cm^3. The weight change due to oxygen incorporation of 0.0390 g corresponds to formation of 0.083 g of alumina. The metal losses due to aluminum dissolution in the electrolyte solution were negligible during oxidation of A-plates. The mass of aluminum incorporated in the alumina layer is equal to the mass decrease of aluminum. The mass of aluminum in the alumina layer was calculated based on its stoichiometry, apparent density and volume. The mass of aluminum was calculated based on a density of 2.7 cm^3/g and a thickness of the metal layer measured at a cross-section of the plate before and after oxidation. The latter was taken from SEM images. The porosity of the alumina layer was estimated to be 20%, the mean pore diameter was 40 nm, and the BET surface area was in the range 10–40 m^2/g.

Oxidation time and anodic current density were optimized with M-plates in a 0.4 M oxalic acid solution at 1.0 °C. A 10–20 μm layer of acrylic coating STAR12E (from Chemtronics®) was deposited to protect the flat side of M-plates from oxidation. After the oxidation process, this coating was removed by soaking in a high purity universal acrylic thinner solution UAT05L (from Electrolube®) at 50 °C. After the electrolysis, the plates were washed twice with distilled water, dried in air at 110 °C for 1 h, cooled and weighed.

A 20 L electrolysis vessel was constructed to produce a large set of anodized plates from the same electrolyte composition (Fig. 1). In this design, two aluminum (Al 99.5) cylindrical cathode foils were placed at a distance of 20 cm from each other. The length of the internal cathode was 75 cm and that of the external cathode was 200 cm. The height of both cathodes was 8 cm. Several geometrical parameters of the impeller were optimized to provide an effective electrolyte circulation from and to the impeller via twelve half-circle openings with a diameter of 3 cm made in the top and bottom parts of the internal cathode. Up to twelve aluminum substrates can be positioned on an aluminum ring between the cathode foils. The aluminum ring was connected to an anode. A PTFE line (carbon filled Polytetrafluorethylen, heat conductivity of 1 W m^{-1} K^{-1}, i.d. = 8 mm, o.d. = 10 mm) for the coolant was fixed at the bottom part of the vessel. The temperature of the electrolyte in the vessel was controlled by a West 6100+ regulator by changing the temperature of coolant in the range from −15 to −5 °C depending on the heat evolved in the process.

2.3. Cu–Cr oxide catalyst deposition

Anodized Al51st plates were degreased with acetone and calcined at 300 °C. The catalysts were prepared by impregnation of the anodic alumina layer by an aqueous solution of copper dichromate, followed by drying under an IR lamp for 1 h and calcination at 450 °C for 4 h. The following conditions of catalyst preparation were varied: concentration of copper dichromate solution (250 or 500 mg/ml), duration of impregnation (0.1–1 h), number of impregnation cycles (1 or 2), mode of removal of excess impregnating solution (washing or wiping). The samples are

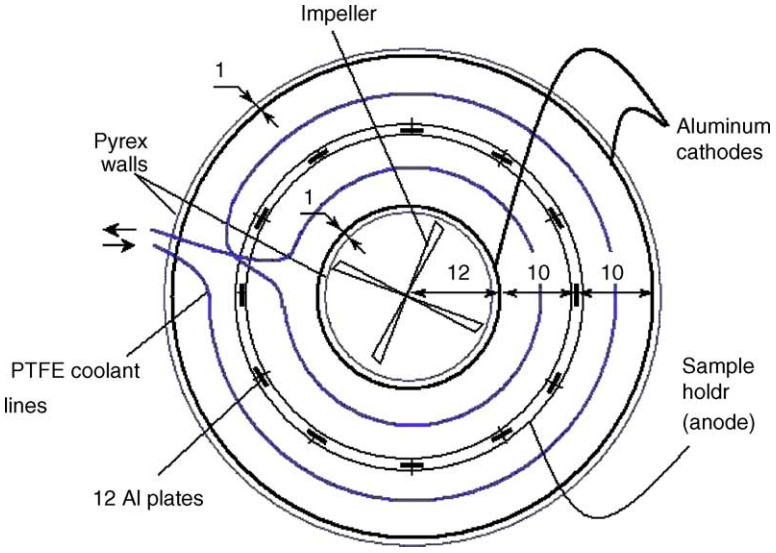

Fig. 1. Schematic view of a 20 l electrolysis vessel. Two aluminum cathode foils of 75 cm × 8 cm and 201 cm × 8 cm were placed at a distance of 20 cm from each other. Twelve half-circle openings with a diameter of 3 cm were made in the top and bottom parts of the internal cathode. A radial impeller was used with a diameter of 125 mm, with four blades,which were fixed to the axis at a distance of 40 mm from the bottom. The blade angle is 30°, and the blade height is 25 mm. The impeller speed was fixed at 160 rpm. Twelve aluminum substrates were positioned on an aluminum ring between the cathode foils. A PTFE line (i.d. = 8 mm, e.d. = 10 mm) for the coolant was fixed at the bottom part of the vessel. All sizes are given in millimetres.

referred to according to their loading with the active component and a number of impregnation cycles. Index ''A'' in the sample name stands for the flat Al plates, index ''M'' denotes the microstructured plates. Number in brackets corresponds to the $CuCr_2O_4$ loading and the Roman number stands for a number of impregnation cycles.

The reference samples of 26 wt.% $CuCr_2O_4/\gamma$-Al_2O_3 catalyst were prepared by incipient wetness impregnation of spherical γ-alumina granules (1.0–1.6 mm, the BET surface area is 193 m^2/g) with an aqueous solution of copper dichromate for 15 min. This was followed by drying under the IR lamp for 1 h and calcination in air at 400, 500 or 700 °C for 4 h to study the effect of the calcination temperature on the phase composition of copper-chromium oxide catalysts. These samples are referred as P(26)-400, P(26)-500, and P(26)-700 hereafter. The BET surface area of samples P(26)-500 and P(26)-700 is 129 and 106 m^2/g, respectively.

2.4. Catalyst characterization

The chemical composition of the samples was determined by inductively coupled plasma atomic emission spectroscopy (ICP-AES) after total dissolution of the sample in hydrochloric acid. The XRD studies were performed in a HZG-4 diffractometer using Cu Kα radiation in the 2θ range of 10–70° with a sweep rate of 1° 2θ/min. X-ray microprobe analysis was performed on a MAP-3 microanalyzer with a probe diameter of ∼1 μm at the working voltage 25 kV and a current of 30–40 nA; Al Kα, Cu Kα and Cr Kα were the analytical lines. Fragments of 5 mm × 5 mm were fixed by epoxy resin in a holder. Textural characteristics of the samples were studied by nitrogen adsorption using an ASAP-2400 instrument. Diffuse reflectance spectra (DRS) were recorded by a spectrophotometer ''Shimadzu'' UV-2501 PC in the range of 11,000–54,000 cm^{-1}. X-ray photoelectron spectra were recorded using a spectrometer VG ESCALAB HP with Al Kα radiation. The carbon 1 s signal at 284.8 eV was used as a reference to calibrate the binding energy scale. The catalytic activity of the combustion catalysts was studied in the model reaction of butane oxidation in a flow setup with a tubular quartz reactor (i.d. of 13 mm) in the temperature range of 200–450 °C. The temperature was measured by a thermocouple placed downstream of the catalyst (granules or stack of plates). The original A or M-plates were cut for smaller fragments (5 mm × 20 mm). These fragments were loaded in the reactor at the distance of ∼0.5 mm from each other. The composition of the initial reaction mixture was 0.2 vol.% butane in air. The flow rate was adjusted to fix the same space velocity of 120,000 h^{-1} with respect to the alumina volume. Butane, O_2, CO, CO_2, and CH_4 concentrations were analyzed using a ''Kristal-2000M'' GC equipped with FID and TCD detectors. A HayeSep S column (3 mm × 2 m) was used for butane separation and an activated carbon SKT column (3 mm × 2 m) was used for CO_2 separation from the gas mixture. Both columns were maintained at 165 °C. A molecular sieve NaX column (3 mm × 2 m) maintained at 20 °C was used for O_2, CO and CH_4 analysis. Neither carbon monoxide nor methane was found in the reaction products. The carbon balance was 95–105%. In some experiments, water was separated and analyzed using a Porapaq T column (3 mm × 2 m) maintained at 150 °C. The catalyst activity was characterized by the temperature dependence of the butane conversion to products of total oxidation (CO_2, H_2O).

3. Results and discussion

3.1. Fabrication of microchannels

We have chosen Al99.5 material for micromachining based on our previous experience to produce microreactors in aluminum [13–16]. However, in case of relatively long 40 mm plates, the results were quite different comparing with those for the 6.5 mm plates applied in [15] and [16]. The examination of microchannels obtained in this study and those in reference [15] revealed that the length of the workpiece has a large impact on material removal characteristics and results in different reproducibility even when the same material was used. In case of 40 mm long microchannels, application of the EDM method with one machining pass gave a relatively large standard deviation (S.D.) of the channel diameter (and the channel to channel distance) from the average values (S.D. = 1.4%), which would make the assembling of the microreactor impossible.

It is well known that Al51st material due to proper combination of alloying components, can be electro discharge machined in a more reproducible way. Indeed, the application of the same method gave a narrow channel diameter distribution of less than 0.34%. However, due to the different evaporation rate of aluminum and alloying components, a rough surface was obtained (R_a = 4.0 μm). In attempt to reduce the surface roughness, the method with two machining passes was applied. In this method, the time interval between the sparks was decreased during the second machining pass. This allowed to obtain an R_a value of 2.0 μm with further improvement of the channel diameter distribution (S.D. = 0.18%). Application of three machining passes deteriorated considerably the S.D. value, which was close to that of the Al99.5 material (S.D. = 1.2%). For the proper assembling of the reactor, a method with two machining passes had to be applied.

3.2. Anodic oxidation

Several studies have shown that anodization processes carried out at room and higher temperatures dramatically decrease the oxide formation current efficiency, leading to severe aluminum dissolution [3,17,18]. Therefore, in this study we decided to carry out the process just above the freezing point of the electrolyte. Aqueous oxalic acid

solutions become saturated above 0.6 M at 0 °C [19]. In our experiments, the oxalic acid concentration was fixed at 0.4 M. No substantial difference was observed in the oxidation behavior of the Al51st alloy machined with a method with one machining pass or with two machining passes. Therefore, the Al51st alloy produced by a method with one machining pass was used for optimization of anodic oxidation experiments.

Several experiments were carried out to investigate the effect of oxidation time on the thickness of anodic coatings (Fig. 2). The alumina layer thickness as a function of oxidation time can be described by the following function in the range between 0 and 48 h:

$$h = 0.55t + 4.6 \times 10^{-2}t^2 - 5.90 \times 10^{-4}t^3, \quad (1)$$

where t is time in hours, h is the layer thickness in microns. The plot of layer thickness versus oxidation time is a typical *S*-curve (Fig. 2). In the beginning of the process, the oxide layer thickness is proportional to the oxidation time. After 5 h the oxidation rate starts increasing. This corresponds to the beginning of the horizontal part of the voltage curve (Fig. 3a). Then, the oxidation rate decreases due to a decrease of the anodization current efficiency with respect to oxide formation. As a result, linear characteristics between layer thickness and oxidation time are again observed in the range between 23 and 30 h with a slope of 1.75 μm/h. At this stage, the oxidation rate more than three times exceeds its initial value. After 30 h, the rate of oxide formation monotonously decreases due to the increasing resistance of a growing alumina layer and as a result decreasing current efficiency with respect to oxide formation. This effect is discussed below.

The schematic view of a cross section of a microstructured plate before and after oxidation is shown in Fig. 4a and b, respectively, where Ox represents the thickness of oxide layer, H represents the initial thickness of the aluminum plate, M represents the thickness of the metal remaining beneath the oxide layer, and R represents the radius of the microchannel. A typical image of the microstructured plate after oxidation is shown in Fig. 4c. If a high anodization current efficiency with respect to oxide formation current is achieved, the ratio E calculated according to Eq. (2) is greater than unity, due to the lower overall density of the porous oxide film compared to the aluminum substrate [19].

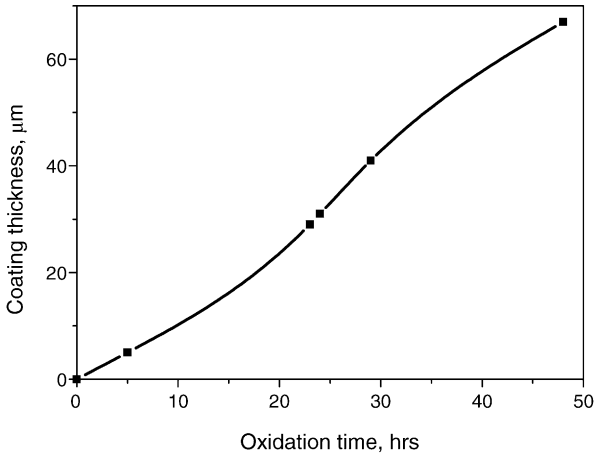

Fig. 2. The thickness of the alumina layer as a function of oxidation time on Al51st. A 0.4 M aqueous solution of oxalic acid was used as electrolyte. Anodic current density: 5 mA/cm^2. Temperature 1.0 ± 0.1 °C. Voltage curve is shown in Fig. 3a.

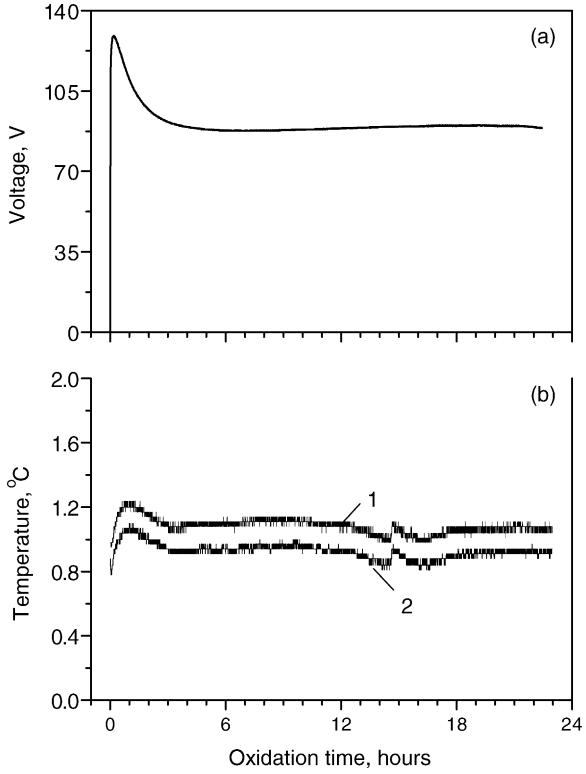

Fig. 3. (a) Voltage and (b) temperature at the top (1) and bottom (2) parts of the electrolyte solution as a function of time. The conditions are the same as those in Fig. 2.

$$E = \frac{\mathrm{Ox}}{M(0) - M} \quad (2)$$

In Eq. (2), Ox is the thickness of oxide layer, $M(0)$ is the initial thickness of the aluminum plate, M is the thickness of the metal remaining beneath the oxide layer. Achieving a high anodization current efficiency is important to avoid possible significant decreases in reactor feature size due to excessive aluminum dissolution. In addition, a high anodization current efficiency promotes the conservation of aluminum metal in the "core" beneath the oxide layer, which allows for improved heat transfer throughout the reactor [19]. The results of anodic oxidation taken at different oxidation times are listed in Table 1. One may see that during a time interval between 23 and 30 h, corresponding to the second linear part of the oxidation rate plot (Fig. 2), the oxidation efficiency remains virtually

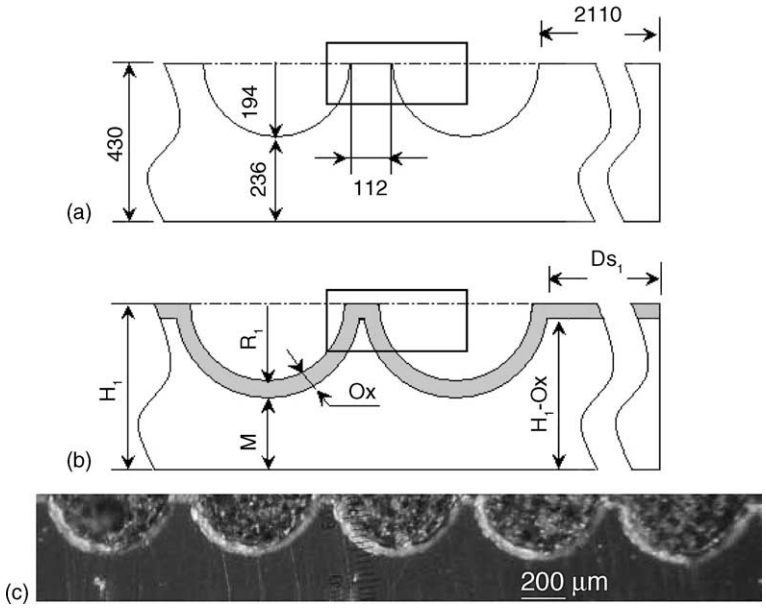

Fig. 4. Schematic view of a cross section of a microstructured plate: (a) before oxidation; (b) after oxidation; and (c) photo of a single plate after oxidation. All sizes are given in microns. Ox represents the thickness of oxide layer, H_1 represents the thickness of the aluminum plate, M represents the thickness of the metal remaining beneath the oxide layer, R_1 represents the radius of the microchannel, and Ds_1 represents the distance between the last channel and the edge of the plate. The area inside the frames is shown in Fig. 11 under a larger magnification.

constant, but decreases considerably when the thickness of the alumina layer exceeds 30 μm.

In the course of oxidation, copper from the Al51st alloy dissolves in the electrolyte and is reduced at the platinum cathodes because its standard reduction potential $E^0_{Cu^{2+}/Cu} = 0.34$ V) is higher than that for protons (0 V). Other elements from the alloy have standard reduction potentials below 0 V, and they cannot be reduced because their concentrations in the solution are far below the concentration of protons (0.4 M). If we assume that all copper from the alloy is dissolved in the electrolyte, we can compare the mass of copper deposited at the cathodes with the mass of copper present in the dissolved volume of the alloy. The Al51st alloy has a density of 2.71 g/cm^3 and contains 0.1 wt.% Cu. The volume of alloy dissolved is calculated based on the data of Table 1 according to the method described in Appendix A. The decrease in the metal volume after oxidation for 23 h gives a value of 0.0396 cm^3 per plate. Eight oxidation runs were carried out for 23 h to provide a higher precision. The total mass of copper, which would be dissolved is

$$m_{Cu} = 8 \times 0.039\,\text{cm}^3 \times 2.71\,\text{g/cm}^3 \times 0.001 = 8.6 \times 10^{-4}\,\text{g} \quad (3)$$

The mass of copper deposited at the cathodes was 3.8×10^{-3} g after eight oxidation runs. The concentration of Cu in the electrolyte solution of 1.1 L was below 10^{-6} M, so the mass of copper in the solution can be neglected in the calculations. The comparison of expected copper mass with the experimental observation clearly demonstrates that the substrate material in the vicinity of microchannels is more than four times enriched by copper after the EDM process comparing to the bulk substrate. However, copper enrichment can be considerably higher, because only the outermost 5 μm of the 29 μm layer create a large resistance to the current, and as a result a voltage maximum is observed in the beginning of the anodic oxidation (Fig. 3a). One may see from Fig. 3b that the heat is effectively removed from the vessel, so the maximum is related to a non-uniform chemical composition of the plates, but not to the differences in the electrolyte temperature.

The metal dissolution rate is higher at the beginning of the oxidation, as one can see from a lower value of the anodization current efficiency after 5 h (Table 1). This can also be explained by a higher concentration of copper and

Table 1
Geometry changes of A151st plates after anodic oxidation at different time intervals and corresponding oxidation efficiency

Oxidation time (h)	L (μm)	R (μm)	M (μm)	H (μm)	E
0	–	194	236	430	–
5	5	199	231	435	1.00
23	29	208	211	448	1.16
24	31	207	209	447	1.15
29	41	204	200	445	1.14
48	67	200	171	438	1.03

E is the oxidation efficiency, $E = \text{Ox}/(M\ (0) - M)$, $M(0)$ is the initial thickness of the aluminum plate, Ox is the thickness of oxide layer, R is the radius of the microchannel, M is the thickness of the metal remaining beneath the oxide layer, H is the overall thickness of the aluminum plate. Oxidation temperature: 1 °C, oxalic acid concentration: 0.4 M, anodic current density: 5 mA/cm^2.

probably other alloying elements in the outermost metal layer. These elements cannot be incorporated into the oxide layer, therefore they are dissolved in the solution, decreasing the overall efficiency of the process. It has to be noted that an intensive gas evolution was observed in the first few hours of the process demonstrating that a part of the current is consumed in the side processes (4) and (5), decreasing overall efficiency:

$$C_2O_4^{2-} \rightarrow 2\,CO_2 + 2e \quad (4)$$

$$H_2O \rightarrow O_2 + 2H^+ + 2e \quad (5)$$

There are three factors, which are responsible for high copper content in the outermost layer. First, copper from the electrode, might be deposited on the microchannels in the EDM process. Secondly, high energy applied during the first machining pass can create a local temperature hot spot at the outer surface of the alloy. This allows migration of the alloying elements from the bulk to the surface. Finally, a gray residue of ca. 1 μm in thickness, present on the surface of the microchannels after a sodium hydroxide-based etch, seems also to create a resistance to the oxidation process. This residue consists of particles of oxide, intermetallics, silicon and copper, which are insoluble in the alkaline solution, but still are quite strongly fixed to the surface.

Under appropriate conditions on properly prepared substrates, an array of nanometer-scale pores can be formed. An average roughness of the alumina surface was 2 μm. SEM at larger magnification revealed the presence of pores with a diameter close to 40 nm (Fig. 5). This data agrees with the observations of others who have attempted to tune pore diameter by adjusting the anodization current density [3,17,18]. Pore size distribution data (not shown) confirmed the presence of the pores with diameter ca. 40 nm. X-ray diffraction analysis of anodized plates (not shown) showed intense peaks of aluminum substrate at 38.5 and 44.8° 2θ. (International Center for Diffraction Data, ICDD 04-0787). No bands related to alumina were found.

3.3. Development of procedure for catalyst deposition

The typical conditions of the catalyst preparation and results of the analysis of Cu–Cr-oxide catalysts are listed in Table 2. The formed copper chromite with spinel structure is dissolved in γ-alumina with a similar structure during calcination of reference samples P(26)-400, P(26)-500, and P(26)-700. In the whole temperature range studied, five peaks are observed in the XRD spectra of reference samples at 29.60, 31.10, 35.19, 37.72, and 42.35° 2θ (not shown). This confirms the formation of a spinel structure (Cu, Cr)$[Cr,Al]_2O_4$ (ICDD 34-0424) with particle size less than 5 nm.

The concentration of copper dichromate solution, duration of impregnation, and number of impregnation cycles were varied and different aftertreatments, viz. washing or removal of impregnating solution by vacuum cleaning or by wiping, were applied in the experiments with A-plates. Washing removed most of Cu and Cr from the support. The mode of removal of excess impregnating solution (wiping or vacuum cleaning) has no influence on the catalyst loadings, but when this operation was omitted (sample A(5.3)-I), the active metals loading in the coatings was higher. Duration of impregnation has no effect on the chemical composition, due to weak chemisorption of copper and chromium from the solution. The absence of chemisorption was proved in an experiment with sample A(0.1)-I. An impregnation time of 17 h, followed by a 5 min washing step, led to trace amounts of copper and chromium

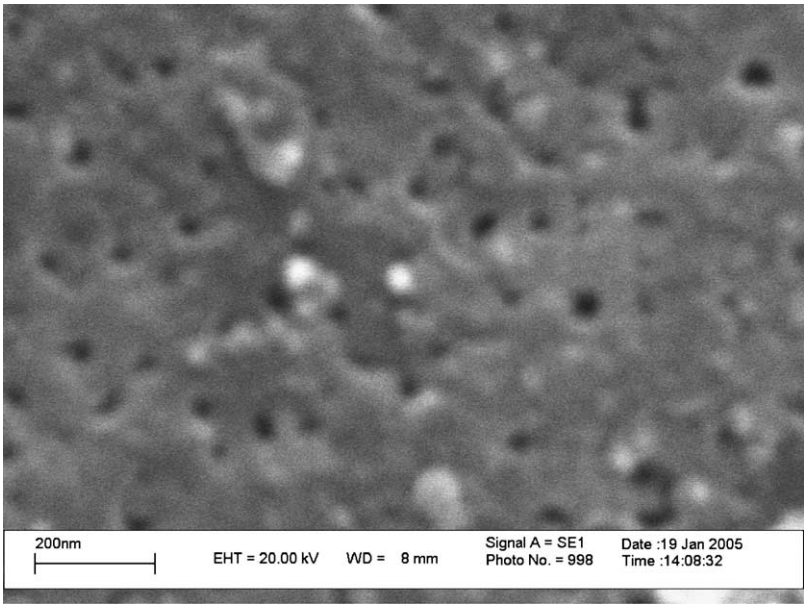

Fig. 5. SEM image of alumina coating on A-plate.

Table 2
Condition of preparation and results of chemical analysis for the supported Cu–Cr-oxide catalysts.

Sample	Concentration of $CuCr_2O_7$ solution (mg/ml)	Impregnation time (h)	After-treatments		Loading[a] wt. %, to mass of Al_2O_3		$CuCr_2O_4$ loading[b] wt.%	Color
			Washing with water[c]	Wiping off the residues of solution	Cu	Cr		
P(26)-500	500	0.25	–	n/a	7.9 ± 0.3	11.2 ± 0.3	26	Black
P(26)-700	500	0.25	–	n/a	7.9 ± 0.3	11.2 ± 0.3	26	Black
A(0.1)-I	250	17	+	+	<0.03	<0.05	<0.1	White
A(0.4)-I	250	0.25	Rinsing	+	0.08 ± 0.05	0.21 ± 0.05	0.4	Yellow
A(2.6)-I	250	0.25	–	+	0.8 ± 0.2	1.1 ± 0.2	2.6	Yellow
A(3.7)-I	500	0.25	–	+	1.1+0.2	1.6 ± 0.2	3.7	Black
A(5.3)-I	500	1.0	–	–	1.6 ± 0.2	2.1 ± 0.2	5.3	Black
A(3.5)-II	250	0.25[d]	–	+	0.8 ± 0.2	1.9 ± 0.2	3.5	Yellow
M(3.7)-I	250	0.25	–	+	1.2 ± 0.2	1.4 ± 0.2	3.7	Gray
M(5.3)-II	250	0.25[d]	–	+	1.6 ± 0.2	2.1 ± 0.2	5.3	Gray

[a] The mass of the alumina layer is 3.8 wt.% of the mass of A samples. The mass of the alumina layer is 9.3 wt.% of the mass of M samples for the coating thickness of 29 μm. In the latter case, volume of a single plate after oxidation, obtained according to the procedure described in Appendix A, is 0.312 cm. Volume of the alumina layer is 0.043 cm^3. Density of the Al51st is 2.7 g/cm^3. Apparent density of the alumina layer is 2.0 g/cm^3.
[b] Calculated with apparent density of the alumina layer of 2.0 g/cm^3.
[c] The sample was kept in water for 1 h.
[d] The sample was dried and calcined after first impregnation.

in the coatings. Therefore, the duration of impregnation was fixed at 0.25 h in further experiments. On the contrary, the concentration of the impregnating solution has a large influence on the chemical composition. The coatings A(0.4)-I, A(2.6)-I prepared with a diluted solution were yellow, while coating A(3.7)-I, prepared from a concentrated solution, was black. The $CuCr_2O_4$ loading was higher in the latter case. Nearly the same loading was achieved after two consecutive impregnations with the diluted solution in sample A(3.5)-II. The color of the plate remains yellow in this case. Thus, the samples with the loadings of Cu up to 1.6 wt.% and Cr up to 2.1 wt.%, based on an apparent density of alumina of 2.0 g/cm^3 (see Section 2.2), were obtained by changing the impregnation conditions.

Element distribution in the coatings was studied by X-ray microanalysis. Fig. 6a and b show similar behavior of the lines of different elements both along the plate and at its cross section. In Fig. 6a, the intensity of Cu Kα follows that of Cr Kα and, in most locations, that of Al Kα indicating interaction of Cr and Cu with each other and with alumina. In Fig. 6b, the maxima of Cu Kα and Cr Kα at the both sides of the plate correspond to the position of alumina layers, while an Al Kα plateau corresponds to a metal layer.

Oxidation states of Cu and Cr were studied by diffuse reflectance spectra (Fig. 7a). DRS of pelletted reference catalysts P(26)-500 and P(26)-700 were also recorded for comparison (Fig. 7b). The spectra of black samples A(3.7)-I and A(5.3)-I (the latter is not shown) have low frequency bands revealed as shoulders at ca 12,500 cm^{-1} corresponding to d–d transitions in Cu^{2+} ion [20], and two bands at higher frequencies of 16,000 and 19,500 cm^{-1} attributed to d-d transitions in Cr^{3+} [20–22], in agreement with DRS of

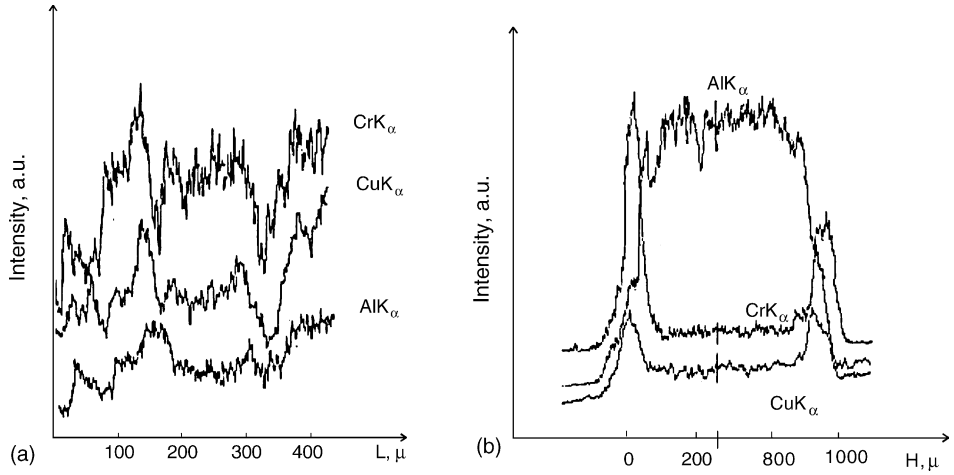

Fig. 6. X-ray microprobe analysis. Intensity of Kα Cr, Kα Cu and Kα Al lines for the sample A(3.5)-II: (a) along the plate and (b) across the plate.

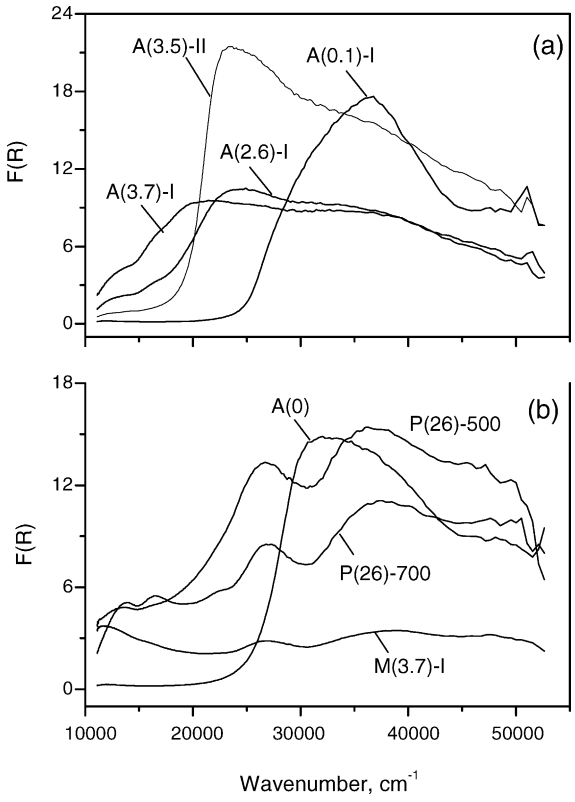

Fig. 7. (a) Diffuse reflectance spectra of catalysts supported on A-plates and (b) diffuse reflectance spectra of samples M(3.7)-I; reference samples P(26)-500, P(26)-700 Sample A(0) represents the blank experiment with a plate without active metals.

the reference samples. Spectrum of A(0.1)-I is close to that of the alumina support, due to a low $CuCr_2O_4$ loading. The spectra of samples A(2.6)-I and A(3.5)-II reveal the presence of an intense wide band near 25,000 cm^{-1}, which may be formed by superposition of two bands at 23,500 and 27,000 cm^{-1}. The position of these bands and their higher intensity with respect to lower energy bands allow the assumption that they are due to charge transfer (CT) transitions in Cr in higher oxidation states: Cr (VI) in CrO_4^{2-} or CrO_3^{-} type compounds [21,22]. This band is very strong, and it is characteristic of fresh catalysts calcined in air. Such catalysts usually contain an admixture of Cr(VI) [21,22], which is responsible for their high initial catalytic activity. Indeed, the intensity of the band at 26,800 cm^{-1} decreases in DRS of P(26)-700 due to partial reduction of Cr(VI) to Cr(III) at high temperature revealing more clearly the bands at 16,500 and 22,500 cm^{-1}.

XPS data listed in Table 3, show that the main signal of copper in all Cu–Cr oxide catalysts studied is $Cu2p_{3/2}$ with almost constant BE = 932.9–933.1 eV. This peak may be assigned to Cu^{2+} ions in the solid solution of $CuCr_2O_4$ [23]. Line deconvolution shows that there are also noticeable admixtures of surface copper carbonate, characterized by the BE ca. 935 eV. This is also confirmed by the BE values of C1s signal for CO_3^{2-} at 290 eV. Some minor amounts of Cu^{+} ions with BE ca. 932 eV are also present in the samples. The

Table 3
Results of XPS study of samples of Cu–Cr oxide catalysts on flat aluminum plates

Sample	Binding energy (eV)					
	Al2s	O1s	C1s	C1s(CO_3)	$Cr2p_{3/2}$	$Cu2p_{3/2}$
A(5.3)-I	119.0	531.0	284.8	289.8	576.7	932.9 935.0
A(0.4)-I	119.2	531.2	284.8	290.0	577.3	933.1
A(3.5)-II	118.9	531.0	284.8	289.7	577.0	932.6 934.9

predominance of Cu^{2+} is supported by the presence of Cu^{2+} ''shake-up'' satellites having maxima in the BE range 933–934 eV for all samples [24,25].

It can be seen, that chromium is present mainly as Cr^{3+} ions, characterized by $Cr2p_{3/2}$ BE values in the vicinity of 577 eV, which, similarly to Cu^{2+} above, may be assigned to $CuCr_2O_4$ [23,24,26]. Line deconvolution and comparison with the reference spectra of Cr_2O_3 obtained in the same spectrometer show that minor amounts of chromium in higher oxidation states (up to +6) may be present in the catalysts. Their overall contribution is lowest for the black sample A(5.3)-I, and higher for yellow samples A(0.4)-I and A(3.5)-II in agreement with the conclusions of the DRS studies of the catalysts.

Catalytic activity of the samples in complete oxidation of butane is presented in Fig. 8. Obviously, sample A(0.4)-I with the lowest $CuCr_2O_4$ loading has the lowest butane conversion. Increasing the $CuCr_2O_4$ loading gives a rise in catalytic activity. However, despite the highest loading of an active component, sample A(5.3)-I has still low activity. This seems to be due to an omitted after-treatment step in which the residues of the impregnating solution were not removed before calcination. These residues could partly block the alumina pores leading to a decrease in activity. It is interesting to note that A(3.5)-II has twice the activity of A(3.7)-I which contains the similar amount of active component. The reason may be due to the presence of chromium in higher oxidation states as shown by DRS and XPS studies. Actually, the activity tests for 40 h showed that the activity of A(3.5)-II is not stable: the butane conversion was lower in the whole range of temperatures studied for the used A(3.5)-II sample. The intensity of the band assigned to Cr in high oxidation states was also decreased in the used A(3.5)-II sample.

3.4. Preparation and characterization of copper chromite catalysts on the microstructured plates

The procedure developed on flat alumina substrate was applied to impregnate the microstructured plates. A diluted copper dichromate solution with a concentration of 250 mg/ml was used for impregnation. Impregnation time was fixed at 0.25 h, calcination for 4 h at 450 °C (see Table 2). The effect of the number of impregnation cycles (1 or 2) was studied.

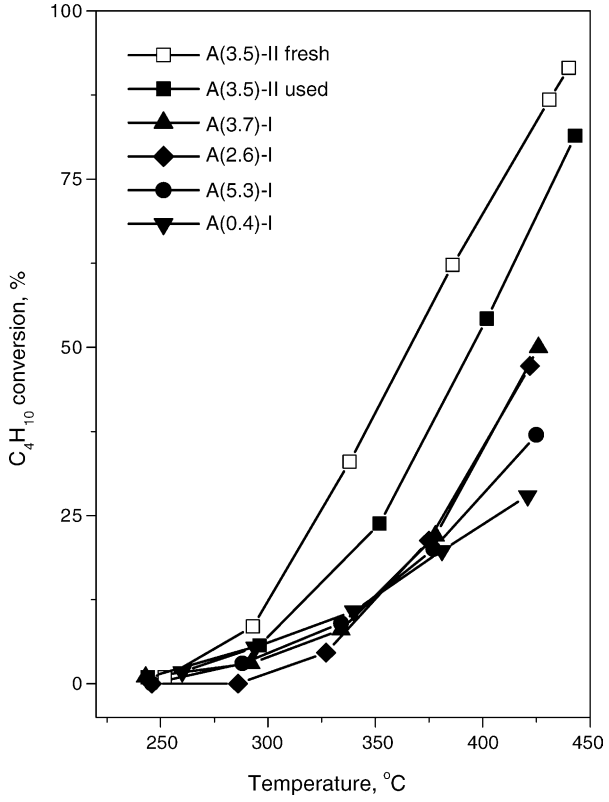

Fig. 8. Butane conversion as a function of temperature on A-plate supported catalysts. Reaction mixture: 0.2% butane in air. Flow velocity is 60 cm^3/min (STP); GHSV = 120,000 h^{-1}.

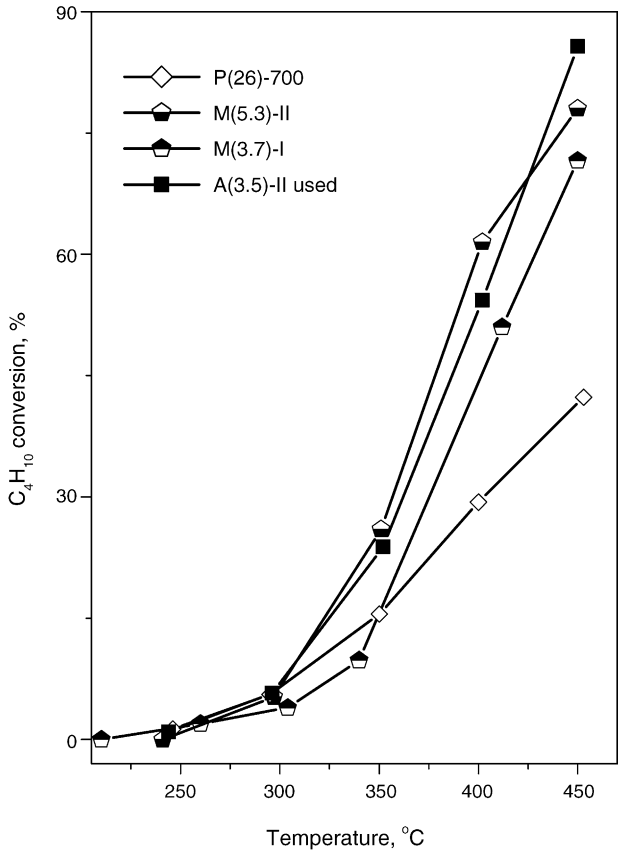

Fig. 9. Butane conversion as a function of temperature on M-plate supported catalysts. Samples A(3.5)-II(used) and P(26)-700 are given for comparison. Reaction conditions are the same as those in Fig. 8.

In contrast to the catalysts supported on A-plates, both samples supported on M-plates had a grey color. SEM images of M-plate supported catalysts revealed that the pores were not blocked after calcination, demonstrating applicability of the developed technique for preparation Cu–Cr oxide catalysts. X-ray diffraction study (not shown) of the M-plate supported catalysts showed two intense peaks of aluminum substrate (occurring at 38.5 and 44.7° 2θ, ICDD 04-0787) and four peaks occurring at 24.51, 33.63, 36.23, and 41.52° 2θ, which can be assigned to the α-Cr_2O_3 phase (ICDD 38-1479) present in trace amounts. A weak broad band was observed in the range of 28–34° 2θ. This band may be assigned to microcrystalline or X-ray amorphous alumina.

In contrast to sample A(2.6)-I, a very weak band at ca. −25,000 cm^{-1} was observed in the DRS spectrum of sample M(3.7)-I prepared under similar conditions (see Fig. 7). The intensity of this band demonstrates the decrease of the Cr content, present in high oxidation states in catalysts prepared on M-plates. This effect can be explained by the differences in structural features and composition of anodic alumina produced on A- and M-plates, due to different distribution of alloying elements in M-plates after the EDM process. The alumina on A-plates seems to stabilize admixtures of Cr in high oxidation states while alumina on M-plates stabilizes Cr^{3+} ions.

Fig. 9 demonstrates that Cu–Cr oxide catalysts prepared on M-plates have activities close to that of used A(3.5)-II sample. The activity of M-samples was higher than that of the reference pelletized catalyst P(26)-700. To quantitatively evaluate the advantages of the catalytic coatings, it is necessary to evaluate the influence of internal diffusion on the reaction rate. The Weisz modulus allows for the estimation of intra-particle diffusion limitations:

$$\psi = \eta\varphi^2, \tag{6}$$

where η is the effectiveness factor, φ is the Thiele modulus.

For a spherical particle:

$$\varphi_p = \frac{r_p}{3}\sqrt{\frac{R_{rxn}}{D_e C_s}} \tag{7}$$

where R_{rxn} is the effective reaction rate, mol m^{-3} s^{-1}; D_e is the effective diffusivity of limiting reactant (butane) in the catalyst pores, m^2 s^{-1}; r_p is the catalyst particle radius, m; and C_s is the concentration of limiting reactant at the catalyst surface, mol m^{-3}.

For the coatings

$$\varphi_c = \mathrm{Ox}\sqrt{\frac{R_{rxn}}{D_e C_s}} \tag{8}$$

If we assume $\eta \cong 1$, the Weisz modulus equations for a spherical particle (ψ_p) and the coating (ψ_c) can be written as follows:

$$\psi_p = \frac{R_{rxn} r_p^2}{9 D_e C_s} \quad (9)$$

$$\psi_c = \frac{R_{rxn} \mathrm{Ox}^2}{D_e C_s} \quad (10)$$

The Weisz modulus below 0.1 ($\psi < 0.1$) indicates that the catalyst layer (particle) is small enough to prevent concentration gradients from forming internally. The Weisz modulus for P(26)-700 is calculated based on the reaction rate value obtained in [27]. In an excess of oxygen, the reaction has the first order with respect to butane and the zero order with respect to oxygen. The reaction rate at 300 °C is equal to 0.115 mol m^{-3} s^{-1} and the activation energy is 75 kJ/mol. The effective diffusivity of butane at 300 and 400 °C is 4.8×10^{-6} and 6.1×10^{-6} m^2 s^{-1}, respectively. These values are obtained using a bed void fraction of 0.5, and particle tortuosity of 3. The reaction rate on the M(5.3)-II coating is calculated using the differential reactor approximation (at conversions below 10%). The reaction rate at 300 °C is equal to 0.170 mol m^{-3} s^{-1}, which is 1.5 times higher than that of P(26)-700. Similar value is obtained for used A(3.5)-II. The activation energy is 81 ± 2 kJ/mol, which is close to the value obtained on P(26)-700. A void fraction of 0.2 (based on the BET data), and layer tortuosity of 1.0 (due to the cylindrical geometry of the pores) were used to calculate the effective diffusivity of butane in the coatings. The Weisz modulus values for P(26)-700 and M(5.3)-II are listed in Table 4. Internal diffusion limitations are observed for P(26)-700 above 370 °C. There is an increasing difference between the catalytic activity of coatings and P(26)-700 in the high temperature range due to the presence of internal diffusion limitations in the latter case. The effectiveness factor for P(26)-700 at 400 °C is ca. 0.8, while the reaction on the coatings is under kinetic control in the whole temperature range studied. This clearly demonstrates the advantages of using catalytic coatings rather than pelletized catalysts.

The Cu–Cr oxide catalysts prepared on M-plates have also a high stability. Fig. 10 demonstrates the activity in butane oxidation for sample M(5.3)-II at 350 °C. One can see that activity stays at the same level for time on stream for at least 40 h.

Table 4
Comparison of the reaction rate and the Weisz modulus for P(26)-700 and M(5.3)-II

Temperature (°C)	P(26)-700		M(5.3)-II	
	R_{rxn} (mol/m^3 s)	ψ_p	R_{rxn} (mol/m^3 s)	ψ_c
300	0.115	0.029	0.170	6.5×10^{-4}
400	1.18	0.322	1.60	0.0083

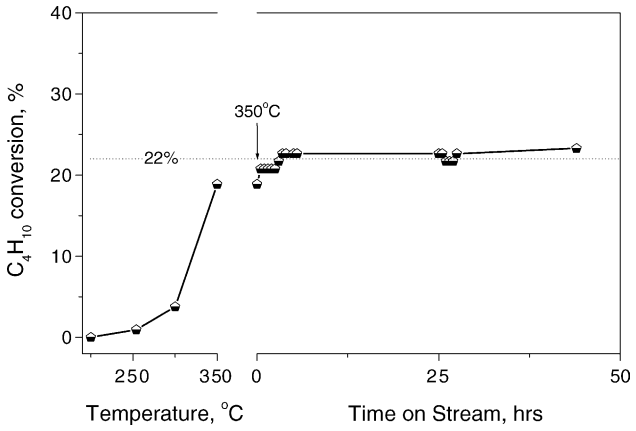

Fig. 10. Butane conversion vs. time on stream for catalyst M (5.3)-II. Temperature: 350 °C. The other conditions are the same as those in Fig. 8.

4. Conclusions

The effect of different electro discharge machining techniques on the geometrical parameters of the micro-structured plates produced in two different aluminum alloys has been studied. Al99.5 material can be applied as a substrate material for machining microchannels with a length to diameter ratio below 50. An alloy with relatively high content of alloying elements (Al51st) should be used in case of microchannels with a high length to diameter ratio of 100. The method with two machining passes has to be applied to decrease the surface roughness of microchannels produced in Al51st to ca. 2.0 μm. A procedure of anodic oxidation of the Al51st alloy has been optimized to produce an oxide layer of 30 μm thickness in a 0.4 M oxalic acid solution under current control conditions. The electrolysis time was optimized to get a maximum anodization current efficiency with respect to oxide formation. The temperature of electrolyte was fixed at 1 °C to avoid extensive dissolution of substrate material. A novel design of the electrolysis cell was proposed and validated to provide a simultaneous oxidation of 12 identical substrates. In this design, the maximum temperature non-uniformity does not exceed 0.2 °C, providing a uniform thickness and uniform pore size distribution. Alumina coatings with an average pore diameter of 40 nm are produced.

The synthesis of copper chromite coatings was performed by impregnation of the alumina coating with an aqueous solution of copper dichromate followed by drying and calcination. The preparation method used provides a uniform metal distribution along the plates. DRS and XPS studies revealed the predominant formation of Cu^{2+} and Cr^{3+} ions with binding energies close to those found in $CuCr_2O_4$. An admixture of chromium in higher oxidation states may be responsible for a higher initial activity of the catalysts in the total oxidation of n-butane. In the course of the reaction, the reduction of high-valent chromium species takes place, which reduces the catalytic activity of these samples by 20–25%. The coatings with only trace amounts

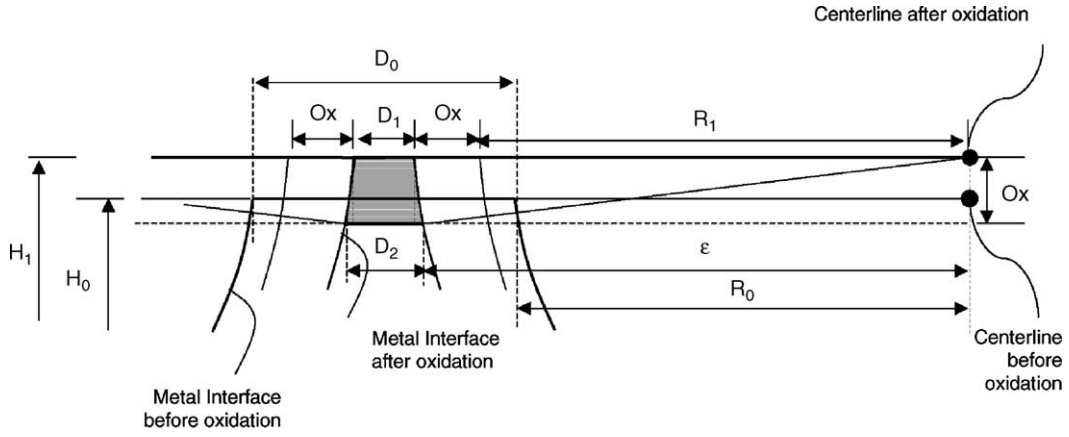

Fig. 11. Schematic view of a part of M-plate with two adjacent microchannels and a metal space in between. The metal–gas interface before oxidation and metal–oxide interface after oxidation are drawn in bold line. The situation before and after oxidation is sketched individually in a height-shifted manner in Fig. 4a and b. The parameter names are the same as those given in Fig. 4. Subindex "0" denotes the initial values of the parameters. Subindex "1" denotes those after oxidation.

of chromium in higher oxidation states demonstrated high and stable activity from the beginning. Even at much lower loadings of active metals, the catalytic activity of the prepared coatings, related to the volume of the alumina layer, is superior to that of pelletized catalysts. Microreactors made according to these procedures can be used for a variety of small-scale total oxidation processes involving combustion of toxic and hazardous chemicals.

Acknowledgements

The financial support by the Netherlands Organization for Scientific Research (NWO) and Russian Foundation for Basic Research (RFBR), project 047.15.007 is gratefully acknowledged. We are grateful for assistance in catalyst characterization to Dr. V.A. Ushakov (XRD), Dr. I.A. Ovsyannikova (X-ray microprobe), Dr. A.I. Boronin and Dr. S.V. Koshcheev (XPS), Dr. T.V. Larina (DRS), Dr. N.A. Rudina (SEM), and Mr. V.V. Kuznetsov (long-term activity tests). Special thanks to Prof. Z.R. Ismagilov for fruitful discussions.

Appendix A. Change of metal volume after oxidation

Fig. 11 demonstrates a part of the channel with a metal part in between. The initial metal volume is

$$V_0 = \left[(N(2R_0 + D_0) - D_0 + 2Ds_0)H_0 - \frac{N\pi R_0^2}{2}\right]L \quad (11)$$

The volume after oxidation is

$$V_1 = \left[(N(2(R_1 + \mathrm{Ox}) + D_1) - D_1 + 2Ds_1)H_1 - \frac{N\pi(R_1 + \mathrm{Ox})^2}{2} - (N-1)S_1 - 2S_2\right]L \quad (12)$$

Subscript "0" denotes the initial values of the parameters. Subscript "1" denotes those after oxidation. S_1 is the area of the gray trapezoid (see Fig. 11),

$$S_1 = \mathrm{Ox}\frac{D_1 + D_2}{2} \quad (13)$$

where

$$D_1 = D_0 - 2\delta \quad (14)$$

$$\delta = R_1 + \mathrm{Ox} - R_0 \quad (15)$$

$$D_2 = D_1 + 2(R_1 + \mathrm{Ox} - \varepsilon) \quad (16)$$

$$\varepsilon = \sqrt{(R_1 + \mathrm{Ox})^2 - \mathrm{Ox}^2} \quad (17)$$

Inserting the expressions for D_1 and D_2 into (13), one arrives at

$$S_1 = \mathrm{Ox}(D_0 + 2R_0 - R_1 - \mathrm{Ox} - \sqrt{(R_1 + \mathrm{Ox})^2 - \mathrm{Ox}^2}) \quad (18)$$

Area S_2 represents the oxide layer on a flat part of M-plates (between the edge and the first channel and between the last channel and the edge). This area can be approximated by the area of the rectangle:

$$S_2 \cong \mathrm{Ox}\, Ds_1 \quad (19)$$

where

$$Ds_1 = Ds_0 - \delta \quad (20)$$

Initial values of parameters are given in Fig. 4a. Values after oxidation for 23 h are given in Table 1.

References

[1] S. Ihm, E. Ruckenstein, Ind. Eng. Chem. Prod. Design Dev. 17 (1978) 110.

[2] G. Patermarakis, C. Pavlidou, J. Catal. 147 (1994) 140.
[3] G. Patermarakis, N. Nicolopoulos, J. Catal. 187 (1999) 311.
[4] J.C. Ganley, K.L. Riechman, E.G. Seebauer, R.I. Masel, J. Catal. 227 (2004) 26–32.
[5] A. Hitoshi, Method for processing anodic oxidation film different in thickness in front and back, Patent JP2001271199 (2001).
[6] G. Wiessmeier, D. Haönicke, J. Micromechan. Microeng. 6 (1996) 285.
[7] K. Toshihiro, K. Shinpei, Apparatus for anodic oxidation-treatment to aluminum or aluminum alloy, Patent JP2004211116 (2004).
[8] Z.R. Ismagilov, M.A. Kerzhentsev, Catal. Rev. Sci. Eng. 32 (1990) 51.
[9] H. Charcosset, P. Turlier, G. Trambouze, J. Chim. Phys. Phys. Chim. Biol. 61 (1964) 1249.
[10] L.V. Feshchenko, V.L. Vlasenko, V.L. Chernobrivets, Khim. Tekhnol. 4 (1982) 12.
[11] R.V. Chesnokova, A.M. Alekseev, A.A. Bondareva, Zh. Neorg. Khim. 12 (1976) 36.
[12] O.V.Korotkikh, Ph.D. thesis, Boreskov Institute of Catalysis, Novosibirsk, Russia, 1995.
[13] E.V. Rebrov, M.H.J.M. de Croon, J.C. Schouten, Catal. Today 69 (2001) 183.
[14] J.C. Schouten, E.V. Rebrov, M.H.J.M. de Croon, Chimia 56 (2002) 627.
[15] E.V. Rebrov, S.A. Duinkerke, M.H.J.M. de Croon, J.C. Schouten, Chem. Eng. J. 93 (2003) 201.
[16] E.V. Rebrov, M.H.J.M. de Croon, J.C. Schouten, Chem. Eng. Res. Des. 81A (2003) 744.
[17] V. Parkhutik, V. Shershulsky, J. Phys. D: Appl. Phys. 25 (1992) 1258.
[18] G. Patermarakis, K. Moussoutzanis, Corrosion Sci. 43 (2001) 1433.
[19] J.C. Ganley, K.L. Riechmann, E.G. Seebauer, R.I. Masel, J. Catal. 227 (2004) 26.
[20] G.L. Castiglioni, A. Vaccari, G. Fierro, M. Inversi, M. Lo Jacono, G. Minelli, I. Pettiti, P. Porta, M. Gazzano, Appl. Catal. A 123 (1995) 123.
[21] B.M. Weckhuysen, A.A. Verberckmoes, A.R. De Baets, R.A. Schoonheydt, J. Catal. 166 (1997) 160.
[22] D.A. Arendarskii, E.A. Paukshtis, Z.R. Ismagilov, E.N. Yurchenko, React. Kinet. Catal. Lett. 28 (1985) 195.
[23] NIST XPS v. Database 3.4, www.nist.gov/srd/online.htm.
[24] D.A. Arendarskii, A.V. Pashis, A. Shepelin, Z.R. Ismagilov, React. Kinet. Catal. Lett. 28 (1985) 211.
[25] D.C. Frost, A. Ishitam, C.A. McDowekk, Mol. Phys. 24 (1972) 861.
[26] C.A. Best, R.G. Squitres, R.A. Walton, J. Catal. 57 (1977) 292.
[27] Z.R. Ismagilov, O.Yu. Podyacheva, M.A. Kerzhentsev, V.N. Bibin, A. Ermakova, G.K. Chermashentseva, Kinetika i Kataliz 29 (1988) 254 (in Russian).

DEVELOPMENT AND OPTIMIZATION OF TOTAL OXIDATION CATALYSTS FOR MICROSTRUCTURED REACTORS

E.V. Matus[1], L.T. Tsikoza[1], I.Z. Ismagilov[1], E.M. Michurin[1], V.V. Kuznetsov[1], E.V. Rebrov[2], R.P. Ekatpure[2], M.A. Kerzhentsev[1]

[1]Boreskov Institute of Catalysis SB RAS, pr. Akademika Lavrentieva, 5, Novosibirsk, 630090, Russia

[2]Eindhoven University of Technology, P.O. Box 513, 5600 MB Eindhoven, The Netherlands

E-mail: matus@catalysis.nsk.su

Microstructured reactor (microreactor) technology creates opportunities for the development of miniature chemical devices, in which several unit operations are integrated. The microreactors are usually made of microstructured solid materials (stainless steel, aluminum and others). They have the reaction channels with diameters of the order of 50–500 μm, the length of about 1-10 cm, and have an inherently large surface-to-volume ratio (10000–50000 m^2/m^3). These properties offer clear advantages such as high mass and heat transfer rates, which are beneficial for attaining the required selectivities and conversions, and enable optimum control of temperature and residence time. Microreactors also have a low hold-up, resulting in an excellent controllability, small safety risks, and low environmental impact. This makes the microreactors specifically suitable for highly exothermic reactions, short contact time reactions, and for the on-demand and safe production of toxic and hazardous chemicals [1,2].

The main goal of this work was development and optimization of preparation methods for active and stable catalysts of total hydrocarbons oxidation in a microreactor. The microstructured plates were made by the spark erosion technique from AlMgSiCu-alloy (94% Al) because of its high thermal conductivity, suitable thermal stability and mechanical properties [3]. The porous Al_2O_3 support for catalyst was produced by anodic oxidation of the AlMgSiCu-alloy in 3.5 wt.% oxalic acid solution at 1-2^oC. The thickness of porous Al_2O_3 layer is close to 30 μm [3]. The Cu-Cr oxide and Pt-systems were chosen as suitable catalytic coatings on microstructured plates for total oxidation reactions. Preliminary experiments with granulated catalysts and flat Al_2O_3/Al plates also were carried out.

The synthesis of Cu-Cr oxide coatings was done by impregnation of plates with the aqueous solution of copper bichromate. The optimization of concentration of copper bichromate solution, duration and number of impregnations was carry out. The impregnation method and deposition by sorption were used for platinum catalytic coatings synthesis. The optimal concentration of chloroplatinic acid solution, temperature and duration of the calcination, conditions of Pt reduction by hydrodgen gas or Na formate were found. The coatings were characterized by

chemical analysis, X-ray microprobe analysis, CO chemisorption, SEM, XPS, ESDR. According to the X-ray microprobe analysis the preparation method provides uniformity of metal (Cu, Cr or Pt) distribution along Al_2O_3/Al plates.

The catalytic activity of supported Cu-Cr oxide and Pt catalysts was tested in butane oxidation as the model reaction. The experiments on C_4H_{10} oxidation were performed in a flow fixed catalyst bed reactor at initial concentration 0.2% vol. C_4H_{10} in air, GHSV 120000 h^{-1} calculated on a volume of the Al_2O_3 layer, in the temperature range 200 – 500°C.

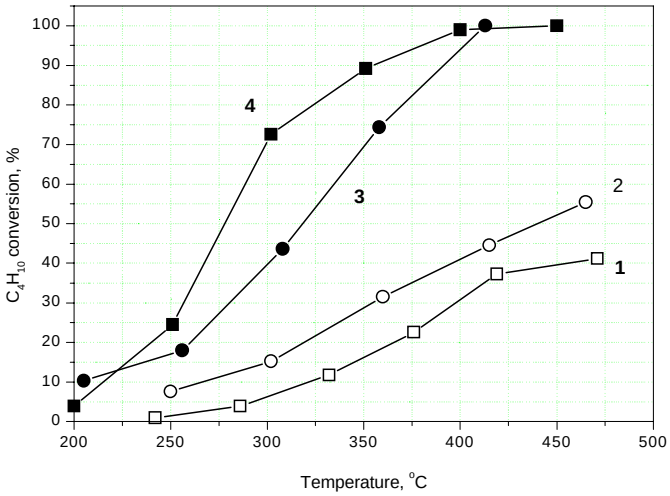

Fig. 1. Conversion in butane oxidation on supported Cu-Cr oxide and Pt catalysts:
1 - Pt catalyst on granulated Al_2O_3 support;
2 - Cu-Cr oxide catalyst on granulated Al_2O_3 support;
3 - Cu-Cr oxide catalyst on flat Al_2O_3/Al support;
4 - Pt catalyst on flat Al_2O_3/Al support.

It was shown that the activity of supported Cu-Cr oxide and Pt catalysts on flat Al_2O_3/Al plates was superior to those of granulated catalysts (Fig. 1).

The activity of supported Cu-Cr oxide and Pt catalysts on microstructured plates is similar to activity of supported Cu-Cr oxide and Pt catalysts on flat Al_2O_3/Al plates, and it was stable during 40 hours of continuous run.

The authors are grateful to Prof. Z.R. Ismagilov, Dr. M.H.J.M. de Croon and Prof. J.C. Schouten for the comments and discussions.

This work was financially supported by project NWO-RFBR «Microstructured Catalytic Reactors for Oxidation of Unsymmetrical Dimethylehydrazyne» 03-03-89004-NWO_a

Литература

1. E.V. Rebrov, S.A. Duinkerke, M.H.J.M. de Croon, J.C. Schouten. J. Chem. Eng. 93 (2003) 201–216
2. E.R. Delsman, M.H.J.M. de Croon, G.J. Kramer, P.D. Cobden, Ch. Hofmann, V. Cominos. J. Chem. Eng. 101 (2004) 123–131
3. I.Z. Ismagilov, R.P. Ekatpure, E.V. Matus, E.V. Rebrov, M.H.J.M. de Croon, L.T. Tsykoza, S.R. Khairulin, M.A. Kerzhentsev, J.C. Schouten. ICOSCAR-2, Delft, The Netherlands, 16-19 October, 2005. (accepted).

Header Design for Flow Equalization in Microstructured Reactors

Evgeny V. Rebrov, Ilyas Z. Ismagilov, Rahul P. Ekatpure, Mart H.J.M. de Croon, and Jaap C. Schouten
Laboratory of Chemical Reactor Engineering, Eindhoven University of Technology, 5600 MB Eindhoven, The Netherlands

DOI 10.1002/aic.11043
Published online November 15, 2006 in Wiley InterScience (www.interscience.wiley.com).

To enhance the uniformity of fluid flow distribution in microreactors, a header configuration consisting of a cone diffuser connected to a thick-walled screen has been proposed. The thick-walled screen consists of two sections: the upstream section constitutes a set of elongated parallel upstream channels and the downstream section constitutes a set of elongated parallel downstream channels positioned at an angle of 90° with respect to the upstream channels. In this approach the problem of flow equalization reduces to that of flow equalization in the first and second downstream channels of the thick-walled screen. In turn, this requires flow equalization in the corresponding cross sections of the upstream channels. The computational fluid dynamics analysis of the fluid flow maldistribution shows that eight parallel upstream channels with a width of 300–600 μm are required per 1 cm of length for flow equalization. The length to width ratio of these channels has to be >15. The numerical results suggest that the proposed header configuration can effectively improve the performance of the downstream microstructured devices, decreasing the ratio of the maximum flow velocity to the mean flow velocity from 2 to 1.005 for a wide range of Reynolds numbers (0.5–10). © 2006 American Institute of Chemical Engineers *AIChE J,* 53: 28–38, 2007
Keywords: design, thick-walled screen, flow maldistribution, microreactor, CFD

Introduction

The demand for high-performance microstructured devices is continuously increasing because of their application in different areas such as high-throughput catalyst testing, kinetic studies of highly exothermic reactions, synthesis and decomposition of hazardous chemicals, and portable hydrogen production. The nonuniformity of fluid flow distribution in the microchannels affects the efficiency of the microreactor. The nonuniformity in the flow distribution is principally attributed to the finite dimensions of the microreactor units, frequently making impossible the use of sufficiently smooth transitions from a cross-sectional shape of the reactor to that of the upstream and downstream pipes. In large-scale chemical reactors, an additional resistance is usually created by the catalyst layer, which may be considered as a part of the flow distribution system. In microstructured reactors, however, the overall pressure drop over the set of microchannels seldom exceeds 5% of the total pressure in the system. Therefore, uniform distribution of flow can be attained only by special equalizing and distributing devices positioned upstream of the reactor unit. Sometimes, it is also necessary to transform one form of the velocity profile into another.[1]

There has been considerable attention in recent years focused on equalizing the fluid flow distribution in microreactor channels. Commenge et al.[2] developed an approximate pressure drop model to investigate the effect of microchannel geometry parameters on the single-phase fluid flow distribution in a multiplate microreactor. This approximate model, based on the resistive network of ducts, can be used to design optimum plate geometries to achieve uniform flow velocity distribution in downstream microchannels. The results of this model were confirmed by finite-volume calculations. Ajmera et al.[3]

Correspondence concerning this article should be addressed to J. C. Schouten at j.c.schouten@tue.nl.
I. Z. Ismagilov is also affiliated with the Laboratory of Environmental Catalysis, Boreskov Institute of Catalysis SB RAS, Prospekt Akademika Lavrentieva, 5, Novosibirsk, 630090, Russia.

developed a novel design of a silicon cross-flow microreactor for parallel testing of porous supported-catalyst beds. The even flow distribution in individual catalyst beds was achieved by bifurcating the inlet channel into 64 parallel microchannels (tree branching concept). The uniform flow distribution in these channels was validated by flow visualization experiments. The flow distribution within the catalysts bed was also analyzed by 2-D computational fluid dynamics (CFD) calculations. Amador et al.[4] studied manifold structures (consecutive and bifurcation) used for even flow distribution in microchannels. The proposed analytical model, analogous to electrical resistance networks, can be effectively used to study the effect of manufacturing tolerances and channel blockages on the flow distribution in downstream microchannels. A CFD- and finite-element method (FEM)–based analysis of the flow distribution in a plate-fin microdevice was reported in several studies.[5,6] It was shown that the even flow distribution in the branched microchannels of the microdevices and in plate-fin (micro-) heat exchangers[7,8] is profoundly affected by the shape of inlet and outlet manifolds.

The geometric parameters and shapes of the reactor units and of the inlet and the outlet parts are highly varied. Therefore, the methods of fluid flow equalization are also different. Meshes (grids) or screens (perforated sheets, etc.) are usually used for equalizing fluid flow distribution in the reactors. By selection of the density of meshes and the local patches, the necessary degree of flow uniformity can be attained.[9] A sheet screen (grid) is the most effective and simple way to distribute fluid flow equally thorough a whole cross section of the reactor. Such a grid creates additional fluid flow resistances, which are equally distributed across the whole cross section of the reactor. The screen-leveling property depends on its geometrical parameters such as the effective (open) cross section and the thickness of the resistance layer (resulting from screens). The resistance of the grid increases with decreasing effective cross section or with increasing thickness of the resistance layer. These parameters define the drag coefficient of the screen, expressed as

$$\zeta_{sc} = \frac{2\Delta p}{\rho \bar{w}_{sc}^2} \tag{1}$$

where $\bar{w}_{sc}$ is the average velocity, ρ is the fluid density, and Δp is pressure drop along the screen. A similar expression can be applied to estimate the resistance of the downstream equipment (such as a microreactor). It is compulsory to use a flow distribution system if the drag coefficient of the resistance layer (ζ) is <1000.[10]

Importantly, there is a clear difference between planar (or thin-walled) and three-dimensional (thick-walled) screens. The former does not have guiding walls, whereas the latter consists of a number of thick bars, whose thickness in the direction of the fluid flow equals or exceeds the spacing between them. In the case of a thin screen (such as gauze), there is a critical value of ζ_{sc} (see Eq. 2) beyond which the degree of fluid flow equalization in a cross section at finite distance downstream from it may considerably differ from the degree of flow spreading upstream of the screen:

$$\zeta_{sc}^{cr} = 3.5\left(\frac{N_0 A_{sc}}{A_0} - 1\right) \tag{2}$$

In this expression, also known as Idelchik's correlation,[9] N_0 is the Coriolis's coefficient and A_{sc} and A_0 are the open cross sections of the screen and the inlet flow duct, respectively.

The internal (hydraulic) diameter of the inlet flow duct of the microreactor is typically between 1 and 4 mm and the inlet duct is sufficiently long, so that at a certain distance from the inlet region of the duct, a constant parabolic velocity profile develops, with maximum at the axis and with zero at the walls:

$$\frac{w}{w_{\max}} = 1 - y^2 \tag{3}$$

It is easy to evaluate the Coriolis coefficient for this case. Assigning the normalized deviation of velocities from the average value as $\Delta\bar{w} = (\Delta w/\bar{w})$, it can be derived that

$$N_0 = \frac{1}{A_0}\int_{A_0}(1+\Delta\bar{w})^3 dA = 1 + \frac{3}{A_0}\int_{A_0}\Delta\bar{w}dA + \frac{3}{A_0}\int_{A_0}\Delta\bar{w}^2 dA + \frac{1}{A_0}\int_{A_0}\Delta\bar{w}^3 dA \tag{4}$$

The second term of this sum equals zero by definition of average velocity, whereas the fourth term is alternating and small, so it can be neglected. Therefore, for a parabolic velocity profile

$$N_0 \approx 1 + \frac{3}{A_0}\int_{F_0}\Delta\bar{w}^2 dA = 1.57 \tag{5}$$

In this way, the critical values of the screen drag coefficient estimated by Eq. 2 are equal to 7.5, 18.5, and 29.5 for A_{sc}/A_0 values of 2, 4, and 6, respectively.

On the other hand, there is an optimum value for the drag coefficient of the flat screen, which can be calculated for $A_{sc}/A_0 \leq 10$ by the following equation:[9]

$$\zeta_{sc}^{opt} = N_0\left(\frac{A_{sc}}{A_0}\right)^2 - 1 \tag{6}$$

It is easy to see that for a planar screen the design criterion $\zeta_{sc}^{opt} < \zeta_{sc}^{cr}$ is satisfied only in a narrow range at $A_{sc}/A_0 < 2.9$; otherwise, planar screens can even amplify the flow nonuniformity downstream of them, giving to the flow profile a distribution that is directly opposite to that of the distribution upstream of the screen.[10,11] Therefore, a planar screen cannot ensure a uniform velocity distribution in a typical range of $A_{sc}/A_0 > 10$ applied in microreaction technology.

This problem does not exist in the case of thick-walled screens because the degree of velocity equalization is virtually the same at all cross sections downstream from them. In this case, the nature of the distribution of the inlet flow under a given set of flow conditions is a function only of the shapes and geometric parameters of the downstream reactor and the inlet flow duct of the screen. If the shape and parameters are specified, the problem of velocity distributions can be solved in a rather general form without taking into account what chemical or technological process occurs within the downstream reactor.

Problems of flow equalization over the cross section of reactors by screens have been investigated for some time.

Initially, those problems were solved empirically. Riman[12] obtained an expression for the value of the drag coefficient, which ensures the specified degree of flow equalization. An approximate determination of the stream function, whose derivatives satisfy the boundary conditions at the channel walls and at the screen, was performed by Taylor and Batchelor.[13] Riman and Cherepkova[14] proposed a method for calculating the distortion of the velocity profile by bars placed in a tube. However, these problems are solved for high Reynolds (Re) numbers, often corresponding to turbulent flow regime, which is not a case in microstructured reactors.

In this article a study on the performance of the header consisting of a fluid flow diffuser and a thick-walled screen with a thickness of parallel bars in the micrometer range is presented. This type of header can effectively equalize the fluid flow distribution in the plate-type microreactors in the laminar flow regime corresponding to $Re < 10$. The study of the fluid flow distribution at the header was investigated by means of the CFD package FLUENT® 6.0.[15] This contribution mainly describes the numerical investigation on the effect of the screen configuration parameters on the flow distribution in a downstream microreactor. Results of the experimental validation of the present configuration are presented elsewhere.[16,17]

Geometry

Physical model

A schematic view of the header is shown in Figure 1. The header consists of a cone diffuser and a thick-walled screen positioned in front of the microreactor. The thick-walled screen consists of two sections positioned with a 90° turn relative each other. The upstream section (U) consists of a set of m elongated parallel upstream channels and the downstream section (D) consists of a set of n elongated parallel downstream channels positioned at an angle of 90° with respect to the upstream channels. Depending on the number of upstream and downstream channels, the screens will be referred to as $[m \times n]$ hereafter. The whole geometry is defined by the following parameters: parameter a is the minimum length between two neighboring downstream channels and parameter b is the distance in cross-sectional view between a top wall of the first downstream channel and a side wall of the upstream channels. In other words, the value b is the overhang of the cross section of upstream channels with respect to the cross section of the first downstream channel. Parameter c is the width of the upstream channels; parameter d is the height of the downstream channels; parameter h is the distance between the neighboring upstream channels; parameters l_{up} and l_{dwn} are the lengths of upstream and downstream channels of the screen, respectively; and $d1$ is the diameter of the channels in the microreactor (R) connected to the downstream channels of the header. $d1$ is usually equal to or slightly lower than parameter d, so the distance in the vertical direction between the channels in the microreactor ($a1$) is equal to or slightly higher than distance a.

In general, the greater the diffuser expansion angle α (Figure 1), the steeper the velocity drop at the walls of the diffuser and the more elongated is the velocity profile, that is, the higher is the ratio of the maximum velocity to the mean velocity, at the entrance to the upstream channels. At constant inlet conditions and constant relative length of the diffuser, there are four principal flow modes, depending on angle α, of the flow diffuser[18] (Table 1). In microreactors it is desirable to avoid large dead volumes; therefore diffusers of type IV are usually applied. This means that an elongated velocity profile is developed with a ratio of the maximum velocity to the mean velocity > 2 at the entrance to the upstream channels.[18]

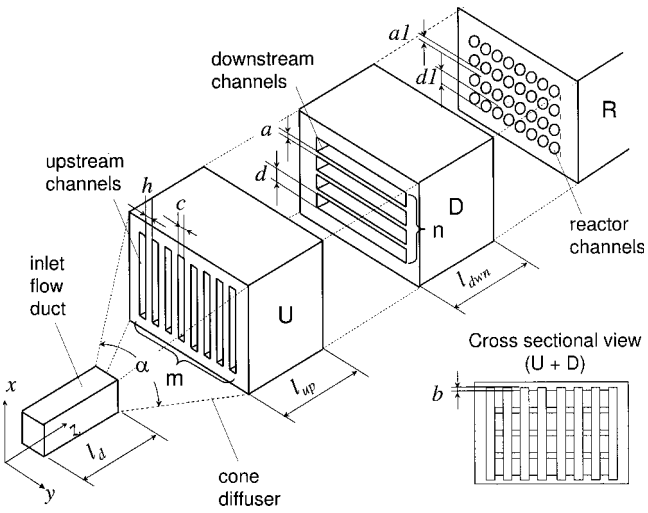

Figure 1. The header consists of a cone diffuser and a thick-walled screen positioned in front of the microreactor.

The thick-walled screen consists of two sections positioned with a 90° turn relative to each other. The upstream section (U) consists of a set of m elongated parallel upstream channels and the downstream section (D) consists of a set of n elongated parallel downstream channels positioned at an angle of 90° with respect to the upstream channels. Parameter a is the minimum length between two neighboring downstream channels; parameter b is the distance in cross-sectional view between a top wall of the first downstream channel and a side wall of the upstream channels; parameter c is the width of the upstream channels; parameter d is the height of the downstream channels; parameter h is the distance between the neighboring upstream channels; parameters l_{up} and l_{dwn} are the lengths of upstream and downstream channels of the screen, respectively. $d1$ is the diameter of the channels in the microreactor (R) connected to the downstream channels of the header. $d1$ is usually equal to or slightly lower than distance d, so the distance in the vertical direction between the channels in the microreactor ($a1$) is equal to or slightly higher than distance a.

Computational domain

In this work, the CFD code FLUENT® 6.0 was used to simulate the fluid flow distribution and pressure drops along the screens. Physical parameters of air [at standard temperature and pressure (STP) conditions] were used throughout this work for definition of the gas-phase properties. The continuity equation and the momentum equation are discretized using a finite-volume method. The semi-implicit SIMPLER algorithm is used in the velocity and pressure conjugated problem. Boundary conditions applied are as follows: inlet fluid Reynolds numbers and outlet pressure are given and no slip occurs on the wall. The convergence criterion is specified to residuals smaller than 1×10^{-6}. The header has two symmetry planes; thus, only one fourth of the screen

Table 1. Principal Flow Modes at the Outlet of the Flow Diffuser, Depending on the Diffuser Expansion Angle α*

	Mode	Diffuser Angle (°)	Flow Description
I	Separation free diffusers	$\alpha \leq 4$	Stable flow
II	Diffusers with local flow separation	$6 < \alpha \leq 14$	Large unsteady flow detachment
III	Diffusers with significant flow separation	$14 < \alpha \leq 40$	Fully developed flow separation: a large part of the diffuser is occupied by a wide recirculation zone
IV	Diffusers with total flow detachment	$\alpha > 40$	Jet flow: the main stream is separated from the diffuser walls over entire perimeter

*From Idelchik and Ginzburg.[18]

was modeled. A mesh independency check was performed on the results of the CFD model. Furthermore, the results of the CFD simulations were verified by measuring flow distribution at the outlets of the downstream channels by laser Doppler anemometry (LDA) as described elsewhere.[16] The experimental results showed good agreement with numerical results for a wide range of Re numbers.

The inlet cone diffuser was not taken into the computational domain. However, the inlet Reynolds numbers in the upstream channels of the screen were assigned with three velocity profiles (see Figure 2). In the case of an uneven number of upstream channels, velocity profiles were determined as follows:

(1) Elongated profile with a ratio of the maximum velocity to the mean velocity ($\bar{w}_{\max}$) of 2.0:

$$w_i^{el} = w_{m+1-i}^{el} = 2\sin^2\left\{\frac{\left[(c+h)(i-1)+\frac{c}{2}\right]}{(c+h)\frac{m-1}{2}+\frac{c}{2}}\frac{\pi}{2}\right\} \tag{7}$$

where $1 \leq i \leq (m+1)/2$.

(2) Parabolic profile with $\bar{w}_{\max}$ of 1.5:

$$w_i^{par} = w_{m+1-i}^{par} = 1.5\left\{1-\left[\frac{(c+h)\left(\frac{m+1}{2}-i\right)}{(c+h)\frac{m-1}{2}+\frac{c}{2}}\right]^2\right\} \tag{8}$$

where $1 \leq i \leq (m+1)/2$.

(3) Uniform profile with $\bar{w}_{\max}$ of 1.0:

$$w_i^{un} = 1 \tag{9}$$

where $1 \leq i \leq m$.

In this way, the mean inlet velocity over all upstream channels is equal in all three cases:

$$\overline{w^{el}} = \overline{w^{par}} = \overline{w^{un}}$$

Similar distributions were used for an even number of upstream channels.

The velocity profile at the each outlet of the downstream channels of the screen was characterized by the flow nonuniformity index, defined as

$$\delta = \frac{100}{\bar{v}}\sqrt{\frac{\sum_{j=1}^{n}\varepsilon_j^2}{(n-1)}} \quad (\%) \tag{10}$$

where $\varepsilon_j = v_j - \bar{v}$, v_j is the area average velocity in the outlet channel j and $\bar{v}$ is the mean velocity over all outlet channels. It should be noted that $\overline{v^{el}} = \overline{v^{par}} = \overline{v^{un}}$. Such a definition of flow nonuniformity also allows us to compare the results obtained at different flow velocities.

Flow nonuniformity was calculated for a [45 × 38] screen at several different values of relative length of the upstream channels (l_{up}^*) using a parabolic profile at the entrance. Figure 3 demonstrates that the flow nonuniformity starts to increase below $l_{up}^* = 7.5$. However, the flow development length is not observed to vary substantially over the range of average flow velocities applied in this study.

Two parameters are introduced herein to evaluate the differences in the flow distribution at the outlet of the downstream channels, that is, the relative outlet flow nonuniformity parameter to evaluate the flow differences between the elongated and uniform inlet profiles, expressed in the following equation:

$$R_j^{el} = 100\frac{v_j^{el} - v_j^{un}}{\bar{v}} \quad (\%) \tag{11}$$

and between the parabolic and the uniform inlet profiles, expressed as

$$R_j^{par} = 100\frac{v_j^{par} - v_j^{un}}{\bar{v}} \quad (\%) \tag{12}$$

Figure 4 presents the numerical results for a [45 × 38] screen with $a = 400$ μm, $b = 260$ μm, $c = 400$ μm, $d = 400$ μm, $h = 400$ μm, $l_{up}/2c = 7.5$, and $l_{dwn}/2d = 7.5$. One can see that the largest differences are observed in the outermost channels.

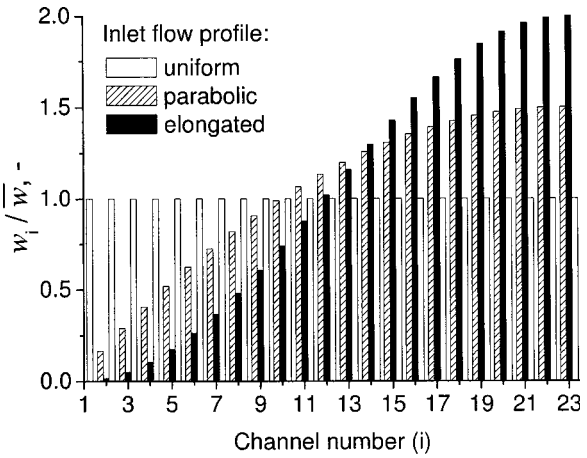

Figure 2. Three different inlet flow profiles (elongated, parabolic, and uniform) assigned to the inlets of the upstream channels of the [45 × 38] screen.

The values are given only for a half of the geometry because of the symmetry.

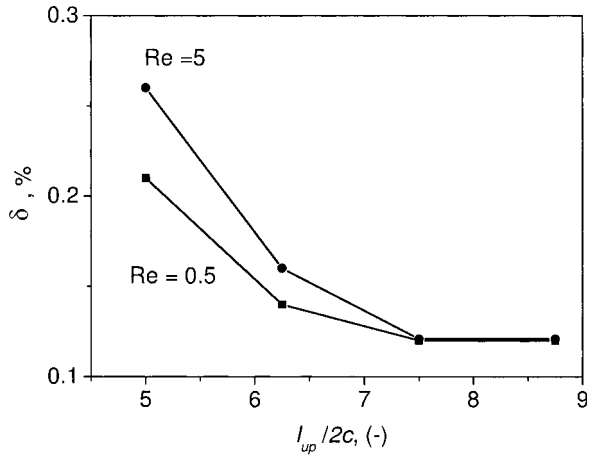

Figure 3. Flow nonuniformity (Eq. 10) as a function of the relative length of the upstream channels (l^*_{up}) at Re of 0.5 and 5.

l^*_{up} is the ratio of the length of the upstream channel (l_{up}) to the hydraulic diameter of the inlet flow duct of the screen.

Furthermore, two parameters, referred to as overall outlet flow nonuniformity parameters, were introduced to compare the differences between the elongated and the uniform (Eq. 13), as well as between the parabolic and the uniform cases (Eq. 14) in different screen configurations. These parameters were evaluated in a wide range of screen parameters:

$$\chi^{el} = \frac{100}{n\bar{v}} \sum_{j=1}^{n} |v_j^{el} - v_j^{un}| \quad (\%) \tag{13}$$

$$\chi^{par} = \frac{100}{n\bar{v}} \sum_{j=1}^{n} |v_j^{par} - v_j^{un}| \quad (\%) \tag{14}$$

The χ^{el} and χ^{par} values are listed in Table 2 for the lowest and highest values of design parameters. It is clear that the values of chosen objective functions are <0.02% for a wide range of applied design parameters. Based on those results it can be concluded that the outlet flow distribution depends only on geometry parameters of the thick-walled screen and does not depend on the inlet distribution at the entrance to the upstream channels of the screen. Therefore, instead of complete modeling of the cone diffuser with the thick-walled screen, a prescribed parabolic flow profile (Eq. 8) was specified at the inlet of the upstream channels. Uniform static pressure of 101.3 kPa was specified at all outlets of the downstream channels. The range of flow velocities studied corresponds to a Reynolds number of 0.5–10. The pressure drop across the screen was always <1.0 Pa.

Optimization of the Header Configuration

At low Reynolds number, the flow is laminar. In this regime there is a linear flow resistance relation between the pressure drop (Δp) along the channel and the volumetric flow rate (Q) through the channel, expressed as

$$Q = G\Delta p \tag{15}$$

where G is a hydraulic conductance. At the interface between the upstream and downstream channels, flow is split up and further redistributed in the downstream channels (Figure 5). To compare the hydraulic resistance of different parts of the thick-walled screen, the entire geometry of the screen was decomposed into even portions. In this approach, the topmost and bottommost portions of upstream channels can be merged together to form a rectangle with height z_{V1}, whereas the middle part can be considered as parallel plates with height z_{V2}. For the screen applied: $z_{V1} = 2(0.5a + b + d)$ and $z_{V2} = 2(a + d)$. Obviously, there is a difference in the hydraulic conductance for the fluid flow between the side and the middle portions of upstream channels represented in the present model by rectangular and parallel plates, respectively. Therefore, to determine the flow rate by the rectangular- and parallel-plate geometry, it is necessary to calculate their hydraulic conductances, for which the pressure drops are identical.

In the present analysis, instead of the actual velocity field entering each downstream channel from the upstream channels, an average value has been taken for the entire downstream channel (Q_{dwn}). This average value depends on the mean velocity over a corresponding part of an upstream channel (Q_{up}) and the b/a ratio of the thick-walled screen. To provide a uniform flow distribution in all the downstream channels, volumetric flow rate Q_{dwn1} has to be equal to Q_{dwn2} and so on. Because of the symmetry of the screen only half of the geometry of the downstream channels has to be considered. In our previous study, a methodology was presented for flow equalization by application of a thick-walled screen in which the b/a ratio was changed from 0 to 1.[19] It was observed that the ratio between the flow rate in the first and the second downstream channels is equal to the ratio of the volumetric flow rates by corresponding cross section of the upstream channel times the height of the corresponding cross sections:

$$\frac{Q_{dwn1}}{Q_{dwn2}} = \frac{Q_{up1}}{Q_{up2}} \frac{z_{up1}}{z_{up2}} \tag{16}$$

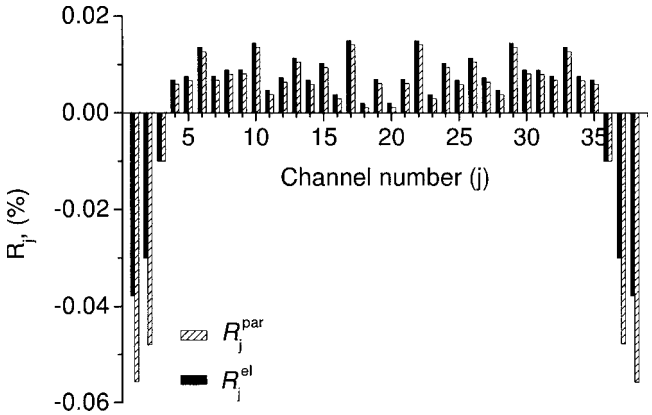

Figure 4. Effect of upstream flow profile on the flow differences at the outlets of the downstream channels of the [45 × 38] screen.

Parameters values: a = 400 μm, b = 260 μm, c = 400 μm, d = 400 μm, h = 400 μm, l^*_{up} = 7.5, and l^*_{dwn} = 7.5. Re = 5.

Table 2. Flow Nonuniformity Parameters χ^{el} and χ^{par} as a Function of Screen Design Parameters *a, c*, and *h**

Average Reynolds Number in the Upstream Channels	Design Parameters (μm)			Objective Functions (%)	
	a	c	h	χ^{el}	χ^{par}
0.5	125	400	400	0.012	0.011
0.5	750	400	400	0.014	0.012
5	125	400	400	0.012	0.011
5	750	400	400	0.014	0.012
0.5	400	300	400	0.010	0.010
0.5	400	800	400	0.012	0.012
5	400	300	400	0.015	0.015
5	400	800	400	0.015	0.015
0.5	400	400	800	0.012	0.010
5	400	400	800	0.014	0.011

*See Eqs. 13 and 14. Screen geometry: [22] × [8]. The following parameters were kept constant: $d = 400$ mm; $l^*_{up} = 7.5$; $l^*_{dwn} = 7.5$; Re = 5.

The correction factor counts for the pressure losses when the fluid moves from the upstream channels to the downstream channels of the screen. The reason for the correction factor can be understood if one observes the flow lines near the interface between the upstream and downstream channels (Figure 6a). For the case described in Mies et al.,[19] when $b = 0.5a$ flow Q_{up1} is less than Q_{up2}, according to the CFD results, flow separation in upstream channels occurs above equidistant plane A12 between the first and second downstream channels. As a result, more fluid goes to the second downstream channel and less to the first one. This arises from the presence of an external wall, which creates an additional resistance to the fluid flow. To distribute flow equally, an additional room for flow distribution has to be created by increasing the area of the rectangle comparing to the area of the parallel plates or, in other words, increasing the b/a ratio to a certain value that is always >0.5.[19]

If the flow is equally distributed between the first and second downstream channels, flow separation between all subsequent downstream channels would always occur in corresponding equidistant planes (A23, A34, etc.) between the adjacent downstream channels (see Figure 6b) as a result of the symmetry of the thick-walled screen geometry. Therefore, the problem of flow equalization in a thick-walled screen at low Re numbers reduces to that of flow equalization in the first and second downstream channels. In other words, the flow by the rectangular- and parallel-plate parts of the upstream channels times their height ratio has to be identical:

$$\frac{0.5a + b + d}{a + d}\frac{Q_{up1}}{Q_{up2}} = 1 \tag{17}$$

For isothermal, steady, incompressible flow of a Newtonian fluid through a duct of the arbitrary cross section, the product of the Fanning friction factor f_F and the Reynolds number is a constant—the Poiseuille number, Po:

$$\mathrm{Po} = f_F\,\mathrm{Re} \tag{18}$$

where $f_F = 2\tau_w/\rho\bar{v}$,[13] and $\bar{v} = \frac{1}{A}\int_A v dA$, $\bar{v}$ is the cross-sectional average velocity, and ρ is the density. The mean wall shear stress τ_w is defined as

$$\tau_w = \frac{D_h}{4}\frac{dp}{dl} \tag{19}$$

where $D_h = 4A/P$ (A is channel cross-sectional area of the upstream channel and P is the upstream channel perimeter).

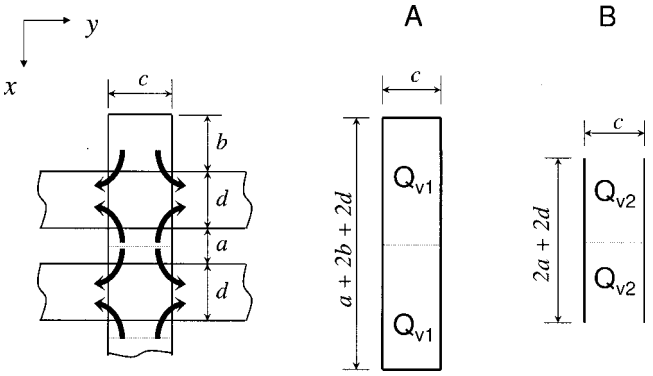

Figure 5. Decomposition of the upstream channel geometry into regular pieces.

(A) Two half rectangles merged together and (B) parallel plates.

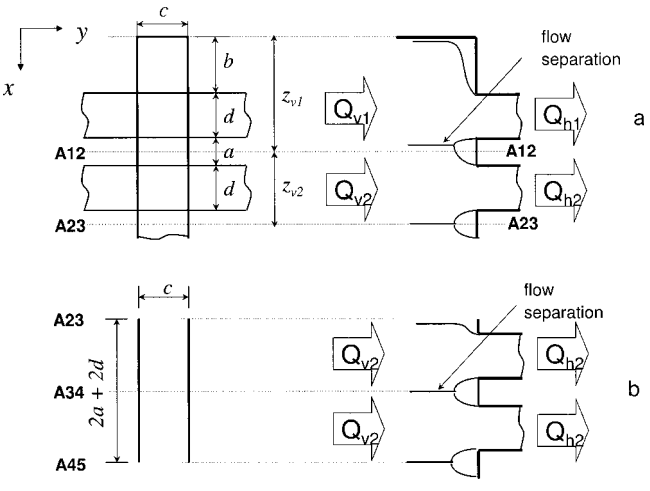

Figure 6. Streamlines for the topmost (bottommost) and middle sections.

A front view of the elementary units of the upstream screen is shown on the left. A cross-sectional view through the centerline of the screen near the interface between the upstream and downstream units is shown on the right.

By combining Eqs. 18 and 19 we can write the Poiseuille number in terms of experimental quantities:

$$\mathrm{Po} = \frac{AD_h^2 \Delta p}{2\eta l_{up} Q} \tag{20}$$

where D_h is the hydraulic radius of an individual upstream channel, Δp is the pressure drop over the upstream channel length l_{up}, η is the viscosity of the fluid, and $Q = \bar{v}A$. By comparing Eqs. 15 and 20, one may conclude

$$G = \frac{AD_h^2}{2l_{up}\eta \mathrm{Po}} \tag{21}$$

The Poiseuille number for developing flow is defined as[20]

$$\mathrm{Po}(t, x^+) = \frac{3.44}{\sqrt{x^+}} + \frac{\dfrac{0.674 + 1.3061t + 0.1222t^2 - 0.6718t^3}{4x^+} + 24P(t) - \dfrac{3.44}{\sqrt{x^+}}}{1 + \dfrac{2.9 \times 10^{-5} + 7.0 \times 10^{-5}t + 9.7 \times 10^{-4}t^2 - 7.8 \times 10^{-4}t^3}{(x^+)^2}} \tag{22}$$

where $P(t) = 1 - 1.3553t + 1.9467t^2 - 1.7012t^3 + 0.9564t^4 - 0.2537t^5$; t is the aspect ratio, $t = c/[a + 2(b + d)]$; and x^+ is the dimensionless length. The Po number depends on both the channel aspect ratio and the dimensionless length of the upstream channels. By combining Eqs. 15 and 21, and assuming that viscosity of the fluid is identical in both channels, Eq. 17 can be rewritten as

$$\frac{0.5a + b + d}{a + d} \times \frac{A_{up1} D_{h-up1}^2}{A_{up2} D_{h-up2}^2} \frac{\mathrm{Po}_{up2}}{\mathrm{Po}_{up1}} = 1 \tag{23}$$

where

$$A_{up1} = (0.5a + b + d)2c \qquad A_{up2} = (a + d)2c$$

$$D_{h-up1} = \frac{(a + 2b + 2d)2c}{a + 2b + c + 2d}$$

and $D_{h-up2} = 2c$. Substituting the values for the cross-sectional areas and the hydraulic diameters into Eq. 23 yields, for flow equalization,

$$\frac{(a + 2b + 2d)^4}{(a + 2b + c + 2d)^2 (2a + 2d)^2} \frac{\mathrm{Po}_{up2}}{\mathrm{Po}_{up1}} = 1 \tag{24}$$

Therefore, at fixed values of design parameters a, c, d, and x^+ the b/a ratio has to be found for which the value of the response function (f) is equal to unity:

$$f = \frac{Q_{dwn1}}{Q_{dwn2}} = \frac{(a + 2b + 2d)^4}{(a + 2b + c + 2d)^2 (2a + 2d)^2} \frac{\mathrm{Po}_{up2}}{\mathrm{Po}_{up1}} \tag{25}$$

Validation of the Approach for the Design of a Thick-Walled Screen

To assess the validity of the thick-walled screen mathematical model, the design results obtained by using this model are compared with CFD simulation results, carried out by use of FLUENT® 6.0. The model predictions obtained at $a = 250$ μm, $c = 300$ μm, $d = 2000$ μm, and $x_{up}^+ = 0.9$ were compared with the CFD results reported in Mies et al.,[19] where the geometry of the diffuser module was similar to that of a thick-walled screen. Figure 7 shows the f-values as a function of parameter a for three different b/a ratios of 0.0, 0.8, and 1.0 applied in Mies et al.[19] Symbols represent the f-values calculated based on the CFD results for the flow distribution between downstream channels 1 and 2. One can observe the rather good agreement between the CFD results and model predictions for all three cases. Furthermore, it can be seen from Figure 7 that the optimum b/a ratio becomes lower at larger distances between downstream channels and vice versa. One can conclude that increasing the separation between the downstream channels shifts the optimum b/a ratio to lower values. Figure 8a demonstrates that, as the b/a ratio increases, more flow goes by the topmost and the bottommost downstream channels. There is a minimum in flow nonuniformity ($\delta = 0.120\%$) at a b/a ratio of 0.75 (Figure 8b). Both lower b/a of 0.73 and higher b/a of 0.77 ratios gave larger values of flow nonuniformity of 0.160 and 0.435%, respectively. CFD simulations give optimum b/a ratios of 0.75 and 0.62 for $a = 250$ and 500 μm, respectively, whereas other design parameters are fixed at the following values: $c = 300$ μm, $d = 400$ μm, and $x_{up}^+ = 0.4$. Predictions made by the present model give optimum values of 0.759 and 0.628, respectively. Thus, there is hardly any difference between results of both designs. The proposed model can be applied for the design of a screen in a wide range of design parameters.

Effect of Design Parameters on Flow Nonuniformity

Effect of the number of the upstream channels (m)

The effect of the number of upstream channels was investigated over a cross section of 12.9 mm (width) × 16 mm (height) by comparing the δ-values obtained in the [22 × 8] screen with those obtained in the [11 × 8] and [8 × 8] geo-

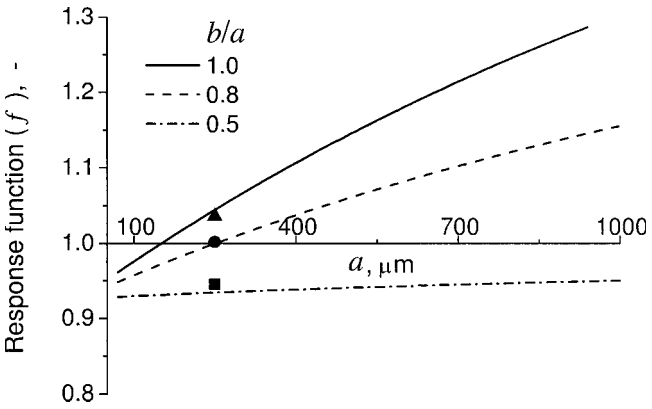

Figure 7. Response function *f* as a function of distance between the downstream channels for three different *b/a* ratios: 0.5, 0.8, and 1.0.

Symbols represent corresponding CFD data.

metries (Figure 9). In the latter cases, parameter h was increased from 300 to 960 and 1500 μm, respectively, other parameters being identical to those mentioned in the beginning of this section. The cross section represents a quarter of the geometry arising from the symmetry. The results were found to be independent of the flow rate with respect to Re numbers ranging from 0.5 to 10.

Increasing the number of upstream channels (m) from 8 to 11 decreases the flow nonuniformity while the optimum b/a ratio remains the same. Further increase of the number of the upstream channels from 11 to 22 does not improve the flow distribution at the outlets of the downstream channels of the screen. This leads to the conclusion that there is an optimum number of upstream channels per unit width of a thick-walled screen beyond which flow nonuniformity remains virtually constant. This number corresponds to one upstream channel per a length of 1260 μm in the y-direction (see Figure 1). In other words, eight upstream channels are required per 1 cm of width of a thick-walled screen to provide a flow nonuniformity $< 0.2\%$. A larger number of channels would considerably hamper the manufacturing of the device, and therefore must be avoided. It should be noted that increasing parameter a from 250 to 500 μm shifts the optimum b/a ratio to the lower values (Figure 9). However, it does not change either the optimum number of upstream channels or the optimum value of the flow nonuniformity parameter (δ). The effect of the b/a ratio on the flow distribution at the downstream channels becomes less important for a screen consisting of a large number of downstream channels ($n > 100$); however, it plays an important role for the screens with a medium ($10 < n < 100$) and it is more dominant for small number of downstream channels ($n < 10$).

Effect of the wall thickness between two neighboring downstream channels (a)

From the discussion in the previous section, it becomes clear that as parameter a increases, the b/a ratio has to be reduced to obtain flow equalization in the whole range of values of parameter a. Therefore, the problem can be formu-

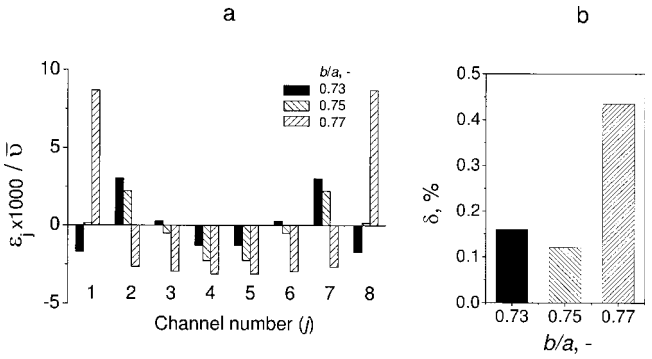

Figure 8. (a) Flow difference in the downstream channels relative to the mean flow in all downstream channels of the [22 × 8] screen as a function of the b/a ratio; (b) flow nonuniformity (δ) as a function of the b/a ratio.

Parameters values: $a = 250$ μm, $c = 300$ μm, $h = 300$ μm, $d = 2$ mm, $l^*_{up} = 7.5$, and $l^*_{dwn} = 7.5$. Re = 5.

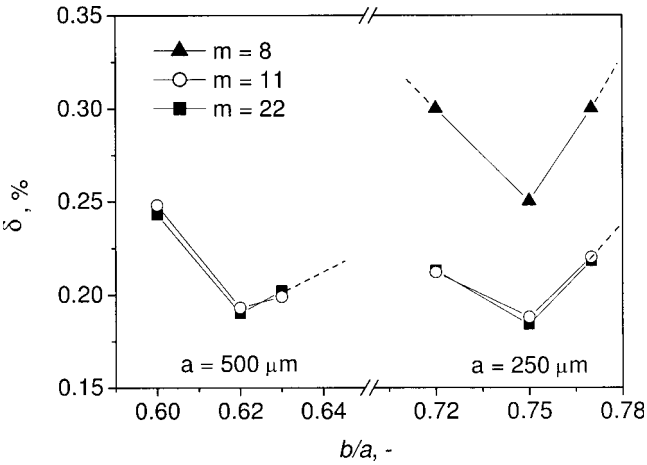

Figure 9. Effect of the number of the upstream channels (m) on the flow nonuniformity at $a = 250$ and 500 μm and different b/a ratios.

Screen geometries of [22 × 8], [11 × 8], and [8 × 8] were applied over a cross section of 12.9 mm (width) × 16 mm (height), corresponding to parameter h of 300 to 960 and 1500 μm, respectively. Other screen parameters were the same as those in Figure 7.

lated as finding an optimum function that minimizes the flow nonuniformity index Ω, defined as

$$\Omega = \left[\frac{1}{a_2 - a_1}\int_{a_1}^{a_2} \frac{(a+2b+2d)^4}{(a+2b+c+2d)^2(2a+2d)^2}\frac{\mathrm{Po}_{up2}}{\mathrm{Po}_{up1}}\,da\right] - 1 \tag{26}$$

The index Ω is the average value of the response function f on the interval of values a between $a_1 = 100$ μm and $a_2 = 1000$ μm, which are within interest for microreactor applications. Several functions with two fitting parameters can be used to describe the ensemble of data points generated by the screen model. In their discrimination, the following criteria were applied:

$$\Omega \le 1 \times 10^{-5} \tag{27}$$

$$\left|f(a,b,c,d,x^+_{up}) - 1\right| \le 0.005 \qquad \text{for} \qquad 100 \le a \le 1000\ (\mu\text{m}) \tag{28}$$

The first criterion is set to minimize the flow nonuniformity in the whole range of values of parameter a. The second criterion states that at any given value of parameter a, the flow nonuniformity should not exceed 0.5%. To satisfy the constraints given by Eqs. 27 and 28, a function for the b/a ratio can be found in the form

$$\frac{b}{a} = P1 + \frac{P2}{a} \tag{29}$$

Figure 10 demonstrates two sets of f-function (see Eq. 25) plots: one at constant b/a ratio of 0.5 and one when the fitting function given by Eq. 29 was applied. It can be seen that the flow equipartition is achieved in the whole range of a-values for different values of parameters c and d if the b/a ratio is a function of the parameter a, and the fitting parame-

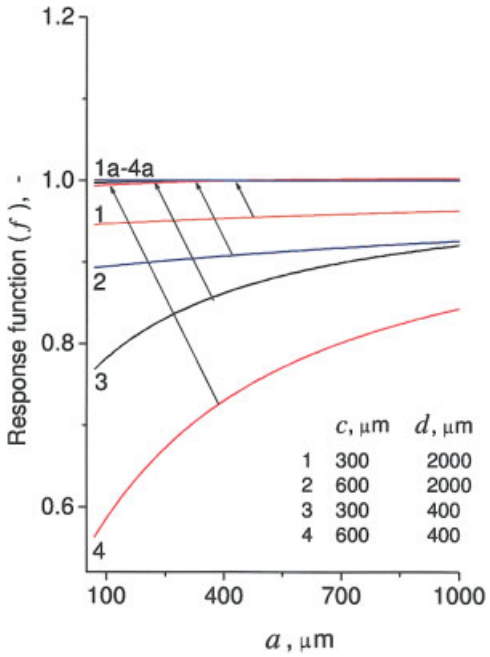

Figure 10. Response function *f* as a function of distance between the downstream channels.

Curves 1–4 are obtained at $b/a = 0.5$. Curves 1a–4a are obtained with the fitting function given by Eq. 29. [Color figure can be viewed in the online issue, which is available at www.interscience.wiley.com.]

ters $P1$ and $P2$ are properly chosen (see Table 3). It can be seen from Table 3 that the parameter $P1$ is always 0.5, whereas parameter $P2$ depends on parameter c and, to a lesser extent, on parameter d. Therefore, the fitting function can be rewritten as follows:

$$b = 0.5a + P2 \tag{30}$$

Equation 30 shows that parameter $P2$ can be neglected if $a \gg 2P2$. If the value of parameter a exceeds the $P2$ value by 20-fold, the contribution of the latter parameter is $<10\%$. Therefore, $P2$ can be neglected if $a > 2.3$ mm because maximum values of parameter $P2$ are found to be about 115 μm (see Table 3). This is a typical situation for monolith reactors. However, microreactors have a typical separation between the adjacent sets of channels (a) of <1 mm, at which the contribution of $P2$ is rather substantial. A complete analysis of the dependency of parameter $P2$ on the design parameters of the screen is beyond the scope of the present study and is reported elsewhere.[21]

Table 3. Fitting Parameters *P1* and *P2* for the Parameter *b*: *b*(*a*) = *P1a* + *P2

c μm	d μm	$P1$	$P2$ μm
300	400	0.500	57.00
300	2000	0.500	56.65
600	400	0.500	115.8
600	2000	0.500	113.4

*The dimensionless length of the upstream channels equals 0.9.

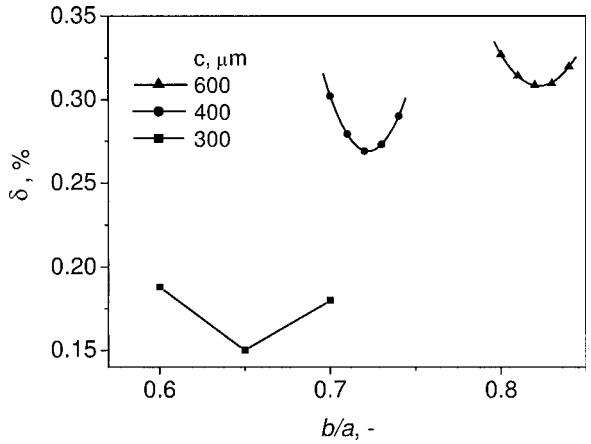

Figure 11. Flow nonuniformity (δ) as a function of *b/a* ratio at different values of parameter *c*: 300, 400, and 600 μm.

Screen geometry of [11 × 8] was applied over a cross section of 12.9 mm (width) × 17.2 mm (height). Parameters values: $a = 400$ μm, $d = 2$ mm, and the sum of parameters c and h was kept constant at 1260 μm. Other screen parameters were the same as those in Figure 7.

Effect of the width of the upstream channels (c)

The width of the upstream channels (c) was varied over a cross section of 12.9 mm (width) × 17.2 mm (height) in the [11 × 8] geometry in the range between 300 and 600 μm to investigate its effect on the flow nonuniformity. In this study, $l^*_{up} = 7.5$, $a = 400$ μm, $d = 2$ mm, and the sum of parameters c and h was kept constant at 1260 μm. When the width of the upstream channel increases from 300 to 600 μm, a minimum flow nonuniformity doubles from 0.155 to 0.31%, whereas the optimum b/a ratio shifts to the higher values (Figure 11). The range of b/a ratios satisfying the design criteria, acceptable in most studies ($\delta < 0.5\%$), becomes more narrow at $c = 600$ μm. A typical precision of micromachining is 10 μm, which can prompt a shift in the b/a ratio of ± 0.02. For example, at $c = 600$ μm, the optimum b/a ratio equals 0.82 ($b = 328$ μm) corresponding to the flow nonuniformity of 0.31%. When the screen is not properly assembled (such as $b = 338$ μm), the δ-value would be 0.33%, generating an increase in the flow nonuniformity of 0.02%. Therefore, the width of upstream channels (c) can be safely set at 600 μm unless very low values of flow nonuniformity ($\delta < 0.15\%$) are desired. The values > 600 μm can also be applied. This, in turn, would require a longer length of the screens to satisfy the criterion: $l^*_{up} = 7.5$.

Conclusions

An original design of a flow distribution header, consisting of a cone diffuser and a thick-walled screen, is proposed for equalizing flow distribution in microstructured reactors having constraints related to flow uniformity and pressure drop. In this design, the degree of flow nonuniformity does not depend on the flow distribution entering the thick-walled screen and is defined by the geometry of the thick-walled screen itself. The diffuser expansion angle plays no role in

equalizing the fluid flow. Therefore, it is recommended to use the diffusers with expansion angle close to 180° (sudden expansion) to minimize the dead volume of the header. The problem of flow equalization in a thick-walled screen at low Reynolds numbers reduces to that of flow equalization in the first (topmost) and second downstream channels of the thick-walled screen. In turn, this requires flow equalization in the corresponding cross sections of upstream channels, which can be modeled by rectangular- and parallel-plate geometries. The influence of different design parameters of a thick-walled screen on the flow nonuniformity has been analyzed by performing a CFD study. At least eight upstream channels with a width of 300 μm are required per 1 cm of width of a thick-walled screen to provide a flow nonuniformity $< 0.2\%$. The width of the upstream channels can be increased to 600 μm. However, this will double the flow nonuniformity and will shift the optimum distance between a top wall of the topmost downstream channel and a side wall of the upstream channel to higher values. The proposed screen configuration can minimize the ratio of the maximum flow velocity to the minimum flow velocity from 2 to 1.005 for a wide range of Reynolds numbers, which in turn can improve the performance of a downstream microreactor.

Acknowledgments

The financial support by the Dutch Technology Foundation (STW, Project No. EPC.5543) by the Nederlands Organization for Scientific Research and (NWO) and the Russian Foundation for Basic Research (RFBR), Project No. 047.015.007, is gratefully acknowledged.

Notation

A = cross-sectional area of a fluid channel, m^2
a = distance between two neighboring downstream channels, m
b = distance in cross-sectional view between a top wall of the first downstream channel and a side wall of the upstream channel, m
c = width of the upstream channels, m
d = height of the downstream channels, m
D_h = hydraulic diameter ($=4A/P$), m
f_F = fanning friction factor ($=2\tau_w/\rho v^2$)
F = open cross section, m^2
G = hydraulic conductance ($=AD_h^2/2l_{up}\eta$Po), m^4 s kg^{-1}
h = distance between two neighboring upstream channels, m
l = channel length, m
l^* = relative length (the length to hydraulic diameter ratio) ($=l/D_h$)
m = number of the upstream channels
N_0 = Coriolis's coefficient (a ratio of true kinetic energy to kinetic energy calculated based on average flow velocity) ($=\int_{A_0} w^3 dA/w_0{}^3A_0$)
n = number of the downstream channels
P = perimeter of the channel, m
Δp = pressure drop, kg m^{-1} s^{-2}
Po = Poiseuille number ($=AD_h^2\Delta p/2\eta l_{up}Q$)
R_j^* = relative flow difference parameter, % ($[(v_j^* - v_j^{un})/\bar{v}] \times 100$). It compares the flow difference in the downstream channels when a prescribed flow profile ($* = par, el$) was applied in the upstream channels instead of the uniform profile.
Re = Reynolds number ($=\bar{v}\rho D_h/\eta$)
Q = volumetric flow rate ($=\bar{v}A$), m^3 s^{-1}
t = aspect ratio
v_j = area-averaged velocity at the outlet of downstream channels j, m/s
$\bar{v}$ = mean velocity over all outlets of the downstream channels, m/s
w = velocity in the upstream channels, m/s
$\bar{w}$ = mean inlet velocity over all upstream channels, m/s
x^+ = dimensionless length of the channel ($=l/D_h$Re)
z = height of a upstream channel, m

Greek letters

α = expansion angle of the flow diffuser, °
δ = flow nonuniformity index ($=(100/\bar{v}) \times [\Sigma_{j=1}^{n}(v_j - \bar{v})^2]/(n-1)$), %
χ^* = overall outlet flow difference parameter [$=(100/n\ \bar{v}) \times \Sigma_{j=1}^{n} |v_j^* - v_j^{un}|$], %. It compares the flow difference in the downstream channels when a prescribed flow profile ($* = par, el$) was applied in the upstream channels instead of the uniform profile.
ε_j = flow difference in channel j relative to the mean flow in all downstream channels ($=v_j - \bar{v}$)
η = fluid viscosity, kg m^{-1} s^{-1}
v = cross-sectional average velocity [$=(1/A)\int_A v d\mathbf{A}$], m s^{-1}
ρ = fluid density, kg/m^3
Ω = flow nonuniformity index $\langle=([1/(a2-a1)]\int_{a1}^{a2} f\,da) - 1\rangle$
ζ = drag coefficient of the screen
τ_w = mean wall shear stress [$=(D_h/4)(dp/dl)$], kg m^{-1} s^{-2}

Superscripts

cr = critical
opt = optimal
el = elongated
par = parabolic
un = uniform

Subscripts

d = diffuser chamber
dwn = downstream channels
i = upstream channel number
j = downstream channel number
o = inlet flow duct
rel = relative
max = maximum
sc = screen
up = upstream channel
1 = above the A12 plane
2 = between the A12 and A23 planes

Literature Cited

1. Rebrov EV, Duinkerke SA, de Croon MHJM, Schouten JC. Optimization of heat transfer characteristics, flow distribution, and reaction processing for a microstructured reactor/heat-exchanger for optimal performance in platinum catalyzed ammonia oxidation. *Chem Eng J*. 2003;93:201–216.
2. Commenge JM, Falk L, Corriou JP, Matlosz M. Optimal design for flow uniformity in microchannel reactors. *AIChE J*. 2002;48:345–358.
3. Ajmera SK, Delattre C, Schmidt MA, Jensen KF. Microfabricated differential reactor for heterogeneous gas phase catalyst testing. *J Catal*. 2002;209:401–412.
4. Amador C, Gavriilidis A, Angeli P. Flow distribution in different microreactor scale-out geometries and the effect of manufacturing tolerances and channel blockage. *Chem Eng J*. 2004;101:379–390.
5. Tonomura O, Tanaka S, Noda M, Kano M, Hasebe S, Hashimoto I. CFD-based optimal design of manifold in plate-fin microdevices. *Chem Eng J*. 2004;101:397–402.
6. Ranganayakulu C, Seetharamu KN. The combined effects of wall longitudinal heat conduction, inlet fluid flow nonuniformity and temperature nonuniformity in compact tube-fin heat exchangers: A finite element method. *Int J Heat Mass Transfer*. 1999;42:263–273.
7. Jiao A, Baek S. Effects of distributor configuration on flow maldistribution in plate-fin heat exchangers. *Heat Transfer Eng*. 2005;26:19–25.

8. Prabhakara RB, Krishna KP, Das SK. Effect of flow distribution to the channels on the thermal performance of a plate heat exchanger. *Chem Eng Proc*. 2002;41:41–58.
9. Idelchik IE. *Handbook of Hydraulic Resistance*. Boca Raton, FL: CRC Press; 1994.
10. Idelchik IE. *Fluid Dynamics of Industrial Equipment: Flow Distribution Design Methods*. London: Hemisphere; 1991.
11. Taganov GI. Equalizing performance of grids in gas and liquid flows. *Trans TsAGI*. 1947;604:14.
12. Riman IS. Modification of velocity profiles in variable cross section ducts by placement of meshes. *Promyshlennaya Aerodin. (Ind Aerodyn)*. 1960;20:216–238.
13. Taylor GI, Batchelor GK. The effect of wire gauze on small disturbances in a uniform stream. *J Mech Appl Math*. 1949;11:1–29.
14. Riman IS, Cherepkova VG. An approximate method for calculation of flow field in a tube filled with thick-walled bars. *Ind Aerodyn*. 1973:30:65–74.
15. *FLUENT Users Guide*. Lebanon, NH: Fluent Inc.; 2005.
16. Mies MJM, Rebrov EV, Deutz L, Kleijn CR, de Croon MHJM, Schouten JC. Experimental validation of the performance of a microreactor for the high-throughput screening of catalytic coatings. *I&EC Res*. 2007, in press.
17. Mies MJM, Rebrov EV, de Croon MHJM, Schouten JC, Ismagilov IZ. *Inlet Section for Micro-Reactor*. Patent PCT/NL2006/050074; 2006.
18. Idelchik IE, Ginzburg YaL.Main results of experimental investigations of conical diffusers. In: *Scrubbing of Industrial Gases*. Moscow: Mashinostroenie; 1974.
19. Mies MJM, Rebrov EV, de Croon MHJM, Schouten JC. Design of a molybdenum high throughput micro-reactor for high temperature screening of catalytic coatings. *Chem Eng J*. 2004;101:225–235.
20. Shah RK, London AL. *Laminar Flow Forced Convection in Ducts*. New York: Academic Press; 1978.
21. Ekatpure RP, Rebrov EV, de Croon MHJM, Schouten JC. Optimization of design parameters of a thick-walled screen for flow equalization in microstructured reactors. *J Micromech Microeng*. 2007, in press.

Manuscript received May 11, 2006, and revision received Sept. 22, 2006.

ELSEVIER

Chemical Engineering Journal xxx (2007) xxx–xxx

Chemical Engineering Journal

www.elsevier.com/locate/cej

Oxidation of organic compounds in a microstructured catalytic reactor

I.Z. Ismagilov [a], E.M. Michurin [a], O.B. Sukhova [a], L.T. Tsykoza [a], E.V. Matus [a], M.A. Kerzhentsev [a], Z.R. Ismagilov [a,*], A.N. Zagoruiko [a], E.V. Rebrov [b], M.H.J.M. de Croon [b], J.C. Schouten [b]

[a] *Boreskov Institute of Catalysis SB RAS, Prospekt Akademika Lavrentieva 5, Novosibirsk 630090, Russia*
[b] *Eindhoven University of Technology, P.O. Box 513, 5600 MB Eindhoven, The Netherlands*

Abstract

A microstructured catalytic reactor for the oxidation of organic compounds has been fabricated from aluminum alloy AlMgSiCu1 (6082 series, Al51st). The catalyst section was assembled of 63 microstructured plates with catalytic coating. In each plate of 416 μm thickness, 45 semi-cylindrical microchannels of 208 μm in radius with a distance in between of 150 μm were electrodischarge machined. A porous alumina layer of 29 ± 1 μm thickness was produced on the plates by anodic oxidation. The resulting coatings were impregnated with an aqueous solution of copper dichromate followed by drying and calcination at 450 °C to produce active catalysts. Kinetics of deep oxidation of organic compounds *n*-butane, ethanol, and isopropanol was studied in the reactor at 150–360 °C and of 1,1-dimethylhydrazine (unsymmetrical dimethylhydrazine, UDMH) at 200–375 °C. Intermediate reaction products in the reactions of alcohols and UDMH oxidation were identified. For UDMH, these are methane, dimethylamine, formaldehyde 1,1-dimethylhydrazone, and 1,2-dimethyldiazene. Nitrogen atoms from the UDMH and N-containing intermediates were shown to convert mainly to N_2. Kinetic parameters of the reactions of *n*-butane and alcohols (rate constants and apparent activation energies) were calculated using kinetic modeling based on a modified method of quickest descent.

Keywords: Microstructured reactor; Electrodischarge machining; Anodic oxidation; Copper chromite; Catalytic combustion; *n*-Butane; Ethanol; Isopropanol; Unsymmetrical dimethylhydrazine; Kinetic modeling

1. Introduction

Since their first appearance in the 1990s, microstructured reactors (microreactors) have found the numerous areas of application in chemical research, development and production due to a number of their advantages compared to conventional reactors, such as miniature dimensions, more precise process control options, higher efficiency and safety [1,2]. One of the examples of processes successfully realized in catalytic microreactors is gas phase oxidation of various compounds, both partial and deep, with such goals as thermal energy production [3,4], generation of H_2 to be further used in the fuel cells and other types of power systems [5,6], purification of air from hazardous volatile organic compounds (VOCs) [7,8], synthesis of valuable chemicals [9,10], etc., as well as kinetic studies of the relevant reaction mechanisms [11–13]. In the latter case, one can rely upon such unique features of microreactors as high uniformity of temperature and concentration profiles among the microchannels, as well as possibility to function in the kinetic rate-controlling regime in wide temperature range [1,2]. Though the mechanisms of gas phase oxidation of several types of compounds in catalytic microreactors have been extensively studied, including hydrogen [11], ammonia [12], carbon monoxide [13], there is still very limited information about the oxidation of organic compounds [14,15].

In this paper, we present results on kinetic testing of a microstructured catalytic reactor with Cu–Cr oxide catalyst supported on anodized aluminum plates, developed for the study of total catalytic oxidation of organic compounds. Model compounds with high heat of combustion, such as *n*-butane ($\Delta H_{c,gas} = -2877.5$ kJ/mol), ethanol ($\Delta H_{c,liq} = -1367.6$ kJ/mol), isopropanol ($\Delta H_{c,liq} = -2006.9$ kJ/mol), and unsymmetrical dimethylhydrazine (UDMH, $\Delta H_{c,liq} = -1978.7$ kJ/mol) were selected for the study, representing different classes of organic compounds—alkanes, alcohols, and hydrazine derivatives. Special attention was paid to UDMH. This compound is a component of the high-energy propellant for liquid-fueled rockets used in Russia, China, and the U.S. UDMH is a highly toxic compound, close to chemical warfare agents according to its effect on biological objects. The

* Corresponding author. Tel.: +7 383 330 62 19; fax: +7 383 339 73 52.
E-mail address: zri@catalysis.ru (Z.R. Ismagilov).

1385-8947/$ – see front matter © 2007 Elsevier B.V. All rights reserved.
doi:10.1016/j.cej.2007.07.036

maximum allowable concentration for UDMH is 0.1 ppm. The U.S. National Institute for Occupational Safety and Health recommends an exposure limit of 0.06 ppm (0.15 mg/m^3) as a ceiling concentration [16]. In Russia the maximum allowable concentration is 0.1 mg/m^3 for working areas and 0.001 mg/m^3 for populated areas [17]. At the moment, there are no specialized industrial facilities for UDMH treatment, as well as no reliable treatment technologies for UDMH, its vapors, and waste containing it, that meet economical and environmental requirements [18]. We believe that for the treatment of hazardous organic compounds microreactor technology using catalytic oxidation is superior to others because of the possibilities, first, to prevent the onset of explosive reaction regimes in microchannels with large surface-to-volume ratios [9,11] and, second, to minimize the occurrence of "hot spots" by using high heat and mass transfer rates and short contact times characteristic for microreactors [12,13]. Furthermore, even if the microreactor fails, small quantity of chemicals released accidentally could be easily contained [1,2].

Microreactor was developed at the Eindhoven University of Technology in several steps using the methods of computational fluid dynamics (CFD) in order to obtain its overall dimensions, first, with the minimal pressure and temperature gradients and, second, with the maximally uniform flow distribution over the inlets of microchannels. The first task was accomplished by using the initially estimated kinetics of *n*-butane oxidation on individual microstructured plates [19]. For the second task, an original type of inlet flow diffuser was developed using the GAMBIT 2.0 and FLUENT 6.1 software [20], also accounting for some earlier diffuser developments [21]. The goal of this paper is to study oxidation kinetics of the above-mentioned organic compounds in the microreactor, with variation of initial concentrations of oxidized compounds and oxygen, gas hourly space velocity (GHSV) and catalyst temperature, and to apply kinetic modeling for the calculation of reaction rate parameters.

2. Experimental

2.1. Microstructured plates

The aluminum alloy AlMgSiCu1 (6082 series, Al51st) was selected as base microreactor material due to its high heat conductivity and the possibility to prepare a strong porous alumina layer by anodic oxidation. For the microreactor fabrication, Al51st plates with a length of 40 mm and a width of 26.62 mm were taken. These plates, being electrodischarge machined (EDM) by the method of "two incisions", provided a surface roughness of microchannel walls (Ra) below 2.0 μm, which was impossible to obtain with pure aluminum. In each plate of 416 μm thickness, 45 semi-cylindrical microchannels of 208 μm in radius with a distance in between of 150 μm were machined [19].

2.2. Coating development

Porous alumina layer was produced by anodic oxidation of the microstructured Al51st alloy plates in 3.5 wt.% oxalic acid solution at 1.0 ± 0.1 °C for 23 h under current-controlled conditions. The produced alumina layer has cylindrical pores with an average diameter of ca. 40 ± 5 nm and a uniform thickness of 29 ± 1 μm. The used method of anodic oxidation is described in detail in [19].

2.3. Catalyst preparation

Method of catalyst preparation was developed and optimized in [19]. Microstructured Al51st alloy plates with the anodic alumina layer were degreased with acetone and calcined at 300 °C. Catalysts were prepared by impregnation of these plates by an aqueous solution of copper dichromate (410 mg/ml) for 20 min. Then, the excess solution was wiped off with filter paper, followed by drying under an IR lamp for 1 h and calcination at 450 °C for 4 h. Characterization of the catalytic coatings by X-ray photoelectron spectroscopy (XPS), electron spectroscopy of diffuse reflectance (ESDR), chemical analysis, and X-ray microprobe analysis showed that the catalyst contains uniformly distributed Cu(II) and Cr(III) oxides having total content of 5 wt.% with respect to the mass of alumina layer [19].

2.4. Microreactor assembling

Microreactor catalyst section is assembled from 63 microstructured plates with catalytic coatings. This section has a size of ca. 27 mm × 34 mm × 40 mm and contains 2835 semi-cylindrical microchannels. Microreactor has inlet section with a specially designed flow diffuser to achieve maximally uniform reaction mixture velocity distribution at the entrance of each microchannel [20,22] and an outlet quench section cooled by water and ethylene glycol to decrease the temperature of gases leaving catalyst section, thus preventing subsequent homogeneous gas phase reactions (Fig. 1).

2.5. Experimental setup

Microreactor is connected to an automatic PC-interfaced experimental setup equipped with the digital mass-flow controllers (Bronkhorst Hi-Tec) for preparation and supply of reaction mixtures and with the temperature controllers. Supply of liquid vapors was performed using saturator with helium as a carrier gas. All the gas lines are placed inside air thermostat heated to 60 °C, where temperature control of all the principal units is provided by a controller "Varta TP 403" and registrator "Oven UKT 38" using chromel–alumel thermocouples with an accuracy of 0.1 °C. Temperature control in the resistively heated microreactor is performed by a controller "West 6100+" and registrator "Voltcraft K204 Datalogger" via another group of chromel–alumel thermocouples, also with an accuracy of 0.1 °C. Prior to each daily experiment, catalyst in the microreactor has undergone oxidative pretreatment cycle for 1 h using approximately the same mixture composition of O_2 and inert gas (N_2 for butane, ethanol, and isopropanol; He for UDMH) as afterwards in the experiment with addition of organic compound to be oxidized, and at the maximal value of temperature to be reached in experiment.

Please cite this article in press as: I.Z. Ismagilov, et al., Oxidation of organic compounds in a microstructured catalytic reactor, Chem. Eng. J. (2007), doi:10.1016/j.cej.2007.07.036

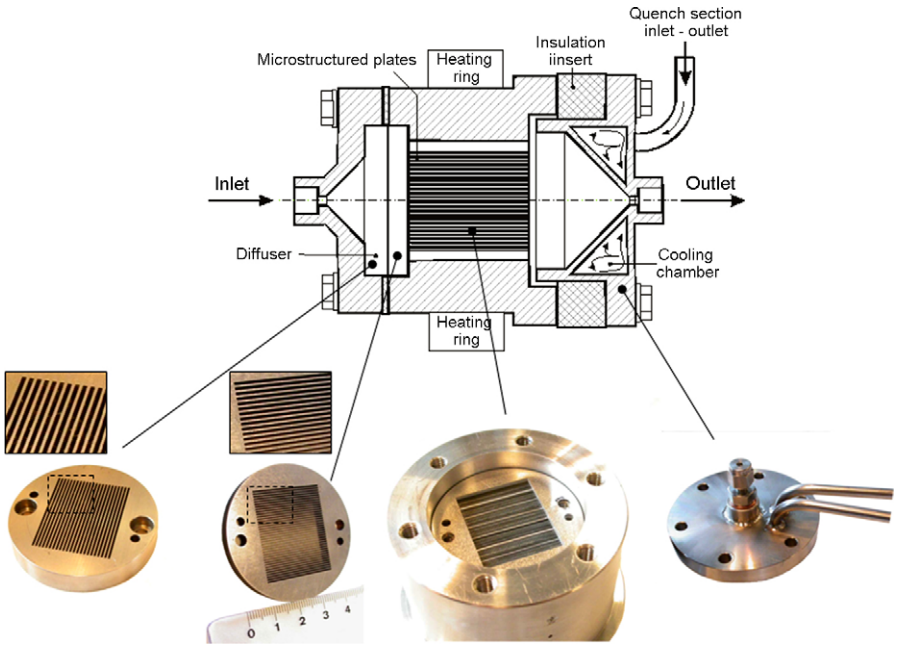

Fig. 1. Cross-section of the catalytic microstructured reactor with photos of its individual parts: vertical and horizontal microchannel sections of inlet flow diffuser, inlet region of microstructured catalytic plates assembled in the housing, quench section with coolant inlet and outlet.

Analysis of the reaction mixtures before and after reactor was performed with a gas chromatograph "Kristall-2000M" equipped with simultaneously operating thermal conductivity detector (TCD) and flame ionization detector (FID).

On the TCD, a stainless steel chromatographic column with diameter of 3 mm and length of 2 m (3 mm × 2 m) with active carbon "SKT" was used for separation and analysis of CO_2 and N_2O. Similar column with NaX molecular sieves was used for the analysis of O_2, N_2, and CO.

For analysis of *n*-butane and alcohols with FID, a stainless steel chromatographic column of 3 mm × 1 m with the sorbent "HayeSep Q-S" was used. Analysis of unsymmetrical dimethylhydrazine and products of its oxidation was performed using a stainless steel column of 2 mm × 3 m with a "Tenax" sorbent.

3. Results and discussions

3.1. *n*-Butane oxidation

Oxidation of *n*-butane with air was studied at initial concentration of 0.2 mmol/l, GHSV in the range of 1600–10,700 h^{-1}, temperature 150–360 °C. The dependencies of *n*-butane conversion on space velocities and temperatures are shown in Fig. 2. Comparison of curves 2 and 3 in Fig. 2 shows that presence of the inlet flow diffuser improves *n*-butane conversion by several % in the whole studied temperature range (example at GHSV = 5360 h^{-1}). This is in qualitative accordance with what is expected based on modeling of such diffuser [20,22] and already tested experimentally in the similar types of microreactors [21]. Oxidation of *n*-butane proceeds with the formation of deep oxidation products CO_2 and H_2O in the whole temperature range (Fig. 3). No products of partial oxidation were detected.

It is known from literature that the Langmuir–Hinshelwood (L–H) type of mechanism is often assumed for the reactions of heterogeneous catalytic oxidation of gaseous organic compounds, such as alkanes, alcohols, and nitrogen-containing ones (see for example [19] and references therein). By applying the L–H approach, the reaction rate order of *n*-butane for its deep catalytic oxidation in the excess of oxygen is close to unity, while for the oxygen this order is close to zero [23,24]. In the case of our microreactor, the observed dependencies of *n*-butane conversion on GHSV (Fig. 2), temperatures (Fig. 3) and initial concentration of oxygen were found to be in agreement with the first and almost zeroth reaction rate orders of *n*-butane and oxygen, respectively, and the rate constants

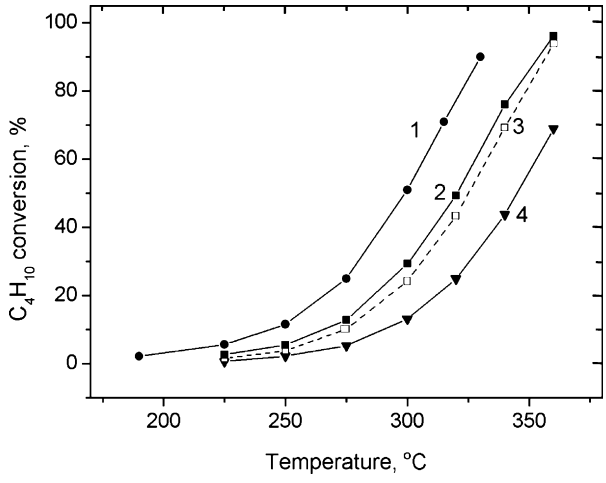

Fig. 2. *n*-Butane conversion vs. temperature upon oxidation with air in the microreactor at initial *n*-butane concentration 0.2 mmol/l and different GHSV values: (1) 1600 h^{-1}, (2) 5360 h^{-1}, (3) 5360 h^{-1} without inlet flow diffuser, (4) 10,700 h^{-1}; GHSV calculated with respect to the volume of catalyst coating.

Please cite this article in press as: I.Z. Ismagilov, et al., Oxidation of organic compounds in a microstructured catalytic reactor, Chem. Eng. J. (2007), doi:10.1016/j.cej.2007.07.036

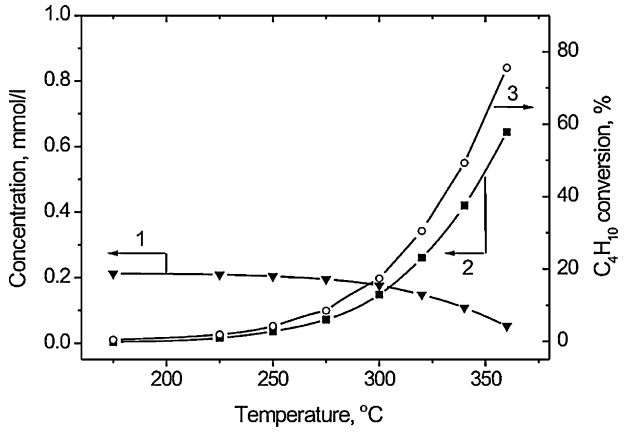

Fig. 3. *n*-Butane concentration (1), CO_2 concentration (2), and *n*-butane conversion (3) vs. temperature upon oxidation in the microreactor with air at initial *n*-butane concentration 0.2 mmol/l and GHSV = 5360 h^{-1}.

k were accordingly calculated using the plug flow approximation.

The Arrhenius plots of calculated dependencies of ln *k* versus 1/*T* for different values of GHSV in the microreactor are shown in Fig. 4 and compared to the one of reference pelletted catalyst 17 wt.%$CuCr_2O_4/Al_2O_3$ with a granule size of 1.0–1.6 mm. The results show that at low temperatures (below 280 °C, on the right-hand side from respective projection on 1/*T* axis) activity of the pelletted catalyst is 1.5–2 times more than that of the microstructured catalyst containing 5 wt.% active component. At higher temperatures the microstructured catalyst exhibits higher efficiency probably due to the absence of diffusion limitations (this is commented further), while the presence of such limitations (internal and external) may affect the reaction rate in case of pelletted catalyst at temperatures above 280 °C. This can be seen in Fig. 4 from the decrease of slope of curve 4 by a factor of 2 on the left-hand side from respective projection on 1/*T* axis. The upper temperature limit for the pelletted catalyst shown in Fig. 4 is 375 °C, and for the microstructured catalyst it is 325 °C. The latter temperature is shown as the limiting one only for the graphical simplicity reasons because, in fact, curves 1–3 hold almost constant slopes (which, in turn, can be interpreted as the continuing absence of diffusion limitations) up to the highest temperature used for *n*-butane oxidation experiments in microreactor, 360 °C (Fig. 3). For the experimental safety reasons, this temperature is approximately 200 °C less than the melting point of Al51st alloy (555 °C) used for microreactor fabrication.

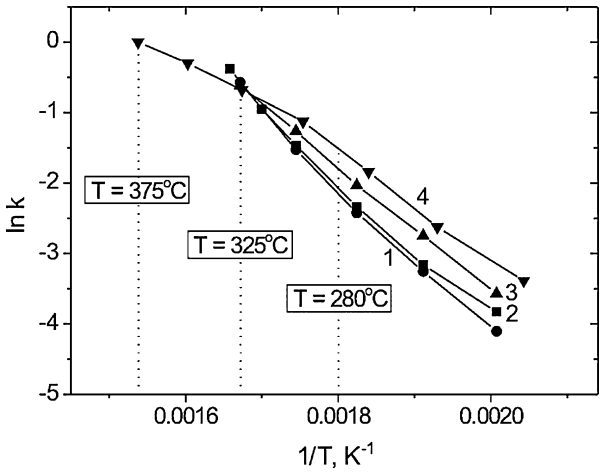

Fig. 4. Temperature dependencies of ln *k* upon *n*-butane oxidation with air at initial *n*-butane concentration 0.2 mmol/l: (1) microreactor, GHSV = 10,700 h^{-1}, (2) microreactor, GHSV = 5360 h^{-1}, (3) microreactor, GHSV = 1600 h^{-1}, (4) pelletted catalyst 17 wt.%$CuCr_2O_4/\gamma$-Al_2O_3, GHSV = 1000 h^{-1}. Projections on 1/*T* axis by dotted lines: temperatures of 280 °C (0.0018 K^{-1}), 325 °C and 375 °C.

Actually, we have shown previously [19] that for the reaction of butane oxidation over pelletted catalyst the Weisz modulus ψ is below 0.1 at 300 °C, indicating the absence of concentration gradients inside granule, but at higher temperatures 350–400 °C this value is over 0.1, which is the evidence that internal diffusion has inhibiting effect on the reaction rate. Calculations show that the value of Weisz modulus remains below 0.1 for the microstructured catalyst at temperatures up to 500 °C, proving that microstructured reactors of this type allow to study intrinsic kinetics in a wide temperature range.

Calculated apparent activation energies of *n*-butane oxidation are within the range of 71–84 kJ/mol, which is close to the literature data [23,24].

3.2. Ethanol oxidation

Ethanol oxidation in the microreactor was studied at ethanol initial concentration in the proximity of 0.45 mmol/l (1 vol.%), oxygen initial concentrations in the range of 4.5–31.2 mmol/l (10–70 vol.%), GHSV in the range of 1600–10,700 h^{-1}, temperature 150–325 °C.

Results of the experiments are shown in Figs. 5–7. At temperatures below 300 °C, the reaction products contain CO_2 and also the products of partial oxidation—acetaldehyde and CO. At higher temperature (325 °C) mainly CO_2 is formed, with concentrations corresponding to the stoichiometry of ethanol deep oxidation. No products of partial oxidation were detected at this temperature (Fig. 5). To verify the results of GC analysis for the reaction mixture of ethanol and its oxidation products, carbon balance data are also included in Fig. 5 for all the temperatures

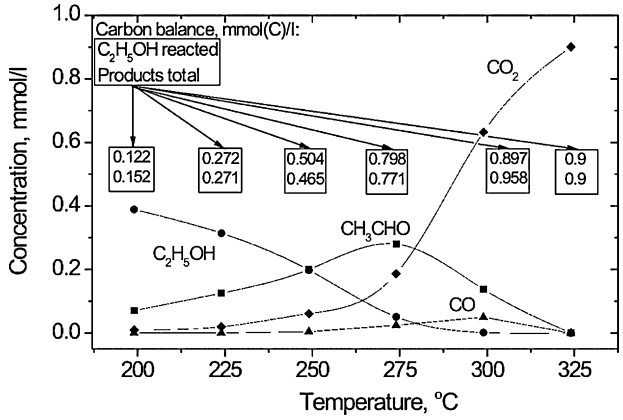

Fig. 5. Temperature dependencies of product concentrations upon ethanol oxidation in the microreactor. Initial concentrations: ethanol 0.45 mmol/l, O_2 8.9 mmol/l (20 vol.%); GHSV = 5360 h^{-1}.

Please cite this article in press as: I.Z. Ismagilov, et al., Oxidation of organic compounds in a microstructured catalytic reactor, Chem. Eng. J. (2007), doi:10.1016/j.cej.2007.07.036

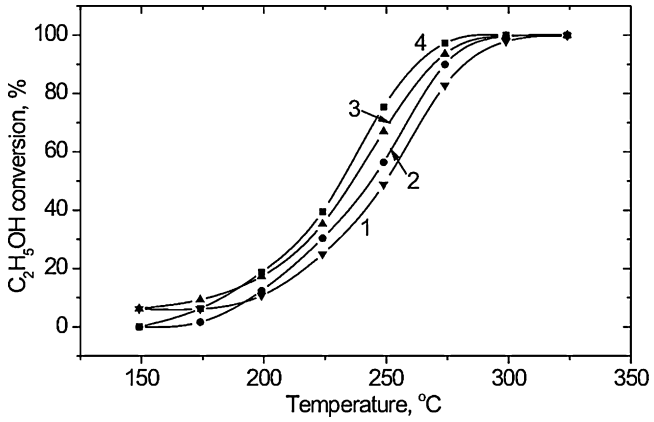

Fig. 6. Temperature dependencies of ethanol conversion upon its oxidation in the microreactor. Initial concentration of ethanol approximately 0.45 mmol/l (1 vol.%). Initial O_2 concentration variable: (1) 4.5 mmol/l (10 vol.%) (ethanol 1.3 vol.%), (2) 8.9 mmol/l (20 vol.%) (ethanol 1.1 vol.%), (3) 22.3 mmol/l (50 vol.%) (ethanol 1.3 vol.%), (4) 31.2 mmol/l (70 vol.%) (ethanol 1.1 vol.%); GHSV = 5360 h^{-1}.

where measurements were made, showing comparison of carbon atom concentrations (mmol/l) in the reacted C_2H_5OH versus total in the products formed (CO_2, CO, and CH_3CHO). Carbon balance appears in overall satisfactory, within relative 10% for all the temperatures except for those around 200 °C. The latter largest deviation can be explained by the uncertainties in GC analysis of products at low concentrations.

Experiments with variation of initial oxygen concentration showed that ethanol conversion increases with oxygen concentration in the medium- and high-temperature range of 200–325 °C (Fig. 6). Some deviations from this general trend are observed in the low-temperature range (150–175 °C), which will be explained further by referring to variations (1.1–1.3 vol.%) in the initial ethanol concentration. Thus, by contrast to *n*-butane, the reaction rate of ethanol oxidation depends both on the concentrations of ethanol and oxygen.

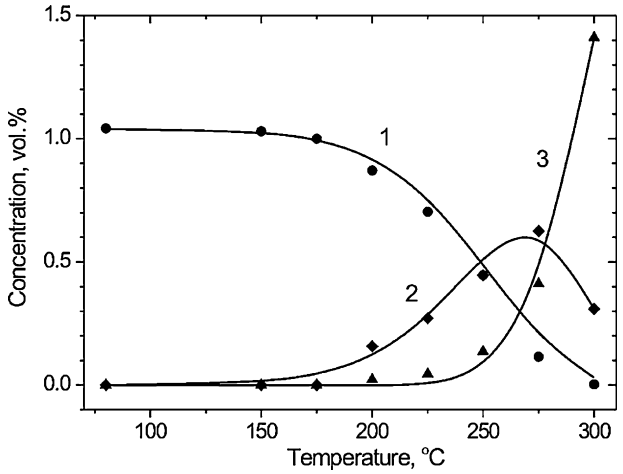

Fig. 7. Composition of reaction products vs. temperature upon ethanol oxidation in the microreactor. Initial concentrations: ethanol 0.45 mmol/l, O_2 8.9 mmol/l (20 vol.%); GHSV = 5360 h^{-1}; (1) ethanol, (2) acetaldehyde, (3) carbon dioxide. The points refer to the experimental data and the lines refer to the results of modeling.

Formation of acetaldehyde as the intermediate reaction product during ethanol oxidation over conventional noble metal and oxide catalysts was as reported previously [25–28]. On the noble metal catalysts Pt/Al_2O_3 [25], Pd/CeO_2–TiO_2 [28], in addition to acetaldehyde, the formation of acetic acid and traces of ethyl acetate and ethylene was observed.

The authors of [26,28] used consecutive reaction schemes for the interpretation of observed results. According to literature, reaction includes the following steps:

$$C_2H_5OH + \tfrac{1}{2}O_2 \rightarrow CH_3CHO + H_2O \quad (1)$$

$$CH_3CHO + \tfrac{5}{2}O_2 \rightarrow 2CO_2 + 2H_2O \quad (2)$$

To obtain formal kinetic equations for the reactions (1) and (2) which would agree with the experimental data, we used software developed at the Boreskov Institute of Catalysis [29], based on a modified method of quickest descent. The quality of experimental data fit for every tested hypothetic kinetic model was estimated by two parameters—the mean absolute deviation of concentrations and the relative confidence interval for model parameters. Criterion of the correctness of obtained results is the invariability of values of the reaction constants for different experimental series.

Based on the analysis of experimental data and on the assumption of consecutive mechanism ((1) and (2)), we suggest the following kinetic model:

$$W_1 = k_1 C_{C_2H_5OH} C_{O_2}^N \quad (3)$$

$$W_2 = k_2 C_{CH_3CHO} C_{O_2}^M \quad (4)$$

where W_i ($i = 1, 2$) are the reaction rates, k_i the apparent rate constants including the product of pre-exponent and activation energy terms $k_i = k_{0,i} \exp(-E_i/RT)$, C_j the steady-state concentration of reagent j in the gas phase, M and N are the reaction rate orders by oxygen.

Our calculations showed that the reaction rate orders with respect to ethanol and acetaldehyde were close to unity. As the first step, model with the first orders with respect to oxygen (M and N) was proposed (Model 1 in Table 1), but the data fit quality appeared to be only moderately good.

Much better results were obtained with Model 2, where reaction orders with respect to oxygen were set as model parameters to be defined. It was shown that the best fit with experimental results was found for Model 2 at values $N = 0.4$ and $M = 0.8$. However, we also tried Model 3 with fixed orders of 0.5 and 1, respectively. Fitting quality in this case was only slightly worse than that for Model 2, but Model 3 seems to be more physically sound because it is more suited to the logic of mass action law and therefore it should be preferred. No special analysis of inter-correlation between kinetic constants was performed, though, to our experience, in case of good quality of solution (low values of relative confidence interval, as it is seen in Table 1) the role of such inter-correlation is not dramatic anyway. All available data points were used simultaneously for the parameter fit. In the given case, when all experimental data belong to similar type of experiments, such approach is reasonable.

Please cite this article in press as: I.Z. Ismagilov, et al., Oxidation of organic compounds in a microstructured catalytic reactor, Chem. Eng. J. (2007), doi:10.1016/j.cej.2007.07.036

Table 1
Kinetic parameters for reaction of ethanol oxidation

Model	$k_{0,1}$ (s^{-1})	$k_{0,2}$ (s^{-1})	E_1 (kJ/mol)	E_2 (kJ/mol)
1	$(9.64 \pm 1.8) \times 10^9$	$(1.48 \pm 0.19) \times 10^{14}$	92.2 ± 1.6	143.5 ± 1.1
2	$(8.56 \pm 0.06) \times 10^7$	$(9.61 \pm 0.69) \times 10^{13}$	75.8 ± 0.6	142.3 ± 0.8
3	$(2.06 \pm 0.2) \times 10^8$	$(3.33 \pm 0.4) \times 10^{15}$	79.1 ± 0.8	157.7 ± 1.0

Model	N_{O_2}	M_{O_2}	Mean absolute deviation of concentrations (%)	Mean relative confidence interval for model parameters (%)
1	1	1	0.064	1.25
2	0.41 ± 0.04	0.82 ± 0.03	0.044	5.07
3	0.5	1	0.047	0.83

The earlier mentioned behavior of ethanol conversion curves in the low-temperature range of Fig. 6 can be explained by the dominating effect of reaction step (1) described by Eq. (3) where, due to the low conversion, steady-state concentration of ethanol is high, close to initial one in the proximity of 1 vol.% (compare with Fig. 5). For the curves 1 and 3, initial concentration of ethanol is 1.3 vol.%, while for the curves 2 and 4, it is 1.1 vol.%, and thus curves 1 and 3 show higher conversion than curves 2 and 4 because of the higher reaction rates for curves 1 and 3, according to the mass action law principle in Eq. (3). Also, based on Eq. (3) applied in the low-temperature range, variation of the initial oxygen concentration seems to make only minor contribution to the ethanol conversion, which can be explained by lower reaction rate order of oxygen compared to ethanol, as well as by low activity of the catalyst at these temperatures. Following the same logic, in the medium- and high-temperature range of Fig. 6, where the steady-state concentration of ethanol is decreasing and the one of acetaldehyde is increasing with a maximum at 275 °C (Fig. 5), conversion of ethanol shows correlation with initial oxygen concentration, according to step (2) described by Eq. (4), where the reaction rate order of oxygen is close to the one of acetaldehyde.

Fig. 7 illustrates good correspondence of the experimental and above outlined Model 3 data which can be used for engineering design of the microreactor. It should be noted that this model represents only a simplified reaction scheme and not the detailed gas-surface mechanism, which will require more experimental data.

3.3. Isopropanol oxidation

Isopropanol oxidation in the microreactor was studied at isopropanol initial concentration of 0.45 mmol/l, oxygen initial concentration in the range of 4.5–31.2 mmol/l (10–70 vol.%), GHSV in the range of 1600–10,700 h^{-1}, temperature 175–325 °C.

Oxidation of isopropanol at $T < 325$ °C proceeds also with formation of the intermediate products of partial oxidation—acetone and CO. In addition, a parallel reaction of isopropanol dehydration with propylene formation takes place (Fig. 8). At $T > 325$ °C mainly the products of deep oxidation—CO_2 and H_2O are formed.

These results agree with literature data [30,31]. The authors of [30] studied chemisorption, decomposition, and oxidation of isopropanol on pure metal oxide catalysts. It was shown that all the catalysts with the exception of Fe_2O_3 and TiO_2 exhibited extremely high selectivity at low temperatures (200 °C) to either RedOx or acidic reaction route products. Redox surface sites yield acetone and acidic surface sites yield propylene. According to [30], Cu(II) and Cr(III) oxides in the microstructured catalyst should be responsible for the acetone formation and acidic sites on the alumina support should catalyze the reaction of isopropanol dehydration with the formation of propylene. At higher temperatures, these products are oxidized with the formation of CO_2 and water.

Literature data and our experimental results allow to propose the following overall simplified reaction scheme for isopropanol oxidation:

$$C_3H_7OH \rightarrow C_3H_6 + H_2O \quad (5)$$

$$C_3H_7OH + \tfrac{1}{2}O_2 \rightarrow C_3H_6O + H_2O \quad (6)$$

$$C_3H_6 + \tfrac{9}{2}O_2 \rightarrow 3CO_2 + 3H_2O \quad (7)$$

$$C_3H_6O + 4O_2 \rightarrow 3CO_2 + 3H_2O \quad (8)$$

In this scheme, neglecting the small amounts of CO formed, we assume that isopropanol is consumed in the parallel reaction of formation of two intermediates—acetone and propylene, which are further oxidized to CO_2 and water. Based on the approach similar to one used above for modeling ethanol oxida-

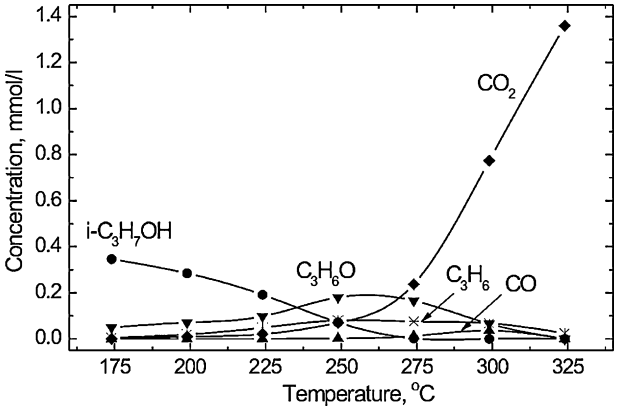

Fig. 8. Temperature dependencies of product concentrations upon isopropanol oxidation in the microreactor. Initial concentrations: isopropanol 0.35 mmol/l, O_2 8.9 mmol/l (20 vol.%); GHSV = 5360 h^{-1}.

Table 2
Kinetic parameters for reaction of isopropanol oxidation

$k_{0,1}$ ($\times 10^7$ s^{-1})	8.32 ± 1.35
$k_{0,2}$ ($\times 10^7$ s^{-1})	4.58 ± 0.07
$k_{0,3}$ ($\times 10^9$ s^{-1})	6.75 ± 1.47
$k_{0,4}$ ($\times 10^{20}$ s^{-1})	1.39 ± 0.32
E_1 (kJ/mol)	81.1 ± 1.4
E_2 (kJ/mol)	71.6 ± 1.4
E_3 (kJ/mol)	95.7 ± 1.8
E_4 (kJ/mol)	210.3 ± 2.1

tion, the following rate equations are proposed:

$$W_1 = k_1 C_{C_3H_7OH} \quad (9)$$

$$W_2 = k_2 C_{C_3H_7OH} C_{O_2}^{0.5} \quad (10)$$

$$W_3 = k_3 C_{C_3H_6} C_{O_2} \quad (11)$$

$$W_4 = k_4 C_{C_3H_6O} C_{O_2} \quad (12)$$

where W_i ($i = 1, 2, 3, 4$) are the reaction rates, k_i the apparent rate constants including the product of pre-exponent and activation energy terms $k_i = k_{0,i} \exp(-E_i/RT)$, C_j is the steady-state concentration of reagent j in the gas phase, the reaction rate orders by oxygen are either 0, 0.5 or 1.

The calculated kinetic parameters for one of the isopropanol oxidation models are given in Table 2. Good correspondence of the modeling and experimental data is illustrated by Fig. 9 (mean deviation of calculated and experimental data was equal to 0.065%, relative confidence interval for the model parameters—1.6%). As in the case of ethanol, it should be noted that these results can be used for the calculation of concentrations of isopropanol oxidation products under different conditions in the microreactor with Cu–Cr oxide catalyst.

3.4. Unsymmetrical dimethylhydrazine oxidation

Unsymmetrical dimethylhydrazine (UDMH) oxidation in the microreactor was studied at an UDMH initial concentration of 0.16–0.4 mmol/l, oxygen initial concentration in the range 8.9–31.2 mmol/l (20–70 vol.%), GHSV in the range of 5360–10,700 h^{-1}, temperature 200–375 °C. UDMH vapors were supplied from the saturator with a helium flow and diluted with helium and oxygen in the mixer to form initial reaction mixtures. Helium was chosen for the reason to measure concentrations of nitrogen formed from UDMH.

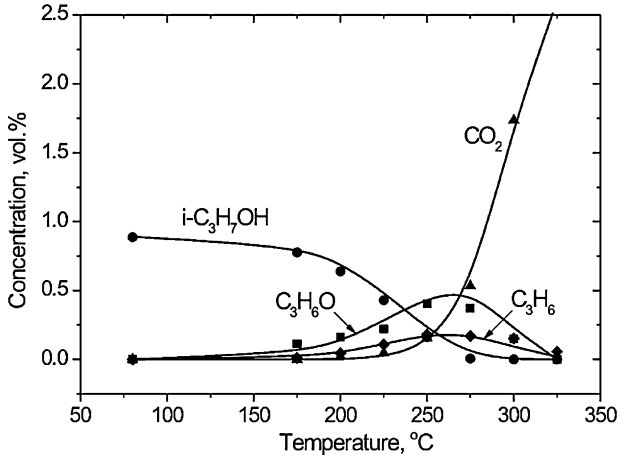

Fig. 9. Composition of reaction products vs. temperature upon isopropanol oxidation in the microreactor. Initial concentrations: isopropanol 0.35 mmol/l, O_2 8.9 mmol/l (20 vol.%); GHSV = 5360 h^{-1}. The points refer to the experimental data and the lines refer to the results of modeling.

Table 3
Concentrations of products of UDMH oxidation (C_j) and total concentrations of carbon ($C_{\Sigma C}$) and nitrogen ($C_{\Sigma N}$) (mmol/l) at different temperatures

T (°C)	C_{CH_4}	C_{DMA}	C_{DDA}	C_{MDMH}	C_{CO_2}	C_{N_2}	$C_{\Sigma C}$	$C_{\Sigma N}$
200	0.0039	0.12	0.03	0.16	0.028	0.11	0.652	0.720
240	0.002	0.156	0.03	0.09	0.045	0.12	0.599	0.636
260	0.002	0.014	0.12	0.10	0.063	0.14	0.533	0.734
300	0.0005	0.0007	0.16	0.02	0.18	0.17	0.541	0.701

Initial concentrations: UDMH 0.4 mmol/l, O_2 8.9 mmol/l (20 vol.%); GHSV = 5360 h^{-1}.

First experiments which were performed at UDMH initial concentration of 0.4 mmol/l, oxygen initial concentration 8.9 mmol/l (20 vol.%), GHSV = 5360 h^{-1}, and temperature in the range of 200–300 °C, showed that UDMH is completely converted to oxidation products already at 200 °C, where its residual concentration was below 0.001 mmol/l. Oxidation products contain CH_4, dimethylamine $(CH_3)_2NH$—DMA, 1,2-dimethyldiazene CH_3–N=N–CH_3—DDA, formaldehyde dimethylhydrazone $(CH_3)_2N$–N=CH_2 (alias methylenedimethylhydrazine—MDMH), CO_2 and nitrogen. Composition of the reaction products is similar to that observed in [32–34] for UDMH oxidation by air over pelletted catalysts. At the temperature of 300 °C only 23% of UDMH was converted to CO_2. Mass balance shows that about 20–30% of carbon and 10–20% of nitrogen should be in the form of some unidentified products (Table 3). Actually, it was found that in addition to the above-listed products, formation of the yellow resinous matter took place, which was deposited in the reactor outlet section and in the outlet tube, eventually blocking the gas passage. This resin could be easily removed by washing with ethanol.

Further experiments were performed at lower UDMH initial concentration (0.16 and 0.3 mmol/l), at higher oxygen initial concentration (9.7 and 34.8 mmol/l (21.7 and 78 vol.%)) and in temperature range extended to 375 °C to reduce formation of the resin. Results of the experiments are given in Figs. 10 and 11.

Results show that at higher temperatures (350–375 °C) the dominating products formed from UDMH are CO_2, N_2 and N_2O (corresponding amounts of H_2O were not analyzed). Small amounts of methane (ca. 0.01 mmol/l) were also detected. Mass balance of carbon and nitrogen is within the accuracy of GC analysis and corresponds to practically total oxidation of UDMH to CO_2. The formed methane is a rather stable compound and its complete oxidation is expected to take place at temperatures over 400 °C. Nitrogen in UDMH is transformed mainly to N_2 with a selectivity of 90% and to N_2O with a selectivity of 10%.

These results generally agree with those previously obtained in experiments performed with a pelletted catalyst of an analogous composition 20 wt.%$Cu_xMg_{1-x}Cr_2O_4/\gamma$-$Al_2O_3$ [32–34].

Please cite this article in press as: I.Z. Ismagilov, et al., Oxidation of organic compounds in a microstructured catalytic reactor, Chem. Eng. J. (2007), doi:10.1016/j.cej.2007.07.036

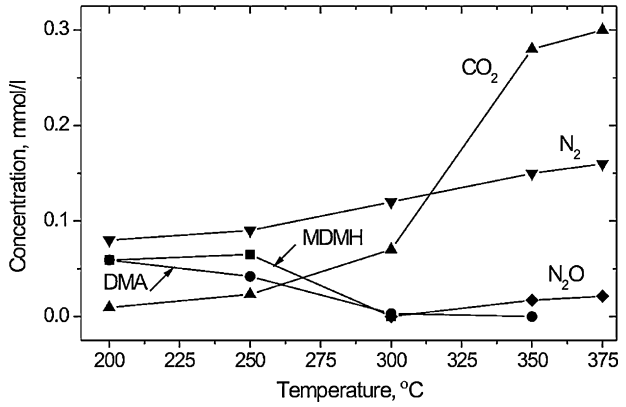

Fig. 10. Temperature dependencies of concentrations of UDMH oxidation products in the microreactor. Initial concentrations: UDMH 0.16 mmol/l in He–O_2 mixture, O_2 9.7 mmol/l (21.7 vol.%); GHSV = 11570 h^{-1}.

Similarly, practically complete UDMH conversion to CO_2 and N_2 was attained over the pelletted catalyst at temperatures over 300 °C and comparable amounts of N_2O and CH_4 were found in the reaction products.

Methane, MDMH, DMA, and DDA are present in the reaction products in wide temperature range. They are already formed in significant quantities at 200 °C. Based on the presence of these compounds at the reactor outlet, and the previous results [32–34], it is possible to suggest a probable L–H type reaction scheme of UDMH heterogeneous catalytic oxidation, proceeding via the following steps:

$$(CH_3)_2N–NH_2 + [] \rightarrow [(CH_3)_2N–NH_2]_{ads} \quad (13)$$

$$[(CH_3)_2N–NH_2]_{ads} + [O]_{ads} \rightarrow [(CH_3)_2N=N]_{ads} + [H_2O]_{ads} \quad (14)$$

$$[(CH_3)_2N=N]_{ads} + [(CH_3)_2N=N]_{ads} \rightarrow [(CH_3)_2N–N=CH_2]_{ads} + [CH_3N=NH]_{ads} \quad (15)$$

$$[(CH_3)_2N–N=CH_2]_{ads} \rightarrow CH_3–N=N–CH_3 + [CH_2]_{ads} \quad (16)$$

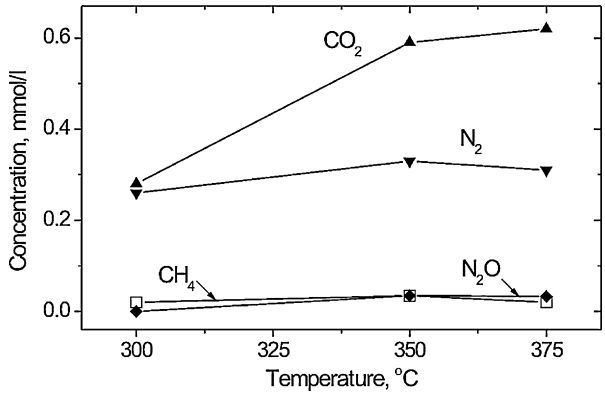

Fig. 11. Temperature dependencies of concentrations of UDMH oxidation products in the microreactor. Initial concentrations: UDMH 0.3 mmol/l in He–O_2 mixture, O_2 34.8 mmol/l (78 vol.%); GHSV = 5360 h^{-1}.

$$[(CH_3)_2N–N=CH_2]_{ads} \rightarrow (CH_3)_2N–N=CH_2 + [] \quad (17)$$

$$4[(CH_3)_2N–N=CH_2]_{ads} + 11[O]_{ads} \rightarrow 4(CH_3)_2NH + 4CO_2 + 2H_2O + N_2 + N_2O + 15[] \quad (18)$$

$$[CH_3N=NH]_{ads} \rightarrow CH_4 + N_2 + [] \quad (19)$$

$$2[CH_3N=NH]_{ads} + 9[O]_{ads} \rightarrow 2CO_2 + 4H_2O + N_2 + N_2O + 11[] \quad (20)$$

where [ ] denotes the active site of catalyst.

The proof of this mechanism and its elucidation still requires additional research.

4. Conclusions

Kinetics of deep oxidation of organic compounds (*n*-butane, ethanol, and isopropanol) was studied in a microstructured reactor with Cu–Cr oxide catalyst in the temperature range of 150–360 °C. Intermediate reaction products in the reactions of alcohols oxidation were identified and reaction schemes were proposed. Kinetic parameters of the reactions (rate constants and apparent activation energies) were estimated using kinetic modeling based on a modified method of quickest descent.

Kinetic studies of oxidation of unsymmetrical dimethylhydrazine (UDMH) were performed in the temperature range of 200–375 °C. Intermediate reaction products were identified (methane, dimethylamine, formaldehyde 1,1-dimethylhydrazone, and 1,2-dimethyldiazene) and a probable reaction scheme was proposed. UDMH was shown to convert mainly to N-containing organic compounds at temperatures below 300 °C, but mainly to CO_2, H_2O, and N_2 at higher temperatures of 350–375 °C. In summary, this work provides one of illustrative examples how the microreactors can be successfully used for catalytic oxidation of organic compounds, which can be applied for energy production, safe and efficient abatement of hazardous VOCs, as well as for kinetic studies of these reactions.

Acknowledgments

The joint support of this work by the Netherlands Organization for Scientific Research (NWO) and Russian Foundation for Basic Research (RFBR) in the frame of Project 047.15.007. is gratefully acknowledged.

References

[1] G. Kolb, V. Hessel, Chem. Eng. J. 98 (2004) 1–38.
[2] L. Kiwi-Minsker, A. Renken, Catal. Today 110 (2005) 2–14.
[3] K. Schubert, J. Brandner, M. Fichtner, G. Linder, U. Schugulla, A. Wenka, Microscale Thermophys. Eng. 5 (2001) 17–39.
[4] J. Vican, B.F. Gajdeczko, F.L. Dryer, D.L. Milius, I.A. Aksay, R.A. Yetter, Proc. Combust. Inst. 29 (2002) 909–916.
[5] A.Y. Tonkovich, S. Perry, Y. Wang, D. Qiu, T. LaPlante, W.A. Rogers, Chem. Eng. Sci. 59 (2004) 4819–4824.

Please cite this article in press as: I.Z. Ismagilov, et al., Oxidation of organic compounds in a microstructured catalytic reactor, Chem. Eng. J. (2007), doi:10.1016/j.cej.2007.07.036

[6] G.-G. Park, S.-D. Yim, Y.-G. Yoon, C.-S. Kim, D.-J. Seo, K. Eguchi, Catal. Today 110 (2005) 108–113.
[7] I. Yuranov, N. Dunand, L. Kiwi-Minsker, A. Renken, Appl. Catal. B 36 (2002) 183–191.
[8] J. Łojewska, A. Kołodziej, P. Dynarowicz-Łątka, A. Wesełucha-Birczyńska, Catal. Today 101 (2005) 81–91.
[9] Y.S.S. Wan, A. Gavrilidis, K.L. Yeung, Trans. IChemE A 81 (2003) 1–7.
[10] S. Walter, S. Malmberg, B. Schmidt, M.A. Liauw, Chem. Eng. Res. Des. A 83 (2005) 1019–1029.
[11] M.T. Janicke, H. Kestenbaum, U. Hagendorf, F. Schüth, M. Fichtner, K. Schubert, J. Catal. 191 (2000) 282–293.
[12] E.V. Rebrov, S.A. Duinkerke, M.H.J.M. de Croon, J.C. Schouten, Chem. Eng. J. 93 (2003) 201–216.
[13] S.K. Ajmera, C. Delattre, M.A. Schmidt, K.F. Jensen, J. Catal. 209 (2002) 401–412.
[14] Y. Suzuki, J. Saito, N. Kasagi, Jpn. Soc. Mech. Eng. Int. J. B 3 (2004) 522–527.
[15] R.M. Tiggelaar, P.W.H. Loeters, P. van Male, R.E. Oosterbroek, J.G.E. Gardeniers, M.H.J.M. de Croon, J.C. Schouten, M.C. Elwenspoek, A. van den Berg, Sens. Actuators 112 (2004) 77.
[16] U.S. Department of Labor, Occupational Safety & Health Administration, Chemical Sampling Information, 1,1-dimethylhydrazine, http://www.osha.gov/dts/chemicalsampling/data/CH_236300.html.
[17] Chemical Search Engine, 1,1-dimethylhydrazine, http://www.chemindustry.com/apps/search?search_term=unsymmetrical-Dimethylhydrazine.
[18] E.W. Schmidt, Hydrazine and Its Derivatives: Preparation, Properties and Applications, 2nd ed., Wiley, New York, 2001.
[19] I.Z. Ismagilov, R.P. Ekatpure, L.T. Tsykoza, E.V. Matus, E.V. Rebrov, M.H.J.M. de Croon, M.A. Kerzhentsev, J.C. Schouten, Catal. Today 105 (2005) 516–528.
[20] M.J.M. Mies, E.V. Rebrov, M.H.J.M. de Croon, J.C. Schouten, I.Z. Ismagilov, Inlet section for micro-reactor, Dutch Patent P6001475PCT (2005).
[21] M.J.M. Mies, E.V. Rebrov, M.H.J.M. de Croon, J.C. Schouten, Chem. Eng. J. 101 (2004) 225–235.
[22] I.Z. Ismagilov, R.P. Ekatpure, E.V. Rebrov, M.H.J.M. de Croon, J.C. Schouten, AIChE J. 53 (2007) 28–38.
[23] Z.R. Ismagilov, O.Yu. Podyacheva, M.A. Kerzhentsev, V.N. Bibin, A. Ermakova, G.K. Chermashentseva, Kinetika i Kataliz 29 (1988) 254 (in Russian).
[24] M. Aryafar, F. Zaera, Catal. Lett. 48 (1997) 173–183.
[25] Z.R. Ismagilov, N.M. Dobrynkin, V.V. Popovskii, React. Kinet. Catal. Lett. 10 (1979) 55–59.
[26] Z.R. Ismagilov, V.N. Bibin, V.V. Popovskii, N.M. Dobrynkin, React. Kinet. Catal. Lett. 23 (1983) 143–147.
[27] P. Larsson, A. Andersson, Appl. Catal. B 24 (2000) 175–192.
[28] R. Lin, M. Luo, Q. Xin, G. Sun, Catal. Lett. 93 (2004) 139–144.
[29] V.N. Tomilov, A.N. Zagoruiko, P.A. Kuznetsov, Proceedings of the 3rd International Conference on "Unsteady State Processes in Catalysis", St. Petersburg, Russia, June 30–July 3, 1998, pp. 172–173.
[30] D. Kulkarni, I.E. Wachs, Appl. Catal. A 237 (2002) 121–137.
[31] L. Gambaro, J. Mol. Catal. A 247 (2006) 31–35.
[32] Z.R. Ismagilov, M.A. Kerzhentsev, I.Z. Ismagilov, V.A. Sazonov, V.N. Parmon, G.L. Elizarova, O.P. Pestunova, V.A. Shandakov, Yu.L. Zuev, V.N. Eryomin, N.V. Pestereva, F. Garin, H.J. Veringa, Catal. Today 75 (2002) 277–285.
[33] I.Z. Ismagilov, V.V. Kuznetsov, A.P. Nemudryi, O.Yu. Podyacheva, Kinet. Catal. 45 (2004) 722–729.
[34] I.Z. Ismagilov, M.A. Kerzhentsev, V.A. Rogov, V.A. Shandakov, Proceedings of the Russian National Conference on "Utilization of Solid Propellant Rocket Engines. Problems and Methodology of Utilization of Composite Solid Rocket Propellants, Waste of Specialized Production and Residues of Liquid Rocket Propellants in the Elements of Rocket and Space Equipment", Federal Research and Production Center "Altai", Biysk, Russia, September 25–28, 2001, pp. 67–74 (in Russian).

Please cite this article in press as: I.Z. Ismagilov, et al., Oxidation of organic compounds in a microstructured catalytic reactor, Chem. Eng. J. (2007), doi:10.1016/j.cej.2007.07.036

Microporous and Mesoporous Materials 123 (2009) 243–252

Contents lists available at ScienceDirect

Microporous and Mesoporous Materials

journal homepage: www.elsevier.com/locate/micromeso

Determination of the Tolman length in the improved Derjaguin–Broekhoff–de Boer theory for capillary condensation of ethanol in mesoporous thin films by ellipsometric porosimetry

Lidia N. Protasova [a,b], Evgeny V. Rebrov [a], Zinfer R. Ismagilov [b], Jaap C. Schouten [a,*]

[a] Department of Chemical Engineering and Chemistry, Eindhoven University of Technology, P.O. Box 513, 5600 MB Eindhoven, The Netherlands
[b] Laboratory of Environmental Catalysis, Boreskov Institute of Catalysis, Pr. Lavrentieva, 5, 630090 Novosibirsk, Russia

ARTICLE INFO

Article history:
Received 9 December 2008
Received in revised form 31 March 2009
Accepted 2 April 2009
Available online 8 April 2009

Keywords:
Ellipsometric porosimetry
Pore size distribution
Derjaguin–Broekhoff–de Boer model
Tolman parameter
Mesoporous films

ABSTRACT

Ethanol adsorption–desorption isotherms on well-organized mesoporous silica and titania films with hexagonal pores structure were studied by ellipsometric porosimetry. The mesopore volume was calculated from the change of the effective refractive index at the end points of the isotherm. An improved Derjaguin–Broekhoff–de Boer (IDBdB) model for cylindrical pores is proposed for the determination of the pore size. In this model, the disjoining pressure isotherms were obtained by measuring the thickness of the ethanol film on a non-porous film with the same chemical composition. This approach eliminates uncertainties related to the application of the statistical film thickness determined via *t*-plots in previous versions of the DBdB model. The deviation in the surface tension of ethanol in the mesopores from that of a flat interface was described by the Tolman parameter in the Gibbs–Tolman–Koening–Buff equation. A positive value of the Tolman parameter of 0.2 nm was found from the fitting of the desorption branch of the isotherms to the experimental data obtained by Low Angle X-ray Diffraction (LA-XRD) and Transmission Electron Microscopy (TEM) measurements in the range of pore diameters between 2.1 and 8.3 nm.

1. Introduction

1.1. Ellipsometric porosimetry

One of the main challenges in using microstructured reactors for heterogeneously catalyzed gas-phase and multiphase reactions is the characterization of the catalytic active phase. The specific surface area in microstructured reactors is generally increased by applying thin porous coatings on the channel walls [1]. Then, the porous layer can be made catalytically active. However, the performance of such catalysts is extremely dependent on the characteristics of the pore volume such as the total porosity, pore size distribution, and porous structure before and after catalysts deposition. The properties of catalytic thin films deposited onto a substrate surface sharply differ from the bulk properties of the material [2,3], therefore characterization of similar pelletized materials cannot provide reliable information.

Consequently, much development has recently taken place for mesoporous film characterization through techniques as Positron Annihilation Lifetime Spectroscopy [4,5] (PALS), Small Angle Neutron and X-ray Scattering (SANS, SAXS), X-ray reflectance, and Rutherford backscattering spectroscopy [6–9]. Most of these techniques can yield precise information on the porosity and pore size distribution, but the interpretation of the ratio of the open/closed pores in a film, which is a fundamental parameter, is not always straightforward. On the other hand, the potential in using optical methods, such as ellipsometric porosimetry [10], for resolving microstructural and dynamic information has not fully been exploited yet. In most cases when ellipsometry is applied in material science, it has been used for determination of the film thickness. The potential in using ellipsometry data for resolving microstructural information has not fully been exploited in the literature so far.

The principle of ellipsometric porosimetry is based on the evaluation of the optical characteristics of a porous film during the vapor adsorption in the pores. Ellipsometric porosimetry is more informative in comparison to classical adsorption porosimetry, and is much simpler than, for example, SANS or positron annihilation methods [11]. In addition to structural characteristics, the heat of adsorption of volatile adsorbates on different surfaces can also be determined via the measurement of the optical characteristics at different temperatures [12–14].

1.2. Data processing

The Kelvin condensation model is widely used for the characterization of porous structures, especially for mesoporous solids,

* Corresponding author. Tel.: +31 (0) 40 247 3088; fax: +31 (0) 40 244 6653.
E-mail address: J.C.Schouten@tue.nl (J.C. Schouten).

1387-1811/$ - see front matter © 2009 Elsevier Inc. All rights reserved.
doi:10.1016/j.micromeso.2009.04.006

while a few authors have reported its underestimation of the pore size in the nanometer region [11,15–18]. Despite that, the Kelvin model was often applied with ellipsometric porosimetry, when methanol, ethanol, or water were used as adsorbates due to the lack of another appropriate model that is accurate enough for mesopores as well as handy enough for widespread use [11,19,20]. Dependence of the relative pressure p/p_0 on the meniscus curvature is described by the Kelvin equation:

$$RT\ln\frac{p}{p_0}=\frac{2v_L\gamma\cos\theta}{R_P}, \tag{1}$$

v_L is the molar volume of the liquid, γ is the surface tension at the solid/liquid interface, R is the universal gas constant, and T is the temperature [21].

At the same time, the pore size can be calculated from the adsorption (or desorption) isotherms in terms of the conventional capillary condensation methods. For example, the methods suggested by Barrett, Joyner, and Halenda (BJH) [22] and by Derjaguin, Broekhoff, and de Boer (DBdB) [21] for estimating the mesopore size, were implemented in various studies. A considerable improvement in the pore range between 2 and 6 nm was achieved by the Kruk–Jaroniec–Sayari (KJS) approach [23]. These authors applied a modified form of the Kelvin equation which incorporates the statistical film thickness (t, adsorbed film on the pore walls) via the Harkins–Jura equation of the following form:

$$t\left(\frac{p}{p_0}\right)=0.1\cdot\left[\frac{60.65}{0.03071-\log\frac{p}{p_0}}\right]^{0.3968}, \tag{2}$$

where t is the thickness in nm measured on a macroporous support.

Neimark et al. demonstrated that the modification of the classical DBdB theory for capillary condensation/evaporation in mesoporous systems, by taking into account the dependence of the surface tension and the disjoining pressure on the pore wall curvature, results in a much better agreement between theory and experiment for a wide range of mesopores [24,25]. According to the classical DBdB theory, the desorption from an open-ended cylindrical pore with a radius R_P and a thickness of the adsorbed film h is determined by the balance of the capillary and disjoining pressures [26,27]:

$$\Pi(h)v_L+\frac{\gamma v_L}{R_P-h}=-RT\ln\frac{p}{p_0}. \tag{3}$$

Eq. (3) contains the disjoining pressure isotherm, $\Pi(h)$, on a flat (non-porous) film with the same thickness h as in the pore. By assuming the complete wetting of the surface, Churaev et al. [28,29] proposed the following form for the disjoining pressure isotherm of the liquid film at the surface of a solid:

$$\Pi_1\exp\left(\frac{-h}{\lambda_1}\right)=-\frac{RT}{v_L}\ln\frac{p}{p_0}, \tag{4}$$

where Π_1 is the strength of the surface force field (which depends on the surface hydrophilicity, or in other words on the number of hydroxyl groups per unit of surface area) and λ_1 is the decay length (λ_1 characterizes the range of structural forces action). This form of isotherm can be used for surfaces characterized by weak interaction with the adsorbed medium, e.g. for adsorption of toluene on mesoporous silicas [30]. Then, the disjoining pressure isotherm $\Pi(h)$ for the liquid absorbate film in a pore is given as follows:

$$\Pi_1\exp\left(\frac{-h}{\lambda_1}\right)+\frac{\gamma}{R_P-h}=-\frac{RT}{v_L}\ln\frac{p}{p_0}. \tag{5}$$

Currently, it is generally accepted that the surface tension for a curved surface of radius ρ $\gamma(\rho)$, on a liquid–vapor interface depends essentially on the radius of the curvature, ρ, for all sizes within the mesopore range [31]. The change in the surface tension in cylindrical mesopores as compared to that on a flat surface is described by the Gibbs–Tolman–Koening–Buff (GTKB) equation [32–34]:

$$\frac{\gamma(\rho)}{\gamma_\infty}=1-\frac{\delta}{\rho}, \tag{6}$$

where γ_∞ is the surface tension for the bulk fluid on a plane surface, and δ is the Tolman length, which is defined as a curvature-correction coefficient in the surface tension of a liquid droplet or a film (in other words, the Tolman length describes the separation between the equimolar surface and the surface of tension). This approach is widely adopted in literature and remains today a commonly-used method for treating adsorption phenomena.

1.3. The Tolman length

In agreement with recent density functional theory (DFT) and molecular simulations, it is generally accepted that the Tolman length is positive for a gas bubble surrounded by a liquid [35–38]. However, in several studies, δ was predicted to be negative (it means that the surface tension of a large droplet is greater than that of the planar one) [39–41]. Miyata et al. [33] suggested that δ has a negative value for a liquid film on a curved solid wall. Using density functional theory, Stecki and co-workers [42,43] investigated the effect of the wall curvature on the surface tension at the liquid–solid interface. They showed that for a fluid in contact with a hard wall, the Tolman parameter can be either positive or negative depending on the bulk density of the fluid and the temperature. For a fluid near a hard wall, Bryk et al. obtained a negative Tolman length [44]. While the sign of δ is still controversial due to a lack of experimental data [45], the magnitude of δ was predicted to be on the order of the molecular size of the adsorbate or the liquid-phase intermolecular distances, i.e. 0.2–0.4 nm for small (mono- and di- and tri-atomic) molecules [32]. This prediction was recently confirmed by various quasi-thermodynamic and statistical–mechanical approaches. A Tolman length of 0.3 ± 0.1 nm was reported for argon and nitrogen [34,46,47]. A constant value of δ of 0.16 nm was reported for water by Gurkov et al. [48]. For water at a water/gas interface, the Tolman length increases from 0.12 to 0.28 nm [49] as the temperature increases from 372 to 615 K. A Tolman length of 0.46 nm at a saturated hydrocarbon/gas interface was found to be almost constant for all paraffins from n-C_5H_{12} to n-$C_{17}H_{36}$ [48]. The latter means that the ratio of the Tolman length to the molecular diameter decreases as the range of interaction between molecules becomes larger. This conclusion was recently confirmed by means of large-scale molecular dynamics simulations [50]. The strength of intermolecular interactions can significantly affect the magnitude of the Tolman length. When the range of interaction is longer than five molecular diameters (e.g. for non-polar fluids), the Tolman length is on the order of a few hundredths of the molecular diameter, which is much smaller than previously reported.

An improved Derjaguin–Broekhoff–de Boer model (IDBdB) with cylindrical pores was applied in earlier studies to describe the adsorption equilibrium [33,47]. This model takes into account both the thickness of the liquid adsorbate film and the deviation in surface tension of the liquid adsorbate in the mesopores from that on a flat interface. However, previous studies rely on the assumptions made either on the Tolman length [33] or adsorbate film thickness [47].

The main purpose of this work is to demonstrate the applicability of an improved Derjaguin–Broekhoff–de Boer model for determination of the pore size distribution of different mesoporous thin films in a wide range of pore diameters. Recent progress in the synthesis of silica and titania mesoporous thin films [51–54], with monosized cylindrical pores ranging between 2 and 9 nm, al-

lows us to make a major improvement in the IDBdB model. In this study, the film thickness was directly measured by ellipsometry on non-porous films with the same chemical composition. This approach eliminates uncertainties related to the application of the statistical film thickness determined via *t*-plots in previous versions of the IDBdB model, which in turns allows considerably increase of the accuracy in the determination of the Tolman length.

2. Description of adsorption and desorption models

2.1. Adsorption model

The relation between the critical film thickness during spontaneous condensation and the capillary radius as a function of the relative pressure for an open-ended cylindrical pore is determined by a system of algebraic Eq. (7) [47]:

$$\begin{cases} \frac{\gamma_\infty (R_P-h-2\delta)}{(R_P-h)^3} - \frac{\Pi_1}{\lambda_1}\exp(\frac{-h}{\lambda_1}) = 0, \\ \frac{\gamma_\infty (R_P-h-\delta)}{(R_P-h)^2} + \Pi_1 \exp(\frac{-h}{\lambda_1}) = -\frac{RT}{v_L}\ln\frac{p}{p_0} \end{cases} \quad (7)$$

The solution of the system of Eq. (7) requires the parameters for the disjoining pressure isotherms: the strength of the surface force field (Π_1) and the decay length (λ_1). These parameters have been obtained on non-porous flat films with the same chemical composition. In other words, the curvature effects of the solid–fluid potential are not considered in these isotherms. In an earlier study, Kowalczyk et al. [47] reported that for mesoporous materials such approach seems to be correct, as they did not observe any differences between the data obtained by this approach and those simulated via DFT methods.

2.2. Desorption model

The desorption of an adsorbate from a cylindrical pore is determined by the Derjaguin equation (Eq. (8)) [55]:

$$-RT\ln\frac{p}{p_0} = \frac{2v_L\gamma_\infty\left(1-\frac{2\delta}{R_P-h}\right) + \frac{2v_L}{R_P-h}\int_h^{R_P}(R_P-h)\Pi(h)dh}{R_P-h}. \quad (8)$$

Following the approach of Miyahara et al. [34], we applied the GTKB equation for the spherical interface in Eq. (8). The thickness of the adsorbate film (h) on the pore walls is given by Eq. (9) [34]:

$$-RT\ln\frac{p}{p_0} = \Pi(h)v_L + \frac{v_L\gamma_\infty\left(1-\frac{\delta}{R_P-h}\right)}{R_P-h}. \quad (9)$$

Combination of Eqs. (8) and (9) gives a relation between the critical film thickness and the critical capillary radius during desorption as a function of p/p_0.

The only unknown parameter is, therefore, the Tolman length. From the preceding section, it can be concluded that this parameter can be either positive or negative depending on the bulk density of the fluid and its magnitude for small molecules varies between 0.15 and 0.4 nm. In this paper, we calculated the condensation and evaporation curves for ethanol adsorption on mesoporous thin films with several values of the Tolman parameter δ to obtain the best agreement with experimental XRD, TEM, and porosity data, the latter being obtained by ellipsometric porosimetry.

3. Experimental

Usually, high vacuum systems are used for ellipsometric porosimetry measurements. The necessity to provide a smooth change of the pressure in the mbar range considerably increases the stabilization time required to reach the intended pressure set-points. Furthermore, heat transfer from the sample holder to the substrate containing the thin film is extremely slow at low pressures. This requires that the substrate material be polished from its back side before the measurements, which increases the costs and the time on sample preparation. In this work, we present a novel design of a flow cell for in situ ellipsometric measurements at ambient pressure. Furthermore, there is a possibility to measure the kinetics of the adsorption process when a surface comes into contact with an adsorbent and a new steady state coverage is reached.

3.1. The optical flow cell

Fig. 1 shows the experimental set-up which consists of a gas mixture preparation section, a flow cell with the sample holder, and an analysis system.

The temperature of the measurements was fixed at 287 ± 0.2 K, unless mentioned otherwise. This temperature was easily maintained with a high precision by a continuous flow of cooling gas (air) and an electrical heater positioned inside the sample table. Ethanol (99.99%) was chosen as the liquid adsorbate because its saturated vapor pressure at 287 K can provide a similar number of data points on the adsorption (and desorption) isotherms as that obtained in nitrogen adsorption studies. The temperature of the outer shell of the flow cell was kept at 303 K. To cover the whole range of the required liquid flow rates, two liquid flow controllers μ-FLOW L01 (Bronkhorst B.V.) for the 25–500 mg h^{-1} range and LIQUI-FLOW® L13 (Bronkhorst B.V.) for the 0.5–10 g h^{-1} range were used (see Fig. 1). Both controllers were with a turndown of 1:20 and a setting time of 4 and 2 s, respectively. A gas flow controller provided flow rates for He between 0.1 and 2.0 L min^{-1} (STP) with a turndown of 1:20 and a setting time of 2 s. The ethanol and He flows were mixed in a CEM system (Controlled Evaporation and Mixing, Bronkhorst B.V.) maintained at 343 K. As a result, ethanol was evaporated and mixed with the He flow. The lowest partial pressure of ethanol was 0.10 mbar corresponding to a p/p_0 ratio of 0.0025 and the highest one, calculated from Antoine's equation [56], was 39 mbar corresponding to a p/p_0 ratio of 0.95. A gas flow rate in excess of 0.4 L min^{-1} (STP) was required for stable operation, far too large to maintain the temperature of the flow cell with high accuracy. Therefore, the flow was split up into two streams and the flow to the cell was controlled at 150 mL min^{-1} (STP) by an additional mass flow controller. The pressure in the cell was maintained at 1.05 bar (just above the highest possible atmospheric pressure) by a back pressure controller. To condense ethanol from the outlet streams, a temperature of 243 K was maintained in the condensing loops by a Lauda thermostat.

3.2. Sample pretreatment and optical measurements

Two samples of mesoporous titania films with different pore sizes (referred to as samples MT1 and MT2) and one with a mesoporous silica film (referred to as sample MS1) deposited on silicon substrates of 10 × 10 mm^2, were investigated. The samples were obtained using non-ionic surfactant Pluronic F127 as a template, Ti(*O*-iPr)$_4$ and TEOS as Ti- and Si-source, respectively, and ethanol as a solvent. The detailed procedure of the sample preparation is described elsewhere [53,54]. Similar non-porous titania and silica films were prepared by the same method without addition of the surfactant (referred to as NT and NS for titania and silica films, respectively). Those were used to determine the thickness of the liquid ethanol film as a function of its relative pressure.

Prior to adsorption, all samples were pretreated following the procedure shown in Fig. 2a and b. The dynamics of the ellipsometric signal (Ψ/Δ) during the pretreatment steps are shown in Fig. 2c.

At first, the samples were evacuated (pressure profile is shown in Fig. 2a), then heated to 573 K with a heating rate of 10 K/min fol-

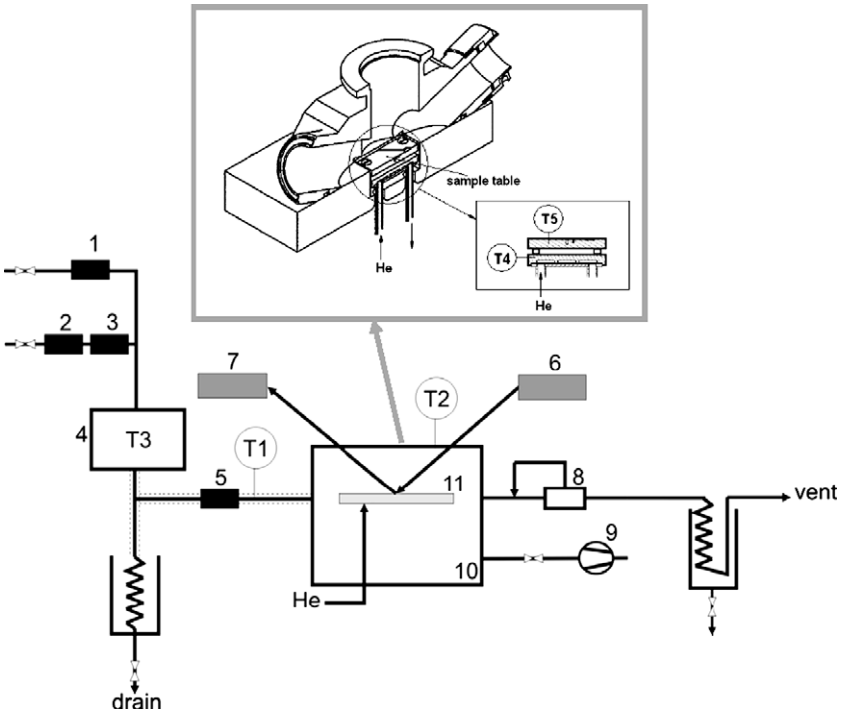

Fig. 1. Schematic view of the ellipsometric porosimetry flow cell set-up: (1) and (5) gas mass flow controllers, (2) and (3) liquid flow controllers, (4) ethanol evaporator, (6) light source of the ellipsometer, (7) detector, (8) back pressure controller, (9) vacuum pump, (10) flow cell, (11) sample table. (T1)–(T5) temperature sensors. An enlarged view of the sample holder is shown in the frame.

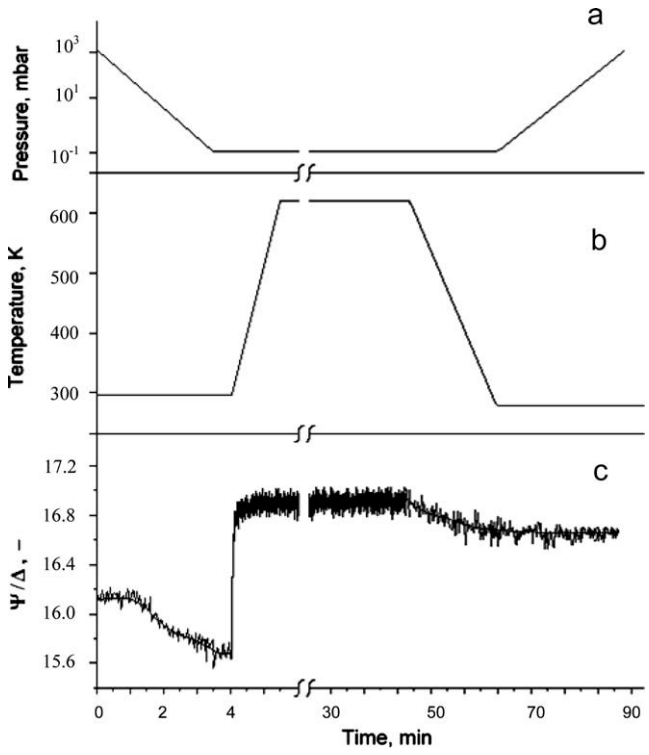

Fig. 2. The sample pretreatment procedure: (a) pressure, (b) temperature, and (c) ellipsometric signal (Ψ/Δ) as a function of the pretreatment time.

lowed by a dwelling interval of 30 min (temperature profile is shown in Fig. 2b). The residual pressure was maintained in the range of 0.08–0.10 mbar during the pretreatment step. To improve the heat exchange between the substrate and the sample holder, a He flow of 1 mL min^{-1} was released into the cell just below the sample. Then, the sample was cooled down to 287 K with a cooling rate of 10 K min^{-1} and the cell was filled with helium till 1.05 bar. After pressure equalization, the cell was closed and the ethanol flow was set at the lowest set-point. After an equalization time of 20 s, a flow of 150 mL min^{-1} was directed to the cell and the adsorption kinetics was monitored by a Woollam M-2000F, EC-400 ellipsometer with a polarised He–Ne laser beam with a wavelength of 633.5 nm incident at an angle of 68.00 ± 0.01° in relation to a plane normal to the surface.

The need to measure the thickness of very thin films, and to characterize thin interlayers requires to take into account all possible uncertainties in the parameters that can affect the accuracy of an ellipsometric measurement. The accuracy depends on the measured angles Δ and Ψ, the angle of incidence ϕ, the refractive index of the substrate, and the wavelength of the light. In this study, the accuracy of the effective refractive index was 0.001, while the uncertainties of the measured angles Δ and Ψ were below 0.01°. The thickness uncertainty at a film thickness in the range 0.1–1.0 nm was 3% at a wavelength of 633.5 nm [57].

Optical measurements were carried out after stabilization of the Ψ/Δ signal, usually in 2–3 min. A typical diffusion time for the achievement of the steady state is $\tau_D \sim \frac{L^2}{D_e}$, where L is the thickness of the film of 10^{-7} m, D_e is the effective diffusivity of ethanol in the porous film, which depends on the porosity and tortuosity. In this study, the minimum porosity was 0.2. The tortuosity in a cubic structure can be modeled with a value of 3. This value is even lower in straight pores of a hexagonal structure. Therefore, the effective diffusivity of ethanol can be estimated as $D_e = \frac{0.2}{3} D_m$, where D_m is the binary molecular diffusion coefficient of ethanol in He determined from the kinetic gas theory. Thus, the diffusion time to reach the steady-state in the pores is ca. 10^{-6} s (1 μs). The flush time of the optical cell is the limiting factor which determines stabilization of the signal. This time is determined by the diffusion of

Table 1
Comparison of different models for pore size determination.

Model	Adsorbate	Correction for the adsorbate layer thickness	Correction for the surface tension (Tolman parameter, nm)	Geometrical correction	Ref.
Kelvin + *t*	Toluene, heptane	Isotherm	–	–	[11]
Kelvin + *t* + *c*	N_2	*t*-plot	–	Geometrical factor	[23]
DBdB	N_2	*t*-plot	–	–	[26]
IDBdB	N_2, Ar	Isotherm	–	–	[47]
IDBdB	N_2	*t*-plot	−0.3	–	[33]
Kelvin + IIC[a]	Water	*t*-plot	–	Geometrical factor	[59]
IDBdB	Ethanol	Isotherm	+0.2	–	Present work

[a] Isotropic inorganic contraction.

Table 2
Fitting parameters of Eq. (9).

Sample	Π_1 (MPa)	λ_1 (nm)
Titania	$(1.92 \pm 0.09) \times 10^8$	0.144 ± 0.005
Silica	$(2.73 \pm 0.05) \times 10^8$	0.134 ± 0.001

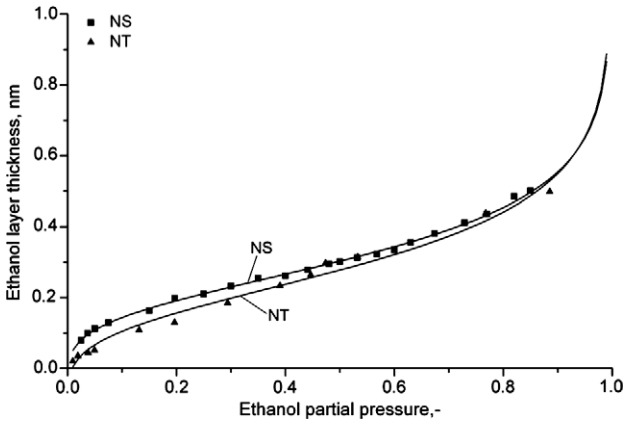

Fig. 3. Ethanol layer thickness as a function of ethanol partial pressure on non-porous films deposited on a silicon substrate. Lines: statistical film thickness curves obtained from Eq. (4). Symbols: adsorption–desorption isotherms at 287 K for samples NS and NT.

ethanol into the stagnant zones of the cell where there is no mass transfer by convection.

After taking the measurement, the flow to the cell was stopped and the ethanol partial pressure was set at a different value. This procedure was repeated until the complete adsorption–desorption curve was recorded.

3.3. Optical data modeling and volumetric pore size determination

The applied optical model consisted of three layers for the porous samples: the silicon substrate layer, the native SiO_2 layer of 3 nm, and a layer of either titania or silica. For the non-porous samples, a layer of ethanol was added to the model. In the latter case, the thickness (t) of the ethanol layer adsorbed onto a non-porous surface and the effective refractive index (n) were found by fitting of the Ψ and Δ values [58]. The thickness of the mesoporous films was changed by less than 1% during the adsorption/desorption process, therefore it was kept constant during the fitting of the experimental data. The refractive index dispersion of the film was modeled using Cauchy's equation (Eq. (10), [58]):

$$n = n_0 + \frac{n_1}{\lambda^2} + \frac{n_2}{\lambda^4}, \tag{10}$$

where λ is the wavelength, and n_0, n_1 and n_2 are fitted parameters. The pore volume was determined from the change in the effective refractive index in the range of 400–1200 nm. The refractive index of the dry (without ethanol) mesoporous film (n_M) and the total non-porous fraction (f_M) were calculated from the change in the effective refraction index (n_{ef}) at the end points of the isotherm using the Bruggeman effective medium approximation (BEMA, Eq.

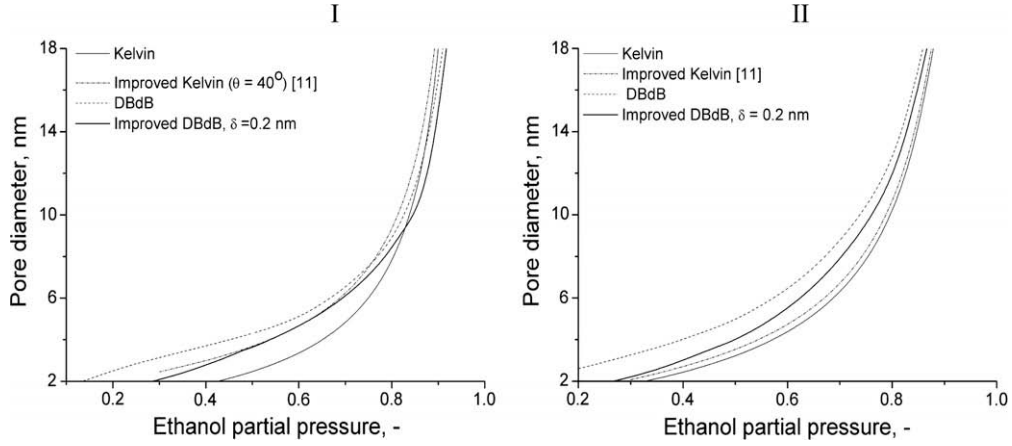

Fig. 4. Prediction of the capillary condensation curves for ethanol adsorption (Panel I) and desorption (Panel II) on titania at 287 K computed via four adsorption models: Kelvin, Improved Kelvin [11], DBdB, and improved DBdB.

Table 3
Pore sizes of mesoporous films determined by different methods.

Sample	Ethanol wetting angle (°)	Porosity (−)	Mean pore size (nm)						
			TEM	$V_p - d_{100}$ model (Eq. (14))	$P - d_{100}$ model (Eq. (17))	EP using desorption models			
						Kelvin	Improved Kelvin	DBdB	IDBdB, δ = 0.2 nm
MT1	40	0.35	2.1	n.d.	n.d.	2.0	2.6	3.0	2.1
MT2	40	0.26	3.5	3.6	3.8	3.0	4.5	4.7	3.6
MS1	30	0.22	8.0	8.3	8.4	6.9	8.3	9.1	8.3

n.d. – not determined.

(11) [59]) and the refractive indexes of air and ethanol (n_m = 1.0 and 1.361 at 633 nm, respectively):

$$f_M \frac{n_M^2 - n_{ef}^2}{n_M^2 + 2n_{ef}^2} + (1 - f_M) \frac{n_m^2 - n_{ef}^2}{n_m^2 + 2n_{ef}^2} = 0. \quad (11)$$

The porous fraction ($1 - f_M$) was determined from n_{ef} with the BEMA model at zero ethanol pressure by fitting the volumetric fraction of the inorganic framework with the air refraction index for the second material (n_p = 1).

Then, the effective refractive index (n_{ef}) as a function of the ethanol partial pressure (p/p_0), was determined by ellipsometry. The isotherm was determined by fitting the volumetric fractions of the inorganic component (f_M), ethanol (f_{ET}), and air with the BEMA model at each relative pressure (Eq. (12)):

$$f_M \frac{n_M^2 - n_{ef}^2}{n_M^2 + 2n_{ef}^2} + f_{ET} \frac{1.361^2 - n_{ef}^2}{1.361^2 + 2n_{ef}^2} + (1 - f_{ET} - f_M) \frac{1.00 - n_{ef}^2}{1.00 + 2n_{ef}^2} = 0. \quad (12)$$

Then, the adsorbed ethanol volume (V_{ET}) is related to the product of the total film volume (V_F), the pore fraction ($1 - f_M$), and the volumetric fraction of the ethanol saturated film (f_{ET}):

$$V_{ET} = V_F(1 - f_M) f_{ET}. \quad (13)$$

The total mesoporous surface area was calculated from the average pore diameter, the total pore volume, and the pore fraction assuming cylindrical pore geometry.

3.4. Low-angle X-ray diffraction and transmission electron microscopy

LA-XRD spectra were recorded on a Rigaku Geigerflex device with CuK_α radiation (40 kV, 40 mA), 0.01°–0.02° 2θ step size, with a counting time of 4.0 s. The TEM images were obtained on a JEM-2010 microscope at 200 kV with a resolution of 0.14 nm. Samples for TEM were prepared by placing a slice of the film removed from the substrate on a copper grid coated with a carbon film and dried under vacuum.

4. Modeling of adsorption–desorption isotherms

Recently, Neimark et al. [60,61] reported that in cylindrical pores desorption takes place at the equilibrium. Their conclusion is based on the arbitrary assignment of the DFT equilibrium transition to the desorption branch of an experimental isotherm. In different studies, Kruk et al. [23] and Morishige and Nakamura [62] proposed to use the adsorption branch of the isotherm for pore size analysis. One of the purposes of this study was to examine a possibility to use the desorption branch in cylindrical pores, if the Tolman parameter as well as the parameters for the disjoining pressure isotherm, $\Pi(h)$ (see Eq. (3)), are known.

Table 1 summarizes the main models used for calculation of the pore size distribution in mesoporous materials. An improved Kelvin model was applied in [11]. According to this model, the pore radius was calculated as the radius of a cylindrical pore with a correction term (t) accounting for the thickness of the layer already adsorbed on the pore walls. Values of t were obtained from the data for the adsorption of the same adsorptive on a non-porous sample having a similar surface and was fitted by the BET equation. This model still overestimates the pore size below 6 nm. A constant correction factor (Kelvin + t + c) in the BJH method was proposed in [23]. However, even with this correction, the pore size of the mesoporous materials above 6 nm was overestimated. For mesoporous films, the unidirectional pore shrinkage associated to the drying and treatment lead to nonsymmetrical models. The spherical to ellipsoidal pore contraction of the inorganic network was taken into account in the Kelvin model modified by a geometric factor (Isotropic Inorganic Contraction (IIC) model) [59]. Calculating the

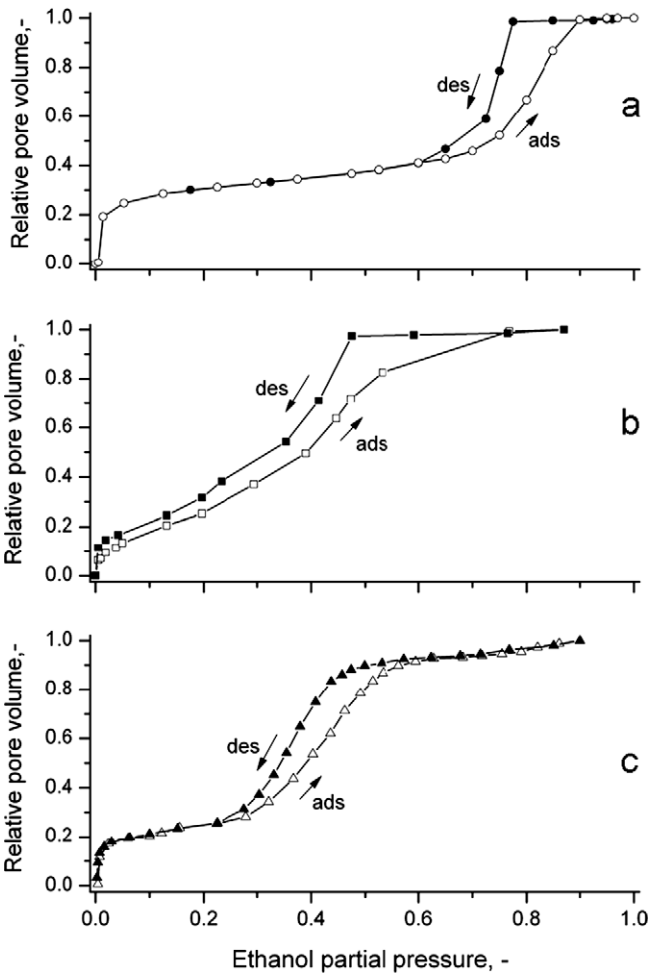

Fig. 5. Experimental ethanol adsorption–desorption isotherms at 287 K for samples: (a) MS1, (b) MT2, (c) MT1. Lines represent a guide for the eye.

pore anisotropy and introducing the liquid–solid contact angle in a modified Kelvin equation allowed the authors to obtain better matching of the mean pore size derived from ellipsometry with that obtained by independent methods. In the IDBdB model applied in this study, the experimental adsorption film thickness of ethanol on the non-porous thin films was directly calculated from the experimental isotherm data by Eq. (4). The obtained parameters for the non-porous silica and titania thin films are listed in Table 2.

Fig. 3 shows the predicted statistical film thickness curves for the silica and titania non-porous thin films. It can be seen that the calculated curves are in a good agreement with the experimental curves but exhibit gradually increasing deviations as the capillary condensation pressures are approached.

A sharp increase of the adsorbed film thickness at a high relative pressure indicates that capillary condensation has occurred on the surface. The silica surface is known to be more hydrophilic than the titania one. As a result, at a given relative pressure, the thickness of the adsorbed ethanol film is higher on the silica surface.

The theoretical adsorption and desorption curves obtained by Kelvin, improved Kelvin [11], DBdB and IDBdB with a Tolman parameter of 0.2 nm models are presented in Fig. 4 Panel I and II, respectively. Since wettability is a crucial factor of the capillary condensation, the liquid–solid contact angle, characterizing the surface energy, is needed to give a correct interpretation of the ethanol adsorption isotherms. The liquid–solid contact angle was experimentally determined for the Kelvin and improved Kelvin adsorption models (Table 3). The adsorption and desorption isotherms on the porous samples calculated from the effective refractive index values are shown in Fig. 5 and the pore size distributions obtained from the theoretical models are shown in Fig. 6.

The pore size was also determined from TEM analysis (Fig. 7) and from the XRD curves (Table 3). In a $V_p - d_{100}$ model, we assumed that the pore diameter (d_{pore}) corresponds to the equivalent cylindrical pore having the same volume as the actual pore with the hexagonal cross section [63]. Taking this into account, the relation between the pore diameter d_{pore}, the pore volume obtained by Eq. (13) at a relative pressure corresponding to complete pore filling, $V_p = V_F(1 - f_M)$, and the d_{100} interplanar spacing can be written as

$$d_{pore} = Cd_{100}\left(\frac{\rho_0^{(s)} \cdot V_p}{1 + \rho_0^{(s)} \cdot V_p}\right)^{1/2}, \tag{14}$$

where $\rho_0^{(s)}$ is the density of the solid framework (2.20 g/cm^3 [63] and 4.23 g/cm^3 [64] for silica and titania with amorphous pore walls, respectively); C is a constant characteristic of the pore geometry (equal to 1.2125 for circular and hexagonal pores).

In a $P - d_{100}$ model, we assumed that the ratio of the pore cross section to that of the hexagonal unit cell cross section equals to the film porosity (P). Porosity values of the films are listed in Table 3. Then, the pore diameter of a hexagonal pore can be determined by Eq. (15) from the unit cell parameter (a_0), and the film porosity (see Appendix 1 for further details):

$$d_{pore} = 2 \cdot \sqrt{\frac{2\sqrt{3} \cdot \left(\frac{a_0}{2}\right)^2 \cdot P}{\pi}}. \tag{15}$$

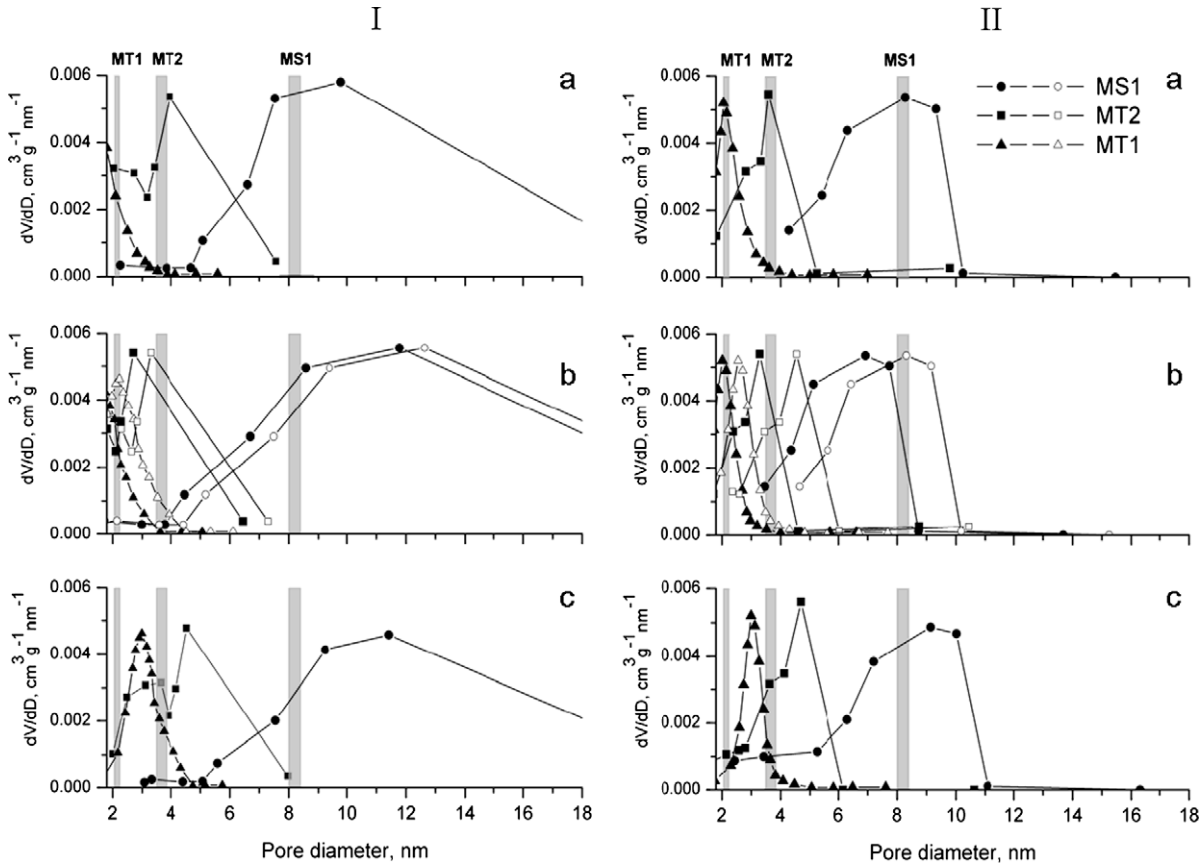

Fig. 6. Pore size distribution (PSD) plots. Panel I: PSD was calculated from the ethanol adsorption isotherms via: (a) IDBdB model with a Tolman parameter of 0.2 nm; (b) Kelvin (solid symbols) and Improved Kelvin [11] (open symbols) models ($\theta = 40°$ for MT1 and MT2, and $\theta = 30°$ for MS1); (c) DBdB model. Panel II: PSD was calculated from the ethanol desorption isotherms via: (a) IDBdB desorption model with a Tolman parameter of 0.2 nm; (b) Kelvin (solid symbols) and Improved Kelvin [11] (open symbols) models; (c) DBdB model. Symbols represent data obtained from the adsorption/desorption isotherms measured by ellipsometric porosimetry. The vertical bars represent the pore size determined by XRD and TEM.

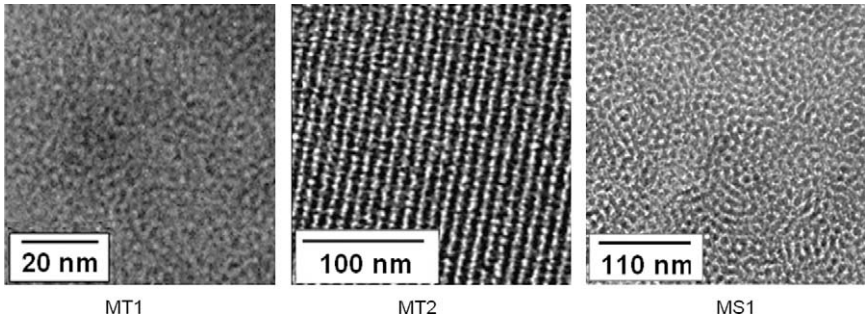

Fig. 7. TEM images of the samples MT1, MT2, and MS1.

Table 4
Deviation of the mean pore sizes determined by EP using different desorption models from that obtained with XRD and TEM.

Sample	Mean pore size[a] (nm)	Deviation from the mean pore size (%)			
		Kelvin	Improved Kelvin [11]	DBdB	IDBdB, δ = 0.2 nm
MT1	2.1	−5	+24	+43	0
MT2	3.6	−17	+25	+31	0
MS1	8.2	−16	+1	+11	+1

[a] Determined from XRD and TEM.

The unit cell parameter (a_0) is determined from

$$a_0 = \frac{2}{\sqrt{3}} d_{100}. \quad (16)$$

The pore diameter can be then determined from the film porosity as follows:

$$d_{pore} = 2R_P = C \cdot d_{100}\sqrt{P}. \quad (17)$$

All adsorption models fail to predict the true pore size. The IDBdB model with a Tolman parameter of 0.2 nm underestimates the pore size below 3 nm and overestimates it above 6 nm (Fig. 6 (Panel Ia)). Both Kelvin and improved Kelvin [11] adsorption models considerably overestimate the pore size above 6 nm (Fig. 6 (Panel Ib)). However, the improved Kelvin model provides a rather good matching with the pore size obtained by other methods in the range below 4 nm. The DBdB adsorption model overestimates the pore size in the whole range of mesopores (Fig. 6 (Panel Ic)).

It appears that the desorption branches of the isotherms are more straightforward for characterization of the film porosity. As reported in literature, the Kelvin desorption model underestimates while the DBdB model overestimates the mean pore size in the whole range of mesopores (Fig. 6 (Panel IIb and c, respectively) and Table 4). The improved Kelvin desorption model [11] satisfactory describes the pore sizes only in a narrow range between 7 and 10 nm. The IDBdB model with a Tolman parameter of 0.2 nm adequately describes the pore size in the whole range of mesopores. The deviation of the mean pore size obtained by EP using the IDBdB model from that obtained by TEM and XRD does not exceed 1%. Different values of the Tolman parameter were taken in the range between 0.10 and 0.40 nm to achieve the least difference between the predictions of the IDBdB model and the true pore size. The best agreement between the theoretical and experimental curves is observed at a value of the Tolman parameter of 0.20 nm (see Fig. 6 (IIa)). It should be noted that positive values of the Tolman parameter mean a thinner film thickness in the pores as compared to that on a flat surface. In these cases, the Tolman correction of the DBdB equation allowed corrections of the pore size values as high as 43% in the range of small pore diameters.

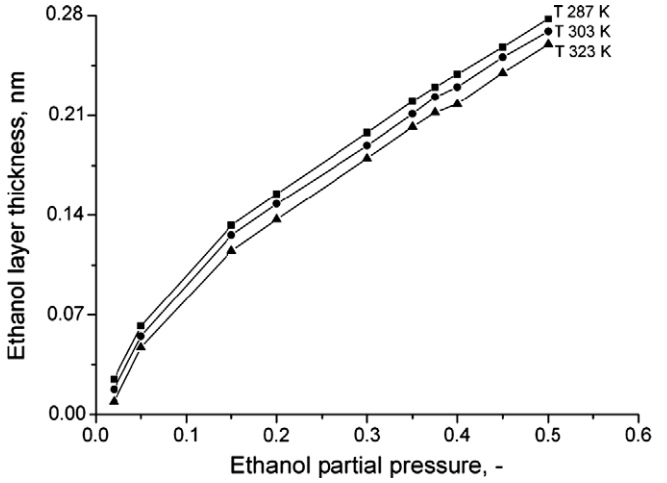

Fig. 8. The ethanol layer thickness as a function of the ethanol relative pressure on a non-porous titania thin film (sample NT) at 287, 303, and 323 K.

The type of disjoining pressure isotherm proposed in this study can be applied for a weak adsorption of an adsorbate on the substrate surface. The value of the energy constant of the BET equation describes the difference between the heat of adsorption for the first layer (E_1) and the subsequent layers (E_L) (Eq. (18)). The latter is equal to the heat of condensation of ethanol of 42.2 kJ/mol [65]:

$$C_{BET} = \exp\left(\frac{E_1 - E_L}{R \cdot T}\right). \quad (18)$$

The dependence of the ethanol layer thickness on the ethanol relative pressure was studied on a non-porous titania thin film at 287, 303, and 323 K (Fig. 8). The constant C_{BET} can be found from the linearization of the BET equation in the range of relative pressures of 0.05–0.35. The values of 9.7, 8.4 and 6.5 were obtained for C_{BET} at 287, 303 and 323 K, respectively. The heat of ethanol adsorption on a non-porous titania film was found to be 47.8 ± 0.3 kJ/mol. A small difference of 5.6 kJ/mol between the heat of adsorption of the first and subsequent layers justifies the choice of Eq. (4) for the disjoining pressure isotherm.

5. Conclusions

A new approach for predicting the pore size distribution of mesoporous thin films using ellipsometric porosimetry has been developed taking into account multilayer adsorption and capillary condensation phenomena. The improved Derjaguin, Broekhoff, and de Boer model was applied for estimating the mesopore size on titania and silica thin films deposited on a silicon substrate. An empirical expression for the disjoining pressure isotherm was

applied to represent the interaction between the adsorbate and the adsorbent in the Broekhoff and de Boer adsorption theory. The parameters in the empirical expression were obtained by fitting the multilayer region of an experimental isotherm on the titania and silica films. Using these parameters, the desorption isotherms of ethanol were predicted and adjusted to the experimental data by fitting the Tolman parameter of the IDBdB model, characterizing the surface tension for a curved surface. The IDBdB desorption model with a positive value of the Tolman parameter of 0.2 nm was found to describe accurately the pore diameter in a wide range of mesopores from 2.1 to 8.3 nm. The results obtained by TEM and XRD were used to validate the IDBdB model. The heat of ethanol adsorption on a non-porous titania film was found to be 47.8 ± 0.3 kJ/mol.

Acknowledgments

The authors thank Dr. M. Creatore for providing the ellipsometer for the porosimetry measurements, and Mr. A. Ishchenko and Dr. A. Berenguer-Murcia for the TEM measurements. The financial support by the Netherlands Organization for Scientific Research (NWO) and the Russian Foundation for Basic Research (RFBR) in frame of the NWO-RFBR Project 047.017.028 is gratefully acknowledged.

Appendix 1

The porosity (P) is calculated as a ratio of the area of the void-space to that of the unit cell:

$$P = \frac{A_p}{A_c}. \tag{A1}$$

The cross section of the unit cell (A_c) and that of a pore (A_p) in a hexagonal structure is calculated as follows (see Fig. A1):

$$A_c = \frac{\sqrt{3}}{2} \cdot a_0^2, \tag{A2}$$

$$A_p = 2\sqrt{3} \cdot R_p^2, \tag{A3}$$

where a_0 is the unit cell parameter and R_p is the pore radius.

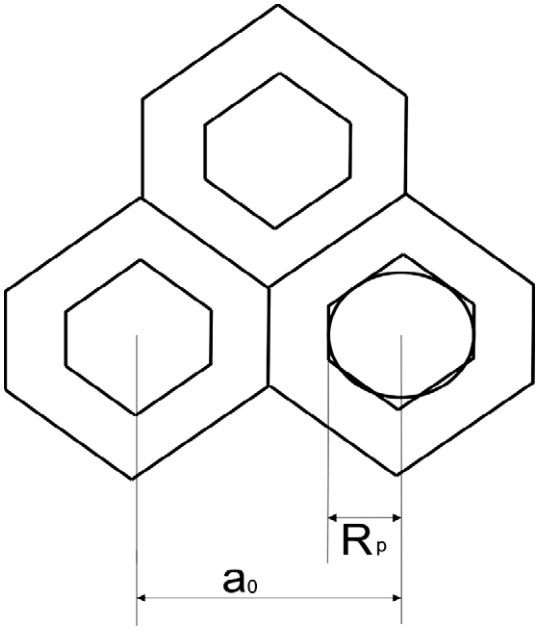

Fig. A1. Schematic representation of a hexagonal porous structure.

Taking into account that $d_{pore} = 2 \cdot R_p = \sqrt{\frac{4 \cdot A_p}{\pi}}$, one can obtain:

$$d_{pore} = 2 \cdot \sqrt{\frac{2\sqrt{3} \cdot \left(\frac{a_0}{2}\right)^2 \cdot P}{\pi}}. \tag{A4}$$

The porosity of a mesoporous thin film can be determined from the change of the effective refractive index at the end point of the isotherm:

$$P = \frac{\frac{n_{sat}^2 - 1}{n_{sat}^2 + 2} - \frac{n_M^2 - 1}{n_M^2 + 2}}{\frac{n_{ET}^2 - 1}{n_{ET}^2 + 2}}, \tag{A5}$$

where n_{sat} is the effective refractive index after pore filling, n_M is the effective refractive index of the empty film, and n_{ET} is the refractive index of ethanol.

References

[1] L. Kiwi-Minsker, A. Renken, Catal. Today 110 (2005) 2.
[2] I.Z. Ismagilov, E.M. Michurin, O.B. Sukhova, L.T. Tsykoza, E.V. Matus, M.A. Kerzhentsev, Z.R. Ismagilov, A.N. Zagoruiko, E.V. Rebrov, M.H.J.M. de Croon, J.C. Schouten, Chem. Eng. J. 135S (2008) S57.
[3] E.V. Rebrov, S.A. Kuznetsov, M.H.J.M. de Croon, J.C. Schouten, Catal. Today 125 (2007) 88.
[4] D.W. Gidley, W.E. Frieze, T.L. Dull, A.F. Yee, E.T. Ryan, H.M. Ho, Phys. Rev. B 60 (1999) R5157.
[5] S. Boskovic, A.J. Hill, T.W. Turney, M.L. Gee, G.W. Stevens, A.J. O'Connor, Prog. Solid State Chem. 34 (2) (2006) 67.
[6] M.R. Baklanov, K.P. Mogilnikov, Microelectron. Eng. 64 (2002) 335.
[7] A. Grill, V. Patel, K.P. Rodbell, E. Huang, M.R. Baklanov, K.P. Mogilnikov, M. Toney, H.-C. Kim, J. Appl. Phys. 94 (2003) 3427.
[8] E. Kondoh, M.R. Baklanov, E. Lin, D. Gidley, A. Nakashima, Jpn. J. Appl. Phys. 40 (2001) L323.
[9] K.P. Mogilnikov, M.R. Baklanov, D. Shamiryan, M.P. Petkov, Jpn. J. Appl. Phys. 43 (2004) 247.
[10] F.N. Dultsev, M.R. Baklanov, Electrochem. Solid State Lett. 2 (1999) 192.
[11] M.R. Baklanov, K.P. Mogilnikov, V.G. Polovinkin, F.N. Dultsev, J. Vac. Sci. Technol. B 18 (2000) 1385.
[12] R.F. Steiger, J.M. Morabito, G.A. Somorjal, R.H. Muller, Surf. Sci. 14 (1969) 279.
[13] C.M.A.M. Mesters, A.F.H. Wielers, O.L.J. Gijzeman, J.W. Geus, G.A. Bootsma, Surf. Sci. 115 (1982) 237.
[14] L.K. Filippov, Chem. Eng. Sci. 19 (1993) 3391.
[15] R. Evans, U.M.B. Marconi, P. Tarazona, J. Chem. Phys. 84 (1986) 2376.
[16] M. Miyahara, T. Yoshioka, M. Okazaki, J. Chem. Phys. 106 (1997) 8124.
[17] A. Saito, H.C. Foley, AIChE J. 37 (1991) 429.
[18] H. Kanda, M. Miyahara, T. Yoshioka, M. Okazaki, Langmuir 16 (2000) 6622.
[19] V. Jousseaume, G. Rolland, D. Babonneau, J.-P. Simon, Appl. Surf. Sci. 254 (2007) 473.
[20] C. Himcinschi, M. Friedrich, S. Frühauf, I. Streiter, S. Schulz, T. Gessner, M. Baklanov, K. Mogilnikov, D. Zahn, Anal. Bioanal. Chem. 374 (2002) 654.
[21] Y. Chen, T. Wetzel, G.L. Aranovich, M.D. Donohue, J. Colloid Interface Sci. 300 (2006) 45.
[22] E.P. Barrett, L.G. Joyner, P.H. Halenda, J. Am. Chem. Soc. 73 (1951) 373.
[23] M. Kruk, M. Jaroniec, A. Sayari, Langmuir 13 (1997) 6267.
[24] P.I. Ravikovitch, A.V. Neimark, Langmuir 18 (2002) 1550.
[25] A.V. Neimark, P.I. Ravikovitch, A. Vishnyakov, J. Phys. Condens. Matter. 15 (2003) 347.
[26] J.C. Broekhof, J.H. de Boer, J. Catal. 9 (1967) 8.
[27] J.C. Broekhof, J.H. de Boer, J. Catal. 9 (1967) 16.
[28] N.V. Churaev, Z.M. Zorin, Adv. Colloid Interface Sci. 40 (1992) 109.
[29] N.V. Churaev, G. Starke, J. Adolphs, J. Colloid Interface Sci. 2 (2000) 246.
[30] L.J.M. Schlangen, L.K. Koopal, M.A.C. Stuart, J. Lyklema, M. Robin, H. Toulhoat, Langmuir 11 (1995) 1701.
[31] R.C. Tolman, J. Chem Phys. 17 (1949) 333.
[32] J.C. Melrose, Ind. Eng. Chem. 60 (1968) 53.
[33] T. Miyata, A. Endo, T. Ohmori, T. Akiya, M. Nakaiwa, J. Colloid Interface Sci. 262 (2003) 116.
[34] M. Miyahara, H. Kanda, T. Yoshioka, M. Okazaki, Langmuir 16 (2000) 4293.
[35] M.A. Anisimov, Phys. Rev. Lett. 98 (2007) 035702.
[36] E.M. Blokhuis, J. Kuipers, J. Chem. Phys. 124 (2006) 074701.
[37] H.M. Lu, Q. Jiang, Langmuir 21 (2005) 779.
[38] A.E. van Giessen, E.M. Blokhuis, J. Chem. Phys. 116 (2002) 302.
[39] K. Koga, X.C. Zeng, J. Chem. Phys. 110 (1999) 3466.
[40] J.C. Barrett, J. Chem. Phys. 111 (1999) 5938.
[41] J.C. Barrett, J. Chem. Phys. 124 (2006) 144705.
[42] A. Samborski, J. Stecki, A. Poniewierski, J. Chem. Phys. 98 (1993) 8958.
[43] A. Poniewierski, J. Stecki, J. Chem. Phys. 106 (1997) 3358.
[44] P. Bryk, R. Roth, K.R. Mecke, S. Dietrich, Phys. Rev. E 68 (2003) 031602.
[45] T.V. Bykov, X.C. Zeng, J. Chem. Phys. 117 (2002) 1851.
[46] P.A. Kralchevsky, T.D. Gurkov, Colloids Surf. 56 (1991) 101.

[47] P. Kowalczyk, M. Jaroniec, A.P. Terzyk, K. Kaneko, D.D. Do, Langmuir 21 (2005) 1827.
[48] T.D. Gurkov, P.A. Kralchevsky, I.B. Ivanov, Colloids Surf. 56 (1991) 119.
[49] S.P. Malyshenko, D.O. Dunikov, Int. J. Heat Mass Transfer 45 (2002) 5201.
[50] Y.A. Lei, T. Bykov, S. Yoo, X.C. Zeng, J. Am. Chem. Soc. 127 (2005) 15346.
[51] T.S. Glazneva, E.V. Rebrov, J.C. Schouten, E.A. Paukshtis, Z.R. Ismagilov, Thin Solid Films 515 (2007) 6391.
[52] O. Muraza, E.V. Rebrov, T. Khimyak, B.F.G. Johnson, P.J. Kooyman, U. Lafont, M.H.J.M. de Croon, J.C. Schouten, Chem. Eng. J. 135S (2008) S99.
[53] E.V. Rebrov, A. Berenguer-Murcia, B.F.G. Johnson, J.C. Schouten, Catal. Today 138 (2008) 210.
[54] E.V. Rebrov, A. Berenguer-Murcia, H.E. Skelton, B.F.G. Johnson, A.E.H. Wheatley, J.C. Schouten, Lab Chip 9 (2009) 503.
[55] B.V. Derjaguin, Acta Phys. Chem. 12 (1940) 181.
[56] M. Goral, P. Oracz, A. Skrzecz, A. Bok, A. Maczynski, J. Phys. Chem. Ref. Data 31 (2002) 701.
[57] D. Chandler-Horowitz, G.A. Candela, J. Phys. 44 (1983) C10–C23.
[58] M. Creatore, S.M. Rieter, Y. Barrell, M.C.M. van de Sanden, R. Vernhes, L. Martinu, Thin Solid Films 516 (2008) 8547.
[59] C. Boissière, D. Grosso, S. Lepoutre, L. Nicole, A. Brunet Bruneau, C. Sanchez, Langmuir 21 (2005) 12362.
[60] A.V. Neimark, P.I. Ravikovitch, A. Vishnyakov, Phys. Rev. E 62 (2000) R1493.
[61] A. Vishnyakov, A.V. Neimark, J. Phys. Chem. B 105 (2001) 7009.
[62] K. Morishige, Y. Nakamura, Langmuir 20 (2004) 4503.
[63] E.A. Ustinov, Langmuir 24 (2008) 6668.
[64] D.R. Lide (Ed.), Handbook of Chemistry and Physics, CRC, New York, 1996.
[65] H. Naono, J. Colloid Interface Sci. 182 (1996) 234.

Catalysis Today 147S (2009) S81–S86

Contents lists available at ScienceDirect

Catalysis Today

journal homepage: www.elsevier.com/locate/cattod

Design of Pt–Sn catalysts on mesoporous titania films for microreactor application

Z.R. Ismagilov [a,*], E.V. Matus [a], A.M. Yakutova [a], L.N. Protasova [a,b], I.Z. Ismagilov [a], M.A. Kerzhentsev [a], E.V. Rebrov [b], J.C. Schouten [b]

[a] Boreskov Institute of Catalysis, Novosibirsk, 630090, Russia
[b] Eindhoven University of Technology, Eindhoven, P.O. Box 513, 5600 MB, The Netherlands

ARTICLE INFO

Article history:
Available online 4 August 2009

Keywords:
Mixed-metal clusters
Pt–Sn
Mesoporous titania
Citral hydrogenation

ABSTRACT

A new generation of nanostructured Pt–Sn/TiO_2 catalytic thin films has been developed by deposition of Pt–Sn mixed-metal precursors from organic solvents on mesoporous TiO_2/Ti films with a thickness of 200–300 nm. The titania sol was obtained by templating a TiO_2 precursor with Pluronic F127 surfactant. The films were prepared on Ti substrates by spin-coating. The influence of the F127/Ti ratio in the range between 0.006 and 0.050, the pH of the titania sol between 1.5 and 2.0, and the aging time between 8 and 240 h on the morphology and porous structure of titania films was investigated. A TiO_2 film with the highest degree of the long-order structure was obtained at a surfactant/Ti molar ratio of 0.009, a pH of 1.5, and an aging time of 24 h. This film has a hexagonal pore structure with a mean pore size of 3.5 nm and a porosity of 25%. A powder titania support with a similar chemical composition and morphology was also produced and used for optimization of an active component deposition. The Pt–Sn carbonyl $[Pt_3(CO)_3(SnCl_3)_2(SnCl_2{\cdot}H_2O)]_n^{-2n}$ clusters were synthesized separately from monometallic precursors. They were loaded onto the TiO_2 supports by impregnation or adsorption. The adsorption of the Pt–Sn precursor for 24 h from an ethanol solution with concentrations of Pt and Sn of 2.0 and 1.2 mg/ml, respectively, followed by a vacuum treatment at 463 K, resulted in Pt–Sn nanoparticles embedded in the mesoporous titania network. An average size of bimetallic nanoparticles was 1.5–2 nm with a narrow particle size distribution. A reaction rate in terms of TOF between 0.2 and 3.3 min^{-1} was observed in the hydrogenation of citral over the Pt–Sn/TiO_2 catalysts. The selectivity to the unsaturated alcohols was as high as 90% at a citral conversion above 95%.

1. Introduction

Multiphase reactions can be performed in structured reactors, which improve heat and mass transfer, allow isothermal operation and provide narrow residence time distribution [1]. There are several application areas, where catalytic microreactors have evident advantages over traditional reactors, among which small-scale energy generation, fuel processing [1,2], and synthesis of fine chemicals [3]. The efficient use of catalytic reactors requires shaping of the catalyst by deposition of thin catalytic films on the inner walls of the reactor channels. Inorganic mesoporous thin films have attracted considerable attention because of their large surface areas and narrow pore size distribution, which make them attractive candidates for catalyst supports [4–6].

The efficiency of catalytic microreactors strongly depends on deposition of uniform catalytic coatings with good adhesion, high surface area, good dispersion of the active component, and high stability. Depending on the geometry of the channel and substrate type, different methods for deposition of thin catalytic porous layers with uniform thickness have been developed, among others, anodic oxidation [7], vapor deposition techniques (ALD, CVD) [8] and sol–gel methods (spin-coating, dip-coating) [4,9].

This study is devoted to the development of mesoporous titania supported novel Pt–Sn bimetallic nanostructured catalysts derived from mixed-metal precursors with desirable stoichiometry between the metals. The unique characteristics of mesostructured titania, namely high surface area, high concentration of hydroxyl groups combined with narrow pore size distribution prevent metal sintering after catalyst deposition. This approach allows a control both of the metal ratio and the loading of the support with the bimetallic nanoparticles. These nanoparticles demonstrate a superior performance in the selective hydrogenation of unsaturated aldehydes to the corresponding unsaturated alcohols (UA) as compared to the "crude" catalysts fabricated via impregnation-reduction methods.

* Corresponding author at: Boreskov Institute of Catalysis SB RAS, Prospekt Akademika Lavrentieva, 5, 630090 Novosibirsk, Russian Federation.
Tel./Fax: +7 383 330 62 19.
E-mail address: zri@catalysis.ru (Z.R. Ismagilov).

0920-5861/$ – see front matter © 2009 Elsevier B.V. All rights reserved.
doi:10.1016/j.cattod.2009.07.046

2. Experimental

2.1. Synthesis of Pt–Sn mixed-metal cluster precursor

The Pt–Sn bimetallic clusters were synthesized by a procedure adopted from Ref. [10]. An aqueous $H_2PtCl_6{\cdot}6H_2O$ (37.5 wt.% Pt, Aurat) solution with a Pt concentration of 2–10 mg/ml was carbonylated at 297 K for 16 h to yield the $H_2[Pt_3(CO)_6]_{10}$ cluster, which converts under CO atmosphere in an organic solvent giving the Chini anion: $[Pt_3(CO)_6]_n^{2-}$, where $n = 5$ or 6. In this study, acetone, ethanol, or tetrahydrofuran (THF) were used as a solvent. In the next step, a desired amount of HCl and $SnCl_2{\cdot}2H_2O$ (98 wt.%, Soyuzkhimprom) was added to the Chini anion solution under CO atmosphere. After a reaction time of 2 h, $[Pt_3(CO)_3(SnCl_3)_2(SnCl_2{\cdot}H_2O)]_n^{-2n}$ mixed-metal clusters were formed. They were isolated by addition of a tetraethyl ammonium chloride solution.

2.2. Preparation of mesoporous titania supports

Titanium substrates (99.99+ wt.% Ti) of $10 \times 10\ mm^2$ with a thickness of 500 μm were cleaned and pretreated as described elsewhere [4]. Immediately prior to the synthesis, the titania layer formed during pretreatment procedures was made super hydrophilic (concentration of surface OH groups $>15/nm^2$) by UV treatment for 2 h to encourage better adhesion of the titania film to the substrate.

A titania precursor sol of composition 1 $Ti(O\text{-}iPr)_4$:0.006–0.050 F127:40 ethanol:1.3 H_2O:0.1 trifluoroacetic acid was synthesized. The solution was prepared by dissolving the templating agent (Pluronic F127, $EO_xPO_yEO_x$, EO = ethylene oxide, PO = propylene oxide, $x = 100$, $y = 65$, BASF) in absolute ethanol, followed by the addition of water and trifluoroacetic acid. Titanium (IV) isopropoxide ($Ti(O\text{-}iPr)_4$, 99.99%, Fluka) was added dropwise to the rapidly stirred solution, and the resulting mixture was left to age under stirring for different time intervals (8–240 h) at room temperature.

Then, a desired amount of the solution was added onto the surface of a titanium substrate and the solvent was evaporated by spin-coating at 1500 rpm for 30 s at a relative humidity of 80%. The samples were dried at room temperature and then calcined at 573 K for 4 h under a residual pressure of 10 mbar with a heating rate of 1 K/min to remove the surfactant [11].

The mesoporous titania powders were prepared by sol–gel method using the same precursors and aging protocol with the only difference that nitric acid was used instead of trifluoroacetic acid. The pH during hydrolysis was varied between 1.5 and 2.0, and the Pluronic F127/$(Ti(O\text{-}iPr)_4$ molar ratio between 0.005 and 0.009. The resulting solution was stirred for 24 h. The solvent was evaporated under an IR-lamp for 3 h, followed by a treatment in a desiccator at 373 K for 1 h and calcination at 823 K for 4 h. The samples represent a white powder.

2.3. Preparation of supported Pt–Sn/TiO_2 catalysts

The $[Pt_3(CO)_3(SnCl_3)_2(SnCl_2{\cdot}H_2O)]_n^{-2n}$ solution was deposited onto the titania support by impregnation or adsorption for time intervals between 24 and 96 h.

For the powder TiO_2, the loading from 20 and 100 ml of solution of the Pt–Sn precursor for 1 g of TiO_2 was used. For the preparation of Pt–Sn catalysts on titania films, 50 titanium plates with TiO_2 films were fixed in a holder and then immersed in 150 ml of an ethanol solution of the Pt–Sn mixed-metal cluster for time intervals between 24 and 96 h. After adsorption, the impregnated TiO_2 materials were washed by a solvent, dried in vacuum and subsequently heated in vacuum at 463 K.

For comparison, the Pt–Sn/TiO_2 powered samples were also prepared by co-impregnation using $H_2PtCl_6{\cdot}6H_2O$ and $SnCl_2{\cdot}2H_2O$ as metals precursors.

The samples are referred to according to their synthesis procedure: the first letter denotes loading mode: "A" and "I" stand for adsorption and impregnation, respectively. The second letter corresponds to the solvent used: "A", "E", and "T" stand for acetone, ethanol, and THF, respectively. The combination of letters at the third place denotes the type of activation treatment: "V" means heated under vacuum at 463 K, "OR" means oxidized (calcined) in O_2 at 673 K and subsequently reduced in a 30 vol.% H_2/Ar flow at 673 K. The number at the end stands for the platinum concentration in the initial solution (mg/ml).

2.4. Characterization of mesoporous titania and Pt–Sn/TiO_2 catalysts

The chemical composition of the prepared catalysts was determined by X-ray fluorescence spectroscopy using a VRA-30 analyzer with a Cr anode of an X-ray tube. The phase composition was determined by X-ray diffraction in the range of 0.5–4° 2-theta.

The morphology of the TiO_2, the average Pt–Sn nanoparticle size and particle size distribution (PSD) were determined with a high-resolution JEOL JEM-2010 transition electron microscope operating at 200 kV with a structural resolution of 0.14 nm. The samples were deposited on perforated carbon supports attached to the copper grids. The local elemental analysis of the samples was carried out by an Energy Dispersive X-ray Analysis (EDX) method using an EDAX spectrometer equipped with a Si (Li) detector with a resolution of 130 eV.

The BET surface area and the porosity of the powder supports and catalysts were determined on a Micromeritics ASAP 2400 instrument using nitrogen adsorption at 77 K. The mesopore volume, mesopore surface area, and the pore size distribution, of the TiO_2 films were determined by ellipsometric porosimetry. The details of the method are described elsewhere [12].

2.5. Catalytic activity test

Two types of catalytic tests were performed: (i) either fifty Pt–Sn/TiO_2/Ti plates were inserted in a holder at a 2 mm separation, or (ii) catalyst pellets with a particle size of 100–200 μm were fixed in a basket. The holder with the catalyst was placed in an autoclave reactor with a total volume of 270 ml. The catalysts were reduced at 523 K under 12 bar of H_2 pressure for 12 h. Then the reactor was cooled to room temperature. The hydrogenation of a 0.01 M citral solution in 2-propanol was performed at 343 K and 12 bar H_2 with the plate holder rotating at 1500 rpm. Analysis was performed by introducing aliquots at established time intervals into a Varian CP-3800 GC equipped with a CP-Sil 5 CB capillary column via an automatic rapid on-line sampler-injector system (ROLSI™). The main reaction products were nerol, geraniol, citrononellal, citronellol and 3,7-dimethyl-1-octanol. The carbon balance was closed within 99% in all experiments.

3. Results and discussion

3.1. Synthesis of mesoporous TiO_2 materials

The samples of TiO_2 powder were prepared via sol–gel route at several different surfactant to titanium ratios 0.005–0.009 and pH of 1.5, 1.8, 2.0. The samples exhibit a IV type isoterms with a hysteresis loop at a N_2 partial pressure of 0.8 which is associated with textural mesoporosity [6,7]. The average pore size is 3.5–6.8 nm and the total pore volume is 0.04–0.16 cm^3/g. The specific surface area increases from 20 to 90 m^2/g with rising F127/Ti molar ratio from 0.005 to 0.008 at a given pH. These data are close to

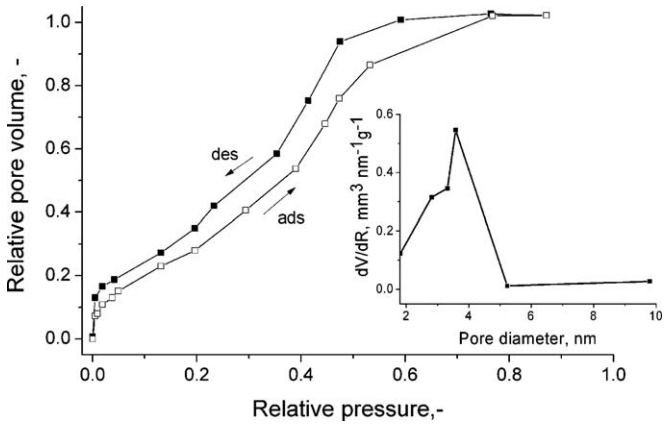

Fig. 1. The ethanol adsorption–desorption isotherms at 287 K and the pore size distribution for the mesoporous titania film. Synthesis conditions: F127/Ti ratio: 0.009, pH: 1.5, aging time: 24 h.

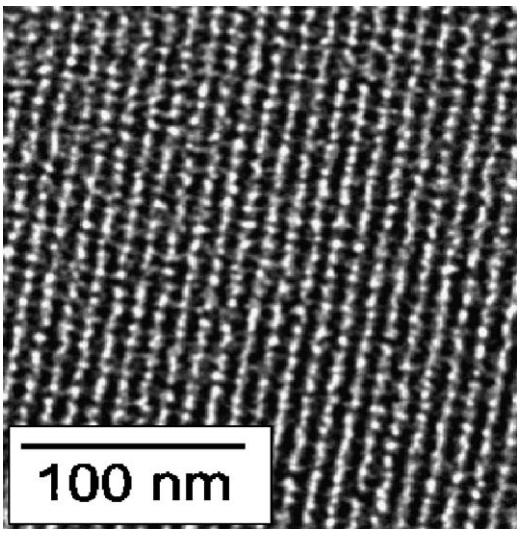

Fig. 2. TEM image of the mesoporous titania film taken after storage in air at room temperature for 2 months. Synthesis conditions are the same as those in Fig. 1.

those reported in literature [13,14]. It seems that the low porosity of the prepared TiO_2 is connected with a high calcination temperature and a long duration of the calcination required for the surfactant removal. Anatase was the only phase in the samples based on the XRD analysis data.

The TiO_2 coatings were synthesized on titania substrates by evaporation-induced self assembly (EISA) assisted sol–gel method at variation of surfactant to titanium ratios, pH and aging time. Typical ethanol adsorption–desorption isoterms are shown in Fig. 1. The type IV isotherm with a H1 hysteresis loop at ethanol partial pressure of 0.3–0.5 indicates to the framework-confined mesopores [13,15]. The increase of the aging time leads to increasing of the sol viscosity, thereby enlarging the thickness of the resulting film. For the titanium films, hexagonal mesostructure was confirmed by LA-XRD and TEM in the whole range of the compositions studied. A typical example of the mesoporous structure is shown in Fig. 2. As the F127/Ti molar ratio increases from 6×10^{-3} to 9×10^{-3}, the unit cell size decreases from 9.3 to 7.0 nm with the substantial increase in open porosity from 14 to 25%.

The surfactant was completely removed even at mild conditions as confirmed by the absence of the absorption bands at 1110, 2850 and 2930 cm^{-1} in the FTIR spectra of the mesoporous titania films. After calcination, the film thickness was reduced to 200 nm, which is almost a half of that in the as-synthesized samples.

3.2. Preparation of Pt–Sn/TiO_2 supported catalysts

To optimize the conditions of Pt–Sn cluster loading onto TiO_2, several synthesis parameters have been systematically varied, among them (i) solvent type (acetone, ethanol, or THF), (ii) concentration of the precursor solution (2.0, 10 mgPt/ml; 1.2, 6.0 mgSn/ml), (iii) the metal precursor to support ratio (20, 100 ml/g), (iv) duration of adsorption (2, 24 h), and (v) type of the activation treatment (calcined in O_2 at 673 K for 4 h and subsequently reduced in a 30 vol.% H_2/Ar flow at 673 K for 2 h, or in vacuum at 463 K for 2 h). In addition, the influence of the nature of the bimetallic precursor (carbonyl mixed-metal cluster or inorganic metal salts) was studied. Table 1 presents the effect of synthesis conditions on the properties of Pt–Sn/TiO_2 powder catalysts.

The metal loading in supported bimetallic catalysts prepared by adsorption of the bimetallic carbonyl precursor depends on the solvent type and increases in a sequence: acetone < ethanol < THF. This seems to be related to a difference in solubility of the precursor in these solvents. Fig. 3 reports TEM images of AE-OR-2 and AT-OR-2 catalysts showing numerous particles 1–3 nm of size. Fig. 4 shows the image of one of these

Table 1
Synthesis conditions and properties of powered Pt–Sn/TiO_2 catalysts.

Sample name	Synthesis conditions				Catalyst composition			Average particle size, nm
	Concentration in solution, mg/ml		Duration of loading, h	Thermal treatment[a]	Pt, wt.%	Sn, wt.%	Pt/Sn molar ratio	
	Pt	Sn						
Mixed-metal cluster precursor								
AA-OR-2	2	1.2	24	OR	0.05	0.04	1.2	0.7
AE-OR-2	2	1.2	24	OR	0.61	0.25	1.5	1.1
AT-OR-2	2	1.2	24	OR	4.04	1.75	1.5	2.2
AE-OR-10	10	6	24	OR	3.55	2.80	0.8	3.2
IE-OR-2	2	1.2	72	OR	3.46	1.33	1.6	n.d.
AE-V-2	2	1.2	24	V	0.61	0.25	1.5	1.5
IT-OR-2	2	1.2	72	OR	3.67	2.29	1.0	1.6
Inorganic metal salt precursor								
IE-OR-33	33	20	0.25	OR	2.16	0.95	1.4	1.8
IA-OR-33	33	20	0.25	OR	2.16	1.05	1.3	1.7

n.d.—not determined.
[a] OR—oxidized (calcined) in O_2 at 673 K for 4 h and subsequently reduced in a 30 vol.% H_2/Ar flow at 673 K for 2 h; V—heated under vacuum at 463 K for 2 h.

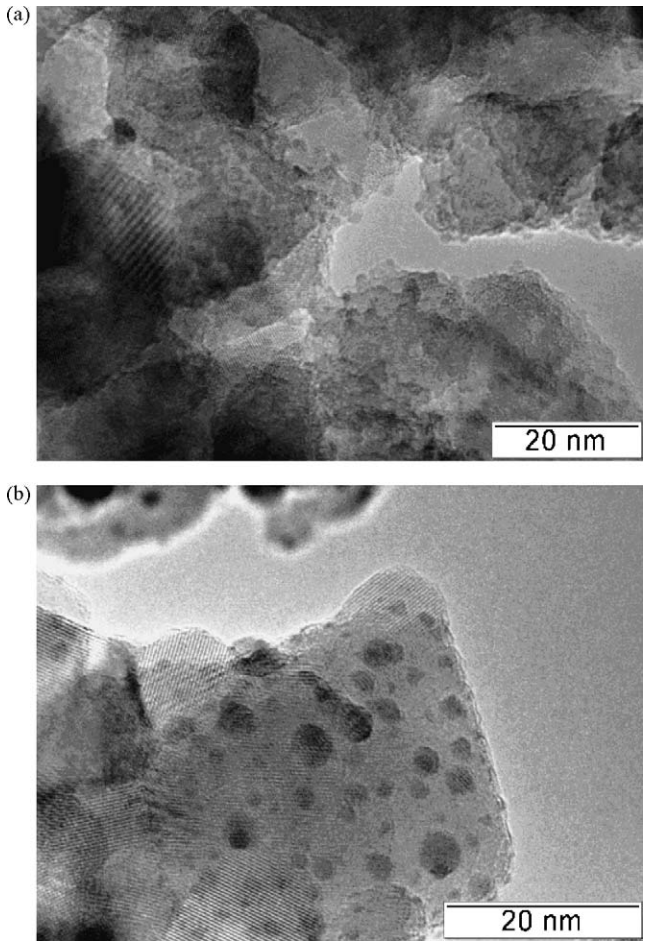

Fig. 3. TEM images of Pt–Sn/TiO_2 catalysts with different metal loadings: (a) 0.61 wt.% Pt, 0.25 wt.% Sn (AE-OR-2, Table 1); (b) 4.04 wt.% Pt, 1.75 wt.% Sn (AT-OR-2, Table 1).

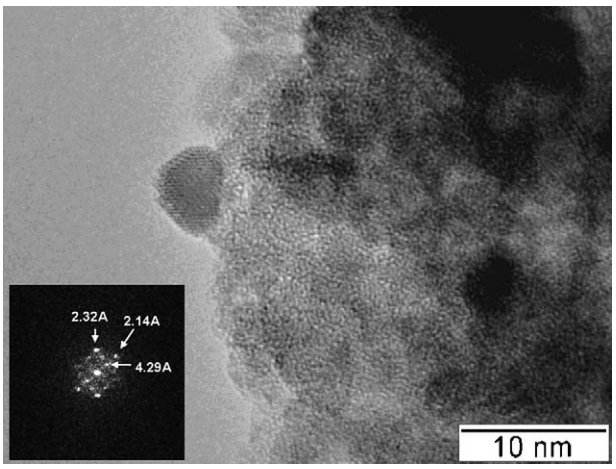

Fig. 4. TEM image of AT-OR-2 sample. Inset: Fourier pattern and lattice spacings.

metal particles. According to the Fourier pattern, this particle has a crystalline structure with lattice spacings of 2.14, 2.32, 4.29 Å. This structure can be assigned to a Pt_3Sn alloy with lattice spacings of $d_{2\,0\,0}$ = 2.0015 Å, $d_{1\,1\,1}$ = 2.3107 Å, and $d_{1\,0\,0}$ = 4.001 Å. The increase of metals content from 0.1 to 0.6 to ca. 4 wt.% Pt resulted in an increase of the average particle size from 1 to 2 nm. At the same time, the PSD pattern changed from mono- to bi-modal (Fig. 5).

The increase of the mixed-metal cluster concentration in the solution (from 2 to 10 mgPt/ml) leads to a proportional rise of the metal loading (from 0.6 to 3.5 wt.% Pt), average particle size (from 1.5 to 3.2 nm) and to a wider PSD in the Pt–Sn/TiO_2 samples. For the both samples, PSD has a monomodal type. It is necessary to note that an increase of the metal precursor to support ratio and the duration of adsorption step also leads to higher metal loadings in the catalysts. When a mixed-metal cluster precursor is deposited by impregnation it allows increasing the metal loading in the catalysts (sample IE-OR-2 and IT-OR-2, Table 1).

The crystalline structure of particles was not significantly affected by the mode of thermal treatment. The Pt_3Sn nanoparticles were observed in the sample after treatment in vacuum (Fig. 6). A vacuum catalyst activation procedure also resulted in a narrow PSD in comparison with that after reduction by hydrogen (compare Figs. 7 and 5a). The range of obtained particle sizes is 0.5–5.1 and 0.5–2.9 nm, respectively for oxidative and vacuum treatments.

The mixed-metal cluster precursor provided a more uniform metal particle size distribution as compared with inorganic metal salt precursors at the practically same average particle size. In particular, for catalysts prepared by co-impregnation from H_2PtCl_6 and $SnCl_2$ precursors, large nanoparticles of 20 nm were also obtained while the average particle size was ca. 2 nm. In these catalysts in addition to Pt_3Sn nanoparticles the Pt and Pt_2Sn_3 particles were observed.

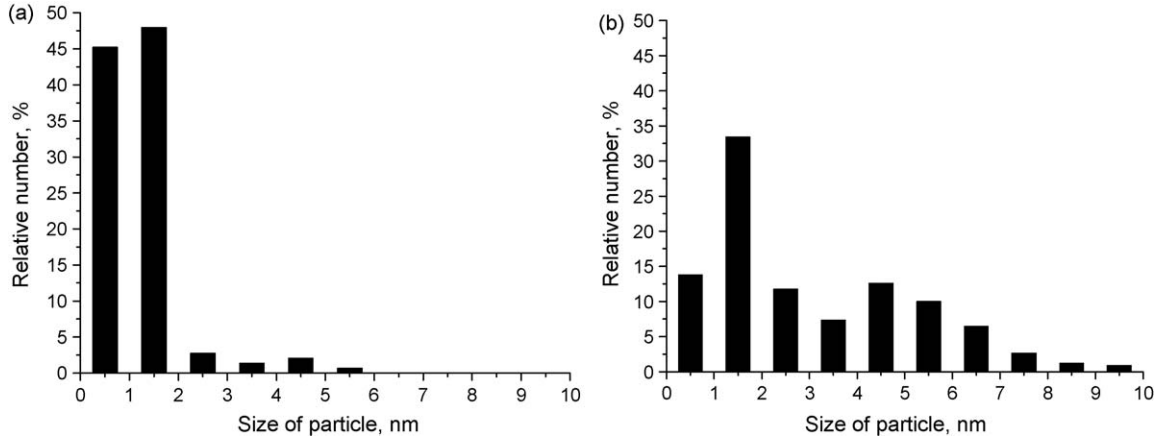

Fig. 5. Size distribution of Pt–Sn particles in the Pt–Sn/TiO_2 catalysts with different metal loading: (a) 0.61 wt.% Pt, 0.25 wt.% Sn (AE-OR-2, Table 1); (b) 4.04 wt.% Pt, 1.75 wt.% Sn (AT-OR-2, Table 1).

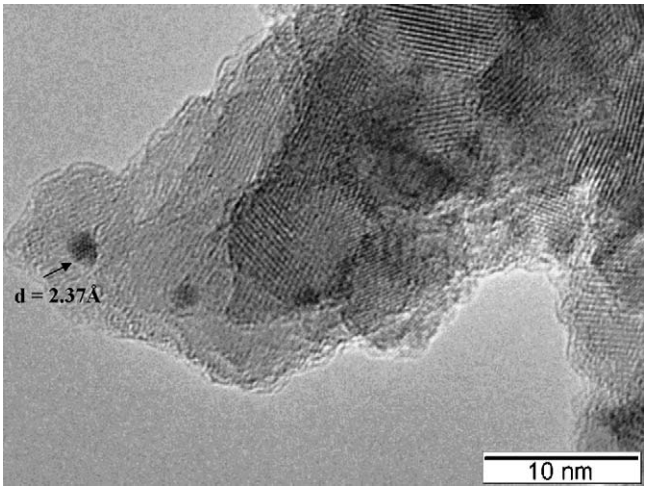

Fig. 6. TEM image of AE-V-2 sample after vacuum treatment at 463 K.

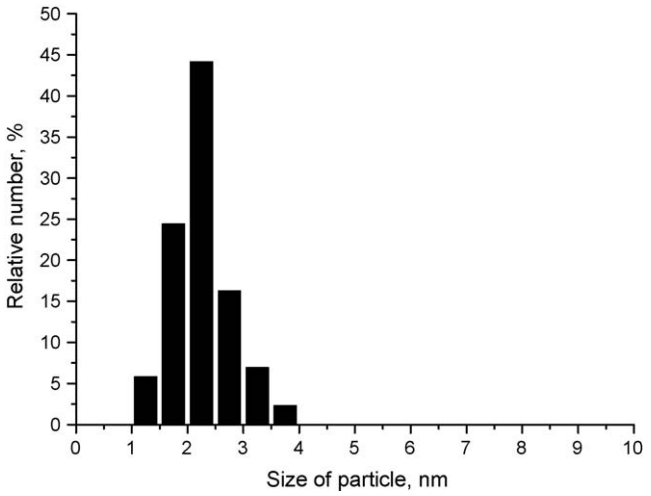

Fig. 8. Size distribution of Pt–Sn particles in the Pt–Sn/TiO_2 catalytic film prepared by adsorption of Pt–Sn–CO anion complex onto TiO_2 film during 24 h.

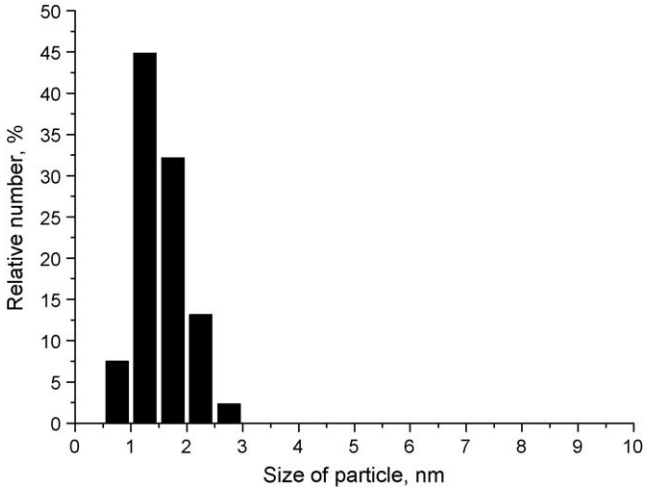

Fig. 7. Size distribution of Pt–Sn particles in the Pt–Sn/TiO_2 catalyst after vacuum treatment at 463 K (AE-V-2, Table 1).

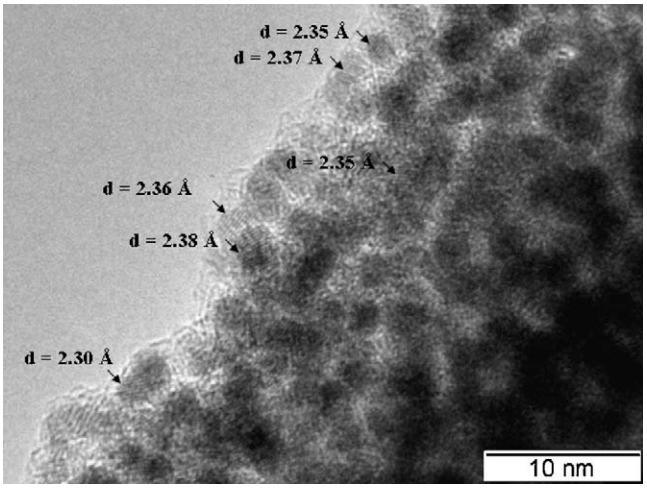

Fig. 9. TEM image of Pt–Sn/TiO_2 catalytic film prepared by adsorption of Pt–Sn–CO anion complex onto TiO_2 film during 24 h.

The prolonged adsorption (96 h) of the mixed-metal cluster precursor from the ethanol solution onto TiO_2 films leads to a decrease of the porosity from 25 to 8% and the average pore size from 3.5 to 1.8 nm. The Pt–Sn/TiO_2 film had a smaller mean pore size as compared to the pure titania support due to a partial pore blockage by the metal nanoparticles. Using TEM, the average Pt–Sn particle size was found to be 9.1 nm. Hence the pore size of the titania film (about 2 nm) is smaller than the average Pt–Sn particle size.

As noted above, for powdered Pt–Sn/TiO_2 catalysts the average particle size is about 1–3 nm. The larger particle size for Pt–Sn/TiO_2

Table 2
Activity and selectivity of powered Pt–Sn/TiO_2 catalysts.

Sample	Initial TOF, min^{-1}	Product selectivity at the 96–98% citral conversion, %			
		Nerol and Geraniol	Citronellal	Citronellol	3,7-Dimethyl-1-octanol
Mixed-metal cluster precursor					
Pt/TiO_2	5.6	3	11	21	65
AA-OR-2	n.d.	n.d.	n.d.	n.d.	n.d.
AE-OR-2	0.06	65	28	6	1
AT-OR-2	0.20	82	7	10	1
AE-OR-10	0.54	90	6	4	0
IE-OR-2	0.35	80	4	16	0
AE-V-2	0.18	39	35	26	0
IT-OR-2	0.14	90	4	6	0
Inorganic metal salt precursor					
IE-OR-33	3.3	85	0	15	0
IA-OR-33	0.32	70	4	17	9

n.d.—not determined.

film is probably connected with a long time of adsorption step (96 h) during its preparation. Actually the reduction of the duration of the adsorption of carbonyl complex anion onto the TiO_2 film from 96 to 24 h leads to the decrease of an average particle size from 9.1 to 2.3 nm (Fig. 8). Fig. 9 shows the TEM image of Pt–Sn/TiO_2 catalytic coatings prepared by adsorption for 24 h. The lattice spacing of the observed nanoparticles is indicative of the bimetallic composition of particles.

3.3. Activity of Pt–Sn/TiO_2 catalysts

The catalytic activity of the Pt–Sn/TiO_2 catalysts was determined in the hydrogenation of citral employing a 0.01 M solution of citral in 2-propanol at 343 K and 12 bar H_2 (Table 2). The activity of a reference Pt/TiO_2 sample characterized by the initial TOF was found to be 5.6 min^{-1} with the selectivity to unsaturated alcohols of 3%. The addition of tin to the Pt/TiO_2 catalysts resulted in TOF lowering and an increase of the selectivity to UA, which is in agreement with previously reported literature data [16,17].

The Pt–Sn/TiO_2 catalysts prepared using Pt–Sn mixed-metal cluster precursor and oxidation–reduction thermal treatment showed a TOF of 0.1–0.5 min^{-1} and a selectivity to UA of 65–90%. In the beginning of the reaction the selectivity to UA is growing with the increase of citral conversion and then stay at the plateau. Most of the citral was converted into UA, while citronellal, citronellol were formed in small amounts. The fully saturated product (3,7-dimethyl-1-octanol) was only observed at high conversion of citral. The samples after vacuum thermal treatment exhibited a lower selectivity to UA at the same TOF in comparison with the samples after OR thermal treatment. The sample obtained using high concentration of Pt in initial solution (10 mg/ml) showed a very high selectivity to UA (90%) and TOF of 0.54 min^{-1}. A higher activity was demonstrated by Pt–Sn/TiO_2 catalyst (IE-OR-33) prepared using combined impregnation of the inorganic salts as metal precursors. This sample showed a TOF of 3.3 min^{-1} and a selectivity to UA of 85%. It can be supposed that such high TOF value is connected with the peculiarity of the composition of bimetallic particles and electronic state of metals. A similar effect was observed over Rh–Sn/SiO_2 catalysts in citral hydrogenation in [18]. The activity of catalysts prepared by co-impregnation was three-folds higher than that of the catalysts prepared via organometallic route and successive impregnation. This could be attributed to an intimate contact between the metals. A metal–metal interaction plays an essential role in the reaction over bimetallic catalytic systems.

4. Conclusions

Mesoporous titania films with hexagonal pore structure and a thickness of 200–300 nm were successfully prepared on Ti substrates by the sol–gel method using the Pluronic F127 as a template. The morphology and porous structure of titania films were regulated by the variation of the F127/Ti ratio in the range between 0.006 and 0.050, the pH of the titania sol between 1.5 and 2.0, and the aging time between 8 and 240 h. Powder titania supports were also produced by the same manner and used for the optimization of catalyst preparation.

Pt–Sn/TiO_2 catalyst films on the Ti plates and powdered Pt–Sn/TiO_2 catalysts were obtained by loading Pt–Sn carbonyl complex anionic species $[Pt_3(CO)_3(SnCl_3)_2(SnCl_2{\cdot}H_2O)]_n^{-2n}$ onto TiO_2 supports. It was shown that the metal content, mean particle size and mode of PSD in the Pt–Sn/TiO_2 catalysts can be varied by changing conditions of the Pt–Sn carbonyl complex adsorption and the thermal treatment of Pt–Sn/TiO_2 catalysts. The mean diameter of anchored bimetallic nanoparticles decrease from 9.1 to 2.3 nm with a reduction of the adsorption duration from 96 to 24 h.

A reaction rate in terms of TOF between 0.2 and 3.3 min^{-1} was observed in the hydrogenation of citral over the Pt–Sn/TiO_2 catalysts with a selectivity to the UA as high as 90% at a citral conversion above 95%.

Acknowledgements

The authors are thankful to A.V. Ishchenko for the assistance with catalyst characterization by HRTEM and EDX. Financial support of this work in the frame of NWO-RFBR 047.017.028 project is gratefully acknowledged.

References

[1] G. Kolb, V. Hessel, Chem. Eng. J. 98 (2004) 1–38.
[2] I.Z. Ismagilov, E.M. Michurin, O.B. Sukhova, L.T. Tsykoza, E.V. Matus, M.A. Kerzhentsev, Z.R. Ismagilov, A.N. Zagoruiko, E.V. Rebrov, M.H.J.M. de Croon, J.C. Schouten, Chem. Eng. J. 135 (2008) S57–S65.
[3] E.V. Rebrov, A. Berenguer-Murcia, H.E. Skelton, B.F.G. Johnson, A.E.H. Wheatley, J.C. Schouten, Lab Chip 9 (2009) 503–506.
[4] T.S. Glazneva, E.V. Rebrov, J.C. Schouten, E.A. Paukshtis, Z.R. Ismagilov, Thin Solid Films 515 (2007) 6391–6394.
[5] O. Muraza, E.V. Rebrov, T. Khimyak, B.F.G. Johnson, P.J. Kooyman, U. Lafont, M.H.J.M. de Croon, J.C. Schouten, Chem. Eng. J. 135 (2008) S99–S103.
[6] E.V. Rebrov, A. Berenguer-Murcia, B.F.G. Johnson, J.C. Schouten, Catal. Today 138 (2008) 210–215.
[7] I.Z. Ismagilov, R.P. Ekatpure, L.T. Tsykoza, E.V. Matus, E.V. Rebrov, M.H.J.M. de Croon, M.A. Kerzhentsev, J.C. Schouten, Catal. Today 105 (2005) 516–528.
[8] M.T. Janicke, H. Kestenbaum, U. Hagendorf, F. Schüth, M. Fichtner, K. Schubert, J. Catal. 191 (2000) 282–293.
[9] K. Haas-Santo, M. Fichtner, K. Schubert, Appl. Catal. A 220 (2001) 79–92.
[10] N.B. Shitova, Y.D. Perfil'ev, L.Y. Al't, G.G. Savel'eva, Russ. J. Inorg. Chem. 46 (2001) 376–381.
[11] L.N. Protasova, E.V. Rebrov, T.S. Glazneva, A. Berenguer-Murcia, Z.R. Ismagilov, J.C. Schouten, J. Catal. (submitted for publication).
[12] L.N. Protasova, E.V. Rebrov, Z.R. Ismagilov, J.C. Schouten, Micropor. Mesopor. Mater. 123 (2009) 243–252.
[13] T.-D. Nguyen-Phan, M.B. Song, E.J. Kim, E.W. Shin, Micropor. Mesopor. Mater. 119 (2009) 290–298.
[14] M.M. Yusuf, H. Imai, H. Hirashima, J. Sol–Gel Sci. Tech. 28 (2003) 97–104.
[15] T.R. Pauly, Y. Liu, T.J. Pinnavaia, S.J.L. Billinge, T.P. Rieker, J. Am. Chem. Soc. 121 (1999) 8835–8842.
[16] J.C.S. Wu, W.-C. Chen, Appl. Catal. A 289 (2005) 179–185.
[17] A.M. Silva, O.A.A. Santos, M.J. Mendes, E. Jordao, M.A. Fraga, Appl. Catal. A 241 (2003) 155–165.
[18] J.N. Coupé, E. Jordão, M.A. Fraga, M.J. Mendes, Appl. Catal. A 199 (2000) 45–51.

Journal of Catalysis 271 (2010) 161–169

Contents lists available at ScienceDirect

Journal of Catalysis

journal homepage: www.elsevier.com/locate/jcat

Control of the thickness of mesoporous titania films for application in multiphase catalytic microreactors

Lidia N. Protasova [a,b], Evgeny V. Rebrov [a], Tatiana S. Glazneva [b], Angel Berenguer-Murcia [c], Zinfer R. Ismagilov [b], Jaap C. Schouten [a,*]

[a] Eindhoven University of Technology, P.O. Box 513, 5600 MB Eindhoven, The Netherlands
[b] Boreskov Institute of Catalysis, Pr. Lavrentieva, 5, Novosibirsk 630090, Russia
[c] Departamento de Química Inorgánica, University of Alicante, Ap. 99 – 03080 Alicante, Spain

ARTICLE INFO

Article history:
Received 14 May 2009
Revised 23 July 2009
Accepted 27 July 2009
Available online 7 March 2010

Keywords:
Mesoporous titania films
Au nanoparticles
Citral hydrogenation

ABSTRACT

A new method of sol–gel polymer template synthesis of mesoporous catalytic thin films has been proposed which allows controlling the chemical nature of the film, the porosity, thickness and loading with an active species. The mesoporous films with a long-order structure can be obtained in a narrow range of surfactant-to-metal precursor molar ratios from 0.006 to 0.009. The catalytic film thickness was varied from 300 to 1000 nm while providing a uniform catalyst distribution with a desired catalyst loading (1 wt. % Au nanoparticles) throughout the film. The films were characterized by TEM, SEM, ethanol adsorption and contact angle measurements. The calcination of the as-synthesized films at 573 K reduced Ti^{4+} sites to Ti^{3+}. A 300 nm thick Au-containing film showed an initial TOF of 1.4 s^{-1} and a selectivity towards unsaturated alcohols as high as 90% in the hydrogenation of citral. Thicker films demonstrated a high selectivity towards the saturated aldehyde (above 55%) and a lower intrinsic catalytic activity (initial TOF of 0.7–0.9 s^{-1}) in the absence of internal diffusion limitations.

1. Introduction

Catalytic microstructured reactors are becoming widely recognized for their unique properties and potential applications in chemical industry [1,2]. Their efficient use requires shaping of the catalyst usually by deposition of catalytic thin films on microchannel walls. Catalytic thin films can be produced on a substrate by different methods such as hydrothermal synthesis [3–7], anodic oxidation [8,9] and evaporation-induced self-assembly (EISA) [10,11]. The latter is a variant of sol–gel synthesis [12–14], where either spin-coating or dip-coating is applied for destabilization of the initial sol. This method enables the formation of highly ordered mesoporous films with various porous hierarchies.

Recently, mesoporous titania thin films have attracted considerable attention in catalysis due to their large surface areas, narrow pore size distribution and favourable surface properties [11,15,16]. The films obtained by either spin-coating or dip-coating have a narrow pore size distribution in the mesopore range but their thickness is limited to 300 nm, which prevents their efficient use in microstructured reactors as the catalyst occupies less than 0.5% of the reactor volume. There are several options to increase the film thickness, such as lowering the rotation speed during spin-coating (or increasing the solvent withdrawal speed during dip-coating) or increasing the viscosity of the initial sol. However, there is a narrow range of conditions leading to the formation of mesoporous structures rather than disordered macroporous films. For the synthesis of sol–gel derived mesoporous titania thin films, the precursors need to be partially hydrolyzed under controlled conditions, so that subsequent polycondensation reactions yield a weakly branched polymeric metal oxide sol [15,17–22]. The rates of hydrolysis and polycondensation reactions are controlled by the surfactant-to-metal precursor ratio, temperature, solution dilution level and pH [15].

The thickness of the mesoporous films can be increased by repeating the spin-coating, aging and calcination steps. Recently the layer-by-layer deposition method of Ag doped silica and titania films has been reported [23]. It is well known that the specific surface area and the mesopore volume can be markedly reduced during calcination, which may also lead to shrinkage of the internal layers in a multilayer film if the surfactant is not completely removed [21]. Therefore it is important to develop a calcination protocol which allows removal of the surfactant at the lowest possible temperature.

In order to assess the feasibility of the proposed deposition method, the catalytic performance of the single and multilayer

* Corresponding author. Fax: +31 40 244 6653.
E-mail address: j.c.schouten@tue.nl (Jaap C. Schouten).

0021-9517/$ - see front matter © 2009 Elsevier Inc. All rights reserved.
doi:10.1016/j.jcat.2009.07.013

coatings should be compared in a catalytic reaction. This has to be fast enough for application in microstructured reactors and should include several subsequent steps to evaluate the performance in terms of both activity and selectivity. Citral hydrogenation has been chosen as a test reaction as this is a multi-step reaction and the presence of internal diffusion limitations substantially decreases the selectivity towards the semihydrogenated products. Gold nanoparticles have been chosen as an active metal to test the performance of structured Au/TiO_2 catalysts in the hydrogenation of citral.

Classical ways of deposition of Au nanoparticles, such as impregnation and deposition–precipitation could provide a uniform distribution with the active metal with a high metal dispersion. Nevertheless, the low reproducibility of these methods severely limits their applicability when applied to manufacturing of structured catalysts. Furthermore, obtaining the desired loading with an active component in a single step is not straightforward [24]. On the other hand, the direct addition of metal nanoparticles into the Ti sol with subsequent aging and evaporation-induced self-assembly provides a good alternative to the post synthesis loading of the active component. The initial size and the chemical composition of the metal nanoparticles can be well controlled in a reduction by solvent method [24].

In view of the tailoring that is possible with microreactors, it is increasingly being recognized that major improvements in the selectivity of reactions can be achieved by changes in the catalyst and/or support structure rather than in process conditions. In this work a method is proposed to increase the thickness of catalytic mesoporous films while maintaining their morphology, long-range order and mesoporous structure. The particle size in a nanostructured catalyst, the pore size and the thickness of the mesoporous support can be independently controlled via a one-pot EISA synthesis. Prior to multi-step synthesis, the surfactant-to-metal precursor ratio should be optimized to obtain stable films with a long-order structure.

Calcination conditions suitable for complete surfactant removal have been investigated by FTIR to obtain crack-free films of known thickness which required complete stabilization of the inorganic framework before the next deposition cycle. The morphology of the films was studied by LA-XRD, TEM and ethanol adsorption–desorption isotherms. The film thickness was determined by ellipsometry and SEM. The strength of the different acid sites was studied by FTIR spectroscopy of adsorbed CO at 77 K. The activity of the resulting Au/TiO_2 catalysts was studied in the hydrogenation of citral.

2. Experimental

2.1. Preparation of mesoporous titania films

Silicon and titanium substrates with a cross-section of $9.8 \times 9.8\ mm^2$ and a thickness of 0.5 mm were used. Prior to film deposition, the surface roughness of the silicon and glass substrates was increased to 500 nm as described elsewhere [13]. Solution A was prepared by mixing titanium isopropoxide (99.99 wt.%, Fluka) and an aqueous HNO_3 solution (65 wt.%, Fluka) under vigorous stirring. Solution B was prepared by dissolving Pluronic F127 (EO_{100}–PO_{65}–EO_{100}, BASF) in ethanol (99.99 wt.%, Aldrich). After stirring for 1 h, solution B was added to solution A. The resulting solution with a molar composition of 1 $Ti(O–iC_3H_7)_4$: 0.005–0.009 Pluronic F127: 40 Ethanol: 1.3 H_2O: 0.13 HNO_3 was stirred for either 8, 15, 25 or 240 hours at 298 K (Fig. 1). After an aging period of 25 h, the solution was deposited on the substrates. The films were produced by spin-coating at 1500 rpm at a relative humidity (RH) of 80%. The as-deposited films were kept at a RH of 80% for 48 h and then were calcined at 573 K for 4 h under a residual pressure of 10 mbar with a heating rate of 1 K min^{-1}.

2.2. Preparation of Au/TiO_2 catalytic mesoporous films

A PVP-stabilized Au colloid solution in ethanol was prepared as shown in Fig. 2 and described elsewhere in detail [25,26].

Poly-*n*-vinyl pyrrolidone (1.14 g) was added to anhydrous ethylene glycol to make solution 1. For solution 2, 0.39 g of $HAuCl_4$ was dissolved in water. Then solution 2 was poured into solution 1 under stirring. The pH of the resulting mixture was adjusted to 9–10 by adding a NaOH solution. The resulting solution was heated at 373 K for 2 h after which it was cooled to room temperature. The prepared nanoparticles were purified as follows: an aliquot containing the desired amount of nanoparticles was treated with a large excess of acetone. This treatment produced the extraction of the protecting polymer to the acetone phase, provoking flocculation of the metallic nanoparticles. After removal of the acetone phase, the purified colloids were redispersed in ethanol [26]. The average size of the Au nanoparticles was obtained by taking several TEM pictures and measuring 100 individual nanoparticles in the colloid solution was found to be 4 nm [24].

A certain amount of the Au colloidal solution, calculated to obtain a 1 wt.% Au loading in the resulting mesoporous film, was mixed with Pluronic F127 at 323 K. Solution A (see Section 2.1) was added and the resulting mixture (solution C) was aged for

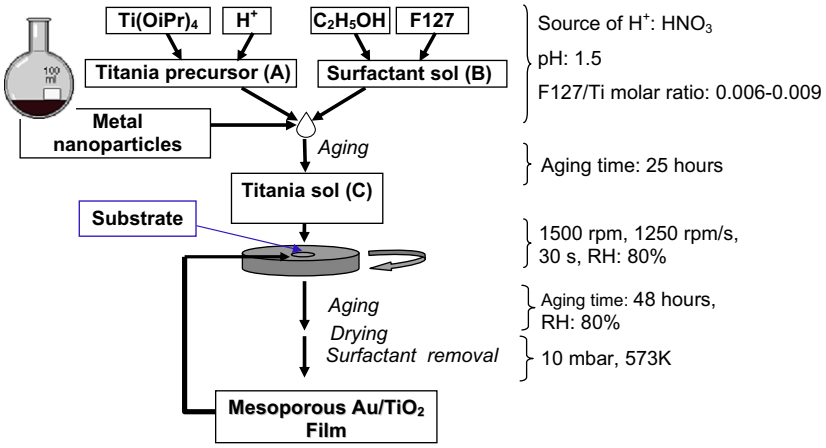

Fig. 1. Sol–gel synthesis of Au/TiO_2 multilayer catalytic coatings.

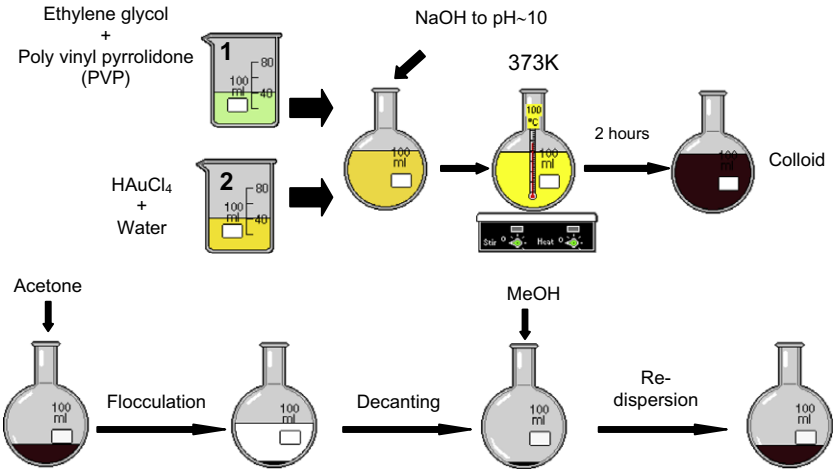

Fig. 2. A schematic view of the reduction by solvent method for the synthesis of Au nanoparticles.

2 h. The precursor/surfactant ratio was chosen to be 0.009, and the pH value was 1.5. The films were deposited on the titanium substrates as described in Section 2.1. Thicker films were prepared from solution C by consecutive repetition of spin-coating, aging and calcinations steps after every deposition (see Fig. 1).

All films are referred to as TiO_2(or Au/TiO_2)-*i*-*a*. The roman numerals (I, II or V) in the first index (*i*) denote the number of deposition cycles. The second index (*a*) stands for the surfactant-to-precursor molar ratio multiplied by 10^3. For example, a catalytic mesoporous film after 2 deposition cycles performed with a surfactant to precursor ratio of 0.009 will be referred as Au/TiO_2-II-9 hereafter.

2.3. Characterization

Low-angle XRD spectra were recorded on a Rigaku Geigerflex device with Cu K_α radiation (40 kV, 40 mA), 0.01–0.02° 2 theta step size, with a counting time of 4.0 s. 2D SAXS was performed with a rotating anode X-ray generator (copper anode operated at 50 kV, 30 mA; small focus) equipped with two adjustable optical systems. The Scanning Electron Micrographs (SEMs) were obtained on a Quanta 3D FEG microscope at 30 kV with a resolution of 1.2 nm. The Transmission Electron Micrographs (TEMs) were obtained on a JEM-2010 microscope at 200 kV with a resolution of 0.14 nm. Samples for TEM were prepared by placing a slice of the film removed from the substrate on a copper grid coated with a carbon film and dried under vacuum.

Surfactant removal was studied by FTIR on a BOMEM MB 102 spectrometer in the 200–4000 cm^{-1} range with a resolution of 4 cm^{-1}. CO adsorption at 77 K and 0.13 and 13 mbar was studied on a Shimadzu FTIR-8300 spectrometer in the region of 400–6000 cm^{-1} with a resolution of 4 cm^{-1} and accumulation of 100 scans. All FTIR studies were performed in a transmission mode on supported films without any destruction of the samples. Each experiment required one sample. Prior to CO adsorption, the sample was pretreated in an IR cell at 673 K for 2 h under a residual pressure of 0.01 mbar to remove adsorbed surface species. The strength of the Brønsted acidic sites is referred to as proton affinity (PA) determined from IR-spectra by Eq. (1):

$$PA_{OH} = PA_0 - \frac{1}{0.00226}\log(\Delta\upsilon_{OH}/\Delta\upsilon_{SiOH}), \quad (1)$$

where a PA_0 of 1390 kJ mol^{-1} is the proton affinity of aerosil hydroxyl groups which is used as standard, a $\Delta\upsilon_{SiOH}$ of 90 cm^{-1} is the frequency shift of the Si–OH vibration, and $\Delta\upsilon_{OH}$ is the frequency shift of the OH vibration. The $\Delta\upsilon_{OH}$ values were obtained from the FTIR differential spectra. The latter were obtained by subtraction of the spectrum of the pretreated sample from the spectrum taken at the maximum saturation value [27].

The mesopore volume of the films and pore size distribution were determined by Ellipsometric Porosimetry (EP) from the desorption branch of the ethanol isotherms at 287 K using the Bruggerman effective media approximation and the improved Deriaguin–Broekhoff–de Boer model. The film porosity was calculated with an accuracy of ±3% based on the change of the effective refractive index between the empty film and the film filled with ethanol [28]. The thickness of the mesoporous films was determined on an M-2000F EC-400 Spectroscopic Ellipsometer (J.A. Woollam Co., Inc.). The applied optical model consisted of three layers: a silicon substrate layer, a native silicon oxide layer of 3 nm and the mesoporous titania layer [28]. The contact angle of a water droplet of 2 μl on the substrates was measured on a Dataphysics OCA 30 device at 293 K and a RH of 40%.

2.4. Catalytic activity

Fifty Au/TiO_2 films were clamped between two concentric rings at a distance of 1 mm from each other. These two rings were connected to a central shaft which was used for stirring. This holder was placed in an autoclave reactor with a total volume of 270 ml. Prior to activity measurements, the catalytic films were reduced *in situ* at 523 K at a H_2 pressure of 12 bar for 12 h to remove the surface oxygen. Then, the reactor was cooled to room temperature. The hydrogenation reaction was performed with 130 ml of a 0.01 M deoxygenated solution of citral in 2-propanol at 343 K and 12 bar H_2 pressure. The stirring speed of the holder equipped with the plates was 1500 rpm. Analysis of the reaction mixture was performed off-line with a Varian CP-3800 gas chromatograph equipped with a CP-Sil 5 CB capillary column (diameter: 1 mm, length: 30 m) and a FID detector. The carbon balance was closed within 99%. The turnover frequency (TOF) was calculated as follows: $TOF = X \cdot n_{C10H16O}/(t \cdot \alpha \cdot D \cdot n_{TiO2})$, where X is the citral conversion, $n_{C10H16O}$ is the initial amount of citral in the reactor, n_{TiO2} is the amount of the titania support in the reactor, α and D are the Au loading and dispersion, respectively, and t is the reaction time. The Au dispersion was estimated as $D \approx 0.9/d_{TEM}$ [29], where d_{TEM} is the average particle size as recorded using TEM (nm).

3. Results and discussion

3.1. Single layer mesoporous titania films

3.1.1. Influence of calcination temperature on the surfactant removal and film thickness

To identify the range of conditions under which stable mesoporous titania films with a long-order structure can be obtained, a series of single layer films were studied by several physical methods immediately after the synthesis as well as after storage in air for 2 months.

Surfactant removal and dehydroxylation during calcination were studied over the sample TiO_2-I-6 by FTIR. The most intense absorption bands of Pluronic F127 were observed in the FTIR spectra of the as-synthesized film at 1110 cm^{-1} and in the 2850–2930 cm^{-1} range (Fig. 3a). These bands were assigned to the C–O–C stretching, CH_2 bending and C–H stretching vibrations (see Table 1). They were used to monitor the surfactant removal during calcination. The formation of the Ti–O–Ti bridges during dehydroxylation of the terminal hydroxyl groups in the amorphous titania walls can be seen after calcination at 473 K (Fig. 3b). The complete removal of surfactant was achieved after calcination at 573 K for 4 h (Fig. 3c). It should be mentioned that film thickness decreases from 350 to 177 nm after calcination at 573 K due to a contraction of the titania framework in the direction perpendicular to the substrate. Therefore it is of importance to obtain complete surfactant removal and stabilization of the inorganic network before deposition of the next layer.

3.1.2. Influence of surfactant content in the sol on film porosity and stability

Fig. 4a–c shows the XRD patterns of the as-synthesized titania films TiO_2-I-6, TiO_2-I-7, (c) TiO_2-I-9, while Fig. 4d–f shows patterns of the same films after storage in air for 2 months (spent films). The average film thickness after calcination was 175 ± 5 nm. The unit cell parameter was calculated from the position of the (200) peak of a P6 mm hexagonal structure. The unit cell decreases from 10.8 nm in TiO_2-I-6 to 8.1 nm in TiO_2-I-9. No long-order structure was observed at a surfactant-to-precursor molar ratios below 6×10^{-3} and above 9×10^{-3} (not shown). All films have a 2D hexagonal structure (see 2D SAXS image in Fig. 4, frame). The pattern consists of well-defined diffraction spots [30], which are distributed along an ellipse rather than a circle. This confirms an anisotropic contraction of the films during calcination [15].

A long-order hexagonal structure was preserved in spent (after storage in air for 2 months) TiO_2-I-9 (Fig. 4f), while at a lower surfactant content (TiO_2-I-*a*, *a* = 6 and 7) it disappeared in the spent films (Fig. 4d and e). The XRD results were confirmed by the TEM image analysis of spent TiO_2-I-9 and TiO_2-I-7 (Fig. 5a and b, respectively). A highly ordered mesoporous domain was observed in the TEM of TiO_2-I-9. The average size of a unit cell, which includes one pore and one pore wall, is 9.0 nm (22 unit cells over 200 nm). This value is close to that obtained from the XRD results.

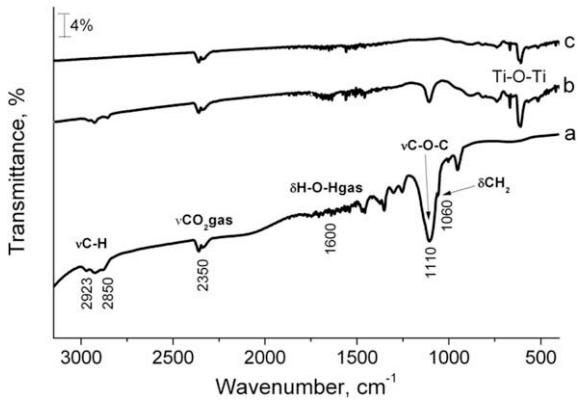

Fig. 3. FTIR spectra of (a) Pluronic F127 surfactant, and TiO_2-I-6 film calcined at (b) 473 K, (c) at 573 K.

Table 1
Vibration frequencies of different groups.

Vibration	Frequency (cm^{-1})	Reference
C–O–C stretching	1110	[46]
CH_2 rocking	1060	[47]
C–H stretching	2850 and 2923	[48]
CO_2 in gas phase stretching	2350	[49]
H–O–H bending	1600	[50]
Ti–O–Ti	430–860	[51]

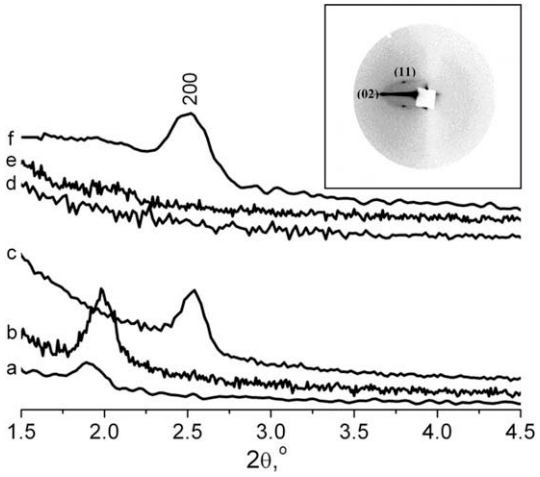

Fig. 4. LA-XRD patterns of mesoporous titania films: (a) TiO_2-I-6, (b) TiO_2-I-7, (c) TiO_2-I-9 as-synthesized, (d) TiO_2-I-6, (e) TiO_2-I-7, and (f) TiO_2-I-9 after storage in air for 2 months. A 2D SAXS image of TiO_2-I-9 is shown in the frame.

Typical adsorption–desorption isotherms of ethanol are shown in Fig. 6. Type IV adsorption isotherm with a hysteresis loop and a narrow PSD was observed, indicating a strong support–adsorbate interaction [31]. The mean pore size increased from 2.5 nm at *a* = 5 to 3.2 nm at *a* = 7 and finally to 3.5 nm at *a* = 9. These values are still lower as compared to 5 nm reported elsewhere [15]. The pore size distribution is narrow with a deviation of ±0.5 nm from the average value. Comparing the XRD, TEM and EP results it can be concluded that the thickness of the pore wall decreases with increasing surfactant content in the sol. The thickness of the pore wall can be calculated by subtracting the unit cell size from the pore size. As the unit cell size decreases, the pore wall thickness also decreases from 8.0 nm in TiO_2-I-6 to 4.5 nm in TiO_2-I-9. At the same time, the film porosity increases from 14% to 25% (Fig. 7). These data yield evidence that increasing the surfactant content increases the mean pore size and the mesopore volume due to a larger micelle size at higher surfactant concentrations in the sol [11].

Thus, a stable hexagonal mesoporous structure was obtained only at a F127/Ti molar ratio of 0.009. This ratio was used for the synthesis of supported titania catalysts with embedded nanoparticles.

3.1.3. Investigation of Lewis and Brønsted acidity by FTIR of adsorbed CO

Both Lewis and Brønsted acidities of the titania surface were determined by CO adsorption. The effect of different surfactant

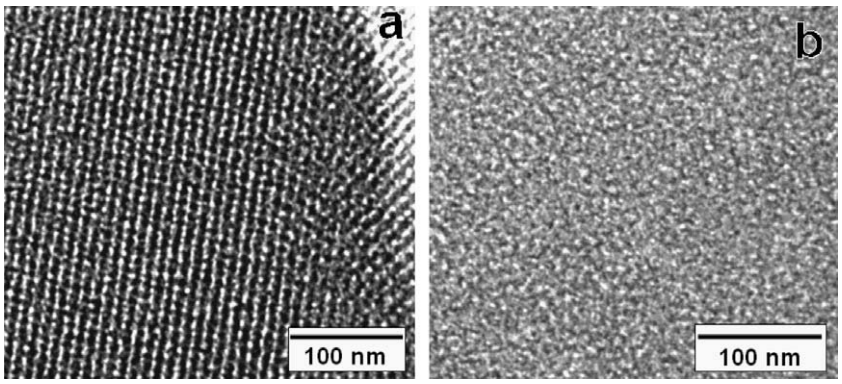

Fig. 5. TEM images of the mesoporous titania films taken after storage in air for 2 months: (a) TiO_2-I-9, and (b) TiO_2-I-7.

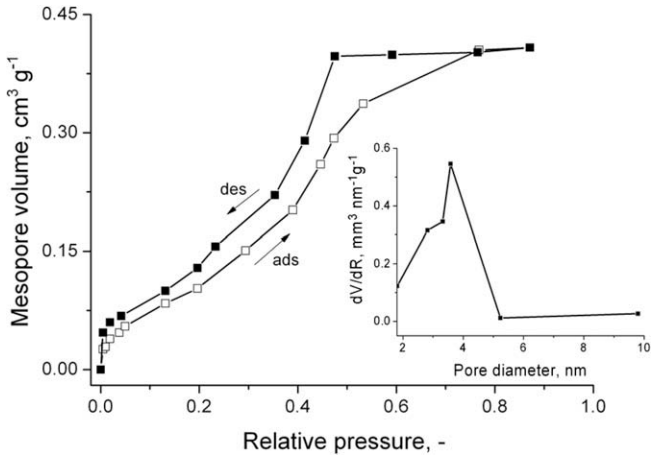

Fig. 6. Ethanol adsorption–desorption isotherms at 287 K and the pore size distribution for the film TiO_2-I-9.

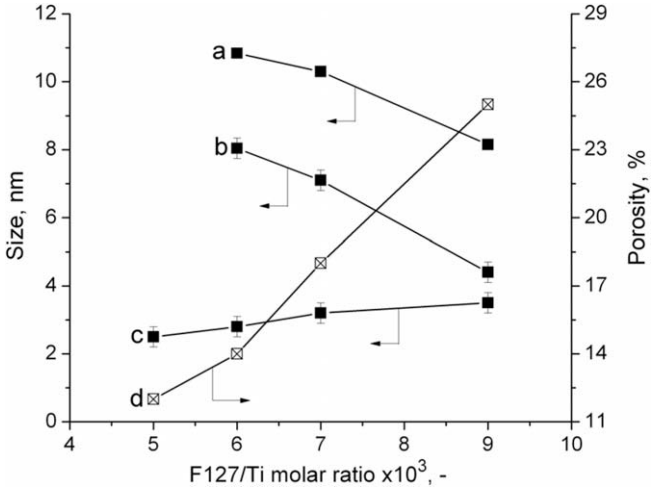

Fig. 7. Dependence of the porosity, pore and unit cell sizes, pore wall thickness of mesoporous titania films on surfactant-to-precursor molar ratio: (a) unit cell size, (b) pore wall thickness, (c) pore size, and (d) porosity.

content was studied over TiO_2-I-5 and TiO_2-I-9 by FTIR of adsorbed CO (Fig. 8). The adsorption bands at 2153 and 2156 cm^{-1} are assigned to CO adsorbed on the Ti–OH groups. The bands at 2141 and 2145 cm^{-1} are related to CO condensed in the mesopores (CO in gas phase) [27], while those at 2123 and 2129 cm^{-1} are

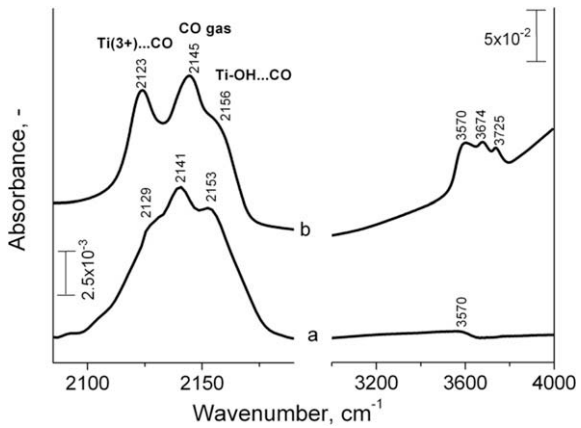

Fig. 8. FTIR spectra of CO adsorbed on: (a) TiO_2-I-9, (b) TiO_2-I-5. Experimental conditions: temperature 77 K, CO pressure 13 mbar. The sample was pretreated in an IR cell at 673 K for 2 h under a residual pressure of 0.01 mbar to remove adsorbed surface species.

characteristic for CO adsorbed on the Ti^{3+} species [32]. In both cases no adsorption band at 2180 cm^{-1} was observed, demonstrating the absence of unsaturated Ti^{4+} sites on the surface [33]. The reduction of the Ti^{4+} sites at 773 K gives the Ti^{3+} sites [34–37]. This effect was observed already at 573 K in [37]. However, further heating to 773 K significantly increased the amount of the reduced

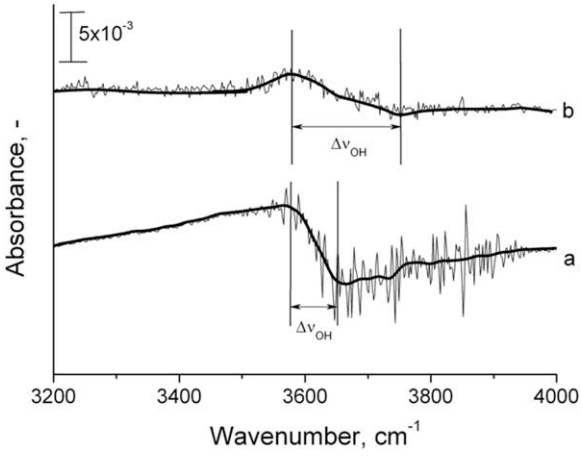

Fig. 9. Differential FTIR spectra of mesoporous titania films: (a) TiO_2-I-9, (b) TiO_2-I-5. Experimental conditions are the same as those in Fig. 8.

Table 2
Acidic properties of titania films determined by IR of adsorbed CO.

Sample	υ_{1CO} (cm^{-1})	υ_{2CO} (cm^{-1})	υ_{OH} (cm^{-1})	$\Delta\upsilon_{OH}$ (cm^{-1})	PA[a] (kJ mol)
TiO_2-I-5	2123	2156	3570, 3674, 3725	168	1270
TiO_2-I-9	2129	2153	3570	98	1373

[a] PA – proton affinity.

sites. In this study, the Ti^{3+} sites were formed after calcination of the mesoporous films at 573 K.

The frequency shift of the OH vibration ($\Delta\upsilon_{OH}$) was obtained from the FTIR differential spectra (Fig. 9, Table 2). The hydroxyl groups in both the films possess strong acidic properties.

Thus, pretreatment at 573 K at low pressure creates reduced Ti^{3+} sites in the mesoporous films.

3.1.4. Influence of porosity on hydrophilic properties

Surface hydrophilicity of films is an important parameter when they are applied in multiphase catalysis. In order to improve the interactions between a heterogeneous catalyst and the reactants flowing in the liquid film, it is of prime importance to ensure good wetting of the surface. High surface hydrophilicity provides stabilization of the liquid flow around the catalyst, which can substantially reduce the pressure drop in the microreactor. The surface concentration of hydroxyl groups was studied before and after UV-treatment by measuring the contact angle of a water droplet on the films obtained with different surfactant-to-precursor ratios (series TiO_2-I-*a*, where *a* = 5, 6 and 7). The initial contact angle was 35, 32 and 30 ± 1° over TiO_2-I-5, TiO_2-I-6 and TiO_2-I-7, respectively. After a UV-treatment for 2 h, the water contact angle decreased to 14 ± 1° over TiO_2-I-5. Samples TiO_2-I-6 and TiO_2-I-7 were more hydrophilic with contact angles of 9 ± 1° and 8 ± 1°, respectively. The film surface became superhydrophilic on all samples after 5 h of UV irradiation. In this state, the highest concentration of surface hydroxyl groups (>15 OH per nm^2) was created on the surface [22]. The difference of hydrophilicizing rate of films is related to their different mesoporosities. The films with a higher mesopore volume and larger surface areas enhance their hydrophilicity owing to the so-called two-dimensional capillary phenomenon [38,39].

Based on the results described above, it can be concluded that there exists a narrow range of the surfactant-to-metal precursor ratios between 0.006 and 0.009 leading to formation of mesoporous titania films with a high degree of long-order structure. The thickness of the pore wall decreases while the porosity and the long-term stability increase with increasing the surfactant content in the initial sol. A higher porosity is beneficial to rapid diffusion of the reactants and products, especially in thicker films. The templating agent can be completely removed from the film by calcination at 573 K at a residual pressure of 10 mbar for 4 h. Under these conditions Ti^{4+} sites are reduced to Ti^{3+}. A F127/Ti molar ratio of 0.009 and optimized calcination conditions were chosen for the synthesis of multilayer films.

3.2. Multilayer mesoporous catalytic titania films

After optimization of synthesis parameters for a single layer, Au-containing catalytic films with two, three and five consequent layers were synthesized and analyzed as described in Section 2.2 (Table 3). The thickness gain was almost the same in the first and second deposition cycles. The similarity of the deposition process indicates that the UV-induced superhydrophilic state of the surface has a minor influence on the thickness of the film layer. However, in the third and fifth deposition runs less material was deposited per deposition cycle. This might be related to an increased surface roughness of the films after multiple depositions. On the surface of spin-coated films derived from alkoxide solutions is often observed the so-called "radiative striation", i.e. circumferential unevenness in thickness or radially extended ridges. Striations can scatter the solution from the next deposition cycle resulting in a smaller growth rate. It can be seen from a cross-sectional view of the film in Fig. 10 that a significantly heterogeneous thickness profile is obtained after five deposition cycles. The mean film thickness is 1 μm; however, the film contains thicker and thinner areas with an on-scale difference of several tens of micrometres. In spite of non-uniform growth rate, a proportional weight gain confirms uniform porosity throughout the film.

Table 3
Characteristics of mesoporous films Au/TiO_2-*i*-9.

Number of deposition cycles	Thickness (nm)	Weight[a] (mg)	Apparent density[b] (g cm^{-3})	Initial TOF (s^{-1})
1	300	0.6	0.40	1.4
2	590	1.1	0.37	0.7
3	660	1.3	0.39	n.d.
5	1000	2.0	0.40	0.9[c]

n.d. – not determined.
[a] Weight is given for fifty films on substrates of 9.8 × 9.8 mm^2.
[b] Apparent density is given as weight divided by the coating volume.
[c] TOF decreased to 0.26 s^{-1} in 16 min.

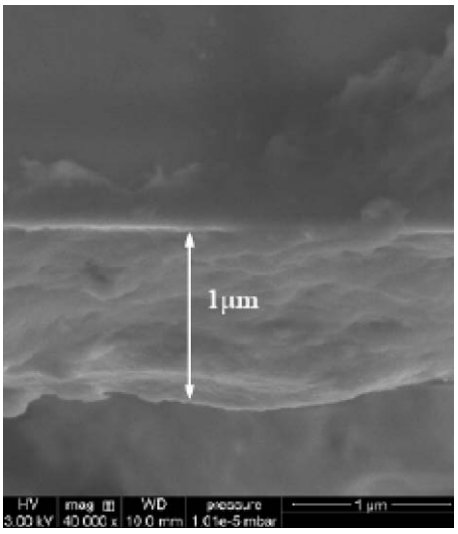

Fig. 10. SEM image of Au/TiO_2-V-9.

A narrow pore size distribution with a mean pore size of 3.1 ± 0.2 nm was observed on the Au/TiO_2-I-9 and Au/TiO_2-II-9 samples according to both TEM and EP analysis (not shown). Both samples had a smaller mean pore size as compared to that of the titania support (3.5 ± 0.2 nm) due to a partial pore blockage by the Au nanoparticles.

3.3. Catalytic tests in the hydrogenation of citral

Citral hydrogenation has been chosen as a test reaction as this is a multi-step reaction and the presence of internal diffusion limitations substantially decreases the selectivity towards the semihydrogenated products (unsaturated alcohols, nerol and geraniol (UCOL) and/or saturated aldehyde citronellal (CAL), Scheme 1). Citral conversion linearly increased with time from the beginning of the reaction, demonstrating the zero reaction order for citral (Fig. 11). A citral conversion of 81.2% was achieved after a reaction

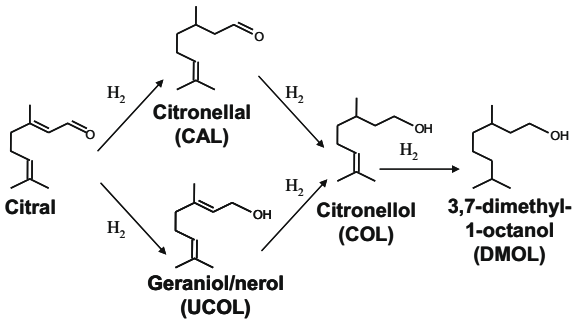

Scheme 1. Main products in citral hydrogenation.

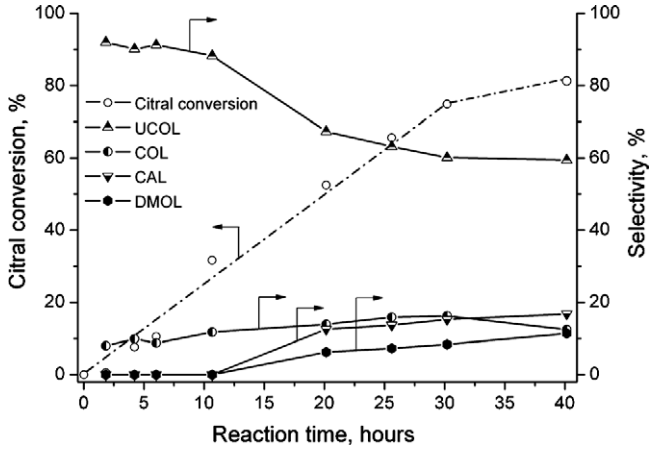

Fig. 11. Citral conversion and products selectivity on Au/TiO_2-I-9 as a function of the reaction time. Reaction conditions: temperature 343 K, 12 bar H_2, 0.01 M citral solution in 2-propanol, stirring speed 1500 rpm, catalyst mass 0.6 mg.

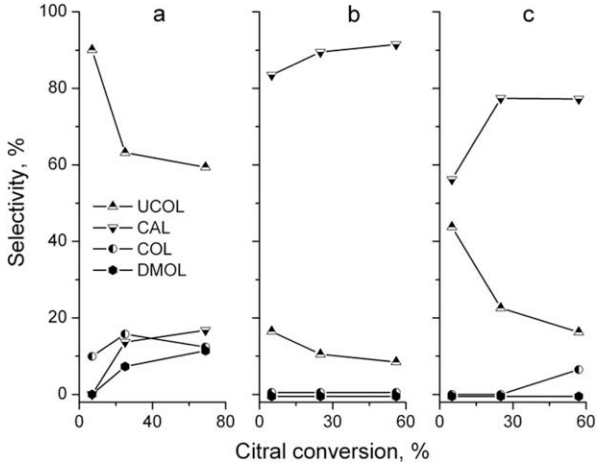

Fig. 12. Selectivity as a function of the citral conversion over (a) Au/TiO_2-I-9; (b) Au/TiO_2-II-9; (c) Au/TiO_2-V-9. Reaction conditions are the same as those in Fig. 11. The weights of the catalytic coatings are 0.6, 1.3 and 2.0 mg for (a), (b) and (c), respectively.

Table 4
Characteristics of the Au/TiO_2-*i*-9 thin films.

Parameter	Value
Apparent density (kg m^{-3})	400
Metal dispersion (–)	0.2
Au loading (wt.%)	1.0
Volumetric reaction rate ($m_L^3\ m_{cat}^{-3}\ s^{-1}$)	1.4
Film porosity (–)	0.3

time of 40 hours over Au/TiO_2-I-9. In the beginning of hydrogenation, UCOL was the main product with a selectivity as high as 90% while the hydrogenation of the C=C double bond was completely suppressed. Further hydrogenation of unsaturated alcohols resulted in the increase of selectivity to citronellol (COL) up to 14.5%. At a citral conversion of 70%, citronellal and 3,7-dimethyl-octanol (DMOL) were produced with a selectivity of 15.3% and 8.4%, respectively (Fig. 12a).

The thicker films (Au/TiO_2-II-9 and Au/TiO_2-V-9) showed a lower selectivity to the unsaturated alcohols as compared with Au/TiO_2-I-9 (Fig. 12b and c). Citronellal was the main product on the multilayered films with a substantial amount of citronellol at the end of the hydrogenation runs. Formation of the fully saturated product (3,7-dimethyl-1-octanol) was not observed.

The maximum coating thickness (h) to avoid internal diffusion limitations can be estimated for a zero-order reaction as $h = c/(k_v/D_e)^{0.5}$, where k_v is the volumetric reaction rate (see Table 4) and D_e is the effective diffusivity in the mesoporous network and c is a constant which depends on the reaction order and the catalyst geometry [40].

The maximum coating thickness for a single plate was found to be 5 μm in the beginning of the reaction run, when the zero-order in citral was observed. This is in line with the observed selectivity patterns. The selectivity towards the fully hydrogenated product was rather low over Au/TiO_2-V-9 even at high citral conversions.

It should be mentioned that at higher citral conversions, the reaction order with respect to citral gradually increased towards 1 and the maximum thickness to avoid internal diffusion limitations decreased to 0.7 μm. Therefore, the effective reaction rate over Au/TiO_2-V-9 was lower than the intrinsic rate observed over Au/TiO_2-II-9. From the effective reaction rate it is possible to estimate the effective diffusion coefficient of citral in catalytic films (D_{eff}) which is related to the molecular diffusion coefficient of citral (D_m) by Eq. (2).

$$D_{eff} = \frac{\varepsilon\sigma}{\tau} D_m \tag{2}$$

For the case considered in this study, $D_{eff} = 9 \times 10^{-12}$ m^2/s, $D_m = 2 \times 10^{-10}$ m^2/s, the tortuosity factor (τ) is assumed to be 1, and the mean porosity (ε) is equal to 0.3 giving the constriction factor (σ) of 0.15. Such a low value for the constriction factor indicates that the Au nanoparticles substantially reduce effective cross-sectional area available for reactant diffusion.

The initial intrinsic reaction rate in terms of TOF was ca. 1.4, 0.7 and 0.9 s^{-1} over Au/TiO_2-I-9, Au/TiO_2-II-9 and Au/TiO_2-V-9, respectively. In the absence of internal diffusion limitations, such differences can be related to different electronic states of the Au nanoparticles in thin (Au/TiO_2-I-9) and thick (Au/TiO_2-II-9, Au/TiO_2-V-9) films. In Au/TiO_2-I-9, the titanium substrate has a much larger influence on the electronic state of the titania film, which might substantially change the electronic properties of the embedded gold nanoparticles. There was also a dramatic change in the selectivity pattern between thin and thick catalytic films (Fig. 12): unsaturated alcohols were the main products over Au/TiO_2-I-9 while the yield of saturated aldehyde was much higher over the thicker films. A similar enhancement of the reaction rate as compared to that over the bulk material was observed in the water–gas shift reaction when a thin film of molybdenum carbide catalyst with a thickness of 50 nm was deposited on a molybdenum substrate [41]. However, this effect mostly disappeared in a thicker film, when the thickness of the Mo_2C layer was increased up to several microns.

It should be mentioned that the transport mechanisms within mesopores can be different. These include Knudsen diffusion, molecular diffusion in disordered domains and diffusion in the capillary-condensed phase [42]. In a three-phase reactor, the catalyst is usually contacted by a single fluid phase. However the pores can be emptied by vaporization, the necessary energy for which is supplied in part by the reaction heat. Reaction in the gas-filled pores can dominate even if the coating is mostly filled with liquid. This might explain observed small deviations in the initial reaction rate between Au/TiO_2-II-9 and Au/TiO_2-V-9.

TEM images of Au/TiO_2-II-9 (both fresh and after reaction) are shown in Fig. 13a and b. Disordered mesoporous domains can be seen after the reaction, however the Au nanoparticles maintained their initial size of 4.5 nm.

From the TEM images it is difficult to assess the location of nanoparticles, however, the following hypothesis may be drawn. Lower diffusivity of citral as compared to that expected in completely open mesopores and smaller pore size in the catalytic films from the EP analysis demonstrate that nanoparticles are partially embedded into the amorphous titania wall. The unit cell, which comprises one pore and the wall between two adjacent pores, is equal to 8.1 nm (Fig. 7). Therefore, the pore wall thickness is estimated to be 4.5 nm. The nanoparticles with a size smaller than the pore wall thickness can be in principle fully embedded into the wall. Even in that case, nanoparticles can be accessible for the reactants via micropores. A significant and unique feature of polymer templated mesoporous titania films is the presence of complimentary microporosity in the amorphous titania walls. These complementary pores interconnect adjacent mesopores which allows reactants to diffuse to the nanoparticles embedded into the wall. However in this study, the mean nanoparticle size is about the same as the pore wall thickness.

On the other hand, if the nanoparticles are located outside the mesoporous network, then the effective diffusivity of citral should be much higher. From the TEM, EP and kinetic measurement analysis, it can be concluded that nanoparticles are partially embedded into the titania wall and to some extent are protruded towards the adjacent mesopore but not fully blocking them.

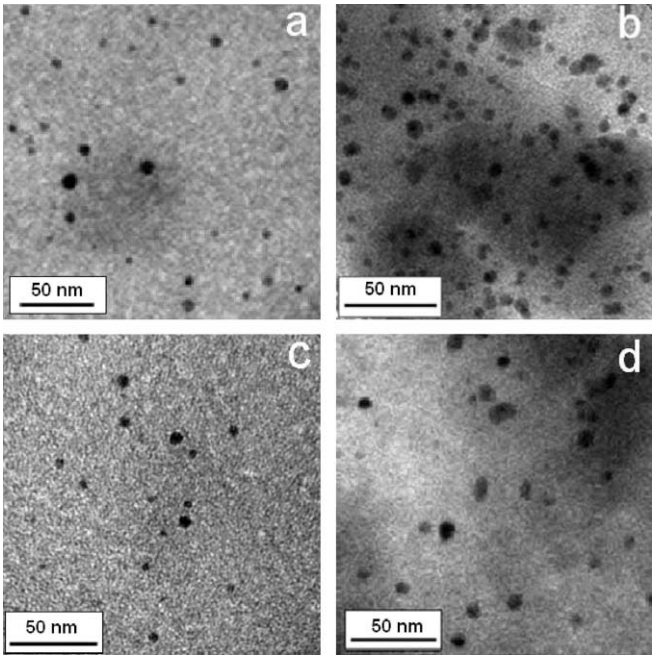

Fig. 13. TEM images of the mesoporous Au/TiO_2 films: (a) fresh Au/TiO_2-II-9, (b) Au/TiO_2-II-9 after reaction, (c) fresh Au/TiO_2-V-9, and (d) Au/TiO_2-V-9 after reaction.

The mean Au particle size in Au/TiO_2-V-9 after the reaction (Fig. 13d) was larger (7.0 nm) as compared to that in the fresh film (Fig. 13c). This film has larger disordered areas which can result in two diffusional pathways characterized by different diffusivities, namely those in the inner pore space and those between the ordered domains (Fig. 13c and d). A slightly larger gold nanopaticle size might be responsible for a higher initial TOF over Au/TiO_2-V-9 as compared to that expected if the intrinsic activity of Au would remain constant.

No deactivation was observed over Au/TiO_2-I-9 and Au/TiO_2-II-9 during the whole reaction period, while the TOF decreased from 0.9 to 0.26 s^{-1} over Au/TiO_2-V-9 within the first hour of reaction. It appears that the agglomeration of Au nanoparticles, which are not fully embedded into mesoporous domain, led to irreversible deactivation [43]. The deactivation could also be due to a partial collapse of the mesoporous network in Au/TiO_2-V-9. As a result, larger mesopores are formed and the Au nanoparticles can be physically blocked. However, a detailed study on the origin of deactivation of Au/TiO_2-V-9 was beyond the scope of this paper and will be reported elsewhere.

The new method of making mesoporous catalytic thin films allows to control the chemical nature of the film, its porous structure, thickness and loading with an active metal, as well as provides the "freedom of choice" of the catalytic species, which can further be fine tuned to fit specific applications. In addition to the Au nanoparticles considered in this study for the hydrogenation of citral, Pd nanoparticles can also be embedded into mesoporous titania films for the selective hydrogenation of phenylacetylene to styrene [44], while PdZn bimetallic nanoparticles can be employed in semihydrogenation of terminal acetylene alcohols to ethylene alcohols [45]. Successful implementation of this method will further depend on the capability of scaling the synthetic protocol from a substrate of a few square centimetres to that of a few meters while maintaining film uniformity.

4. Conclusions

Control of the thickness of mesoporous titania films deposited on a variety of substrates was achieved by multiple spin-coating. The thickness gain with each deposition cycle consistently decreased from ca. 300 nm per cycle in the first cycle to 200 nm in the last cycle. Gold nanoparticles with an average size of 4.5 nm were embedded in mesoporous titania films by the condensation of metal oxide species via self-assembly in the presence of a known amount of gold colloids. The complete surfactant removal leading to thermally stable mesoporous films was achieved at 573 K under a residual pressure of 10 mbar within 4 h. Under these conditions the Ti^{4+} sites were reduced to Ti^{3+} which might be responsible for a high selectivity to the unsaturated alcohols in the hydrogenation of citral over Au-containing supported catalysts.

Acknowledgments

The authors thank Dr. M. Creatore from Eindhoven University of Technology, Department of Applied Physics for providing an ellipsometer, Mr. V. Kuznetsov and Dr. E.A. Paukshtis from Boreskov Institute of Catalysis (Novosibirsk, Russia) for help in the FTIR study, Dr. P.A. Albouy from Laboratoire de Physique des Solides, Université Paris-Sud, France for 2D SAXS measurements, Mr. A. Ishchenko from Boreskov Institute of Catalysis and Mr. S. Çelebi from Eindhoven University of Technology, Department of Chemical Engineering and Chemistry for the TEM-measurements, and Mr. C. Buijs from Eindhoven University of Technology, Department of Chemical Engineering and Chemistry for SEM-measurements. The financial support by the Netherlands Organization for

Scientific Research (NWO) and the Russian Foundation for Basic Research (RFBR) in frame of NWO-RFBR Project 047.017.028, is gratefully acknowledged.

References

[1] V. Hessel, S. Hardt, H. Löwe, A. Müller, G. Kolb, Chemical Micro Process Engineering, Wiley, Belgium, 2005.
[2] V. Hessel, S. Hardt, H. Löwe, Chemical Micro Process Engineering: Fundamentals, Modelling and Reactions, Wiley, Belgium, 2004.
[3] E.V. Rebrov, G.B.F. Seijger, H.P.A. Calis, M.H.J.M. de Croon, C.M. van den Bleek, J.C. Schouten, Appl. Catal. A 206 (2001) 125.
[4] M.J.M. Mies, J.L.P. van den Bosch, E.V. Rebrov, J.C. Jansen, M.H.J.M. de Croon, J.C. Schouten, Catal. Today 110 (2005) 38.
[5] M.J.M. Mies, E.V. Rebrov, J.C. Jansen, M.H.J.M. de Croon, J.C. Schouten, Microporous Mesoporous Mater. 106 (2007) 95.
[6] M.J.M. Mies, E.V. Rebrov, J.C. Jansen, M.H.J.M. de Croon, J.C. Schouten, J. Catal. 247 (2007) 328.
[7] O. Muraza, E.V. Rebrov, J. Chen, M. Putkonen, L. Niinistö, M.H.J.M. de Croon, J.C. Schouten, Chem. Eng. J. 135S (2008) S117.
[8] E.V. Rebrov, M.H.J.M. de Croon, J.C. Schouten, Catal. Today 69 (2001) 183.
[9] I.Z. Ismagilov, R.P. Ekatpure, L.T. Tsykoza, E.V. Matus, E.V. Rebrov, M.H.J.M. de Croon, M.A. Kerzhentsev, J.C. Schouten, Catal. Today 105 (2005) 516.
[10] D. Grosso, F. Cagnol, G.J. de. A.A. Soler-Illia, E.L. Crepaldi, H. Amenitsch, A. Brunet-Bruneau, A. Bourgeois, C. Sanchez, Adv. Funct. Mater. 14 (2004) 309.
[11] L. Malfatti, P. Falcaro, H. Amenitsch, S. Caramori, R. Argazzi, C.A. Bignozzi, S. Enzo, M. Maggini, P. Innocenzi, Microporous Mesoporous Mater. 88 (2006) 304.
[12] O. Muraza, E.V. Rebrov, T. Khimyak, B.F.G. Johnson, P.J. Kooyman, U. Lafont, P.A. Albouy, M.H.J.M. de Croon, J.C. Schouten, Stud. Surf. Sci. Catal. 162 (2006) 167.
[13] T.S. Glazneva, E.V. Rebrov, J.C. Schouten, E.A. Paukshtis, Z.R. Ismagilov, Thin Solid Films 515 (2007) 6391.
[14] O. Muraza, E.V. Rebrov, T. Khimyak, B.F.G. Johnson, P.J. Kooyman, U. Lafont, M.H.J.M. de Croon, J.C. Schouten, Chem. Eng. J. 135 (2008) S99.
[15] E.L. Crepaldi, G.J. de A.A. Soler-Illia, D. Grosso, F. Cagnol, F. Ribot, C. Sanchez, J. Am. Chem. Soc. 125 (2003) 9770.
[16] Y. Zhang, A.H. Yuwono, J. Li, J. Wang, Microporous Mesoporous Mater. 110 (2008) 242.
[17] D.M. Antonelli, Microporous Mesoporous Mater. 30 (1999) 315.
[18] U.-H. Lee, H. Lee, S. Wen, S. Mho, Y.-U. Kwon, Microporous Mesoporous Mater. 88 (2006) 48.
[19] D. Grosso, F. Babonneau, C. Sanchez, G.J. de A.A. Soler-Illia, E.L. Crepaldi, J. Sol–Gel Sci. Technol. 26 (2003) 561.
[20] J. Sabataityteÿ, I. Oja, F. Lenzmann, O. Volobujeva, M. Krunks, Preliminary communication, C.R. Chimie 9 (2006) 708.
[21] Y.K. Hwang, K.-C. Lee, Y.-U. Kwon, The Royal Society of Chemistry, Chem. Commun. (2001) 1738.
[22] M. Wark, J. Tschirch, O. Bartels, D. Bahnemann, J. Rathouskyr', Microporous Mesoporous Mater. 84 (2005) 247.
[23] M.C. Fuertes, M. Marchena, M.C. Marchi, A. Wolosiuk, G.J.A.A. Soler-Illia, Small 5 (2009) 272.
[24] E.V. Rebrov, A. Berenguer-Murcia, B.F.G. Johnson, J.C. Schouten, Catal. Today 138 (2008) 210.
[25] P. Lu, T. Teranishi, K. Asakura, M. Miyake, N. Toshima, J. Phys. Chem. B 103 (1999) 9673.
[26] S. Domínguez-Domínguez, A. Berenguer-Murcia, D. Cazorla-Amorós, A. Linares-Solano, J. Catal. 243 (2006) 74.
[27] E.A. Paukshtis, IR-spectroscopy in heterogeneous acid–basic catalysis, Science, Russia, Novosibirsk, 1992, p. 47.
[28] L.N. Protasova, E.V. Rebrov, Z.R. Ismagilov, J.C. Schouten, Microporous Mesoporous Mater. 123 (2009) 243.
[29] M. Boudart, Kinetics of Heterogeneous Catalytic Reactions, Princeton University Press, Princeton, NJ, 1984. p. 26.
[30] M. Klotz, P.-A. Albouy, A. Ayral, C. Menager, D. Grosso, A. van der Lee, V. Cabuil, F. Babonneau, C. Guizard, Chem. Mater. 12 (2000) 1721.
[31] IUPAC Recommendations, Pure Appl. Chem. 66 (1994) 1739.
[32] G. Busca, H. Saussey, O. Saur, J.C. Lavalley, V. Lorenzelli, Appl. Catal. 14 (1985) 245.
[33] K. Kim, Bull. Korean Chem. Soc. 11 (1990) 396.
[34] T. Ekou, A. Vicente, G. Lafaye, C. Especel, P. Marecot, Appl. Catal. A 314 (2006) 73.
[35] Y. Li, B. Xu, Y. Fan, N. Feng, A. Qiu, J.M.J. He, H. Yang, Y. Chen, J. Mol. Catal. A 216 (2004) 107.
[36] P. Mäki-Arvela, J. Hajek, T. Salmi, D.Yu. Murzin, Appl. Catal. A 292 (2005) 1.
[37] L. Bonneviot, G. Haller, J. Catal. 113 (1988) 96.
[38] M.M. Viana, T.D.S. Mohallem, G.L.T. Nascimento, N.D.S. Mohallem, Braz. J. Phys. 36 (2006) 1081.
[39] J.C. Yu, J. Yu, W. Ho, J. Zhao, J. Photochem. Photobiol. A 148 (2002) 331–339.
[40] C.N. Satterfield, Mass Transfer in Heterogeneous Catalysis, MIT Press, England, Cambridge, 1970.
[41] E.V. Rebrov, S.A. Kuznetsov, M.H.J.M. de Croon, J.C. Schouten, Catal. Today 125 (2007) 88.
[42] R. Valiullin, J. Karger, R. Glaser, Phys. Chem. Chem. Phys. 11 (2009) 2833.
[43] P. Konova, A. Naydenov, C. Venkov, D. Mehandjiev, D. Andreeva, T. Tabakova, J. Mol. Catal. A 213 (2004) 235.
[44] E.V. Rebrov, A. Berenguer-Murcia, H.E. Skelton, B.F.G. Johnson, A.E.H. Wheatley, J.C. Schouten, Lab Chip 9 (2009) 503.
[45] E.V. Rebrov, E.A. Klinger, A. Berenguer-Murcia, E. Sulman, J.C. Schouten, Org. Process. Res. Dev. (2009), doi:10.1021/op900085b.
[46] A. Dey, S. Karan, S.K. De, Solid State Ionics 178 (2008) 1963.
[47] J.K. Walters, R.J. Newport, J. Phys.: Condens. Matter 7 (1995) 1755.
[48] P.J. Kruegearn, D.J. Jan, Can. J. Chem. 48 (1970) 3236.
[49] J. Heidberg, E. Kampshoff, R. Kiihnemuth, O. Schönekiis, Surf. Sci. 269/270 (1992) 120.
[50] A. Grodzicki, P. Piszczek, J. Mol. Struct. 443 (1998) 141.
[51] Y. Kim, M. Yoon, J. Mol. Catal. A 168 (2001) 257.

CHAPTER 9
Synthesis and study of supports and catalysts. Oxygen-permeable perovskite membranes

КИНЕТИКА И КАТАЛИЗ Том 29, вып. 1, 1988

УДК 541.128.35 : 541.18.02 : 546.623—36 : 539.4.015

ИССЛЕДОВАНИЕ КАТАЛИЗАТОРОВ И РЕАКЦИЙ КАТАЛИТИЧЕСКОГО ОКИСЛЕНИЯ

III. ФОРМИРОВАНИЕ ТЕКСТУРЫ ПСЕВДОБЕМИТОВ ПРИ ГРАНУЛЯЦИИ ЖИДКОСТНЫМ МЕТОДОМ СФЕРИЧЕСКИХ НОСИТЕЛЕЙ ДЛЯ КАТАЛИЗАТОРОВ КГТ

ШЕПЕЛЕВА М. Н., ШКРАБИНА Р. А., ОККЕЛЬ Л. Г., ЗАЙКОВСКИЙ В. И., ФЕНЕЛОНОВ В. Б., ИСМАГИЛОВ З. Р.

Исследованы изменения текстуры псевдобемитных гидроксидов алюминия на стадиях пептизации и коагуляции при жидкостном формовании гранул Al_2O_3. Осадки, полученные при 291—310 К, с морфологией свежеосажденного псевдобемита и преимущественно коагуляционными связями легко дезагрегируются кислотой, что позволяет после коагуляции получать гранулы с однородно-пористой структурой и высокой прочностью. При температуре осаждения 368—375 К и образовании в гидроксидах кристаллизационных контактов дезагрегации кислотой не происходит. Варьированием соотношения осадков первого и второго типов можно получать гранулы Al_2O_3 с заданными структурно-механическими характеристиками, отвечающими требованиям к носителям катализаторов полного окисления, используемым в каталитических генераторах тепла.

В каталитических генераторах тепла (КГТ) при сжигании топлив в кипящем слое используются катализаторы, получаемые нанесением активного компонента на сферические гранулы носителя диаметром 0,4—3,0 мм [1]. В качестве носителей применяются оксиды алюминия, получаемые методом жидкостного формования. К катализаторам сжигания топлив предъявляется ряд особых требований, в том числе высокая механическая прочность. Очевидная связь механической прочности гранул и текстурных характеристик оксида алюминия определяет необходимость изучения формирования текстуры кислородсодержащих соединений алюминия на всех стадиях получения сферических гранул, а именно приготовления пластифицированной массы из псевдобемитного гидроксида путем обработки его кислотой (стадия пептизации) и формования гранул в растворе аммиака (стадия коагуляции).

По [2] структурно-механические свойства конечного продукта — гранулированного γ-Al_2O_3 — существенно зависят от степени агрегации исходного осадка, его морфологии. Наличие крупных агрегатов, образовавшихся в ходе синтеза и старения, препятствует уплотнению осадка при сушке, приводит к росту суммарной пористости и снижению механической прочности гранул. Цель данной работы — более детальное исследование особенностей формирования пористой структуры псевдобемитных осадков с разной морфологией на стадиях пептизации и коагуляции. Основное внимание уделено изменениям морфологии агрегатов, которые исследовали как непосредственно методом электронной микроскопии, так и косвенно — по результатам измерения усадки, пористой структуры и прочности гранул.

МЕТОДИКА ЭКСПЕРИМЕНТА

В качестве объектов исследования выбраны гидроксиды алюминия (ГА), полученные осаждением из растворов алюмината натрия азотной кислотой в условиях, обеспечивающих получение осадков с разной морфологией и степенью агрегирования. Образец 1 осаждали при 291 К,

образец 2 — при 305—310 К, образец 3 — при 368—375 К. Образцы 4—5 получены смешением гидроксидов 1 и 3. Пептизацию осадков для получения пластифицированной массы (ПМ) проводили азотной кислотой до величины кислотного модуля $M_к$ (г-моль HNO_3 на 1 г-моль Al_2O_3), равной 0,17 для образцов 1 и 2; 0,065 для образца 4; 0,15 для образца 5 и в диапазоне 0,06—0,50 для образца 3. Стадию коагуляции проводили в растворе аммиака с концентрацией 18—21% в течение 30—60 с, далее гранулы гидроксида (Г) промывали, сушили и прокаливали при 823 К в токе воздуха для получения γ-Al_2O_3.

Рентгенофазовый анализ (РФА) проводили с помощью аппарата ДРОН-1,5 на монохроматизированном медном излучении. По данным РФА все образцы представляют собой псевдобемит, образец 1 содержит также незначительное количество аморфной фазы. Размер частиц оценивали по области когерентного рассеяния (о. к. р.). Электронно-микроскопические исследования (ЭМ) проводили на микроскопе JEM-100-CX. Истинную плотность ρ измеряли по гелию на приборе Autopycnometer-3200. Пористую структуру и удельную поверхность ($S_{уд}$) исследовали путем анализа изотерм адсорбции азота, измеренных при 77,5 К на автоматической адсорбционной установке Digisorb-2600 (распределение объемов пор по эффективным радиусам горл в диапазоне до 100 нм). Эффективные радиусы горл в диапазоне 4—10^7 нм исследовали методом ртутной порометрии на приборе Porosizer-9300. Для получения сопоставимых данных при анализе использовали десорбционную ветвь области капиллярно-конденсационного гистерезиса. Измерение механической прочности (P, кг/см^2) гранул проводили после прокаливания при 823 К, усадки $\Delta l/l_0$ — после сушки при 383 К (l_0 — начальный диаметр гранулы, Δl — изменение диаметра при сушке) по методикам, описанным в [2].

РЕЗУЛЬТАТЫ И ИХ ОБСУЖДЕНИЕ

Сводка основных результатов приведена в таблице. По данным ЭМ гидроксид, осажденный при 291 К (образец 1-ГА), состоит из крупных (более 100 нм) агломератов произвольной формы, составленных из во-

Характеристики исходных гидроксидов, пластифицированных масс и сформованных гранул

Образец	$S_{уд}$, м^2/г	Объем пор с радиусом (нм), см^3/г				V_{Σ}, см^3/г	$\Delta l/l_0$,%	P, кг/см^2
		<4	4—30	30—100	>100			
ГА	254	0,332	0,071	0,004	0,17	0,577	42	80
1 ПМ	180	0,132	0,002	—	—	0,134		
Г	300	0,294	0,012	0,001	—	0,307	46	215
ГА	230	0,314	0,060	0,001	—	0,374	47	90
2 ПМ	229	0,351	0,057	—	—	0,408		
Г	275	0,355	0,013	0,001	—	0,368	49	210
ГА	93	0,125	0,140	0,095	0,585	0,945	0	
3 ПМ	55	0,069	0,102	0,055	0,375	0,601		
Г	90	0,083	0,124	0,080	0,500	0,784	0	
ГА эксп	130	0,183	0,100	0,060	0,150	0,498	28	7
расч	139	0,184	0,120	0,069	0,210	0,583		
4 ПМ эксп	157	0,171	0,028	0,075	0,110	0,384		
расч	123	0,087	0,073	0,039	0,090	0,289		
Г эксп	123	0,166	0,073	0,080	0,120	0,443	30	40
расч	150	0,143	0,092	0,057	0,150	0,442		
ГА эксп	228	0,270	0,140	0,050	—	0,460	33	50
расч	200	0,240	0,102	0,043	—	0,385		
5 ПМ эксп	235	0,240	0,050	0,040	—	0,330		
расч	122	0,104	0,050	0,025	—	0,179		
Г эксп	195	0,200	0,070	0,030	—	0,300	37	120
расч	203	0,200	0,065	0,036	—	0,304		

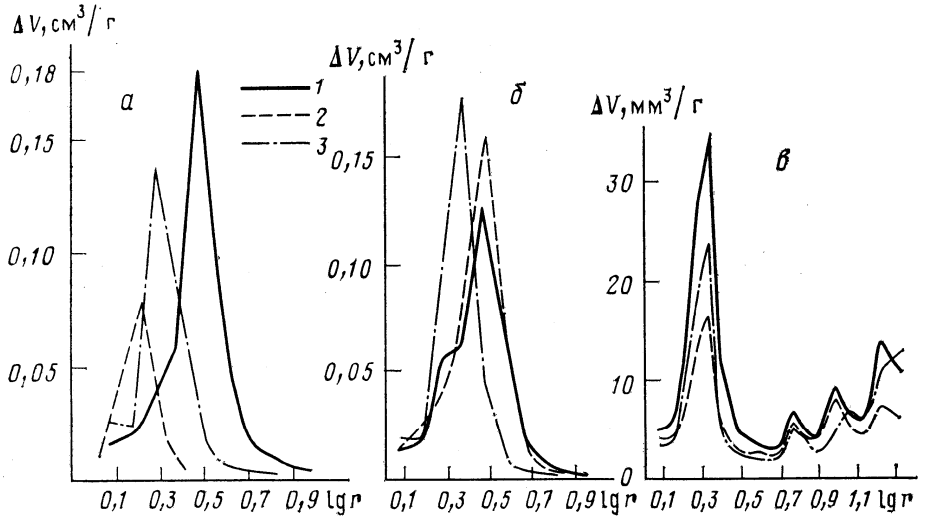

Рис. 1

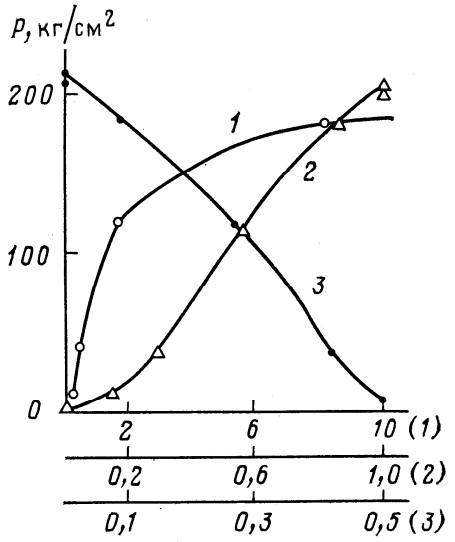

Рис. 2

Рис. 1. Распределение объема пор по радиусам для образцов: *а*—1, *б*—2, *в*—3; *1*—ГА, *2*—ПМ; *3*—Г

Рис. 2. Зависимость прочности гранул Al_2O_3 (P, кг/см²) от величин $V_{в.ф.}/V_{ма}'$ (*1*), X, г/г сухого смешанного осадка (*2*) и $V_{ма}'$, см³/г (*3*)

локон и игл шириной $h \sim 4$ нм и длиной $l \sim 20$—40 нм, и сферических частиц диаметром ~ 4 нм. Влагосодержание образца 1, определенное при 383 К, равно 4,36 г H_2O/г сухого ГА. При сушке закатанных из него гранул происходит значительная усадка, причем экспериментально измеренное значение $\Delta l/l_0$ равно рассчитанному из соотношения

$$\left(\frac{\Delta l}{l_0}\right)_p = 1 - \left(\frac{V_\varepsilon + 1/\rho}{W_{ГА} + 1/\rho}\right)^{1/3},$$

где $W_{ГА}$— объем влаги, удаляемой при сушке, V_ε— полученный из экспериментальных данных суммарный объем пор. В структуре высушенного ГА можно выделить две характерные области распределения пор: область тонких пор с максимумом распределения $r_1 \approx 3$ нм — расчет из результатов адсорбционных измерений (рис. 1, *а*) и область макропор со средним размером $r_2 \approx 200$ нм — данные ртутной порометрии. Область макропор, как следует из данных ЭМ, соответствует промежуткам между крупными агрегатами, а тонких пор — порам в агрегатах между частицами малых размеров.

Кислотная обработка при интенсивном механическом перемешивании (образец 1-ПМ) сопровождается по данным ЭМ переходом к разупорядоченной структуре из игл и волокон с h до 3 нм. Имевшиеся в исходном образце крупные агрегаты после такой обработки исчезают.

Расчетная усадка увеличивается до 52%. Соответственно изменяются и структурные характеристики: макропоры полностью исчезают, максимум распределения тонких пор смещается к 1,7 нм. Величина о. к. р. по данным РФА при кислотной обработке не меняется и равна 4 нм. Таким образом, в данном случае сушка приводит к образованию плотноупакованной однороднопористой системы, величина суммарной пористости которой, рассчитанная как $\varepsilon = V_\varepsilon\rho/(1+V_\varepsilon\rho)$, равна 0,26. Столь низкие значения пористости, как и наблюдающееся снижение $S_{уд}$, могут объясняться заполнением части пористого пространства образовавшимися низкомолекулярными соединениями алюминия. Влияние начальной агрегации в данном случае полностью устраняется благодаря эффективному распаду агрегатов, первичные частицы в которых, очевидно, взаимосвязаны лишь ван-дер-ваальсовскими и электростатическими силами (коагуляционные контакты по [3]).

Коагуляция в аммиаке с образованием гранул гидроксида (образец 1-Г) приводит к некоторому снижению степени усадки (расчетная ее величина 47%, экспериментальная — 46%). Суммарный объем пор увеличивается ($\varepsilon = 0{,}45$), но их распределение по размерам остается довольно узким с максимумом при $r = 2$ нм (рис. 1, *а*), макропоры отсутствуют. Такие изменения пористой структуры обусловлены увеличением прочности «скелета», образовавшегося при нейтрализационной коагуляции гидроксида. Отсутствие макропор указывает на достаточно однородное пространственное размещение в геле ГА коагуляционных контактов, поскольку при сушке образование зон локальной агрегации в объеме должно сопровождаться появлением пор между агрегатами. Из сопоставления структурно-механических характеристик образцов 1-ГА и 1-Г видно, что необходимая при приготовлении жидкостным методом гранул обработка устраняет макропоры, что приводит к значительному росту механической прочности (почти в 3 раза). Распределение объема более тонких пор изменяется при этом несущественно.

Исходный гидроксид, осажденный при 305—310 К (образец 2-ГА), имеет начальную влажность $W_{ГА} = 3{,}66$ г H_2O/г сухого ГА. По данным ЭМ этот осадок состоит из мелких игл ($h = 3$—7 нм, l до 50 нм), упакованных в агрегаты размером <100 нм. На снимках также наблюдаются участки с волокнистой структурой и небольшое количество сферических частиц размером 3—5 нм. Величина о. к. р. 3 нм. В данной серии обработка гидроксида как кислотой (образец 2-ПМ), так и аммиаком (образец 2-Г) мало влияют на текстурные характеристики осадка (таблица). Суммарный объем и распределение пор почти сохраняются при незначительном росте доли более тонких пор для образца 2-ПМ. Расчетная усадка во всех случаях составляет 44—45%. Размеры пор в области максимумов их распределения по объемам равны для образцов этой серии 3,1; 3,1 и 2,5 нм соответственно (рис. 1, *б*). Столь малое влияние обработки на текстурные характеристики обусловлено низкой степенью агрегации в исходном состоянии.

Гидроксид 3, осажденный при 368—375 К, имеет влажность $W_{ГА} = 0{,}95$ г H_2O/г сухого ГА. По данным ЭМ осадок преимущественно состоит из крупных агрегатов в виде пластин с размерами $\geqslant 100$ нм. Края пластин образованы плотной упаковкой игл толщиной до 20 нм, которые, в свою очередь, состоят из тонких игл с h до 4 нм. Морфология таких агрегатов близка к описанной для бемита [4], о. к. р. по данным РФА составляет 15—17 нм. Гранулы, закатанные из ГА-3, не дают усадку при сушке (расчетная усадка 10^{-3}%) и имеют очень низкую прочность. Кислотная обработка при интенсивном перемешивании не позволила получить пригодную для формования массу даже при увеличении кислотного модуля до 0,3—0,5. Из данных ЭМ видно, что диспергирование не происходит, заметна только размытость границ агрегатов. При всех $M_к$ образовывалась быстро расслаивающаяся суспензия, не обладающая необходимыми вязкотекучими свойствами, поэтому стадию коагуляции имитировали путем смешивания суспензии с водным раствором аммиака.

Все образцы этой серии имеют сходную разнородно-пористую структуру с характерными максимумами распределения объема мезопор при $r \approx 2{,}2$ нм (рис. 1, *в*) и большим объемом макропор. Величина пористости агрегатов при допущении, что все мезопоры с размерами до 100 нм находятся в их объеме, изменяется в диапазоне 0,4—0,5. Положения максимумов распределения и относительный объем пор разного размера мало изменяются в ходе последовательных обработок: объем пор с размерами до 4 нм составляет 10—13%, в диапазоне 4—30 нм — 15—17%, 30—100 нм — 9—10%, более 100 нм — 62—64% от V_ε. При анализе распределений, рассчитанных по адсорбционным ветвям капиллярно-конденсационного гистерезиса изотерм адсорбции, получены аналогичные результаты. Наиболее близки по структурным характеристикам образцы 3-ГА и 3-Г. Снижение суммарного объема пор и $S_{уд}$ образца 3-ПМ может быть объяснено образованием при большой $M_к$ растворимых соединений алюминия и их осаждением при сушке на периферийной части агрегатов.

Эти результаты позволяют полагать, что подобные агрегаты практически не диспергируются в рассмотренных условиях, несмотря на довольно развитую внутреннюю поверхность и пористость. Такая стабильность, по-видимому, обусловлена наличием кристаллизационных контактов между первичными частицами в агрегатах исходного ГА. Формование жидкостным методом ГА-3 оказалось возможным лишь при смешении его с осадками типа 1 и 2. При смешении ГА-1 и ГА-3 получены образцы 4 ($X=0{,}29$) и 5 ($X=0{,}55$), где X — доля высокодисперсного ГА-1 (г/г сухого смешанного осадка). Кислотная обработка этих образцов и последующая коагуляция не приводят к заметным изменениям морфологии крупных агрегатов.

Смешанные гидроксиды представляют особый интерес для анализа особенностей взаимного размещения в них ГА-1 и ГА-3, их влияния на пористую структуру и, в конечном итоге, на прочность гранул γ-Al_2O_3. Обозначим гидроксиды 1 и 3 в составе смешанного осадка фазами 1 и 3. Инертность фазы 3 позволяет допустить, что мезопористая структура смешанных образцов пропорциональна объему мезопор в фазах 1 и 3. В этом случае объемы мезопор с определенным диапазоном размеров могут быть оценены по соотношению $\Delta V_i = \Delta V_1 X + \Delta V_3 (1-X)$, где ΔV_1 и ΔV_3 — объемы мезопор в соответствующих образцах серий 1 и 3. Аналогично можно оценить и $S_{уд}$. Результаты этих расчетов приведены в таблице. Видно, что в области пор с размерами до 100 нм для образцов типа ГА и Г расчетные и полученные из измерений величины довольно близки. Отсутствие аддитивности для образцов типа ПМ, по-видимому, связано с введением разных количеств кислоты в ГА-1 и ГА-3. Аддитивность также не выполняется и в области макропор, что объясняется размещением части высокодисперсной фазы 1 в промежутках между агрегатами фазы 3 (для образцов серии 4 расчетный объем макропор почти в 3 раза больше измеренного).

Для анализа размещения фаз 1 и 3 представим модель строения полученных смешением гидроксидов в простейшем виде: грубодисперсные агрегаты фазы 3 образуют каркас, в макропорах которого размещена высокодисперсная фаза 1. Допустим, что упаковка агрегатов каждой фазы не зависит от наличия второй фазы. При этом условии объем макропор, образующихся в единице массы смешанного ГА без учета фазы 1, равен $V'_{ма} = V_3(1-X)$, где V_3 — объем макропор в образцах серии 3. Объем, занимаемый высокодисперсной фазой 1, равен $V_{в.ф.} = (V_1 + 1/\rho_1)X$, где V_1 и ρ_1 — объем мезопор и истинная плотность. Как видно из таблицы, расчетный объем макропор $V_{ма} = V'_{ма} - V_{в.ф.}$ для образцов серии 4 близок к измеренному экспериментально ($V_{в.ф.}/V'_{ма} \approx 0{,}5$), а в образцах серии 5 макропоры отсутствуют ($V_{в.ф.}/V'_{ма} \approx 1{,}6$) и механическая прочность этих гранул велика. Эти же закономерности выполняются и для других полученных смешением образцов. Так, для ГА с $X=0{,}147$ (образец 6) расчетная величина объема макропор равна 0,30, а экспериментальное значение 0,36 см³/г. При $X=0{,}855$ (образец 7) макропо-

ры отсутствуют. Соотношение $V_{в.ф.}/V'_{ма}$ и прочность гранул составляют 0,29 и 11 кг/см² у образца 6 и 8,3 и 180 кг/см² у образца 7.

Отметим, что при $V_{в.ф.}/V'_{ма}<1$ экспериментально измеренный объем макропор во всех случаях несколько больше расчетного. Это указывает на некоторое снижение плотности упаковки агрегатов грубодисперсной фазы в присутствии высокодисперсной. Однако экспериментальные данные в удовлетворительном приближении описываются рассмотренной выше простейшей моделью. На рис. 2 показана зависимость механической прочности гранул Al_2O_3 от параметров X, $V_{в.ф.}/V'_{ма}$ и $V'_{ма}$. Видно, что появление макропор сопровождается резким снижением прочности. В области $V_{в.ф.}/V'_{ма}>1$, где макропористый каркас заполняется высокодисперсной фазой, прочность изменяется сравнительно слабо. В то же время зависимость прочности от величины X, включающая $X=1$ (образец 1), говорит о практически пропорциональной зависимости прочности от доли высокодисперсной фазы.

Полученные результаты показывают, что гидроксиды алюминия, синтезированные при 291—310 К, с морфологией, характерной для свежеосажденного псевдобемита, дезагрегируются азотной кислотой, что позволяет получать гранулы Al_2O_3 с однородно-пористой структурой и высокой механической прочностью. Даже при длительном старении подобные осадки сохраняют способность достаточно полно дезагрегироваться [2], что свидетельствует о преимущественно коагуляционном характере связи между первичными частицами. Осадки, полученные при 368—375 К и имеющие морфологию, характерную для бемита, не дезагрегируются при кислотной обработке, что указывает на образование кристаллизационных контактов между первичными частицами. Формование таких осадков возможно только при их смешении с легкодиспергируемыми осадками.

Структурно-механические свойства гранул Al_2O_3, получающихся при смешении ГА, определяются текстурой исходных осадков и их соотношением. При введении диспергируемого осадка в количестве $X<0,5$ ($V_{в.ф.}/V'_{ма}<1$) образуются гранулы Al_2O_3 с бидисперсной структурой, величина их механической прочности убывает пропорционально объему макропор, не заполненных фазой высокодисперсного осадка. Избыток легко диспергируемого осадка ($X>0,5$; $V_{в.ф.}/V'_{ма}\geqslant 1$) устраняет макропоры и приводит к получению гранул со структурно-механическими характеристиками, близкими к характеристикам гранул из ГА, осажденных при низких температурах.

Таким образом, изменения, происходящие с текстурой псевдобемитных гидроксидов алюминия на стадиях пептизации и коагуляции при жидкостном формовании гранул Al_2O_3, существенно зависят от морфологии исходных осадков, которая определяется как условиями их синтеза, так и длительностью хранения. Найденные закономерности позволяют целенаправленно синтезировать алюмооксидные носители катализаторов для каталитических генераторов тепла с заданными характеристиками.

Авторы выражают благодарность Э. М. Мороз и Т. Д. Камбаровой за снятие и расшифровку рентгенограмм.

ЛИТЕРАТУРА

1. *Боресков Г. К., Левицкий Э. А., Исмагилов З. Р.*//Журн. Всесоюз. хим. о-ва им. Д. И. Менделеева. 1984. Т. 29. № 4. С. 379.
2. *Шепелева М. Н., Фенелонов В. Б., Шкрабина Р. А., Мороз Э. М.*//Кинетика и катализ. 1986. Т. 27. № 5. С. 1202.
3. *Ребиндер П. Н.* Физико-химическая механика дисперсных структур. М.: Наука, 1966. С. 3.
4. *Дзисько В. А.* Основы методов приготовления катализаторов. Новосибирск: Наука, 1983. С. 58.

Институт катализа СО АН СССР,
Новосибирск

Поступила в редакцию
19.I.1987

Applied Catalysis, 55 (1989) 75–80
Elsevier Science Publishers B.V., Amsterdam — Printed in The Netherlands

Study of Structural and Mechanical Properties of Granulated Alumina Supports Using X-Ray Microprobes

I.A. OVSYANNIKOVA

Institute of Catalysis, Prosp. Akad. Lavrentieva, 5, Novòsibirsk 630090 (U.S.S.R.)

G.I. GOL'DENBERG

Special Bureau for Catalyst Design, ul. Tikhaya 1, Novosibirsk 630058 (U.S.S.R.)

and

N.A. KORAYABKINA, R.A. SHKRABINA and Z.R. ISMAGILOV*

Institute of Catalysis, Prosp. Akad. Lavrentieva 5, Novisibirsk 630090 (U.S.S.R.)

(Received 20 February 1989, revised manuscript received 21 June 1989)

ABSTRACT

Defects on surfaces of porous granulated supports (using alumina as an example) were examined by X-ray spectral microanalysis and the relationship between defects and the mechanical strength of spherical granules was determined. The mechanical strength of the granules depends significantly on their imperfections (micro cracks with a size of $>10^3$ nm), which is determined quantitatively from the Al Kα intensity profile. The regularities found are also valid for complex (Mg/Al_2O_3) systems.

INTRODUCTION

A knowledge of factors determining the mechanical strength of dispersed granulated materials is necessary for the development of highly durable catalysts and supports for fluidized bed reactors. In many studies, the dependence of mechanical strength on pore structure ($r_p < 10^3$ nm) and elastic internal tension arising during the formation of support and catalyst structures has been considered [1–4], taking into account the mutual arrangement of the particles forming the framework and the type of contacts between them [5].

0166-9834/89/$03.50

An X-ray method for evaluating defects has been developed for the assessment of the catalyst mechanical strength [3].

Studies on the dependence of mechanical strength on macro defects ($> 10^3$ nm) in granulated porous materials are less numerous. Typically, such a dependence has been considered in studies on high-temperature ceramics [6–8]. There is some evidence in favour of a relationship between the mechanical strength and the size of pores (macropores) (10^2–10^4 nm) [9].

The objective of this work was to examine defects on surfaces of porous granulated supports (using alumina as an example) by X-ray spectral microanalysis and to determine the relationship between defects and the mechanical strength of granules.

EXPERIMENTAL AND RESULTS

The investigation was performed using a JS M-35 scanning microscope with a 35-DDS adjustment for microanalysis. Spherical granules of alumina supports were fixed in copper cartridges with epoxy resin or Wood's alloy. The granules were then polished to half their diameter with control of the surface quality, and a ca. 200 Å carbon layer was sputtered to ensure sufficient conductivity. The Al Kα line intensity was measured by reflection of thallium phthalate (TAP) at a monocrystal plane and registered by a flow proportional counter. The Al Kα intensity profile was recorded at a sample movement of 20 μm/min with a recording-tape velocity of 20 mm/min. The probe current was 40 nA and that of absorbed electrons was 10 nA.

The mechanical strength of spherical granules was determined under static conditions, as described [10], and calculated as the ratio of breaking force to cross-section of the granule. The average value of the mechanical strength (R_{av}) was calculated as the arithmetic mean of the value for 30 granules.

Spherical granules (diameter 1–3 mm) of alumina were examined. The characteristics obtained are given in Table 1.

As shown previously [11], when applying a microanalyser supplied with vertical spectrometers and definite recording conditions, the radiation intensity profile sample scanning reflects the relief of the surface. A porous sample naturally has a rough surface owing to pores and macro defects which cause changes in intensity even at a constant composition of the sample provided that the size of the pores (defects) is commensurate with the probe diameter (1–2 μm). As found experimentally, scanning of alumina samples with a low mechanical strength leads to sharp variations in the Al Kα radiation intensity; the higher the sample strength, the smaller is the amplitude of the intensity variations (Fig. 1).

For the quantitative characterization of the intensity curve associated with the mechanical strength of granules, a sample fragmentation parameter was used. Obviously, a decrease in mechanical strength can occur if macro cracks

TABLE 1

Properties of Al_2O_3 supports

Sample No.	Phase composition	Content of Mg^{2+} (wt.-%)	V_Σ (cm^3/g)	$V_{r<10\,nm}$ (cm^3/g)	$V_{r>10-100\,nm}$ (cm^3/g)	R_{av} (kg/cm^2)
1	γ-Al_2O_3	–	0.55	0.40	0.15	130
2	γ-Al_2O_3	–	0.50	0.40	0.10	130
3	γ-Al_2O_3	–	0.52	0.42	0.10	110
4	γ-Al_2O_3	–	0.35	0.35	–	240
4a	α-Al_2O_3 (from sample 4)	–	0.30	–	0.30	180
5	γ-Al_2O_3	–	0.31	–	–	310
6	$Mg/Al_2O_3^a$	1.5	0.38	0.38	–	430
7	$Mg/Al_2O_3^a$	3.0	0.25	0.25	–	540

[a]Solid solution with γ-Al_2O_3 structure.

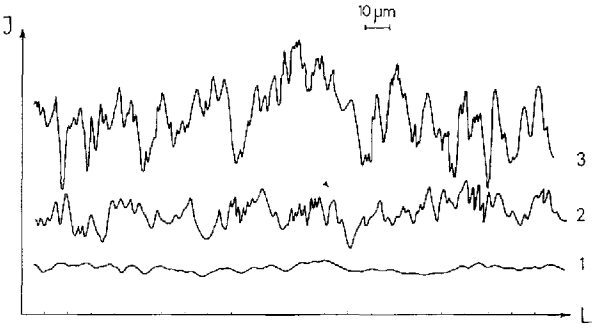

Fig. 1. Intensity of Al Kα radiation for spherical alumina granules with different mechanical strength: 1, $R_{av}=310$ kg/cm^2; 2, $R_{av}=240$ kg/cm^2; 3, $R_{av}=110$ kg/cm^2.

between fragments are deep and the fragments are small, i.e., a large number of particles correspond to unit length of scanning. Therefore, the parameter should include the number of particles per unit length of scanning, n/L, where n is the total number of particles per length L; the depth of defects can be characterized by the area limited by the intensity curve and an intermediate line, S/L. Thus, from the intensity curves one can calculate the parameter $B=KnS/L^2$. The coefficient K is introduced to provide the possibility of comparing records taken at different rates and scales with respect to intensity.

A comparison of the values of B and mechanical strength obtained is shown in Fig. 2. It should be taken into account that an average value of the strength may differ considerably from the values for individual granules, whereas results of microprobe analysis characterize individual properties of the granules.

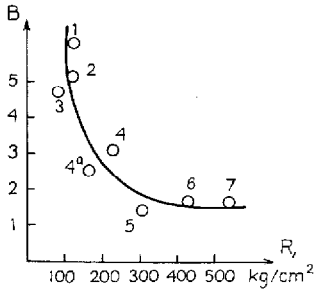

Fig. 2. Plot of degree of fragmentation of samples (B) vs. mechanical strength of granules (R). Numbers of samples as in Table 1.

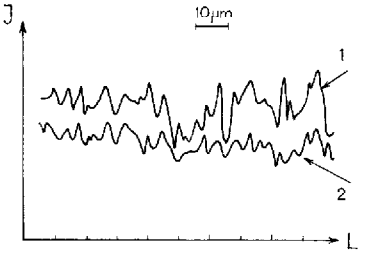

Fig. 3. Intensity of (1) Al Kα and (2) Mg Kα radiation for Mg/Al_2O_3 containing 1.5 wt.-% Mg^{2+} (sample 6, Table 1).

For the construction of the plot (Fig. 2), average values of B for 2–5 granules were used.

Based on the results obtained, we conclude that the mechanical strength of spherical alumina granules is strongly related to their fragmentation at the level of micrometre size. Other structural methods do not provide information on pores over this range. In the samples studied, pores larger than 100 nm were not detected (see Table 1).

Alumina samples additionally containing Mg^{2+} cations (samples 6 and 7, Table 1) were also studied using the same approach. Al Kα and Mg Kα radiation intensities were recorded on scanning the same part of the sample. At low concentrations of Mg^{2+} (ca. 1.5%) the Al Kα and Mg Kα intensity profiles are almost identical (Fig. 3), which is in agreement with X-ray analysis results indicating the formation of a solid MgO–Al_2O_3 solution in this concentration region.

At concentrations exceeding the solubility limit, excess Mg^{2+} cations can reside in macro defects of the matrix, as follows from the Al Kα and Mg Kα intensity profiles (Fig. 4). In this instance B can be calculated from a new intensity curve for Al Kα obtained by substracting the area under the Mg Kα curve from that for Al Kα, taking into account the scale coefficient.

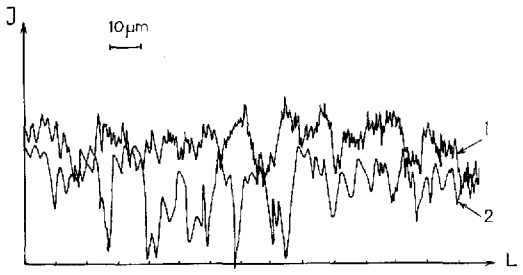

Fig. 4. Intensity of (1) Al Kα and (2) Mg Kα radiation for Mg/Al_2O_3 containing 3 wt.-% Mg^{2+} (sample 7, Table 1). The Mg Kα intensity is ten times higher than that of Al Kα.

TABLE 2

Mechanical strength of Al_2O_3 granules determined by different methods

No.	Sample	Mechanical strength (kg/cm^2)	
		Microanalysis data	Measured as in ref. 10
1	γ-Al_2O_3	235	225
2	Mg/γ-Al_2O_3	250	300
3	δ-Al_2O_3	195	180
4	Mg/δ-Al_2O_3	330	330

As can be seen in Fig. 2, the experimental dependence $R = f(B)$ remains valid for the Mg/Al_2O_3 system (points 6 and 7).

Additional support for such a dependence comes from the data listed in Table 2, which shows that the mechanical strength of additionally studied alumina samples (found from the plot in Fig. 2) is very close to that measured for these samples.

In addition, it can be seen in Table 1 and 2 and Fig. 2 that the dependence $R = f(B)$ is valid for the various modifications of alumina (γ-, δ- and α-Al_2O_3).

CONCLUSION

This X-ray microanalysis of granulated alumina systems has indicated that the mechanical strength of granules depends significantly on their imperfections (micro cracks with a size of $> 10^3$ nm), as determined quantitatively from the Al Kα intensity profile. The regularities found remain valid for complex (Mg/Al_2O_3) systems; in addition, an analysis of the Al Kα and Mg Kα curves provides more detailed information about the effect of the second cation on the structural and mechanical properties of alumina.

REFERENCES

1 P.A. Rebinder, in Physico-Chemical Mechanics of Dispersed Materials, Nauka, Moscow, 1966, p. 5.
2 E.D. Shchukin and S.I. Kontorovich, Kinet. Katal., 9 (1968) 872.
3 E.D. Shchukin, S.I. Kontorovich, Zh.G. Malikova, et al., Dokl. Akad. Nauk SSSR, 173 (1967) 139.
4 S.I. Kontorovich, K.A. Lavrova, G.M. Plavnik, et al., Dokl. Akad. Nauk SSSR, 199 (1971) 1360.
5 E.D. Shchukin, Kinet. Katal., 6 (1965) 641.
6 G. Bisson and C. Prieur, Rev. Int Hautes Temp. Refract., 19 (1982) 269.
7 J.E. Ritter, Jr., and R.W. Davidge, J. Am. Ceram. Soc., 67 (1984) 432.
8 Y. Matsuo, K. Kitakami and S. Kimura, J. Mater. Sci., 22 (1987) 2253.
9 V.A. Dzisko, T.S. Vinnikova, L.M. Kefeli and I.A. Ryzhak, Kinet. Katal., 7 (1966) 859.
10 E.D. Shchukin, A.I. Bessonov and S.A. Paranskii, Mechanical Tests of Catalysts and Sorbents, Nauka, Moscow, 1971.
11 I.A. Ovsyannikova, G.I. Gol'denberg, V.B. Fenelonov and V.Yu. Gavrilov, Izv. Sib. Otd. Akad. Nauk SSSR, Ser. Khim., 8 (1986) 3.

Improvement of the Hydrocarbon-Ammonia Granulation Method for Production of Spherical Alumina with Variable Properties

M. N. SHEPELEVA, R. A. SHKRABINA, Z. R. ISMAGILOV

Institute of Catalysis, Siberian Branch of the USSR Academy of Sciences, Novosibirsk, USSR

The physico-chemical processes, taking place at the main stages of alumina formation into spherical granules by the hydrocarbon-ammonia granulation method (HAG method) were studied. It was possible to develop the scientific basis of preparation of granules with variable characteristics, to establish the optimal conditions for each stage and to improve the apparatus.

The alumina granules obtained by the improved HAG method are distinguished by having a perfect spherical shape, wide texture characteristics range and high mechanical strength. These granules can be used both in fixed and fluidised bed processes.

Alumina is widely used as an adsorbent, catalyst component or support. The development of the chemical industry, diversification of application areas and severity of process conditions place new requirements on the alumina quality [1, 2].

It is known that not only the preparation method, but also the procedure of moulding into granules influence the product's characteristics. This work is devoted to the development of the hydrocarbon-ammonia granulation method (HAG method) which allows the obtaining of spherical alumina granules, particularly important for the processes in a moving or fluidized bed. The results obtained during the past 5 years helped to form the scientific basis for the preparation of alumina spheres and established the technological conditions in laboratory, semi-industrial and industrial installations.

The process of granulation includes the sequence of several technological steps: raw material preparation, dosing and mixing of the components, formation of granule structure development etc. [3]. In our case the following stages were considered:

1. aluminium hydroxide plastication;
2. preparation of spherical granules of aluminum hydroxide;
3. thermal treatment.

The HAG method can be realized in batch or continuous equipment, the main part of the installation is the granulation column. The continuous type installations are more productive. In this appartus the granules are carried by a liquid stream from the bottom of the column to the drying oven. The principle is presented in Fig. 1. It is useful to consider separately the processes taking place at each technological stage.

PLASTICATION

At this stage, aluminium hydroxide is converted into a slurry which can flow from the spinnerets of the moulding device. As a rule, the aluminium hydroxide is used as a gel or powder. Acids which form water soluble aluminium salts are used as plasticizers.

The investigation of colloid processes proceeding at this stage [4, 5] have shown that three types of aluminium hydroxide exist: completely disagregatable, completely agregatable and partially disagregatable. The use of the first type aluminium hydroxide leads to the production of fine pore (the pore volume is approximately equal to the volume of micropores $V < 10$ nm), strong (10–50 MPa crushing pressure) alumina granules with high bulk density (0.6–0.9 g/cm^3). The second type hydroxides could be moulded by the HAG

method only after mixing them with the first type hydroxides. It is possible to obtain alumina granules with a wide range of pore volume, specific area (from 70 to 300 m^2/g), bulk density (0.4–0.7 g/cm^3) and strength (10–30 MPa) depending on the ratio of the first and second types hydroxide concentration in the mixture, which then belongs to the third type. The plastication conditions and the choice of the acid (plasticizer) determine the granules structural and mechanical characteristics. This determines the importance of the plastication stage in the over-all HAG process. Substantial changes in the texture of aluminium hydroxide at this stage are the distinctive feature of this granulation method in comparison with other methods in which the hydroxide is not practically subjected to chemical treatment.

The success of plastication lies in the proper choice of solid phase — water — acid ratio which establishes the required rheological properties of the slurry. The maximum alumina concentration should not exceed 30 wt. %, the minimum should not drop below 10 wt. %. These restrictions are given by rheological properties — the excess of solid phase results in a thick non-flowing mass, considerable decrease in solid phase concentration gives excessively flowing slurry and loss of spherical shape. It is particulary important to monitor this factor carefuly in mass preparation from powdered aluminium hydroxides when the amount of water added determines the alumina concentration. When an aluminium hydroxide gel containing 20–30 % of alumina is used, water addition at the plastication stage is not necessary.

Rheological properties are also affected by the concentration of the acid. This concentration is expressed as the acid module (M) which is equal to the acid/alumina mole ratio. It has been established that its value determines the maturation time and life-time. During the maturation, the heterogeneous system obtained after component mixing becomes quasi-homogeneous due to the swelling. The acid concentration and the temperature in the reactor-plasticator influence the maturation rate. Mature slurry posesses tixotropic properties which are manifested as a rapid drop in slurry viscosity, the preservation of low viscosity within a certain time and a further viscosity increase up to the change from a liquid into a gel. This viscosity increase is reversible: under repeated agitation the gel becomes liquid. The necessary condition of apparatus operation is

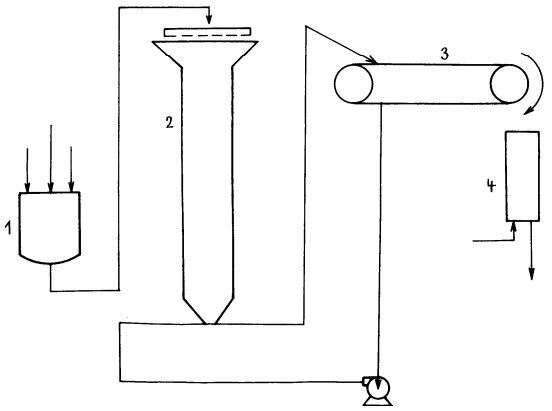

Fig. 1. The principle of a HAG method installation: 1-reactor — plasticator, 2-column, 3-drying aggregate, 4-calcination oven

the production of a slurry with a sufficiently long set time (τ).

As our experiments have shown τ should lie in the range of 15–25 min for the production of granules with 2–3 mm in diameter. It has been established that M influences considerably the τ value (Fig. 2). Up to the present time, the M value was determined for each hydroxide charge by empirical means which led to the production of excessively fluid or excessively stiff masses. Any deviation from the required value leads to the deterioration of the product and semiproduct characteristics.

Optimal M value (M_{opt}), at which τ lies in the required range but maturation time is minimal, has been found and its dependence on the aluminium hydroxide properties and preparation conditions has been established. In a general case, the M_{opt} value depends on the solid phase concentration in the slurry, on the amount and nature of admixtures, plastication temperature and agitation intensity. Provided the three last parameters are fixed, M_{opt} depends on moisture content in the hydroxide and its specific area. When nitric acid is used as plasticizer, the following formula is applicable:

$$(M_{opt})_{calc} = S + W \qquad (1)$$

where S is specific area of aluminium hydroxide [m^2/g], W moisture content in aluminium hydroxide [g H_2O/g alumina] and α, β are coefficients: $\alpha = (6.5 \pm 1.6) \times 10^{-8}$, $\beta = (22.7 \pm 3.2) \times 10^{-3}$.

The use of formula (1) excludes the necessity of empirical evaluation of M_{opt} and gives good agreement of

Table 1. The influence of nature of acidic plasticizer on the structural and mechanical properties of alumina

Acid	Bulk density	Specific area [m^2/g]	Crushing strength [MPa]	Pore volume [cm^3/q]	
				V_p	$V_r > 10$ nm
HNO_3	0.84	320	32	0.25	0.01
HCl	0.84	320	31	0.25	0.01
CH_3COOH	0.83	310	28	0.33	0.04

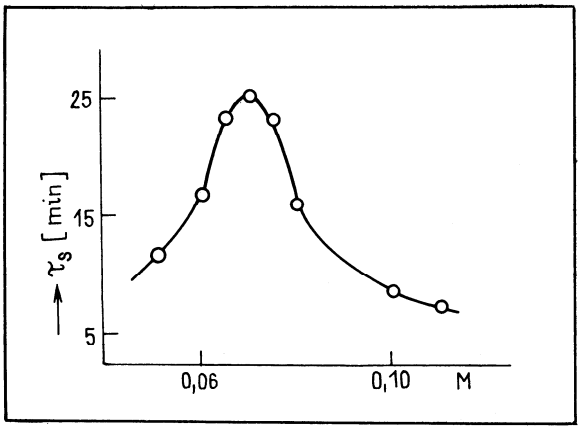

Fig. 2. The dependence of slurry setting time τ_s the acid module M

calculated and experimental values of acid modulus. Nitric, hydrochloric and acetic acids are usually applied for the plastication. HCl and HNO_3 affect the aluminium hydroxide similarly. CH_3COOH is a weaker plasticizer, because the resulting alumina granules have increased pore volume and are less strong (Table 1).

The investigation of plasticated slurries allowed the discovery of the cause of unreproducibility of properties of alumina granules obtained from the same sample in case of unpredicted installation stop or in case of fresh sample mixed with residues from previous batches. It is found that the ability to reverse "setting--liquefection" interchange gradually disappears. After a certain time which amounts to from several days to several months, the agitation results only in a short-time viscosity decrease; the system sets again rapidly. Later the mixture cannot be liquified by agitation and loses its ability to be moulded by the HAG method.

Fig. 3. The dependence of granule strength S on the storage time τ

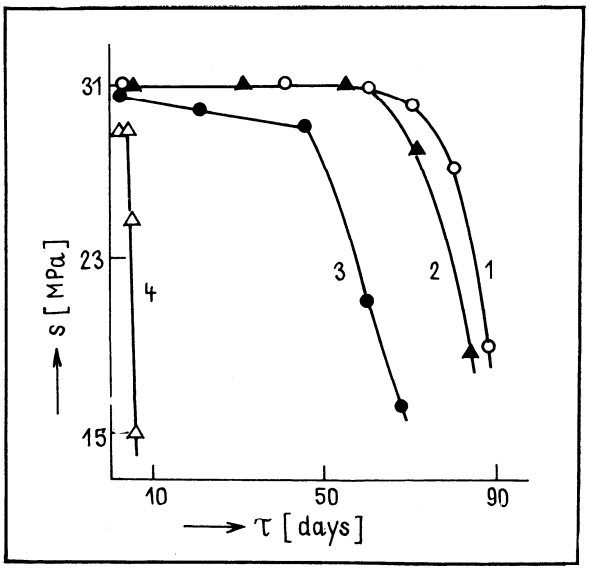

Further we have discovered that the use of slurries, aged for a long time, leads to deterioration of granule shape and to changes of their characteristics.

Fig. 3 shows the dependence of strength of alumina granules on the time of storage, calculated from the moment of preparation till moulding. The granule strength remains constant during a certain storage time. The use of older slurries leads to the production of alumina granules with decreased strength. Other granule characteristics such as specific area; total pore volume (V_p) and bulk density also change but these changes are not so pronounced as the strength and spheric shape.

Thus, the investigation of plastication process enabled us to establish the following: a) this breaks ground for the textural and mechanical characteristics of alumina granules; b) the rheological properties and process technological characteristics of the slurry depend on the correct choice of solid phase concentration and on the nature and amount of acid added; c) the mixing of slurries with different storage time is impermissible.

PRODUCTION OF SPHERIC ALUMINA GRANULES

This stage is carried out in two steps:

a) sphere formation in hydrophobic medium;
b) coagulative setting of granules with the fixation of spheric shape.

Sphere formation

A hydrocarbon liquid (HL) with a density less than that of coagulant and much less than that of the mass being moulded is usually applied as hydrophobic medium.

In the layer of HL a drop of the slurry is subjected to surface tension forces which tighten it into a sphere. This stage breaks ground for the granule shape and the majority of defects. The drops have time for sphere formation in air during the time from their take-off from the spinnerets till the immersion into HL.

The data concerning the influence of H_{hl} on the properties of alumina granules are listed in Table 2. At low H_{hl} the spheres are not formed. The optimal H_{hl} is about 5—15 mm. Further increase in H_{hl} leads to the granules getting hung up at the hydrocarbon — ammonia interface and their sticking together. The experiments were made also with hexadecane and tridecane but diesel fuel was generally used.

Granule hardening

In the HAG method the granules harden as a result of coagulant action. This process can proceed completely, if the coagulant uniformly penetrates the granules, or partially if granules harden on surface only. These "shell" granules lose their shape in drying and

Fig. 4. The dependence of strength of alumina granules S on their time in ammonia solution τ (NH_4OH)

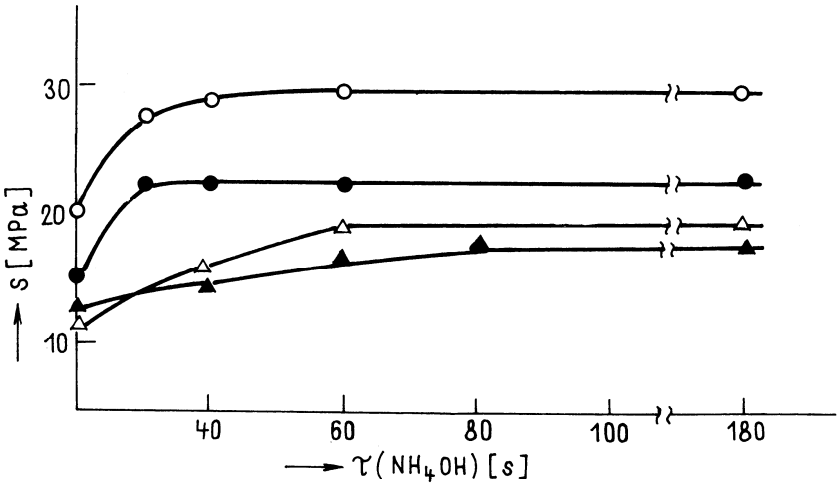

calcination ammonia solution is generally used as coagulant. It is necessary to provide complete interaction between the slurry and the coagulant for the preparation of high strength alumina granules. In continuous moulding, the dependence of granule characteristics on the time they remain in ammonia solution has been investigated. Fig. 4 shows the dependence of granule strength on the time they remain in ammonia solution. The granules from slurries with solid phase concentration $G < 25$ % and $M < 0.1$ harden within 30s of being in 16–19 % ammonia solution. At $M > 0.1$ only partial surface hardening occurs during this time. The increase of the time they remain up to 60–80 s and simultaneous rise in ammonia concentration up to 19–21 % leads to production of uniformly impregnated granules. Thus, special attention should be paid to the following factors: correct choice of the height of the hydrocarbon layer allows the obtaining of spherical alumina granules, a decrease in the frequency of their faults and a reduction of the amount of waste. The treatment of aluminium hydroxide with optimal amount of the acid and 30–60 s time in the coagulant solution is sufficient for complete granule hardening and maximum strength attainment.

THERMAL TREATMENT OF GRANULES

Drying and calcination processes are necessary stages of material preparation from wet precipitates. The texture and other physical properties of catalysts and supports are developed at these stages. Phase transformation also proceeds in the thermal treatment.

The basis of these processes and methods of their execution have been well investigated, therefore our

Table 2. The influence of HL layer height H_{hl} on the properties of alumina granules

H_{hl} [mm]	Alumina characteristics			
	Bulk density [g/cm^3]	Strength [MPa]	Target fraction yield [%]	Shape of granules
2	0.82	28	30	flattened
5	0.84	32	98	spherical
20	0.84	32	70	spherical, many stuck together

Table 3. The influence of drying conditions on alumina granule characteristics

Drying granules			Alumina characteristics			
Method	T [°C]	τ [h]	S_{sp} [m^2/g]	V_g [cm^3/q]	Strength [MPa]	Yield of fraction [%]
In air flow	20	48	270	0.37	18.2	98
In drying box	110	4	270	0.36	10.4	90
Under heater	200	0.5	270	0.35	10.0	90
Same	40–200	0.5	270	0.35	11.2	98

Calcination conditions				Alumina characteristics				
T [°C]	τ [h]	Rate of temperature increase [K/h]	Air flow [h^{-1}]	Granule bed height [mm]	Bulk density [g/cm^3]	S_{sp} [m^2/g]	V_p [cm^3/q]	Strength [MPa]
500	4	400	–	5	0.85	170	0.35	30.0
500	4	400	1000	5	0.84	240	0.29	31.2
500	4	400	1000	20	0.84	210	0.31	28.7
500	4	650	1000	5	0.84	210	0.32	29.0
500	4	250	1000	5	0.84	250	0.25	33.1
700	4	400	1000	5	0.85	200	0.33	30.9

Table 4. The dependence of structural and mechanical properties of alumina granules on calcination conditions

work pays special attention only to the choise of drying and calcination conditions at which it is possible to obtain high-strength alumina granules with well developed porous structure.

Granule drying

Drying was carried out by several methods: in air flow, in drying box, in aggregates with moving net ribbon and heaters above it. The experimental results are shown in Table 3. It can be seen that the drying method does not considerably affect the specific area and pore volume but strongly affects the strength of granules and the yield of desired fraction. Sharp moisture removal from the granules leads to their destruction and formation of deep fractures. Granules of the highest strength were obtained when drying in air was applied. This is a well known and widely recommended method, especially for the drying of fine porous materials. It cannot be used, however, for continuous processes. The conditions providing sufficiently rapid drying from moisture content 70–80 % to 30–40 %, when granules acquire free-flowing properties, were to be found. It was established that the decrease of initial drying temperature and gradual temperature increase while drying facilitates the increase of granule strength.

Granule calcination

The calcination of granules with bidisperse or broad-pore structure does not present great difficulty. The calcination of fine pore samples is more complicated. The dependence of granule properties on calcination temperature, rate of gaseous products removal and granule bed height has been investigated; the results are presented in Table 4. It is evident that the rate of temperature increase and bed height rise facilitate the sintering of fine pores which leads to the rise of total pore volume and to the drop in specific area and granule strength. The increase of air flow slows down the sintering process while the granule strength and specific area increase. Thus in the thermal treatment, the formation of final granule structure proceeds, specific area, total pore volume and volumes of micro-and macropores increase, as well as granule strength. Carrying this stage out in optimal conditions allows the obtaining of low fault granules with high yield of desired fraction.

The investigation of physico-chemical processes taking place at the main stages of alumina moulding by the HAG method enables to develop the scientific bases of preparation of granules with variable characteristics, to establish the optimal conditions for each stage and to improve the apparatus.

Alumina granules obtained by the improved HAG method are distinguished by having a perfect spherical shape, wide-pore texture and high strength. These granules can be used both in fixed and fluidised bed processes.

REFERENCES

[1] Dziko, V. A.: The Principles of Catalyst Preparation Methods. Novosibirsk, Nauka 1983.

[2] Trimm, D. L., Stanislav, A.: Appl. Catal. *21* (1986), No. 2, 215.

[3] Klassen, P. V., Grishaev, I. G.: The Principles of Granulation Technique. Moscow 1982.

[4] Shepeleva, M. N., Fenelonov, V. B., Shkrabina, R. A.: Kinetika i Kataliz *27* (1986), No. 5, 1202.

[5] Shepeleva, M. N., Shkrabina, R. A., Okkel, L. G. et al.: Kinetika i Kataliz *20* (1988), No. 2, 195.

[6] Shepeleva, M. N., Shkrabina, R. A., Ismagilov, Z. R.: in The Problems of Kinetics and Catalysis. Chemical Principles of Catalyst Mounding. Ivanovo 1988.

Adsorption-Contact Method of Drying of Thermolabile Materials

I.ZH. ZAINIEVA*, R.A. SHKRABINA, Z.R. ISMAGILOV, V.F. KOMAROV
Institute of Catalysis, Siberian Branch of the USSR Academy of Sciences, Novosibirsk, USSR

The main stages of adsorption-contact method (ACT-method) of drying of thermolabile materials are studied. The optimal conditions of ACD are established.
The main requirements of the adsorbents (spherical alumina) for ACD are formulated in the results of detailed investigation of the physico-chemical and structure-mechanical characteristics of adsorbents of a wide range in the course of multicyclic regeneration.

The adsorption-contact drying method (the ACD method) is known to be one of the ways of intensification of thermally unstable material drying. This method is based on the immediate contact of damp material with a dry porous adsorbent able to adsorb vapours and pick up moisture [1]. After separation of wet adsorbent from dry material the former is regenerated for repeated use.

The following experimental results are presented in this work: first, on adsorption-contact moisture transfer from crystalline, thermal unstable ammonium salts depending on the temperature, adsorbent quantity and structural properties; second, on the character of channels of porous structure and mechanical strength of adsorbent under ACD (i.e. under repeated ACD cycles) with the aim of making a choice of adsorbent with optimum porous structure and stable strength characteristics.

The investigation of moisture removal patterns by the ACD method has been carried out in a laboratory mass-transfer drum with a speed of rotation 2-27 rpm. During the selection of adsorbents preference was given to γ-aluminas, which in contrast to silica-gels, zeolites and carbons exhibit increased mechanical strength and water resistance. The experiments were carried out at temperature 293± 5 K for ammonium bicarbonate and at 293-333 K for ammonium oxalate.

In Figs. 1 and 2 the kinetic curves of ammonium bicarbonate and oxalate drying under the contact of spheric γ -alumina (d =2-3 mm) are presented. It is seen from these pictures that the increase in amount of adsorbent (n) in the contacting mixture allows obtaining the required residual moisture content (U_k) within a shorter time interval (τ) under the same experimental temperature. Thus the tenfold increasing of adsorbent amount permits reducing the drying time for ammonium oxalate by a factor of 11 and for ammonium bicarbonate by a factor of 3. For ammonium oxalate the reduction of drying time is observed also with the increasing of temperature from 293 to 333 K (Fig. 2b). Special experiments with different drum rotation rate - 2,9,30 and 87 rpm allow establishing the independence of drying speed on the mixing intensity in the range investigated.

The plot of drying rate versus the volume of selected pore size of the adsorbent is presented in Fig. 3. The drying rate is shown to increase with increase of pore volume with $r <$ 4 nm and r = 4-10 nm, and decrease with pore volume with $r >$ 10 nm.

The results presented show that the use of ACD process for ammonium bicarbonate and ammonium oxalate allows

Fig. 1. The dependence of moisture concentration in ammonium bicarbonate on the contact time with γ-alumina at 293 K; n = 0.5 (1), n = 1.0 (2), n = 3.0 (3)

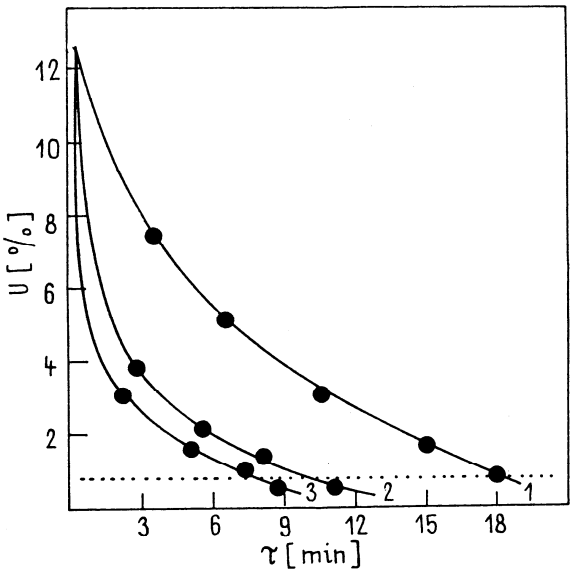

* Institute of Catalysis
Siberian Branch of the USSR Academy of Sciences
pr.Lavrentieva 5
630 090 Novosibirsk
USSR

Fig. 2. The dependence of moisture concentration in ammonium oxalate on its contact time with γ-alumina

a) $n = 0.5$;
293 K (1)
313 K (2)
333 K (3)

b) 313 K;
$n = 0.1$ (1)
$n = 0.3$ (2)
$n = 0.5$ (3)
$n = 1.0$ (4)

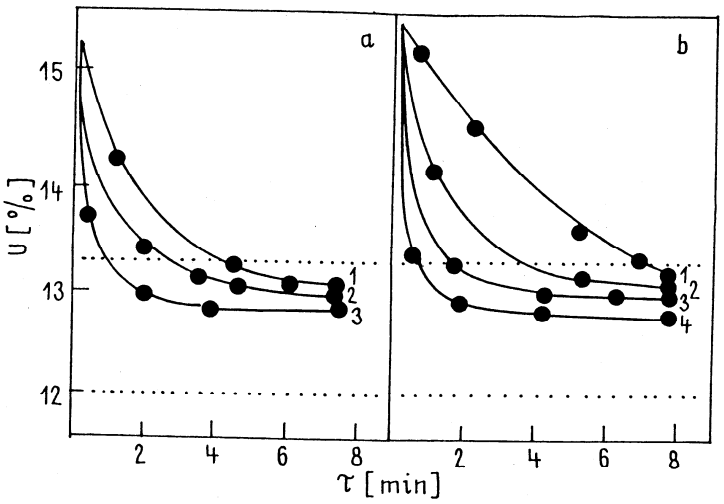

reducing the drying time by a factor 8 - 10 and also to dry products with a higher initial moisture content, their quality being related to the established standard. Pilot tests of ACD of ammonium salts confirmed the results of the laboratory tests and demonstrated this drying method to be promising.

In the course of contact mass transfer under ACD the moisture content in dryed material (we'll call it „the moisture donor" in a general case) is reduced and the moisture content in the adsorbent (acceptor) increases, which affects the moisture transfer mechanism. The process, in turn, can be limited by one of 3 specific stages:

a) Mass transfer in the donor bulk;
b) Mass transfer through the donor-acceptor boundary;
c) Mass transfer in the acceptor bulk.

The mass transfer through the donor-acceptor boundary can proceed via different ways:

a) Vapour transfer via evaporation from the donor and condensation on the acceptor;
b) Condensate transfer along the interconnected system of pores filled with condensate;
c) Condensate transfer along the polymolecular film through interconnected structure regions not filled with the condensed phase.

Part of liquid phase can additionally be evaporated to the volume of mass transfer apparatus (the pressure considerably rises in the experiments with increased temperature).

The experimental kinetic data analysis allows selecting three stages of the drying process:

1. rapid drying,
2. the decrease of drying rate,
3. very slow moisture exchange.

Each stage can be described satisfactorily by the 1st order equation:

$$U/\Delta\tau = \beta(U - U_p)$$

where β is mass transfer coefficient, U_p equilibrum moisture content.

The computer treatment of data performed reveals the dependence at each stage and leads to several approximations. The 1st stage corresponds mostly to the liquid phase capillary transfer. In this case practically momentary moisture removal from surface and from microcapillaries proceeds.

Generally, the rate of capillary transfer is proportional to the ratio of surface tension to liquid viscosity, both quantities decrease with temperature, that can explain the temperature dependence. The effectivity of ACD in this case is connected with the formation of local pressure and temperature gradients between the cooling donor and heating by adsorption acceptor. At the 2nd stage the moisture is removed from the microcapillaries and this period is longer than that of the 1st stage. Thus as the latter stage lasts generally 1-2 minutes, the former may last 10 minutes or more. Obviously the vapour phase transfer proceeds along with the liquid phase

Fig. 3. The dependence of amonia salts drying rate on the volume of pores with $r = 4$nm (1), $r = 4$-10 nm (2), and $r >$ 10 nm (3) in adsorbent

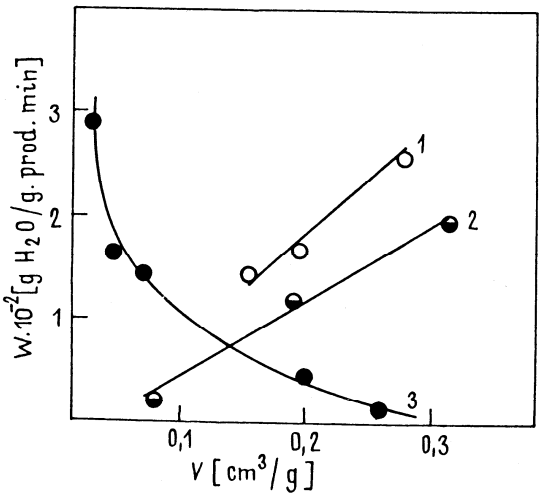

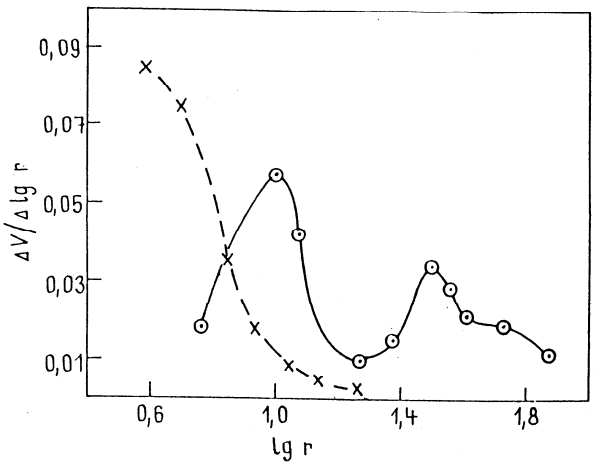

Fig. 4. Differential curves of pore volume-radii distribution for the starting sample 1 (dotted line) and after 100 regeneration cycles (solid line)

moisture transfer. At the 3rd stage, apparently the most strongly bounded adsorbed moisture is removed. For this stage practically no dependence on T and n was observed. The analysis of β value obtained shows that the presence of adsorbent contributes substantially to the 1st drying stage, 70% of moisture being removed at this stage. An increase of the mass transfer coefficient depending on temperature and adsorbent amount is clearly observed. At the 2nd and 3rd stage this dependence is much less pronounced.

Thus on the basis of both the laboratory investigation and the tests in industrial conditions it can be concluded that the rate of the moisture removal from ammonia salts depends on both the pore size distribution of the adsorbent and its amount in the mixture and on temperature. On the other hand it does not depend in the investigated range on the rate of mass transfer and drum rotation.

During the ACD process the moisture transfer from dried material to the volume of adsorbent pores proceeds, and the moisture content in the adsorbent reaches 5-10 mass % depending on drying conditions, which leads to the reduction of the drying rate. Therefore for the optimization of the water removal process it is necessary to remove the adsorbend moisture from the adsorbent in order to restore its adsorption capacity, i. e. regeneration becomes necessary.

It should be taken into account that the adsorbent passes by turns through the stages of low temperature moisture adsorption in mass transfer apparatus and the stage of high temperature desorption in the regenerator. Each of these stages makes its specific demands on the adsorbent, its physico-chemical properties and strength characteristics. The succesful application of the particular adsorbent in ACD conditions depends obviously not only on high adsorption capacity, but to a large extent on the stability of its structural and mechanical properties in the process of a lengthy operation.

The results of investigations of porous structure and mechanical strength changes at repeated ACD cycles, with the aim of selection of adsorbent with stable adsorption and machanical characteristics, are presented in this work.

According to the literature data available one of the causes of adsorbent mechanical strength decrease [2-5] are gradients of temperature and moisture capacity in the bulk of the porous material. As a result, the bulk-strained state appears which in turn can cause cracks leading to the local and complete destruction of material [6]. Under repeated ACD cycles of drying and moistening structure defects are gradually accumulated, which affect the strength properties of the porous material [7].

Adsorbents with a high mechanical strength (manufactured on the basis of spheric active alumina) have been selected as the objects of the investigation. This choice was made because none of the industrial adsorbents (on the basis of zeolites, silica gels and active carbons) is applicable for ACD, because of poor mechanical strength of zeolites and carbons and because of poor water stability of silica gels.

Multicyclic adsorbent regeneration has been carried out in conditions usually accepted in industrial practice [8], i.e. in a fixed bed under atmospheric pressure and at temperature 523 K.

The following methods have been used for the investigation of structural characteristics of adsorbents before and after regeneration: argon thermodesorption for specific area determination, the volume - picnometric method for true density determination, the mercury porosimetry and nitrogen adsorption on the automatic sorption device Dijisorb-3600 for pore volume and its radii distribution (V,r) determination. The X-ray diffraction to determine the phase composition of samples has been carried out on the type Dron-1,5 apparatus with the use of monochromatic copper radiation [9]. Granule strength has been determined under

Fig. 5. The dependence of average crush strength on the number of regenerations at 523 K

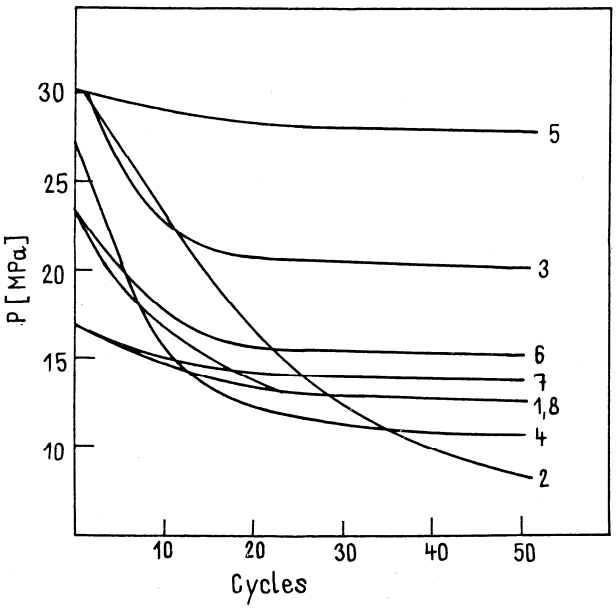

Table 1. The main structural-mechanical properties of spheric adsorbents on the basis of alumina

No	Content of γ - Al_2O_3 [%]	Bulk density [g/cm^3]	Spheric area [m^2/g]	True density [g/cm^3]	Total pore volume [cm^3/g]	Pore volume [cm^3/g] (% from V)			Mechanical strength		
						r < 4 nm	r = 4-10 nm	r > 10 nm	P_{av}, crush [MPa]	W.10^{-3} [J/cm^2]	V_{fric} [%/min]
1	100	0.84	220	3.23	0.40	0.15(37)	0.22(54)	0.03(9)	21.0	140	0.22
2	100	0.77	220	3.25	0.47	0.31(65)	0.15(32)	0.01(2)	29.0	180	0.33
3	100	0.85	210	3.29	0.41	0.11(27)	0.29(71)	0.01(2)	31.0	190	0.37
4	85+15%	0.69	220	3.42	0.58	0.21(36)	0.36(62)	0.01(2)	26.0	200	0.19
5	100	0.94	190	3.22	0.33	0.13(39)	0.20(60)	-	30.0	280	0.15
6	100	0.68	205	3.26	0.57	0.09(16)	0.41(61)	0.13(23)	21.0	140	0.18
7	50+50%	0.83	180	3.29	0.42	0.10(24)	0.31(74)	0.01(2)	16.0	110	0.22
8	45+55%	0.82	260	3.31	0.43	0.13(30)	0.24(56)	0.01(2)	16.0	110	0.22

static (crush, P_{av}) and dynamic (impact, W_{sp}, abrasion V_{ab}) conditions [10]. The main phisico-chemical characteristics of samples investigated are listed in Table 1. The samples 1-8 are spheric alumina granules 2-3 mm in diameter. The samples 1-6 were produced by the liquid moulding method from pseudoboehmite hydroxide obtained by redeposition technique [11]. The sample 4 obtained from pseudoboehmite was prepared by gibbsite thermodestruction technology [9]. The samples 7,8 have been produced by the mechanical moulding method from gibbsite thermochemical activation product [12]. In contrast to the samples 4,7,8 obtained by untraditional techniques, the adsorbents obtained from industrial pseudoboehmite aluminium hydroxide (1,2,3,5,6) are 100% γ - alumina (Table 1). An inhomogeneous composition of samples is probably due to the preparation conditions.

The finest porous adsorbents under consideration are the samples 2 and 5. They have 36-65% of pores with average r < 4 nm. For the sample 1 the amount of cycles has been raised to 100. In the course of multicycle regeneration the samples were taken after each 10 cycles for complete analysis of porous structure for measurement of mechanical strength.

The experimental data obtained suggest that 50-100 regeneration cycles slightly increase the bulk density of samples by approximately 10%, the value of their specific area decreases and their porosimetric pore volume rises (Fig. 4). Similar data have been obtained for the other samples.

The carrying out of 100 moisture thermodesorption cycles leads to slight changes of adsorbent porous structure. The observed decrease of fine (4-10 nm) pores volume and increase of larger pores (4-10 nm) volume is obviously connected, first, with blocking part of the adsorbent finest pores by some amount of moisture, and second, with destruction of fine pores and formation of larger pores.

The main results of determination of adsorbent strength characteristics in the course of multicycle regeneration are presented in graphic form. As can be seen from Fig. 5, the average crush strength decreases practically for all samples investigated with the increase of number of regenerations. The main changes are observed during the first 10-20 cycles,further changes being minor. It should, however, be noted that for samples presented the strength drop proceeds via different ways: the largest one, by 34-50%, is observed for samples 1,2 and practically there is no change for sample 5. The treatment of experimental data in the coordinates of relative sample strength versus micropores volume reveals in these samples the following relationship: the higher is the pore volume with r > 4 nm in the initial sample, the sharper is the strength drop after cycles of saturation-regeneration. Fig. 6 shows, that at micropores volume of more than 0.15 cm^3/g (samples 1,2,4) the strength drop amounts to 60-30%. Results obtained are in good agreement with the data of [10], presuming the destruction of micropores in the first turn because of thermal desorption, leading to mechanical property deterioration.

It has been established simultaneously, that one can succeed in the adsorbent strength preservation at high level by increasing the relative content of pores with r from 4 to 10 nm in the samples. The investigation of dynamic strength changes of sample granules also shows (Fig. 7) the strength drop at first of 10-20 cycles, but further increase of W_o values was observed for several samples. This we presume to be connected with the fact that the main macro-microdefects of structure, which lower granule impact stability, vanished at

Fig. 6. The dependence of average relative crush strength of samples after 50 regeneration cycles on the content of pores with r = 4 nm in these samples

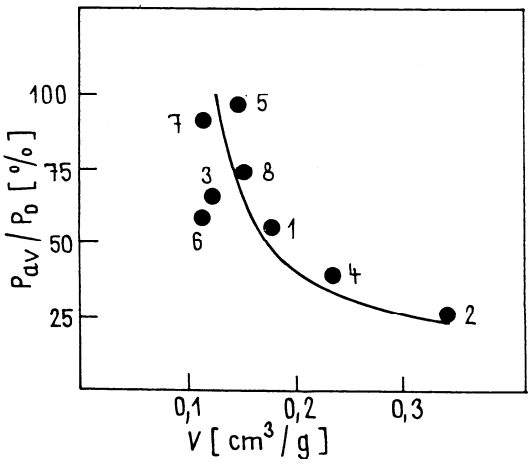

that moment, and the reconstruction of structural formations ceased. An analysis of the relation of adsorbents porous structure to their stability to destructive mechanical loads leads to the conclusion that adsorbents with porous structure represented mainly by pores with r from 4 to 10 nm can be recommended for successful use in the ACD processes. The content of micropores with $r > 4$ nm in the adsorbent should not exceed 0.1 cm^3/g. As is shown by the data of samples friction stability determined after multicyclic regeneration, samples with high friction quality characteristics (i.e. susceptible to the friction degradation to a greater extent), become even less stable to the influence of friction loads after 50 cycles.

An important indicator of adsorbent performance stability is their moisture stability. Results of moisture stability investigation have shown the lowering of this parameter for the finest porous samples, with microporosity factor $V_{mi}/V_s = 30–70\%$.

Thus, as has been shown by the experimental data analysis, the character of mechanical properties changes of adsorbent samples investigated in the process of moisture adsorption and thermal desorption depends first upon the porous structure and does not depend on phase composition and preparation conditions of alumina.

Detailed investigation of physico-chemical and structure-mechanical characteristics of adsorbents of a wide range in the course of multicyclic regeneration allows the formulation of the main requirements of the adsorbents for ACD:

1. The adsorbent performance stability is determined by its porous structure and does not depend practically on preparation technology providing the same adsorbent porous structure. It is reasonable to use the adsorbents with the main pore volume represented by pores with r = 4-10 nm. The content of micropores with $r < 4$ nm should be minimal, not exceeding 0.15 cm^3/g.

2. Strength characteristics should fit several requirements: static crush strength $P > 180$ kg/cm^2; static impact strength not less than $130.10^{-3} J/cm^2$, frictive degradation rate should not exceed 0.30 %/min.

The investigation carried out enables us to establish the optimal conditions of ACD of thermolabile ammonium salts-bicarbonate and oxalate and to formulate the main requirements of the adsorbents, which provide their long and effective performance.

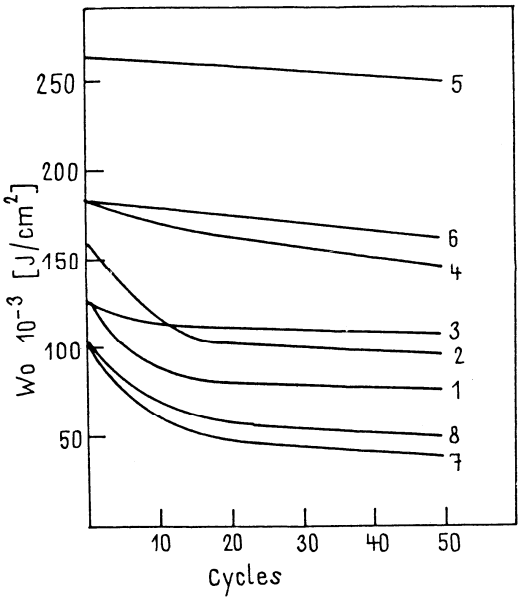

Fig. 7. The dependence of sample impact strength on the number of regeneration cycles

REFERENCES

[1] Anufrieva, V.P., Boreskov, G.K., Levitskii, E.A. et al.: S. U. No. 928878 (1986).

[2] Schukin, E.D., Dukarevich, M.V., Kantorovich, S.I., Rebinder, P.A.: Dokl. Akad. Nauk SSSR *165* (1965), 1109.

[3] Susdaltseva, S.F., Skvortsova, E.I., Margolis, L.Ya.: Dokl. Akad. Nauk SSSR *201* (1971), 415.

[4] Veber, V.I., Tabachkova, I.I., Kundo, N.N.: Zhurn. Prikl. Khim. 1 (1977), 1061.

[5] Poleshko, G.D., Schnip, V.A.: Zav. Lab. *48* (1982), 69.

[6] Rapport, D.M.: Trudy UfNII 3 (1960), 249.

[7] Ostrikov, N.S.: Thesis, Kiev 1967.

[8] Lukin, V.D., Antsipovitsh, I.S.: The regeneration of adsorbents. Chimiya, Leningrad 1983.

[9] Shkrabina, R.A.: Thesis, Novosibirsk 1982.

[10] Schukin, E.D., Bessonov, A.I., Poranskii, S.A.: Mechanical testing of adsorbents and catalysts. Nauka, Moscow 1971.

[11] Lainer, A.I., Eremin, N.I., Lainer, Yu.A. et al.: The production of glinozem. Metalurgija, Moscow 1978.

[12] Buianov, R.A., Krivoruchko, O.P., Zolotarskii, B.P.: Izv. SO AN SSSR, ser. khim. 4 (1986), 39.

Applied Catalysis, 69 (1991) 65–73
Elsevier Science Publishers B.V., Amsterdam

Interrelation between structural and mechanical characteristics of spherical alumina granules and the initial hydroxide properties

Z.R. Ismagilov*, M.N. Shepeleva, R.A. Shkrabina and V.B. Fenelonov

Institute of Catalysis, Novosibirsk 630090 (USSR)

(Received 7 February 1990, revised manuscript received 17 August 1990)

Abstract

The properties are studied of a wide range of aluminium hydroxides of pseudoboehmite structure obtained by settling under conditions providing the gradual growth of primary particles and crystallinity level. The spherical granules of alumina are obtained by the method of hydrocarbon–ammonia moulding. Colloidal-chemical processes taking place during the formation of granules are studied; reasons are determined for obtaining the fine and coarse porous granules of alumina from aluminium hydroxides, which distinguish themselves by the type of contacts between primary particles. The correlation is investigated between the structural and mechanical characteristics of the alumina granules and the shrinkage ratio of the initial aluminium hydroxide under drying.

Keywords: aluminium hydroxide, spherical granules, catalyst preparation (colloidal processes).

INTRODUCTION

Porous, spherical granules of alumina are often used as adsorbents, supports and catalyst components. Their wide application is due to their high surface area, their developed and readily variable porous structure, their thermal shock resistance, thermal stability and mechanical strength [1–3].

One of the most widespread methods for preparing spherical alumina granules is based on the hydrocarbon–ammonia moulding [4–6] process according to the scheme:

$$\text{Aluminium hydroxide gel} \xrightarrow{\text{Peptizer}} \text{sol} \xrightarrow[+\text{Coagulant}]{\text{Sphere-forming substance}}$$

$$\text{Gel in the form of sphere} \xrightarrow{\text{Heat treatment}} \text{Spherical granules of } \gamma\text{-}Al_2O_3$$

According to this scheme a wet precipitate or gel of aluminium hydroxide is first peptized, up to the moment at which a viscid sol is formed. The sol is sprayed in drops into a layer of hydrocarbon liquid, under which conditions

0166-9834/91/$03.50

spheres are formed. There is a coagulant present under the liquid layer and the granules which pass through the layer grow hard and turn into resistant spherical granules of γ-Al_2O_3 after heat treatment.

Refs. 7 and 8 report the special features required for the formation of pseudoboehmite aluminium hydroxides having a porous structure with the use of nitric acid as a peptizer and ammonium hydroxide as a coagulant. On the basis of these reports it is concluded that the role of the aggregation of the primary particles in the initial hydroxides determines the structural and mechanical properties of the alumina granules obtained.

Expanding the concepts developed in refs. 7 and 8 in this work, our major attention was paid to the study of new methods by which it may be possible to predict the structural and mechanical characteristics of alumina on the basis of the properties of the initial hydroxide. Attention was also given to a search for a particular method for the evaluation of the suitability of any given hydroxide in the preparation of alumina granules having the characteristics required.

EXPERIMENTAL

Spherical granules were prepared by the addition of nitric acid to an aluminium hydroxide in the amount of 0.15 mol or less per mol of alumina, and then introducing the sol so obtained dropwise into a two-layer column (hydrocarbon liquid above, ammonia solution below). Drying and calcination of the granules at 500–600 °C leads to the production of γ-Al_2O_3.

The total content of moisture in the hydroxide (ΣW, g H_2O/g of wet hydroxide) was calculated from the change of mass of the aluminium hydroxide upon heat treatment at temperatures ranging from 20 to 800 °C. The value of the specific surface area A was determined by the adsorption of argon in hydroxide specimens desiccated at 110 °C, and in aluminium oxide calcined at 500 °C. The pore volume V_p and the size distribution of the pore radii were determined with a Porosizer-2300 mercury intrusion porosimeter; true density ρ was determined by helium adsorption using an Autopicnometer-3200 apparatus. The phase composition of the specimens was determined by X-ray diffraction using a Dron-1.5 apparatus, with monochromated copper emission; the size of the coherent dispersion (s.c.d.) of the pseudoboehmite aluminium hydroxide particles was determined by the method of approximation using the line [1.4.0, 0.3.0] ($2\theta = 49°$). Electron microscopy was carried out with the help of the JEM-CX microscope. The morphology and the range of particle dimensions were studied with a magnification of 5×10^4. The mechanical strength of the alumina granules, S, was evaluated by mechanical loading up to the crushing point between the two parallel plates.

RESULTS AND DISCUSSION

A wide range of gelatinous aluminium hydroxides of pseudoboehmite structure were prepared for subsequent study. Their characteristics are shown in Table 1 and Fig. 1.

The conditions for the synthesis of the aluminium hydroxides during the settling phase were chosen so that in the series of specimens 1–5 displayed a growth in particle size and degree of crystallinity. Thus, if specimen 1, according to its phase composition is a pseudoboehmite with an s.c.d. of ca. 3 nm in association with a trace quantity of an amorphous phase, then specimen 2 comprises pseudoboehmite only, and specimen 5 is the transition modification from pseudoboehmite to boehmite.

TABLE 1

Characteristics of aluminium hydroxides and oxides

No.	ΣW (g/g)	A (m^2/g)	ρ (g/cm^3)	s.c.d. (nm)	φ (%)	Bulk density (g/cm^3)	A (m^2/g)	V_p (cm^3/g)	$V_{r>100\ nm}$ (cm^3/g)	S (MPa)
1	0.85	370	2.67	3	42	0.84	320	0.04	0	22
2	0.81	380	2.61	5	41	0.80	280	0.20	0	19
3	0.78	250	2.74	7	30	0.75	250	0.39	0.04	10
4	0.72	200	2.74	13	22	0.69	250	0.42	0.19	4
5	0.59	140	2.79	15–17	0	—	240	0.68	0.47	0

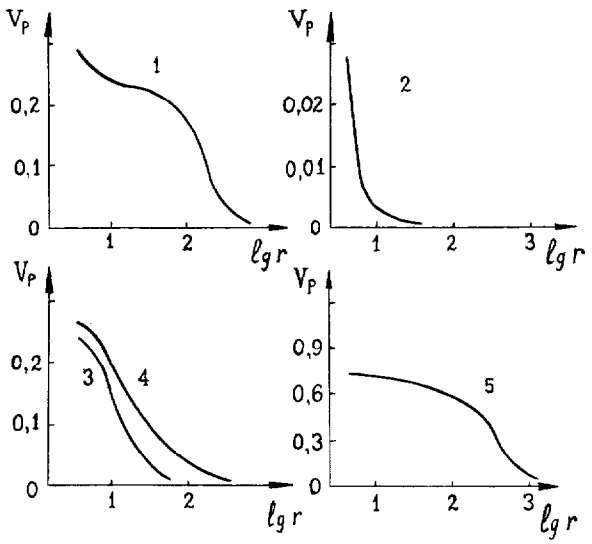

Fig. 1. Distribution of pore volumes, V_p (cm^3/g), with radii, r (nm) of aluminium hydroxides dried at 110°C (spec. 1–5).

From the data of Table 1 it is evident that, as the pseudoboehmite particle size increases, the quantity of total moisture ΣW decreases, the value of A falls off, and the true density of ρ increases. According to the electron microscope data, the morphology of pseudoboehmite secondary aggregates changes simultaneously with the primary particle growth. Hydroxide 1 is formed by coarse loose aggregates, consisting of needles and fibres of size $4\times$ (20–40) nm. Specimen 2 is formed by the needles 3×50 nm in size, packed in small aggregates. The sizes of the needles in the specimens 3 and 4 increase up to $7\times$ (50–100) nm, and thus they are packed in aggregates which increase in size. Specimen 5 consists of large aggregates in the shape of plates of size greater than 100 nm, the edges of the plates being formed by the close packing of needles up to 20 nm thick. The size of aluminium hydroxide aggregates determines their porous structure (Fig. 1). The relatively large volume of pores, V_p, and macropores, $V_{r>100\ nm}$, can be explained by the presence of large aggregates in specimen 1. In specimen 2 a small quantity of aggregated particles formed from a great number of needles in the shape of a plate causes a low pore volume; the pore space texture of this specimen is generally determined by the fine needle sizes. The increasing aggregation of particles when progressing from specimen 2 to specimens 3 and 4 is accompanied by the growth of the average value of pore volume. A great number of pores become accessible to mercury (growth of V_p), and as a result the volume of the pores increases sharply over the range of 10–100 nm (specimen 3) and then, as a result of the formation of the larger particles and aggregates, the growth in V_p is caused by a growth in the volume of the pores having a radius of more than 100 nm (specimen 4). In specimen 5 the major share is formed by pores having a radius of more than 100 nm.

Study of the changes in morphology and sizes of aluminium hydroxide aggregates during the chemical interactions taking place during the process of hydrocarbon–ammonia moulding shows that the hydroxides can be divided into 3 groups.

In the first group (specimens 1 and 2), the action of an acid peptizer leads to a complete destruction of the initial aggregates into particles of 3–5 nm in size. In hydroxides of the second group (specimens 3 and 4) some aggregates interacting with the peptizer are conserved in their initial state. The fifth hydroxide can be related to the third group since its particle size and morphology remain unchanged after the acid treatment. The principle scheme of the processes taking place in aluminium hydroxides of the first and third groups upon the action of a peptizer and a coagulant in turn is presented in Fig. 2.

Upon examination of the results of the experiments conducted according to the ideas developed by Rebinder and co-workers [9], we suppose that the conditions under which the aluminium hydroxides are synthesized determine not only the morphological structure of the particles but also the type of structure. Depending on the type of coalescence contact between the particles, the structures formed may be subdivided into two main types: (i) thixotropic coagula-

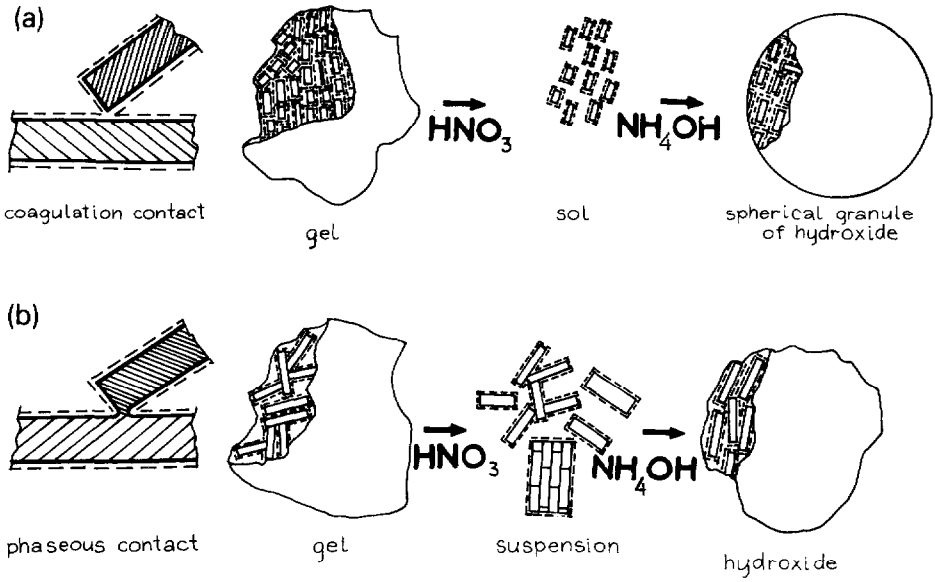

Fig. 2. Principle scheme of processes taking place in aluminium hydroxides of the 1 (a) and 3 (b) groups by subsequent action of a peptizer and coagulant.

tion structures connected by van der Waals or electrostatic forces, slightly resistant but plastic and elastic, owing to the preservation of the ion-solvation sheath at a point of contact (Fig. 2a); (ii) crystallization structures connected by the forces of chemical interaction with either point or phase contact between the particles (Fig. 2b).[α]

In accordance with this classification, aluminium hydroxides of the first group (specimens 1 and 2) consist of aggregates with weak coagulation contacts between the particles, which recover after rupture.

The introduction of an acid, thus increasing the thickness of the electric double layer, is enough to break the contacts in a structure. As a result of this, a hydroxide is almost completely peptized, dispersing in the limit into its primary particles (Fig. 2a). This becomes apparent in a rheological state of mass, leading to the state conversion of the hydroxide from solid into liquid. When such a mass is submerged in the ammonia solution after spraying as drops, a rapid coagulation takes place at the expense of the rupture (or contraction) of the ion-solvent sheath. Small, mobile particles of an aluminium hydroxide are packed close together. The final result is the production of aluminium hydroxide granules having a fine, porous, monodispersed structure.

Systems consisting of phase contacts and chemical bonds between primary

[α]According to the terms accepted by S. Gregg and K. Sing [10], aggregates are formed from loosely bonded particles, and agglomerates are formed from the strongly bonded particles.

particles remain practically unpeptized by acid (group 3, specimen 5). In the quantity which is used in our method of granulation (i.e. 0.07–0.15 moles of nitric acid per mole of alumina), no changes in morphology and aggregate size take place on introducing such a system into ammonia. An increase of acid addition leads only to the hydroxide being dissolved. In order to investigate the properties of the resulting alumina, nitric acid and ammonium hydroxide were consequently added to specimen 5 and the hydroxide was then dried and calcined.

The particles in the hydroxides of the intermediate type (group 2, specimens 3 and 4) are bonded by contacts of both types; the degree of dispersion under the influence of the action of the peptizer depends on the relation between the numbers of contacts.

Calcination of the aluminium hydroxide granules in the temperature range of 500–600 °C permits production of spherical γ-Al_2O_3. The nature of particle packing, as defined by peptization and coagulation of the initial hydroxide, remains unchanged throughout the subsequent stages of alumina preparation and determines its porous structure, specific surface area, and strength. The characteristics of the prepared spherical granules of γ-Al_2O_3 are given in Table 1.

It is evident that the destruction of aluminium hydroxide aggregates and subsequent compact coagulation of the small particles formed leads to the production of fine porous alumina granules with high values of specific surface area, bulk density and strength (specimens 1 and 2). As opposed to this, preservation of the coarse aggregates in aluminium hydroxide (specimen 5) after a peptization–coagulation cycle causes the presence of macropores even in the final alumina.

The results obtained explain the reason for the production of fine and wide porous alumina granules from various aluminium hydroxides as well as the possibility to use them in the hydrocarbon–ammonia moulding.

We also searched for an appropriate experimental test of an initial hydroxide which would permit us to evaluate beforehand (i.e. before the peptization–coagulation cycle is conducted) its suitability for the production of the spherical alumina having the required structural and mechanical properties. Practical experience showed that it was rather difficult to establish a correlation between the properties of the aluminium hydroxide and the subsequent alumina.

Investigation of the hydroxides conducted by the X-ray method did not yield a direct result. The conditions of synthesis of a hydroxide mainly determined the packing of the primary particles, their dispersity, size distribution, and the degree of interlayer separation. However, we could not determine any consistently directed change in these parameters, nor their connection with the properties of the final alumina granules.

The research conducted on the aluminium hydroxide porous structures showed that, for specimen 1 as well as for specimen 5, synthesized under extremely different conditions, the coarse aggregates and macropores are char-

acteristic. For specimen 1 there is no relation between the hydroxide and oxide volumes of the pores, and their values in specimen 5 are close to each other. Hence the selection of hydroxides according to their porous structure is impossible.

In our search for a convenient aluminium hydroxide quality index, we paid attention to the value of its drying shrinkage. This index is widely used to characterize the final products, the properties of which vary with time or during heat treatment. Shrinkage can have a negative influence (e.g. leading to formation of cracks in granules) or a positive one (decreasing the total volume of pores, i.e. increasing the density).

In order to determine the shrinkage, φ (%), an initial aluminium hydroxide was shaped spherically, and the diameter was measured before (d_0) and after d_F) drying:

$$\varphi = \frac{(d_0 - d_F)}{d_0} \times 100\%$$

Fig. 3 shows the dependence of the strength S, volume of pores V_p, and bulk density of Δ of alumina granules on the value of the initial hydroxide shrinkage.

Using this correlation, one can evaluate the possible values of the texture and mechanical indices of the alumina granules in terms of the potential shrinkage of the aluminium hydroxide during drying.

It is known that the humidity of the material influences its shrinkage value, which could distort the correlation given in Fig. 3. However, the values of the

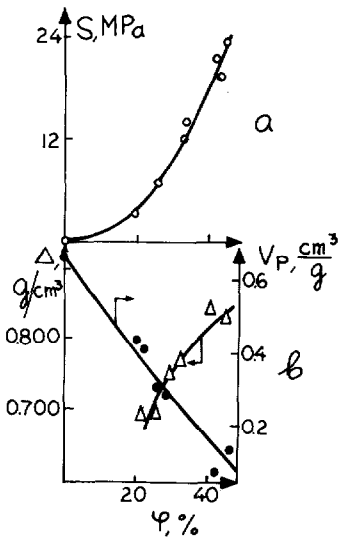

Fig. 3. Dependence of the alumina granule strengths, S (MPa), pore volume, V_p (cm^3/g), and bulk density, Δ (g/cm^3), on the value of initial hydroxide shrinkage, φ.

total humidity, which are all close to each other, are characteristic of the gel-like aluminium hydroxides investigated. Besides this, the method of hydrocarbon–ammonia moulding demands the following humidity values for the forming hydroxides: ΣW must be in the region of 0.70–0.85 g/g. This is connected with the rheological properties of the mass produced during peptization. The drier hydroxides do not display any liquid-flow properties when they are treated with acid. The use of wetter hydroxides leads to deformation of the granules.

However, in our case the most significant thing is that shrinkage depends on the real degree of aggregation of the aluminium hydroxide (i.e. its morphology and the type of contacts between the particles). The small-sized aggregates, as well as those of large sizes which are porous with coagulation contacts, are distorted and packed during drying. Removal of water from between the aggregates, together with ion-solvent sheath moisture, lead to closer positioning of the particles. In this case shrinkage of a hydroxide is significant. As opposed to this, the coarse, close aggregates with phase contacts are not destroyed upon drying and do not form a compact texture. In this case, shrinkage is insufficient.

From this a direct connection between the potential shrinkage of aluminium hydroxide during drying and its ability to be peptized under the influence of a small quantity of acid may be observed.

SUMMARY

It has been shown in this work that, depending on the conditions of preparation, pseudoboehmite aluminium hydroxides can consist of aggregates with coagulation or phase type contact between the primary particles. In the first case, hydroxides are completely disaggregated by acid, which allows the production of very strong, homogeneously porous granules of alumina. Precipitates with phase contacts are not disaggregated by acid treatment, which leads to the production of macroporous, low-strength alumina granules.

It has been determined that the shrinkage of aluminium hydroxide on drying is a total criterion which takes account of the moisture and structural characteristics of the aluminium hydroxides. It is appropriate to use this quality index for an initial substance in order to forecast the structural and mechanical characteristics of the spherical alumina prepared by the hydrocarbon–ammonia moulding method.

ACKNOWLEDGEMENTS

The authors are grateful to E.M. Moroz and V.I. Zaikovskii for carrying out the X-ray and microscopic investigations.

REFERENCES

1 V.A. Dzisko, A.P. Karnaukhov and D.V. Tarasova, Physical and Chemical Base of the Oxide Catalyst Synthesis, Novosibirsk, 1987.
2 D.L. Trimm and A. Stanislaus, Appl. Catal., 21 (1986) 215.
3 K.P. Coolboy and H.L. Fleming, Chem. Eng. Prog., 80 (1984) 63.
4 G.S. John, Spheroidal Platinum-Group Catalysts Production, U.S. Patent 2805206.
5 Ya.R. Katsobashvili and N.S. Kurkova, Zh. Prikl. Khim., 39 (1966) 2424.
6 A. Olechowska, I. Berak and M. Popowich, Prsem. Chem., 52 (1973) 439.
7 M.N. Shepeleva, V.B. Fenelonov, R.A. Shkrabina and Z.R. Ismagilov, Kinet. Katal. 27 (1986) 1202.
8 M.N. Shepeleva, R.A. Shkrabina, L.G. Okkel and Z.R. Ismagilov, Kinet. Katal., 29 (1988) 195.
9 P.A. Rebinder, Physical and Chemical Mechanics of Dispersed Structures, Moscow, p. 3, 1966.
10 S.J. Gregg and K.S.W. Sing, Adsorption, Surface Area and Porosity, Academic Press, London, 1983.

Applied Catalysis, 78 (1991) 175–184
Elsevier Science Publishers B.V., Amsterdam

Production of spherical granules of alumina with controlled porous structure

M.N. Shepeleva*, R.A. Shkrabina, V.B. Fenelonov and Z.R. Ismagilov

Institute of Catalysis, Siberian Branch of the USSR Academy of Sciences, Prosp. Akad. Lavrentieva 5, Novosibirsk 630090, (USSR), fax. (+7-383)2355756 or (+7-383)2350259

(Received 20 October 1990, revised manuscript received 18 May 1991)

Abstract

Structural changes of aluminium hydroxides at main technological stages are studied to produce spherical alumina with a given volume of pores. Two hydroxides essentially different in morphology, particle size and type of bond between primary particles have been synthesized. A collected of alumina with varied volumes of pores and effective radii has been obtained using a mixture of hydroxides of both types. We show how to calculate the volumes of meso- and macropores as well as the specific surface area of alumina and its precursors on the basis of the characteristics of each hydroxide and their ratio in the mixture.

Keywords: aluminium hydroxide, granulated alumina, mechanical strength, porous structure, pseudoboehmite, spherical particles, textural characteristics.

INTRODUCTION

Porous granules of alumina are widely used as carriers, catalysts and adsorbents [1–3]. It is known that for each technological process it is necessary to use granules with textural characteristics which are optimal for exploitation. A great deal of the literature is devoted to the investigation of the influence of the initial products properties and reprocessing conditions on the final alumina characteristics [4–5]. However, the production of alumina granules with the correct porous structure required for a given process has been a complex problem so far and has been largely solved by using empirical sampling.

In this paper a method is shown for calculating the parameters of alumina porous structure using the characteristics of initial hydroxide. The peculiarities of spherical alumina production with a diameter of 1–3 mm are investigated. Such granules can be used both in the stationary and in the fluidized bed, the latter being especially actual for the current modern intensive chemical production industry.

Granules of spherical shape can be produced by mechanical (pouring, dispersive drying, etc.) and coagulation–chemical methods (moulding in oil, in

coagulant, etc.). The first group of these methods is relatively simple from the point of view of textural changes of product during its manufacture: aluminium hydroxide texture is retained in the moist or dry granules and then undergoes some changes during thermal processing at temperatures of 500–700 °C in the process of γ-alumina preparation. Therefore one can obtain γ-alumina with the required characteristics only by the use of an appropriate hydroxide. However, variations in hydroxide synthesis are rather limited and this is the reason why a wide series of alumina cannot be obtained by such means.

In the methods based on chemical influence a change in structure of aluminium hydroxide occurs at each technological stage. This, on the one hand, enables us to produce alumina with different proportions of micro-, meso- and macropores, but, on the other hand, makes the prediction of the final product properties difficult.

For the production of alumina with substantially variable structural characteristics it was necessary to investigate the textural changes of hydroxides at the main technological stages and to mix two (or more) hydroxides in the required proportion.

EXPERIMENTAL

Aluminium hydroxide with a pseudoboehmite structure was chosen as the object of the investigation. The aluminium hydroxide was prepared from a solution of sodium aluminate which was treated with nitric acid under conditions which enabled the production of precipitates with different morphology [6]. Sample 1 was precipitated at 291 K and pH 8.5; sample 2 was precipitated at the same pH and 393 K. The remaining samples were produced by mixing samples 1 and 2. Spherical granules of alumina were obtained by the hydrocarbon–ammonia method of moulding. The method consists of (i) the conversion of aluminium hydroxide into the fluid mass (sol) during treatment with nitric acid (plastification stage); (ii) transformation of the mass into spheres in the hydrocarbon layer and the hardening of granules in the coagulant (moulding stage); and (iii) the thermal processing giving γ-alumina [7–8].

Electron-microscopy studies were carried out with the help of a JEM-100-CX microscope. True density ρ was measured by helium with an autopycnometer-3200 instrument. The porous structure and specific surface area A were investigated by the analysis of nitrogen adsorption isotherms measured at 77.5 K on an automatic adsorption unit Digisorb-2600 (distribution of pores volume on the radii up to 100 nm). The effective necks radii in the range 4–10 nm were studied by the mercury intrusion porosimetry method with a Porosizer-2300. To obtain comparable data in the analysis we used a desorption branch of the capillary condensational hysterisis area. Porosity of particle packing ϵ was calculated by the formula:

$$\epsilon = V_\Sigma \rho / (1 + V_\Sigma \rho). \quad (1)$$

The total volume of pores V_Σ was determined by the data sum of mercury porosimetry (V_p) and from the nitrogen adsorption isotherms ($V_r < 4$ nm). The mechanical strength of granules S was measured by pressing between two parallel plates.

RESULTS AND DISCUSSION

Investigation of the aluminium hydroxides produced by the physical–chemical methods showed their substantial differences. An hydroxide precipitated at 291 K (AH-1) has a humidity of 85 wt.-%. Its specific surface area after drying at 380 K is 370 m^2/g and its average size of primary particles is 3 nm. The hydroxide precipitated at 373 K (AH-2) has a lower water content — 59 wt.-%, its specific surface area is 140 m^2/g and the size of the primary particles is 15–17 nm.

According to the electron microscopy data (Fig. 1a) AH-1 contains agglomerates of random shape consisting of fibres and needles h ca. 4 nm wide and l ca. 20–40 nm, and spherical particles with a diameter of about 4 nm. AH-1 dried at 291 K contains a considerable quantity of thin pores which make a major contribution to the total volume of pores V_Σ. Two characteristic regions in the distribution of pores can be distinguished in the structure of the dried AH-1: the region of thin pores with a distribution maximum r_1 ca. 3 nm [calculated from the results of adsorption measurements (see Fig. 2)] and the region of macropores with an average size r_2 200 nm [mercury porosimetry data (see Fig. 3)]. The region of macropores (the electron microscopy data) corresponds to the space between large aggregates, and the region of thin pores corresponds to pores in the aggregates between the particles of small size.

Hydroxide 2 according to the electron microscopy data (Fig. 1b) consists primarily of large aggregates in the form of plates with sizes greater than 100 nm. The pore volume V_p of AH-2 is large (Fig. 4), the preferential pore radius being more than 100 nm. Edges of plates are formed by compact packed needles with a thickness up to 20 nm which, in their turn, consist of thin needles of ca. 4 nm in size. The maximum of the mesopores distribution corresponds to an r value of ca. 2.2 nm (Fig. 2). The porosity of the aggregates is $\epsilon = 0.4$ assuming that all the mesopores with $r < 100$ nm are within these aggregates' volume.

The treatment of AH-1 with acid (0.17 mole per mole alumina) leads to the production of plastificated mass PM-1 having a disordered structure consisting of needles and fibres about 3 nm thick (Fig. 1c). Structural characteristics change accordingly: macropores disappear, V_Σ sharply decreases (Fig. 3), the maximum of the distribution of thin pores shifts to 1.7 nm (Fig. 2). Low-molecular aluminium compounds formed during the acid treatment fill some part of the porous space in the dried PM-1 sample and as a result the measured

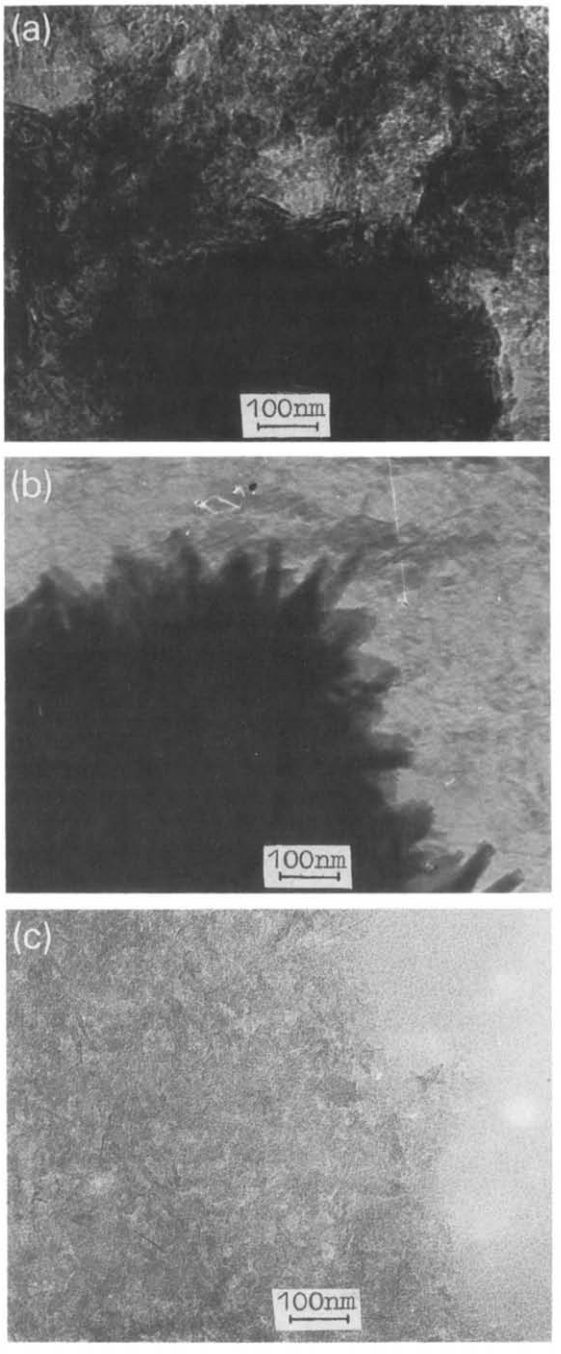

Fig. 1. Electron microscopic photographs of (a) AH-1, (b) AH-2 and (c) PM-1.

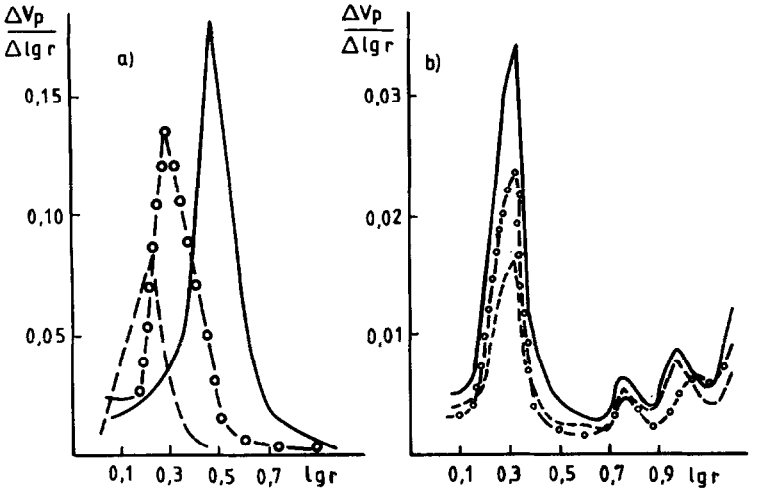

Fig. 2. Micropore volume distribution of (a) sample 1 and (b) sample 2. (——) AH; (---) PM; (-o-o) G.

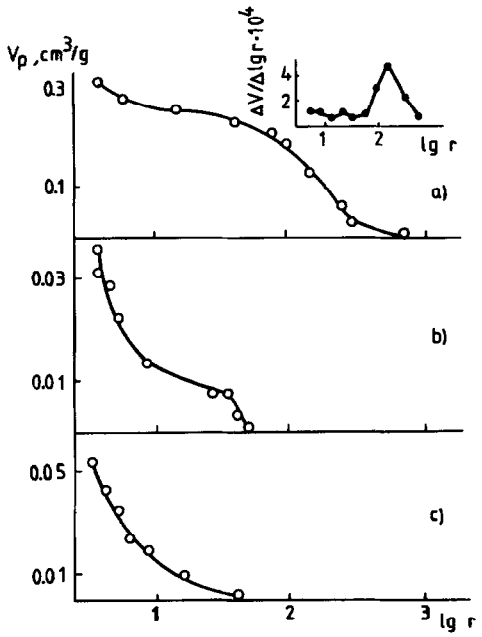

Fig. 3. Cumulative pore volume distribution of sample 1. (a) AH; (b) PM; (c) G. T=380 K.

porosity value ϵ is small and amounts to 0.26. This can also explain the decrease of A from 370 (AH-1) to 215 m^2/g (PM-1). Thus, acid treatment of AH-1 leads to an effective breakdown of original aggregates, primary particles

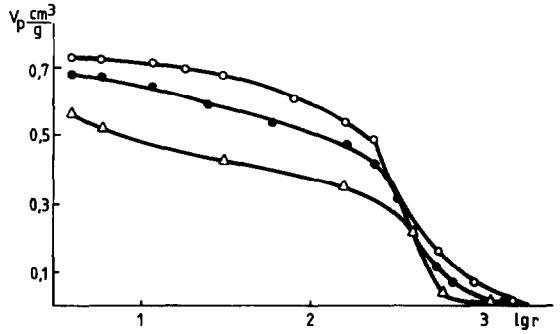

Fig. 4. Cumulative pore volume distribution of sample 2. (○) AH; (△) PM; (●) G.

which are bounded only by weak Van der Waals or electrostatic forces [9].

Hardening of the hydroxide granules (G-1) in the coagulant (NH_4OH solution) at the next technological stage is accompanied by compact packing of thin needles according to the data of electron microscopy. An increase in the strength of the "skeleton" of the formed system consisting of stiffly fixed needles leads to some growth of V_p (Fig. 3), and an increase in porosity up to 0.45, and a shift in the maximum of the mesopores radii distribution to 2 nm (Fig. 2).

But macropores do not appear in G-1. From the comparison of the structural–mechanical characteristics of AH-1 and G-1 samples it can be seen that the chemical treatment necessary for the preparation of granules, removes macropores. In this case the changes in distribution of the thinner pores volume is negligible. When G-1 is calcined producing γ-alumina textural characteristics change slightly.

Treatment of AH-2 reveal a different picture. Acid treatment with intensive mixing does not allow us to produce the mass that is suitable for moulding even when the acid concentration is increased to 0.3–0.5 g mol/g mol alumina. The electron microscopy data show that no dispersion of aggregates occur in this case and only diffusion of boundaries appears.

After PM is kept in coagulant and dried it transforms into powder. All the samples of the AH–PM–G series have a similar structure of heterogeneous porosity with a characteristic distribution maxima for the volume of mesopores with r ca. 2.2 nm (Fig. 2) and a large volume of macropores. The porosity of the aggregates during treatment by acid and ammonia lies within the range of $\epsilon = 0.4–0.5$. In this case the location of the distribution maxima and the relative volume of pores having different sizes change very little. Distribution analyses, calculated over adsorption branches of capillary–condensational hysteresis of the adsorption isotherms gave the following results: the volume of pores with necks up to 4 nm constitutes 10–13%; the volume of pores in the range 4–30 nm is 15–17%; in the range 30–100 nm, 9–10%; and in the range greater than 100 nm, 62–64% of V_Σ. Samples AH-2 and G-2 have the most similar structural

characteristics. Some decrease in the total volume of pores (Fig. 2) and A of the PM-2 sample (from 140 m^2/g in AH-2 up to 110 m^2/g in PM-2) can be explained by the formation of soluble aluminium compounds and by their precipitation on the peripheral parts of aggregates during drying.

These results allow us to assume that such aggregates practically do not disperse under the given conditions in spite of a rather well-developed inner surface and porosity. Such stability is due to the presence of chemical bonds between the primary particles in the aggregates of the initial AH-2 [9]. The calcination of G-1 granules and G-2 powder leads to the production of alumina whose characteristics are given in Table 1.

Using a mixture of aluminium hydroxides with very different textural characteristics is one of the means by which we can obtain a wide range of granulated alumina.

Let us analyze the peculiarities of the AH-1 and AH-2 mutual locations during their mixing and their influence on the porous structure of the final alumina granules. The low reactivity of AH-2 allows us to assume that the mesoporous structure of the mixed samples is proportional to the volume of mesopores in samples 1 and 2. In this case the volume of mesopores in a given size range can be determined by the following relation:

$$V_i = V_1X + V_2(1-X), \tag{2}$$

where V_1 and V_2 are the volumes of mesopores in the AH–PM–G series of the samples 1 and 2 correspondingly, cm^3/g; and X is the part of AH-1 in the mixture, g/g. The specific surface area of the samples can be similarly estimated:

$$A_i = A_1X + A_2(1-X), \tag{3}$$

where A_1 and A_2 are the specific surfaces areas of samples 1 and 2 in the series AH–PM–G correspondingly, m^2/g.

The results of the calculations of A_i and the volumes of mesopores V_i for sample 3 at $X=0.55$ and sample 4 at $X=0.29$ are compared with experimental data in Table 2. It can be seen that the values calculated and obtained from

TABLE 1

Characteristics of the spherical Al_2O_3 produced from AH-1 and AH-2

Al_2O_3 characteristics	AH-1	AH-2
1. Bulk density, g/cm^3	0.84	–
2. Specific surface area, m^2/g	320	240
3. V_p, cm^3/g	0.04	0.88
4. V (r=10–100 nm), cm^3/g	0.01	0.14
5. V (r>100 nm), cm^3/g	0	0.70
6. Strength, MPa	22	0

TABLE 2

Calculated and experimental characteristics of AH, PM and G samples from the aluminium hydroxide mixture

Sample No.	X (g/g)	Series		A (m^2/g)	Volume of pores (cm^3/g) with a radius (nm)			V_Σ (cm^3/g)
					<4	4-100	>100	
3	0.55	AH	calc.	260	0.24	0.10	–	0.38
			exp.	250	0.27	0.14	–	0.46
		PM	calc.	170	0.10	0.07	–	0.17
			exp.	280	0.24	0.09	–	0.33
		G	calc.	250	0.20	0.10	–	0.30
			exp.	270	0.20	0.10	–	0.30
4	0.29	AH	calc.	210	0.18	0.19	0.21	0.58
			exp.	200	0.18	0.16	0.15	0.49
		PM	calc.	140	0.09	0.07	0.09	0.29
			exp.	220	0.17	0.10	0.11	0.38
		G	calc.	190	0.14	0.10	0.15	0.44
			exp.	210	0.16	0.08	0.12	0.44

measurements of samples of AH and G are rather similar in pore area with sizes up to 100 nm. The absence of additivity for the samples of PM-type is probably due to the injection of different amounts of acid into AH-1 and 2. In the area of macropores there is no additivity either which is explained by the location of some highly dispersive phase 1 in the space between the aggregates of phase 2. For the samples of series 4 the calculated volume of macropores is almost three times larger than the measured volume (these data are not included in Table 2).

To complete the analysis of the location of hydroxides 1 and 2 we have introduced a structural model of samples produced by mixing them in their simplest form: roughly dispersed AH-2 aggregates form a frame, in the macropores of which highly dispersive AH-1 is located. Let us assume that the aggregate packing at each phase does not depend on the presence of the other phase. According to this condition the volume of macropores formed in the unit of mass of the mixed aluminium hydroxide, without taking into consideration phase 1, is equal to

$$V'_{ma} = V_2(1-X), \tag{4}$$

where V_2 is the volume of macropores for sample 2 in the series AH–PM–G. The volume occupied by highly-dispersive phase 1 is equal to

$$V_{hd} = \left(V_1 + \frac{1}{\rho_1}\right)X \tag{5}$$

where ρ_1 is true density of sample 1, g/cm^3. Then the calculated volume of macropores $V_{ma}^{calc.}$ is equal to

$$V_{ma}^{calc.} = V'_{ma} + V_{hd}. \quad (6)$$

As can be seen from Table 2 the calculated volume values of macropores for the series of sample 4 are rather similar to the experimental values but exceed them, on the average by 20%. The observed minor differences can be associated with the inadequacy of the model which has been used for the calculations: actually, the phases influence each other; in this case phase 1, being more finely dispersed, can contribute to the increase in the packing density and to the growth of particle sizes in phase 2. In the samples of series 3 the absence of macropores is shown both by experimental data and theoretical calculations.

In order to test the obtained regularities the precipitates with X from 0.15 to 0.85 has been produced by mixing samples 1 and 2.

The experimentally measured volume of macropores at $X < 0.5$ was found to be somewhat larger than the calculated volume in all the cases. This indicates a decrease in the packing density of aggregates of the roughly dispersed phase in the presence of the highly dispersed phase. However, experimental data are satisfactorily described by the above simple model as well. At $X > 0.5$ macropores are absent in the samples according to both experimental data and theoretical calculations.

As is shown in Table 3, the synthesis of aluminium hydroxide by mixing of precipitates allows us to obtain wide porous granules with an effective radius (r_{ef}) = 200–500 nm with a low bulk density of alumina (sample 5), very fine porous and compact granules the major volume of pores in which is not determined by mercury porosimetry (i.e., $r \ll 4$ nm), (sample 9) as well as oxides with poly- and bidispersive distribution of pores (samples 6–8).

Eqns. (2–6) make it possible to predict textural characteristics not only of

TABLE 3

Characteristics of Al_2O_3 granules produced from the mixed aluminium hydroxides

Sample No.	X (g/g)	Bulk density (g/cm^3)	A (m^2/g)	V_p (cm^3/g)	$V(r, \text{nm})$, cm^3/g					S (MPa)
					<10		10–100	>100		
					Exp.	Calc.	Calc.	Exp.	Calc.	
5	0.15	0.44	240	0.87	0.08	0.19	0.12	0.60	0.59	2.3
6	0.22	0.48	250	0.63	0.12	0.10	0.11	0.41	0.47	4.1
7	0.38	0.54	290	0.54	0.18	0.10	0.09	0.26	0.31	8.3
8	0.65	0.63	300	0.25	0.20	0.04	0.05	0	0.02	13.2
9	0.85	0.82	310	0.019	0.015	0.003	0.02	0	0	22.4

the mixed hydroxides and semiproducts but also of the final alumina granules. Agreement between calculated and experimental results is sufficiently good.

Thus, the degree of disaggregation of the mixed aluminium hydroxides affected by the acid at the plastification stage depends on the quantity of easily dispersive hydroxide.

Structural–mechanical properties of alumina granules, produced from such hydroxides are determined by the texture of the original precipitates and from their proportion in the mixture.

Injection of the AH-1-precipitate with $0.2 < X < 0.5$ ($V_{hd}/V'_{ma} < 1$) leads to the formation of alumina granules with a wide collection of pores. At $X < 0.2$ the main volume is occupied by macropores. The mechanical strength value of such granules decreases proportionally to the growth of V'_{ma}. The excessive highly-dispersive precipitate at $X > 0.5$ ($V_{hd}/V'_{ma} > 1$) gradually fills the space between the aggregates which leads to the disappearance of macropores. At $X > 0.8$ the characteristics of alumina granules from AH-1 and mixed hydroxides practically coincide and the mechanical strength abruptly increases.

Thus, by varying the structural characteristics of the final product according to a given method, it is possible to produce carriers and adsorbents for a wide range of processes, and the high values of the mechanical properties of the granules (samples 6 and 9) make it possible for us to use them in the moving or fluidized bed.

REFERENCES

1 D.L. Trimm and A. Stanislaus, Appl. Catal., 21 (1986) 215.
2 K.P. Coolboy and H.L. Fleming, Chem. Eng. Prog., Symp. Ser., 80 (1984) 63.
3 F. Dirksen, Chemsa, 9 (1983) 122.
4 V.A. Dzisko, A.P. Karnaukhov and D.V. Tarasova, Physical-Chemical Basis of Oxide Catalysts Synthesis, Nauka, Novosibirsk, 1978, p. 384 (in Russ.).
5 Ya.P. Katsobashvili, N.S. Kurkova, W.S. Lichobabenko and E.A. Levitskij, Izv. Akad. Nauk SSSR, Otd. Khim. Nauk, 1 (1961) 245.
6 M.N. Shepeleva, V.B. Fenelonov, R.A. Shkrabina and E.M. Moroz, Kinet. Katal., 27 (1986) 1202.
7 US Patent 2 805 206 (1953).
8 Ya.P. Katsobashvili, N.S. Kurkova and E.A. Levitskii, Khim. Prom., 1 (1962) 26.
9 Z.R. Ismagilov, M.N. Shepeleva, R.A. Shkrabina and V.B. Fenelonov, Appl. Catal., 69 (1991) 65.

УДК 541.128.13 : 541.128.35 : 546.623 : 541.18.02 : 539.4.01

М. Н. ШЕПЕЛЕВА, З. Р. ИСМАГИЛОВ, Р. А. ШКРАБИНА, И. А. ОВСЯННИКОВА

ИССЛЕДОВАНИЕ КАТАЛИЗАТОРОВ И РЕАКЦИЙ КАТАЛИТИЧЕСКОГО СЖИГАНИЯ

X. ОСОБЕННОСТИ СОЗДАНИЯ ПРОЧНЫХ НОСИТЕЛЕЙ ДЛЯ КАТАЛИЗАТОРОВ КИПЯЩЕГО СЛОЯ С ПРИМЕНЕНИЕМ ЖИДКОСТНОГО ФОРМОВАНИЯ

Исследованы прочностные характеристики гранул Al_2O_3, полученных методом жидкостного формования из гидроксидов алюминия с различной способностью пептизироваться. Показаны пути повышения прочности гранул, сокращения разброса механических показателей. Оценены максимально возможные значения прочности реальных дефектных структур.

Внедрение в промышленность процессов с использованием кипящего слоя тормозится из-за отсутствия катализаторов и носителей, способных выдержать одновременное действие химических, механических и гидродинамических нагрузок. Один из путей увеличения надежности носителей и катализаторов — применение изначально высокопрочных гранул.

Для характеристики прочности, как правило, используют усредненный по выборке показатель. Между тем для реальной структуры твердого тела характерно наличие дефектов, количество которых в пористых системах существенно выше, чем в монокристалле [1]. Очевидно, что срок годности образца будет определяться количеством гранул с прочностью ниже средней, содержащих наибольшее число дефектов. Кроме того, интерес представляют гранулы с прочностью выше средней.

Как показано в [2], прочность гранул может изменяться в зависимости от условий получения пористых тел, свойств материала частиц, образующих структуру, а также от одновременного действия различных факторов. Например, по данным [3], при одинаковых условиях формирования структуры разброс величины прочности единичного контакта может достигать шести порядков вследствие геометрической и энергетической неоднородности поверхности взаимодействующих частиц.

Цель работы — изучение возможности получения прочных гранул Al_2O_3 с достаточно узким разбросом механических показателей, пригодных для эксплуатации в качестве носителей катализаторов для каталитических генераторов тепла (КГТ), а также поиск путей снижения количества малопрочных гранул. Данная работа является продолжением исследований, начатых в [4].

МЕТОДИКА ЭКСПЕРИМЕНТА

Оксид алюминия формовали в сферические гранулы жидкостным методом. Метод основан на последовательно проводимых обработках гидроксида алюминия пептизатором и коагулянтом. Операции при приготовлении гранул и методы определения характеристик Al_2O_3 описаны в [4]. При определении прочности на раздавливание для выборки из 30 шт. рассчитывали среднее значение $P_{ср}$, а также минимальное P_{min} из пяти наименьших значений и аналогично максимальное P_{max} значение.

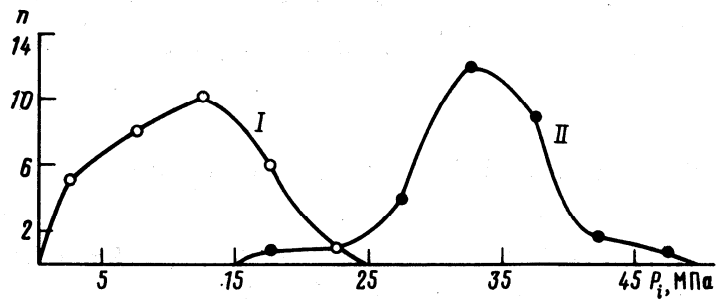

Рис. 1. Гистограммы значений прочности P_i образцов I и II (n – число гранул с указанным интервалом значений P_i)

Использовали гидроксид алюминия псевдобемитной структуры с влажностью 78 мас.% и размером первичных частиц 8—10 нм (ГА-I). Получаемые из таких гидроксидов гранулы Al_2O_3 обладают $P_{ср} \leqslant 12$ МПа [5]. С целью повышения прочности конечного продукта мехобработкой ГА-I был получен гидроксид ГА-II.

РЕЗУЛЬТАТЫ И ИХ ОБСУЖДЕНИЕ

Структурно-механические характеристики гранул Al_2O_3, полученных формованием ГА-I (образец 1) и ГА-II (образец 2), представлены в табл. 1.

На рис. 1 приведены гистограммы образцов 1 и 2. Дисперсия значений прочности σ (в предположении нормального закона распределения) составляет 5,3 и 6,1 соответственно.

В [6] для различных партий промышленных и опытных образцов оксида алюминия, алюмосиликатов, цеолитов и других катализаторов приведены значения $\sigma/P_{ср}$, достигающие 50%. Наилучшими в [6] считаются образцы с $\sigma/P_{ср}$=20—30%. В данной работе для образца 1 получены значения $\sigma/P_{ср}$=49%, для образца 2 $\sigma/P_{ср}$=18%, т. е. условия приготовления последнего обеспечивают получение гранул с высокими и стабильными результатами.

Исследование большого числа образцов сферического Al_2O_3 показало, что в зависимости от условий приготовления возможны различные сочетания числа низко- и высокопрочных гранул в выборке при достаточно близком значении $P_{ср}$. Кривые распределения гранул по прочности могут существенно отличаться от приведенных на рис. 1, возможны также значительные отклонения от нормального распределения. Очевидно, что износ при эксплуатации в кипящем слое в таких образцах будет различаться, несмотря на примерно одинаковые $P_{ср}$.

Гистограммы образцов 1 и 2 перекрываются только в узкой области $15<P_i<25$. Это свидетельствует о том, что из гидроксидов алюминия, подобных по свойствам ГА-I, в принципе, невозможно приготовить гранулы γ-Al_2O_3 с $P_i>25$ МПа (так же как из ГА-II получается незначительное число гранул с $P_i \approx 50$ МПа). Однако из различий прочности образцов 1, 2 можно сделать вывод о возможности повышения прочности гранул Al_2O_3, если воздействие производится не на уровне изменения условий технологического режима, а на уровне существенного изменения свойств исходного гидроксида алюминия или путем введения дополнительных технологических стадий.

Таблица 1

Характеристики сферических гранул Al_2O_3

Образец	Насыпная плотность, г/см³	S, м²/г	$V_{пор}$, см³/г	$P_{ср}$, МПа	P_{min}, МПа	P_{max}, МПа
1	0,69	260	0,45	11	3	19
2	0,80	210	0,28	33	24	42

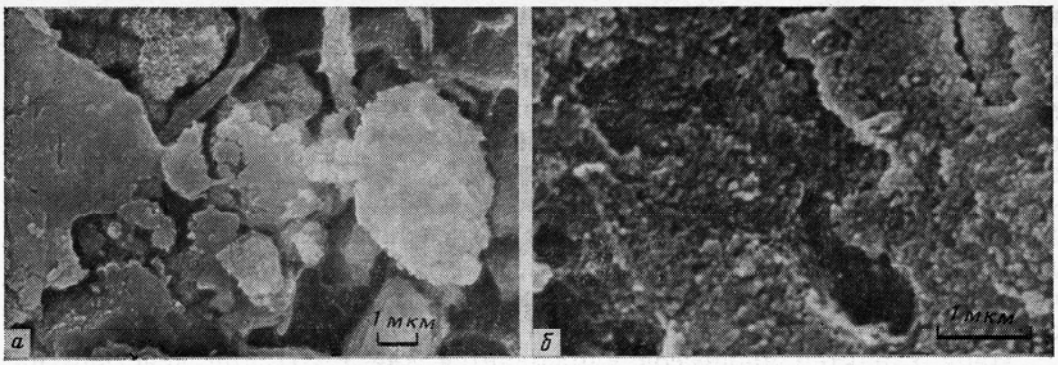

Рис. 2. Электронные микрофотографии: *а* – образец 1 (×6000); *б* – образец 2 (×15 000)

Поскольку прочность гранул связана с плотностью упаковки частиц в них, то для решения поставленных задач было изучено изменение размеров и морфологического строения агрегатов ГА-I и ГА-II на основных этапах получения гранул Al_2O_3.

В [5] показано, что условием получения достаточно прочных гранул Al_2O_3 жидкостным методом является глубокая дезагрегация вторичных частиц гидроксида алюминия под действием пептизатора и последующее уплотнение структуры в результате воздействия коагулянта. Необходимая для получения прочных и плотных структур глубина процессов дезагрегации — реагрегации возможна, если частицы в исходном гидроксиде связаны преимущественно ван-дер-ваальсовыми силами (коагуляционный характер контактов между частицами). Для ГА-I характерна малая степень диспергируемости при кислотной обработке [5]. Это связано с преимущественно фазово-кристаллизационным контактным взаимодействием первичных частиц, образовавшихся при синтезе гидроксида. Условия синтеза такого гидроксида не исключают образования определенного количества коагуляционных контактов между частицами. Поскольку в подобных контактах частицы разделены прослойкой дисперсионной среды, то путем различных воздействий можно варьировать их прочность.

По данным электронной микроскопии ГА-I состоит из плотных агрегатов, по краям которых различимы иглы шириной h=5—10 нм и длиной $l \approx 50$ нм. Обработка ГА-I кислотой на стадии пептизации приводит к распаду некоторых агрегатов на частицы коллоидных размеров ($\leqslant$100 нм). Изменения формы и размеров оставшихся агрегатов не наблюдается. Система остается полидисперсной, как и в исходном состоянии. На стадии твердения уже сформованной гранулы при действии коагулянта (раствора аммиака) частицы и агрегаты закрепляются в пространственной сетке. Сушка и прокаливание практически не изменяют размеры частиц при переходе от ГА-I к оксиду. Чередование разнообразных по форме и размеру частиц (от 0,1 до 10 мкм) с крупными порами наблюдается как на внутреннем срезе гранулы (рис. 2, *а*), так и на внешней поверхности. Естественно предположить, что хаотическое распределение в объеме гранулы агрегатов различного размера образует структуру, не соответствующую плотной случайной упаковке частиц. Проведенные в соответствии с [7] расчеты показали, что плотность свободной упаковки частиц в сухих гранулах ГА-I $\varepsilon^{I}_{ГА}$=0,45, в то время как наибольшая плотность случайной упаковки подобной полидисперсной системы приблизительно оценивается равной $\varepsilon^{I}_{п.с.у.}$=0,35. Прокаливание гранул ГА-I незначительно влияет на размер частиц, усадка при этом невелика (2—5%), плотность упаковки частиц $\varepsilon^{I}_{Al_2O_3}$=0,58. Эти данные позволяют сделать вывод о том, что главной причиной низ-

кой прочности образца 1 является невозможность создания малопористой системы вследствие неоднородности размеров агрегатов, образующих гранулу, и произвольного размещения в ее объеме. Вероятность попадания агрегата определенного размера в данную гранулу имеет статистический характер, в связи с чем возможны большие отклонения значений прочности каждой гранулы от $P_{ср}$.

По-видимому, для плохо диспергирующихся систем, подобных ГА-I, диапазон разброса прочности может быть сокращен только до определенной величины. По нашим данным, для лучших образцов Al_2O_3, полученных с соблюдением всех требуемых условий приготовления, $\sigma/P_{ср}$ составляет ~40%.

Иной характер процессов наблюдается для ГА-II при действии на него пептизатора и коагулянта. Если исходный ГА-II состоит из агрегатов размером до 1000 нм, образованных иглами с h=5 нм и l=50—100 нм, то пептизированный ГА-II представляет бесструктурную массу из тонких игл и отдельных частиц, по форме близких к сферическим. Коагулированный ГА-II образован мелкими агрегатами из упакованных в пачки игл, при этом $\varepsilon^{II}_{ГА}$=0,32. Плотность случайной упаковки системы частиц с формой, близкой к сферической (при факторе формы $\Phi \approx 1$ по [7]) $\varepsilon^{II}_{п.с.у.}$ составляет ~0,25. Гранулы Al_2O_3, обладающие мелкозернистой структурой, имеют $\varepsilon^{II}_{Al_2O_3}$=0,46 и большую прочность — результат увеличения числа контактов в единице объема и их упрочнения при термообработке с переходом от коагуляционного типа в кристаллизационный.

Наблюдения показали, что практически все гранулы образца 2 на внутреннем срезе содержат поры достаточно крупных (до 1 мкм) размеров (рис. 2, *б*). По всей видимости, одной из основных причин их образования является поэтапное прохождение процесса коагуляции пептизированной массы: первоначально быстро при контакте периферийной части гранулы с раствором аммиака, далее с торможением, вызванным диффузией коагулянта в глубь гранулы. Подтверждением служит тот факт, что прочность гранул с диаметром 1,5—2,0 мм, как правило, больше прочности гранул диаметром 2,0—3,0 мм в 1,2—1,5 раз. Кроме того, внешняя поверхность высокопрочной гранулы, на которой коагуляция прошла мгновенно, макродефектов не содержит.

Любые отклонения от оптимальных условий приготовления будут особенно отражаться на гранулах Al_2O_3 с $P_{ср}$>20 МПа. При этом под «оптимальными» понимаются усредненные условия с некоторым колебанием параметров, имеющим место при реальном проведении процесса получения гранул. Отклонения в более «мягкую» сторону обусловят появление гранул с P_i>$P_{ср}$, количество и размер дефектов в которых минимальны; и, наоборот, незначительные изменения в форме и размере гранул, скорости их прохождения в коагулянте, температуры сушки и т. п. могут существенно снизить P_i. Эффект «чуткого реагирования» особопрочных материалов на незначительные изменения внешних условий описан в [8]. В связи с этим разброс значений прочности в высокопрочных образцах так же сложно снизить, как и в низкопрочных, хотя причины их появления различны.

В рамках проводимых исследований представлялось необходимым оценить максимально возможную прочность образцов, получаемых из ГА с различными свойствами. При этом в отличие от других исследователей мы не сопоставляли реальную P_i с прочностью идеального монокристалла данного химического состава или бездефектного поликристалла. Например, расчет по формулам, предложенным в [9], дает прочность гранул Al_2O_3, полученных из ГА-II, в пределах $(1—3)10^4$ МПа. Такие прочности для реальных дефектных структур недостижимы и на практике не требуются. Однако оценка возможности упрочнения гранул путем синтеза оптимальной дисперсной структуры, минимизации внут-

Таблица 2

Экспериментальные и стандартные значения коэффициента фрагментарности для образцов 1 ($P_{ср}$ и $P_{ср}'$=11 и 21 МПа) и 2 ($P_{ср}$ и $P_{ср}'$=33 и 34 МПа)

P_i, МПа	$B_i^{эксп}$	$B_{ст}$	P', МПа	P_i, МПа	$B_i^{эксп}$	$B_{ст}$	P', МПа
Образец 1				Образец 2			
3,7	4,15	≫5	12,0	24,8	2,25	2,10	24,0
8,0	2,18	>5	24,0	33,8	1,43	1,40	34,0
15,8	1,64	3,20	31,0	43,1	1,10	1,10	45,0

ренних напряжений, создания прочных кристаллизационных контактов между частицами и агрегатами позволяет определить достигнутый уровень разрешения этой задачи и наметить пути совершенствования технологии.

С этой целью с помощью рентгеноспектрального микроанализа были определены параметры фрагментарности $B_i^{эксп}$ и проведено их сравнение со стандартным параметром $B_{ст}$. Расчет $B_i^{эксп}$ и стандартная кривая $B_{ст} - P_{ст}$ приведены в [4, 10]. Ранее было показано, что параметр фрагментарности характеризует разупорядоченность упаковки агрегатов в грануле и макродефекты в структуре. Профили интенсивности характеристического $K_{\alpha Al}$ записаны от осколков гранул, полученных после определения их P_i.

Из табл. 2 видно, что для низкопрочного образца 1 значения $B_i^{эксп}$ существенно меньше значений $B_{ст}$, соответствующего данной P_i. При этом разброс $B_i^{эксп}$ достаточно велик. В соответствии с представлениями, развитыми в [4], это свидетельствует о том, что прочность материала фрагментов существенно выше прочности гранулы в целом. При отсутствии в гранулах большого количества дефектов (супермакропор) их прочность приближалась бы к значениям, определенным по кривой $B_{ст} - P_{ст}$ при соответствующем $B_i^{эксп}$. Определенные этим методом значения «теоретически возможной» прочности (P') приведены в табл. 2. Для образца 1 $P' \gg P_i$, в то время как для высокопрочного образца 2 $P_i \approx P'$. Следует отметить, что для образца 2 разброс $B_i^{эксп}$ невелик, в то время как значения P_i различаются почти в 2 раза. Это является дополнительным подтверждением сильного изменения механических показателей высокопрочных материалов при появлении незначительной разупорядоченности в структуре. Данные табл. 2 свидетельствуют о том, что дефектность гранул образца 1 снижает среднее значение прочности всей партии с возможного $P'_{ср}$=21 МПа до реального $P_{ср}$=12 МПа. В то же время для высокопрочного образца 2 $P_{ср} \approx P_{ср}'$. Следовательно, материал фрагментов образца 1 может обеспечить более высокую прочность гранул при снижении количества и размеров дефектов. Пути залечивания макродефектов известны — применение наполнителей, клеев, сжатие гранулы при формовании и др. По-видимому, при использовании плохо пептизирующихся гидроксидов алюминия типа ГА-I для повышения прочности гранул необходимо использовать дополнительные технологические приемы, которые дадут возможность, кроме того, снизить разброс механических показателей.

Для образца 2 эти пути неприемлемы: введение дополнительных веществ или обволакивающих оболочек в тонкопористых образцах (эффективный радиус пор <10 нм) приводит к росту размеров пор, а также к образованию непрочных поверхностных слоев. Поскольку из ГА-II возможно получение отдельных гранул с P_{max}=40—50 МПа, то реальными способами увеличения P_{min} и $P_{ср}$ является создание достаточно одинаковых для всех гранул и максимально приближенных к оптимальным условий приготовления. Известным способом удаления дефектов структуры является высокотемпературное прокаливание. Эксперимен-

тально установлено снижение разброса прочности при получении α-Al_2O_3 из образца с $P_{ср}>20$ МПа. Прокаливание при 1500—1600 К низкопрочного образца разброс P_i практически не изменяет.

Таким образом, создание носителей и катализаторов, способных не разрушаться под воздействием химических, термических и динамических нагрузок, возникающих в аппаратах с кипящим слоем, должно идти по пути поиска условий приготовления высокопрочных гранул, а также снижения количества низкопрочных гранул в образце. Отклонение значений прочности от среднего — результат дефектности получаемой структуры.

Авторы благодарят В. И. Зайковского и Г. И. Гольденберга за проведение электронно-микроскопических исследований.

СПИСОК ЛИТЕРАТУРЫ

1. *Ребиндер П. А., Щукин Е. Д.* // Успехи физ. наук. 1972. Т. 108. № 1. С. 3.
2. *Бабак В. Г., Амелина Е. А., Щукин Е. Д. и др.* // Докл. АН СССР. 1972. Т. 206. № 1. С. 132.
3. *Щукин Е. Д., Юсупов Р. К., Амелина Е. А. и др.* // Коллоид. журн. 1969. Т. 31. № 6. С. 913.
4. *Шепелева М. Н., Исмагилов З. Р., Овсянникова И. А. и др.* // Кинетика и катализ. 1991. Т. 32. № 1.
5. *Шепелева М. Н., Шкрабина Р. А., Оккель Л. Г. и др.* // Кинетика и катализ. 1988. Т. 29. № 1. С. 195.
6. *Щукин Е. Д., Паранский С. А., Бессонов А. И.* Механические испытания катализаторов и адсорбентов. М.: Наука, 1971. С. 25.
7. *Фенелонов В. Б., Заграфская Р. В.* // Моделирование пористых материалов. Новосибирск: ИК СО АН СССР, 1976. С. 60.
8. *Перцов Н. В., Данилова Ф. Б., Бабак В. Г. и др.* // Докл. АН СССР. 1975. Т. 222. № 5. С. 1085.
9. *Степанов И. А.* // Изв. АН Латв. ССР. Сер. физ. и техн. наук. 1985. № 2. С. 83.
10. *Ovsyannikova I. A., Goldenberg G. I., Koryabkina N. A. et al.* // Appl. Catalysis. 1989. V. 55. P. 75.

Институт катализа СО АН СССР,
Новосибирск

Поступила в редакцию
26.09.89

ELSEVIER

Catalysis Today 24 (1995) 269–271

CATALYSIS TODAY

Synthesis of mechanically strong and thermally stable spherical alumina catalyst supports for the process of methane dimerization in a fluidized bed

Z.R. Ismagilov [a], R.A. Shkrabina [a], N.A. Koryabkina [a], F. Kapteijn [b]

[a] *Boreskov Institute of Catalysis, Novosibirsk, Russia*

[b] *Delft University of Technology, Delft, The Netherlands*

1. Introduction

It is known that methane dimerization occurs at 650–850°C, and catalysts which operate under fluidized bed conditions should have the high mechanical strength and thermal stability to comply with severe conditions of this process. It is evident that these properties of catalysts depend mainly on the support properties. One of the most widely used methods to increase the strength and the stability of supports and catalysts is chemical modification with various compounds.

This work is devoted to the development of the method of chemical modification for the preparation of thermally stable spherical alumina with high mechanical strength.

2. Results

Formation of the spherical granules was carried out by the hydrocarbon–ammonia moulding method [1]. The following compounds were used to prepare modified alumina: lanthanum, cerium and magnesium nitrates, and sol SiO_2.

Alumina supports were impregnated with aqueous solution of the salts. In some experiments a special impregnation method was used: the spherical granules of hydroxide were impregnated with aqueous solution of salts [2]. Sol SiO_2 was added to aluminium hydroxides before the hydrocarbon–ammonia moulding.

The amount of modificator added was varied between 1 and 13 wt.-%. Sintering tests were carried out at 900–1300°C at different heating time in order to study the stabilizing and strengthening effects of a modifying element on the phase transformation, surface area and mechanical strength.

The results obtained show that modified spherical alumina properties depend on the method of the introduction of chemical compounds. This is connected with the different nature of the interaction between aluminium compounds and modifying additives.

Magnesium introduction to aluminium hydroxide granules allows to increase sharply the strength of granules (1.5–2 times) in comparison with pure alumina after calcination at 550°C. Introduction of magnesium does not cause support texture to change. It was shown that the increase in durability of modified low-temperature support is due to component interaction and formation of cation–anion type solid solution based on the γ-alumina structure. The samples of spherical granules (diameter 1–3 mm) obtained by the new method have mechanical strength ca. 50 MPa and

SSDI 0920-5861(95)00041-0

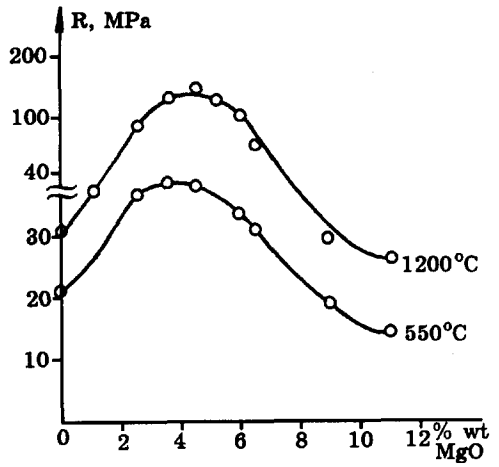

Fig. 1. Mechanical strength of alumina granules (R) versus MgO concentration and temperature.

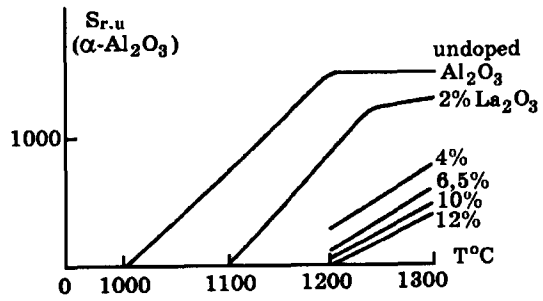

Fig. 2. Dependence of α-Al_2O_3 content in the θ-Al_2O_3/α-Al_2O_3 system on CeO_2 concentration.

contain 2–3 wt.-%. MgO. Fig. 1 illustrates the dependence of the mechanical strength of spherical alumina on the MgO content at different temperatures.

The method of lanthanum introduction influences the support thermal stability. Thus, the incipient wetness impregnation of oxide granules is more efficient as compared with the introduction of the lanthanum salt into aluminium hydroxide granules. The stabilizing effect of lanthanum was assumed to result from the formation of intermediate X-ray amorphous compounds with the transient Al_2O_3 forms. The phase $La_2O_3 \cdot 11Al_2O_3$ is observed only at 1100°C and γ-alumina is detected at this temperature also. The dependence of the α-Al_2O_3 line intensity on La_2O_3 concentration at different temperatures is shown in Fig. 2. It is seen that the higher is the temperature the more La_2O_3 additive should be introduced to decrease α-Al_2O_3 content. When the formation of $La_2O_3 \cdot 11Al_2O_3$ is completed (at 1300°C) the stabilizing effect seems to end, and alumina not involved in the interaction exists as α-Al_2O_3 only. It is shown that the phase lanthanum aluminate which forms preferably when the salt is added to aluminium hydroxide granules does not provide the stabilizing effect.

Unlike La_2O_3–Al_2O_3 system, the method of cerium introduction has no influence on the thermal stability of Al_2O_3. The thermal stability of alumina was shown to increase only at low content of CeO_2 (ca. 5 wt.-%) and only a part of cerium introduced was found to interact with alumina.

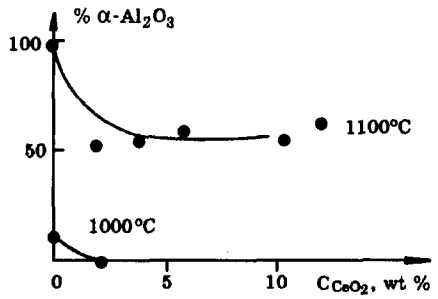

Fig. 3. Integral intensity of lines (d/n=2.085) for α-Al_2O_3 versus temperature and concentration of lanthanum.

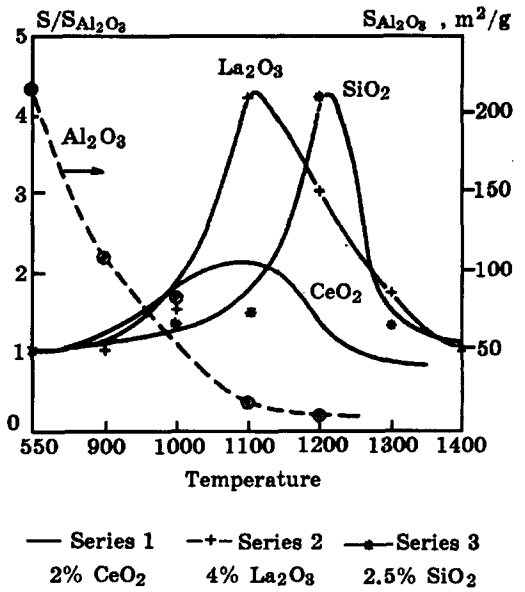

Fig. 4. The efficiency of various additives at different temperatures.

Fig. 3 shows the influence of CeO_2 content on the amount of α-Al_2O_3 formed at different temperature.

Thus, the results obtained allow to conclude that alumina promotion with cerium provides a less profound effect on the thermal stability of the support than that with lanthanum. That is connected with the limited interaction of cerium with the support.

The role of lanthanum and cerium in the increase of thermal stability is discussed in [3,4], where the X-ray study of these systems was carried out to establish dependencies on the method of introduction, type of alumina and amount of additives.

The introduction of silica-sol into plastic mass before hydrocarbon–ammonia moulding also allows the increase of the thermal stability of alumina. For instance, at SiO_2 content 2–3 wt.-% the specific surface area of alumina (S_{BET}) after sintering at 1200°C increases 3–4 times in comparison with pure alumina.

Comparison of the efficiency of La_2O_3, CeO_2, and SiO_2 (characterized by change in S_{BET}) shows that up to 1100°C the best additive is La_2O_3, and SiO_2 promotor is the most effective at 1200°C. The data are represented in Fig. 4.

Thus, the optimal conditions were chosen to prepare strong and thermally stable alumina support, which can be used for the preparation of fluid bed methane dimerization catalysts.

3. References

[1] M.N. Shepeleva, R.A. Shkrabina and Z.R. Ismagilov, Technology Today, 3 (1990) 150.
[2] N.A. Koryabkina, Z.R. Ismagilov and R.A. Shkrabina et al., Appl. Catal., 72 (1991) 63.
[3] R.A. Shkrabina, N.A. Koryabkina and Z.R. Ismagilov et al., Kinet. Katal., (in press).
[4] N.A. Koryabkina, R.A. Shkrabina and Z.R. Ismagilov et al., Kinet. i Katal., (in press).

React. Kinet. Catal. Lett., Vol. 54, No. 1, 181-191 (1995)

RKCL2563

POROUS STRUCTURE OF ALUMINA CERAMIC SUPPORTS FOR GAS SEPARATION MEMBRANES, I. PREPARATION AND STUDY OF THE EXTRUSION MASSES

R.A. Shkrabina, B. Boneckamp*, P. Pex*, H. Veringa* and Z.R. Ismagilov

Boreskov Institute of Catalysis, Novosibirsk 630090, Russia
*ECN, Petten, The Netherlands

Received July 4, 1994
Accepted July 27, 1994

The properties of aluminium-containing compounds and the compositions of extrusion pastes have been studied to obtain materials with good plastic properties. To prepare these masses aluminium hydroxide (as binder) and α-alumina powders (as additives) were used. It was shown that there is an optimal correlation between binder and additive for preparation of the extrusion pastes with good plastic properties.

INTRODUCTION

The pore structure of materials used as catalysts or membrane supports is one of their most important characteristics. Same additional specific properties come into play when porous ceramic supports are applied as membranes. These membrane supports should have a relatively low specific surface area and a well defined monomodal pore distribution.

Most gas-separating processes occur at high temperature and pressure. So, the ceramics used as membrane supports should possess mechanical and thermal stability.

Alumina ceramics are widely used as supports for catalysts

and membranes. A large number of publications are devoted to the study of alumina ceramics and the method of their preparation. So, it is a matter of common knowledge that chemical modifications by B, Ca and Mg considerably increase the mechanical strength of γ- and α-alumina [1-4]. The pore structure of alumina ceramics depends on the thermal treatment conditions and on the pore structure of initial components (hydroxide or oxide). The burning out of organic additives also permits to change the pore structure of ceramics [5,6].

Aluminium hydroxide and α-alumina powder were used in this work as the initial components for the preparation of extrusions.

The goal of this paper is to study the effect of properties of the starting components as well as quantitative composition of extrusion mass on the pore structure of alumina ceramics. This manuscript consists of two parts. The first part is devoted to the preparation and study of extrusion masses.

EXPERIMENTAL

The following aluminium-containing compounds were used to prepare alumina membrane supports.

Aluminium hydroxide powder with the pseudoboehmite structure produced in Russia (hydroxide-R);

Aluminium hydroxide powder with the pseudoboehmite structure manufactured by Condea Co. (Disperal RS);

α-Alumina powder obtained upon hydroxide-R calcination at 1200 °C for 4 h (α-R');

α-Al_2O_3 powder produced by ALCOA (α-Alc).

Table 1 presents the basic physico-chemical properties of the starting components.

The suitability of masses for extrusion was estimated with a laboratory machine (type "Force Gauge"), which measures the breaking force (F in Newton) as a relative characteristic of the rheological mass properties.

To prepare extrusion masses, we have used a binder made from the mixture of aluminium hydroxide with a pseudoboehmite

Table 1

Properties of starting aluminium compounds

No.	Compound	Phase composition	Cryst. size (Å)	S BET (m^2/g)	Porosity (%)	Aver. pore diam. (μm)	Particle size (μm)	Admixture (wt.%)
1	Hydroxide (hydr.-R)	Pseudoboehmite structure	50	220 (550 °C)	-	0.01 (550 °C)	<30	NO_3^- <0.5
2	Hydroxide (Disperal RS)	Pseudoboehmite with amorphous aluminium component	100	240 (550 °C)	-	~0.01 (550 °C)	~10	NO_3^- -3.5 C -0.55
3	Porous oxide (α-R)	α-Al_2O_3	>1000	10	50	0.1	3÷10	-
4	Dense oxide (α-Alc)	α-Al_2O_3	>1000	~4	-	1	3÷5	-

structure (see Table 1), nitric acid and/or water. The capability of the pseudoboehmite to react with strong acids and to form aluminium water-soluble basic salts is widely used for the binder preparation [7-9]. Such basic salts were shown to form multinuclear oxocompounds soluble in intermicellar liquids between primary particles of hydroxide and to convert the mixture of hydroxide, water, and acid into a peptized mass [10,11].

Preliminary experiments have shown that the binder with a high content of anhydrous Al_2O_3 (44-50 wt.%) can be directly used for extrusion. In this case the porous structure of ceramics is primarily specified by conditions of thermal treatment of the extrusions and by texture characteristics of the initial hydroxide. It is known that during transformation of aluminium hydroxide to alumina, pseudomorphism is observed, i.e. the initial particle arrangement in hydroxide aggregates is preserved in alumina and this determines its porous structure [6].

Amount of acid used in binder preparation is calculated as mol HNO_3 per mol Al_2O_3 and characterized by the acid modulus (Ma).

RESULTS AND DISCUSSION

1. Effect of properties of aluminium hydroxides on the rheological characteristics of extrusion masses

Figure 1 shows the effect of binder rheological properties (defined as the α-Al_2O_3 equivalent concentration in the binder) on α-Al_2O_3 amounts added upon preparation of masses suitable for extrusion. These data were obtained for hydroxide-R (used for binder preparation) and dense α-Al_2O_3; the weight fraction of the latter was calculated with respect to binder + additive mixture (curve 1). Note that this effect is characterized by three regions of alumina concentration in the binder.

In the first region (concentration of alumina in the binder is lower than 35 wt.% and that of dense α-alumina <80 wt.%), the mass converts to a more fluid dispersion than the initial binder when no force is applied to it. This means that the mixture has dilatant properties and cannot be used for extrusion.

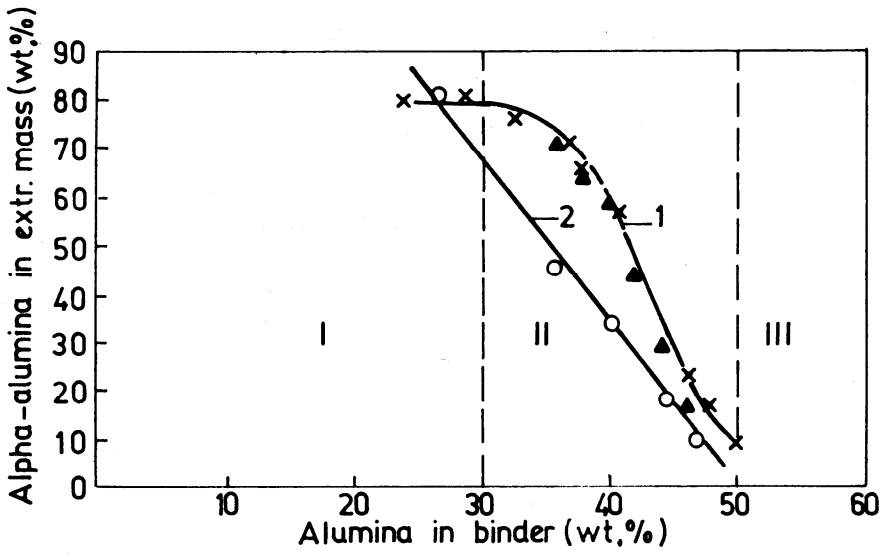

Fig. 1. Dependence of α-alumina content in extrusion masses on the alumina concentration in the binder
Curve 1 - for binders prepared from hydroxide-R with acid (x) and Disperal RS without acid (▲);
Curve 2 - for binder prepared from Disperal RS (with acid)

Only at >80 wt.% of α-alumina additive is the mass suitable for extrusion. However, this mass exhibits high value of load-stress (more than 60 N) and is rather stiff.

We failed to prepare binders with the alumina concentration exceeding 50 wt.% (third region); the water amount required for preparation of such alumina-rich mixture is quite insufficient to dissolve aluminium basic salts and to convert the mixture to a homogeneous plastic mass.

Only binders with 30-50 wt.% alumina concentration are suitable for the preparation of extrusion masses containing α-alumina additive (second region).

The higher the alumina concentration in a binder, the smaller the additional amounts of α-alumina needed to prepare the extrusion mass.

Note that the same curve is valid for Disperal RS when the binder is prepared without acid (Fig. 1). But at the same con-

centration of the equivalent α-Al_2O_3, binders prepared with water and acid exhibit quite different rheological properties than those prepared with water only (Fig. 1, curve 2). The following explanation might be accepted. The phase composition of Disperal RS is a mixture of pseudoboehmite aluminium hydroxide and amorphous hydroxide (the background in X-ray patterns at $2\theta < 14^\circ$ and a smeared line intensity at $2\theta = 49^\circ$ evidence this fact). The amorphous hydroxide is known [6] to be stabilized by anionic groups because it is a mixture of X-ray amorphous hydroxide and basic aluminium salt. The chemical analysis of Disperal RS verifies this fact (Table 1). The calculations indicate that this amount of anions, in terms of acid concentration, corresponds to an acid modulus of ~0.04. This acid amount is sufficient [12] for the formation of the soluble basic salts and for the transformation of the hydroxide gel to a plastic mass. At excess acid ($M_a > 0.1$), the plastic mass is transformed to a gel [13] due to formation of the normal $Al(NO_3)_3$ salt and coagulation of hydroxide particles.

Due to these processes, the binder prepared from Disperal RS with acid has a lower plasticity and higher load-stresses than those obtained from hydroxide-R or Disperal RS+H_2O (at similar Al_2O_3 concentrations). It follows that we can add smaller amounts of α-Al_2O_3 powder to such binders for preparation of masses applicable for extrusion.

It is evident that the crystal and morphological structure of the hydroxide applied for binder preparation as well as the properties of α-Al_2O_3 additive also affect this dependence of the amount of α-alumina additive on alumina concentration in the binder.

Figure 2 presents the diagram for extrusion masses prepared using a mixture of various hydroxide binders (with 40 wt.% Al_2O_3 concentration in each) at approximately equal acid contents (M_a = 0.04-0.02) and dense α-Al_2O_3. In addition to hydroxide-R and Disperal RS, we have also used aluminium hydroxides of Condea GmbH Co. with various sizes of pseudoboehmite/boehmite primary particles. The initial particle sizes (in the

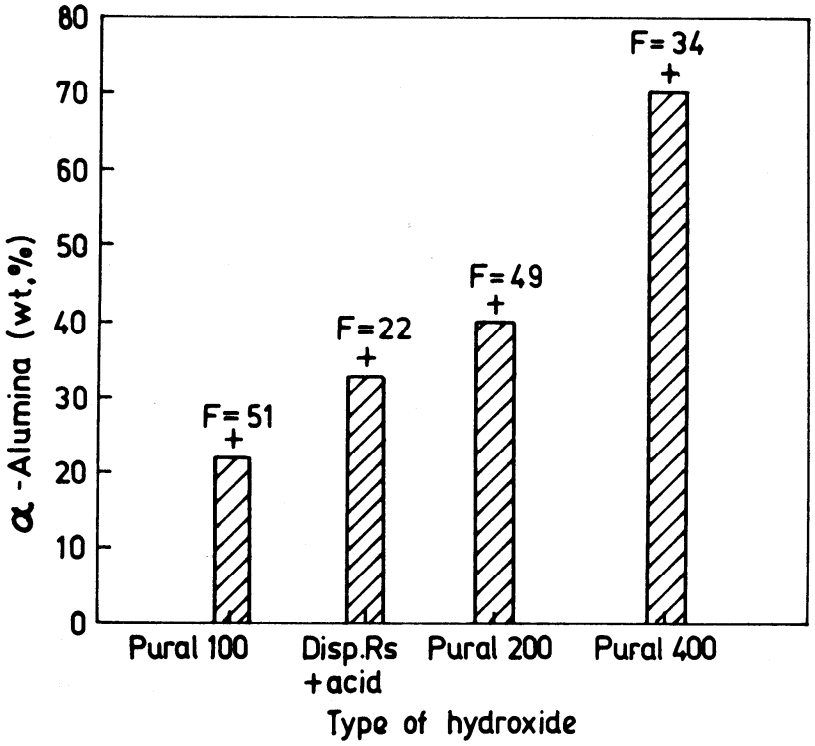

Fig. 2. α-Alumina content in extrusion masses prepared with binders from different types of hydroxide. Alumina concentration in each binder is equal to 40 wt.%

coherent dissipation region) are ~150 Å (Pural 100), 200-300 Å (Pural 200) and 400-550 Å (Pural 400). At similar Al_2O_3 contents in the binder, the amount of α-Al_2O_3 needed for extrusion mass preparation is quite different. Rheological properties (load-stress values) of the extrusion masses obtained from these binders are also different.

This phenomenon may be explained as follows. With increasing crystallite size of boehmite/pseudoboehmite particles, the number of coagulation types of contacts between the initial particles decreases. It is known [9] that only these contacts can be broken upon hydroxide interaction with the acid and this destruction accounts for the plastic mass formation. For coarsely-dispersed Pural 400 with predominantly crystallization contacts, full destruction with only basic salt formation is high-

ly improbable [9]. This hydroxide interaction with nitric acid causes the appearance of normal salts and additional water formation, decreasing the Al_2O_3 content in the binder. Thus, larger amounts of α-Al_2O_3 additive are needed for extrusion mass formation.

For Pural 100 (although the fraction of crystallization type contacts in this hydroxide is less than for Pural 400), the binder with 40 wt.% alumina concentration has less plasticity than the binder from other hydroxides. This may be connected with the formation of a smaller amount of water soluble basic salts under these conditions (desired M_a and alumina concentration). This is the reason why a smaller amount of α-alumina can be added to this binder during extrusion mass preparation.

2. Effect of α-Al_2O_3 additive on extrusion mass properties

It is evident that the extrusion mass properties are determined among other factors by the porous structure of components. Here we would like to discuss the effect of different porous structures of α-Al_2O_3 additives on the rheological characteristics and component composition in extrusion masses. Table 2 presents compositions of suitable extrusion masses prepared from hydroxide-R and Disperal RS binders together with dense and/or porous α-Al_2O_3 additives.

The table suggests that the binder with the same rheological properties (concentrations of equivalent α-Al_2O_3) requires different amounts of porous and dense α-Al_2O_3 added upon preparing masses suitable for extrusion (compare samples 1,4 and 9,10). This is due to the fact that porous α-Al_2O_3 adsorbs some water from the binder, thus providing a decrease of the water volume fraction in the extrusion mass. The table also lists the volume ratio of components in the extrusion masses. In our calculations we took into account that porous α-Al_2O_3 adsorbs 35% water.

Comparison of results of adding of the same amounts of α-Al_2O_3 (dense or porous) shows that the content of Al_2O_3 in the binder should be lower if we use the porous one (compare

Concentration of components in extrusion masses prepared from aluminium hydroxide (as binder) and mixtures of dense (α-Alc) and porous (α-R) alumina powder

≠	Conc. alum. in bind (wt.%)*	Σα (wt.%)		Hydr. (wt.%)	Water (wt.%)	Σα (vol.%)		Hydr. (vol.%)	Water (vol.%)	F, N
		α-Alc	α-R			α-Alc (*)	α-R (*)	(*)	(*)	
					Disperal RS					
1	32	75	-	10.5	14.5	51	-	9.5	39.5	26
2	41	44	-	30.5	25.5	24	-	22	54	26
3	32 (35)	44	19	16	21	(44)	(18)	(13)	(43)	30
4	35	34	18	22	26	(34)	(16)	(17)	(49)	32
5	32 (34)	-	44	23	33	(33)	(33)	(15)	(52)	29
					Hydroxide-R					
6	29	80	-	8	12	57	-	7	36	23
7	42	53	-	26	21	31	-	20	49	31
8	33 (36)	16	32	23	29	(8)	(26)	(16)	(50)	28
9	30 (32)	52	18	12	18	30	(14)	(16)	(40)	30
10	25 (30)	-	53	16	31	(41)	(41)	(11)	(48)	23

(*) In brackets are shown the alumina concentrations calculated with 35% water adsorption by porous α-alumina

samples 2,5 and 7,10).

Using dense and porous α-Al_2O_3 mixtures as additives and varying the binder concentration, extrusion masses with similar rheological properties can be prepared (samples 3,4,8,9).

The dense or porous α-Al_2O_3 additives (or their composites) used for the preparation of extrusion masses enable one to control the properties of extrusion masses and to regulate the porous structure of ceramics.

Thus, the results obtained allow to choose the optimal alumina concentration in the binder and the compositions of α-alumina-additives and binder for regulation of the plastic properties of extrusion masses.

REFERENCES

1. M. Stranik, M. Honalla, Hercules David M.: J. Catal., 104, 396 (1987).
2. E.Z. Golosman, A.L. Kljachko-Gurvich, V.J. Jakerson, G.P. Epishko, E.V. Pristavko, A.M. Rubinshtain: Kinet. Katal., 13, 1035 (1972).
3. N.A. Koryabkina, Z.R. Ismagilov, R.A. Shkrabina, E.M. Moroz, V.A. Ushakov: Appl. Catal., 72, 63 (1991).
4. E.M. Moroz, V.N. Kuklina, V.A. Ushakov: Kinet. Katal., 28, 699 (1987).
5. N.F. Ermolenko, M.D. Efros: in "Regulation of pore structure of oxide adsorbents and catalysts", p. 350. Nauka, Tekhnika, Minsk 1971.
6. V.A. Dzisko, A.P. Kharmauchov, D.V. Tarasova: in "Physicochemical base of oxide catalysts synthesis", p. 384. Nauka, Novosibirsk 1978.
7. N.S. Smorgunenko, E.A. Levitskii: Izv. Akad. Nauk Belor. Ser. Khim. Nauk, 2, 43 (1966).
8. I.G. Frolov: in " Colloidal Chemistry", p. 320. Khimiya, Moscow 1980.
9. Z.R. Ismagilov, M.N. Shepeleva, R.A. Shkrabina, V.B. Fenelonov: Appl. Catal., 69, 65 (1991).
10. J.J. Fripiat, F. van Vauwelaert, H. Boomans: J. Phys.

Chem., 69, 2458 (1965).
11. J.N. Mukherjec: Kolloid. Z., 63, 36 (1993).
12. M.N. Shepeleva, R.A. Shkrabina, Z.R. Ismagilov, V.B. Fenelov: in "Proc. Intern. Symp. Preparation of Catalysts V" (G. Poncelet, P.A. Jacobs, P. Grange and B. Delmon, editors), p. 583. Elsevier Science Publishers, Amsterdam 1991.
13. V.A. Dzisko: in "The bases of the preparation methods of catalysts", p. 264. Nauka, Novosibirsk 1983.

React. Kinet. Catal. Lett., Vol. 54, No. 1, 193-201 (1995)

RKCL2564

POROUS STRUCTURE OF ALUMINA CERAMIC SUPPORT FOR GAS SEPARATION MEMBRANES, II. STUDY OF POROUS STRUCTURE OF CERAMIC COMPOSITION

R.A. Shkrabina, B. Boneckamp[+], P. Pex[+], H. Veringa[+] and Z.R. Ismagilov

Boreskov Institute of Catalysis, Novosibirsk 630090, Russia
[+] ECN, Petten, The Netherlands

Received July 4, 1994
Accepted July 7, 1994

Porous structure changes of alumina ceramic membrane supports have been studied in the preparation process. It is shown that the porous structure can be controlled without burning out additives and variations of thermal treatment conditions, but taking into account the properties of initial aluminium-containing components and their content in extrusion masses.

INTRODUCTION

This part is the continuation of the study reported previously [1] and is devoted to the investigation of the properties of the ceramic obtained from the extrusion masses described in [1]. Here we will discuss the porous structure of a ceramic material containing two types of α-alumina: (i) one obtained from hydroxide-binder, and (ii) α-alumina added to the binder upon the preparation of extrusion masses.

EXPERIMENTAL

We have used a piston-type extruder (5 mm/min crosshead speed) for extrusion, of single tubes (with 10 mm outer and 8 mm inner diameters) or cylinder (with 4 mm diameter).

The tubes and cylinders obtained were dried at room temperature under static conditions. Dried samples were fired; the heating rate of the samples was constant and equal to 100 ^{o}C per 1 h at 550-1200 ^{o}C.

Mercury porosimetry was used to study the porous structure of ceramics.

Sample texture was analyzed by scanning electron microscopy.

Gas permeability and bubble point measurements for ceramic tubes were performed by the methods described in [2,3].

RESULTS AND DISCUSSION

Table 1 presents the porous structure data of ceramics prepared from the extrusion masses listed in ref. [1], Table 2.

Ceramics prepared from hydroxides without α-Al_2O_3 additive in extrusion masses (samples 11,12) have a monodisperse distribution of pores with a predominant pore diameter of 0.1 μm. Note that ceramics obtained from the hydroxides studied are somewhat different. The α-Al_2O_3 ceramics prepared from Disperal RS has a lower specific surface area and pore volume, and therefore a lower porosity as compared to those obtained from hydroxide-R. This is associated with the active sintering upon decomposition of Disperal RS containing significant amounts of anions (see ref. 1, Table 1). It is known that NO_3^-, F^-, and other anions intensify the γ-Al_2O_3 conversion to α-Al_2O_3 due to chemisorption of the acid gases (HF, HNO_3) released upon hydroxide decomposition [4]. Such chemisorbed compounds change the nature of primary particles: their defectiveness and capability to arrange close-packed aggregates increase. These factors intensify the process of α-Al_2O_3 formation and increase the size of corundum crystals. Besides, the acid gases lead to creation of hydrothermal conditions favoring the formation of coarsely-

Table 1

Porous structure of cylindrical ceramic granules prepared with dense and porous α-Al_2O_3 additives*

No.	Content of α-Al_2O_3 in extrusion mass (wt.%)			Porosity (%)	V_Σ (cm^3/g)	Diameter of pores (μm)			S BET (m^2/g)
	dense	porous	total			average	d_1	d_2	
					Disperal RS				
1	75	-	75	33	0.124	0.229	0.4	0.15	2.1
2	44	-	44	40	0.172	0.192	0.35	0.15	3.6
3	44	19	63	44	0.205	0.226	0.4	0.15	3.6
4	34	18	52	47	0.226	0.215	0.6	0.20	4.2
5	-	44	44	57	0.342	0.221	1.0	0.15	6.2
					Hydroxide-R				
6	80	-	80	33	0.122	0.442	0.4	0.2	0.5
7	53	-	53	42	0.185	0.213	0.5	0.1	3.5
8	16	32	48	57	0.332	0.237	0.8	0.1	5.6
9	52	18	70	44	0.195	0.278	0.45	0.15	3.0
10	-	53	53	61	0.394	0.174	1.0	0.1	9.0
11	Disperal RS		-	37	0.149	0.113	-	0.113	5.3
12	Hydroxide-R		-	49	0.245	0.102	-	0.102	9.6

*Samples are numbered as in Table 2 [1]. Sintering conditions for dried cylindrical alumina were the following:

550 °C, 8 h → 1000 °C, 4 h → 1200 °C, 2 h

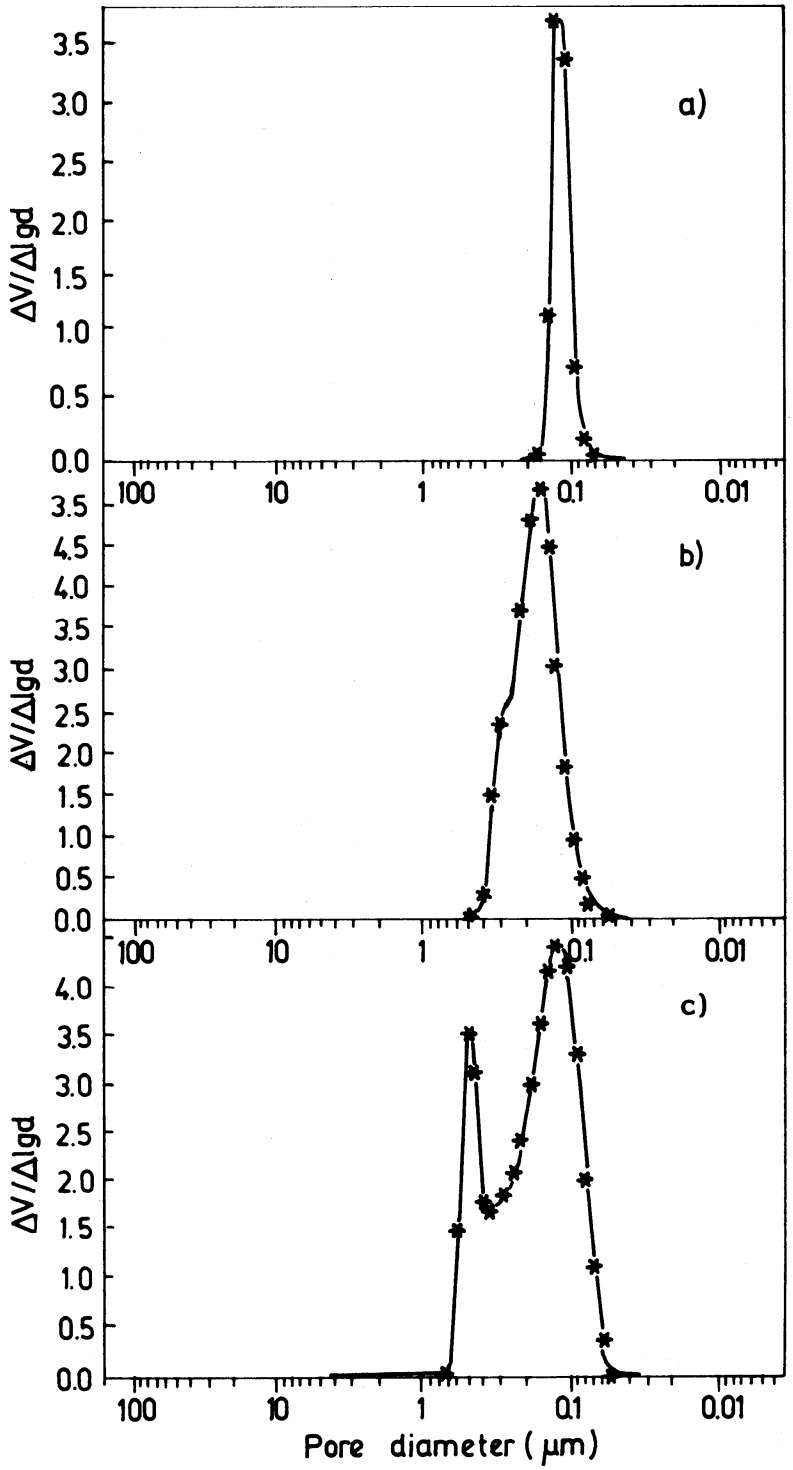

Fig. 1. Differential pore size distibutions for cylindrical alumina ceramics prepared from extrusion masses with different contents of α-alumina additives:
a) without α-alumina; b) 33 wt.% α-alumina;
c) 59 wt.%
Initial components: Disperal RS and α-Alcoa

dispersed starting crystals, which, in turn, cause the appearance of α-Al_2O_3 with a lower specific surface area and porosity.

The α-Al_2O_3 powder added to the extrusion mass provides changes of the ceramic porous structure, associated with the arrangement of various types of α-Al_2O_3 forming the ceramics and with the porous structure of α-Al_2O_3 additive. The data of Table 1 (samples 1,2,6,7) and the pore size distribution for ceramics at various α-Al_2O_3 additive contents (Fig. 1) support this fact. The higher the α-Al_2O_3 content, the lower the porosity and specific surface. The appearance of pores with large diameters takes place. SEM micrographs of the samples (Figs 2-4) suggest changes in the ceramic particle arrangement upon adding various amounts of α-Al_2O_3. The data of Table 1 indicate also that the increasing of fraction of porous α-Al_2O_3 alumina additives (in extrusion masses) leads to increasing S_{BET} and

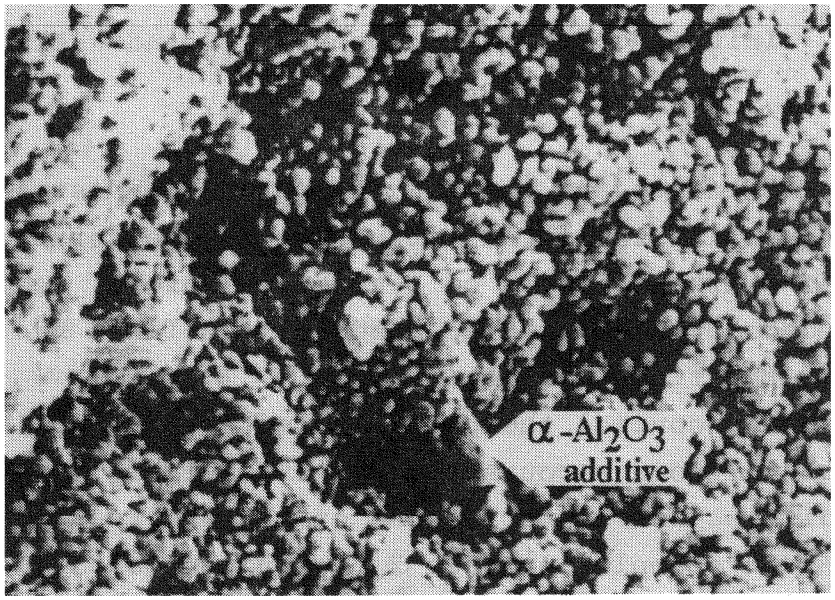

Fig. 2. SEM micrographs for ceramic tubes (for fraction) prepared from extrusion masses with different contents of α-alumina additives: 9 wt.%
Initial components: Disperal RS and α-Alcoa

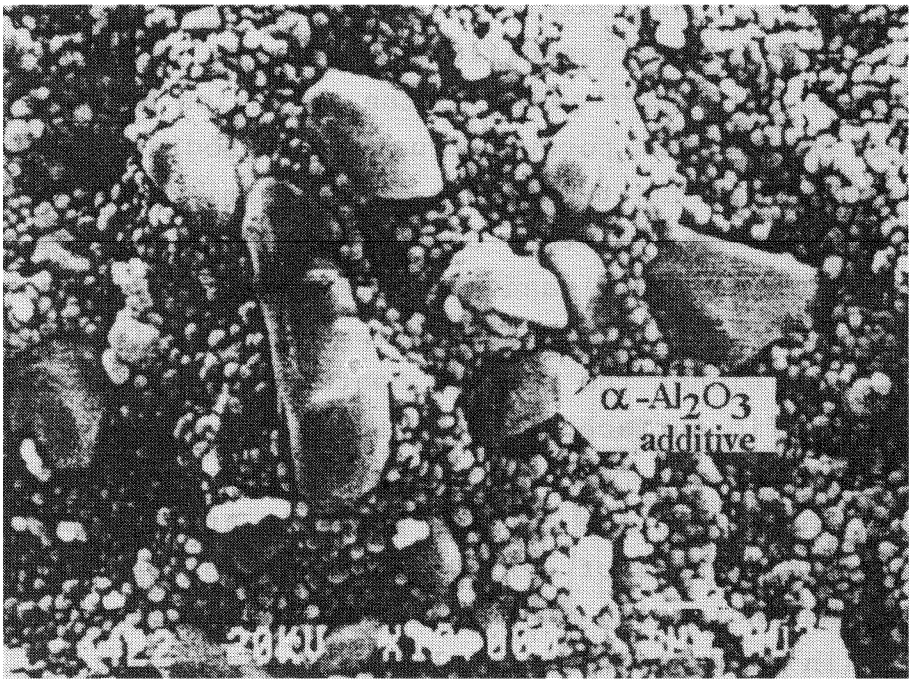

Fig. 3. SEM micrographs for ceramic tubes (for fraction) prepared from extrusion masses with different contents of α-alumina additives: 17 wt.%
Initial components: Disperal RS and α-Alcoa

porosity of ceramics and changes the pore size distribution.

Consequently, the porous structure of the ceramics obtained from different types of α-alumina (porous, dense additives and decomposed hydroxide binder) is defined by their correlation in the final product.

So, we can control the porous structure of alumina ceramic products without recourse to the extensively used burning out of additives and to variations of thermal treatment conditions. As an example,in Table 2 the properties of ceramic tubes prepared on the basis of the data obtained are given. It is seen that there is a good reproduction of the tube pore structure as compared with a cylindrical ceramic (sample 2, Table 1) with the same composition. Moreover, the properties of these ceramic tubes satisfy the requirements to membrane supports.

Table 2

Properties of the ceramic tubes*

Characteristic	Value
Alumina concentr. in binder (wt.%)	42
Correlation between components in extrusion mass wt.% (vol.%):	
- dense α-alumina (α-Alc)-addition	44(24)
- water	25(54)
- hydroxide	31(22)
Load-stress (ext.mass) (N)	43
Properties of ceramic tubes:	
length (l), mm	100-800
-outer diameter (Øout) (mm)	13
-inner diameter (Øinn) (mm)	7
-total shrinkage (%)	
l	13
Øout	12
Øinn	14
-Porosity (%)	41
-total pore volume (cm^3/g)	0.173
-average pore diameter (μm)	0.164 (d_1~0.15;d_2~0.37)
$-S_{BET}$ (m^2/g)	4.2
Bubble point (length of tube 160 mm)	
Pressure, bar (number of defects)	6.3(4);6.56(4)
Total number of defects	8
Defects size (μm)	0.46-0.43
Gas permeability at 1 bar (He)	0.0237×10^{-4} mol/m^2 s Pa

* For the binder preparation aluminium hydroxide Disperal RS was used. Drying of the tubes was performed on a rolling table. Sintering conditions were the following:
550 °C, 8 h → 800 °C, 2 h → 1000 °C, 2 h → 1200 °C, 2 h

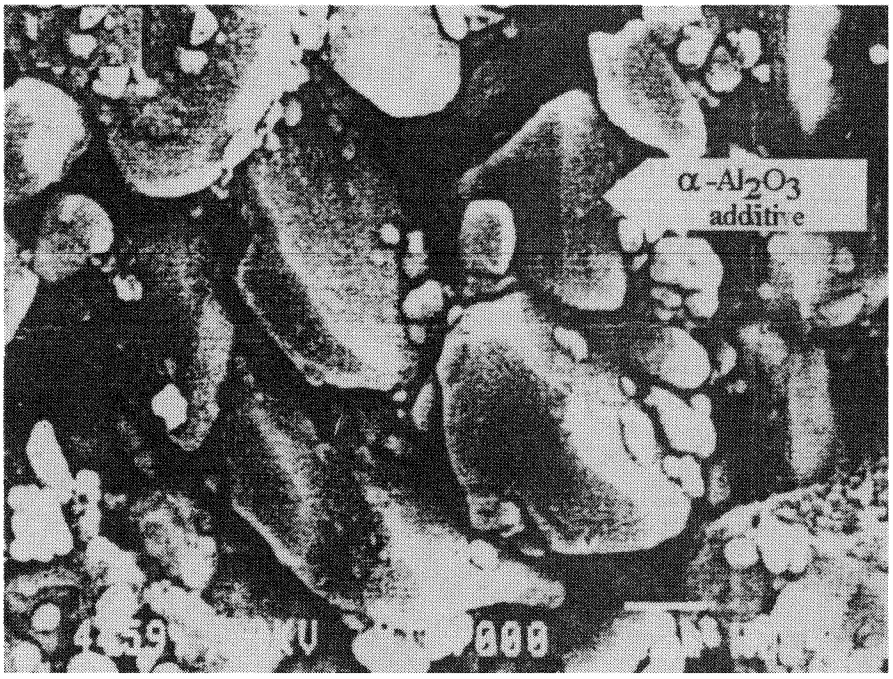

Fig. 4. SEM micrographs for ceramic tubes (for fraction) prepared from extrusion masses with different contents of α-alumina additives: 80 wt.%
Initial components: Disperal RS and α-Alcoa

Thus, the data obtained suggest that if the porous structure of the initial aluminium-containing components is known (taking into account the requirements for the extrusion moulding masses), it is possible to prepare starting compositions ensuring the desired porous structure of the alumina ceramics.

REFERENCES

1. R.A. Shkrabina, B. Boneckamp, P. Pex, H. Veringa, Z.R. Ismagilov: React. Kinet. Catal. Lett., 54. 181 (1995).
2. Vassilis T. Zaspalis: Thesis "Catalytically active ceramic membranes", 1990, Twente University, The Netherlands.
3. A.G.M. Leenaars: Thesis "Preparation, structure and separation characteristics of ceramic alumina membranes", 1984, Petten, The Netherlands.
4. N.E. Ermolenko, M.D. Efros: in "Regulation of pore structure of oxide adsorbents and catalysts", p. 350. Nauka and Tekhnika, Minsk 1971.

ELSEVIER

Catalysis Today 29 (1996) 427–431

CATALYSIS TODAY

Synthesis of a mechanically strong and thermally stable alumina support for catalysts used in combustion processes

N.A. Koryabkina *, R.A. Shkrabina, V.A. Ushakov, Z.R. Ismagilov

Boreskov Institute of Catalysis, Pr. Ak. Lavrentieva, 5, Novosibirsk, 630090, Russia

Abstract

It is shown that simultaneous modification of spherical alumina by bi- and three-valence cations (that are strengthening and thermally stabilizing additives, respectively) by a special method leads to the formation of supports with unique properties. These results are due to the specific interaction between the additives and alumina.

Keywords: Aluminium supports

1. Introduction

The interest in high-temperature catalyst application, such as jet engines or gas turbines, has evolved in recent years. In this application, goal temperatures will be in the range of 1100–1400°C. It is evident that an important role in developing efficient and stable catalyst systems belongs to the support and its behavior at high temperature.

Previously, the authors proposed a new method of preparation of alumina with high mechanical strength [1]. We have also studied the conditions for the formation of thermally stable alumina support doped with lanthanum [2,3]. The understanding of the mechanism of strengthening upon Mg^{2+}-doping and phase stabilization upon La^{3+}-doping allows to suggest the special procedure of double modification of support with Mg and La cations for the preparation of alumina support with unique properties.

2. Experimental

Spherical alumina hydroxide ($d = 1.4$–2.0 mm) was prepared by method of hydrocarbon–ammonia moulding [4]. The initial reagent for the moulding procedure was aluminum hydroxide of pseudo-boehmite structure prepared according to Ref. [5]. The introduction of magnesium ions into spherical granules of aluminum hydroxide, with subsequent drying at 100°C and thermal treatment (at 550°C for 4 h) was carried out as described in Ref. [1]. The magnesium content in samples, 3.2 wt.-% MgO, was optimal for the preparation of the strongest support [1–3]. The resulting γ-alumina was further used as an initial material for lanthanum introduction.

The subsequent lanthanum introduction was performed by incipient impregnation with a lanthanum nitrate solution. Then the samples were

* Corresponding author. Fax. (+7-383) 2397352, (+7-383) 2355766.

SSDI 0920-5861(95)00315-0

dried in air at ambient temperature for 10 h and at 100°C for 4 h. The thermal treatment was carried out in air stream with a space velocity of 1000 h^{-1} at 550°C for 4 h. Sintering tests were carried out at 900–1400°C at different duration of calcination in order to study the stabilizing and strengthening effects of modifying elements on the phase transformation, surface area and mechanical strength.

X-ray analysis of the samples was carried out in a diffractometer HZG-4 with the copper radiation as in [1,7].

The mechanical crushing strength of the granules was determined as in [1].

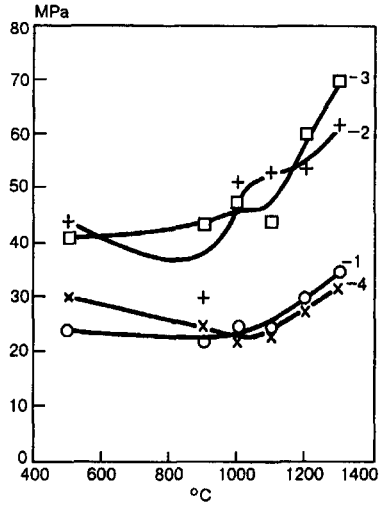

Fig. 1. The dependence of mechanical strength on the calcination temperature. The numbers of samples are same as in Table 1.

3. Results and discussion

Table 1 presents the properties of spherical alumina after high temperature calcination, prepared via the special procedure, in comparison with earlier published data [1–3].

The dependence of mechanical strength of doped aluminas on the calcination temperature are shown in Fig. 1. The introduction of magnesium increases the mechanical strength of granules by a factor 1.5–2.0 in comparison with pure alumina. The introduction of the second cation–lanthanum results in the increase of mechanical strength at high temperatures (1200–1300°C). At the same time, introduction of lanthanum preserves thermal stability with additional increase of efficiency at high temperatures. In Fig. 2, surface areas of doped samples are presented relative to that of the undoped alumina as a function of the calcination temperature.

X-ray of the system Mg–La–Al_2O_3 has shown that the solid solution of Mg–La–γ-Al_2O_3 is formed with the introduction of Mg and La into alumina. The parameter of the cell

Table 1
The structural and mechanical properties of high temperature alumina supports

No.	Additives (wt.-%)	S_{BET} (m^2/g)	α-Al_2O_3 content (%)	Mechanical strength (average) (MPa)
1200°C				
1	–	8	100	28
2	3% MgO [1,2]	7	100	54
3	5% La_2O_3 [3]	29	15	35
4	12% La_2O_3 [3]	24	trace	34
5	3% MgO + 5% La_2O_3	23	15	65
6	3% MgO + 12% La_2O_3	27	trace	60
1300°C				
1	–	5	100	30
2	3% MgO	6	100	62
3	5% La_2O_3	8	100	44
4	12% La_2O_3	12	100	35
5	3% MgO + 5% La_2O_3	14	100	65
6	3% MgO + 12% La_2O_3	24	trace	70

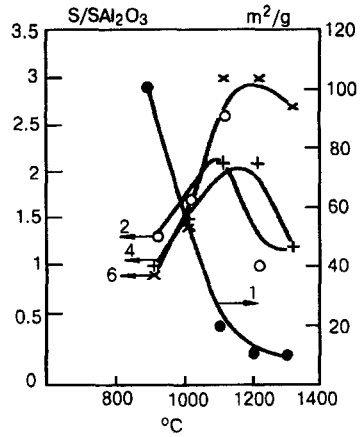

Fig. 2. Specific surface areas of the doped samples relative to that of alumina as a function of the calcination temperature. The numbers of samples are same as in Table 1.

was 7.942; at the same time the coefficient B, which is determined as the ratio of the heights of lines 311 and 222 in γ-Al_2O_3 structure and characterizes structural changes in a support, slightly increased to 1.90. This is probably due to the substitution of aluminum ions for lanthanum in the structure of the solid solution Mg–γ-Al_2O_3. This solid solution begins to decompose with the formation of α-Al_2O_3 and 2 $MgO \cdot La_2O_3 \cdot 11\ Al_2O_3$ (ASTM 26-873) under thermal treatment at 1200°C. Mixed solid solutions of magnesia and lanthania in γ-Al_2O_3 containing 10 and 12 wt.-% La_2O_3, respectively, completely decompose at 1400°C.

The observation that the thermal stability of double modified alumina (Mg–La–Al_2O_3) is higher than that of La_2O_3–Al_2O_3 system apparently can be adequately explained on the basis of the 'hydroxide model' of the structure of low-temperature alumina [7] and the analysis of the possible paths of the structural rearrangement of solid solutions upon thermal treatment [8]. According to this model, which was derived on the basis of the full-profile X-ray analysis of diffraction patterns, γ-Al_2O_3 has a protospinel structure, slightly different from the spinel one, and is assigned to compounds of the common formula:

$$C_{(x1)}A_{(x2)}[D_{(y1)}B_{(y2)}]O_{(32-z)}\{OH\}_{(z)}$$

where A and B are spinel tetrahedral and octahedral cation positions; C and D are 'protospinel' cation positions considered in respect to spinel structure as defects. These positions are

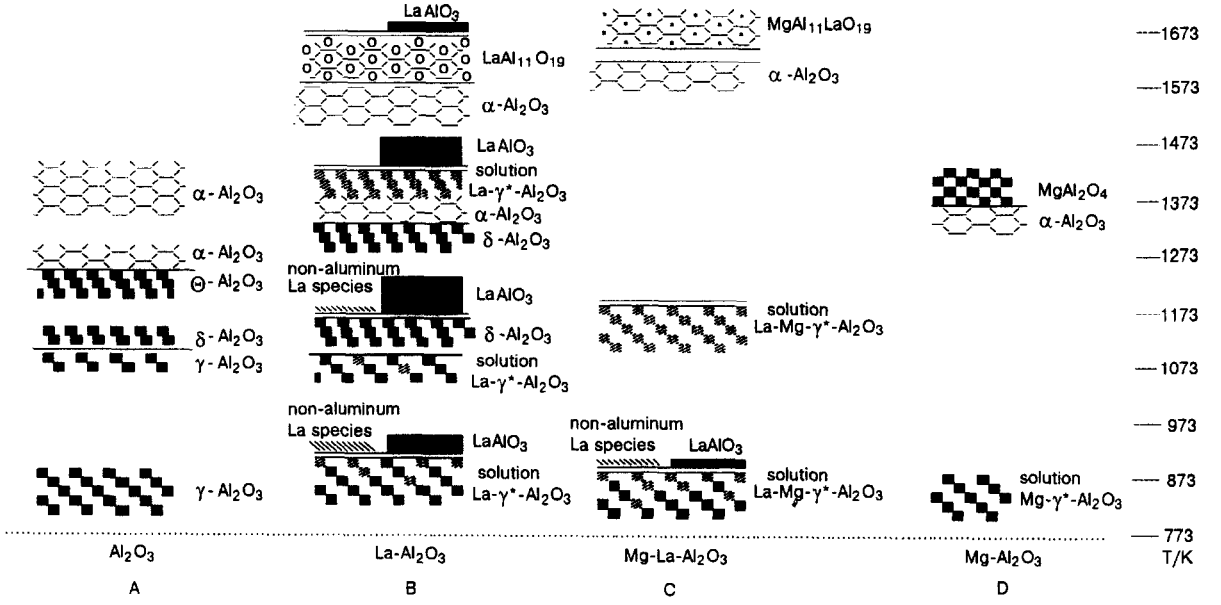

Fig. 3. Scheme of the changes of the structure and phase composition of aluminas doped with magnesium (ca. 3 wt.-%) and lanthanum (ca. 10 wt.-%) upon the increase of temperature.

present as an alternative set of cation positions in spinel structure.

Low-temperature solid solutions formed in γ-Al_2O_3 have principally a similar structure, differing only in the values of x, y, and z coefficients. As the temperature is raised, simultaneously with the resulting removal of OH groups and the perfection of cubic anionic framework, the process of the compact filling of cationic positions takes place. This process can occur in two principally different ways:

(1) Through the preferential filling of octahedral positions by Al at the expense of the packing of the defective (imperfect) positions. The final result of this process is the formation of stoichiometric spinel AB_2O_4. This way of structural rearrangement of Al_2O_3 is typical for alumina solutions of Mg [9], Ni [10], i.e., cations with the preference for tetrahedral cationic positions.

(2) Through the preferential filling of tetrahedral positions by Al. In this case new positions, untypical for spinel and low-temperature alumina, in practically cubic anionic framework are occupied. This mode of structural rearrangement is characteristic for alumina itself and alumina solutions of Cr [10] and possibly La [6], i.e., cations with the preference for octahedral cationic positions. The final result of the structural rearrangement is the transition from practically cubic closely packed anionic framework to the hexagonal one (with the formation of α-Al_2O_3 and solid solutions on its basis).

The changes observed in the structure and phase composition of alumina doped with magnesium (ca. 3 wt.-%) and lanthanum (ca. 10 wt.-%) upon the increase of temperature are illustrated in Fig. 3:

3.1. Pure alumina (Fig. 3a)

This scheme is based on earlier data [7,8].

3.2. The low-temperature solid solution containing lanthanum ions (Fig. 3b)

Upon lanthanum introduction a low-temperature solid solution is formed, with the structure similar to that of γ-Al_2O_3. In contrast to aluminum ions, lanthanum ions fill only octahedral positions, their presence in transient structures creates additional limitations for structural rearrangement with the formation of δ-, or α-Al_2O_3 [6].

3.3. The low-temperature solid solution containing magnesium ions (Fig. 3d)

The low-temperature solid solution containing magnesium ions has a structure similar to that of the low-temperature alumina, with magnesium replacing aluminium in tetrahedral positions (A and C). As the temperature increases, a preferential filling of octahedral positions takes place, while the occupation of defective positions decreases. At temperatures above 1000°C, owing to the diffusion of magnesium ions, the decomposition of the solid solution to α-Al_2O_3 and stoichiometric $MgAl_2O_4$ occurs; the latter has a cubic anionic framework, and its cationic framework has 24 occupied positions (2/3 of which are octahedral ones). The degree of the decomposition increases with the increase of magnesium introduced.

3.4. The system La_2O_3–MgO–Al_2O_3 (Fig. 3c)

After thermal treatment at 823 K, lanthanum appears to be present both in the composition of the low-temperature solid solution Mg–La–γ-Al_2O_3, and in the form of finely dispersed particles of lanthanum oxide. Coexistence of Mg and La, different in the preference for filling particular cationic positions in the anionic oxygen framework, in a solid solution based on the structure of γ-Al_2O_3 does not permit the realization of the ways of solid solution structural rearrangement typical for each of the cations. Moreover, the stabilization of a 'loose' structure of the low-temperature solution favors the admittance of lanthanum ions into the sup-

port structure. No formation of lanthanum aluminate is observed upon temperature increase, as opposed to the system La_2O_3–Al_2O_3, because in this case the preferential process is apparently the diffusion of lanthanum ions into the structure of the mixed solid solution. At temperatures above 1200°C two compounds with hexagonal packing of oxygen framework (α-Al_2O_3 and $MgAl_{11}LaO_{19}$) coexist in the system.

4. Conclusion

The modification of γ-Al_2O_3 by a composition of two-valence (Mg) and three-valence (La) cations, increases mechanical strength and thermal stability of alumina. Thermal stability of the doped alumina results from the suppression of structural rearrangement of low-temperature solid solutions with a rise of temperature.

References

[1] N.A. Koryabkina, Z.R. Ismagilov, R.A. Shkrabina, V.A. Ushakov and E.M. Moroz, Appl. Catal., 72 (1991) 63.
[2] Z.R. Ismagilov, R.A. Shkrabina and N.A. Koryabkina, Second Workshop Meeting C–C Hydrocarbon Conversion, Abstr., (1994) 58.
[3] Z.R. Ismagilov, R.A. Shkrabina, N.A. Koryabkina and F. Kapteijn, Catal. Today, (1995) in press.
[4] M.N. Shepeleva, R.A. Shkrabina and Z.R. Ismagilov, Technol. Today, 3 (1990) 150.
[5] R.A. Shkrabina, Z.R. Ismagilov, M.N. Shepeleva, S.R. Lohokari, M.S. Vaidya and D.R. Sane, Proc. 10 Nat. Symp., 11 (1990) 30.
[6] N.A. Koryabkina, R.a. Shkrabina, E.M. Moroz and V.A. Ushakov, Proc. EPDIC-3, in press.
[7] V.A. Ushakov and E.M. Moroz, Kinet. Katal., 26 (1985) 968 (in Russian).
[8] V.A. Ushakov, E.M. Moroz and E.A. Levitskii, Kinet. Katal., (1985) 1206 (in Russian).
[9] E.M. Moroz, V.N. Kuklina and V.A. Ushakov, Kinet. Katal., 28 (1987) 699.
[10] E.M. Moroz, O.A. Kirichenko, V.A. Ushakov and E.A. Levitskii, React. Kinet. Catal. Lett., 28(1) (1985) 9.

КИНЕТИКА И КАТАЛИЗ, 1997, том 38, № 1, с. 128–132

УДК 542.973:546.65'623:541.68

ИССЛЕДОВАНИЕ РЕАКЦИЙ И КАТАЛИЗАТОРОВ СЖИГАНИЯ ТОПЛИВ. XVII. ВЛИЯНИЕ ЛАНТАНА И ЦЕРИЯ НА СТРУКТУРНО-МЕХАНИЧЕСКИЕ СВОЙСТВА ОКСИДА АЛЮМИНИЯ

© 1997 г. Н. А. Корябкина, Р. А. Шкрабина, В. А. Ушаков, М. Лаусберг*, Ф. Каптейн**, З. Р. Исмагилов

Институт катализа им. Г.К. Борескова СО РАН, Новосибирск

**Университет г. Делфт, Нидерланды*

***Университет г. Амстердам, Нидерланды*

Поступила в редакцию 31.08.95 г.

Исследованы зависимости структурно-механических свойств оксида алюминия, промотированного ионами La и Ce, от температуры прокаливания (873–1573 K) и от содержания вводимых элементов. Наибольший эффект стабилизации удельной поверхности ($S_{уд}$) наблюдается при 1173–1473 K. В области температур наилучшая стабилизация $S_{уд}$ достигается при введении ~5 вес. % La_2O_3. Показано, что при $T > 1173$ K происходит стабилизация пористой структуры в модифицированных образцах. Механическая прочность гранул, содержащих ионы лантана и церия, возрастает с ростом температуры. Полученные результаты позволяют установить взаимосвязь между найденными ранее закономерностями влияния ионов лантана и церия на полиморфные превращения в оксиде алюминия в зависимости от условий термообработки и структурно-механическими свойствами модифицированного оксида алюминия.

Данная работа является продолжением исследования закономерностей модифицирования оксида алюминия ионами La и Ce [1, 2] и посвящена изучению структурно-механических свойств сферического оксида алюминия, промотированного этими элементами.

МЕТОДИКА ЭКСПЕРИМЕНТА

Исследования проводили на тех же образцах сферического оксида алюминия (d = 1.4–2.0 мм), что и в работах [1, 2].

Ионы La и Ce вводили пропиткой по влагоемкости гранул γ-Al_2O_3 из растворов солей азотной кислоты. Образцы серии I готовили пропиткой γ-Al_2O_3, полученного традиционным способом переосаждения; образцы серии II – пропиткой γ-Al_2O_3, полученного из продукта терморазложения гиббсита, согласно [3]. Содержание добавки варьировали в пределах 1–13 вес. % (в пересчете на оксид). Далее образцы всех серий сушили на воздухе при комнатной температуре в течение 10 ч, а затем при 383 K в течение 10 ч. Термообработку осуществляли в токе воздуха (объемная скорость 1000 $ч^{-1}$) при 823 K в течение 4 ч, а затем при 1173–1573 K в течение 2 ч. В специальных опытах термообработку проводили при 1273 K в течение 2, 5, 10, 20 и 30 ч.

Распределение вводимых элементов в грануле Al_2O_3, изученное методом рентгеноспектрального микроанализа на сканирующем микроскопе ISM-35C, во всех исследованных образцах было равномерным[1].

Удельную поверхность ($S_{уд}$) образцов определяли методом БЭТ по термодесорбции аргона.

Механическую прочность гранул на раздавливание измеряли по стандартной методике на приборе МП-9С. Среднюю прочность ($P_{ср}$) рассчитывали из объема выборки не менее 30 гранул.

Пористую структуру исследовали методом ртутной порометрии на приборе Porosiger-9300.

Рентгенографический анализ образцов осуществляли на дифрактометре HZG-4 аналогично [1, 2].

РЕЗУЛЬТАТЫ И ИХ ОБСУЖДЕНИЕ

Удельная поверхность

На рис. 1 показано, как изменяется при термообработке $S_{уд}$ модифицированных лантаном и церием образцов относительно удельной поверхности чистого оксида алюминия. Здесь же представлены и абсолютные значения удельной поверхности немодифицированного Al_2O_3 ($S_{Al_2O_3}$). Наиболее значительно $S_{Al_2O_3}$ снижается при тем-

[1] Авторы благодарят И.А. Овсянникову за исследование синтезированных образцов.

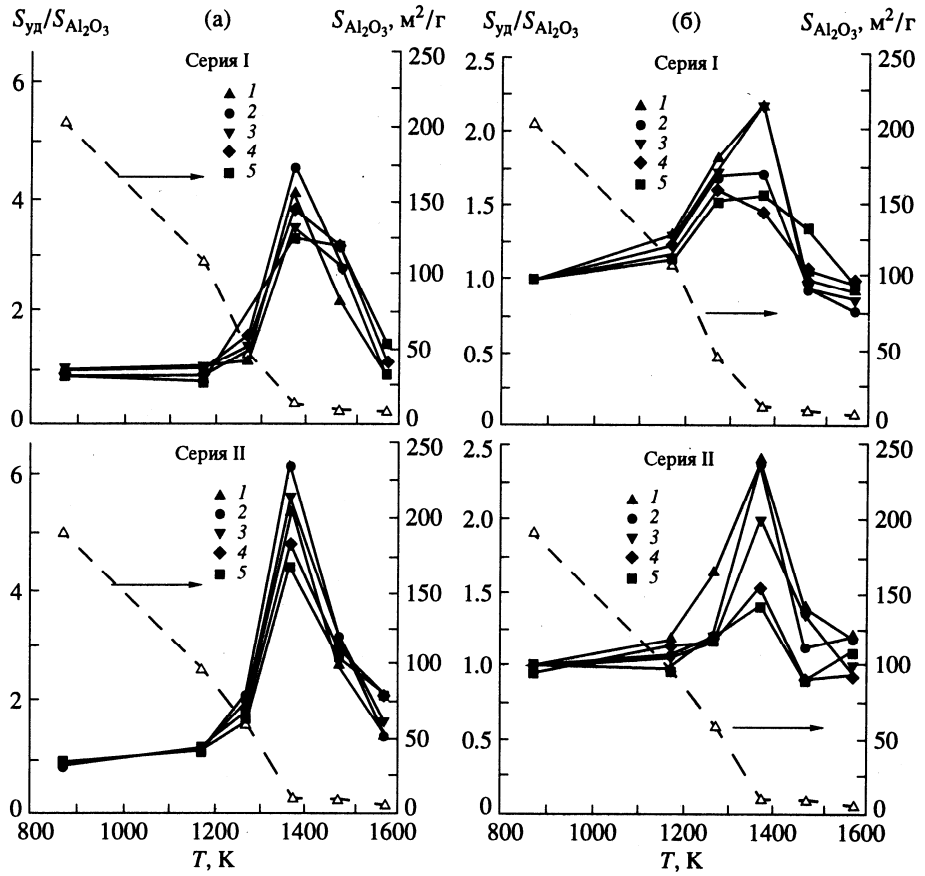

Рис. 1. Зависимости отношения удельной поверхности образцов оксида алюминия серий I и II, модифицированных La_2O_3 (а) и CeO_2 (б) к удельной поверхности "чистого" оксида алюминия от температуры прокаливания при концентрации добавок, вес. %:

1 – 2; *2* – 5; *3* – 8; *4* – 10; *5* – 12. Пунктиром показана зависимость удельной поверхности Al_2O_3 ($S_{Al_2O_3}$) от температуры прокаливания.

пературе ~1373 K. Эффект стабилизации удельной поверхности модифицированных образцов Al_2O_3 сильнее всего проявляется в области температур 1173–1473 K. Так, при температуре прокаливания 1373 K $S_{уд}$ модифицированных лантаном образцов в 3–6 раз (в зависимости от способа приготовления исходного оксида алюминия и количества введенной добавки) превышает $S_{Al_2O_3}$. Эффект стабилизации удельной поверхности наиболее выражен в случае образцов серии II, содержащих 5% La_2O_3 (рис. 1а). Это является результатом эффективного взаимодействия вводимого катиона с носителем с образованием твердого раствора, имеющего структуру соответствующей формы оксида алюминия.

Удельная поверхность образцов, модифицированных церием, независимо от способа приготовления Al_2O_3 в области температур 1173–1473 K превышает $S_{Al_2O_3}$ только в 1.2–2.2 раза (рис. 1б). Из рис. 1 видно, что лантан оказывает более сильное стабилизирующее действие на удельную поверхность оксида алюминия, чем церий.

Следует отметить, что при $T \geq 1473$ K в системе La_2O_3–Al_2O_3 эффект стабилизации $S_{уд}$ с ростом содержания La_2O_3 более выражен, чем в системе CeO_2–Al_2O_3. Это связано с присутствием в ней гексаалюмината лантана $La_2O_3 \cdot 11Al_2O_3$, содержание которого увеличивается с ростом концентрации La_2O_3 и который, как известно [4], имеет слоистую структуру, способствующую сохранению при высоких температурах большой $S_{уд}$. В системе CeO_2–Al_2O_3 гексаалюминаты церия не обнаружены [2].

Пористая структура

Изменения пористой структуры образцов обеих серий при введении модифицирующего катиона были изучены при температурах 873 и 1373 K

Влияние модифицирующих добавок (5 вес. %) и температуры прокаливания на текстуру оксида алюминия

Добавка	823 K			1373 K		
	V_Σ, см^3/г	$r_{эф}$, Å	$S_{уд}$, м^2/г	V_Σ, см^3/г	$r_{эф}$, Å	$S_{уд}$, м^2/г
			Серия I			
Нет	0.29	53	205	0.28	360	11
La_2O_3	0.32	54	185	0.38	100	56
CeO_2	0.30	60	185	0.30	280	25
			Серия II			
Нет	0.60	66	195	0.40	590	11
La_2O_3	0.52	64	170	0.60	150	65
CeO_2	0.52	65	185	0.52	460	20

(таблица). Как видно, при 873 K пористая структура модифицированных образцов практически не отличается от структуры чистого Al_2O_3. При более высокой температуре прокаливания образцы с лантаном и церием ведут себя по-разному. Так, объем пор (V_Σ) образцов CeO_2–Al_2O_3 как и "чистого" Al_2O_3, практически не изменяется при 1373 K по сравнению с 823 K. Средний радиус пор ($r_{эф}$) у этих образцов при 1373 K становится в ~1.3 раза меньше, чем у "чистого" Al_2O_3.

В системе La_2O_3–Al_2O_3 при 1373 K наблюдается увеличение V_Σ по сравнению с "чистым" Al_2O_3. При этом эффективный радиус пор у образцов с лантаном становится в три раза меньше, чем у образцов CeO_2–Al_2O_3. Следовательно, происходит торможение спекания, причём более эффективное в системе La_2O_3–Al_2O_3.

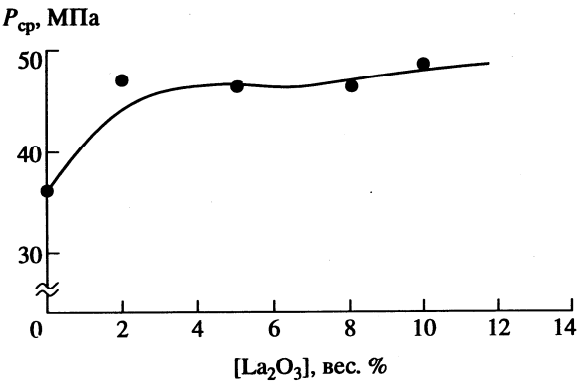

Рис. 2. Зависимость прочности гранул оксида алюминия от содержания La_2O_3 в носителе (образцы серии I) при 873 K.

Механическая прочность гранул

Поскольку механическая прочность и механическая стабильность гранул являются важнейшими характеристиками катализаторов, работающих в кипящем слое, нами специально было рассмотрено влияние модифицирующих добавок на прочность гранул Al_2O_3 и ее изменение в ходе термической обработки.

При введении 2 вес. % La_2O_3 прочность ($P_{ср}$) образцов при 823 K возрастает, а при дальнейшем увеличении концентрации модифицирующей добавки практически не меняется (рис. 2). Аналогичная зависимость наблюдается и в случае промотирования церием. Возможно, это связано с увеличением прочности единичных контактов между первичными частицами оксида алюминия вследствие образования высокодисперсных (рентгеноаморфных) соединений лантана (и, соответственно, церия) с оксидом алюминия [1, 2] и "цементирования" этими соединениями контактов между частицами. Известно [5], что увеличение прочности единичных контактов способствует общему увеличению прочности гранулированных материалов.

На рис. 3 показано, как изменяется в зависимости от температуры прокаливания механическая прочность гранул "чистого" оксида алюминия и промотированных лантаном и церием образцов серии I. При T < 1173 K исследованные образцы практически не различаются между собой. С повышением температуры до 1373 K происходит резкое увеличение $P_{ср}$ для гранул "чистого" оксида алюминия и церийсодержащих образцов. Наибольший прирост прочности наблюдается в системе 5 вес. % CeO_2–Al_2O_3. Образцы, содержащие 5 вес. % La_2O_3, увеличивают свою прочность только при $T \geq$ 1473 K, и по этому показателю образцы не отличаются от "чистого" оксида алюминия. Очевидно, что с точки зрения механической прочности оксид церия является более эффективной добавкой, чем оксид лантана. По-видимому, изменение прочности модифицированных образцов связано с фазовым составом исследованных систем. Согласно данным [2], и как было отмечено выше, в модифицированных церием образцах при T < 1173 K кроме фаз Al_2O_3 и CeO_2 присутствует высокодисперсное церийсодержащее соединение, которое не фиксируется рентгенографически, по-видимому, из-за своей очень низкой концентрации. При повышении температуры оно, вероятно, образует прочные фазовые контакты с частицами оксида алюминия. Поскольку механическая прочность образцов не зависит от содержания CeO_2 во всей исследованной области температур, то можно предположить, что количество этого рентгеноаморфного соединения во всех образцах одинаково, независимо от концентрации CeO_2. Следовательно, можно полагать, что улуч-

шение механической прочности гранул связано не с увеличением числа контактов, а только с упрочнением единичных контактов вследствие взаимодействия первичных частиц Al_2O_3 с добавкой.

В системе La_2O_3–Al_2O_3 [1] при $T > 1473$ K образуются α-Al_2O_3 и гексаалюминат лантана, что, возможно, не обеспечивает сохранения высокой прочности единичных контактов.

Изменение структурно-механических свойств носителей при длительной термообработке

Нами было проведено исследование изменения $S_{уд}$ образцов La_2O_3–Al_2O_3 и CeO_2–Al_2O_3 с оптимальным содержанием добавки (5% La_2O_3 и 2% CeO_2) в условиях длительной термообработки при 1273 K (рис. 4).

Наиболее резкое изменение $S_{уд}$ всех образцов наблюдается в первые 5 ч прокаливания. Увеличение времени термообработки приводит к дальнейшему, хотя и не столь резкому, снижению удельной поверхности немодифицированных образцов, а $S_{уд}$ образца серии II, содержащего лантан, практически не меняется.

После 30 ч термообработки наибольшую удельную поверхность сохраняют образцы с лантаном, приготовленные из оксида алюминия, полученного на основе продукта терморазложения гиббсита (серия II).

Что касается образцов, содержащих церий, то способ получения исходного оксида алюминия не влияет на эффект стабилизации их поверхности в условиях длительной (30 ч) термообработки при 1273 K.

Уменьшение $S_{уд}$ образцов при длительном прокаливании связано с изменением фазового состава. В первые часы прокаливания при 1273 K образуется δ-Al_2O_3, и это сопровождается изменением морфологии частиц и их компоновки. После 2 ч термообработки в чистом оксиде серии I обнаруживаются только следы α-Al_2O_3, а в образце серии II его образуется до 50% [1, 2]. Дальнейшее увеличение времени прокаливания чистого оксида алюминия способствует завершению фазового перехода в α-Al_2O_3, что также способствует снижению удельной поверхности. Если в образцах серии II этот переход завершается после 20 ч термообработки, то в образцах серии II – после 10 ч. Во всех образцах, модифицированных лантаном, с увеличением времени термообработки растет количество δ-фазы, а следы α-Al_2O_3 появляются только после 30 ч прокаливания. В образцах, промотированных церием, содержание δ-фазы также растет, однако следы α-Al_2O_3 появляются уже после 20 (серия I) или даже 10 ч (серия II) прокаливания. При этом существенного увеличения дисперсности частиц CeO_2 не наблюдается.

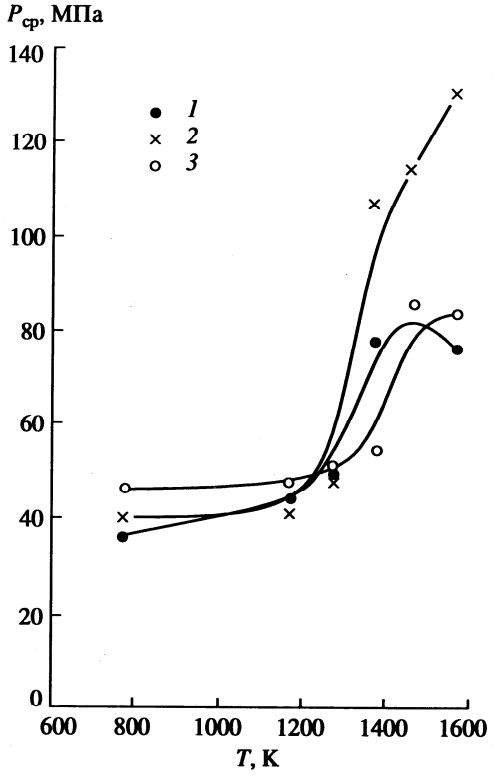

Рис. 3. Влияние температуры прокаливания на механическую прочность образцов серии I: *1* – чистый Al_2O_3; *2* – 5% CeO_2/Al_2O_3; *3* – 5% La_2O_3/Al_2O_3.

Важно также отметить, что в ходе длительной термообработки (при 1273 K) прочность модифицированных образцов не снижалась, что свидетельствует об их механической стабильности. Так, прочность гранул лантансодержащих образцов серий I и II после 30 ч термообработки при 1273 K составляла 58.5 и 33.0 МПа соответственно, а прочность гранул церийсодержащих образцов тех же серий – 54 и 30 МПа.

Полученные данные хорошо согласуются с результатами рентгенографического исследования систем La_2O_3–Al_2O_3 и CeO_2–Al_2O_3 [1, 2]. Так, при введении лантана в γ-оксид алюминия образуется твердый раствор оксида лантана на базе структуры γ-Al_2O_3, в котором ионы алюминия частично замещены ионами лантана. Это создает дополнительные ограничения на перестройку структуры с образованием δ-, θ- и α-Al_2O_3. С указанными процессами связано сохранение большой удельной поверхности и улучшение прочностных характеристик модифицированных образцов при высоких температурах.

При модифицировании оксида алюминия оксидом церия, в отличие от модифицирования оксидом лантана, не отмечено значительного эф-

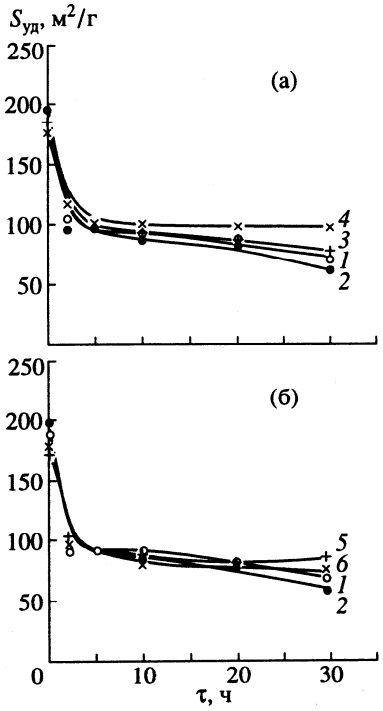

Рис. 4. Влияние времени термообработки образцов 5% La_2O_3/Al_2O_3 (а) и 2% CeO_2/Al_2O_3 (б) при 1273 K на их удельную поверхность: *1* – Al_2O_3 (серия I); *2* – Al_2O_3 (серия II); *3* – La_2O_3/Al_2O_3 (серия I); *4* – La_2O_3/Al_2O_3 (серия II); *5* – CeO_2/Al_2O_3 (серия I); *6* – CeO_2/Al_2O_3 (серия II).

фекта стабилизации дисперсной структуры Al_2O_3. Это, как показано ранее [2], объясняется ограниченным взаимодействием оксида алюминия и ионов церия.

Модифицирование оксида алюминия ионами La и Ce улучшает термомеханическую стабильность образцов, которую мы характеризовали коэффициентом термомеханической стабильности (**КТС**), определяемым как отношение минимальной прочности (P_{min}) гранул, прокаленных при заданной температуре, к P_{min} при 873 K [6]. Для всех образцов КТС > 3, и этот показатель не снижался в процессе длительной термообработки. Отметим, что для чистого Al_2O_3 КТС ≤ 1 [6].

Полученные результаты подтверждают и дополняют найденные ранее авторами закономерности влияния ионов лантана и церия на полиморфные превращения и связанные с ними изменения структурно-механических свойств оксида алюминия.

Модифицирование оксида алюминия ионами лантана и церия позволяет получать алюмооксидные носители, устойчивые к воздействию высоких температур.

СПИСОК ЛИТЕРАТУРЫ

1. *Шкрабина Р.А., Корябкина Н.А., Ушаков В.А. и др.* // Кинетика и катализ. 1996. Т. 37. № 1. С. 116.
2. *Корябкина Н.А., Шкрабина Р.А., Ушаков В.А. и др.* // Кинетика и катализ. 1996. Т. 37. № 1. С. 124.
3. *Shkrabina R.A., Ismagilov Z.R., Shepeleva M.N. et al.* // Proc. 10 Nat. Symp. New Delhi, 1990. Part II. P. 30.
4. *Masato M., Koichi E., Hiromichi A.* // J. Catal. 1987. V. 103. P. 385.
5. *Ребиндер П.А., Щукин Е.Д., Марголис Л.Я.* // Докл. АН СССР. 1964. Т. 154. № 3. С. 695.
6. *Исмагилов З.Р., Шкрабина Р.А., Шепелева М.Н., Корябкина Н.А.* // Мат. II. Всесоюз. совещ. Новосибирск, 1989. С. 111.

Jointly published by
Elsevier Science B.V., Amsterdam
and Akadémiai Kiadó, Budapest

React.Kinet.Catal.Lett.
Vol. 60, No. 2, 225-231
(1997)

RKCL2852

POROUS ALUMINA AS A SUPPORT FOR CATALYSTS AND MEMBRANES. PREPARATION AND STUDY

Z.R. Ismagilov, R.A. Shkrabina, N.A. Koryabkina, A.A. Kirchanov, H. Veringa* and P. Pex*
Federal Scientific Center,
Boreskov Institute of Catalysis, Novosibirsk 630090, Russia
*ECN, Petten, The Netherlands

Received October 2, 1995
Accepted January 13, 1997

Abstract

Porous alumina as single tubes and as a multihole structure with controlled properties has been prepared. It is shown that the porous structure of these supports can be controlled without burning out additives but by a variation of the ratio between the main alumina component (α-Al_2O_3) and aluminium hydroxide (binder) in the extrusion masses and thermal treatment conditions. Gas permeability measurements have been used for the characterization of the supports. The properties of the ceramics are shown to satisfy the requirements of membrane supports.

Keywords: Ceramic, alumina supports, porous structure, gas permeability, mechanical strength

INTRODUCTION

Alumina is widely used as a material for the preparation of granulated catalyst supports. For many years aluminas are also applied as membrane supports.

The pore structure of support materials is one of the most important characteristics, and the preparation of ceramics with required properties is an important problem to be solved.

0133-1736/97/US$ 12.00.

The known route for obtaining the required pore structure - burning out organic additives - does not allow modification of the pore structure over a wide range and, for instance, to produce high temperature ceramics with pore diameters <1000 Å. In Refs [1,2] we have shown that a variation of the ratio of raw materials (aluminium hydroxide and α-Al_2O_3 powder) in the extrusion masses allows to regulate the pore structure of alumina ceramics prepared from these masses. This work is the continuation of the study reported previously [1,2].

EXPERIMENTAL

We used a screw-type extruder VP-100 with a vacuum system (residual pressure 0.5-0.7 bars, screw rate 35 mm/min) for extrusion of single tubes and multihole structure. Specially constructed dies allowed to produce single tubes (ST) and a multihole structure (MHS) with the following sizes:

for ST - outer diameter 4-5 mm, inner diameter 1.5-2.0 mm;

for MHS - outer diameter 50 mm, inner diameter of a channel 1.0-1.5 mm; wall thickness 1.0-1.5 mm.

Single tubes were dried at room temperature for 24 h using a rolling table. Samples with the multihole structure were dried at room temperature for 24 h in air-isolated equipment in static conditions. Both types of dried samples were sintered under the regime worked out earlier [2] :

$$550°C, 8\ h \longrightarrow 800°C, 2\ h \longrightarrow 1000°C, 2\ h \longrightarrow 1200°C, 2\ h.$$

The heating rate was constant (100°C/h).

Nitrogen desorption measurements were used to determine the specific surface area (S_{BET}).

Mercury porosimetry was used to study the porous structure of ceramics (total volume of pores, V_{tot}, average pore diameter, D_{av}).

Gas permeability (G/P) and defectness of ceramics were measured at different pressures by the method and equipment described in Refs [3-5]. The scheme of the installation for the G/P measurement is shown in Fig. 1.

Mechanical strength (forming side, P_{av}) was determined by crushing an individual single tube (length *ca.* 10 mm) or a fragment of the multihole structure (size 10x10 mm) between two parallel plates in static conditions. The P_{av} value was calculated as the ratio of the load-stress to the section of the area tubes (wall thickness x length) or that of the multihole structure (length x width).

Photographs of the ceramic samples (as single tubes and the multihole structure) are presented in Fig. 2.

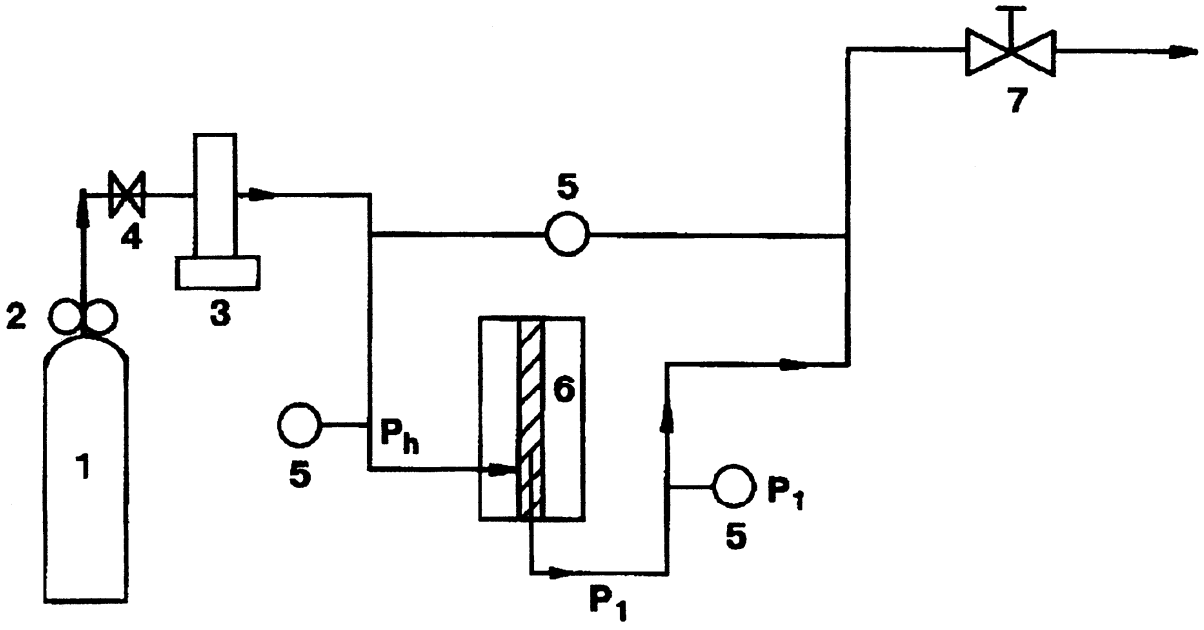

Fig. 1. Scheme of the installation for gas permeability measurements. 1. Nitrogen cylinder, 2. Pressure reducer valve, 3. Flow controller, 4. Flow regulating valve, 5. Pressure transducers, 6. Permeation cell, 7. Valve

RESULTS AND DISCUSSION

The alumina ceramics prepared were applied as membrane supports for the gas separation. It is known that these ceramic supports should have well-defined properties. For our work, the supports should have the following properties: porosity 40-50%; pore diameter 0.1-0.2 μm with a monomodal distribution of pores; size of defects <0.4 μm; permeability $>10^{-5}$ mol/m^2 s Pa.

On the basis of the results obtained earlier [1,2], the following compositions of the extrusion masses were used for the preparation of ceramics with a required pore structure:

Single tubes:

32 wt.% aluminium hydroxide (binder) + 44 wt.% α-Al_2O_3 (dense) + 24 wt.% H_2O.

Multihole structure:

27 wt.% aluminium hydroxide (binder) + 37 wt.% α-Al_2O_3 (dense) + 20 wt.% H_2O + 16 wt.% clay.

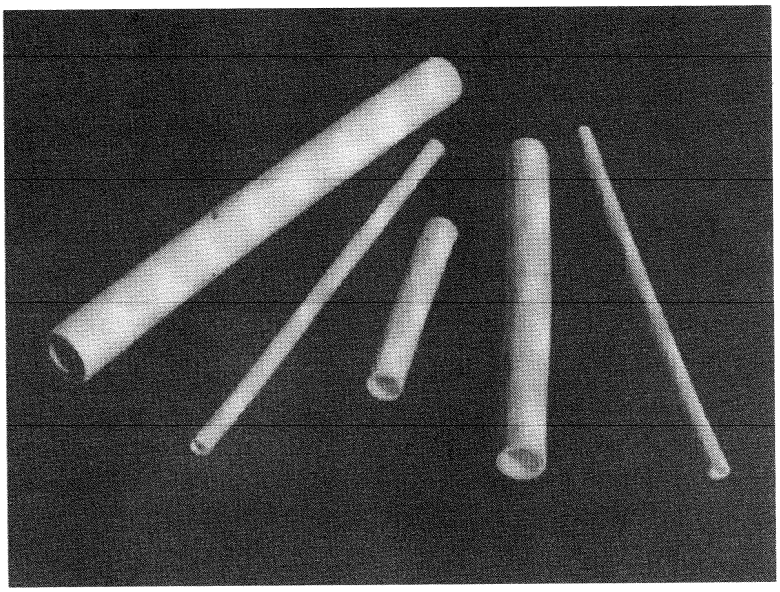

a)

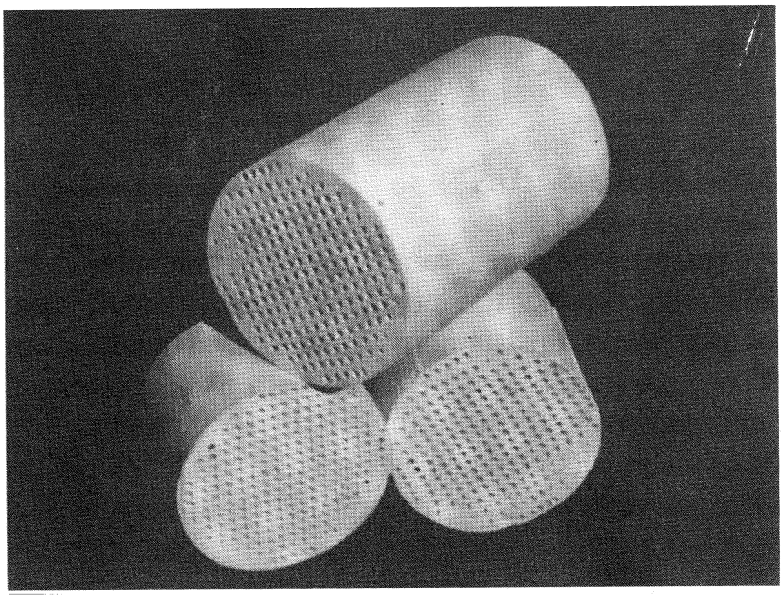

b)

Fig. 2. Photographs of ceramic samples: a) Single tubes b) Multihole structure

Table 1

Properties of ceramic samples (single tubes and multihole structure)

Sample No.	S_{BET} (m^2/g)	V_{tot} (cm^3/g)	D_{av} μm	P_{av} (kg/cm^2)	Porosity (%)	Shape of samples
1	5.3	0.17	0.12	7.5	40	ST
2 (MgO)	9.0	0.16	0.09	13.0	39	ST
3 (MgO)	2.5	0.16	0.12	210	40	MHS

In preliminary experiments it was shown that the addition of clay (<20 wt.%) allowed to improve plastic properties of the extrusion masses without changing the pore structure of the alumina ceramics prepared from these masses.

The properties of the ceramics obtained are presented in Table 1. Samples 2 and 3 contained 2.5 wt.% MgO. As shown earlier [6,7], it provided an increase in the mechanical strength of final ceramics. It can be seen that the pore structure of the samples prepared satisfy the requirements of membrane supports.

Table 2

The G/P value as a reproduction of measurements and preparations

Sample No.	Number of tubes	Pore structure		G/P x10^6 (mol/m^2 s Pa)
		V_{tot}(cm^3/g)	D_{av} (μm)	
1	1	0.28	0.10	15.30
	2			13.60
	3			14.70
2	4	0.18	0.15	21.64
	5			22.90
	6			21.11
3	7	0.17	0.12	21.28
	8			20.64
	9			22.93
	10			22.93
	11			23.52
	12			23.39
4	13	0.19	0.16	22.90
	14			23.39
5	15	0.26	0.09	15.64
	16			15.30

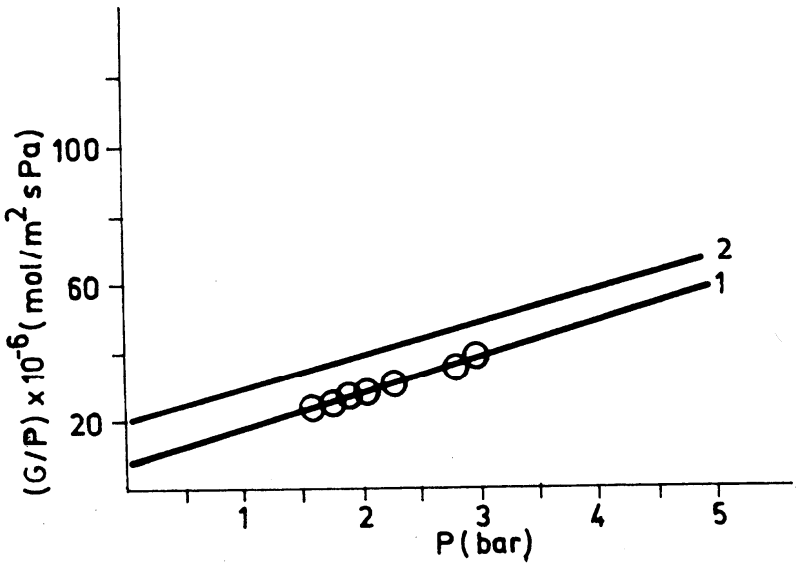

Fig. 3. A typical curve for the dependence of the gas permeability (G/P) on mean pressure. Size of testing tube: length - 96.3 mm, outer diameter 4.4 mm, inner diameter 2.9 mm. 1 - for nitrogen, 2 - for helium

It is known that permeability is one of the main characteristics of membrane supports. Therefore, in this work special attention was paid to the gas permeability measurements. In preliminary experiments the instrumental error and measurement reproducibility were tested by 8-10 measurements of the G/P value for the same tube. The static error was shown to be equal to 6%. Table 2 presents the data on the reproducibility of the G/P value for different tubes. Individual tubes of each sample turned out to have very similar properties.

Figure 3 presents a typical curve for the dependence of the G/P value on mean P (Table 3, sample 4). In this Table main characteristics of membrane supports are listed. Note that we characterized the defectness of the support outer surface by the number and size of defects determined by the bubble point at fixed pressure.

One can see that the samples prepared have no defects on the outer surface and mean G/P values satisfy the requirements of membrane supports [3-5] for gas separation processes.

Table 3

Properties of ceramic tubes

Sample No.	$S_{BET}(m^2/g)$	$V_{tot}(cm^3/g)$	Number of defects (at bubble pressure, bar)	G/P x 10^6 in N_2 (mol/m^2 s Pa)
1 (l=10 cm)	5.3	0.17	absence (<6.9)	21.28
2 (l=10 cm)	6.1	0.22	absence (<5.9)	23.39
3 (l=10 cm)	8.2	0.18	absence (<6.4)	22.93
4 (l=10 cm)	3.4	0.15	absence (7)	17.91

Thus, the results obtained extend the possibilities of the pore structure control compared to the chemical method of the burning out of organics and allow to prepare alumina ceramics with required properties.

Acknowledgement. The work was supported by a grant of NWO in the Netherlands.

REFERENCES

1. R.A. Shkrabina, B. Boneckamp, P. Pex, H. Veringa, Z.R. Ismagilov: *React. Kinet. Catal. Lett.*, **54**, 181 (1995).
2. R.A. Shkrabina, B. Boneckamp, P. Pex, H. Veringa, Z.R. Ismagilov: *React. Kinet. Catal. Lett.*, **54**, 193 (1995).
3. A.G.M. Leenaars: *Thesis: "Preparation, structure and separation characteristics of ceramic alumina membranes"*, Petten, ECN, The Netherlands 1984.
4. R.J. van Vuren, B. Boneckamp, R.I.R. Uhlhorn, K. Keiser, H.J. Veringa, A.I. Burggraaf: *Materials Science Monographs (High Tech. Ceramics)*, p.2235, Elsevier, Amsterdam 1987.
5. V.T. Zaspalis: *Thesis: "Catalytically active ceramic membranes"*, Twente University, The Netherlands 1990.
6. I.A. Ovsyannikova, G.I. Goldenberg, N.A. Koryabkina, R.A. Shkrabina, Z.R. Ismagilov: *Appl. Catal.*, **55**, 75 (1989).
7. N.A. Koryabkina, R.A. Shkrabina, V.A. Ushakov, E.M. Moroz, Z.R.Ismagilov: *Appl.Catal.*, **72**, 63 (1991).

Jointly published by
Elsevier Science B.V., Amsterdam
and Akadémiai Kiadó, Budapest

React.Kinet.Catal.Lett.
Vol. 60, No. 2, 243-250
(1997)

RKCL2850

METAL FOAM SUPPORTED PEROVSKITE CATALYSTS

O.Yu. Podyacheva, A.A. Ketov, Z.R. Ismagilov, V.A. Ushakov, *A. Bos and *H.J. Veringa

Federal Scientific Center, Boreskov Institute of Catalysis,
Novosibirsk 630090, Russia
*ECN, P.O.BOX 1, 1755 ZG Petten, The Netherlands

Received October 2, 1995
Accepted January 13, 1997

Abstract

The impregnation technique and the polymer coating method were applied to synthesize a $LaCoO_3$ perovskite catalyst on a metal foam support. The synthesized catalysts were examined by X-ray diffraction analysis, BET method, scanning electron microscopy. The perovskite phase was characterized by temperature-programmed reduction and diffused reflectance electron spectroscopy. The activity of the catalysts was tested in the methane oxidation reaction.

Keywords: Metal foams, perovskite catalysts, methane combustion

INTRODUCTION

Metal supports for catalysts endow them with useful characteristics which are unattainable for catalysts on ceramic supports. Metal supported catalysts are strong and resistant to high temperatures, and therefore can be applied in high temperature combustion processes for environmentally clean energy production. An important advantage of these catalysts is in their high heat conductivity. This property makes them attractive for endothermic processes, where high heat transfer is required.

It is well known that the most active catalysts for high temperature methane combustion are mixed oxides, preferably perovskites ABO_3. Among numerous combinations of A and B cations the highest level of activity was exhibited by the perovskites with the $LaMnO_3$ and $LaCoO_3$ chemical composition [1].

0133-1736/97/US$ 12.00.

The present work is devoted to the preparation and characterization of $LaCoO_3$ perovskite catalysts supported on Ni and Ni-Cr foam materials.

EXPERIMENTAL

The Ni and Ni-Cr foam supports were synthesized by the powder metal slip casting technique and electrolysis method using procedures described, for example, in Refs [2, 3]. The impregnation technique and the polymer coating method were applied to deposit a $LaCoO_3$ perovskite phase on the support surface. The preliminary washcoating of the metal surface was required in both cases. The impregnation technique was used to support a perovskite phase on the surface of metal foams washcoated with porous alumina. After two impregnation steps, the quantity of the perovskite phase was within the 10 - 12 wt.% interval. The polymer coating method was developed to support the perovskite on the surface of the metal foam covered with a dense alumina layer. In this procedure, the perovskite powder and a polymer as a binder were used [4]. The massive $LaCoO_3$ perovskite powder was prepared by the co-precipitation technique. The supported perovskite catalysts contained about 10-20 wt.% of the perovskite phase.

The catalysts synthesized were characterized by XRD analysis, BET method and scanning electron microscopy. The activity of the catalysts was tested in methane oxidation using a flow-circulating system. The reaction mixture was 1% CH_4 in air. The perovskite phase was characterized by temperature-programmed reduction (TPR) and diffuse reflectance electron spectroscopy (DRES).

RESULTS AND DISCUSSION

High mechanical strength and thermal stability are the main requirements to metal foam materials to be used as catalyst supports for high temperature combustion processes. Ni and Ni-Cr foam supports were synthesized by the combination of powder metal slip casting and electrolysis methods to increase the mechanical strength of the support material. Figure 1 demonstrates the Ni-Cr foam support prepared in a sectional view. The metal foam consists of two different types of layers: a porous material formed due to burning of the polymer matrix, and a dense one deposited by electrolysis. SEM revealed that the external dense layer also contained a certain amount of pores. The metal foam samples were impregnated with a $NiCr_2O_7$ solution to remove these pores. SEM showed that when treated, the surface became smooth and did not contain any pores. The mechanical strength and thermal stability of the metal foams after the procedure

happened to be sufficient to use this material as a catalyst support for a high temperature combustion process.

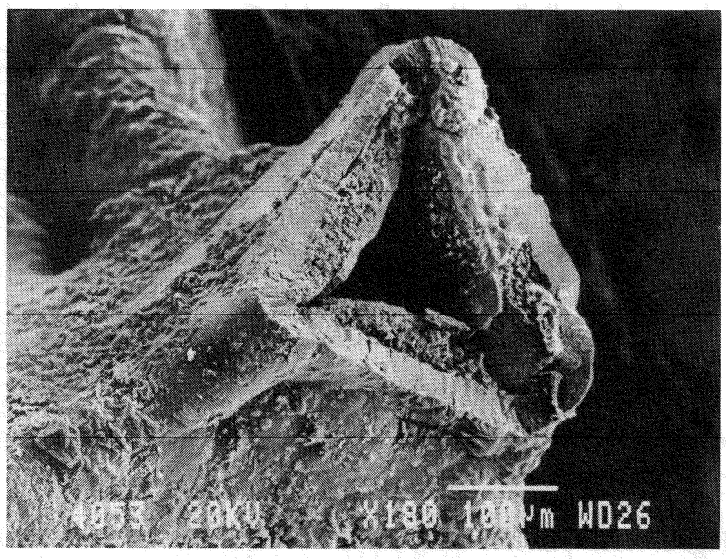

Fig.1. Scanning electron micrograph of the Ni-Cr foam (in a sectional view)

XRD analysis showed the formation of the perovskite phase in catalysts synthesized both by the impregnation technique and by the polymer coating method. XRD patterns of $LaCoO_3$/Ni synthesized by the polymer coating method calcined at different temperatures are given in Fig.2. These diffractograms show that only the perovskite phase is detected. The content of other phases that can be formed during the coating procedure is below the detection limit. The perovskite phase did not change with the increase of the calcination temperature up to 1000°C.

Specific surface area of the supported perovskite catalysts was about 2-3 m^2/g, whereas that of the massive $LaCoO_3$ catalyst was equal to 10 m^2/g.

Data on the activity of the synthesized catalysts in methane oxidation are presented in Fig.3. It is obvious that the activity of massive and supported catalysts referred to the quantity of perovskite phase are comparable. However, it is necessary to note that in the case of supported perovskite catalyst, we have a catalyst of complex geometry and high mechanical strength. These advantages of perovskite catalysts supported on metal foams compared to massive ones allow one to utilize them in a high temperature combustion process with high gas dynamic flows.

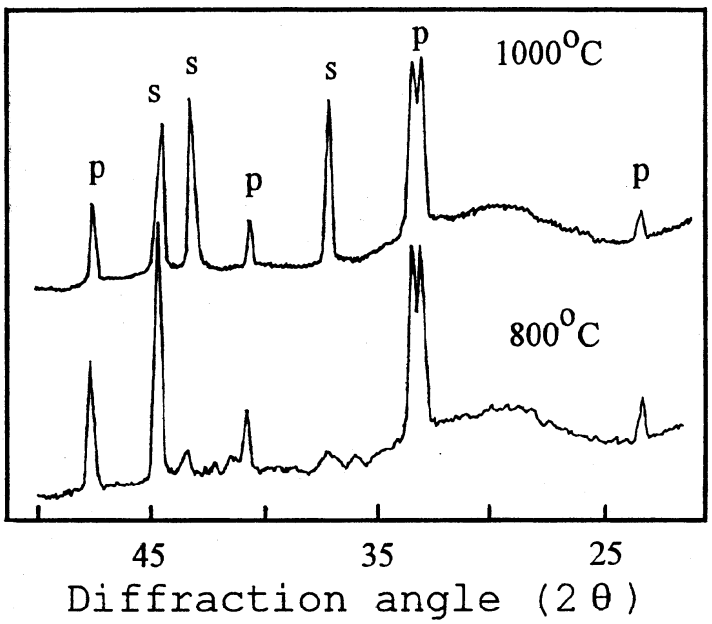

Fig. 2. XRD patterns of $LaCoO_3$/Ni calcined at 800 and 1000°C

TPR experiments were performed to characterize the perovskite phase supported on the metal foam material. The reduction mixture was 10% H_2 in Ar, flow rate - 40 mL/min, heating rate - 10°C/min. The TPR spectrum of the unsupported $LaCoO_3$ catalyst shows two forms of absorption: a low temperature one and a high temperature one (Fig. 4). The ratio between them is approximately 1. The TPR spectra of the supported perovskite catalysts also have the low temperature and high temperature forms of absorption (Fig. 4), but the ratio of these two forms depends on the preparation method of the perovskite phase. The perovskite powder is used in the polymer coating method, therefore, the TPR spectrum of the supported catalyst does not considerably differ from that of the unsupported one. On the contrary, the TPR spectra of supported perovskite catalysts prepared by the impregnation technique are considerably different. The high temperature form of absorption becomes the main component in the TPR spectrum. Thus, the TPR data show that the preparation method influences the properties of the perovskite phase in supported perovskite catalysts.

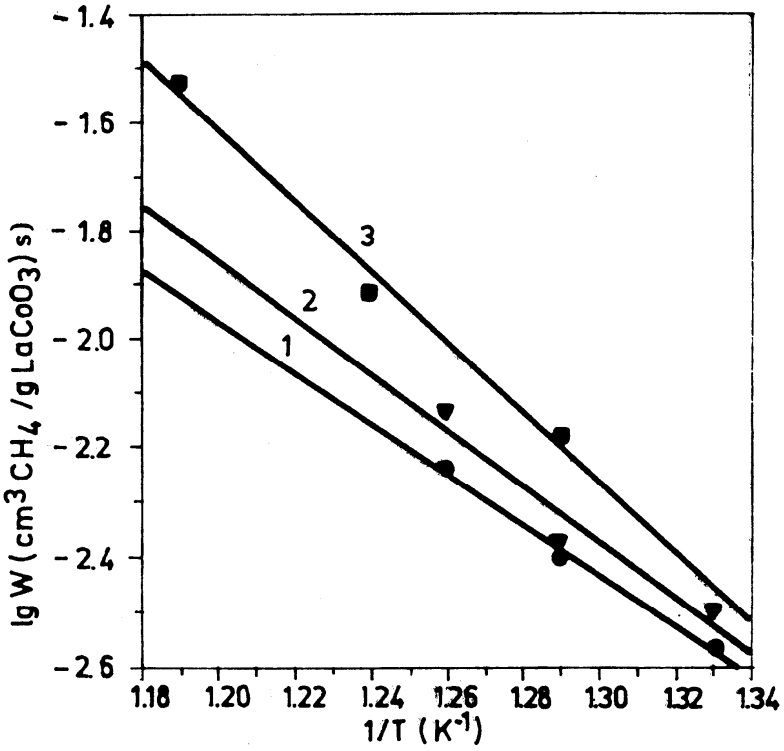

Fig. 3. Temperature dependence of methane oxidation on: 1 - $LaCoO_3$, massive, 2 - 19% $LaCoO_3$/Ni (polymer coating), 3 - 13% $LaCoO_3$/Ni (impregnation technique)

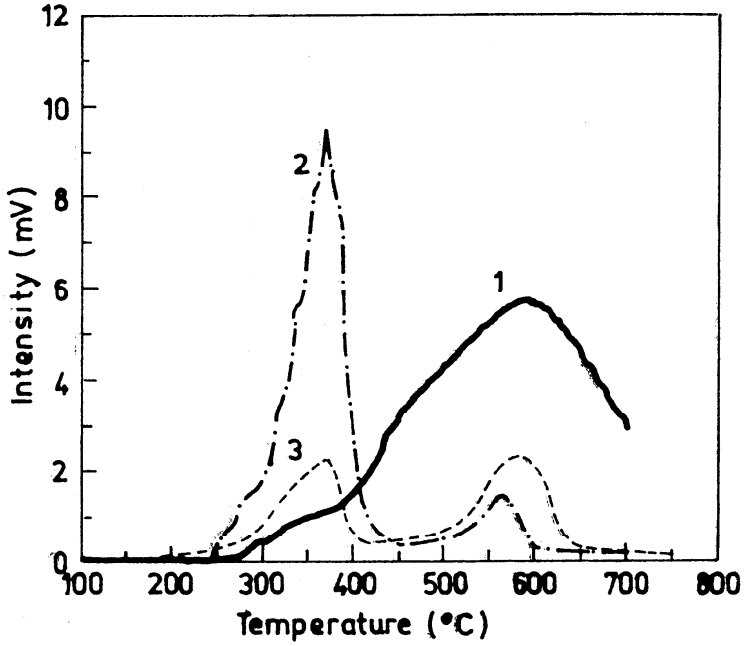

Fig. 4. TPR spectra of: 1 - $LaCoO_3$/Ni (impregnation technique); 2 - $LaCoO_3$/Ni (polymer coating); 3 - $LaCoO_3$

This suggestion was confirmed by diffuse reflectance electron spectroscopy. Massive and supported perovskite catalysts were examined by DRES. The following catalysts were used: massive $LaCoO_3$, 10% $LaCoO_3$/Ni (impregnation technique), 12%$LaCoO_3$/Ni (polymer coating). The catalysts were calcined at 800 and 1000°C. The spectra of the supported catalysts were recordered against the Ni support as reference and, therefore, the spectra consisted of bands corresponding to the perovskite phase only.

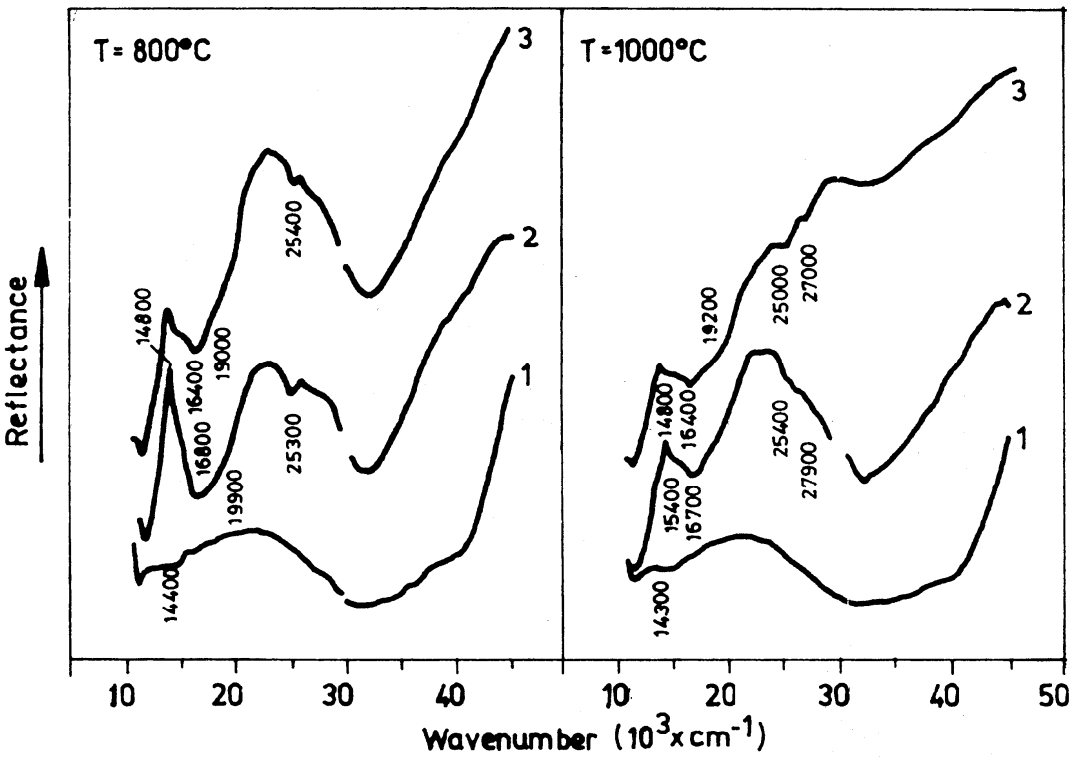

Fig. 5. DRES spectra of perovskite catalysts calcined at 800 and 1000°C: 1 - $LaCoO_3$; 2 - $LaCoO_3$/Ni (impregnation technique); 3 - $LaCoO_3$/Ni (polymer coating)

The DRES spectrum of massive $LaCoO_3$ calcined at 800 and 1000°C consists of two bands: a band at 14300-14400 cm^{-1} corresponding to Co^{2+} in tetrahedral coordination and a weak band at 23000-26000 cm^{-1} corresponding to Co^{3+} in octahedral coordination (Fig. 5). The spectrum of 10% $LaCoO_3$/Ni (impregnation technique), calcined at 800°C consists of the following reflectance bands: 16800, 19900, 25300 cm^{-1}. After the calcination at 1000°C, the DRES spectrum includes a shoulder at 15400 and bands at 16700, 25400 and 27900 cm^{-1}. The bands at

16700 and 16800 cm^{-1} can be ascribed to Co^{2+}_{Td} in coordination deformed by the crystal lattice field of the support. The shoulder at 15400 cm^{-1} may belong to Co^{2+}_{Td} in coordination without deformation. The bands at 25300, 25400, 27900 cm^{-1} correspond to Co^{3+}_{Oh}. There are no great changes in the spectra of the catalysts with the increase of calcination temperature, except for the band at 15400 cm^{-1}, which becomes more significant in the catalyst calcined at 1000°C. The catalyst calcined at 800°C contains a band at 19900 cm^{-1}, which can be ascribed to $Co(H_2O)_6^{2+}$. The spectrum of 12% $LaCoO_3$/Ni (polymer coating), calcined at 800°C consists of bands at 14800, 16400, 19000, 25400 cm^{-1}, whereas the spectrum of the catalyst calcined at 1000°C contains bands at 14800, 16400, 19200, 25000 and 27000 cm^{-1}. The 14800 cm^{-1} band may belong to Co^{2+}_{Td}, the 16400 cm^{-1} band to Co^{2+} in tetrahedral coordination deformed by crystal lattice field of support, the 19000 and 19200 cm^{-1} bands - to $Co(H_2O)_6^{2+}$ and the bands at 25000, 25400 and 27000 cm^{-1} - to Co^{3+}_{Oh}. The rise of the calcination temperature leads to an increase in the quantity of Co^{3+} in octahedral vacancies.

Comparing the spectra of the massive perovskite catalyst with those of the perovskite catalysts supported by different techniques, the following conclusions can be made.

a) The 14300 cm^{-1} band corresponding to Co^{2+} in tetrahedral coordination disappears from the spectrum of the supported perovskite catalyst synthesized by the impregnation technique, whereas it is present in the spectrum of that prepared by the polymer coating method. This band is shifted to higher frequencies in the spectrum of the perovskite catalyst supported by the polymer coating method due to the influence of the crystal field of the support. Therefore, it can be supposed that the interaction between the active component and support is much greater in the supported perovskite catalyst synthesized by the impregnation technique than that in the catalyst synthesized by the polymer coating method.

b) The supporting of $LaCoO_3$ on the metal foam support leads to an increase in the quantity of Co^{3+} in octahedral coordination. The rise of the calcination temperature causes changes in the quantity of Co^{3+}_{Oh}: it increases for 12% $LaCoO_3$/Ni (polymer coating) and decreases for 10% $LaCoO_3$/Ni (impregnation technique).

Thus, in this work it is shown that the preparation routes proposed (the impregnation technique and the polymer coating method) can be used to synthesize perovskite catalysts supported on metal foam materials. The method of the active component deposition influences the properties of the perovskite phase. The catalysts synthesized combine the gas dynamic characteristics of foam supports and the catalytic activity of massive perovskites. The catalysts developed can be recommended for the application in a high temperature combustion process with high gas dynamic flows.

Acknowledgement. This research was subsidized by a grant of the Dutch Organization for Scientific Research NWO in a scientific program between the Netherlands and Russian Federation.

REFERENCES

1. H. Arai, T. Yamada, K. Eguchi, T. Seiyama: *Appl. Catal.*, **26**, 265 (1986).
2. GB Patent No. 2070957, B 01 J 35/04, 16.09.1981.
3. GB Patent No. 1557485, C 23 J 7/00, 12.12.1979.
4. Z.R. Ismagilov, O.Yu. Podyacheva, A.A. Ketov, A. Bos, H.J. Veringa: *Proc. MRS Meeting* 1994, Boston, USA. **368**, 321 (1995).

ELSEVIER

Catalysis Today 47 (1999) 51–71

CATALYSIS TODAY

New technology for production of spherical alumina supports for fluidized bed combustion

Z.R. Ismagilov*, R.A. Shkrabina, N.A. Koryabkina

Boreskov Institute of Catalysis, Pr.Ak.Lavrentieva, 5, Novosibirsk 630090, Russian Federation

A stract

Fluidized bed catalytic combustion has proved to be very promising for industrial application. The milestone problem is the development of support and catalyst with a high mechanical and thermal stability. We have developed a new technology for production of alumina supports with desired spherical shape, texture and structure. In this paper several pathways to produce aluminum hydroxide of a pseudoboehmite structure including conventional and new technologies are discussed. Properties of spherical granules depend on the method of granulation and most attention has been paid to development and optimization of hydrocarbon–ammonia molding to produce uniform alumina spheres. Several methods to estimate mechanical strength of spherical aluminas are applied to evaluate mechanical durability of prepared catalysts in a fluidized bed. Optimization of high quality spheres production focused on study of the effect of initial hydroxide properties and molding conditions on properties of the final product. Modification of spherical alumina with oxides of Mg, Ce, La and Si proved to be effective to substantially improve the mechanical and thermal stability. This effect is most pronounced when pairs of these dopes are introduced simultaneously.

Keywords: Aluminum hydroxide; Pseudoboehmite; Gibbsite amorphization; Spherical alumina; Fluidized bed; Granulation; Hydrocarbon–ammonia molding; Mechanical strength; Thermal stability; Modification by Mg, La, Ce, Si; Double modification

1. Introduction

It is known [1–6] that the properties of the initial hydroxide determine not only the type of aluminas, but also their thermal stability. One should consider this fact when choosing an appropriate oxide as a catalyst support. The transformation routes show that χ-Al_2O_3 exhibits the lowest thermal stability. The most widely used industrial support is γ-Al_2O_3 obtained from pseudoboehmite because:

- it is quite easy to control its properties at the preparation stages;
- this hydroxide can react with acids yielding pastes suitable for molding.

Below we shall concentrate in more detail on the problems in the production of pseudoboehmite and γ-Al_2O_3 with desired properties.

Catalytic oxidation, including the catalytic combustion of fuels, is one of the main directions of R D at the Institute of Catalysis. Combustion of fuel–air mixtures that are close to stoichiometry is a highly exothermic process, and we proposed to use fluidized

*Corresponding author.

0920-5861/99/$ – see front matter
PII: S0920-5861(98)00283-1

bed catalytic reactors [7–10], the so-called catalytic heat generators (CHGs).

Besides, CHG used for the fuel combustion imposes severe demands on the catalyst, which should retain its activity and resistance to attrition in the fluidized bed where local thermal shocks occur. Apparently, the properties of the catalyst are determined by those of the support (its mechanical strength and thermal stability). We have formulated the following demands on the catalysts and supports to be used in the process [10–12]:

- Support granules should have a regular spherical shape and be 1–3 mm in size with a narrow particle size distribution (1.0–1.4, 1.6–2.0, 2.0–2.5 mm, etc.) to avoid catalyst losses due to mechanical attrition and uptake caused by the non-uniform particle size distribution.
- Support and catalyst granules should be strong enough to avoid cracking during the operation. The average strength of spherical granules should not be less than 18 MPa.
- Support (and catalyst) should retain their key properties during the operation when local overheating up to 1000°C occurs on the catalyst granules.

Taking all these requirements into account [10,12] we have concentrated on the development of spherical supports for CHG catalysts on the basis of γ-Al_2O_3.

2. Pathwa s to produce aluminum h droxide of a pseudo oehmite structure

It is known [1–6] that γ-alumina is the dehydration product of aluminum monohydrate with a boehmite or pseudoboehmite structure. Pseudoboehmite differs from boehmite by having additional water molecules inserted into the interlayer space roughening the structure [1]. Monohydrate with primary particles smaller than 250 Å is a highly dispersed and chemically active hydroxide. It has a higher specific surface area and can produce soluble basic salts in the reaction with acids. These salts serve as good binders in molding [13]. That is why this highly dispersed hydroxide is used to produce granular γ-Al_2O_3 with desired properties.

2.1. Conventional technologies

A periodic precipitation from solutions of sodium aluminate with acids or from solutions of aluminum salts (nitrates, sulfates) with an alkali (NaOH, NH_4OH) is the most industrially recognized method for synthesis of pseudoboehmite aluminum hydroxide. In both cases gibbsite is used as a raw material to prepare the solutions of aluminum compounds. Precipitation conditions (pH, temperature), time and temperature of precipitate aging and other process parameters determine the properties of hydroxide, such as porous structure (at 110°C), dispersity, arrangement of primary particles in secondary aggregates, etc.

Detailed information about the conventional procedure of pseudoboehmite synthesis is given in [1,14].

Regarding the precipitation temperature, we distinguish the so-called ''cold'' (about 20°C) and ''hot'' (about 100°C) precipitation. It will be shown below that the properties of pseudoboehmite hydroxides obtained via the cold and hot precipitation are substantially different. That is why the so-called ''mixed'' pseudoboehmite hydroxides are used in the industry. The hydroxides of the cold and hot precipitation are mixed usually in a ratio of 1:3 to provide better filtering and washing from impurities.

Recently, continuous precipitation methods have been developed. In this case precipitation is conducted in a single flow at 40–50°C followed by aging at 30–35°C [15].

2.2. New technologies

Pseudoboehmite synthesis via gibbsite amorphization and processing has recently become quite popular. There are many amorphization procedures, such as mechanical or mechano-chemical activation [16,17]; pulse heating in a flow of flue gases [18], in a hot air flow [19], or in the fluidized catalyst bed where the heat for amorphization is supplied by catalytic fuel combustion [7–12]. Further processing of this amorphous product yields hydroxide of the pseudoboehmite type.

The process of gibbsite amorphization in CHGs has been developed at BIC and commercialized in Russia [6,7,12]. Fig. 1 shows a schematic view of a CHG. In this reactor heating of powdered gibbsite occurs with a

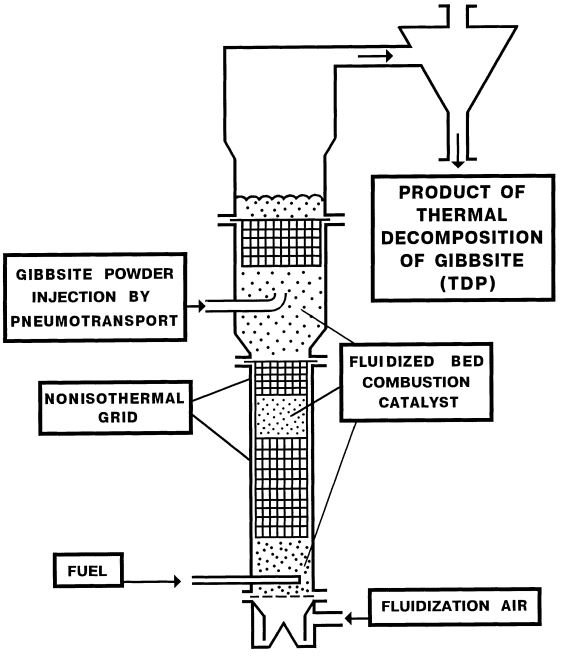

Fig. 1. Scheme of catalytic heat generator for thermal decomposition of gibbsite.

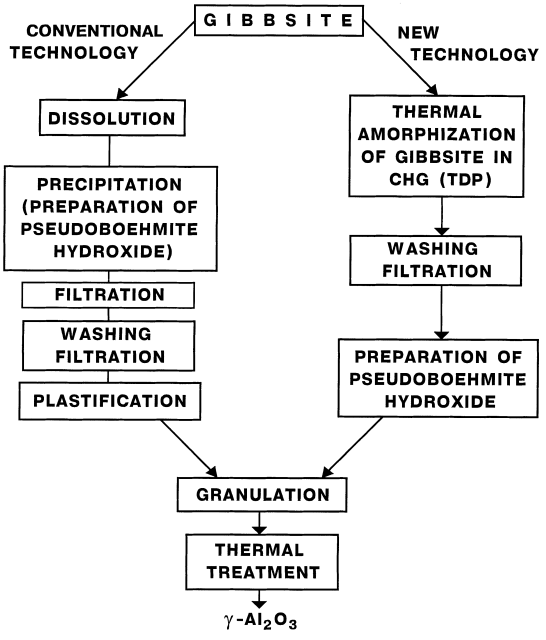

Fig. 2. Scheme of preparation of γ-Al_2O_3.

very short residence time (less then 0.1 s), and gibbsite amorphization occurs simultaneously with its dehydration.

The resulting thermal decomposition product (TDP) of gibbsite has a higher reactivity. It allows us to produce pseudoboehmite hydroxide avoiding conventional stages of gibbsite dissolving and reprecipitation.

Table 1 shows the TDP properties as compared to those of the initial gibbsite.

Pseudoboehmite formation from TDP occurs at 110–120°C in acidic medium (pH∼3–4) as described elsewhere [6,20,21]. The pseudoboehmite content in the final product attains 80–90%, while its dispersity (estimated by the coherent dissipation region, c.d.r.) does not exceed 100 Å.

Fig. 2 is a schematic representation of the pseudoboehmite hydroxide production according to the new CHG technology as compared with the traditional procedure.

Table 1
Main properties of thermal decomposition product (TDP)

Product	S_{BET} (m^2/g) (110°C)	Water content (wt%)	Chemical activity[a] (wt%)
Gibbsite	1	34	∼8
TDP	250	10–13	85

[a]Chemical activity is determined as the amount of Al^{3+} ions transferred to the solution under dissolution in 5 N NaOH at 60°C as described in [6].

2.3. *Properties of pseudoboehmite aluminum hydroxide*

A variety of methods used for the pseudoboehmite hydroxide production leads to different properties of solids which are compared in Table 2.

Note that the morphology of the pseudoboehmite is also different. TEM was used to study the packing of the primary particles into secondary aggregates and the morphology of samples 1–3 [22–24].

Sample 4 obtained via salt precipitation consisted of the roughly packed secondary aggregates formed by fibers made of thin (∼40 Å) needles.

Pseudoboehmite produced by continuous precipitation (sample 5) was an assembly of small needles 20–30 Å closely packed in fibers ∼15 000 Å long. Large

Table 2
Effect of preparation conditions on the properties of pseudoboehmite hydroxide

Preparation procedure	Preparation conditions		H_2O content (wt%)	S_{BET} (m^2/g)	Primary particle size (Å)	Pore volume (cm^3/g) (radius, r, Å)		
	pH	t (°C)				V_Σ	40	40–1000
(1) Reprecipitation (cold precipitation)	8.5	20	85	270	~30	0.572	0.322	0.075 (1000, 0.175)
(2) Reprecipitation (hot precipitation)	8.5	100	59	110	150–180	0.945	0.125	0.235 (1000, 0.585)
(3) Mixed hydroxide (cold:hot=1:1)	–	–	75	220	50, 150	0.460	0.270	0.190
(4) Acid precipitation	7	70	81	290	~40, 120	1.410	0.210	0.790 (1000, 0.410)
(5) Continuous precipitation	8.5	40	80	250	30–40	0.314	0.154	0.058 (1000, 0.102)
(6) Gibbsite thermal decomposition in CHG	3–4	130	75	200	50, 150	0.480	0.270	0.210

shapeless aggregates were scarce (unlike in sample 1). Therefore, morphologically this type of pseudoboehmite is similar to the ordinary one containing needles packed in fibers [1].

Pseudoboehmite produced from TDP (sample 6) was similar by its morphology to that produced by the mixed precipitation method (sample 3). It consisted of needles and almost spherical particles packed in large aggregates as plates larger than 1000 Å.

3. Preparation of spherical granules and methods of propert control

3.1. Methods of granulation

Fig. 3 presents the methods used to produce spherical granules and shows the size of granules produced by each method. Let us consider the peculiarities of different granulation methods.

3.1.1. Rotating pan granulation

A round rotating dish is one of the best known methods to produce spherical granules [25–27]. Oxide or hydroxide powders in the presence of water or binding solutions are fed into the dish and the small rotating particles develop layer by layer into larger spherical granules. Rotation of wet extrudates, whose height and diameter are approximately the same, is also used to produce spherical shape of granules. The latter method does not allow one to produce a narrow particle size distribution, and the particle diameter is as a rule larger than 2 mm. Besides, the strength of the alumina granules does not exceed 10 MPa. These disadvantages make it impossible to use such granules in a moving or fluidized bed.

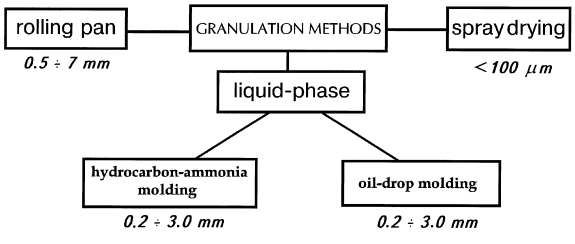

Fig. 3. Granulation methods of spherical alumina production.

3.1.2. Gas phase granulation (spray drying)

This method is a suitable technique to produce microspherical particles not exceeding 0.1 mm. In a spray dryer a hydrogel or a sol (solid content less than 20 wt% [25]) is sprayed through nozzles into a heated zone. Catalytic cracking in moving beds is an example of a process involving a catalyst produced by this procedure. However, these microspherical granules can hardly be used in the fuel combustion at high linear flow rates.

3.1.3. Liquid-phase molding

In this method special die plates with cylindrical holes are used to produce drops of an aluminum hydroxide sol, which then gets into an oil layer at the top of the column and thus assumes a spherical shape due to the surface tension. Further on, these granules congeal during their moving down through the gelating media layer (gel-formation). Two technologies are distinguished depending on the congealing conditions: oil and hydrocarbon–ammonia molding.

3.1.4. Oil molding

In this case a spherically shaped sol (containing, e.g., hexamethylenetetramine (HMTA) [28] or an organic monomer [29] is introduced into a hot oil ($\sim$90°C) [27]. Congealing of the sol occurs either by means of neutralization with ammonia or due to HMTA decomposition (or monomer polymerization). The method provides formation of uniform spherical granules. But the use of the hot oil and the necessity to keep the sol drops for quite a long time (10 min) under such severe conditions to complete the HMTA decomposition or the polymerization are obvious drawbacks.

3.1.5. Hydrocarbon–ammonia molding

The sequence of main stages and a principal schematic view of the hydrocarbon–ammonia molding (HAM) [30,31] is represented in Figs. 4 and 5.

Aluminum hydroxide is treated by an acid-peptizer to obtain a flowing (plastic) sol. Then the sol drops through a die plate into the liquid hydrocarbon layer on top of the molding column, where it assumes a spherical shape due to the surface tension. Further on, spherical sol granules move down into the ammonia solution. The sol transforms to a gel in the coagulant

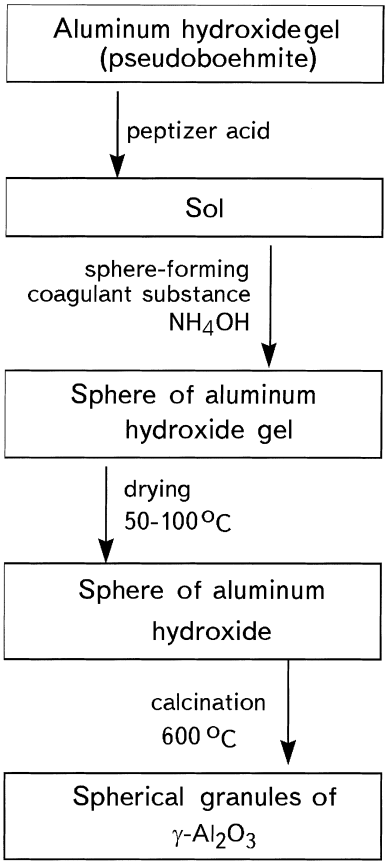

Fig. 4. The main stages of the hydrocarbon–ammonia molding.

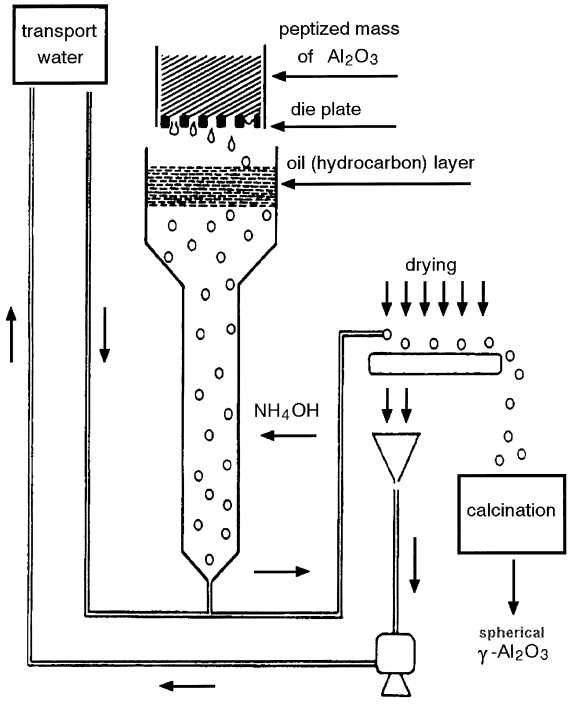

Fig. 5. Principal scheme of the hydrocarbon–ammonia molding technology.

media, and thus granules are congealed. Then the spherical granules of the gel are dried and calcined to produce spherical alumina.

The main physical and chemical processes occurring during all the molding stages, and the effects of technological parameters on the properties of the final spherical alumina bodies are discussed in [7,22–24,30–33].

Colloidal processes occurring at the plasticizing stage, namely how the pseudoboehmite morphology (degree of aggregation) and the amount of acid affect the texture of both hydroxide and spherical alumina, were studied in [23,24,30–33]. Only the hydroxide with contacts due to coagulation between the primary particles appears to disaggregate in the acid. No disaggregation occurs in the hydroxides with contacts due to crystallization. Contacts between the primary particles in the hot-precipitation pseudoboehmite (sample 2, Table 2) belong to the crystallization type due to chemical interactions, and this hydroxide cannot be peptized by acid to produce the sol for HAM [30–33]. In the cold and continuous precipitation hydroxides (samples 1 and 5, Table 2, respectively), the primary particles are bound by electrostatic or van der Waals forces. Both types of contacts are present in the mixed (sample 3, Table 2), acid-precipitation or TDP-originated hydroxides (samples 4 and 6, Table 2, respectively). Therefore, these hydroxides can be used to produce a plastic mass by acid treatment.

The stage of the sphere formation includes two steps:

- spherical granules formation in a hydrophobic medium of a liquid hydrocarbon layer by means of surface tension;
- congealing of the spheres.

There is an optimal height of the hydrophobic liquid layer because the residence time affects the shape and uniformity of granules. The residence time in the coagulant – NH_4OH solution, its concentration and

temperature influence the rate of coagulation; the uniformity of coagulant diffusion into the granule also affects the properties of the spherical alumina produced [30].

The porous structure of the hydroxide, and thus of the resulting alumina, has been shown to depend on the properties of the initial hydroxide. Thus, with the cold-precipitation samples (sample 1, Table 2) the sol formed during peptization looses its macropores, since the large secondary aggregates decompose. The gel after coagulation also does not contain macropores, and therefore, the spatial arrangement of coagulation contacts in the gel is not uniform enough.

The porous structure of the mixed-precipitation hydroxides at the stages of peptization–coagulation depends on the ratio between cold- and hot-precipitation hydroxides in the mixed precipitate. The higher the contribution of the hot-precipitation hydroxide, the less are the changes in the porous structure during peptization–coagulation [23]. Thus the volume of mesopores (300–1000 Å) in samples 3 (Table 2) changed insignificantly.

Samples 5 and 6 (Table 2) had the same behavior during the coagulation process as their analogs in morphology (samples 1 and 3).

In general, HAM allows one to produce spherical γ-Al_2O_3 granules from the aluminum hydroxide of pseudoboehmite structure containing coagulation contacts between the primary particles. But the properties of γ-Al_2O_3, e.g. mechanical strength, and thermal stability, depend on the morphology and the pore structure of the initial hydroxide.

3.2. *Methods to estimate the mechanical strength of granules*

A high mechanical strength is one of the demands on γ-Al_2O_3-supported catalysts for CHG equipment with the fluidized catalyst bed. There is a variety of methods to determine this key parameter and it is important to choose the most appropriate method, which adequately reflects the mechanical impact on the spherical granules in the fluidized bed of the CHG apparatuses.

Apparently, the term ''mechanical strength'' includes different characteristics, such as resistance to crushing and to attrition, resistance to thermal and mechanical shock, etc.

As regards testing procedures, static and dynamic methods are used [34,35]. Methods determining the crushing strength of individual granules between two parallel plates belong to the first type. Attrition and impact loads are usually tested under dynamic conditions.

Taking into account results obtained earlier [35–40], we used the following strength measurements:

- crushing strength;
- attrition strength;
- impact strength.

Fig. 6 shows schematically mechanical stresses on granules in the methods we used to determine the mechanical strength.

Sample strength according to the first method (P, MPa) was calculated as the arithmetic mean from values determined for 30 granules. The minimum and maximum sample strengths were determined as the arithmetic mean for five granules possessing the minimum (P_{min}) or maximum (P_{max}) strength. Since the granules of minimum strength were the first to be crushed, it was important to fix this particular parameter, P_{min}.

Attrition strength determined by the second method was characterized by two attrition rates: V_1 (%/min) at

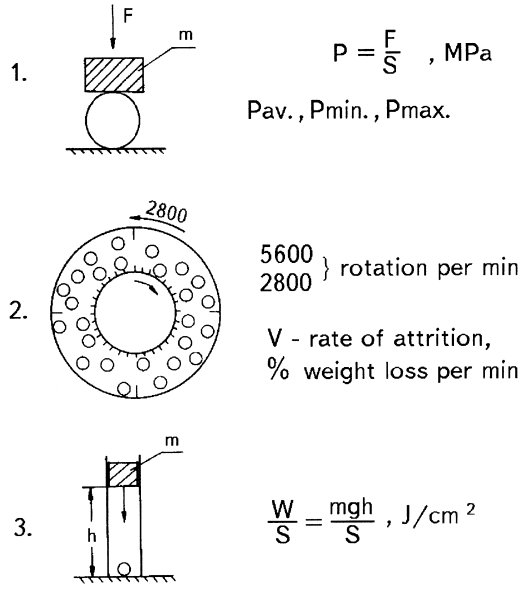

Fig. 6. Basic schemes of mechanical testing.

the initial part, and V_2 (%/min) over the stationary part of the kinetic curve in the coordinates "attrition (%)-versus-time (min)" at fixed attrition degrees (15% or 30%). We adjusted the process so that no crushing of granules occurred.

Impact strength was measured under multiple loads on each granule in a chosen set of 50 pieces to complete crushing at a constant energy $_o=mgh$, where m is the mass of the load falling from height (h). The number of cycles (impacts), K, before crushing of the granule and the number of granules (n) crushed after K impacts were fixed.

Granules of crushing strength below 10 MPa failed to resist loads under the attrition conditions chosen, they crushed during testing. Samples with an average crushing strength over 10 MPa were undergoing pure attrition, its rate being practically constant and equal to 0.22%/min. No crushing is observed and an important demand is formulated: the mechanical strength of granules should exceed 10 MPa to avoid crushing under dynamic conditions.

We used the third method in order to study the impact strength.

Fig. 7 shows the kinetic energy providing a 50% crush of the granules ($_{sp}$, J/cm^2) versus crushing strength (MPa). Apparently, the impact strength is proportional to the crushing strength. Therefore, the stronger the granule under static test conditions (P_{av}), the less fragile it is.

Such a $_{sp}$-versus-P_{av} function is true for aluminas independent of their phase composition. However, we found that δ- and α-Al_2O_3 were more fragile at the same P_{av} than γ-Al_2O_3 (Fig. 8).

The above results show that the stronger the individual granules according to the static method, the better they resist attrition and impact.

3.3. *Effect of initial hydroxide properties on the mechanical strength of the support*

In this section results on the mechanical strength of spherical γ-Al_2O_3 obtained from the pseudoboehmite hydroxides synthesized via various methods will be discussed.

Table 3 presents the main properties of spherical γ-Al_2O_3 obtained from the pseudoboehmites described in Table 2. The numbering of samples corresponds to that of Table 2. Note that as it is not possible to obtain spherical γ-Al_2O_3 via HAM from the hot-precipitation hydroxide (sample 2, Table 2), there are no data for γ-Al_2O_3 from this hydroxide. Pseudoboehmite synthesis from TDP has been described elsewhere [6,7].

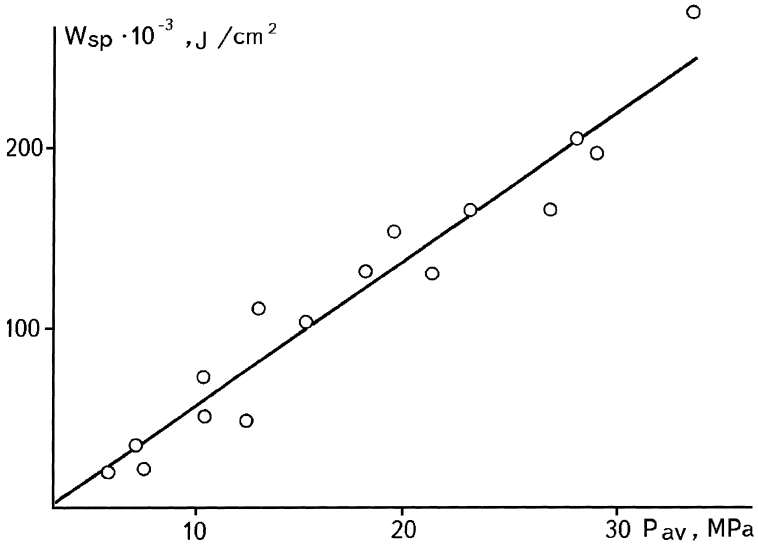

Fig. 7. Critical specific kinetic energy $_{sp}$ as a function of P_{av}.

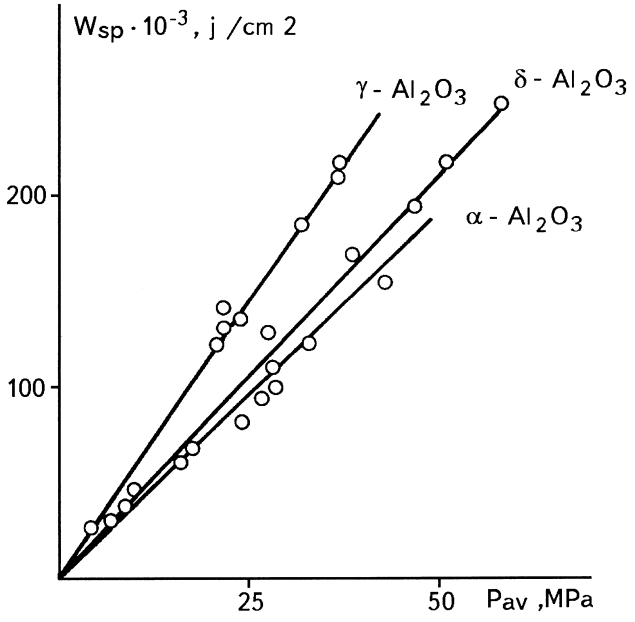

Fig. 8. $_{sp}$- versus-P_{av} for various modifications of alumina.

Table 3 shows that the porous structure and the mechanical strength of the γ-Al_2O_3 are determined by the properties of the parent hydroxide.

Therefore, the character of contacts between the primary particles in aluminum hydroxide of the pseudoboehmite structure not only plays a key role in HAM, but also affects the structure and mechanical properties of γ-Al_2O_3.

The question rises whether one can change the character of the contacts in the aluminum hydroxide with the aim of further use for HAM.

Dispersing is a well known way to change the crystal structure and energy states of solids. Mechanical activation may improve the solid reactivity [41]: surface properties change, partial amorphization occurs, solubility improves, etc. All these processes do not depend on the changes of the particle size.

The influence of the milling intensity on the texture of reprecipitated aluminum hydroxides (AHs), on their properties and on the properties of the resulting Al_2O_3 is reported in [33]. It has been shown that mechanical activation resulted in crushing of the initial aggregates and some changes in the character of binding between the primary particles. So secondary aggregates decomposed by rupture of bonds between primary particles during the peptization

Table 3
Properties of spherical γ-Al_2O_3 (granule diameter 2–3 mm)

No.	Bulk density (g/cm^3)	S_{BET} (m^2/g)	V_{Σ} (cm^3/g)	Volume of pores with radius (r, Å) (cm^3/g)				Mechanical strength P (MPa)		
				40–100	100–1000	1000–10 000	10 000	P_{av}	P_{max}	P_{min}
1	0.86	290	0.40	0.39	0.01	–	–	21	25	14
3	0.67	240	0.44	0.18	0.05	0.21	–	8	9	5
4	0.39	280	1.59	0.78	0.35	0.098	0.37	7	8	5
5	0.75	250	0.36	0.35	0.01	–	–	20	22	16
6	0.51	230	0.63	0.41	0.22	–	7	9	6	
7 (after grind. hydr.)	0.81	230	0.34	0.35	–	–	–	25	46	15
8 (from milled TDP)	0.80	225	0.40	0.40	–	–	–	24	42	14

stage. Increasing the milling intensity above the optimal magnitude resulted in a decrease of the specific surface and the total volume of pores (V_{Σ}) and the volume of pores with r 1000 Å. At a very high milling intensity the excess surface energy accumulated and the particles once again started to aggregate spontaneously, their surface and volume becoming partially inaccessible for the measurements.

TEM and X-ray spectroscopy evidenced the profound changes of the hydroxide structure with mild influence on the granulometry of the hydroxide powder. Therefore, mainly strong crystallization contacts between the particles are changed to weak coagulation contacts during disaggregation induced by mechanical activation. Using the AH milling, one can change the character of the contacts and thus affect the mechanical strength of γ-Al_2O_3 granules. Table 3 presents the properties of γ-Al_2O_3 (sample 7) obtained from the milled AH with mixed contacts between the secondary aggregates (sample 3, Table 2) [33]. In the case of spherical γ-Al_2O_3 preparation from the milled TDP (sample 8) the milling reduced the polydispersity of the TDP fractional composition to a minimum and increased its chemical activity thus reducing the optimal autoclave operation time and acid consumption. As in the case of reprecipitated hydroxide, we obtained a strong alumina with a monodisperse structure.

Using the approach suggested in [42,43], one can estimate the possible strength of a perfectly structured granule. According to very approximate estimates, P should exceed 100 MPa for a granule 1–3 mm in diameter. Such essential differences between the real and calculated strength values can be explained by large (micron scale) defects.

Inner cavities and cracks can be attributed to the macrodefects. A mosaic structure forming when the granule consists of separate weakly bound fragments is a defect as well. The size of defects and their disposition in the granule affect its strength essentially. X-ray analysis was used to study the defectness of granules with regard to their mechanical strength [44–46]. Curves of the Al K_{α} irradiation intensity with oscillations typical for each sample were obtained for the inner cuts of granules.

Scanning of weaker samples showed that the irradiation intensity oscillated intensively indicating numerous defects and microcracks which reduced the granule strength. The higher the strength the smaller the amplitude of the intensity oscillations.

3.4. Influence of molding conditions on the mechanical strength

The type of initial hydroxide and its ability to disaggregate in acids determines the specific surface, the porous structure and the strength of the γ-Al_2O_3 granules. Meanwhile, molding in the hydrocarbon liquid as well as granule solidification in the coagulant solution mostly affect the defectness of the shape, the inner cavities, the tensions and the other factors that essentially determine the granule strength.

It has been shown in [30] that the range of the interaction of the plastic sol (PS) with the coagulant (NH_4OH solution) depends on its concentration and the time of the granule stay in ammonia. In the same paper one can find the data on how the PS aging time, acid module, acid type and hydrocarbon layer height influence the mechanical strength, the shape and the fractional composition of the granule. The effects of the Al_2O_3 concentration in the PS, the ammonia solution and the PS temperatures have also been studied. The water amount in the plastic sol appears to have a less drastic effect than the ratio of capillary compression and skeleton rigidity. In the systems with weak skeletons (poorly crystallized or mechanically activated AH), capillary forces provide dense and strong γ-Al_2O_3 granules even if comparatively large amounts of water are removed. On the contrary, in the systems with rigid skeletons (roughly disperse AH) the macropores resist drying and calcination resulting in a decrease of the granule strength.

3.5. Thermal stability and its estimation

γ-Al_2O_3 is the most thermally stable alumina [1], since its transition to α-Al_2O_3 starts at the highest temperature. χ-Al_2O_3 is the least stable. Note that for all low-temperature aluminas transition to α-Al_2O_3 completes at 1200°C independent of their properties. According to Saalfeld [47], χ-Al_2O_3 has the most disordered structure characterized by various occupations of the Al^{3+} vacancies in the oxygen lattice. This factor determines the low thermal stability of this particular alumina, since Al^{3+} diffusion from the tetrahedral vacancies into the octahedral ones is easier

as the rhombic lattice of κ-Al_2O_3 is deformed. It is known [1] that in the low-temperature aluminas Al^{3+} occupies tetrahedral and octahedral vacancies, whereas in α-Al_2O_3 it occupies only the octahedral ones. Therefore, transition of aluminas into α-Al_2O_3 involves Al^{3+} diffusion into the octahedral vacancies and is accompanied by lattice rearrangements.

At present, there are many methods to produce γ-Al_2O_3-based spherical supports. Principal and technological adjustments yield supports possessing different properties (phase composition in particular). In [48], for instance, γ-Al_2O_3-based supports with various contents of χ-Al_2O_3 were studied at different calcination temperatures. Let us consider these results in more detail.

Fig. 9 shows how the crushing strength depends on the χ-Al_2O_3 content in the initial alumina (550°C) during its calcination. Apparently, the strength of spherical granules decreases during the calcination. The lowest strength was observed after thermal treatment at 900–1100°C independent of the alumina type. The crushing strength, P_{av}, starts to increase at 1200°C when the transition to α-Al_2O_3 completes, and bulk sintering sets on.

We can explain the decrease of the granule strength in the above temperature range in the following way. It is known that the transition to the high-temperature oxides, like δ-, κ-, and θ-Al_2O_3, causes a 2–3-fold increase of the primary particle size. Thus the radii of pores also increase at almost the same pore volume [49]. Sintering occurs by a surface diffusion mechanism, when particles stick together, but their centers do not approach each other (no porosity decrease, no shrinkage).

As a result, the number of contacts between the elementary particles imposed to mechanical tensions drops [40], and the strength of the whole granule also decreases. If this process is complicated by different rates of phase transitions and by change of structural parameters (as indeed occurs in the (γ+χ)-Al_2O_3 system), it is quite natural to expect drastic changes of mechanical properties. As the polymorphous transitions yielding α-Al_2O_3 come to the end, the granule strength increases independent of the initial phase composition of the alumina. The reason is that bulk sintering occurs at T 1200°C. According to the assumptions of Saalfeld [47], this sintering yields a coarsely disperse α-Al_2O_3 with primary particles larger than 700 Å. The strength of such particles and the area of contacts between them increase with sintering.

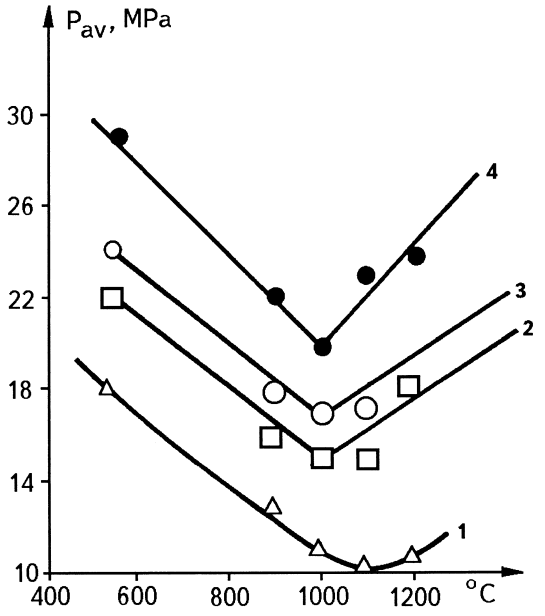

Fig. 9. Dependence of P_{av} on the calcination temperature for aluminas of different contents of χ-phase in samples after treatment at 550°C: (1) 50% χ-+50% γ-Al_2O_3; (2) 30% χ-+70% γ-Al_2O_3; (3) 20% χ-+80% γ-Al_2O_3; (4) 100% γ-Al_2O_3.

Similar results showing the effect of the calcination temperature on the alumina strength were reported in [50,51], and the reasons for such complicated temperature dependence of the strength of alumina granules obtained during calcination of γ-Al_2O_3 were discussed.

Therefore, we may focus on several important items concerning the thermal stability.

1. Stability of the low-temperature aluminas is determined by the set-on temperature of polymorphous transitions, i.e., the temperature at which the high-temperature modifications and α-Al_2O_3 appear.
2. Change of the specific surface related to the porous structure of the alumina may serve as an indirect characteristic of the thermal stability.
3. Mechanical strength is a key parameter determining the thermal stability of Al_2O_3.

As for spherical γ-Al_2O_3 used as the support for catalysts working in moving or fluidized beds, the

above results show that we managed to design the support with the best thermal stability and mechanical strength.

However, it is still necessary to improve these supports, since high-temperature processes, such as methane oxidation, combustion of off-gases, etc., impose more and more severe demands on supports and catalysts.

New approaches are required to solve this problem. Chemical modification of aluminum oxide/hydroxide by various dopings can be the way to improve the properties of the final product.

4. Alumina modification as a method to control its main properties

4.1. Modifiers and ways of their introduction

Modifiers can be divided into mineralizers and stabilizers according to their effect on materials (alumina in our case).

Mineralizers are substances that accelerate the changes of the basic material. For γ-Al_2O_3 these substances accelerate sintering and polymorphous transformations during the calcination lowering the temperature at which the high-temperature oxides and α-Al_2O_3 form. Oxides of copper [52,53], manganese [54–56], molybdenum and vanadium [55,56], fluorine and chlorine compounds [57], TiO_2 [55,58], etc. are among such substances.

Stabilizers are substances that decelerate the changes of the basic material. Zr and Y compounds [59–61], SiO_2 [62–65], and B_2O_5 [66–68] have such an influence on γ-Al_2O_3.

Besides, there are modifiers that improve the strength of alumina, such as compounds of Ba [69], B [67,68], Ca [70], and Mg [71,72]. Note, however, that data on the role of modifiers on alumina properties are contradicting.

We shall show below that this controversy about the role and mechanism of some additives is caused by the fact that different researchers use varying doping methods. The main differences lie in the

- dopant form (salt, hydroxide, oxide);
- introduction procedure (co-precipitation, alumina impregnation, hydroxide impregnation, oxide mixing, etc.);
- dopant amount;
- calcination conditions (rate of temperature rise, residence time at the given temperature, etc.);
- method of producing ''pure'' alumina and its properties.

In our research work we have stated and grounded main approaches to be used for alumina modification:

1. The most efficient dopes allowing the control of the alumina properties are: Mg – as a strengthening dope; La, Ce, Si as dopes improving the thermal stability.
2. In each metal/alumina system we verified the introduction method, the dope amount, the type of the low-temperature alumina, and the calcination conditions with regard to the properties of alumina obtained.
3. We have also designed special introduction procedures to obtain the optimum dope contents and studied the mechanisms of their modifying action.

Mg, La, Ce were introduced from the nitrate solutions, SiO_2 was introduced as the sol.

Let us now discuss the results obtained for each system. In all systems we studied two types of supports:

1. Spherical γ-Al_2O_3 (d=1.4–2.0 or 2.0–3.0 mm) prepared from commercial pseudoboehmite hydroxide.
2. Spherical γ-Al_2O_3 (d=1.4–2.0 or 2.0–3.0 mm) obtained via the TDP processing.

Spherical granules were produced using the HAM method.

4.2. Mg/Al_2O_3 system

Main results obtained with this system are reported in [73–80]. Mg was introduced from its aqueous nitrate solution either via incipient wetness impregnation of spherical γ-Al_2O_3 (two types) or by impregnating spherical granules of aluminum hydroxide precursors of oxides 1 and 2. We have designed an original impregnation procedure and apparatus, which are described elsewhere [73,75]. In [74] detailed studies of the Mg/alumina system have been published and the mechanism of the strengthening effect of Mg has been suggested. We have shown that only when

Mg^{2+} is introduced into aluminum hydroxide granules (independently of how the latter are prepared), Mg strengthens the γ-Al_2O_3 granules.

Summing up all the data we may draw the following conclusions:

1. Alumina strengthening occurs due to the formation of cation–anion solid solutions of Mg in alumina.
2. Such solid solutions form only from the solid solutions of pseudoboehmite structure when Mg is introduced into aluminum hydroxide.
3. Cation–anion solid solutions decrease the defectness of granules on a micron scale.

4.3. La/Al_2O_3 system

Results of a complex study of the effect of lanthanum cations on the thermal and mechanical stability (phase composition, mechanical strength, specific surface) of alumina depending on the introduction procedure and dope amount, calcination temperature and time are described in [81–84]. Even a small amount of the dope (up to 5% with La_2O_3) causes deceleration of the α-Al_2O_3 formation. At higher concentrations the transition of θ- to α-Al_2O_3 is completely suppressed and alumina is stabilized either in θ-form or in a mixture of γ- and δ-forms.

Therefore, it is possible to stabilize the transient forms of alumina up to 1200°C. Key factors determining the thermal stability of alumina in the La_2O_3–Al_2O_3 system are:

1. The effect of lanthana at the same introduction procedure is determined by the type of alumina used.
2. The introduction procedure of lanthana has a drastic effect on the change of the thermal stability. Thus, La introduction via the oxide granule impregnation (series I and II) is more efficient in comparison to the La salt introduction into AH granules.
3. There is an optimum amount of La for each introduction procedure and each type of initial γ-Al_2O_3 which completely suppresses the phase transitions in Al_2O_3.

The observed results allow us to conclude that the lanthana stabilizes the transition aluminas when a solid solution of La ions forms in the structure of the low-temperature aluminas. The presence of La in the alumina lattice prevents the diffusion of Al ions and the rearrangements into the high-temperature forms.

For convenience, in the next section we shall consider phase transitions observed in the Ce/Al_2O_3 system. Then in a separate section we shall unite the results concerning the main physical–chemical and structure–mechanical properties of alumina modified with La or Ce.

4.4. Ce/Al_2O_3 system

We performed our studies with the same samples of spherical aluminum hydroxide and oxide. We introduced Ce from its salts exactly as in the La/Al_2O_3 system, and we performed calcination in the same manner as well. The Ce content calculated as CeO_2 ranged from 1 to 13 wt% [85].

Like in the La_2O_3–Al_2O_3 system the strongest stabilization effect at the same way of Ce introduction was observed with the samples obtained from amorphous aluminum hydroxide (series II). This was proved by the largest absolute difference in the content of δ- and α-Al_2O_3 in these samples as compared to that of the pure support. The stabilizing effect is related to the stronger interaction of the dope with the alumina, as the latter contained χ-Al_2O_3 besides γ-Al_2O_3 due to peculiarities of its preparation. Most probably, not only γ-Al_2O_3, but also χ-Al_2O_3 interacts with Ce ions. The latter is more defective and disordered. That is why we observed no χ- and κ-Al_2O_3 at 550°C and 900°C, respectively, as in the La_2O_3–Al_2O_3 system (unlike in the non-doped aluminum of the series).

In comparison to the La_2O_3–Al_2O_3 system, CeO_2–Al_2O_3 never shows a phase in which Ce has reacted with Al_2O_3 in the X-ray patterns in the whole temperature range studied. Most likely, the Ce–Al_2O_3 system has two Ce-containing phases: (i) Ce oxide not interacting with alumina and imposing no stabilizing effect; (ii) highly disperse Ce compounds with alumina, which are not revealed in the X-ray patterns, but nevertheless affect the thermal stability of alumina. We failed to identify this phase. However, we believe in its existence judging from the fact that the intensities of CeO_2 profiles in mechanical mixtures and in our samples did not coincide at the same

concentration of Ce oxide. This assumption is confirmed by the X-ray studies performed on Pt–Ce–Al_2O_3 [86]. This paper discusses a highly disperse product forming at 550°C. This product results from the Ce interaction with the support and is Ce aluminate with a perovskite-like structure. This interaction is quite limited (not more than 5 mass% CeO_2 interacts with Al_2O_3).

Note that according to the data of other researchers [87], who used complex physical–chemical methods to study the thermal stability of alumina modified by Ce, the latter stays mainly as a disperse phase on the surface non-interacting with alumina. The authors of [87] explain this phenomenon by the fact that Ce has a weaker effect on the stability of alumina than La whose ions enter the alumina structure.

Thus, X-ray studies of two systems, La_2O_3–Al_2O_3 and CeO_2–Al_2O_3, prepared with the same alumina samples according to the same procedure and calcined at the same conditions allow us to conclude that alumina stabilization by Ce is weaker than by La. Such a behavior relates to the limited character of the interaction of ceria with the support.

4.5. *Structure and chemical properties of spherical alumina modified with La and Ce ions*

One of the publications [88] concerns the structural–mechanical properties of alumina modified by La and Ce ions.

4.5.1. *Specific surface area*

The specific surface area of doped aluminas was shown to be stabilized at temperatures ranging from 900°C to 1200°C. Thus at 1100°C the specific surface area of La-modified alumina was 3–6 times larger (depending on the alumina preparation procedure and dope amount) than that of ''pure'' alumina. The most pronounced stabilization effect was observed for samples containing 5% of La_2O_3. Therefore, the dope cation interacted actively with the support producing a solid solution with the structure of the corresponding alumina form.

The specific surface area of Ce-modified alumina exceeded that of ''pure'' alumina only by a factor of 1.2–2 upon calcination within the 900–1200°C range independent of the alumina preparation conditions.

Note that the stabilization effect on the BET surface area was more pronounced in the system La_2O_3–Al_2O_3 than in CeO_2–Al_2O_3 also at T 1200°C. The reason is the presence of lanthanum hexaaluminate, $La_2O_3{\cdot}11Al_2O_3$, whose concentration increases with the content of La_2O_3. Hexaaluminate is known [89] to have a layered structure that retains its large surface at high temperatures. In the CeO_2–Al_2O_3 system no cerium hexaaluminates were registered [90]. CeO_2 or Ce^{3+} compounds with alumina were coarsely disperse and had a small BET surface area [91].

4.5.2. *Pore structure*

We have studied the pore structure of samples for both doped and undoped alumina at 550°C and 1100°C. At 550°C the pore structure of modified samples practically did not differ from that of pure alumina. As the temperature increased, La- and Ce-modified samples behaved differently. Thus the pore volume (V_Σ) of CeO_2–Al_2O_3 practically did not change at 1100°C in comparison to that at 550°C as in pure alumina, whereas the average pore radius was 1.3 times smaller than for pure alumina.

In the La_2O_3–Al_2O_3 system V_Σ increased in comparison to that of non-modified alumina at 1100°C, the effective pore radius being three times less than for CeO_2–Al_2O_3. Therefore, sintering was certainly decelerated, and decelerated more efficiently for La_2O_3–Al_2O_3.

4.5.3. *Granule strength*

Since mechanical strength and mechanical stability are the main properties of the granular catalysts working in the fluidized bed (under local overheating), the effect of modifying dopes on the strength of alumina granules and the change of the sample strength in calcination was studied in [88].

Fig. 10 shows how the mechanical strength of granules (P_{av}) depends on the calcination temperature for ''pure'' alumina and for alumina doped by La and Ce. Apparently, at T 900°C all samples had the same mechanical strength. Raising the calcination temperature to 1100°C resulted in an increase of P_{av} for the ''pure'' alumina granules, which was very sharp for the samples containing 5 wt% of CeO_2. The strength of the samples containing 5 wt% of La_2O_3 increased only at T 1200°C. La-doped samples thus did not differ in this parameter from the ''pure'' alumina.

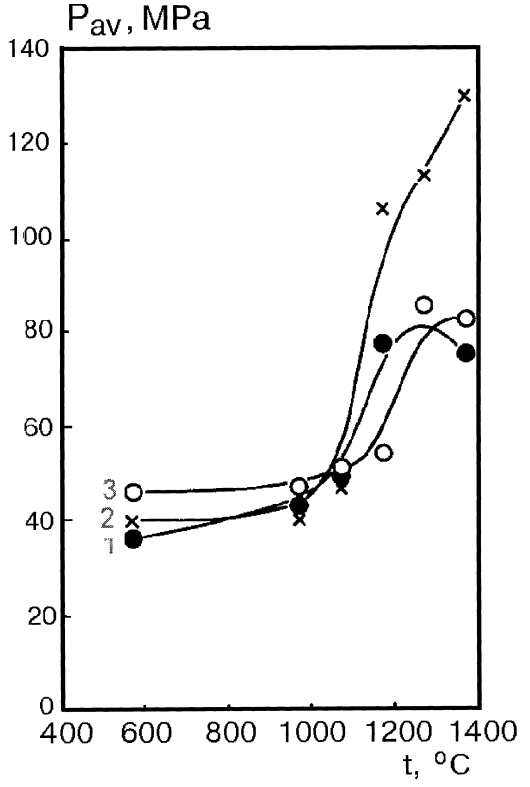

Fig. 10. Influence of calcination temperature on mechanical strength of alumina: 1 – pure Al_2O_3; 2 – 5% CeO_2/Al_2O_3; 3 – 5% La_2O_3/Al_2O_3.

Obviously, CeO_2 is a more efficient dope than La_2O_3 with regard to the mechanical strength. Most likely, the strength of modified samples changes with the transformation of the phase composition of these samples. According to the data obtained in [85], at T 900°C a highly disperse Ce-containing phase is present besides the Al_2O_3 and CeO_2 phases. It is not registered by the X-ray analysis due to the very low content. Since the mechanical strength of samples does not depend on the Ce content over the whole temperature range, we assume that the content of this X-ray amorphous phase is the same in all samples and does not depend on the concentration of CeO_2. Therefore, the strengthening is caused by an increase of the number of contacts, but by the strengthening of single contacts due to the interaction of the primary alumina particles with the dope.

For the La_2O_3–Al_2O_3 system [81] the low-temperature X-ray amorphous compound decomposes at T 1200°C producing α-Al_2O_3 and La hexaaluminate, thus not providing a high strength of the single contacts.

4.5.4. *Study of structural–mechanical properties of supports after calcination for prolonged periods of time*

In order to investigate how La–Al_2O_3 and Ce–Al_2O_3 behave during prolonged calcination at 1000°C, we have studied the change of S_{BET} for samples with the optimum dope content (5% of La_2O_3 or 2% of CeO_2). These data are shown in Fig. 11.

The sharpest change of S_{BET} occurred for all the samples during the first 5 h of calcination. A longer calcination decreased S_{BET} of non-modified samples, but not of the La-containing sample.

La-samples of alumina obtained from the gibbsite TDP (series 11) had the largest specific surface area after calcination for 30 h. For Ce-samples, stabilization of the surface area after 30 h calcination at 1000°C did not depend on the way of the alumina preparation.

S_{BET} dropped during calcination for a long period of time activation due to a change in the phase composition. δ-Al_2O_3 formed during the first hours of calcination at 1000°C, changing the particle morphology and package. As it is shown in [81,85], the pure oxide of the above spherical δ-Al_2O_3 support (1) had only the traces of α-Al_2O_3 after 2 h calcination, whereas there was up to 50% of α-Al_2O_3 in a differently prepared alumina sample, viz. the δ-Al_2O_3 support (2) produced via TPD processing. A longer calcination of pure alumina facilitates the phase transition to α-Al_2O_3 reducing S_{BET}. For some aluminas this transition was completed after calcination for 20 h. However, in other aluminas this transition was over already after 10 h. The content of the δ-phase grew with calcination time in all samples modified by La, but the traces of α-Al_2O_3 appeared only after 30 h. In the Ce-doped samples the δ-Al_2O_3 content also grew, but α-Al_2O_3 traces appeared after 20 h for one and after 10 h for another alumina. Meanwhile, the dispersity of CeO_2 particles did not increase.

Note that the modified samples did not lose their strength during a long time calcination at 1000°C, and were mechanically stable. The granule strength of La-doped samples of above δ-Al_2O_3 supports (1) and (2)

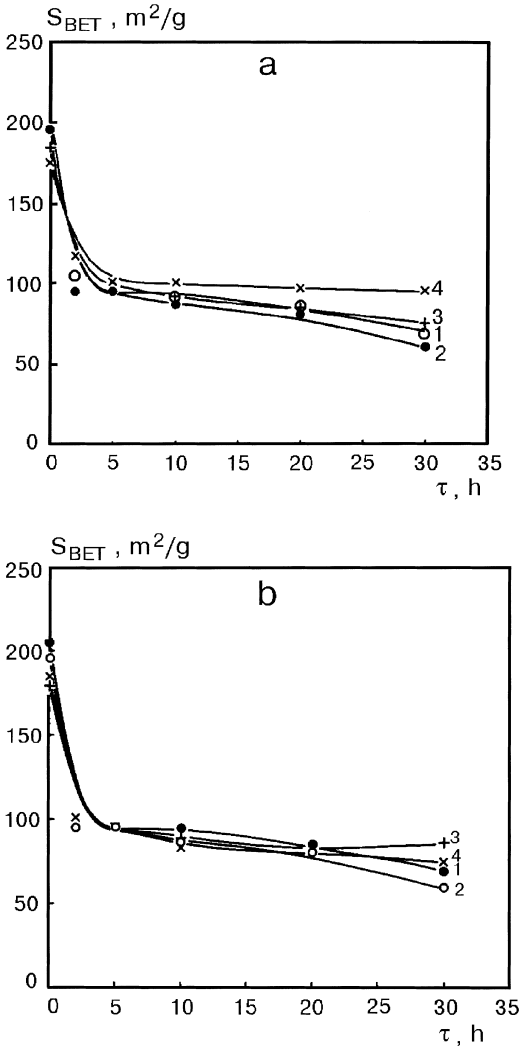

Fig. 11. Influence of calcination time at 1000°C on S_{BET} of alumina: (a) with 5% La_2O_3. 1 – Al_2O_3 support (1); 2 – Al_2O_3 support (2); 3 – La_2O_3/Al_2O_3 support (1); 4 – La_2O_3/Al_2O_3 support (2); (b) with 5% CeO_2. 1 – Al_2O_3 support (1); 2 – Al_2O_3 support (2); 3 – CeO_2/Al_2O_3 support (1); 4 – CeO_2/Al_2O_3 support (2). Support (1): spherical γ-Al_2O_3 prepared from commercial pseudoboehmite; support (2): spherical γ-Al_2O_3 produced by TDP processing.

after calcination for 30 h at 1000°C was 58.5 and 33 MPa, respectively. With the Ce-doped samples it was 54 and 30 MPa, respectively.

The results obtained agree well with our X-ray data on the La_2O_3–Al_2O_3 and CeO_2–Al_2O_3 systems. Thus La introduction into γ-Al_2O_3 produces a solid solution of La oxide based on the γ-Al_2O_3 structure where La ions substitute Al. This imposes limitations on the transitions to δ-, θ- and α-Al_2O_3. So, a large specific surface area is retained, and the mechanical properties of modified samples better resist high temperatures.

Unlike La_2O_3–Al_2O_3, alumina modified by CeO_2 does not show essential stabilization of the disperse structure of Al_2O_3. This is caused by the limitations on the interaction of alumina with Ce ions.

Therefore, modifying alumina with La and Ce ions, one can obtain alumina supports well resisting the effect of high temperatures.

4.6. Alumina containing two dopes simultaneously

Properties of alumina modified by the cations of two- or three-valent metals and interaction mechanisms discussed in Section 4.5.4 allow us to assume that introducing simultaneously two elements into alumina we may obtain a new family of supports exhibiting unique behavior. Moreover, studying such systems we may confirm or oppose our assumption on the mechanisms of the dope effects.

Below we shall consider the properties of alumina simultaneously containing Mg and La or Si and La dopes.

4.6.1. Mg–La/Al_2O_3 system and its properties

The X-ray studies show [81,84] that Mg and La ions present together in alumina improve its thermal stability, which is estimated from the content of α-Al_2O_3 formed at the given temperature, in comparison to the earlier studied La_2O_3–Al_2O_3 system.

Mg and La ions simultaneously present in alumina stabilize the solid solutions based on the γ-Al_2O_3 structure. The co-existence of Mg and La that favor to occupy different cation positions in the oxygen anion lattice in the γ-Al_2O_3-based solid solution does not allow the rearrangement of the solid solution structure typical for other ions. Moreover, the stabilized ''rough'' structure of the low-temperature solid solution facilitates the entrance of La into the support structure. Unlike the La_2O_3/Al_2O_3 system, here La ions diffuse mainly into the structure of solid mixed La–Mg/γ-Al_2O_3 at rising temperatures. If the solid La solution in alumina at T 1200°C yields $La_2O_3{\cdot}11Al_2O_3$, the solid La–Mg–γ-Al_2O_3 solution produces $2MgO$–$La_2O_3{\cdot}11Al_2O_3$. Both compounds

have a hexagonal packing of the oxygen lattice, as α-Al_2O_3, and are related, but have a higher symmetry.

Stabilization of Mg and La ions in the respective tetrahedral and octahedral positions hinders the Al ion diffusion yielding the high-temperature oxides. Calcination at 1400°C shows that it is necessary to optimize the ratio of Mg and La cations in the structure to stabilize the low-temperature solid solution. We may consider the mixed solution La–Mg–γ-Al_2O_3 with Mg:La∼1:1 as a low-temperature form of $2MgO–La_2O_3·11Al_2O_3$. To transit into the high-temperature form, this solid solution must be appropriately ordered with regard to the cation position occupation by La and Mg. According to the diffraction data, an La deficit yields a set of solid solutions or stoichiometric aluminum–magnesium spinel.

Therefore, the thermal stability of alumina simultaneously doped with two- and three-valent cations preferring to occupy different cation positions in the oxygen lattice of the low-temperature alumina results from the hindering of structure rearrangements in the structure of the mixed low-temperature solid solutions at increasing temperatures.

Structural–mechanical properties of alumina simultaneously doped with two- and three-valent cations have been studied in [84]. It was shown that the mechanical strength and thermal stability increased in this case.

4.6.2. *Mg–Ce/Al_2O_3 system*

As in the case of Mg–La/Al_2O_3, Mg was introduced into the spherical alumina hydroxide granules and cerium into γ-Al_2O_3 via incipient wetness impregnation with nitrate solutions. Sample properties were studied after calcination at 550–1300°C.

X-ray methods used to study the phase composition of alumina doped with Mg and Ce showed that Mg and Ce ions present in alumina did not increase its thermal stability in comparison to the CeO_2/Al_2O_3 and MgO–La_2O_3/γ-Al_2O_3 systems.

This effect is caused by the fact that only a small part of Ce introduced is able to interact with the support to stabilize as Ce^{3+} and slightly improve the thermal stability. The interaction product decomposes at higher temperatures, yielding a separate phase of cerium oxide, α-Al_2O_3 and a stoichiometric spinel. The major part of Ce introduced during impregnation transforms from Ce^{3+} to Ce^{4+} due to peculiarities of Ce chemistry to give the CeO_2 phase having no effect on the thermal stability of the support.

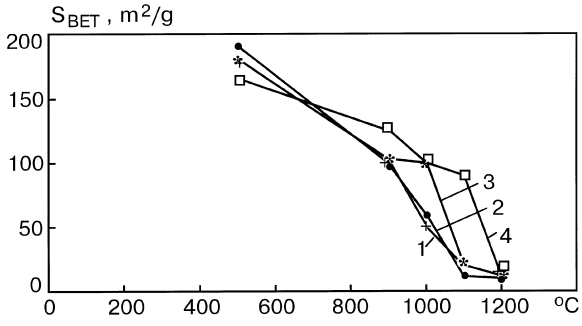

Fig. 12. Dependence of S_{BET} of alumina on temperature: 1 – pure Al_2O_3; 2 – 2.5% MgO/Al_2O_3; 3 – 5% CeO_2/Al_2O_3; 4 – Mg–Ce/Al_2O_3.

Note that unlike the system $MgO–La_2O_3–Al_2O_3$, $MgAl_{11}CeO_{19}$ (ASTM 26-879) was not formed here at T 1100°C. In the former system La almost completely interacts with the support yielding $MgAl_{22}LaO_{19}$ at the same temperatures.

Fig. 12 shows how the specific surface area of modified alumina changed with the calcination temperature. For comparison, we present data for ''pure'' alumina within the same figure (curve 1). Apparently, aluminas containing both Mg and Ce had the largest specific surface area at 900–1000°C. The specific surface area of the aluminas modified solely with Mg and of ''pure'' alumina, decreased in the above temperature range. Ce-doped alumina retained its surface up to 1100°C.

Fig. 13 and Table 4 show how the sample strength depended on the calcination temperature. Apparently, only the samples containing both Mg and Ce or Mg alone retained their high mechanical strength that even increased with temperature.

All the data obtained for the Mg–Ce/Al_2O_3 system prove that two- and three-valent cations both present in alumina enhance the effects of each other and allow one to improve the thermal and mechanical stability of alumina (though not so considerably as in Mg–La/Al_2O_3).

Therefore, only if a uniform solid mixed solution of ions forms in the low-temperature alumina, it is possible to obtain a support exhibiting high thermal stability. Moreover, the ions introduced must occupy respective tetrahedral or octahedral cation positions in the structure.

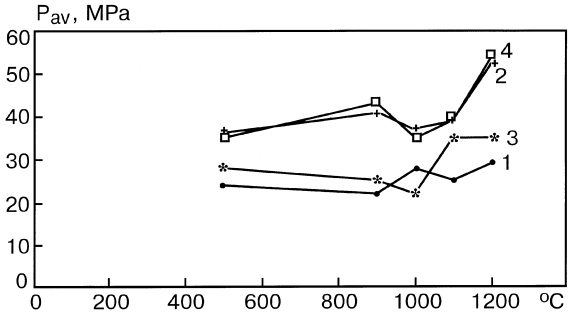

Fig. 13. Influence of calcination temperature on mechanical strength of alumina: 1 – pure Al_2O_3; 2 – 2.5% MgO/Al_2O_3; 3 – 5% CeO_2/Al_2O_3; 4 – Mg–Ce/Al_2O_3.

4.6.3. *La–Si/Al_2O_3 system*

It is known that SiO_2 introduced into alumina may substantially improve its thermal stability [63–66,92].

For us it was interesting to compare the SiO_2/Al_2O_3 system with Si–La/Al_2O_3. As shown in [83,93–95], introduction of SiO_2 (sol) into the plasticized paste of pseudoboehmite aluminum hydroxide obtained from TDP before molding allowed us to increase the thermal stability of alumina. So, S_{BET} of modified Al_2O_3 at 1200°C was 2.5 times higher than that of pure alumina.

Based on all our data, we have chosen the following composition to synthesize Si–La/Al_2O_3:

$$2.5\%\ SiO_2 + 5\%\ La_2O_3 + 92.5\%\ Al_2O_3$$

SiO_2 was introduced as a sol into the plasticized paste of TDP before HAM. Lanthanum was introduced into the spherical granules (diameter 2–3 mm) of γ-Al_2O_3 via incipient wetness impregnation with La nitrate solution. Then the granules were dried at 110°C and calcined at 550–1300°C (2 h at each temperature).

Table 4
Properties of spherical alumina

No.	Dope	S_{BET} (m^2/g)	Strength (MPa)	Phase composition
550°C				
1	–	200	24	γ-Al_2O_3
2	La	180	26	γ^*-Al_2O_3
3	Si	210	22	γ-Al_2O_3
4	Ce	185	21	γ-Al_2O_3+CeO_2
5	Mg	180	44	γ^*-Al_2O_3
6	La–Si	190	32	γ^*-Al_2O_3
7	La–Mg	160	38	γ^*-Al_2O_3
8	Ce–Mg	180	38	γ^*-Al_2O_3+CeO_2
1200°C				
1	–	7	28	α-Al_2O_3
2	La	29	35	$LaAlO_3$ (traces)+α-Al_2O_3+$La_2O_3{\cdot}11Al_2O_3$
3	Si	40	28	γ-Al_2O_3+40% α-Al_2O_3
4	Ce	14	35	α-Al_2O_3+CeO_2
5	Mg	10	60	$MgAl_2O_4$+α-Al_2O_3
6	La–Si	80	38	γ^*-Al_2O_3+δ-Al_2O_3 (∼50%)
7	La–Mg	23	65	α-Al_2O_3+$MgAl_{11}LaO_{19}$+γ^{**}-Al_2O_3
8	Ce–Mg	23	60	$MgAl_2O_4$+α-Al_2O_3+CeO_2
1300°C				
1	–	6	30	α-Al_2O_3
2	La	28	44	α-Al_2O_3+La_2O_3+$La_2O_3{\cdot}11Al_2O_3$
3	Si	28	30	α-Al_2O_3
4	Ce	8	36	α-Al_2O_3+CeO_2
5	Mg	6	65	$MgAl_2O_4$+α-Al_2O_3
6	La–Si	26	48	α-Al_2O_3 (traces)+θ-Al_2O_3+$La_2O_3{\cdot}11Al_2O_3$ (traces)
7	La–Mg	14	70	α-Al_2O_3+$MgAl_{11}LaO_{19}$
8	Ce–Mg	10	65	$MgAl_2O_4$+α-Al_2O_3+CeO_2

γ^* – solid solution of Me cation on the base of γ-Al_2O_3.
γ^{**} – continuous number of low temperature solid solutions of La and Mg cations.

Table 4 shows the main properties of the system synthesized and compares it with ''pure'' alumina and alumina containing solely SiO_2 (2.5%) or La_2O_3 (5 wt%).

Apparently, La and Si both present in the system decelerated the phase transitions in alumina at rising temperatures. Thus the specific surface area remained large. The best stabilization effect was observed at T=1000°C. At 1100°C S_{BET} of the samples containing La–Si was twice higher than that of La/Al_2O_3 and Si/Al_2O_3. Calcination at 1300°C removed the difference between the S_{BET} of La/Al_2O_3, Si/Al_2O_3 and ''pure'' alumina, while the S_{BET} of $La–Si/Al_2O_3$ was 3–4 times higher. Note that the phase composition of these systems was considerably different. The α-Al_2O_3 phase appeared in $La–Si/Al_2O_3$ only at T=1300°C as traces. No lanthanum aluminate phase was registered in all high-temperature samples (T 1000°C) of the combined system. Lanthanum hexaaluminate appeared only at 1300°C. There were no other compounds indicating the interaction of La and Si oxides.

Note that the stabilization effect for the $La–Si/Al_2O_3$ system was far higher than that of $Mg–La/Al_2O_3$. Thus 15% of α-Al_2O_3 formed in $Mg–La/Al_2O_3$ after calcination at 1200°C (see Table 4), and S_{BET} of this sample was four times smaller than that of $La–Si/Al_2O_3$ containing no α-Al_2O_3 at this temperature. At 1300°C there was only α-Al_2O_3 in $Mg–La/Al_2O_3$ (5 wt% La_2O_3), whereas this phase was present only as traces in $La–Si/Al_2O_3$.

5. Conclusion

The data obtained in the fundamental studies allowed us to suggest a technological solution for the synthesis of spherical alumina with high mechanical strength and thermal stability.

Such alumina supports for catalysts operating in moving- or fluidized bed reactors can be prepared via the hydrocarbon–ammonia molding of pseudoboehmite aluminum hydroxide.

We suggested a new technology to produce pseudoboehmite aluminum hydroxide based on the thermal decomposition of gibbsite in the catalytic heat generator.

New spherical supports with unique properties were synthesized by modifying alumina with various dopes.

References

[1] B.C. Lippens, J.J. Steggerda, Physical and Chemical Aspects of Adsorbents and Catalysts, Academic Press, New York, 1970, p. 171.
[2] D.I. Trimm, A. Stanislaus, Appl. Catal. 21 (1986) 215.
[3] H.C. Stumpf, A.R. Russel, J.W. Newsome, C.M. Tucker, Ind. Eng. Chem. 45 (1953) 819.
[4] S.J. Wilson, J. Solid State Chem. 30 (1979) 247.
[5] T. Ono, Y. Ohguchi, O. Togari, in: G. Poncelet, P. Grange, P. Jacobs (Eds.), Preparation of Catalysis III, Elsevier, Amsterdam, 1983, p. 631.
[6] R.A. Shkrabina, Ph.D. Thesis, Institute of Catalysis, Novosibirsk, 1982 (in Russian).
[7] R.A. Shkrabina, Z.R. Ismagilov, M.N. Shepeleva et al., Proceedings of the 10th National Symposium on Catalysis Recent Development – Catalysis, Theory and Practicals, Madras, 18–21 December 1990, p. 30.
[8] G.K. Boreskov, E.A. Levitskii, Z.R. Ismagilov, J. Vses. obtsh. im Mendeleeva 29 (4) (1984) 379 (in Russian).
[9] Z.R. Ismagilov, M.A. Kerzhsenzev, J. Vses. obtsh. im Mendeleeva 35 (1) (1990) 43 (in Russian).
[10] Z.R. Ismagilov, M.A. Kerzhenzev, Catal. Rev.-Sci. Eng. 32 (1990) 51.
[11] Z.R. Ismagilov, R.A. Kerzhenzev, R.A. Shkrabina, Rus. Chim. J. 37 (1993) 48 (in Russian).
[12] Z.R. Ismagilov, R.A. Shkrabina, M.A. Kerzhenzev, G.B. Barannik, React. Kinet. Catal. Lett. 55(2) (1995) 489.
[13] Ya.Z. Kazobashvili, G.M. Micheev, Neftepererabotka neftechim., Moscow 12 (1964) 11 (in Russian).
[14] V.A. Dzisko, A.P. Karnaukhov, D.V. Tarasova, Physicochemical Basis of Oxide Catalysts Synthesis, Nauka, Novosibirsk, 1978, p. 300 (in Russian).
[15] V.V. Plaksina, Yu.N. Fomichev, M.E. Levinter, in: R.A. Buyanov (Ed.), Scientific Basis of Catalysts Preparation, Institute of Catalysis, Novosibirsk, 1983, p. 216 (in Russian).
[16] G.M. Gusev, L.G. Shumskaya, N.M. Lyamina, Dokl. AN SSSR 235 (1977) 921 (in Russian).
[17] S.M. Paramzin, Yu.D. Pankratiev, O.P. Krivoruchko et al., Izv. SO AN SSSR, Ser. Chim. 4 (1984) 33 (in Russian).
[18] Rhone Poulenc, Eur. Patent N 55164 (1981).
[19] Leuna Werke, Patent DDR N 203 038 (1983).
[20] R.A. Shkrabina, E.M. Moroz, E.A. Levitskii et al., Kinet Katal. 22 (1981) 1603 (in Russian).
[21] Yu.K. Vorobiev, R.A. Shkrabina, E.A. Levitskii, Kinet. Katal. 22 (1981) 1595 (in Russian).
[22] M.N. Shepeleva, R.A. Shkrabina, V.B. Fenelonov, Z.R. Ismagilov, Appl. Catal. 78 (1991) 175.
[23] M.N. Shepeleva, V.B. Fenelonov, R.A. Shkrabina, E.M. Moroz, Kinet. Katal. 27 (1986) 1202 (in Russian).
[24] M.N. Shepeleva, R.A. Shkrabina, L.G. Okkel et al., Kinet. Katal. 29 (1988) 195 (in Russian).
[25] P.V. Klassen, I.G. Grishaev, The Basis of Granulation Methods, Chimiya, Moscow, 1982 (in Russian).
[26] H. Shubert, Chem. Ing. Thechnol. 47 (1975) 86.
[27] C. Perego, P.L. Villa, Proceedings of the Third Seminar of Catalysis, Rimini, Chapter 2, 19–24 June 1994, Italy, p. 25.

[28] Rhone Poulenc, US Patent 4 273 620 (1965).
[29] Labofina French Patent 2 261 056 (1975); 2 261 057 (1975).
[30] M.N. Shepeleva, R.A. Shkrabina, Z.R. Ismagilov, Technol. Today 3 (1990) 150.
[31] M.N. Shepeleva, R.A. Shkrabina, Z.R. Ismagilov, V.B. Fenelonov, in: G. Poncelet, P.A. Jacobs, B. Delmon (Eds.), Proceedings of the Fifth Symposium on Preparation of Catalysts, Elsevier, Amsterdam, 1991, p. 583.
[32] Z.R. Ismagilov, M.N. Shepeleva, R.A. Shkrabina, V.B. Fenelonov, Appl. Catal. 69 (1991) 65.
[33] M.N. Shepeleva, R.A. Shkrabina, Z.R. Ismagilov et al., Kinet. Katal. 32 (1991) 132 (in Russian).
[34] R.A. Rebinder, E.D. Shchukin, L.Ya. Margolis, Dokl. AN SSSR 154 (1964) 695 (in Russian).
[35] L.Ph. Melgunova, Z.R. Ismagilov, R.A. Shkrabina, Proceedings of the European Congress on Catalysis, vol. 1, (EUROPACAT-1): Book of Abstracts V.2.-Montpellier, France, 2–3 September 1993, p. 992.
[36] Z.R. Ismagilov, M.N. Shepeleva, R.A. Shkrabina et al., Proceedings of the Workshop on The Problems of Strength of Granulated Supports and Catalysts, Novosibirsk, 10–13 October 1987, p. 40 (in Russian).
[37] R.A. Rebinder, Physico-chemical Mechanics of Dispersed Materials, Nauka, Moscow, 1966 (in Russian).
[38] E.D. Schukin, A.Yu. Bessonov, S.A. Paranskii, Mechanical Testing of Catalysts and Sorbents, Nauka, Moscow, 1971, p. 115 (in Russian).
[39] D.I. Titelman, A.P. Shlakov, A.I. Kruindel, N.A. Karabajyan, Metody Analiza i Kontrolja 5 (1983) 34 (in Russian).
[40] L.V. Kovalskaya, Ph.D. Thesis, Grozny, 1983 (in Russian).
[41] E.G. Avvakumov, Mechanical Methods of Chemical Processes Activation, Nauka, Novosibirsk, 1986 (in Russian).
[42] N.V. Perzev, Ph.B. Danilova, V.G. Babak et al., Dokl. AN SSSR 222 (1975) 1085 (in Russian).
[43] I.A. Stepanov, Izv. AN Latv. SSR. Ser. Phys. i Tech. Nauk. 2 (1985) 83 (in Russian).
[44] M.N. Shepeleva, Z.R. Ismagilov, R.A. Shkrabina, I.A. Ovsyannikova, Kinet. Katal. 32 (1991) 455 (in Russian).
[45] Z.R. Ismagilov, N.A. Koryabkina, I.A. Ovsyannikova, R.A. Shkrabina, Kinet. Katal. 32 (1991) 494 (in Russian).
[46] I.A. Ovsyannikova, G.I. Goldenberg, N.A. Koryabkina, R.A. Shkrabina, Z.R. Ismagilov, Appl. Catal. 55 (1989) 75.
[47] H. Saalfeld, Neues Jahrb. Mineral Abhanell. 95 (1960) 1.
[48] Z.R. Ismagilov, R.A. Shkrabina, M.N. Shepeleva, N.A. Koryabkina, Proceedings of the Second All-Union Workshop on Catalyst Deactivation, Ufa, 10–13 May 1989, p. 111 (in Russian).
[49] V.N. Kuklina, L.M. Plyasova, L.M. Kepheli, E.A. Levitskii, Kinet. Katal. 12 (1971) 1078 (in Russian).
[50] B.M. Phedorov, V.M. Balashov, A.S. Berenblyum, Kinet. Katal. 31 (1990) 673 (in Russian).
[51] B.M. Phedorov, V.I. Nechoroshev, I.A. Zhukov, A.S. Berenblyum, Kinet. Katal. 32 (1992) 190 (in Russian).
[52] E.M. Moroz, O.A. Kirichenko, V.A. Ushakov, E.A. Levitskii, React. Kinet. Catal. Lett. 28 (1985) 9.
[53] O.A. Kirichenko, V.A. Ushakov, E.M. Moroz, Z.R. Ismagilov, React. Kinet. Catal. Lett. 38 (1989) 307.
[54] P.G. Tsyrulnikov, V.S. Salnikov, A.S. Noskov, Proceedings of the 11th International Conference on Modern Trends in Chemical Kinetics and Catalysis, Novosibirsk, Part 2, 13–15 November 1995, p. 402.
[55] K. Gauguin, M. Granulier, D. Papee, Catalysis for Control of Automobile Pollution, Washington, 1975, p. 147.
[56] B.S. Porekh, S.W. Weller, J. Catal. 55 (1978) 58.
[57] T.V. Antipina, V.V. Yuschenko, J. Phys. Chem. 50 (1976) 2921 (in Russian).
[58] H. Sabiro, I. Yoshio, Y. Masahiro, S. Shigeyuki, J. Ceram. Soc. Jpn. 94 (1986) 400.
[59] M. Johnson, J. Catal. 123 (1990) 245.
[60] Patent USA 4 708 946 (1987).
[61] K. Akita, Y. Hisao, M. Shimplei, Proceedings of the Eighth Jap–USSR Catalysis Seminar, Tokyo, 29–31 October 1986, p. 24.
[62] C. Thierry, L. Jean-Luc, Patent France 2 697 832 (1994).
[63] M.N. Shepeleva, B.R. Bunimovich, O.A. Kirichenko et al., in: A. Samachov (Ed.), Scientific Bases of Catalyst Preparation, Institute of Catalysis, Novosibirsk, 1983, p. 234 (in Russian).
[64] R.K. Iler, J. Am. Cer. Soc. 47 (1964) 339.
[65] E. Yoldas Bulent, J. Mater. Sci. 11 (1976) 465.
[66] Patent USA 3 956 186 (1976).
[67] N.F. Ermolenko, M.D. Efros, Vesti AN BSSR, Ser. Chim. Nauk. 3 (1973) 5 (in Russian).
[68] V.A. Peregudov, N.V. Kochetkova, E.V. Gorotshankin, V.N. Anochin, Proceedings of the Nauchno-techn. Conference, Moscow Chim. Techn. Institute (branch), Novomoskovsk, part 2, 6–11 February 1984, p. 8 (in Russian).
[69] M. Masato, E. Koichi, A. Himomichi, J. Chem. Lett. 2 (1986) 151.
[70] V.L. Ermak, T.L. Pashkova, G.M. Belotserkovskii, I.Ya. Tyuryaev, Catalysts of Basic Organic Synthesis, Leningrad, 1973, N. 68, p. 77 (in Russian).
[71] D.K. Nukherjee, B.N. Samaddar, J. Trans. Indian. Ceram. Soc. 48 (1989) 23, 35.
[72] A.W. Kaysser, M. Sprissler, C.A. Handwerker, J.E. Blendell, J. Am. Ceram. Soc. 70 (1987) 339.
[73] Russian Patent Appl. N94 007 256, pr.15.03.94.
[74] N.A. Koryabkina, Ph.D. Thesis, Institute of Catalysis, Novosibirsk, 1993 (in Russian).
[75] Pat. Rus. Fed. 1 660 276, 25.08.1989.
[76] N.A. Koryabkina, G.S. Litvak, R.A. Shkrabina, Z.R. Ismagilov, Kinet. Katal. 34 (1993) 913 (in Russian).
[77] N.A. Koryabkina, Z.R. Ismagilov, R.A. Shkrabina, E.M. Moroz, V.A. Ushakov, Appl. Catal. 72 (1991) 63.
[78] N.A. Koryabkina, Z.R. Ismagilov, R.A. Shkrabina, E.M. Moroz, V.A. Ushakov, Kinet. Katal. 32 (1991) 1013 (in Russian).
[79] Z.R. Ismagilov, N.A. Koryabkina, N.A. Rudina, G.I. Goldenberg, I.A. Ovsyannikova, R.A. Shkrabina, Kinet. Katal. 32 (1991) 494 (in Russian).
[80] I.A. Ovsyannikova, G.I. Goldenberg, N.A. Koryabkina, R.A. Shkrabina, Z.R. Ismagilov, Appl. Catal. 55 (1989) 75.
[81] R.A. Shkrabina, N.A. Koryabkina, V.A. Ushakov, E.M. Moroz, M. Lausberg, Z.R. Ismagilov, Kinet. Katal. 37 (1996) 116 (in Russian).

[82] Z.R. Ismagilov, R.A. Shkrabina, N.A. Koryabkina, V.A. Ushakov, Kinet. Katal., 38, N1 (1997) 133 (in Russian).
[83] Z.R. Ismagilov, R.A. Shkrabina, N.A. Koryabkina, F. Kapteijn, Catal. Today 24 (1995) 269.
[84] N.A. Koryabkina, R.A. Shkrabina, V.A. Ushakov, Z.R. Ismagilov, Catal. Today 29 (1996) 427.
[85] N.A. Koryabkina, R.A. Shkrabina, V.A. Ushakov, E.M. Moroz, M. Lausberg, Z.R. Ismagilov, Kinet. Katal. 37 (1996) 124 (in Russian).
[86] V.A. Drozdov, P.G. Tsirulnikov, V.V. Popovskii et al., Kinet. Katal. 27 (1986) 721 (in Russian).
[87] M. Ozava, M. Kimura, A. Isogai, J. Les Common Met. 162 (1990) 297.
[88] R.A. Shkrabina, N.A. Koryabkina, V.A. Ushakov, M. Lausberg, Z.R. Ismagilov, F KapteijnKinet. Katal., 38, N1 (1997) 128 (in Russian).
[89] J.L. Duplan, H. Praliaud, Appl. Catal. 67 (1991) 325.
[90] H. Yamashita, A. Kato, N. Watanad, S. Matsuda, Nippon Kagaki Kaishi (1986) 1169.
[91] A.B. Kiss, G. Keresztur, L. Farkas, Spectrochim. Acta 36 (1980) 653.
[92] B. Beguin, E. Gazbowski, M. Primet, J. Catal. 127 (1991) 595.
[93] R.A. Shkrabina, N.A. Koryabkina, Z.R. Ismagilov, V.A. Ushakov, L.T. Tsykoza, D.A. Arendarskii, Proceedings of the Seventh Nordic Symposium Catalysis, Book of Abstracts, Turku, Finland, 2–4 June 1996, p. 31.
[94] Z.R. Ismagilov, R.A. Shkrabina, N.A. Koryabkina, Proceedings of the 11th International Congress on Catalysis – 40th Anniversary, Baltimore, USA, 30 June–5 July 1996, p. 100.
[95] N.A. Koryabkina, R.A. Shkzabina, Z.R. Jsmagilov, Proceedings of conference "The problems of Catalyst Deactivations", Ufa, (1989), Part I, 18 (in Russian)..

ELSEVIER

Catalysis Today 51 (1999) 411–417

CATALYSIS TODAY

Application of plasma spraying in the preparation of metal-supported catalysts

Z.R. Ismagilov[a,*], O.Yu. Podyacheva[a], O.P. Solonenko[b], V.V. Pushkarev[a], V.I. Kuz'min[b], V.A. Ushakov[a], N.A. Rudina[a]

[a]*Boreskov Institute of Catalysis, Pr. Ak.Lavrentieva 5, 630090, Novosibirsk, Russian Federation*
[b]*Institute of Theoretical and Applied Mechanics, Institutskaya st. 4/1, 630090, Novosibirsk, Russian Federation*

A stract

Catalysts supported on metals are widely used today, but room still remains for further improvement of catalyst characteristics. The subject of this paper is the application of a plasma spray for the deposition of alumina coatings on metal substrates of different geometry (plates, foams) for subsequent synthesis of catalysts. The alumina layer sprayed successfully solves two different problems: (i) it serves as a washcoat on which a catalyst is synthesized, and (ii) it protects the metal surface from oxidation at high temperatures.

Keywords: Plasma spraying; Metal-supported catalysts; Washcoating

1. Introduction

The development of new environmentally clean and energy safe technologies is one of today's important tasks. Examples are gas and oil processing, motor fuel production, catalytic removal of VOCs from gas streams and purification of wastewater containing organic compounds. Catalysts to be used in these processes must possess high thermal stability and wear resistance properties.

Application of metal substrates as catalyst supports is becoming more common. Metals have some advantages that make their application in catalysis more attractive than ceramic supports. Their advantages include their high mechanical strength and heat conductivity characteristics. Protection of catalytic coatings against mechanical shock and chemical exposure to the reaction medium and the conservation of the catalytic activity at high temperatures are the main problems when metal-supported catalysts are used. The preparation of materials with strong contact between the catalytic layer and the metal surface at high temperatures is also a very complicated task.

Plasma spray technology offers the possibility of preparing solid surface coatings on metals which will exhibit high mechanical and thermal stabilities. The application of plasma spray methods makes it possible to support both preliminary inert washcoats as well as catalytically active coatings.

Plasma spray of washcoatings of alumina, titania, zirconia, etc., will allow one to solve successfully the problem of adhesion of the active component to the metal surface and to protect the metal-substrates from

*Corresponding author. Tel.: +7-3832-35-02-59; fax: +7-3832-39-73-52; e-mail: zri@ns.catalysis.nsk.su

0920-5861/99/$ – see front matter
PII: S0920-5861(99)00030-9

aggressive medium and improve their durability for high temperature use. Moreover, the plasma spray method will give an opportunity to design composite materials consisting of different combinations of plasma-sprayed catalytic and protective layers.

It is important to note that there are no strict limitations on the geometry of granulated or monolithic supports when plasma spray methods are used. Both substrates of simple geometry (flat surfaces) and complex substrates (foam materials and honeycomb monoliths) can be applied successfully.

Although plasma spray techniques are well-developed and in common use today, information on the application of these methods in catalysis is rather scarce. Traditionally, plasma spraying is applied when the formation of dense, non-porous protective layers is necessary and this makes the direct use of this method in catalysis rather complicated.

A number of papers have shown that the porous structure of sprayed coatings depends significantly on the jet outflow regime (laminar, transient or turbulent): the chemical composition and flow rate of the plasma-forming gas, the plasma torch power, the spraying distance, etc. For example, an increase of the plasma-forming gas flow rate and spraying distance leads to a growth of the porosity of the coating and this is accompanied by lower adhesion [1–3]. Changing the particle size of the powder sprayed also allows regulation of the physicochemical characteristics of the layers deposited: the phase composition, the porosity, the specific surface area and the thermal conductivity properties [4,5].

Several publications have been devoted to the application of plasma spraying for the synthesis of catalysts. Two different approaches have been used for the synthesis of catalysts: (i) preliminary spraying of a gradient layer with various additives, followed by deposition of an active component; and (ii) direct spraying of a catalytically active component on a support surface [6–8].

The subject of this paper is the application of direct current (dc) plasma torch [9,10] with the interelectrode insert (IEI) for the atmosphere plasma spraying of the alumina coatings under different regimes of the jet outflow (laminar, transient or turbulent) on the metal substrates of different geometries (plates, foams) for subsequent synthesis of catalysts.

2. Experimental conditions and procedure

Operating modes of plasma torch with IEI (see [9,10]) were provided by the variation of the plasma-forming gas (air) flow rate over a wide range (from 0.5 up to 2.5 g/s); this made it possible to change the velocity of the particles and their aggregate state, and therefore, the coating micro- and macrostructure over the wide range. The main regimes of the plasma torch operation and outflowing jets are presented in Table 1.

The main advantages of the plasma torch used [9,10], as compared with conventional plasma torches are: (i) application of IEI provides a possibility to increase the plasma torch power by increasing the arc voltage (rather than the arc current, as usually); this increasing the continuous operating life of the plasma torch electrodes; (ii) the detected frequency of the arc shunting in plasma torches of this type is one or two orders of magnitude higher in comparison with the large scale shunting (low-frequency) in plasma generators with a self-setting arc length, other conditions being equal; (iii) within a specific range and at equal gas flow rate, pressure, discharge chamber diameter, arc current and other parameters, the mean mass temperature of the gas at the outlet of the output electrode of a plasma torch with IEI is always higher than in a plasma generator with a self-setting arc mean length; this is explained by a higher electric field of the turbulent arc and by a possibility of varying the IEI length; (iv) realization of a ''diffusive'' arc attachment on the anode surface provides an axial symmetry of the exhausting plasma flow, this increasing the stability and reproducibility of the parameters of the high-temperature flow in the repeated torch activation; (v) the use of air as a working gas, when there are no strict requirements to the gas composition, reduces substantially the cost of plasma technologies and speeds up the equipment pay-back and (vi) the use of the plasma torch operating mode with a quasi-laminar jet outflow makes possible new effective technologies of powder (primarily oxide) materials and surface treatment.

The principal scheme of the powder plasma spraying set-up, used in this work, is presented in Fig. 1. Alumina powders differing in phase composition and particle size (α-Al_2O_3 20–80 and γ-Al_2O_3 90–500 μm) were used to spray a washcoating layer on titanium plates and nickel foam materials. The active phase was

Table 1
Main regimes of the plasma torch operating and outflowing jets

Flow rate of plasma-forming gas (air) G_g (g s^{-1})	0.5	0.75	1.0	1.25	2.0	2.5
Arc current I (A)	255	250	245	240	220	210
Arc voltage U (V)	180	200	210	220	250	270
Efficiency of electric energy utilization η (%)	45	50	60	65	70	72.5
Effective thermal power of outflowing plasma jet (kW)	20.6	25.0	30.8	34.3	38.5	41.1
Regime of the plasma jet outflow and approximate length of powder thermal treatment zone in axial direction, L_r (m)	Laminar	Laminar–transient	Transient	Transient	Turbulent	Turbulent
	0.15	0.09	0.075	0.06	0.05	0.05
Mean-mass temperature of plasma prior to powder injection section/K	8450	7600	7400	7150	6400	6150
Mean-mass velocity of plasma prior to powder injection section (m s^{-1})	460	570	720	815	1020	1160
Characteristic times of heating (ms) corresponding to particles of different size (mkm)						
20	0.96	0.6	0.46	0.35	0.24	0.22
40	1.5	0.96	0.71	0.55	0.38	0.33
70	2.1	1.3	1.0	0.77	0.54	0.49
90	2.4	1.6	1.1	0.89	0.65	0.58
200	3.9	2.5	1.9	1.5	1.1	0.99
300	5.3	3.4	2.6	2.0	1.5	1.3
400	6.5	4.1	3.1	2.5	1.8	1.6
500	7.6	4.8	3.6	2.9	2.1	1.8

synthesized by impregnation of the plasma sprayed layer with lanthanum and cobalt cations. In some cases, the modification of the plasma-sprayed layer was provided by the deposition of lanthanum-containing γ-Al_2O_3 to increase the specific surface area of the washcoating layer. For comparison, the same catalysts on Ni foam supports were synthesized using the technique described in reference [11], which includes a direct synthesis of a γ-Al_2O_3-containing washcoat on the metal surface by a chemical method without the formation of plasma-sprayed layer.

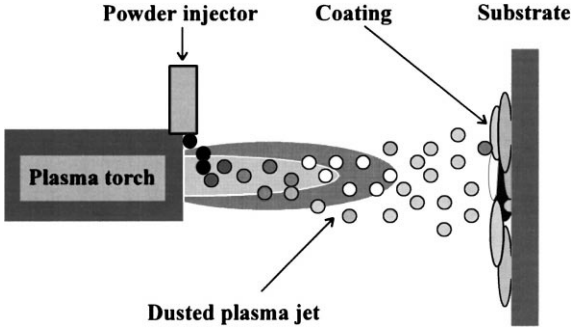

Fig. 1. Schematic diagram of the plasma spray set-up.

X-ray analysis of the samples was carried out using a HZG-4 diffractometer with copper radiation in the 2θ range of 20–55°. To specify the parameters of the solid solutions and of the perovskite composition, the data were obtained in the range of 2θ of 62–72°. The specific surface areas of the samples were measured by the BET method and the pore volumes of the sprayed layers were calculated using the water capacity technique. The morphology of the catalysts was characterized by SEM. The catalytic activity was

Table 2
Properties of γ-Al_2O_3 after plasma treatment and cooling in water

Particle size (μm)	Flow rate ($g\ s^{-1}$)	Regime	Specific surface area ($m^2\ g^{-1}$)	Phase composition	I_α/I_γ[a]
90–200	0.5	Laminar	2.2	α-Al_2O_3, γ-Al_2O_3	30
90–200	1.0	Transient	22	α-Al_2O_3, γ-Al_2O_3	13
200–300	0.5	Laminar	19	α-Al_2O_3, γ-Al_2O_3	25
200–300	1.0	Transient	76	α-Al_2O_3, γ-Al_2O_3	11
300–400	0.5	Laminar	67	α-Al_2O_3, γ-Al_2O_3	8
300–400	1.0	Transient	104	α-Al_2O_3, γ-Al_2O_3	6
400–500	0.5	Laminar	119	α-Al_2O_3, γ-Al_2O_3	

[a] I_α/I_γ ratio of intensities of line d/n=2.085 (α-Al_2O_3) and d/n=1.990 (γ-Al_2O_3).

tested for the methane oxidation reaction in a flow set-up; the reaction mixture was 1% CH_4 in air with a volume velocity of 400 h^{-1}.

3. Result and discussion

As mentioned before, the jet outflow regime and powder particle size define physicochemical characteristics of coatings sprayed. A preliminary study of the influence of the plasma regimes on the properties of alumina powders plasma treated and cooled in water has been performed. The results for γ-Al_2O_3 powder are presented in Table 2.

A comparison of cross-section views of initial and plasma-treated and cooled in water particles of γ-Al_2O_3 showed that in the latter case the pellet consists of a core and a shell (Fig. 2). The densities of these two basic areas are different. A comparison of the scanning electron micrographs of the initial and the plasma-treated and cooled in water particles and the analysis of XRD data allow us to suggest that the particle core consists of γ-Al_2O_3 phase, while the particle shell is made of α-Al_2O_3. It seems that the use of large particles for spraying and high cooling velocities leads to the formation of a cool core and a hot melted shell. This conclusion was confirmed by the numerical modeling of the temperature distributions inside the particles of γ-Al_2O_3. The method used is described in reference [10]; it took into account the temperature gradient under heating and complicated aggregate state of the particle.

At the same time, experiments on the plasma spraying of alumina of different phase composition and particle size on titanium plates showed that the properties of plasma sprayed layers are quite similar and do not depend significantly on the jet outflow regime used (Table 3).

When α-Al_2O_3 was sprayed on titanium plates, the coatings were characterized by a low specific surface area; meanwhile, their pore volume increased when the spraying regime was changed from laminar to turbulent.

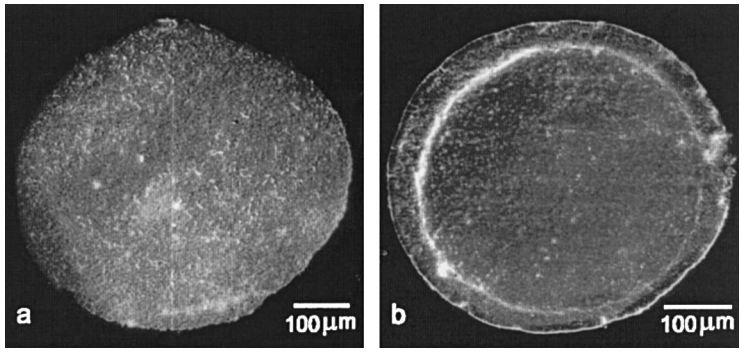

Fig. 2. Micrograph of a cross-section view of (a) initial and (b) plasma-treated γ-Al_2O_3 particles.

Table 3
Properties of alumina sprayed on titanium plates

Particle size (μm)	Type of alumina sprayed	Flow rate ($g\ s^{-1}$)	Regime of plasma jet outflow	Specific surface area (m^2g^{-1})	Phase composition	Pore volume ($cm^3\ g^{-1}$)
40	α-Al_2O_3	0.75	Laminar–transient	0.2	α-Al_2O_3	0.052
40	α-Al_2O_3	1.25	Transient	0.2	α-Al_2O_3	0.065
40	α-Al_2O_3	1.75	Turbulent	0.2	α-Al_2O_3	0.167
90–200	γ-Al_2O_3	0.5	Laminar	0.2	α,θ-Al_2O_3	0.068
90–200	γ-Al_2O_3	0.75	Laminar–transient	0.4	α,θ-Al_2O_3	0.075
90–200	γ-Al_2O_3	1.0	Transient	0.6	α,θ-Al_2O_3	0.166

It was established that the dependence of the regime on the coating properties was the same when γ-Al_2O_3 was sprayed. Moreover, in the latter case, the spraying regime influenced the quantitative proportions of the α-Al_2O_3 and θ-Al_2O_3 phases of the coatings and their specific surface areas. The maximum pore porosity and minimum α-Al_2O_3 phase content were registered when a transient jet outflow regime was used.

The disagreement in the data for the phase compositions and the specific surface area for γ-Al_2O_3 powders plasma treated and cooled in water and for γ-Al_2O_3 sprayed on Ti plates may be explained by significant differences in the quenching rate in the experiments performed. The formation of dense layers when γ-Al_2O_3 was sprayed on titanium plates was confirmed by scanning electron microscopy (Fig. 3). It is obvious that the contact between the alumina and the metal surface was rather strong and uniform. The sprayed layer had a complicated structure, consisting of dense areas and macropores of different forms and sizes.

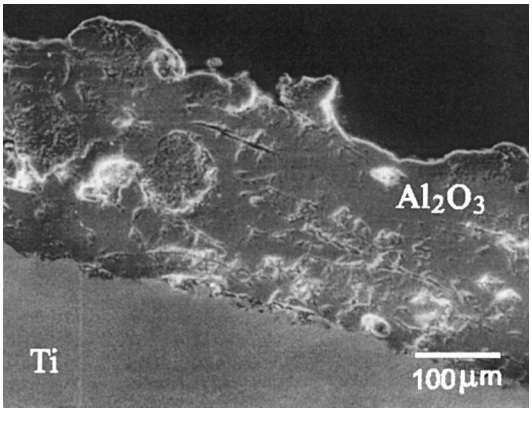

Fig. 3. Micrograph of a cross-section view of γ-Al_2O_3 plasma-sprayed on Ti.

The direct deposition of the active La–Co component on these supports leads to the formation of $LaCoO_3$ and Co_3O_4 phases, as shown by XRD. The quantities of the supported active component did not exceed 2 wt% because of the low porosity of the sprayed alumina layer. A modification of the sprayed layer by La-containing γ-Al_2O_3 allowed an increase of this value by one order of magnitude. The phase composition of the modified catalyst after the deposition of the active La–Co component was more complex. Besides the presence of the $LaCoO_3$ and Co_3O_4 phases, $LaAlO_3$ perovskite was also formed.

The procedure described was applied to the synthesis of catalysts on Ni foam supports. The external surface of α-Al_2O_3 sprayed on the metal foam support had a complex structure; there were a number of splats differing in appearance and thickness (Fig. 4). The modification of the plasma-sprayed alumina coating by La-containing γ-Al_2O_3 leads to the formation of a top layer on the plasma sprayed alumina (Figs. 5 and Fig. 6). SEM showed also the presence of an intermediate region sprayed between a top layer consisting of γ-Al_2O_3 and dense plasma sprayed α-Al_2O_3 coating. This layer is probably formed at the end of the spraying process (the ''switching off'' moment) when a moderate temperature regime is realized, this leading to the formation of a layer with higher porosity than the basic one.

The SEM study of catalysts supported on Ni foams coated by plasma-sprayed alumina and modified by La-containing γ-Al_2O_3 revealed that the La–Co component was concentrated in the modifying layer (Fig. 6). XRD showed the formation after calcination at 1000°C of the main $LaAlO_3$ phase and a solid solution based on γ-Al_2O_3.

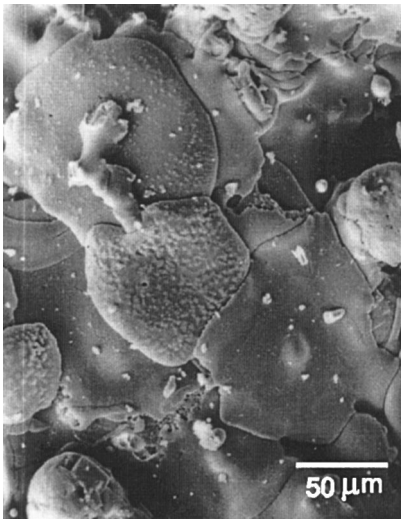

Fig. 4. Micrograph of plasma-sprayed alumina on a Ni foam support.

Changes of the characteristics of the samples following various temperature treatments were examined by XRD and BET measurements and their activities for the methane oxidation reaction were also determined. An increase of the calcination temperature from 600°C to 1000°C caused a decrease in the BET area of the samples from 20 to 8 m^2/g, while the temperature to give 50% methane conversion increasing from 460°C to 610°C.

The properties of the catalysts developed were compared with those of catalysts having the same phase composition and BET surface area but synthesized without the use of a plasma-sprayed alumina layer. The catalysts calcined at temperatures from 600°C to 1000°C demonstrated the same level of activity as catalysts synthesized using the plasma technique. A difference in the activity between these types of catalysts appeared when the duration of calcination at 1000°C was increased from 3 to 9 h. There was no decrease in the activity of the catalyst with a plasma-sprayed alumina layer whereas the temperature to give 50% conversion rose from 600°C to 655°C for the catalyst prepared without a plasma-sprayed layer (Fig. 7). It appeared that a plasma-sprayed washcoating layer consisting of alumina on a Ni foam support prevented the nickel from

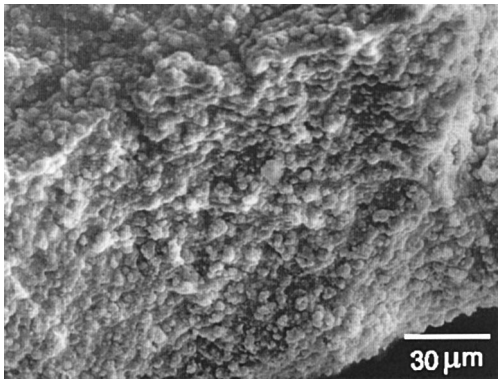

Fig. 5. Micrograph of a modifying γ-Al_2O_3 layer supported on a plasma-sprayed alumina.

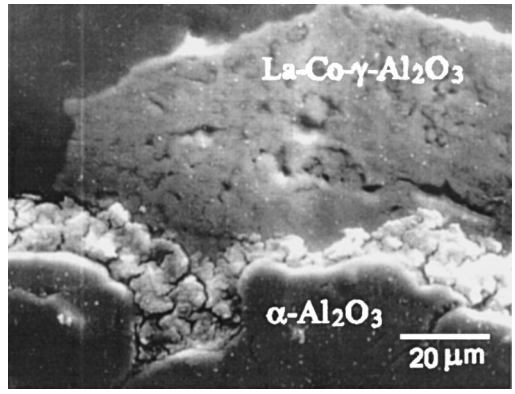

Fig. 6. Micrograph of a cross-section view of a catalyst consisting of La–Co on a Ni foam support.

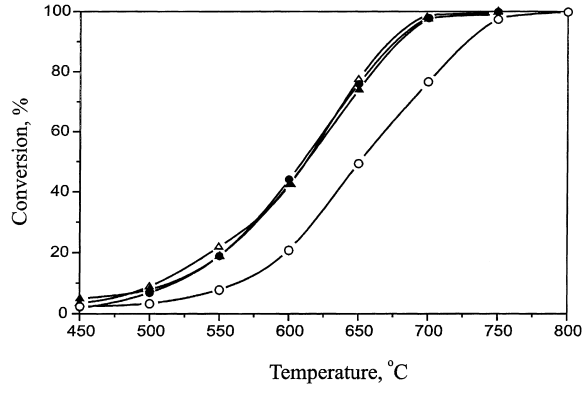

Fig. 7. Temperature dependencies of methane conversion (1% CH_4 in air) on catalysts: (▲) La–Co/Ni, plasm., T_{calc}=1000°C for 3 h; (△) La–Co/Ni, T_{calc}=1000°C for 3 h; (●) La–Co/Ni, plasm., T_{calc}=1000°C for 9 h; (○) La–Co/Ni, T_{calc}=1000°C for 9 h.

becoming oxidized more successfully and increased the thermal stability of the catalyst.

4. Conclusion

In this paper we have presented our first results of a comprehensive study of catalysts prepared on metal supports for high temperature combustion developed using plasma spray methods. Undoubtedly, application of the plasma spray technology in this area is very promising. Experiments performed on metal supports of different geometry have shown that a sprayed alumina layer has a strong and uniform adhesion to the metal surface. The gradient layer sprayed successfully solves two different problems: (i) it serves as a washcoat on which a catalyst can subsequently be synthesized; and (ii) it protects the metal surface from oxidation at high temperatures.

Acknowledgements

This research was subsidized by a grant from the Siberian Division of the Russian Academy of Sciences in the frame work of the Integrated Program (grant no. 28, ''Physical Processes at Contact Boundaries during Production of Heterogeneous Materials and Coatings'').

References

[1] T. Yoshida, Appl. Chem. 66 (1994) 1223.
[2] J. Ilavsky, J. Forman, P. Chraska, J. Mater. Sci. Lett. 11 (1992) 573.
[3] S. Uematsu, T. Senda, Proceedings of the Eighth International Symposium on Plasma Chemistry, vol. 4, Tokyo, 31 August–4 September 1987, p. 1958.
[4] D.J. Varacalle, Proceedings of the Third Material Resources Society Symposium, Reno, 5–9 April 1988, Pittsburgh, p. 541.
[5] Ke-Shun Shi, Z-Y. Qian, M-S. Zhuang, J. Am. Ceram. Soc. 71 (1988) 924.
[6] J.V. Gorynin, B.V. Farmakovskii, A.P. Khinsky, Patent USA, no. 5 204 302 (1991).
[7] H.R. Khan, H. Frey, J. Alloy. Compounds 190 (1993) 209.
[8] S.V. Dozmorov, A.N. Pestryakov, SU Patent no. 1 695 978 (1989).
[9] V.I. Kuz'min, O.P. Solonenko, M.F. Zhukov, Proceedings of the Fourteenth International Thermal Spray Conference, 25–28 May 1995, Kobe, Japan, p. 1091.
[10] O.P. Solonenko, in: O.P. Solonenko, M.F. Zhukov (Eds.), Thermal Plasma and New Materials Technology. Vol. 2. Investigation and Design of Thermal Plasma Technologies, vol. 7, Cambridge/Interscience, UK, 1995, p. 97.
[11] O.Yu. Podyacheva, A.A. Ketov, Z.R. Ismagilov, V.A. Ushakov, A. Bos, H.J. Veringa, React. Kinet. Catal. Lett. 60 (1997) 243.

КИНЕТИКА И КАТАЛИЗ, 2000, том 41, № 3, с. 433–438

УДК 542.973:546.654'623'46

ИССЛЕДОВАНИЕ РЕАКЦИЙ И КАТАЛИЗАТОРОВ СЖИГАНИЯ ТОПЛИВ

XIX. ТЕРМОСТАБИЛЬНОСТЬ ОКСИДА АЛЮМИНИЯ, СОДЕРЖАЩЕГО ОДНОВРЕМЕННО ДОБАВКИ ЛАНТАНА И КРЕМНИЯ

© 2000 г. Р. А. Шкрабина, В. А. Ушаков, Н. А. Корябкина, З. Р. Исмагилов

Институт катализа им. Г.К. Борескова СО РАН, Новосибирск

Поступила в редакцию 30.10.98 г.

Методом рентгенофазового анализа и измерением прочности и удельной поверхности исследована термическая стабильность системы La–Si/Al_2O_3 в зависимости от содержания вводимых элементов и температуры прокаливания. Обсуждены механизмы взаимодействия этих элементов с оксидом алюминия. Показано, что взаимодействие катионов кремния и лантана начинается уже при низких температурах (~500°C). Высказано предположение, что заполнение катионом кремния тетраэдрических, а катионом лантана – октаэдрических позиций в решетке γ-оксида алюминия приводит к значительному повышению его термической стабильности. Так, при 1200°C в тройной системе сохраняется до 50% γ-Al_2O_3, и только при 1300°C начинает формироваться α-Al_2O_3.

Работа является продолжением исследований влияния модифицирования оксида алюминия катионами Mg, La, Ce, [1–3], La–Mg [4, 5] и Ce–Mg [6] на его свойства и посвящена изучению алюмооксидных систем, одновременно содержащих добавки лантана и кремния.

МЕТОДИКА ЭКСПЕРИМЕНТА

Кремний вводили в виде золя или порошка оксида кремния в золь гидроксида алюминия псевдобемитной структуры, полученного по методу, описанному в [7], перед формованием сферических гранул, а лантан вводили в сферические гранулы (диаметр 2–3 мм) γ-Al_2O_3 пропиткой по влагоемкости из раствора нитрата лантана. Сферические гранулы получали методом углеводородно-аммиачного формования [8], далее гранулы сушили при 110°C и прокаливали при температурах 550–1300°C (2 или 4 ч при каждой температуре).

Рентгенографический анализ образцов проводили на дифрактометре HZG-4 аналогично [1–3].

Удельную поверхность ($S_{уд}$) образцов определяли методом БЭТ по термодесорбции аргона.

Механическую прочность гранул на раздавливание измеряли по стандартной методике на приборе МП-9С. Среднюю прочность ($P_{ср}$) рассчитывали из выборки объемом не менее 30 гранул.

РЕЗУЛЬТАТЫ И ИХ ОБСУЖДЕНИЕ

Результаты исследования влияния ионов кремния на структурно-механические свойства оксида алюминия в процессе его термообработки представлены в табл. 1. Увеличение содержания SiO_2 (добавленного в виде кремнезоля) приводит к снижению содержания α-Al_2O_3 при 1200°C, а при содержании 33 вес. % SiO_2 (образец 4) наблюдается продукт взаимодействия его с Al_2O_3 – муллит. Интересно отметить, что при 1300°C в этом образце наряду с муллитом появляется и α-SiO_2, что свидетельствует об ограниченном взаимодействии с оксидом алюминия. При введении кремния в виде кристобалита (образцы 5 и 6) эффект стабилизации не наблюдается. Для сравнения в табл. 2 представлен фазовый состав кремнийоксидной системы, полученной при прокаливании кремнезоля. Видно, что вплоть до 900°C она представляет собой рентгеноаморфную фазу, а уже при 1000°C фиксируется только фаза кристобалита. Следует отметить, что в исследованных нами алюмокремниевых системах, в которых SiO_2 вводился в виде золя, при 1000°C фаза кристобалита не наблюдается.

Полученные результаты, свидетельствующие о взаимном стабилизирующем влиянии катионов алюминия и кремния в алюмокремниевых оксидах, позволяют предположить, что это влияние обусловлено взаимодействием оксидов.

Необходимо отметить, что с увеличением содержания SiO_2 (добавленного в виде золя) возрастает не только термическая, но и механическая стабильность. Прочность гранул с 33% SiO_2 при 1200°C в ~5 раз выше, чем у чистого α-Al_2O_3 (табл. 1).

Влияние на термическую стабильность температуры и времени прокаливания наиболее де-

Таблица 1. Влияние добавок SiO_2 на свойства сферического оксида алюминия (d = 2–3 мм)

№ образца	SiO_2, %	$S_{уд}$, $м^2/г$	$P_{ср}$, МПа	Фазовый состав
		550°C, 4 ч*		
1	0	240	19	γ-Al_2O_3
2	2.5 (золь)	240	19	γ-Al_2O_3
3	14.5 (золь)	240	22	γ-Al_2O_3
4	33.0 (золь)	250	17	γ-Al_2O_3 + аморфная фаза
5	2.0 (кристобалит)	210	19	γ-Al_2O_3
6	14.5 (кристобалит)	220	16	γ-Al_2O_3
		1200°C, 4 ч*		
1	0	8.6	26	α-Al_2O_3
2	2.5 (золь)	40	29	40% α-Al_2O_3 + δ-Al_2O_3
3	14.5 (золь)	44	51	30% α-Al_2O_3 + δ-Al_2O_3
4	33.0 (золь)	30	130	2% α-Al_2O_3 + δ-Al_2O_3 + следы муллита
5	2.5 (кристобалит)	10	29	α-Al_2O_3 + α-SiO_2
6	14.5 (кристобалит)	12	14	α-Al_2O_3 + α-кристобалит
		1300°C, 2 ч*		
1	0	6	34	α-Al_2O_3
2	2.5 (золь)	7.9	29	α-Al_2O_3
3	33.0 (золь)	6.5	135	α-Al_2O_3 + α-SiO_2 + муллит
		1400°C, 2 ч*		
1	0	2.9	38	α-Al_2O_3
2	2.5 (золь)	3.0	31	α-Al_2O_3
3	33.0 (золь)	4.0	145	α-Al_2O_3 + α-SiO_2 + муллит

* Условия термообработки модифицированного оксида алюминия.

тально было исследовано для образцов, содержащих 2.5 вес. % SiO_2. Длительная (в течение 24 ч) термообработка показала, что стабильность этих образцов существенно выше, чем у "чистого" Al_2O_3. После прокаливания в первом случае потери $S_{уд}$ за счет спекания составляют 8% (при 1000°C), ~6% (при 1100°C) и 12% (при 1200°C), в то время как у "чистого" оксида алюминия эти изменения составляют 30% (при 1000°C), ~70% (при 1100°C) и 40% (при 1200°C).

Что касается термостабильности "чистого" Al_2O_3, то эти результаты подтверждают ранее опубликованные нами данные о резком изменении свойств оксида алюминия, полученного из продукта терморазложения гиббсита при 1100°C [1–3]. За счет неоднородности фазового состава низкотемпературного оксида (наличие χ-фазы, наряду с γ-Al_2O_3) происходит не только резкое уменьшение механической прочности гранул, но и резкое уменьшение $S_{уд}$.

Таблица 2. Зависимость от температуры фазового состава в кремнеоксидной системе, полученной из золя

Температура прокаливания, °C	Фазовый состав
550	Рентгеноаморфная фаза
900	Рентгеноаморфная фаза более окристаллизованная, чем при 550°C
1000	Кристобалит

На основании анализа полученных нами результатов для синтеза и исследования алюмооксидной системы, содержащей одновременно катионы La и Si, была выбрана следующая композиция:

$$2.5\%\ SiO_2 + 5\%\ La_2O_3 + 92.5\%\ Al_2O_3.$$

В табл. 3 представлены основные свойства синтезированной системы в сравнении с "чистым" Al_2O_3 и оксидом алюминия, содержащим только SiO_2 (2.5 вес. %) или только La_2O_3 (5 вес. %). Как видно из таблицы, введение одновременно лантана и кремния приводит к значительному замедлению фазовых превращений в оксиде алюминия и связанному с этим сохранению достаточно высокого значения удельной поверхности при высокотемпературной обработке. Наибольший эффект термостабилизации наблюдается при

Таблица 3. Свойства модифицированного различными катионами сферического оксида алюминия

№ образца	Модифицирующая добавка	$S_{уд}$, м^2/г	$P_{ср}$, МПа	Фазовый состав
			550°C	
1	–	200	24	γ-Al_2O_3
2	La	180	26	γ*-Al_2O_3
3	Si	240	19	γ-Al_2O_3
4	La–Si	190	32	γ**-Al_2O_3
			900°C	
1	–	100	20	γ-Al_2O_3 + κ-Al_2O_3 + δ-Al_2O_3
2	La	100	25	γ*-Al_2O_3 + 50% δ-Al_2O_3
3	Si	125	20	γ-Al_2O_3 + δ-Al_2O_3
4	La–Si	120	35	γ**-Al_2O_3
			1000°C	
1	–	60	26	50% α-Al_2O_3 + κ-Al_2O_3 + δ-Al_2O_3
2	La	110	25	γ*-Al_2O_3 + 50% δ-Al_2O_3
3	Si	95	25	γ-Al_2O_3 + δ-Al_2O_3
4	La–Si	110	35	γ**-Al_2O_3
			1100°C	
1	–	11	27	α-Al_2O_3
2	La	64	23	[γ- + δ- + α- (сл)] Al_2O_3 + $LaAlO_3$ (сл) + $La_2O_3 \cdot 11Al_2O_3$ (сл)
3	Si	50	28	[δ- + α- (сл)]Al_2O_3
4	La–Si	100	37	γ**-Al_2O_3
			1200°C	
1	–	7	28	α-Al_2O_3
2	La	29	35	$LaAlO_3$ (сл) + α-Al_2O_3 + $La_2O_3 \cdot 11Al_2O_3$
3	Si	40	29	40% α-Al_2O_3 + δ-Al_2O_3
4	La–Si	80	38	γ**-Al_2O_3 + δ-Al_2O_3 (~50%) (более окристаллизован)
			1300°C	
1	–	6	30	α-Al_2O_3
2	La	8	44	$LaAlO_3$ + α-Al_2O_3 + $La_2O_3 \cdot 11Al_2O_3$
3	Si	8	29	α-Al_2O_3
4	La–Si	26	48	α-Al_2O_3 (сл) + θ-Al_2O_3 + $La_2O_3 \cdot 11Al_2O_3$ (сл)

Примечание. γ* – твердый раствор La^{3+} в γ-Al_2O_3; γ** – аморфизованный γ-Al_2O_3; сл – следы.

$T > 1000$°C. Так, при 1100°C $S_{уд}$ образца, содержащего La и Si, в ~2 раза выше, чем для систем La/Al_2O_3 и Si/Al_2O_3; при 1200°C значительная разница в величине удельной поверхности между этими системами сохраняется, а при 1300°C для La–Si/Al_2O_3 $S_{уд}$ в ~3–4 раза выше, чем для La/Al_2O_3, Si/Al_2O_3 и "чистого" Al_2O_3, для которых различия в $S_{уд}$ нивелируются. Это обусловлено тем, что фазовый состав исследованных систем существенно различается. Фаза α-Al_2O_3 в La–Si/Al_2O_3 проявляется только при 1300°C и только в следовых количествах. В этой системе после высокотемпературных обработок (>1000°C) не обнаружена фаза алюмината лантана (в отличие от системы La/Al_2O_3, как показано в [2]). Гексаалюминат лантана появляется только при 1300°C. Следует также отметить отсутствие продуктов взаимодействия оксидов лантана и кремния. Фаза γ-Al_2O_3 присутствует даже при 1200°C, хотя в более окристаллизованном виде по сравнению с образцом, прокаленным при 550°C.

Интересно отметить, что эффект стабилизации для системы La–Si/Al_2O_3 существенно выше по сравнению с системой Mg–La/Al_2O_3. Так, при одинаковом содержании La_2O_3 (5 вес. %) после термообработки при 1200°C в Mg–La/Al_2O_3 (по данным [5]) образуется 15% α-Al_2O_3 и $S_{уд}$ этого образца в ~4 раза ниже, чем для La–Si/Al_2O_3, в ко-

тором фаза α-Al_2O_3 не фиксируется (табл. 3, образец 4). При 1300°C в системе Mg–La/Al_2O_3 присутствует только α-Al_2O_3 (наряду со смешанным твердым раствором магния и лантана в оксиде алюминия [5]), а для La–Si/Al_2O_3 фаза α-Al_2O_3 фиксируется лишь в следовых количествах.

В спектрах ЯМР ^{29}Si образца 2.5% SiO_2–Al_2O_3 (золь), прокаленного при 550°C и 900°C, сигналы со сдвигами, характерными для атомов кремния, связанных через кислородный мостик с алюминием, отсутствуют. Это, вероятно, связано с низкой концентрацией таких связей (Si–O–Al). При этом, однако, фиксируются небольшие отклонения значений химических сдвигов, которые не могут быть однозначно объяснены взаимодействием между катионами алюминия и кремния, но позволяют предположить вероятность такого взаимодействия[1].

Следовательно, результаты, полученные с использованием методов ЯМР и РФА, не позволяют уверенно говорить о взаимодействии компонентов в Si–Al- и La–Si–Al-системах. Тем не менее, косвенные доказательства этого взаимодействия имеются:

1) образование рентгеноаморфного оксида в системе 33% SiO_2–Al_2O_3 (табл. 1) при 550°C и муллита при 1200°C, в то время как чистый рентгеноаморфный SiO_2 уже при 1000°C превращается в кристобалит (табл. 2);

2) формирование аморфизованного γ-Al_2O_3, стабильного вплоть до 1200°C, при введении в оксид алюминия одновременно кремния и лантана (табл. 3).

Причину стабилизации γ-Al_2O_3 при высоких температурах, как и в случае магний-лантановой системы, можно объяснить, по нашему мнению, только на основе гидроксо-оксидной модели устройства низкотемпературных оксидов алюминия, анализируя пути перестройки структуры твердых растворов на основе этих оксидов при термообработке [9, 10].

Согласно указанной модели, η- и γ-Al_2O_3 имеют протошпинельную структуру, описываемую формулой

$$A^*_{x_1}A^*_{x_2}B^*_{y_1}B^*_{y_2}O_{32-z}(OH, \ldots)_z,$$

где A и B – шпинельные тетра- и октаэдрические позиции катионов, а A* и B* – протошпинельные катионные позиции, рассматриваемые с точки зрения структуры шпинели в качестве дефектов. Структура стабилизирована присутствуем в анионном каркасе гидроксильных групп. Общее содержание катионов алюминия составляет ~18.5 вместо 24, как в случае шпинели. Низкотемпературные растворы на основе протошпинсли в целом имеют близкую структуру, но отличаются значениями коэффициентов x, y, z.

С ростом температуры, по мере удаления протонов и совершенствования кубического анионного каркаса катионные позиции заполняются все более плотно. Этот процесс может протекать принципиально различными путями:

1. За счет возрастающего заполнения преимущественно октаэдрических позиций, при этом параллельно уменьшается заполнение дефектных позиций. Конечным результатом протекания процесса по этому пути является образование стехиометрической шпинели AB_2O_4. Этот путь характерен для системы, содержащей магний.

2. За счет увеличения заполнения преимущественно тетраэдрических позиций катионов. В этом случае заполняются новые, нехарактерные для шпинели и низкотемпературных форм оксида алюминия катионные позиции. По мере повышения температуры происходит образование последовательно δ-, θ-форм или твердых растворов на их основе. Такой путь перестройки структуры характерен для собственно оксида алюминия и для системы, содержащей лантан. Конечным результатом этого пути перестройки структуры является переход от практически кубического плотноупакованного кислородного анионного каркаса к гексагональному (с образованием либо α-Al_2O_3, либо твердых растворов на ее основе, либо гексаалюминатов).

Известно [11], что в зависимости от координации ионные радиусы катионов, упомянутых в статье, составляют для октаэдрического окружения: Al^{3+} = 0.053 нм, Si^{4+} = 0.040 нм, La^{3+} = 0.106 нм; для тетраэдрического окружения: Al^{3+} = 0.039 нм, Si^{4+} = 0.026 нм. Ионы алюминия могут легко замещаться на ионы меньшего размера, такие, как кремний. Плотная кубическая упаковка кислорода позволяет размещать без искажения решетки ионы радиусом не более 0.075 нм.

Введение кремния в оксид алюминия приводит к новой ситуации, обусловленной особенностями его свойств (заряд 4+ и предпочтение тетраэдрического кислородного окружения). При неизменности структуры низкотемпературной формы оксида замещение алюминия на кремний должно приводить к появлению избыточного положительного заряда катионной подрешетки, который может быть уменьшен путем удаления части протонов, как наиболее подвижных элементов структуры. В то же время удаление протонов из состава анионной подрешетки протошпинели и связанное с ним нарушение электронейтральности молекулы является движущей силой перестройки структуры переходных форм оксида алюминия и твердых растворов на их основе с ростом температуры. Таким образом, замещение ионов

[1] Авторы благодарят А.В. Носова за полезное обсуждение результатов.

алюминия ионами кремния с параллельным удалением протонов делает ненужным процесс перестройки структуры низкотемпературного оксида при повышении температуры, и, соответственно, содержание катионов должно остаться практически неизменным, а структура низкотемпературного оксида должна как бы "заморозиться".

В РФА это проявляется в виде практически неизменной дифракционной картины для низкотемпературной формы оксида алюминия. При достаточно большом замещении структура искажается, возможно становится более низкосимметричной, но сохраняющей практически кубической анионный каркас, что проявляется в размывании дифракционной картины.

Замещение алюминия на кремний в структурс низкотемпературной формы оксида алюминия имеет два ограничивающих фактора: количество гидроксильных групп и количество заполненных алюминием тетраэдрических позиций, но, очевидно, первый фактор является определяющим. Это в свою очередь означает, что состав продукта взаимодействия SiO_2 и Al_2O_3 будет определяться конкуренцией двух процессов: скоростью замещения алюминия на кремний и скоростью удаления гидроксильных групп с образованием анионных вакансий, поскольку оба эти процесса направлены на увеличение положительного заряда в ячейке.

Конечным результатом термических превращений продукта взаимодействия SiO_2 и Al_2O_3 является муллит. Хотя ему приписывают химическую формулу $Al_6Si_2O_{13}$, однако структурные исследования показывают, что он соответствует формуле $Al_{6-x}Si_xO_z$, где по разным данным x = = 1.016–1.48 и z = 9.0508–9.74. Если рассмотреть утроенную ячейку муллита, объем которой почти точно соответствует объему ячейки шпинели, то можно оценить изменения в заполнении катионной и анионной подрешеток при переходе от структуры чистой низкотемпературной формы оксида алюминия к муллиту. Такая утроенная ячейка приближается к формуле $Al_{14}Si_4O_{29}$, а например, γ-Al_2O_3 имеет, согласно нашей модели, протошпинельную структуру, описываемую формулой $A^*_{1.75}A_{6.75}B^*_{1.0}B_{9.0}O_{23.5}(OH)_{8.5}$. Сравнение этих формул показывает, что, как говорилось выше, степень заполнения катионной подрешетки практически осталась неизменной. Потеря протонов из анионного каркаса частично компенсирована замещением половины имевшихся в тетраэдрических позициях ионов алюминия ионами кремния, а частично, при росте температуры термообработки, удалением анионов с образованием анионных вакансий. Замещение алюминия на ионы кремния и удаление из кубического анионного каркаса почти 10% анионов привело в конечном счете к искажению структуры – к переходу от кубической симметрии к орторомбической.

Появление лантана в структуре оксида алюминия приводит к существенным искажениям решетки, поскольку размер катиона достаточно велик. Даже в α-Al_2O_3 растворимость лантана не превышает 10 мол. %. Мы полагаем, что рыхлая структура γ-Al_2O_3, в которой возможно образование дефектов анионной подрешетки, способствует ограниченной растворимости лантана, достаточной для повышения общей термостабильности системы.

Присутствие в системе лантана, как и в случае магний-лантановой системы, благоприятствует вхождению ионов кремния в структуру носителя и создает дополнительные диффузионные ограничения для перестройки структуры твердого раствора при высоких температурах.

Таким образом, при промотировании алюмооксидных носителей смесью двух катионов – кремния и лантана – удается достичь стабилизации структуры низкотемпературных форм оксида алюминия за счет формирования устойчивого твердого раствора.

В [12] – в единственной, известной авторам работе – наблюдалась фаза, представляющая собой продукт взаимодействия SiO_2 и Al_2O_3. Авторы показали, что способ приготовления смешанных Si- и Al-содержащих ксерогелей влияет на формирование фаз – предшественников муллита. Если ксерогели формировались при быстром гидролизе то образовывалась шпинельная фаза, близкая по составу к $SiO_2 \cdot 6Al_2O_3$. Из шпинельной фазы в процессе термообработки кристаллизовалась фаза муллита. Упоминание о шпинельной фазе имеется также в работе [13], в которой авторы исследовали продукты механоактивации каолинита после их термообработки. Выше 900°C в механоактивированном каолините фиксируются следы шпинели, доля которой возрастает после прокаливания при 1000°C. Дальнейшее увеличение температуры приводит к увеличению доли муллита.

Таким образом, проведенные в данной работе рентгенографические исследования, а также известные литературные данные позволяют говорить о наличии низкотемпературного взаимодействия оксида алюминия с оксидом кремния. Кроме того, подтверждается ранее высказанная точка зрения на механизм стабилизации γ-Al_2O_3, при введении лантана [2, 4–6]. Это дает основание предполагать, что в системе La–Si/Al_2O_3 катионы лантана и кремния усиливают действие друг друга в отношении стабилизации структуры оксида алюминия.

СПИСОК ЛИТЕРАТУРЫ

1. *Koryabkina N.A., Ismagilov Z.R., Shkrabina R.A. et al.* // Appl. Catal. 1991. V. 72. № 1. P. 63.

2. *Шкрабина Р.А., Корябкина Н.А., Ушаков В.А. и др.* // Кинетика и катализ. 1996. Т. 37. № 1. С. 116.

3. *Корябкина Н.А., Шкрабина Р.А., Ушаков В.А. и др.* // Кинетика и катализ. 1996. Т. 37. № 1. С. 124.

4. *Корябкина Н.А., Шкрабина Р.А., Ушаков В.А. и др.* // Кинетика и катализ. 1997. Т. 38. № 1. С. 128.

5. *Ушаков В.А., Шкрабина Р.А., Корябкина Н.А., Исмагилов З.Р.* // Кинетика и катализ. 1997. Т. 38. № 1. С. 133.

6. *Исмагилов З.Р., Шкрабина Р.А., Корябкина Н.А.* Алюмооксидные носители: производство, свойства и применение в каталитических процессах защиты окружающей среды. Новосибирск: Наука, 1998. 100 с.

7. *Shkrabina R.A., Ismagilov Z.R., Shepeleva M.N. et al.* // Proc. 10 Nat. Symp. Recent Develop. in Catalysis. New Delhi, 1990. Pt. II. P. 30.

8. *Шепелева М.Н., Шкрабина Р.А., Оккель Л.Г. и др.* // Кинетика и катализ. 1988. Т. 29. № 1. С. 195.

9. *Ушаков В.А., Мороз Э.М.* // Кинетика и катализ. 1985. Т. 26. № 4. С. 968.

10. *Ушаков В.А., Мороз Э.М., Левицкий Э.А.* // Кинетика и катализ. 1985. Т. 26. № 5. С. 1200.

11. *Cook L.P.* "Phase equilibria of alumina" in Alumina chemicals: science and technology handbook / Ed. Hart L.D. Westerville, Ohio: Am. Ceram. Soc. J., 1990, p. 49.

12. *Okada K., Otsuka N.* // J. Am. Ceram. Soc. 1986. V. 69. № 9. P. 652.

13. *Muller D., Gessner W., Behrens H.-J., Schler G.* // Chem. Phys. Lett. 1981. V. 799. № 1. P. 59.

КИНЕТИКА И КАТАЛИЗ, 2000, том 41, № 5, с. 728–735

УДК 542.973:546.665'623'46–31:539.4.01:542.49

ИССЛЕДОВАНИЕ РЕАКЦИЙ И КАТАЛИЗАТОРОВ СЖИГАНИЯ ТОПЛИВ

XX. ТЕРМОСТАБИЛЬНОСТЬ И ДРУГИЕ СВОЙСТВА СИСТЕМЫ CeO_2–MgO–Al_2O_3

© 2000 г. Н. А. Корябкина, Р. А. Шкрабина, В. А. Ушаков, З. Р. Исмагилов

Институт катализа им. Г.К. Борескова СО РАН, Новосибирск

Поступила в редакцию 17.02.99 г.

Исследовано влияние одновременного введения катионов магния и церия на формирование структуры и свойства оксида алюминия, полученного из гидроксидов различного фазового состава, при термообработке в области температур 773–1573 K. При температурах <1273 K наблюдается эффект стабилизации величины удельной поверхности образцов. Показано, что модифицированный катионами Mg и Ce сферический оксид алюминия приобретает высокую механическую прочность после прокаливания при $T > 1373$ K. Модифицированные образцы, прокаленные при 1573 K, обладают некоторой каталитической активностью в реакции окисления CH_4.

Соединения церия широко используют для модифицирования трехфункциональных катализаторов нейтрализации выхлопных газов автотранспорта, поскольку они способствуют диспергированию активного компонента на поверхности носителя и замедляют фазовые превращения в γ-Al_2O_3. Кроме того, CeO_2 является аккумулятором кислорода, он также способен создавать новые активные центры или модифицировать существующие. Исследованию перечисленных свойств соединений церия посвящен ряд публикаций [1–4]. Как правило, объектами таких исследований являются композиции на основе оксида алюминия, промотированного только ионами церия, и приготовленные на их основе катализаторы. Свойства Al_2O_3, модифицированного одновременного несколькими катионами, изучены мало.

Настоящая работа является продолжением цикла исследований, посвященных оптимизации состава носителей на основе оксида алюминия, которые характеризуются повышенной термостабильностью и одновременно улучшенными механическими характеристиками. Результаты исследования систем La_2O_3–Al_2O_3 и CeO_2–Al_2O_3 описаны в работах [5–7]. Выполнено рентгенографическое исследование генезиса фазового состава композиции La_2O_3–MgO–Al_2O_3 в области температур 823–1673 K [8].

В настоящей статье рассмотрены условия формирования сферических носителей на основе оксида алюминия, модифицированного путем последовательного введения ионов магния и церия, и изменение их свойств при термообработке в области температур 823–1573 K.

ЭКСПЕРИМЕНТАЛЬНАЯ ЧАСТЬ

В работе использованы гидроксиды алюминия различного фазового состава:

– промышленный гидроксид алюминия псевдобемитной структуры с содержанием псевдобемита 100% (**серия 1**);

– гидроксид алюминия ПТ, полученный переработкой аморфного гидроксида алюминия по технологии терморазложения [9] и содержащий 85% (**серия 2**) или 65% (**серия 3**) псевдобемита;

– оксид алюминия, полученный прокаливанием гиббсита при 773 K с содержанием бемита менее 10% (**серия 4**).

Сферический оксид алюминия (d = 1.4–2.0 мм) серий 1–3 был приготовлен методом углеводородно-аммиачного формования гидроксидов алюминия [9]. Образцы серии 4 использовали в виде порошка, поскольку гиббсит непригоден для формования углеводородно-аммиачным методом.

Введение ионов магния в образцы серий 1–3 осуществляли из водного раствора азотнокислой соли магния путем пропитки им сферических гранул гидроксида алюминия. Затем образцы сушили при 383 к и подвергали термообработке при 823 K в течение 4, как описано в работе [10]. В образцы серии 4 магний вводили путем пропитки порошка оксида алюминия с последующей сушкой (383 K) и термообработкой (823 K, 4 ч). Содержание MgO в образцах серий 1–4 составляло 4.5, 3.2, 2.6 и 3.8 вес. % соответственно.

Модифицированные оксиды алюминия использовали в качестве исходных носителей, в которые вводили ионы церия путем пропитки по влагоемкости водным раствором нитрата церия. Далее образцы сушили на воздухе при комнатной температуре в течение 10 ч, а затем при 383 K в

Таблица 1. Свойства модифицированных алюмооксидных носителей, прокаленных при 773 K

№ образца	[MgO], вес. %	[CeO_2], вес. %	Насыпная плотность, г/см^3	$S_{уд}$, м^2/г	$P_{ср}$, МПа
Серия 1					
1	–	–	0.78	230	30
2	4.5	–	0.80	215	45
3	4.5	5.3	0.82	220	55
4	4.5	12.9	0.89	150	60
Серия 2					
5	–	–	0.7	220	24
6	3.2	–	0.75	180	44
7	3.2	2	0.81	180	44
8	3.2	5.6	0.83	165	49
9	3.2	13.4	0.93	155	49
Серия 3					
10	–	–	0.69	180	17
11	2.6	–	0.88	175	26
12	2.6	5.6	0.89	165	49
13	2.6	12.8	0.97	155	44
Серия 4					
14	–	–		150	–
15	3.8	–	–	140	–
16	3.8	5.3	–	130	–
17	3.8	12.6	–	120	–

течение 4 ч. Термообработку осуществляли в токе воздуха при 823 K в течение 4 ч. Дальнейшее прокаливание проводили при температурах 1173, 1273, 1373, 1473 или 1573 K в течение 2 ч. Содержание церия в расчете на CeO_2 составляло от 2 до 14 вес. %.

Удельную поверхность ($S_{уд}$) образцов определяли по термодесорбции аргона методом БЭТ с точностью 10%.

Механическую прочность гранул на раздавливание измеряли на приборе МП-9С по стандартной методике. Среднюю прочность ($P_{ср}$) рассчитывали для выборки из не менее, чем 30 гранул.

Каталитическую активность образцов проверяли в реакции окисления метана в проточном реакторе в области температур 373–973 K (в условиях как повышения, так и понижения температуры). Объем катализатора составлял 2 см^3; скорость газового потока 30 см^3/ч; объемная скорость 3600 ч$^{-1}$; газовая смесь содержала 1 мол. % CH_4 в воздухе.

Рентгенографический анализ образцов проводили на дифрактометре HZG-4 аналогично тому, как это делалось в работе [5].

РЕЗУЛЬТАТЫ ЭКСПЕРИМЕНТОВ

Удельная поверхность и прочность модифицированных образцов

Свойства модифицированных образцов оксида алюминия, прокаленных при 773 K, представлены в табл. 1. В образцах серий 1–3 по мере увеличения содержания второго катиона (Ce) отмечается увеличение насыпной плотности и прочности сферических гранул. Для порошкообразных образцов серии 4 эти характеристики не определяли.

В табл. 2 приведены данные об изменении прочностных характеристик образцов в зависи-

Таблица 2. Прочность сферических алюмооксидных носителей, прокаленных при различных температурах

№ образца	[MgO], вес. %	[CeO_2], вес. %	$P_{ср}$, МПа				
			773 K	1173 K	1273 K	1473 K	1573 K
Серия 1							
1	–	–	30	33	40	45	50
2	4.5	–	45	55	88	116	125
3	4.5	5.3	55	50	55	173	183
4	4.5	12.9	60	56	58	205	282
Серия 2							
5	–	–	24	21	24	30	43
6	3.2	–	44	40	51	60	75
7	3.2	2	44	40	35	60	75
8	3.2	5.6	49	43	35	61	78
9	3.2	13.4	49	43	35	65	90
Серия 3							
10	–	–	17	14	14	13	15
11	2.6	–	26	28	34	43	45
12	2.6	5.6	49	50	41	70	87
13	2.6	12.8	44	54	46	65	91

Таблица 3. Влияние химического модифицирования на удельную поверхность Al_2O_3

№ образца*	$S_{уд}$, $м^2/г$ ($S_{уд}^{мод}/S_{уд}^{Al}$)				
	773 K	1173 K	1273 K	1473 K	1573 K
			Серия 1		
1	220	110	90	10	5
2	215	90 (0.8)	60 (0.7)	9 (0.9)	5 (1.0)
3	220	110 (1.0)	110 (1.2)	8 (0.8)	7 (1.4)
4	150	110 (1.0)	110 (1.2)	7 (0.7)	4 (0.8)
			Серия 2		
5	190	100	80	10	5
6	180	120 (1.2)	50 (0.6)	11 (1.1)	11 (2.2)
7	180	130 (1.2)	100 (1.2)	11 (1.1)	–
8	165	125 (1.2)	100 (1.2)	11 (1.1)	9 (1.8)
9	155	120 (1.2)	80 (1.0)	10 (1.0)	8 (1.6)
			Серия 3		
10	170	100	60	7	5
11	175	105 (1.0)	50 (0.8)	10 (1.4)	5 (1.0)
12	165	130 (1.3)	90 (1.5)	14 (2.0)	7 (1.4)
13	155	110 (1.1)	90 (1.5)	12 (1.7)	6 (1.2)
			Серия 4		
14	155	–	50	30	7
15	140	–	50 (1.0)	30 (1.0)	7 (1.0)
16	130	–	50 (1.0)	40 (1.3)	7 (1.0)
17	120	–	60 (1.2)	30 (1.0)	7 (1.0)

* Состав образцов см. в табл. 1.

мости от температуры термообработки. Прочность всех образцов, модифицированных магнием, с ростом температуры увеличивается. Прочность образцов, модифицированных одновременно магнием и церием и прокаленных ниже 1473 K, остается постоянной, а при более высокой температуре значительно возрастает. Наиболее прочными являются образцы серии 1, содержащие 12 вес. % CeO_2, а максимальное относительное увеличение прочности наблюдается для образцов серии 3.

Изменения удельной поверхности образцов в зависимости от температуры термообработки представлены в табл. 3. Введение церия в оксид алюминия, содержащий катион Mg^{2+}, приводит к тому, что при $T \le 1273$ K, независимо от типа гидроксида алюминия, использованного для приготовления образца, $S_{уд}$ остается не менее высокой, чем у исходного оксида алюминия. Наибольшее сильный эффект такого рода, оцениваемый по относительному изменению удельной поверхности при данной температуре термообработки $S_{уд}^{мод}/S_{уд}^{Al}$, где $S_{уд}^{мод}$ и $S_{уд}^{Al}$ – удельная поверхность модифицированного образца и "чистого" оксида алюминия соответственно, отмечен для образцов серий 2 и 3. При 1473 K положительное действие CeO_2 на $S_{уд}$ проявляется только на образцах серии 3 и, в незначительной степени, на образце серии 4, содержащем ~5 вес. % CeO_2.

Результаты рентгенографических исследований

Рентгенографическое исследование алюмооксидных носителей, промотированных магнием и церием и подвергшихся термообработке при температурах 773–1573 K, позволило выявить присутствие четырех фаз: твердых растворов на базе низкотемпературных форм оксида алюминия, α-Al_2O_3, CeO_2 и $MgAl_2O_4$.

Твердые растворы на базе низкотемпературных форм оксида алюминия. Представленные в табл. 4 результаты рентгенофазового анализа носителей свидетельствуют о том, что независимо от природы исходного гидроксида алюминия при введении в образцы серий 1–3 азотнокислого магния после термообработки при 773 K образуются

твердые растворы $MgO–Al_2O_3$ со структурой низкотемпературных форм оксида алюминия. Эти растворы характеризовали параметром решетки a и коэффициентом B, который равен отношению интенсивностей линий 311/222, отвечающих структуре шпинели, и характеризует происходящие в образце структурные изменения. Изменение коэффициента B в системе $MgO–Al_2O_3$ от 1.2–1.3 (величины характерной для "чистого" оксида алюминия) до 3 является свидетельством образования твердого раствора со структурой, близкой к структуре γ-Al_2O_3; значения B от 3 до 25 характерны для нестехиометрических шпинелей различной степени дефектности, а $B = 25$ – для стехиометрической шпинели [11]. Изменения коэффициента B, как и параметра решетки a (табл. 4), свидетельствуют о взаимодействии Mg^{+2} с Al_2O_3 при температуре 773 к. Параметры структуры твердых растворов зависят от содержания добавки. В то время как немодифицированные образцы (серии 2 и 3) представляют собой двухфазную систему (γ-Al_2O_3 + χ-Al_2O_3), содержание χ-фазы в которой зависит от условий переработки продукта терморазложения гиббсита (**ПТ**), модифицированные носители, полученные из ПТ, однородны по фазовому составу. Большее относительное изменение параметра решетки образца 11 (с содержанием χ-Al_2O_3 35%) по сравнению с образцом 2, полученным из промышленного псевдобемита, указывает на то, что χ-компонент носителей, как более разупорядоченная и дефектная фаза, принимает участие в образовании твердого раствора. К тому же в образцах 6 и 11 после их термообработки при 1273 К не отмечалось образования фазы к-Al_2O_3, характерной для полиморфных превращений χ-Al_2O_3 и присутствующей в немодифицированных образцах.

Отдельно следует остановиться на образцах серии 4. При 773 К немодифицированный носитель представляет собой практически чистый χ-Al_2O_3 (содержание γ-Al_2O_3 не превышает 10%). Его параметры незначительно увеличиваются при введении магния. Если для определения параметров кубической структуры достаточно установить положение одной линии, как это и делалось в настоящей работе, то параметры более низкосимметричных структур определяют по большему числу линий, удовлетворяющих определенным требованиям. Поэтому изменения в структуре твердого раствора на базе χ-Al_2O_3, структура которого относится к гексагональному типу, мы оценивали по изменениям межплоскостного расстояния d/n. Эта величина до и после термообработки составляла соответственно 0.1397 и 0.1401 нм. Если для немодифицированного образца после термообработки при 1273 К характерно присутствие к-Al_2O_3 со следами α-Al_2O_3, то в модифицированном образце имеется нестехиометрическая шпинель с параметром a = 0.7942 нм

Таблица 4. Фазовый состав модифицированных алюмооксидных образцов с различным содержанием оксида магния после их термообработки при 773 К

№ образца*	[MgO], вес. %	Фазовый состав	a, нм	B
		Серия 1		
1	–	γ-Al_2O_3	0.7915	1.15
2	4.5	γ-Al_2O_3**	0.7940	1.52
		Серия 2		
5	–	(γ + 15%χ)-Al_2O_3	0.7915	1.34
6	3.2	γ-Al_2O_3**	0.7952	1.82
		Серия 3		
10	–	(γ + 35%χ)-Al_2O_3	0.7915	1.30
11	2.6	γ-Al_2O_3**	0.7962	1.54
		Серия 4		
14	–	(γ + 90%χ)-Al_2O_3	–	–
15	3.8	(γ + 90%χ)-Al_2O_3**	–	–

* Состав образцов см. в табл. 1.

** Твердый раствор со структурой γ-Al_2O_3.

и следы к-Al_2O_3. Дальнейшее повышение температуры до 1473 К приводит лишь к незначительному росту параметра a до величины 0.7952 нм. При 1573 К наблюдается распад нестехиометрической шпинели на стехиометрический оксид $MgAl_2O_4$ и α-Al_2O_3.

Вид дифракционных картин всех изученных образцов, модифицированных одновременно магнием и церием и прокаленных при 773 К, свидетельствует об образовании твердого раствора (магния и, возможно, церия) со структурой низкотемпературных форм оксида алюминия. Образцы серии 2 характеризовались параметром ячейки a = 0.7944–0.7952 нм (ошибка измерения ±0.0003 нм), причем в отличие от системы $La_2O_3–MgO–Al_2O_3$, величина a и коэффициент B не изменялись с увеличением концентрации добавки, в данном случае церия. При дальнейшем повышении температуры термообработки вплоть до 1273 К параметры твердых растворов также оставались неизмененными. После термообработки при температуре 1373 К в каждом образце наблюдается образование широкого круга твердых растворов, вплоть до стехиометрической шпинели. В образце, обработанном при 1473 К и выше, присутствует единственное алюмомагнийоксидное соединение – стехиометрическая шпинель $MgAl_2O_4$.

Дифракционные картины образцов серии 4, модифицированных одновременно магнием и церием и прокаленных при 773 К, указывают на образование твердого раствора ионов модификаторов в оксиде алюминия на базе структуры χ-Al_2O_3. При повышении температуры до 1273 К

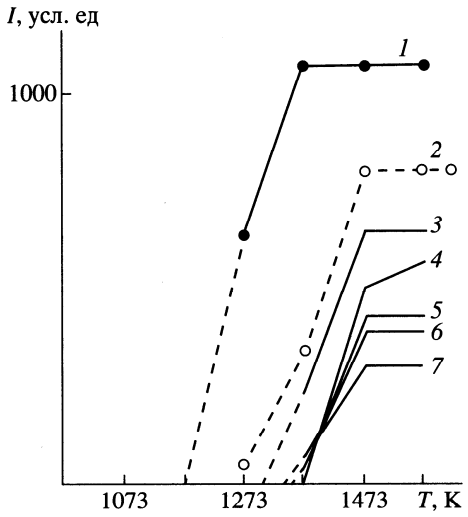

Рис. 1. Зависимость интенсивности линии α-Al_2O_3 d/n = 0.3479 нм от температуры термообработки и содержания введенного церия в системе CeO_2–MgO–Al_2O_3: *1* – Al_2O_3, *2* – MgO–Al_2O_3, *3–7* – CeO_2–MgO–Al_2O_3 с содержанием CeO_2 2 (*3*), 5 (*4*), 8 (*5*), 10 (*6*) и 12% (*7*).

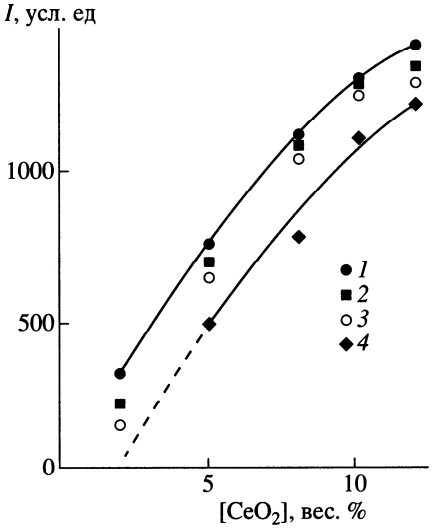

Рис. 2. Зависимость интенсивности линии CeO_2 d/n = = 0.3110 нм от содержания введенного церия в системе CeO_2–MgO–Al_2O_3 при температурах термообработки, K: *1* – 773, *2* – 1173, *3* – 1373, *4* – 1573.

происходит совершенствование структуры твердого раствора: дифракционная картина соответствует образованию нестехиометрической шпинели с параметром a = 0.7942 ± 0.0003 нм. Кроме того, отмечено присутствие следовых количеств к-Al_2O_3. При температуре термообработки 1473 K нестехиометрическая шпинель распадается на стехиометрическую шпинель $MgAl_2O_4$ и α-Al_2O_3.

α-Al_2O_3. Подробное исследование влияния концентрации введенного CeO_2 на образование α-Al_2O_3 и дисперсность частиц оксида церия проводили на примере образцов серии 2, при этом концентрацию CeO_2 варьировали от 2 до 14 вес. %. На рис. 1 показано, как изменяется интенсивность линии d/n = 0.3479 нм в зависимости от температуры термообработки и содержания введенного церия (наблюдаемое уменьшение интенсивности линий с ростом содержания церия частично обусловлено происходящим при этом изменением поглощения рентгеновских лучей в образце). Как видно, по мере увеличения содержания церия температура начала образования α-Al_2O_3 повышается, при этом наиболее сильные изменения вызывает введение первых 5% оксида церия.

CeO_2. Во всех образцах системы CeO_2–MgO–Al_2O_3 после термообработки при 773 K обнаруживается оксид церия, исключение составляет образец с содержанием 2% CeO_2 серии 2. По мере увеличения температуры размер частиц оксида церия увеличивается от 60–80 Å (при 773 K) до 400–500 Å (при 1573 K). Рост интегральной интенсивности линии с увеличением температуры термообработки образцов серий 1–3 указывает на возрастание содержания оксида церия (рис. 2). Увеличение содержания CeO_2 происходит, вероятно, за счет той части церия, которая после приготовления осталась в состоянии Ce^{3+} и частично вошла в структуру носителя или находилась в виде высокодисперсных частиц. Этот результат аналогичен закономерностям, установленным ранее для системы Ce/Al_2O_3 [6].

Интегральная интенсивность линий оксида церия в образцах серии 4 изменяется с ростом температуры при содержании 5% CeO_2 не более чем на 15%, а при содержании 12% CeO_2 остается неизменной. Это, по-видимому, обусловлено тем, что в структуру носителя входит ограниченное количество церия и его доля по мере роста общего содержания церия до 12% уменьшается настолько, что становится ниже чувствительности метода. В отличие от образцов на носителе γ-Al_2O_3 в случае χ-Al_2O_3 твердый раствор претерпевает значительно бóльше структурные изменения при переходе от низкотемпературного твердого раствора к стехиометрической шпинели. В образцах с γ-Al_2O_3 все превращения протекают в рамках шпинельной структуры, а в образцах с χ-Al_2O_3 имеет место переход от твердых растворов на базе гексагональной упаковки к структуре кубической нестехиометрической шпинели. В результате этого процесса и нестабильности соединений Ce^{3+}

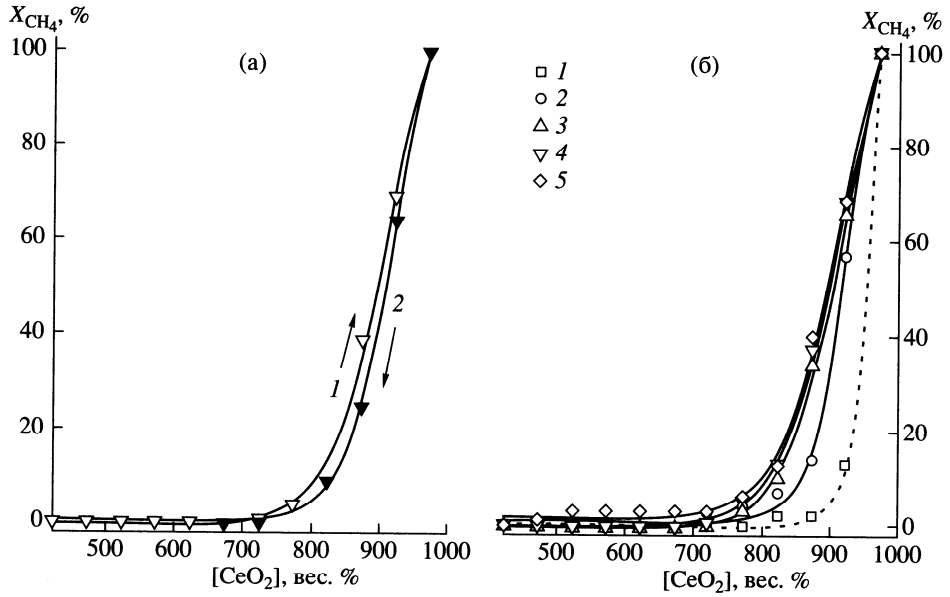

Рис. 3. Зависимость конверсии метана от температуры реакции: а – на образце 9 в условиях повышения (*1*) и понижения (*2*) температуры; б – в пустом реакторе (*1*), на Mg–La/Al_2O_3 (*2*) и на образцах 12 (*3*), 9 (*4*) и 3 (*5*).

происходит выход церия из состава твердого раствора.

$MgAl_2O_4$. Образование стехиометрической шпинели во всех образцах начинается при температуре термообработки выше 1273 K, а после 1473 она становится единственным магнийалюмооксидным соединением.

Каталитическая активность

Термическая стабильность алюмооксидных носителей является одной из важнейших характеристик катализаторов высокотемпературных процессов полного окисления различных топлив. Поэтому образцы модифицированного оксида алюминия испытывали в реакции полного окисления метана. На рис. 3 представлены типичные кривые конверсии метана (x_{CH_4}) модифицированном катионами магния и церия оксиде алюминия, прокаленным при 1573 K. Исследованные образцы обладают некоторой каталитической активностью независимо от природы используемого оксида алюминия и количества введенных добавок. На рис. 3б для сравнения показана кривая конверсии метана в пустом реакторе. Видно, что в присутствии модифицированного оксида алюминия окисление протекает не только в газовой фазе, но и на поверхности носителя. Интересно отметить, что высокотемпературный оксид алюминия, модифицированный одновременно лантаном и магнием, менее активен в этой реакции (рис. 3б).

Каталитическая активность церийсодержащих образцов, очевидно, обеспечивается присутствием Ce^{3+}, который, согласно нашим предположениям, присутствует в образцах серий 1–3. Кривые конверсии метана на образце 9 в условиях повышения и понижения температуры реакции представлены на рис. 3а. Как видно, эти кривые не совпадают, что, по-видимому, связано с окислением Ce^{3+} до Ce^{4+} в условиях реакции. Образованием Ce^{4+} объясняют снижение каталитической активности образцов и авторы работ [1–4].

ОБСУЖДЕНИЕ РЕЗУЛЬТАТОВ

Проблемы применения соединений церия для термической стабилизации переходных форм оксида алюминия исследуются достаточно интенсивно [12–15]. Эффект термической стабилизации приписывают воздействию церий содержащих соединений на оксид алюминия. В системе CeO_2–MgO–Al_2O_3, как и в системе CeO_2–Al_2O_3, возможны следующие формы существования церия:

– в виде оксидной фазы CeO_2 [16, 17];

– в составе твердого раствора Al_2O_3 и Ce^{3+}, который образуется на промежуточном этапе формирования алюмината церия с перовскитоподобной структурой [18];

– в виде алюмината церия с перовскитоподобной структурой $CeAlO_3$ [19, 20];

– в виде ионов церия, стабилизированных на поверхностных дефектах структуры оксида алюминия;

– в виде некристаллической дисперсной фазы на поверхности носителя.

Согласно данным работы [7], в которой использовали комплекс физических методов для исследования термической стабильности оксида алюминия, модифицированного ионами церия, последний существует в основном в виде дисперсной фазы на поверхности оксида алюминия. Эта дисперсная фаза не взаимодействует с Al_2O_3. Именно этим обстоятельством авторы [17] объясняют более слабое повышение термической стабильности образцов под действием церия по сравнению с лантаном, ионы которого способны входить в структуру носителя. Другие исследователи [16] связывают эффект повышения термической стабильности с присутствием поверхностного дисперсного Ce^{4+}, однако признают, что он не способен оказывать длительное стабилизирующее воздействие из-за интенсивной сегрегации. С другой стороны, показано [21], что Ce^{3+} даже в низкой концентрации эффективен как стабилизатор низкотемпературных форм оксида алюминия.

Результаты проведенного нами рентгенографического исследования двух систем, La_2O_3–Al_2O_3 и CeO_2–Al_2O_3, приготовленных в одинаковых условиях, позволили заключить, что церий оказывает значительно более слабый стабилизирующий эффект, чем лантан [5, 6]. Это различие, по нашему мнению, обусловлено образованием при введении лантана твердого раствора на базе структуры γ-Al_2O_3 с замещением алюминия на лантан, что в свою очередь, накладывает диффузионные ограничения на переход к высокотемпературным формам оксида алюминия и образование α-Al_2O_3. Ограниченный характер взаимодействия церия с γ-Al_2O_3 и нестабильность соединений Ce^{3+} являются причинами меньшей эффективности иона Ce в качестве стабилизирующей добавки.

Рентгенографическое исследование показало, что совместное присутствие ионов магния и церия в оксиде алюминия не приводит к существенному повышению термостабильности оксида алюминия (которую оценивают по количеству образовавшегося при данной температуре α-оксида) по сравнению с термостабильностью ранее исследованных систем CeO_2–Al_2O_3 и La_2O_3–MgO–Al_2O_3. Природа носителя (γ-Al_2O_3, смесь χ-Al_2O_3 + + γ-Al_2O_3, χ-Al_2O_3) оказывает определенное влияние на взаимодействие церия с носителем (см. табл. 3). Наибольший эффект стабилизации структуры носителя при введении CeO_2 отмечен в серии 3, где содержание χ-Al_2O_3 составляет 35%, т.е. с увеличением доли χ-Al_2O_3 эффективность действия модификатора увеличивается. Наиболее показательны в этом отношении результаты термообработки при 1473 K (табл. 3). Казалось бы, наиболее сильное влияние оксид церия должен оказывать на термостабильность оксида алюминия в виде χ-Al_2O_3, однако на практике этого не наблюдалось. По-видимому, существует как оптимальная концентрация вводимого церия, так и оптимальный состав продукта терморазложения, т.е. смеси χ-Al_2O_3 + γ-Al_2O_3. Следует отметить, что продукт терморазложения гиббсита не является простой механической смесью, поскольку технологические этапы его формирования являются существенно иными, чем этапы формирования составляющих его компонентов [9]. Это приводит к изменению характера его взаимодействия, например, с магнием (табл. 4): сильное изменение параметра решетки твердого раствора отмечено даже при примерно двукратном снижении количества введенного магния. В то же время наблюдается минимальное взаимодействие с чистым χ-Al_2O_3. Вероятно, одной из причин этого является и синергетическое действие двух модификаций оксида алюминия, γ-Al_2O_3 и χ-Al_2O_3, отмеченные ранее для систем CeO_2–Al_2O_3 [5] и La_2O_3–Al_2O_3 [6].

На рис. 4 представлена схема изменения фазового состава двух исследованных систем – La_2O_3/MgO–Al_2O_3 и CeO_2/MgO–Al_2O_3 – при введении 10% модифицирующего компонента. При введении лантана с ростом температуры усиливается взаимодействие с носителем, и на базе его структуры формируется достаточно однородный смешанный твердый раствор ионов лантана и магния, который характеризуется высоко термостабильностью. При введении церия лишь ограниченная его часть взаимодействует с носителем – алюмомагниевым твердым раствором, стабилизируясь в состоянии Ce^{3+} и обеспечивая незначительное повышение термостабильности системы. Продукт взаимодействия по мере повышения температуры разрушается с выделением отдельной фазы CeO_2 и, соответственно, α-оксида и стехиометрической алюмомагниевой шпинели. Основная же часть вводимого церия из-за особенностей химии соединений церия уже на стадии нанесения переходит из состояния Ce^{3+} в состояние Ce^{4+} и образует при термообработке отдельную фазу CeO_2, которая не оказывает влияния на термостабильность носителя. На ограниченный характер взаимодействия указывает также отсутствие образования при температурах выше 1373 K соединения $MgAl_{11}CeO_{19}$. Этим данная система отличается от системы La_2O_3/MgO–Al_2O_3, для которой при практически полном взаимодействии введенного лантана с носителем характерно образование при указанных температурах соединения $MgAl_{11}LaO_{19}$.

Таким образом, модифицирование оксида алюминия последовательным введением катионов

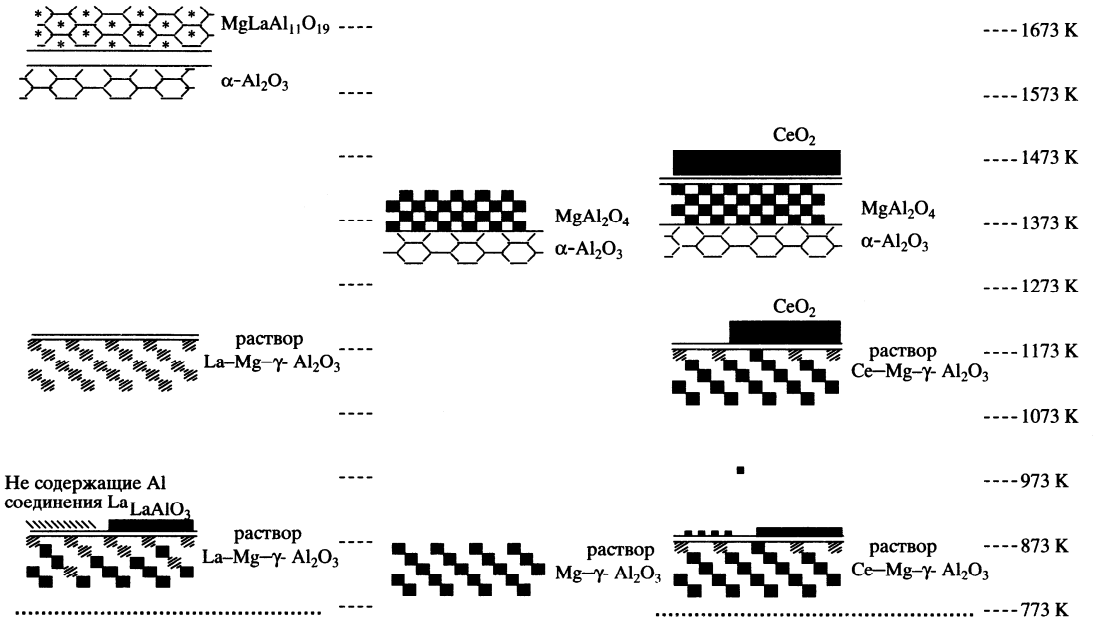

Рис. 4. Схема изменений фазового состава систем La–Mg–γ-Al_2O_3, Mg–γ-Al_2O_3 и Ce–Mg–γ-Al_2O_3 в зависимости от температуры термообработки.

магния и церия хотя и повышает термическую стабильность оксида алюминия, но эффективность добавок не столь велика, как в ранее исследованных системах CeO_2–Al_2O_3 и La_2O_3–MgO–Al_2O_3. С другой стороны, церийсодержащие алюмооксидные носители могут быть с успехом использованы для приготовления катализаторов полного окисления, поскольку сами эти носители обладают некоторой активностью в реакции окисления метана.

СПИСОК ЛИТЕРАТУРЫ

1. *Keiski, Harkonen M., Lahti A. et al.* // 3rd Intern. Congr. on Catalysis and Automotive Polution Control. Brussels, 1994. Preprints. V. 1. P. 53.
2. *Tagliaferri, Padeste L., Baiker A.* // 3rd Intern. Congr. on Catalysis and Automotive Polution Control. Brussels, 1994. Preprints. V. 1. P. 81.
3. *Tagliaferri, Kopler R.A., Baiker A.* // 4th Intern. Congr. on Catalysis and Automotive Polution Çontrol. Brussels, 1997. Preprints. V. 1. P. 9.
4. *Gonzales-Velasco, Botas J.A., Ferret R., Gutierrez-Ortiz M.A.* // 4th Intern Congr. on Catalysis and Automotive Polution Control. Brussels, 1997. Preptints. V. 1. P. 19.
5. *Шкрабина Р.А., Корябкина Н.А., Ушаков В.А. и др.* // Кинетика и катализ. 1996. Т. 37. № 1. С. 116.
6. *Корябкина Н.А., Шкрабина Р.А., Ушаков В.А. и др.* // Кинетика и катализ. 1996. Т. 37. № 1. С. 124.
7. *Корябкина Н.А., Шкрабина Р.А., Ушаков В.А. и др.* // Кинетика и катализ. 1997. Т. 38. № 1. С. 128.
8. *Ушаков В.А., Шкрабина Р.А., Корябкина Н.А., Исмагилов З.Р.* // Кинетика и катализ. 1997. Т. 38. № 1. С. 133.
9. *Ismagilov Z.R., Shkrabina R.A., Koryabkina N.A.* // Catal. Today. 1999. V. 47. P. 51.
10. *Koryabkina N.A., Ismagilov Z.R., Shkrabina R.A. et al.* // Appl. Catal. 1991. V. 72. P. 63.
11. *Мороз Э.М., Куклина В.Н., Ушаков В.А.* // Кинетика и катализ. 1987. Т. 28. С. 699.
12. *Yao H.C., Yu-Yao Y.F.* // J. Catal. 1984. V. 86. P. 54.
13. *Yu-Yao Y.F., Kammer J.T.* // J. Catal. 1987. V. 106. P. 307.
14. *Su E.C., Rothschild W.G.* // J. Catal. 1986. V. 99. P. 506.
15. *Su E.C., Montreuil C.N., Rothschild W.G.* // Appl. Catal. 1984. V. 17. P. 75.
16. *Chrch J.S., Cant N.W., Trimm D.L.* // Appl. Catal. A: General. 1993. V. 101. P. 105.
17. *Ozawa M., Kimura M., Isogai A.* // J. Less Common Metals. 1990. V. 62. P. 297.
18. *Kaufherr N., Mendelovici I., Steinberg M.* // J. Less Common Metals. 1984. V. 107. P. 281.
19. *Che M., Kibblewhity J.F.J., Tench A.J.* // J. Chem. Soc., Faraday Trans. 1923. V. 69. P. 857.
20. *Shyu J.Z., Weber W.H., Gandhi H.S.* // J. Phys. Chem. 1998. V. 92. P. 4964.
21. *Appel L.G., Perez C.A.C., Eon J.G., Schmal M.* // Environ. Catal / Ed. Genti G. et al. Proc. 1st World Congr., Environmental Catalysis for a Better World and Life. Risa, 1995. P. 391.

ELSEVIER

Chemical Engineering Journal 82 (2001) 355–360

Chemical Engineering Journal

www.elsevier.com/locate/cej

Short communication

A catalytic heat-exchanging tubular reactor for combining of high temperature exothermic and endothermic reactions

Z.R. Ismagilov [a,*], V.V. Pushkarev [a], O.Yu. Podyacheva [a], N.A. Koryabkina [a], H. Veringa [b]

[a] *Boreskov Institute of Catalysis, Lavrentiev Avenue 5, 630090 Novosibirsk, Russia*

[b] *ECN, P.O. Box 1, 1755 ZG Petten, The Netherlands*

Received 16 June 2000; accepted 3 November 2000

Abstract

A multifunctional catalytic heat-exchanging (HEX) tubular reactor for combining exothermic and endothermic reactions has been developed and tested for catalytic methane oxidation and methane steam reforming. The methane combustion and steam reforming catalysts were synthesized on the heat-conducting metal foam support materials by application of preliminary plasma spraying of alumina in order to increase adhesive properties of the active layer. The HEX rector with perovskite-supported catalyst on Ni-Cr foam material on the external surface of the HEX tube and with Ni containing reforming catalyst on the internal Ni foam was successfully tested in methane combustion reaction combined with methane steam reforming.

Keywords: Catalytic heat exchanging reactor; Methane combustion; Methane steam reforming

1. Introduction

Many of industrial chemical processes, such as methane steam reforming and methane pyrolysis are endothermic and consequently consume heat. The natural gas flame combustion is one of the main sources of thermal energy supply for these processes. The temperature of methane combustion flame is higher than 1500°C and it leads to substantial heat loss and high thermal NO_x emission. The promising way to solve problems of heat consumption efficiency and NO_x abatement is use of the catalytic heat exchangers. The catalytic heat exchanger composed with a combustion catalyst supported on the metallic foam on one side of the reactor wall provides a good heat transfer for another endothermic reaction proceeding on the other side of the wall; thus, preventing energy loss and giving low NO_x emission due to low temperature catalytic combustion.

Metal foam materials having unique structure are very attractive to be used as a catalyst support in the catalytic combustion. In this case, the problem of the preparation of catalytic coatings on metal surface with high adhesive and strong mechanical properties for durable exploitation at high temperatures appears, therefore, the new ways of synthesis are required. Plasma spray technique gives a good possibility to support oxide coatings on metal surfaces exhibiting high adhesive and mechanical characteristics. The application of plasma spray methods makes it possible to support both preliminary inert washcoats as well as catalytically active coatings.

Plasma spraying of washcoatings of alumina, titania, zirconia, etc. will allow one to solve successfully the problem of the adhesion of the active component to the metal surface and to protect the metal support substrates from aggressive medium and improve their durability for high temperature use. Moreover, the plasma spray method will give an opportunity to design composite materials consisting of various combinations of plasma-sprayed catalytic and protective layers.

Although plasma spray technique is well developed and in common use today, information on the application of these methods in catalysis is rather scarce. Traditionally, plasma spraying is used for development of dense, non-porous protective layers and it should be modified for application of this method in catalyst synthesis.

A number of papers have shown that the porous structure of sprayed coatings depends significantly on the jet outflow regime (laminar, transient or turbulent): the chemical composition and flow rate of the plasma-forming gas, the plasma torch power, the spraying distance, etc. For example, an

* Corresponding author. Tel.: +7-3832-341219; fax: +7-3832-397352.
E-mail address: z.r.ismagilov@catalysis.nsk.su (Z.R. Ismagilov).

increase of the plasma-forming gas flow rate and spraying distance leads to a growth of the porosity of the coating and this is accompanied by lower adhesion [1–3]. Changing the particle size of the powder sprayed also allows regulation of the physicochemical characteristics of the layers deposited: the phase composition, the porosity, the specific surface area and the thermal conductivity properties [4,5].

Therefore, successful application of the plasma spraying techniques for the synthesis of catalysts requires a comprehensive study of the influence of the various parameters of the plasma spraying and properties of the spraying materials on the coatings obtained.

The technique of plasma spraying of alumina on the metal foams was developed [6,7]. The prospects of the application of the plasma spraying technique for the preparation of the combustion catalysts on the metal foams were shown on the example of the synthesis of the perovskite containing catalyst. Intermediate alumina layer was formed by plasma spraying. The plasma sprayed alumina was then modified by La-containing γ-alumina, and La-Co perovskite catalyst was supported by an impregnation procedure.

The subject of this paper is the development of combustion catalyst on metal foams by plasma spraying to be used in catalytic heat exchangers for methane steam reforming and determination of its optimal operation parameters.

2. Experimental

Alumina powders differing in phase composition and particle size (α-Al_2O_3 20–80 mkm and γ-Al_2O_3 90–200 mkm) were used to spray an intermediate layer on titanium plates and Ni, Ni-Cr foam materials under laminar, transient and turbulent regimes of the plasma jet outflow (Fig. 1). The modification of the plasma-sprayed layer was provided by the deposition of lanthanum-containing γ-Al_2O_3 to increase the specific surface area of the intermediate layer. For comparison, the same catalyst on Ni foam support was prepared by direct deposition of a γ-Al_2O_3-containing washcoat on the metal surface by a chemical method without deposition of preliminary plasma-sprayed layer [8].

The X-ray analysis of the samples was carried out using a HZG-4 diffractometer with copper radiation in the 2θ range of 20–55°. To specify the parameters of the solid solutions and of the perovskite composition, the data were obtained in the range of 2θ of 62–72°. The specific surface areas of the samples were measured by the BET method and the pore volumes of the sprayed layers were calculated using the water capacity technique. The morphology of the catalysts was characterized by SEM (REM-100U, Russia).

A thermal cycling technique was used for investigation of the adhesion of the catalytic coating on the surface of the metal foam support. The experiments were performed as follows. First, a catalyst was heated to 900°C; then, it was dipped into water and dried in air. After drying, the operation was repeated. The number of thermal cycles needed for achievement of a stationary figure on the weight loss curve was used as criteria.

A metal foam heat-exchanging (HEX) reactor has been manufactured by placing the thermally stable high-permeable metal foam on both internal and external surfaces of the stainless steel metal tube: o.d. = 20 mm, i.d. = 18 mm (Fig. 2). The metal foams were prepared by duplication of a foamed polymer matrix, impregnated by metal salts with subscquent thermal treatment and reduction. The alumina was sprayed on external metal foam and perovskite (La-Co) combustion catalyst was deposited on this oxide layer by an impregnation or suspension technique. The methane reforming Ni-based catalyst was loaded from its slurry directly on the internal foam.

A laboratory set-up has been built for catalytic heat exchangers testing. A catalytic metal foam HEX tubular reactor was axially placed into a quartz tube (Fig. 3) insulated with rock wool to reduce heat loss. The mixture of fuel gas (methane and/or hydrogen) with air was injected into the external combustion catalyst of heat exchanger. A preheated steam–methane mixture with temperature 100–300°C was fed into the internal Ni-containing reforming catalyst.

The spatial temperature distribution in the reactor, in the combustion catalyst and the gas phase above it was measured with the aid of 10 chromel–alumel thermocouples, and two thermocouples were used to measure the inlet and outlet temperature of the reforming reactor. The H_2, CO, CH_4 and CO_2

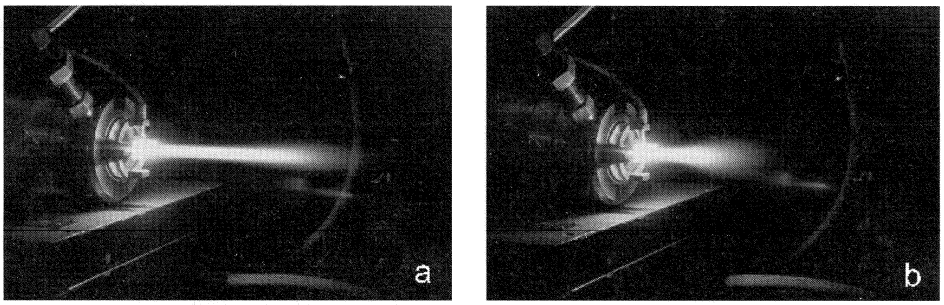

Fig. 1. Laminar (a) and turbulent (b) plasma jet outflow.

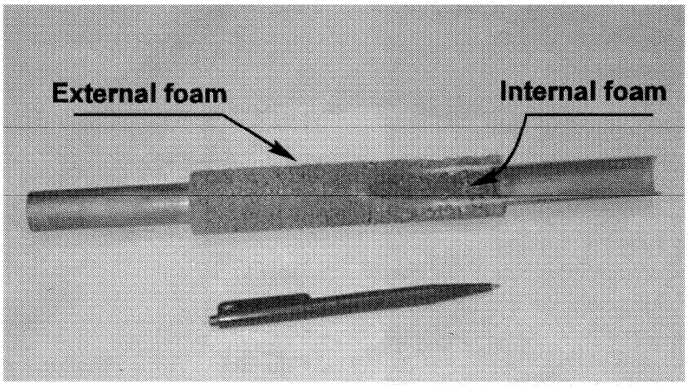

Fig. 2. Catalytic heat-exchanging reactor with metal foam deposited on the internal and external surfaces of a metal tube.

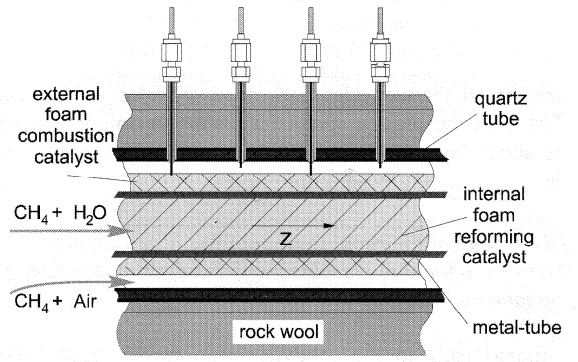

Fig. 3. Longitudinal section of the catalytic metal foam heat-exchanging reactor.

concentrations were measured with a gas-chromatograph equipped with TCD and column with activated carbon.

On the external surface of the catalytic heat-exchanger, the exothermic catalytic combustion of H_2 and/or CH_4 took place

$$CH_4 + 2O_2 = CO_2 + 2H_2O, \quad \Delta H = -802.28\,\text{kJ mol}^{-1}$$

$$H_2 + \tfrac{1}{2}O_2 = H_2O, \quad \Delta H = -241.81\,\text{kJ mol}^{-1}$$

Heat released in the above reactions transferred through the metal wall of the heat exchanger into the internal chamber, where it was consumed in the endothermic methane steam reforming process

$$CH_4 + H_2O = CO + 3H_2O, \quad \Delta H = 206.4\,\text{kJ mol}^{-1}$$

3. Results and discussion

3.1. Study of the combustion catalyst on metal support synthesized by the application of plasma spraying of the intermediate layer

Experiments on the plasma spraying of alumina of different phase composition and particle size on titanium plates showed that the properties of plasma sprayed layers are quite similar and do not depend significantly on the jet outflow regime used (Table 1). When α-Al_2O_3 was sprayed on titanium plates, the coatings were characterized by a low specific surface area; meanwhile, their pore volume increased when the spraying regime was changed from laminar to turbulent. It was established that the dependence of the regime on the coating properties was the same when γ-Al_2O_3 was sprayed. Moreover, in the latter case, the spraying regime influenced the quantitative proportions of the α-Al_2O_3 and θ-Al_2O_3 phases of the coatings and their specific surface areas. The maximum porosity and minimum α-Al_2O_3 phase content were registered when a transient jet outflow regime was used. The low rates of hardening when

Table 1
Properties of alumina sprayed on Ti plates

Sprayed alumina	Particle size (mkm)	Regime	Specific surface area (m^2/g)	Phase composition	Pore volume (cm^3/g)
α-Al_2O_3	30	Laminar	0.2	α-Al_2O_3	0.052
α-Al_2O_3	30	Transient	0.2	α-Al_2O_3	0.065
α-Al_2O_3	30	Turbulent	0.2	α-Al_2O_3	0.167
γ-Al_2O_3	90–200	Laminar	0.2	α,θ-Al_2O_3	0.068
γ-Al_2O_3	90–200	Transient	0.4	α,θ-Al_2O_3	0.075
γ-Al_2O_3	90–200	Turbulent	0.6	α,θ-Al_2O_3	0.166

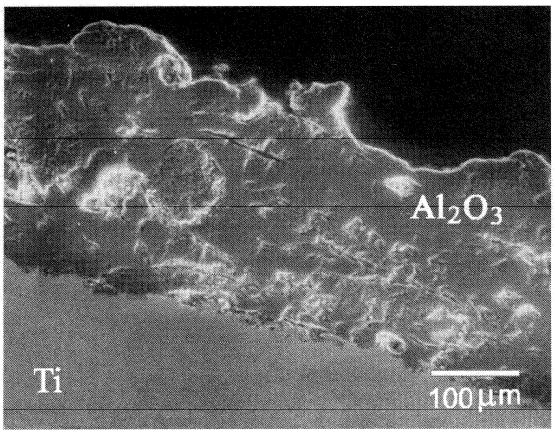

Fig. 4. Micrograph of cross-section view of Al_2O_3 plasma sprayed on metal surface.

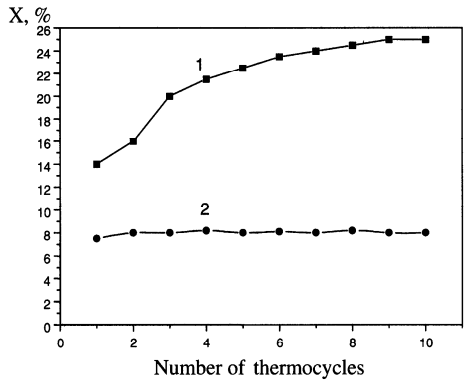

Fig. 5. Dependence of the catalyst weight loss on number of thermocycles, $X(\%) = (m_0 - m_n)/m_0$, where m_0 is initial catalyst weight, m_n the catalyst weight after n thermocycles: (1) $LaCoO_3$/La-γ-Al_2O_3/Ni-Cr foam; 2) $LaCoO_3$/La-γ-Al_2O_3/α-Al_2O_3/Ni-Cr foam, plasma sprayed α-Al_2O_3.

alumina was sprayed on metal surface lead to the transformation of γ-Al_2O_3 predominantly to the α-Al_2O_3 and θ-Al_2O_3 phases. When both γ-Al_2O_3 and α-Al_2O_3 were sprayed on Ti plates, the coatings were characterized by strong adhesive properties and had a complicated structure consisting of dense areas and macropores of different forms and sizes (Fig. 4). It is obvious that the contact between the alumina and the metal surface was rather strong and uniform.

The direct deposition of the active La-Co component on these supports led to the formation of $LaCoO_3$ and Co_3O_4 phases, as shown by XRD. The quantities of the supported active component did not exceed 2 wt.% because of the low porosity of the sprayed alumina layer. A modification of the sprayed layer by La-containing γ-Al_2O_3 allowed to increase this value by one order of magnitude. The phase composition of the modified catalyst after the deposition of the active La-Co component was more complex. Besides the presence of the $LaCoO_3$ and Co_3O_4 phases, minor quantities of $LaAlO_3$ perovskite and solid solutions based on γ-Al_2O_3 were registered. Increasing of La content in the modifying layer led to the decrease of the relative content of $LaAlO_3$ and the solid solution based on γ-alumina phases. Phase composition of the catalyst synthesized without preliminary spraying of intermediate alumina layer was identical to that described above. Thus, it can be concluded that presence of the plasma spayed alumina layer does not affect the genesis of the formation of the perovskite active component, catalyst phase composition depend only on the composition of the modifying layer. Meanwhile, the experiments on thermal cycling (Fig. 5) have revealed that the presence of the plasma sprayed alumina layer on the metal surface allows to improve substantially the adhesive properties of the active layer. It was found that in the catalyst prepared by a chemical method the substantial destruction of the active layer continuously proceeds during each of 10 thermocycles performed, whereas in the catalyst with the plasma sprayed alumina the minor loss of the active layer is observed only after the first thermocycle.

3.2. Testing of the metal foam catalytic heat exchanger in the steam reforming combined with catalytic combustion of methane and methane–hydrogen mixture

Experiments in the catalytic HEX reactor have been performed to determine the effectiveness of heat transfer and the parametric sensitivity of conditions of stable performance of catalytic combustion with simultaneous heat transfer to steam reforming. The following parameters were varied in the experiments: gas hour space velocity (GHSV), fuel concentration in gas, steam–methane mixture flow rate. The following values were obtained under observed steady state operation modes: the temperature profile along the combustion catalyst bed and the gas phase above it, inlet and outlet steam–methane mixture temperature, fuel conversion and composition of the outlet gases. Methane and methane–hydrogen mixture were used as a fuel. Before each experiment, the HEX reactor was preheated by introducing of air–methane–hydrogen mixture (5.5% CH_4, 10% H_2, 25,000 h^{-1}). When reactor temperature was reached the value of 750°C, the desired operational parameters were set.

3.2.1. The influence of the combustion catalyst layer thickness

The thickness of metal foam with a combustion catalyst on it is an important factor to stable operation of combustion reactor. The thickness of catalytic foam was varied in a range 2–5 mm in the experiments with the combustion of methane and methane–hydrogen mixtures. As it has been found, the thickness of catalytic foam <2.5 mm was

Table 2
Steam reforming of methane supported by catalytic combustion of methane in catalytic heat-exchanging reactor

Combustion zone of heat-exchanger	
Maximum catalyst temperature, T_{max} (°C)	1007
GHSV (20°C, 1 bar, h^{-1})	10000
CH_4 concentration, Co_{CH_4} (%)	6.0
CH_4 conversion, X_{CH_4} (%)	99.9
Adiabatic temperature rise, T_{ad} (K)	1400
Steam reforming zone	
GHSV (20°C, 1 bar, h^{-1})	7100
CH_4 concentration, Co_{CH_4} (%)	38.5
H_2O/CH_4 mole ratio	1.6
$T_{gas,in}$ (°C)	101
$T_{gas,out}$ (°C)	543
CH_4 conversion, X_{CH_4} (%)	50

Table 3
Steam reforming of methane supported by catalytic combustion of methane–hydrogen mixture in catalytic heat-exchanging reactor[a]

Combustion zone of heat-exchanger	
Maximum catalyst temperature, T_{max} (°C)	865
GHSV (20°C, 1 bar, h^{-1})	19200
CH_4 concentration, Co_{CH_4} (%)	6.1
H_2 concentration, Co_{H_2} (%)	9.7
CH_4 conversion, X_{CH_4} (%)	74.9
H_2 conversion, X_{H_2} (%)	97.6
Adiabatic temperature rise, T_{ad} (K)	1720
Steam reforming zone	
GHSV (20°C, 1 bar, h^{-1})	7100
CH_4 concentration, Co_{CH_4} (%)	38.5
H_2O/CH_4 mole ratio	1.6
$T_{gas,in}$ (°C)	265
$T_{gas,out}$ (°C)	723
CH_4 conversion, X_{CH_4} (%)	63.5

[a] Range of operation parameters.

insufficient for effective methane combustion in our experimental conditions, after preheating the temperature of catalytic layer dropped fast to the ambient temperature. As was found the optimal thickness of combustion catalyst layer is 4–5 mm.

3.2.2. *The influence of composition of combustion gas*

When methane was used for combustion the methane conversion in combustion reaction in the HEX reactors was close to 100% (Table 2). The temperature profile along HEX reactor was not uniform with a maximum 1037°C on the combustion catalyst. The efficiency of steam reforming was close to thermodynamic figure (conversion CH_4 50%) for the temperature profile attained in the internal reforming catalyst.

From literature survey it's known [9] that selectivity of the endothermic methane steam reforming reaction

$$CH_4 + H_2O = CO + 3H_2,$$
$$\Delta H = -206.4\,kJ\,mol^{-1} \text{ (main reaction)}$$

$$CO + H_2O = CO_2 + H_2,$$
$$\Delta H = 41.0\,kJ\,mol^{-1} \text{ (side reaction)}$$

is maximal at the temperature range 750–900°C and H_2O/CH_4 ratio equal 1.2–4. Therefore, in our experiments, we tried to maintain the temperature profile in combustion catalyst layer in this range.

Addition of certain amount of hydrogen to combustion mixture has a positive effect on to the steam reforming catalyst performance. The temperature profile in the combustion catalyst layer becomes more uniform in the range of 850–900°C (Fig. 6). Methane conversion in reforming

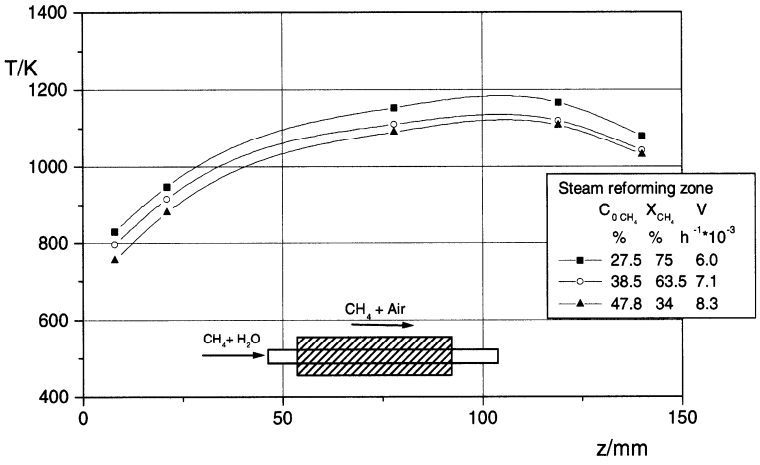

Fig. 6. Temperature profile in the combustion catalyst bed. Combustion of methane–hydrogen mixture with simultaneous steam reforming in heat-exchanging reactor.

section increases to 65% (Table 3) due to better uniformity of the temperature profile in the reforming catalyst as well.

4. Conclusion

The methane combustion catalyst of perovskite structure was synthesized on the heat-conducting Ni-Cr foam support materials by means of preliminary plasma spraying of alumina in order to increase adhesive properties of the active layer. It was shown that plasma sprayed alumina does not change the genesis of the formation of the perovskite active component but allows to improve substantially the adhesive properties of the active layer at high temperature.

This technique of catalyst preparation was used for development of tubular catalytic heat exchangers for combination: catalytic combustion of CH_4 and steam reforming of CH_4. The optimum stable operation of catalytic heat exchangers was obtained by the varification of the composition of the combustion mixture and thickness of the combustion catalyst layer.

Acknowledgements

This work is supported by NWO grant in 1997–1999, The Netherlands.

References

[1] T. Yoshida, Appl. Chem. 66 (1994) 1223.
[2] J. Ilavsky, J. Forman, P. Chraska, J. Mater. Sci. Lett. 11 (1992) 573.
[3] S. Uematsu, T. Senda, in: Proceedings of the 8th International Symposium on Plasma Chemistry, Vol. 4, Tokyo, 31 August–4 September 1987, p. 1958.
[4] D.J. Varacalle, in: Proceedings of the 3rd Symposium on Materials Research Society, Reno, Nev., April 1988 – Pittsburgh (PA), 1988, p. 541.
[5] K.-S. Shi, Z.-Y. Qian, M.-S. Zhuang, J. Am. Ceram. Soc. 71 (1988) 924.
[6] Z.R. Ismagilov, O.Y. Podyacheva, O.P. Solonenko et al., Catal. Today Vol. 51 (1999) 411.
[7] Z.R. Ismagilov, O.P. Solonenko, O.Y. Podyacheva, et al., in: Proceedings of the 13th International Symposium on Plasma Chemistry, Vol. 4, Beijing, China, 1997, pp. 1880–1885.
[8] O.Y. Podyacheva, A.A. Ketov, Z.R. Ismagilov, V.A. Ushakov, A. Bos, H.J. Veringa, React. Kinet. Catal. Lett. 60 (1997) 243.
[9] J.R. Rostrup-Nielsen, Catalytic steam reforming, in: J.R. Andersen, M. Budart (Eds.), Catalysis Science and Technology, Springer, Berlin, 1984, Vol. 5, p. 1.

КИНЕТИКА И КАТАЛИЗ, 2003, том 44, № 6, с. 879–885

УДК 541.128.3:542.943.7:547.211:546:711'623–31:541.18.02

ИССЛЕДОВАНИЕ РЕАКЦИЙ И КАТАЛИЗАТОРОВ СЖИГАНИЯ ТОПЛИВ. XXI. СИНТЕЗ И ИССЛЕДОВАНИЕ МОДИФИЦИРОВАННЫХ Mn–Al–O-КАТАЛИЗАТОРОВ ДЛЯ ВЫСОКОТЕМПЕРАТУРНОГО ОКИСЛЕНИЯ

© 2003 г. Л. Т. Цикоза, З. Р. Исмагилов, В. А. Ушаков, В. В. Кузнецов, И. А. Овсянникова

Институт катализа им. Г.К. Борескова СО РАН, Новосибирск

Поступила в редакцию 18.10.2002 г.

Исследован фазовый состав и активность в реакции окисления метана нанесенных Mn–Al–O-катализаторов в зависимости от состава алюмооксидного носителя (γ-Al_2O_3 с различным содержанием χ-Al_2O_3, модифицированный индивидуальными оксидами Mg, La или Ce, а также смесью оксидов Mg + La или Mg + Ce) и температуры прокаливания (500, 900 и 1300°C). Показано, что Mn–Al–O-катализаторы, приготовленные на основе γ-оксида алюминия, содержащего χ-Al_2O_3 и модифицированного добавками Mg, La или Ce, более активны и термостабильны (вплоть до 1300°C) по сравнению с образцами на основе чистого γ-Al_2O_3. Сделан вывод, что более высокая степень разупорядоченности структуры χ-Al_2O_3 по сравнению с γ-Al_2O_3 способствует более глубокому взаимодействию марганца и модифицирующих добавок с носителем на ранних стадиях синтеза и образованию при 1300°C Mn–Al-соединений сложного состава (твердых растворов и/или гексаалюминатов), которые и обеспечивают стабильность и высокую активность катализаторов в окислении метана.

Оксиды переходных металлов известны как высокоэффективные катализаторы глубокого окисления. Их реакционная способность зависит от энергии связи металла с кислородом, причем наиболее активны оксиды кобальта, меди и марганца [1], конкурирующие в ряде процессов с катализаторами на основе благородных металлов. Однако практическое использование массивных (без носителя) оксидных катализаторов ограничено их недостаточно высокими эксплуатационными характеристиками, такими как удельная поверхность, механическая прочность и термическая устойчивость, хотя существует принципиальная возможность решения этих вопросов, как это показано, например, для массивного оксида меди [2, 3].

Наиболее распространенным методом получения и совершенствования каталитических свойств оксидов является их формирование на поверхности носителя с заданными физико-химическими и структурно-механическими характеристиками. Активность, отнесенная к единице общей поверхности катализатора, в этом случае снижается по сравнению с массивным оксидом, однако активности в расчете на единицу массы катализаторов и массивных образцов могут быть соизмеримы при гораздо меньшем содержании активного компонента [2, 4, 5].

Несмотря на то, что прочность связи металла с кислородом в оксиде марганца меньше, чем в оксидах кобальта и меди [1], катализаторы на его основе наиболее перспективны для использования в высокотемпературных процессах благодаря своей сравнительно высокой термической устойчивости. Так, по данным [6] массивный гопкалит ($CuO : MnO_2 = 1 : 2$) и гопкалит, смешанный в количестве 40 мас. % с оксидом алюминия, сохраняют достаточно высокую активность в сжигании бутана после прокаливания их при 800–1000°C. При этом показано, что температура 50%-ной конверсии бутана на образце гопкалит–оксид алюминия ниже, чем на массивном гопкалите, и равна, соответственно, ~250 и ~300°C (для образцов, прокаленных при 800°C) и ~370 и ~450°C (для образцов, прокаленных при 1000°C).

Это связано со специфической особенностью системы Mn–Al–O – увеличением активности после термической обработки катализатора MnO_x/γ-Al_2O_3 при 900–1000°C, а образцов MnO_x/α-Al_2O_3 – при 700–1000°C. Как показано в [7], термоактивацией является диспергирование активного компонента на поверхности носителя. Такое свойство послужило основой для создания технологии получения промышленного Mn–Al–O-катализатора ИКТ-12-40 [8], имеющего высокую активность в реакциях полного окисления вплоть до 1000°C.

По данным [7, 8] активным компонентом системы Mn–Al–O, при синтезе которой используются низкотемпературные формы оксида алюминия, является дисперсная фаза с приблизительным составом $Mn_3O_{4.2}$ и дефектной шпинельной структурой. В ее формировании при температурах ниже 1000°C решающую роль играет фаза α-Al_2O_3, образование которой при этих температурах стимулируется минерализующим действием нанесенного марганца. Однако после прокалива-

ния выше 1000°C эта дисперсная фаза переходит в более окристаллизованную и менее активную фазу Mn_3O_4.

По тем же данным использование α-Al_2O_3 в качестве исходного носителя вместо γ-Al_2O_3 при температурах выше 850°C уже не приводит к выигрышу в активности катализатора.

Сведения о модифицировании системы Mn–Al–O добавками оксидов РЗЭ и других металлов – известного способа повышения термической устойчивости γ-оксида алюминия [9, 10] – ограничены в [7, 8] упоминанием о слабом положительном действии некоторых добавок до температур 750–800°C.

В настоящее время одной из актуальных задач высокотемпературного сжигания, например, метансодержащего сырья является создание эффективных и устойчивых катализаторов, позволяющих проводить процессы окисления при 1200–1300°C. Для совершенствования оксидных катализаторов целесообразно искать пути повышения термической стабильности и сохранения в указанном диапазоне температур высокой активности Mn–Al–O-системы, которая, по крайней мере, при 900–1000°C наиболее активна среди оксидов.

Ранее нами было показано [11, 12], что использование в качестве носителя для Mn–Al–O-катализаторов γ-оксида алюминия, содержащего разупорядоченный χ-Al_2O_3 и модифицированного добавками оксида La, Ce и Mg, является одним из перспективных направлений совершенствования этих катализаторов.

В настоящей работе с целью определения оптимального состава Mn–Al–O-катализатора, отвечающего требованиям высокотемпературных (вплоть до 1300°C) условий использования, проведен анализ фазового состава модифицированных Mn–Al–O-катализаторов и их активности в реакциях глубокого окисления в зависимости от содержания фазы χ-Al_2O_3 в исходном носителе, химической природы модифицирующей добавки и температуры прокаливания.

МЕТОДИКА ЭКСПЕРИМЕНТА

Mn–Al–O-катализаторы готовили пропиткой по влагоемкости носителя раствором азотнокислого марганца с последующей сушкой и прокаливанием на воздухе при заданной температуре в течение 4 ч. Содержание марганца во всех катализаторах равно ~5 мас. % (в расчете на MnO_2).

В качестве носителей использовали полученный методом углеводородно-аммиачного формования [10] сферический оксид алюминия на основе γ-Al_2O_3 с различным содержанием χ-подобного Al_2O_3: **1** – чистый (γ-Al_2O_3), **2** – 15% χ-Al_2O_3, **3** – 35% χ-Al_2O_3. Основные их характеристики (удельная поверхность, пористая структура) близки. Модифицирование носителей 1–3 добавками оксидов Mg, La и Ce проводили в соответствии с [12].

Каталитическую активность характеризовали двумя параметрами: 1) скоростью реакции окисления бутана при 400°C ($w \times 10^2$, $см^3/г^{-1}\ с^{-1}$) в проточно-циркуляционной установке при начальной концентрации углеводорода 0.5 об. % и скорости циркуляции 1000 л/ч; 2) температурой 50%-ного окисления метана в проточной установке при мольном отношении CH_4: воздух = 1 : 99 и объемной скорости 1000 $ч^{-1}$.

Содержание Mn, Mg, La и Ce в образцах (мас. % в расчете на оксиды) определяли химическим анализом. Удельную поверхность ($S_{уд}$, $м^2/г$) образцов измеряли по тепловой десорбции аргона. Рентгенофазовый анализ проводили на аппарате HZG-4, (CuK_α-излучение) в области 2Θ = 10–70 со скоростью 1 град/мин. Рентгеноспектральный микроанализ (спектры излучения MnK_α и AlK_α) проводили на приборе МАР-3 с диаметром зонда ~1 мкм при напряжении 25 кВ и токе 30–40 нА.

РЕЗУЛЬТАТЫ И ИХ ОБСУЖДЕНИЕ

Катализаторы на немодифицированном носителе. По данным РФА (табл. 1) при нанесении марганца на чистый (немодифицированный) носитель **1**, после прокаливания при 500°C на поверхности γ-Al_2O_3 формируется высокодисперсная фаза MnO_2 (образец № 1). В случае носителя **2** наряду с фазой MnO_2 наблюдается уширение линий носителя, что может указывать на начало взаимодействия его с катионами марганца (образец № 7). С увеличением содержания χ-Al_2O_3 (носитель **3**) взаимодействие усиливается, о чем свидетельствует еще большая размытость линий носителя и изменение параметра его решетки по сравнению с исходным (образец № 12). При этом окристаллизованная фаза оксида марганца не обнаружена. Это, видимо, связано с формированием твердого раствора марганца в структуре носителя.

Повышение температуры прокаливания до 900°C приводит к появлению во всех этих системах фазы α-Al_2O_3 (1–4%), а сам носитель представляет собой смесь δ- и γ-форм оксида алюминия (δ-Al_2O_3 не более 30%). Вероятно, ионы марганца присутствуют в твердых растворах на основе δ- и α-Al_2O_3. Как отмечено в [7, 8], образование при 900°C фазы α-Al_2O_3 обусловлено минерализующим действием на γ-оксид алюминия введенного марганца и косвенно подтверждает наличие взаимодействия между ними.

О взаимодействии марганца с носителем при 900°C свидетельствует отсутствие индивидуальных оксидных фаз марганца как в образце № 1 (за счет твердофазной реакции между MnO_2 и γ-Al_2O_3), так и в катализаторе № 12 (за счет совершенствования структуры низкотемпературного твердого

Таблица 1. Фазовый состав Mn–Al–O-катализаторов (содержание Mn ~ 5 мас. % в расчете на MnO_2)

№ образца	Модифиц. добавка – мас. %	Фазовый состав		
		500°C	900°C	1300°C
		Носитель **1** (γ-Al_2O_3)		
1	–	MnO_2 (D ~ 80 Å) + γ-Al_2O_3 (a ~ 7.910 Å)	α-Al_2O_3 (~1%) + + (δ* + γ*)-Al_2O_3	α-Al_2O_3 + (Mn, Al)$[Al]_2O_4$ (a ~ 8.125 Å) + + (Mn, Al)[Mn, Al]$_2O_4$ (a ~ 8.290 Å)
2	MgO-4.5	β-Mn_2O_3 (D ~ 180 Å) + + γ*-Al_2O_3 (a ~ 7.952 Å)	γ*-Al_2O_3 (a ~ 7.956 Å)	α-Al_2O_3 + (Mn, Mg)$[Al]_2O_4$ (a ~ 8.147 Å)
3	MgO-4.5 La_2O_3-5	β-Mn_2O_3 (D ~ 180 Å) + + γ*-Al_2O_3 (a ~ 7.952 Å)	γ*-Al_2O_3 (a ~ 7.963 Å)	–
4	MgO-4.5 La_2O_3-12	γ*-Al_2O_3 (a ~ 7.952 Å)	γ*-Al_2O_3 (a ~ 7.970 Å)	α-Al_2O_3 + (Mn, Mg)$Al_{11}LaO_{19}$
5	MgO-4.5 CeO_2-5	β-Mn_2O_3 (D ~ 50 Å) + CeO_2 + + γ*-Al_2O_3 (a ~ 7.952 Å)	CeO_2 + γ*-Al_2O_3 (a ~ 7.963 Å)	CeO_2 + α-Al_2O_3 + следы (Mn, Mg)$[Al]_2O_4$ (a ~ 8.140 Å)
6	MgO-4.5 CeO_2-12	β-Mn_2O_3 (D ~ 50 Å) + CeO_2 + + γ*-Al_2O_3 (a ~ 7.952 Å)	CeO_2 + γ*-Al_2O_3 (a ~ 7.970 Å)	–
		Носитель **2** (85% γ-Al_2O_3 + ~15% χ-Al_2O_3)		
7	–	MnO_2 (D = 80 Å) + + р/а структура, близкая к γ-Al_2O_3 (a ~ 7.910 Å)	β-Mn_2O_3 + α-Al_2O_3 (~2%) + + (δ* + γ*)-Al_2O_3	α-Al_2O_3 + (Mn, Al)$[Al]_2O_4$ (a ~ 8.097 Å) + + (Mn, Al)[Mn, Al]$_2O_4$ (a ~ 8.285 Å)
8	MgO-4.5	β-Mn_2O_3 (D ~ 180 Å) + + γ*-Al_2O_3 (a ~ 7.952 Å)	α-Al_2O_3 (следы) + + γ*-Al_2O_3 (a ~ 7.965 Å)	α-Al_2O_3 + следы (Mn, Mg)$[Al]_2O_4$ (a ~ 8.130 Å)
9	MgO-4.5 La_2O_3-5	γ*-Al_2O_3 (a ~ 7.952 Å)	γ*-Al_2O_3 (a ~ 7.956 Å)	α-Al_2O_3 + (Mn, Mg)$Al_{11}LaO_{19}$
10	MgO-4.5 La_2O_3-12	γ*-Al_2O_3 (a ~ 7.952 Å)	γ*-Al_2O_3 (a ~ 7.956 Å)	α-Al_2O_3 (следы) + следы (Mn, Mg)$[Al]_2O_4$ (a ~ 8.120 Å) + +(Mn, Mg)$Al_{11}LaO_{19}$
11	MgO-4.5 CeO_2-5	CeO_2 + γ*-Al_2O_3 (a ~ 7.952 Å)	CeO_2 + γ*-Al_2O_3 (a ~ 7.956 Å)	CeO_2 + α-Al_2O_3 + + (Mn, Mg)$[Al]_2O_4$ (a ~ 8.127 Å)
		Носитель **3** (65% γ-Al_2O_3 + ~35% χ-Al_2O_3)		
12	–	Р/а структура, близкая к γ-Al_2O_3, (a ~ 7.917 Å)	α-Al_2O_3 (~4%) + + (δ* + γ*)-Al_2O_3	α-Al_2O_3 + (Mn, Al)$[Al]_2O_4$ (a ~ 8.117 Å) + + (Mn, Al)[Mn, Al]$_2O_4$ (a ~ 8.277 Å)
13	MgO-4.5	γ*-Al_2O_3 (a ~ 7.952 Å)	α-Al_2O_3 (следы) + + γ*-Al_2O_3 (a ~ 7.963 Å)	–
14	MgO-4.5 La_2O_3-5	»	γ*-Al_2O_3 (a ~ 7.967 Å)	α-Al_2O_3 + (Mn, Mg)$[Al]_2O_4$ (a ~ 8.113 Å) + + (Mn,Mg)$Al_{11}LaO_{19}$
15	MgO-4.5 La_2O_3-12	»	»	–
16	MgO-4.5 CeO_2-5	CeO_2 (D ~ 60Å) + γ*-Al_2O_3 (a ~ 7.952 Å)	CeO_2 (D ~ 90 Å) + γ*-Al_2O_3 (a ~ 7.971 Å)	CeO_2 (D ~ 500 Å) + α-Al_2O_3 + + (Mn, Mg)$[Al]_2O_4$ (a ~ 8.123 Å) + + следы (Mn, Mg)$Al_{11}CeO_{19}$
17	MgO-4.5 CeO_2-12	CeO_2 + γ*-Al_2O_3 (a ~ 7.952 Å)	CeO_2 + γ*-Al_2O_3 (a ~ 7.964 Å)	CeO_2 + α-Al_2O_3 + + (Mn, Mg)$[Al]_2O_4$ (a ~ 8.123 Å) + + (Mn, Mg)$Al_{11}CeO_{19}$

Примечание. γ*-Al_2O_3 – твердый раствор на основе шпинельной структуры γ-Al_2O_3 с параметром ячейки a, Å, указанным в скобках; δ*-Al_2O_3 – твердый раствор на основе δ-Al_2O_3.
р/а – рентгено-аморфный.

раствора марганца в (γ,χ)-Al_2O_3). Однако в катализаторе № 7 при 900°C найдена фаза β-Mn_2O_3, и это может свидетельствовать о том, что твердофазное взаимодействие MnO_2 с носителем, уже имеющим поле 500°C признаки низкотемпературного твердого раствора, видимо, затруднено по сравнению с взаимодействием MnO_2 с γ-Al_2O_3 в случае носителя **1**.

При 1300°C во всех образцах наблюдаются α-Al_2O_3 и высокотемпературные Mn-содержащие фазы: частично обращенная шпинель (Mn, Al)[Mn, Al]$_2O_4$ и шпинель (Mn, Al)[Al]$_2O_4$. Обе шпинели присутствуют в соизмеримых количествах на носителях **1** и **2**, а в случае носителя **3** формируется преимущественно обращенная шпинель.

Катализаторы на носителе, модифицированном лантаном или церием. При модифицировании лантаном (5 и 12 мас. % La_2O_3) в Mn–Al–O-катализаторах, приготовленных на носителях **1–3**, параметр решетки при 500 и 900°C практически соответствует исходному носителю, независимо от содержания в нем фазы χ-Al_2O_3. При этом окристаллизованные Mn-содержащие фазы не наблюдаются. При 1300°C формируется смешанный гексаалюминат (**ГА**) состава $MnLaAl_{11}O_{19}$. Минерализующее влияние марганца подавляется, и фаза α-Al_2O_3 появляется только при 1300°C.

При модифицировании церием (5 и 12 мас. % CeO_2) в катализаторах на носителях **1–3** при 500 и 900°C изменение параметра решетки исходного носителя при введении марганца также незначительно, и окристаллизованные Mn-содержащие фазы не наблюдаются. Во всех образцах, вплоть до 1300°C, присутствует оксид CeO_2, размер частиц которого, как показано на примере образца № 16 (табл. 1), с ростом температуры увеличивается. При этом фаза α-Al_2O_3, как и в случае модифицирования лантаном, наблюдается только при 1300°C. Кроме того, при 1300°C в образцах на носителях **2** и **3**, содержащих фазу χ-Al_2O_3, с повышенным содержанием церия, обнаружены следы смешанного ГА вероятного состава $MnAl_{11}CeO_{19}$.

Катализаторы на носителе, модифицированном магнием. При модифицировании магнием носителей **1–3** характер взаимодействия катионов марганца с оксидом алюминия иной и в значительной мере определяется фазовым составом исходного носителя. Так, по данным табл. 1, при 500°C одновременно с образованием твердого раствора магния в оксиде алюминия на поверхности носителей **1** и **2** формируется грубодисперсная фаза β-Mn_2O_3 (образцы № 2, 8). И только в случае носителя **3** Mn-содержащие фазы отсутствуют (образец № 13). При повышении температуры до 900°C происходит совершенствование твердого раствора и увеличение параметра его решетки. Окристаллизованные оксидные формы Mn во всех случаях отсутствуют, что свидетельствует об усилении взаимодействия Mn^{3+} с Al_2O_3 в присутствии алюмомагниевого твердого раствора. При 1300°C наблюдаются две фазы – α-Al_2O_3 и смешанный твердый раствор (Mn, Mg)[Al]$_2O_4$, параметр решетки которого соответствует ~50%-ному замещению магния на марганец.

Катализаторы на носителе, модифицированном добавками Mg + La или Mg + Ce. При модифицировании Mn–Al–O-катализаторов на основе носителей **1–3** добавками Mg + La или Mg + Ce сохраняются те же закономерности в формировании фазового состава, что и в случае образцов, модифицированных только магнием, но присутствие La или Ce усиливает взаимодействие катионов марганца с носителем. Так, при 500°C оксидная фаза β-Mn_2O_3 проявляется только в образцах, приготовленных на носителе **1** (образцы № 3, 5, 6, табл. 1), тогда как в катализаторах аналогичного состава на носителях **2** (образцы № 9–11) и **3** (образцы 14–17) оксидные фазы марганца не обнаружены. Следует заметить, что окристаллизованные Mn-содержащие фазы отсутствуют и в образце № 4, содержащем 12% La.

При 900°C происходит совершенствование смешанных твердых растворов с увеличением параметров их решетки, а оксидные фазы марганца отсутствуют во всех образцах. Как и в случае катализаторов, модифицированных индивидуальными оксидами La или Ce, во всех указанных выше Mg–La- и Mg–Ce-содержащих катализаторах (табл. 1) при этой температуре фаза α-Al_2O_3 отсутствует. Это обусловлено стабилизирующим действием добавок La и Ce на термическую устойчивость оксида алюминия [12].

После прокаливания при 1300°C во всех катализаторах, модифицированных двумя оксидами, наблюдается фаза α-Al_2O_3. Марганецсодержащие соединения в катализаторах с добавками Mg + La представлены ГА состава (Mn, Mg)$Al_{11}LaO_{19}$, а в образцах с оксидами Mg + Ce – твердыми растворами на основе шпинели (Mn, Mg)[Al]$_2O_4$. При этом параметры решетки твердых растворов соответствуют замещению в шпинели 25–40% магния на марганец. В Mg–La-образцах на носителях **2** и **3**, содержащих χ-Al_2O_3, обнаружены следы твердых растворов состава (Mn, Mg)[Al]$_2O_3$, а в Mg–Ce-образцах – фаза ГА состава (Mn, Mg)$Al_{11}CeO_{19}$ (табл. 1).

Рентгеноспектральный микроанализ. Результаты рентгеноспектрального микроанализа подтверждают выводы об усилении взаимодействия марганца с носителем при наличии и увеличении содержания в нем фазы χ-Al_2O_3. Так, в приповерхностном слое немодифицированного Mn–Al–O-катализатора на носителе **1**, не содержащем χ-Al_2O_3 (рис. 1, **А**), при 500°C отсутствует взаимодействие оксидов марганца и алюминия (антибатность профилей спектров MnK_α и AlK_α). После прокалива-

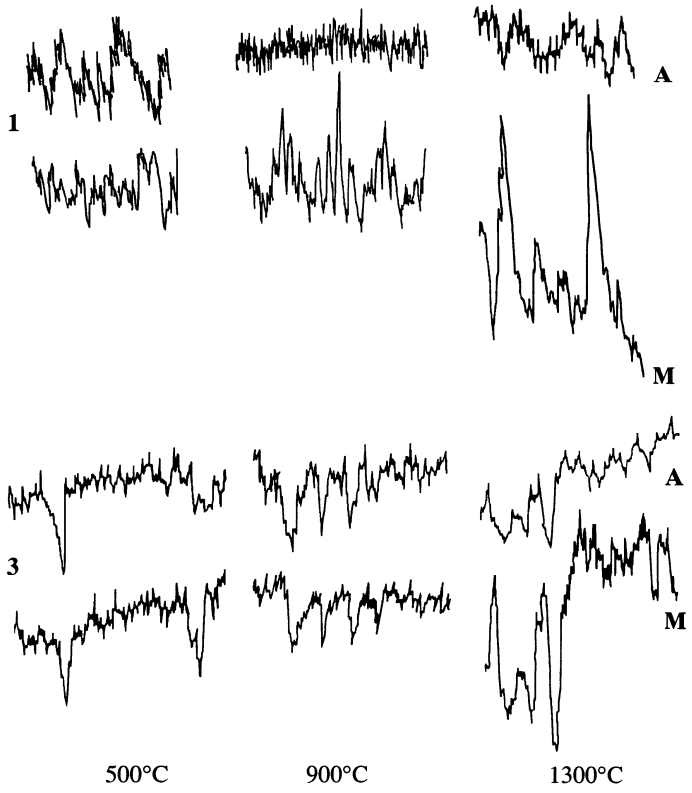

Рис. 1. Результаты рентгеноспектрального микроанализа: интенсивность излучения AlK_α (**A**) и MnK_α (**M**) для немодифицированных Mn–Al–O-катализаторов, приготовленных на носителях **1** и **3** и прокаленных при температурах 500, 900 и 1300°C (при записи интенсивности K_αMn использовалась шкала в 20 раз большая, чем для K_αAl).

ния катализатора при 900°C наблюдается некоторая корреляция в положении минимумов и максимумов спектров MnK_α и AlK_α, что свидетельствует о наличии слабого взаимодействия этих компонентов. При 1300°C связь образующейся Mn-содержащей фазы с носителем заметно ослаблена, и распределение этой фазы на поверхности носителя имеет неоднородный характер. В немодифицированных катализаторах на носителях **2** и **3**, содержащих χ-Al_2O_3 (рис. 1, **M**), уже при 500°C характер спектров MnK_α и AlK_α свидетельствует о наличии взаимодействия между оксидами марганца и алюминия, усиливающегося с ростом температуры прокаливания.

Активность катализаторов в реакции окисления бутана. В табл. 2 представлены данные об удельной поверхности и активности исследуемых катализаторов в реакции окисления бутана. С ростом температуры прокаливания удельная поверхность всех катализаторов уменьшается, однако можно отметить ее более высокие абсолютные значения при 1300°C для модифицированных образцов, за исключением образцов № 10, 11, модифицированных церием. По данным табл. 1 это отклонение может быть связано с образованием при этой температуре грубодисперсного CeO_2.

Катализаторы № 1–3, прокаленные при 500°C, имеют примерно равную активность, независимо от содержания χ-Al_2O_3 в носителе. После обработки при 900°C наблюдается рост активности (или термоактивация [7, 8]), наиболее существенный для образца № 3 с высоким содержанием χ-Al_2O_3.

На катализаторах, модифицированных магнием (образцы № 4–6), эффект термоактивации при 900°C незначителен, хотя слабое влияние присутствующей в носителе фазы χ-Al_2O_3 все же имеет место. Добавки La (образцы № 7–9) заметно повышают активность прогретых при 500°C катализаторов однако после прокаливания при 900°C эти образцы по активности уступают немодифицированным. Аналогичный характер изменения активности наблюдается и для Ce-содержащих катализаторов (образцы № 10, 11), но в этом случае абсолютные значения активности прокаленных при 500°C образцов ниже, чем для La-содержащих катализаторов.

Таблица 2. Удельная поверхность и активность Mn–Al–O-катализаторов различного состава в реакции глубокого окисления бутана (содержание Mn ~ 5 мас. % в расчете на MnO_2)

№ образца	Состав носителя		$S_{уд}$, $м^2/г$, после прокаливания			$w \times 10^2$, $см^3\ г^{-1}\ с^{-1}$ после прокаливания		
	исходный носитель (фазовый состав)	модифицирующая добавка, мас. %	500°C	900°C	1300°C	500°C	900°C	1300°C
1	**1** (γ-Al_2O_3)	–	176	105	3.2	0.52	0.85	0.08
2	**2** (85% γ-Al_2O_3 + 15% χ-Al_2O_3)	–	192	115	2.3	0.47	1.41	0.18
3	**3** (65% γ-Al_2O_3 + 35% χ-Al_2O_3)	–	222	112	–	0.52	1.58	–
4	**1**	MgO-4.5	156	110	4.0	0.45	0.44	0.09
5	**2**	»	165	108	4.3	0.43	0.64	0.58
6	**3**	»	190	105	–	0.69	0.71	–
7	**1**	La_2O_3-5	138	102	4.3	1.70	0.78	0.08
8	**2**	»	164	114	3.9	1.86	0.91	0.67
9	**3**	»	187	134	3.7	1.41	0.72	0.46
10	**1**	CeO_2-5	139	91	0.6	1.51	0.80	0.02
11	**2**	»	160	115	2.6	1.21	0.89	0.50
12	**1**	MgO-4.5 La_2O_3-5	119	81	9.7	1.00	0.48	0.10
13	**2**	»	150	108	6.3	1.70	0.60	0.32
14	**3**	»	155	112	6.9	1.20	0.60	0.44
15	**2**	MgO-4.5 CeO_2-5	153	100	3.5	1.02	0.58	0.28
16	**3**	»	158	103	4.9	1.00	0.59	0.82

После прокаливания при 1300°C, независимо от состава катализаторов, их активность снижается. При этом катализаторы на носителях **2** и **3** в несколько раз активнее образцов близкого состава, приготовленных на носителе **1**.

Активность катализаторов в реакции окисления метана. На рис. 2 представлены данные по каталитической активности в реакции окисления метана прокаленных при 1300°C Mn–Al–O-образцов, приготовленных на основе модифицированных носителей **2** и **3**. Температура 50%-ного превращения метана для этих образцов составляет 520–550°C, что на 80–110°C ниже, чем для промышленного катализатора ИКТ-12-40, содержащего вдвое больше марганца [8]. При этом наибольшую активность имеет катализатор на основе носителя **3**, модифицированного добавкой Mg + Ce (как и в окислении бутана, см. образец № 16, табл. 2). Следует заметить, что увеличение содержания марганца в исследуемых модифицированных катализаторах до уровня ИКТ-12-40 (~10 мас. % в расчете на MnO_2) снижает температуру 50%-ного превращения метана на ~20–30°C.

Таким образом, Mn–Al–O-катализаторы, приготовленные на основе γ-оксида алюминия, содержащего χ-Al_2O_3 и модифицированного добавками Mg, La или Ce, являются более активными и термостабильными (вплоть до 1300°C) по сравнению с образцами на основе чистого γ-Al_2O_3, в том числе, и с катализатором ИКТ-12-40 [8]. Следует подчеркнуть, что только наличие фазы χ-Al_2O_3 в исходном носителе или модифицирование γ-Al_2O_3 вышеуказанными добавками не дает желаемого результата. Можно полагать, что более высокая степень разупорядоченности структуры χ-Al_2O_3 по сравнению с γ-Al_2O_3 способствует более глубокому взаимодействию марганца и модифицирующих добавок с носителем на ранних стадиях синтеза и образованию при 1300°C высокотемпературных Mn–Al-соединений сложного состава

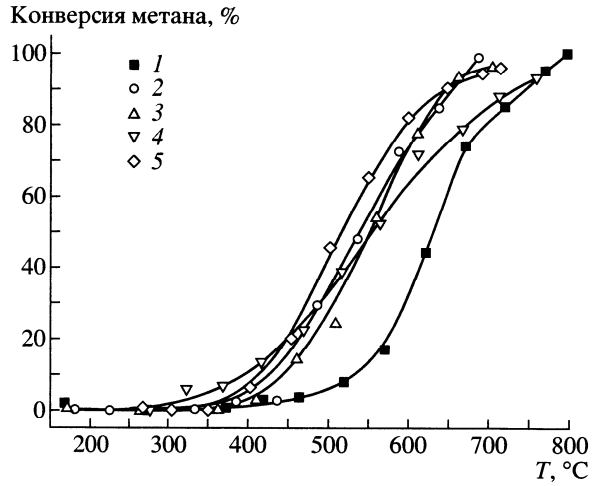

Рис. 2. Активность Mn–Al–O-катализаторов, прокаленных при 1300°C, в реакции окисления метана: *1* – ИКТ-12–40; *2* – Mn/носитель **2** + La_2O_3; *3* – Mn/носитель **2** + MgO; *4* – Mn/носитель **2** + CeO_2; *5* – Mn/носитель **3** + (MgO + CeO_2).

(твердых растворов и/или гексаалюминатов), которые и обеспечивают стабильность и высокую активность модифицированных Mn–Al–O-катализаторов в окислении метана.

Авторы выражают благодарность Р.А. Шкрабиной и Н.А. Корябкиной за предоставление образцов модифицированного оксида алюминия и участие в обсуждении результатов.

СПИСОК ЛИТЕРАТУРЫ

1. *Поповский В.В.* Дис. ... докт. хим. наук. Новосибирск: ИК СО РАН, 1973.
2. *Цикоза Л.Т.* Дис. ... канд. хим. наук. Новосибирск: ИК СО РАН, 1980.
3. А. с. 609549 СССР. Б.И. 1978. № 21.
4. А. с. 810256 СССР. Б.И. 1981. № 9.
5. А. с. 787082 СССР. Б.И. 1980. № 46.
6. *Jaworska–Golas Z., Mista W., Wrzyszcz J., Zawadzkil M.* // Catal. Lett. 1994. V. 24. № 1, 2. P. 133.
7. *Цырульников П.Г., Сальников В.С., Дроздов В.А., Стукен С.А., Бубнов А.В., Григоров Е.И., Калинкин А.В., Зайковский В.И.* // Кинетика и катализ. 1991. Т. 32. № 2. С. 439.
8. *Пат.* 2063803 РФ, 1996.
9. *Shaper H., Doesburg E.B.M.* // Appl. Catal. 1983. V. 7. № 2. P. 221.
10. *Ismagilov Z.R., Shkrabina R.A., Koryabkina N.A.* // Catal. Today. 1999. V. 47. № 1–4. P. 51.
11. *Tsykoza L.T., Shkrabina R.A., Koryabkina N.A., Ushakov V.A., Shikina N.V., Ismagilov Z.R.* // 7th Nordic Symp. on Catal., Åbo/Turku, Finland, 1996. Book of abstr. P. 32.
12. *Tsykoza L.T., Ismagilov Z.R., Shkrabina R.A., Koryabkina N.A., Shikina N.V., Arendarskii D.A., Ushakov V.A., Kalinkin A.V.* // Memorial G.K. Boreskov Conf., Novosibirsk, Russia, 1997. Abstr. Pt. II. P. 410.

Study of Supported Catalysts Synthesized by the Use of Plasma Technique

O. Yu. PODYACHEVA[1], N. V. SHIKINA[1], Z. R. ISMAGILOV[1], V. A. USHAKOV[1], A. I. BORONIN[1], N. A. RUDINA[1], I. A. OVSYANNIKOVA[1], S. A. YASHNIK[1], O. P. SOLONENKO[2], A. A. MICHAL'CHENKO[2] and H.VERINGA[3]

[1]*G. K. Boreskov Institute of Catalysis, Siberian Branch of the Russian Academy of Sciences, Pr. Akademika Lavrentyeva 5, Novosibirsk 630090 (Russia)*

E-mail:pod@catalysis.nsk.su

[2]*Institute of Theoretical and Applied Mechanics, Siberian Branch of the Russian Academy of Sciences, Ul. Institutskaya 4/1, Novosibirsk 630090 (Russia)*

[3]*ECN, P. O. Box 1, 1755 ZG Petten (The Netherlands)*

Abstract

Some prospects of application of plasma spraying technique for the synthesis of supported catalysts are demonstrated. It was shown that Mn-containing catalysts deposited on γ-Al_2O_3 by means of plasma spraying demonstrate superior activity in methane oxidation reaction compared with those of reference catalysts prepared via standard conventional route. Gradient alumina layer sprayed on the surface of metal supports of different geometry improves the performance characteristics of combustion catalysts on metal supports during long term operation at high temperatures. A catalytic heat-exchanging (HEX) tubular reactor for combining exothermic combustion and endothermic methane steam reforming has been developed. The methane combustion and steam reforming catalysts were synthesized on the heat-conducting metal foam support materials by application of preliminary plasma spraying in order to increase adhesive properties of the active layer. The HEX reactor with perovskite or Pt supported catalyst on Ni–Cr foam material on the external surface of the HEX tube and with Ni containing reforming catalyst on the internal Ni foam was successfully tested in methane combustion reaction combined with methane steam reforming.

INTRODUCTION

Last years works on the synthesis of catalysts with substantially improved or new unique properties by the use of plasma techniques have been intensively carried out. Although most of the papers are devoted to the preparation of bulk catalysts, some efforts are undertaken to manufacture supported catalysts for different applications, *i. e.* selective hydrogenation, combustion processes, *etc.*

This paper focuses on the development of supported catalysts by the use of plasma spraying technique. Direct current plasma torch [1] with interelectrode insert and diffusive attachment of arc on anode surface was used for synthesis of Mn-containing catalysts supported on alumina as well as alumina coatings on metal surfaces of different geometry (plates, foams) with subsequent deposition of combustion catalysts.

EXPERIMENTAL

Operating modes of plasma torch with the interelectrode insert were provided by the variation of the plasma-forming gas (air) flow rate over a wide range (from 0.5 up to 2.5 g/s) [2]. The main regimes of the plasma torch operation and outflowing jets are presented in Table 1.

Powders of pure γ-alumina or γ-alumina impregnated by $Mn(NO_3)_2$ were injected into the plasma jet outflow and quenched in water. Influence of powder size (90–1000 μm), regime of plasma jet outflow (laminar or turbulent) and Mn content (5 or 17 % mass) on the

TABLE 1

Main regimes of the plasma torch operating and outflowing jets

Flow rate of plasma-forming gas (air), G_g, g s^{-1}	0.5	0.75	1.0	1.25	2.0	2.5
Arc current, I, A	255	250	245	240	220	210
Arc voltage, U, V	180	200	210	220	250	270
Efficiency of electric energy utilization, η, %	45	50	60	65	70	72.5
Effective thermal power of outflowing plasma jet, kW	20.6	25.0	30.8	34.3	38.5	41.1
Regime of the plasma jet outflow and approximate length of powder thermal treatment zone in axial direction, L_r, m	Laminar, 0.15	Laminar-transient, 0.09	Transient, 0.075	Transient, 0.06	Turbulent, 0.05	Turbulent, 0.05
Mean-mass velocity of plasma prior to powder injection section, m s^{-1}	460	570	720	815	1020	1160

properties of catalysts synthesized in a plasma jet outflow (plasma catalysts) was studied. Reference catalysts having identical chemical composition were prepared using standard conventional route, *i. e.* the calcination of γ-alumina impregnated by $Mn(NO_3)_2$ at 550 °C for 4 h.

Alumina powders differing in phase composition and particle size (α-Al_2O_3 20–80 and γ-Al_2O_3 90–500 μm) were used to spray an intermediate (gradient) layer on titanium plates and Ni, Ni–Cr foam materials under laminar, transient and turbulent regimes of the plasma jet outflow [3]. Various combustion catalysts ($LaCoO_3$, Pt, Pd, $LaMnAl_{11}O_{19}$) were deposited on Ni–Cr foams covered by plasma sprayed alumina layer by means of impregnation or suspension techniques [2, 4].

Phase composition of the catalysts was studied by XRD analysis, specific surface area of the samples was measured by BET method, pore volume of the sprayed layers was calculated using water capacity technique. The morphology of the catalysts was studied by SEM. Active component distribution in alumina was defined by X-ray microprobe analysis, whereas catalyst surface was examined by XPS. Catalysts were tested in methane oxidation reaction in a flow set-up; the reaction mixture was 1 % CH_4 in air with a space velocity 1000 h^{-1}.

RESULTS AND DISCUSSION

γ-Al_2O_3

Study of the influence of the regimes of jet outflow on the properties of alumina powders treated in plasma and quenched in water has been performed. The results for γ-Al_2O_3 powder are presented in Table 2.

A comparison of cross section views of initial and plasma treated particles of γ-Al_2O_3 showed that in the latter case the pellet consists of a core and a shell (Fig. 1). Densities of these two basic areas are different. Analysis of scanning electron micrograph and XRD data (see Table 2) allows the assumption that the particle core consists of γ-Al_2O_3 phase, while the particle shell is formed by α-Al_2O_3. It seems that the use of large particles for spraying and high quenching velocities lead to the formation of a cold core and a hot melted shell.

Mn–γ-Al_2O_3

XRD analysis showed the presence of β-Mn_2O_3 and γ-Al_2O_3 phases in all Mn-containing reference catalysts, independent on the content of Mn and particle size of the samples. Phase composition of the plasma catalysts is more com-

TABLE 2

Properties of γ-Al_2O_3 after plasma treatment and quenching in water

Particle size, μm	Flow rate, g s^{-1}	Regime	Specific surface area, $m^2 g^{-1}$	Phase composition	I_α/I_γ^*
90–200	0.5	Laminar	2.2	α-Al_2O_3, γ-Al_2O_3	30
90–200	1.0	Transient	22	α-Al_2O_3, γ-Al_2O_3	13
200–300	0.5	Laminar	19	α-Al_2O_3, γ-Al_2O_3	25
200–300	1.0	Transient	76	α-Al_2O_3, γ-Al_2O_3	11
300–400	0.5	Laminar	67	α-Al_2O_3, γ-Al_2O_3	8
300–400	1.0	Transient	104	α-Al_2O_3, γ-Al_2O_3	6
400–500	0.5	Laminar	119	α-Al_2O_3, γ-Al_2O_3	

*I_α/I_γ – ratio of intensities of line d/n = 2.085 (α-Al_2O_3) and d/n = 1.990 (γ-Al_2O_3).

plicated. It depends on the Mn content, particle size as well as the regime of plasma jet outflow. The Mn-containing phases are registered in plasma catalysts with particle size equal to 100–200 μm. It was found that Mn is present in solid solutions of Mn–Al–O composition based on spinel structure and having different cell sizes (a = 7.940–8.242 Å).

X-ray microprobe analysis revealed that the active component in reference catalysts is uniformly distributed inside the particle (Fig. 2, *a*). Discrepancy between K_αMn and K_αAl profiles is observed. This fact correlates with XRD data showing the formation of crystalline β-Mn_2O_3 phase in reference catalysts. Analysis of K_αMn and K_αAl profiles of plasma catalyst allows us to conclude that Mn is transferred to the catalyst surface (see Fig. 2. *b*). XPS confirmed that Mn concentration on the surface of the plasma catalyst exceeds the ones of the reference catalyst by 50 %. The XPS spectra of plasma and reference catalysts present one O 1*s* photoline at 531 eV corresponding to the lattice oxygen of alumina. Meantime, the chemical states of manganese in plasma and reference catalysts are different: binding energy of Mn $2p_{3/2}$ photoline of plasma catalysts is 641.6 eV, whereas that of reference catalysts is 640 eV.

Plasma catalysts demonstrate superior activity in methane oxidation reaction (Fig. 3). Temperature of 50 % methane conversion for plasma catalyst with the content of active component 5 % mass is lower than the temperature of 50 % methane conversion for reference catalyst by 90 °C, whereas for catalysts with content of active component 17 % mass by 120 °C. This fact can be probably explained by increased concentration of manganese on the surface of plasma catalyst as well as by formation of active Mn-containing surface phases invisible for XRD analysis.

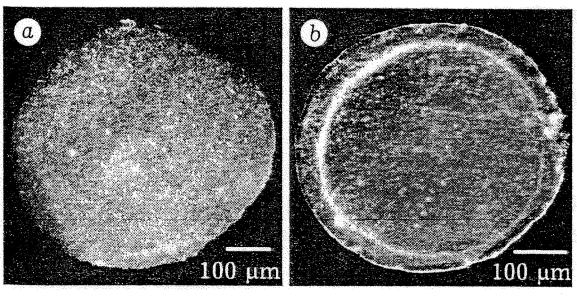

Fig. 1. Micrographs of a cross-section view of initial (*a*) and plasma-treated γ-Al_2O_3 particles (*b*).

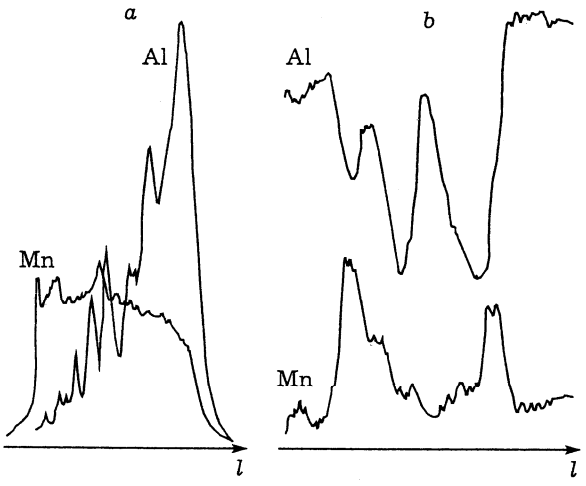

Fig. 2. X-ray microprobe spectra (K_αMn, K_αAl) of cross section of particles of catalyst 17 % Mn_2O_3/γ-Al_2O_3, 100–200 μm: *a* – reference catalyst, *b* – plasma catalyst (laminar regime of plasma jet outflow).

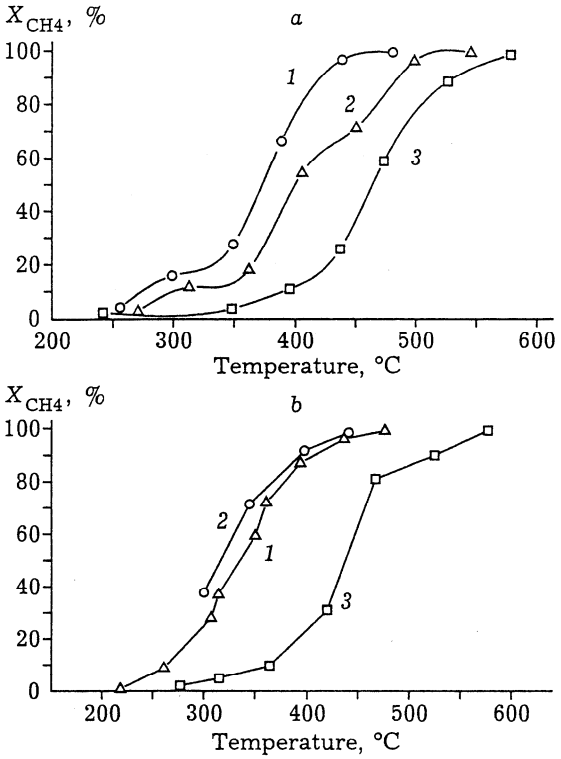

Fig. 3. Temperature dependencies of methane conversion (1 % CH_4 in air, 1000 h^{-1}) on catalysts: *a* – 5 % Mn_2O_3/γ-Al_2O_3, *b* – 17 % Mn_2O_3/γ-Al_2O_3 synthesized using turbulent (*1*) or laminar (*2*) regime of jet outflow and conventional (*3*) route.

Thus, plasma technique allows the synthesis of Mn-containing catalysts deposited on γ-Al_2O_3 with substantially improved properties compared with those of reference catalysts prepared via conventional route.

Alumina-metal supports

Experiments on the plasma spraying of alumina of different phase composition and particle size on titanium plates have shown that

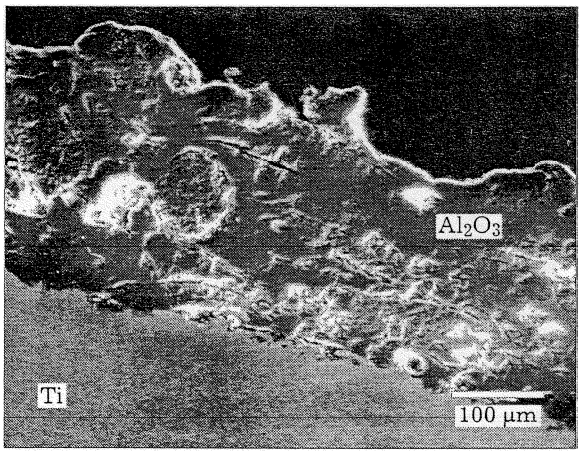

Fig. 4. Micrograph of cross section view of Al_2O_3 plasma sprayed on metal surface.

the properties of plasma sprayed layers are quite similar and do not depend on the jet outflow regime used (Table 3).

When α-Al_2O_3 is sprayed on titanium plates, the coatings are characterized by a low specific surface area and their pore volume increases when the spraying regime is changed from a laminar to a turbulent one. It has been established that the dependence of the regime on the coating properties is the same when γ-Al_2O_3 is sprayed. Moreover, in the latter case the spraying regime influences the quantitative proportions of α-Al_2O_3 and θ-Al_2O_3 phases of the coatings and their specific surface area. The maximum porosity and minimum α-Al_2O_3 phase content were found when a transient jet outflow regime was used.

The formation of dense layers when γ-Al_2O_3 was sprayed on titanium plates was shown by scanning electron microscopy (Fig. 4). It is obvious that the contact between alumina and the metal surface is rather strong and uniform. The

TABLE 3

Properties of alumina sprayed on titanium plates

Particle size, μm	Type of alumina sprayed	Flow rate, g s^{-1}	Regime of plasma jet outflow	Specific surface area, m^2 g^{-1}	Phase composition	Pore volume, cm^3 g^{-1}
40	α-Al_2O_3	0.75	Laminar-tansient	0.2	α-Al_2O_3	0.052
40	α-Al_2O_3	1.25	Transient	0.2	α-Al_2O_3	0.065
40	α-Al_2O_3	1.75	Turbulent	0.2	α-Al_2O_3	0.167
90–200	γ-Al_2O_3	0.5	Laminar	0.2	α,θ-Al_2O_3	0.068
90–200	γ-Al_2O_3	0.75	Laminar-transient	0.4	α,θ-Al_2O_3	0.075
90–200	γ-Al_2O_3	1.0	Transient	0.6	α,θ-Al_2O_3	0.166

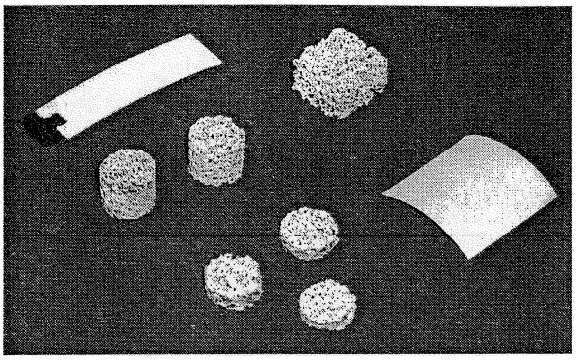

Fig. 5. Plasma sprayed samples of different surface geometry.

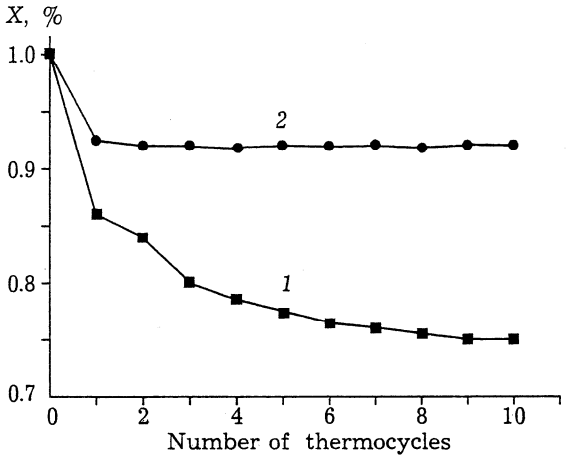

Fig. 6. Dependence of the catalyst mass loss on number of thermocycles, X, % = m_n/m_0 (m_0 – initial mass, m_n – mass after n thermocycles): *1* – $LaCoO_3/La-\gamma-Al_2O_3/Ni-Cr$ foam; *2* – $LaCoO_3/La-\gamma-Al_2O_3/\alpha-Al_2O_3/Ni-Cr$, plasma sprayed $\alpha-Al_2O_3$ layer.

sprayed layer has a complicated structure consisting of dense areas and macropores of different forms and sizes.

Taking into account that phase composition and BET area of plasma sprayed alumina do not depend significantly on the properties of alumina powders used for spraying, α-alumina with particle size 40 μm was sprayed on metal supports of different geometry (Fig. 5).

Combustion catalysts on metal foams

It was shown in [2] that the genesis of an active component in the combustion catalyst is not affected by the presence of the plasma sprayed α-alumina on the metal foam. Meanwhile, the experiments on thermal cycling have revealed that the presence of the plasma sprayed alumina layer on the metal surface allows to improve the adhesive properties of the active layer (Fig. 6). It was found that in the catalyst prepared by a pure chemical method the substantial destruction of the active layer continuously proceeds during each of 10 thermocycles performed, whereas in the catalyst with the plasma sprayed alumina the loss of the active layer is observed only after the first thermocycle.

Different types of combustion catalysts were synthesized on Ni–Cr foam supports covered by dense α-alumina gradient layer using plasma spraying technique. Comparative analysis of the initial activity of metal foamed catalysts calcined at 1000 °C and having different types of active components allowed finding the best compositions for methane combustion at high temperatures: $Pd/CeO_2-\gamma-Al_2O_3$ > $LaMnAl_{11}O_{19}/La-Al_2O_3$-$Pd-LaCoO_3$ > $LaCoO_3/La-\gamma-Al_2O_3$. Thermal stability of these catalysts was studied during long time catalyst operation at the following conditions: 8.6 % CH_4 in air, GHSV = 10 000 h^{-1}, T = 1000 °C. The activity of catalysts was measured after 3, 6, 10, 20 and 50 h of operation. The catalysts tested for 50 h can be arranged into the following sequence according to their activity: $LaMnAl_{11}O_{19}/La-Al_2O_3$ > $Pd/CeO_2-\gamma-Al_2O_3$ >> $Pd-LaCoO_3$ > $LaCoO_3/La-\gamma-Al_2O_3$.

Thus, gradient alumina layer sprayed on the surface of a metal support successfully serves as a washcoat on which active component can be deposited and improves thermal stability of the catalysts.

Heat-exchanging reactors

A catalytic heat-exchanging (HEX) tubular reactor for combining exothermic combustion and endothermic methane steam reforming has been developed [4]. The methane combustion and steam reforming catalysts were synthesized on the heat-conducting metal foam support materials by application of preliminary plasma spraying in order to increase adhesive properties of the active layer. The HEX reactor with perovskite or Pt supported catalyst on Ni–Cr foam material on the external surface

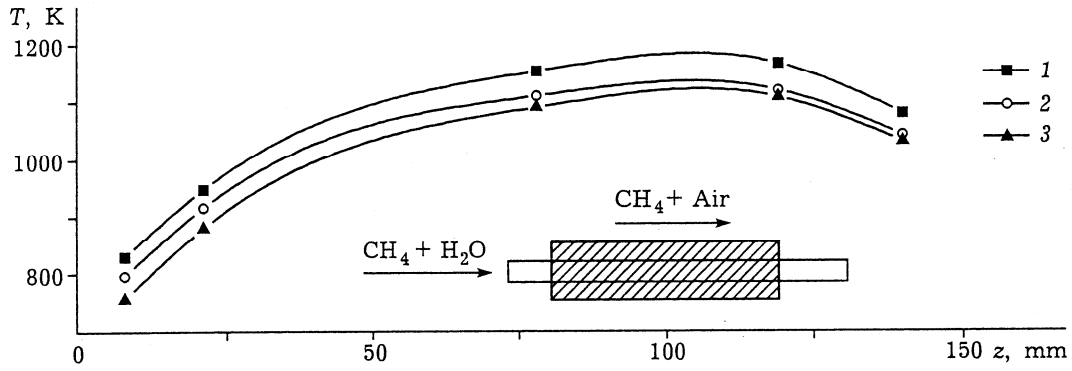

Fig. 7. Temperature profile in the combustion catalyst bed. Combustion of methane-hydrogen mixture with simultaneous steam reforming in heat-exchanging reactor: $C_0(CH_4)$, %: 27.5 (*1*), 38.5 (*2*), 47.8 (*3*); X_{CH_4}, %: 75 (*1*), 63.5 (*2*), 34 (*3*); V, $h^{-1} \cdot 10^{-3}$: 60 (*1*), 7.1 (*2*), 8.3 (*3*).

of the HEX tube and with Ni containing reforming catalyst on the internal Ni foam was successfully tested in methane combustion reaction combined with methane steam reforming (Fig. 7).

CONCLUSION

Some prospects of application of plasma spraying technique for the synthesis of supported catalysts are demonstrated. Plasma spraying technique successfully allows to synthesise the supported catalysts with enhanced catalytic activity properties and to improve the performance characteristics of combustion catalysts on metal supports during long term operation at high temperatures.

Acknowledgements

This work was supported by the grant of the Siberian Branch of the Russian Academy of Sciences in the frame of the Integrated Program 2000–2002; NWO grant in 1997–1999, The Netherlands and INTAS grant 99–1044.

REFERENCES

1 V. I. Kuz'min, O. P. Solonenko, M. F. Zhukov, Proc. 14th Intern. Thermal Spray Conf., 25–28 May 1995, Kobe, Japan, pp. 1091–1096.
2 Z. R. Ismagilov, O. Yu. Podyacheva, O. P. Solonenko *et al.*, *Catal. Today*, 51 (1999) 411.
3 Z. R. Ismagilov, O. P. Solonenko, O. Yu. Podyacheva *et al.*, Proc. 13th Intern. Symp. on Plasma Chemistry, Beijing, China, 1997, vol. 4, pp. 1880–1885.
4 Z. R. Ismagilov, O. Yu. Podyacheva, V. V. Pushkarev *et al.*, *Studies in Surface Sci. and Catal.*, 130 (2000) 2759.

Physica Scripta. Vol. T115, 740–743, 2005

EXAFS Study of Nb Doped $Sr(Co/Fe)O_{3-x}$ Perovskites

V. V. Kriventsov[1]*, D. I. Kochubey[1], Z. R. Ismagilov[1], O. Yu. Podyacheva[1] and A. P. Nemudry[2]

[1]Boreskov Institute of Catalysis, Lavrentiev prosp. 5, Novosibirsk, 630090, Russia
[2]Institute of Solid State Chemistry and Mechanochemistry, Kutateladze 18, Novosibirsk, 630128, Russia

Received June 26, 2003; accepted December 17, 2003

PACS numbers: 61.10.Ht; 82.65.Jv; 82.65.My

Abstract

The local structure of the Fe, Co and Nb surroundings of niobium doped $Sr(Co/Fe)O_{3-x}$ perovskites was studied by EXAFS spectroscopy. The samples were prepared by ceramic method at $T = 1250\,^{\circ}C$. In order to vary the oxygen content, the samples were (*i*) slowly cooled in the furnace, (*ii*) quenched in liquid N_2 and electrochemically oxidised. According to EXAFS data, the Nb and Fe cations occupy octahedral positions even at low oxygen content. At the same time, the Co cations seemingly occupy highly distorted octahedral positions. It should be noted that the mean Co-O distance (∼1.84 Å) is much shorter than the mean Fe-O (∼1.92 Å) distance in this case. It was assumed that oxygen vacancies are mainly located near cobalt cation positions.

1. Introduction

Nonstoichiometric oxides $Sr(Co/Fe)O_{3-x}$ exhibiting the mixed electron/oxygen conductivity, are intensively studied as candidate oxygen membranes for catalytic partial methane oxidation and syn.gas production reactors [1–3].

Distribution and location of oxygen vacancies in a nonstoichiometric oxide are important for understanding the mechanism of oxygen transportation (the main functional property of an oxide) and structural transformations in the membrane material regarding the oxygen concentration.

Doping or introduction of different cations into the nonstoichiometric oxide crystal structure is a promising way to improve permeability, chemical and mechanical stability of oxygen membranes.

XRD is usually used to obtain information on the structure of doped oxides. Unfortunately, this method has a number of drawbacks. First, nonstoichiometric oxides can possess a number of point defects as oxygen vacancies, providing a distortion of the cation local surrounding. Since these vacancies are likely disordered, the standard diffraction methods can not be used for their analysis.

The second problem arises when oxides are doped by cations of elements with close scattering abilities. Sometimes these cations are located in several non-equivalent crystallographic positions and one should establish how different chemical element cations are distributed among these positions.

To distinguish them, one should apply some special techniques such as anomalous diffraction (using synchrotron radiation) along with the standard methods.

The above problems can be solved by EXAFS, which is both the local and selective method. This method permits one to study local structure of every chemical element surroundings regardless of the sample crystallization degree.

In this work EXAFS spectroscopy was used to study the $SrCo_{0.7}Fe_{0.2}Nb_{0.1}O_{3-x}$ perovskites with different oxygen concentrations.

2. Experimental

The $SrCo_{0.7}Fe_{0.2}Nb_{0.1}O_{3-x}$ samples were synthesized from stoichiometric amounts of $SrCO_3$, Fe_2O_3, Co_3O_4, and Nb_2O_5, which were thoroughly mixed in an AGO-2 planetary ball mill. Prior to this, ethanol was added to the reagents to prepare a paste-like mixture which was then treated in a mill for 30 seconds. After drying and calcination at 950 °C for 8 h, the mixture was retreated in a mill for 30 s. The pellets prepared from the oxide mixture were placed into a furnace at 1250 °C and held there for 12 h. To prepare $SrCo_{0.7}Fe_{0.2}Nb_{0.1}O_{3-x}$ with low oxygen concentration $(3 - x) \sim 2.5$, the samples were quenched in liquid nitrogen, if the samples were slowly cooled in the furnace oxygen content increased to $(3 - x) \sim 2.7$. The samples electrochemically oxidized in 1 M KOH [4] possessed the highest value $(3 - x) \sim 2.9$. According to XRD the samples with different oxygen content were monophasic and all X-ray reflections were indexed in perovskite cubic cell. The increase of oxygen concentration in $SrCo_{0.7}Fe_{0.2}Nb_{0.1}O_{3-x}$ samples is accompanied by the slight decrease of perovskite cubic parameter. XRD study was carried out on DRON-3M diffractometer with graphite monochromator using CuK_α radiation. Samples $SrCoO_{2.5}$, $SrFeO_{2.5}$ (brownmillerite type) and $SrCoO_3$, $SrFeO_3$ (perovskite type) were used as reference samples.

EXAFS spectra of the Nb-K, Co-K, Fe-K edges for all the samples were obtained at the EXAFS Station of Siberian Synchrotron Radiation Center (SSRC). The storage ring VEPP-3, with electron beam energy of 2 GeV and an average stored current of 80 mA, has been used as the source of radiation. The X-ray energy was monitored with a channel cut Si(111) monochromator. The all EXAFS spectra of the Nb-K, Co-K, Fe-K edges were recorded under transmission mode, using two ionization chambers as detectors. The samples were prepared as pellets with thickness varied to obtain a 0.5–1.0 jump at the Nb-K, Co-K, Fe-K absorption edges. The EXAFS spectra were treated using the standard procedures [5]. The radial distribution function of atoms (RDF) was calculated from the EXAFS spectra in $k^3\chi(k)$ as the modulus of Fourier transform at the wave number interval 3.8–12.0 $Å^{-1}$. Curve fitting procedure with EXCURV92 [6] code was employed to determine precisely the distances and coordination numbers in similar wave number intervals after preliminary Fourier filtering using the known XRD data for the $SrCoO_{2.5}$, $SrFeO_{2.5}$ (brownmillerite type) and $SrCoO_3$, $SrFeO_3$ (perovskite type) bulk compounds. Debye-Waller factors are fixed (all the values are equal to 0.005 $Å^2$).

EXAFS spectra of the cobalt, iron and niobium local surrounding were used to calculate effective coordination

*e-mail: kriven@inp.nsk.su

Table I. *EXAFS data (R – distances (Å); N – effective coordination numbers) describing Fe and Co local surroundings for reference samples.*

	Reference samples							
	$SrFeO_{2.5}$		$SrFeO_3$		$SrCoO_{2.5}$		$SrCoO_3$	
Bond type	*R*, Å	*N*	*R*, Å	*N*	*R*, Å	*N*	*R*, Å	*N*
Fe-O, Co-O	1.92	2.7	1.92	3.3	1.82	2.0	1.88	3.7
Fe-Sr, Co-Fe	3.19	0.8	3.29	1.5	3.19	1.1	3.25	1.1
Fe-Fe, Co-Co	3.96	1.7	3.95	7.5	3.87	1.5	3.86	5.6

Table II. *EXAFS data (R – distances (Å); N – effective coordination numbers) describing Nb local surrounding for $SrCo_{0.7}Fe_{0.2}Nb_{0.1}O_{3-x}$ samples.*

	$SrCo_{0.7}Fe_{0.2}Nb_{0.1}O_{3-x}$					
	$x \sim 0.5$		$x \sim 0.3$		$x \sim 0.1$	
Bond type	*R*, Å	*N*	*R*, Å	*N*	*R*, Å	*N*
Nb-O	1.95	6.2	1.95	6.9	1.94	7.7
Nb-Sr	3.35	1.9	3.36	3.0	3.34	3.9
Nb-Co, Fe	3.98	3.6	3.95	6.3	3.93	9.1

Table III. *EXAFS data (R – distances (Å); N – effective coordination numbers) describing Co local surrounding for $SrCo_{0.7}Fe_{0.2}Nb_{0.1}O_{3-x}$ samples.*

	$SrCo_{\mathbf{0.7}}Fe_{\mathbf{0.2}}Nb_{\mathbf{0.1}}O_{\mathbf{3-x}}$					
	$x \sim 0.5$		$x \sim 0.3$		$x \sim 0.1$	
Bond type	*R*, Å	*N*	*R*, Å	*N*	*R*, Å	*N*
Co-O	1.82	1.7	1.85	2.3	1.93	3.2
Co-Sr	3.19	0.6	3.22	0.7	3.33	1.3
Co-Co, Fe	3.89	1.4	3.89	2.7	3.94	4.9

Table IV. *EXAFS data (R – distances (Å); N – effective coordination numbers) describing Fe local surrounding for $SrCo_{0.7}Fe_{0.2}Nb_{0.1}O_{3-x}$ samples.*

	$SrCo_{0.7}Fe_{0.2}Nb_{0.1}O_{3-x}$					
	x ~ 0.5		x ~ 0.3		x ~ 0.1	
Bond type	*R*, Å	*N*	*R*, Å	*N*	*R*, Å	*N*
Fe-O	1.93	3.5	1.94	3.8	1.93	5.1
Fe-Sr	3.28	0.9	3.34	1.7	3.32	2.3
Fe-Co, Fe	3.93	2.8	3.94	5.0	3.93	7.0

numbers and distances Me-O and Me-Me in three coordination spheres (Tables I–IV). This way was chosen to analyze coordination numbers, because both doping and a change in the oxygen stoichiometry result in changes in average coordination numbers and distortion degrees of the coordination polyhedron. All nearby Me-O distances merge into one peak due to insufficient spatial resolution of the method. In this case, effective coordination number becomes the only available value providing the information on a true change in the coordination number due to oxygen vacancies and differences between interatomic Me-O distances.

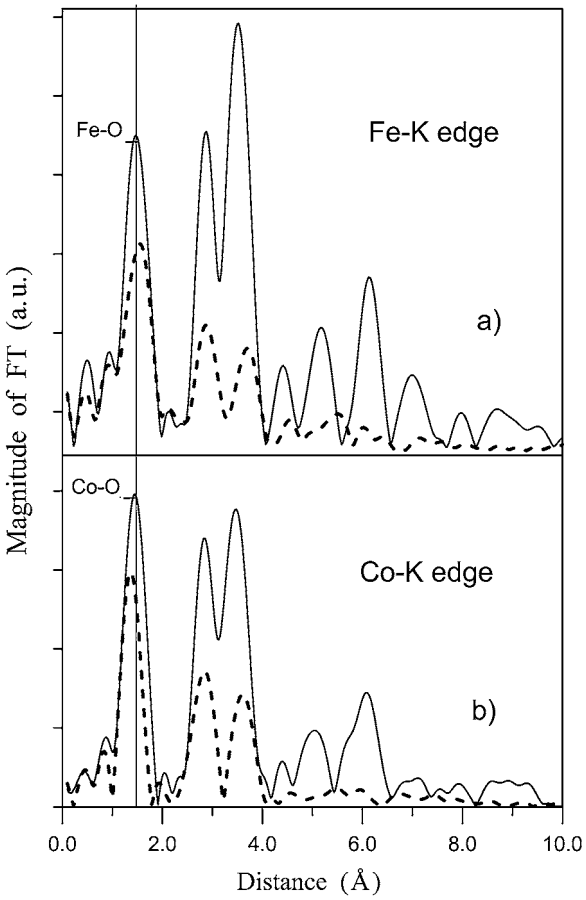

Fig. 1. Radial distribution function (RDF) curves describing a) Fe and b) Co local surrounding of reference samples: (solid line) – $SrFeO_3$, $SrCoO_3$; (dashed line) – $SrFeO_{2.5}$, $SrCoO_{2.5}$.

3. Results and Discussion

RDF curves, describing Fe and Co local surroundings, of reference samples are shown in Fig. 1. RDF curves, describing Co, Fe, Nb local surroundings of $SrCo_{0.7}Fe_{0.2}Nb_{0.1}O_{3-x}$ samples are presented in Fig. 2–4. EXAFS data (*R* – distances (Å); *N* – effective coordination numbers) for $SrCo_{0.7}Fe_{0.2}Nb_{0.1}O_{3-x}$ and reference samples are shown in Tables I–IV. XRD data, for reference and $SrCo_{0.7}Fe_{0.2}Nb_{0.1}O_{3-x}$ samples, are presented in Table V.

Structural data on cubic perovsikte AB_3 ($A = Sr$, $B = Co$, Fe, Nb) suggest that 6 oxygen atoms are observed in the cation first coordination sphere in position B. The second and third coordination spheres contain 8 strontium atoms and 6 metal atoms, respectively. The latter sphere can involve all metals, excepting strontium. A particular composition of the third coordination sphere depends on distribution of three metal cations through the compound bulk.

Reference samples: Diffraction data on samples $SrMeO_{3-x}$ ($Me = Co$, Fe; $x = 0.5, 0.0$) (Table V) comply with the literature evidence [7–10]. The oxides whose composition approximates the ideal perovskite $SrMeO_3$ have a cubic structure, but their effective coordination numbers (Fig. 1, Table I) for first spheres (Me-O) are low for both iron and cobalt containing perovskites. This indicates that random microdistortions exist in the structure as the long-range ordering (manifesting itself in diffraction) preserves. Note that the distortion degrees are close in both compounds.

Samples $SrMeO_{2.5}$ are crystallized in the brownmillerite type. It is of interest that for the cobalt sample, the unit cell parameter

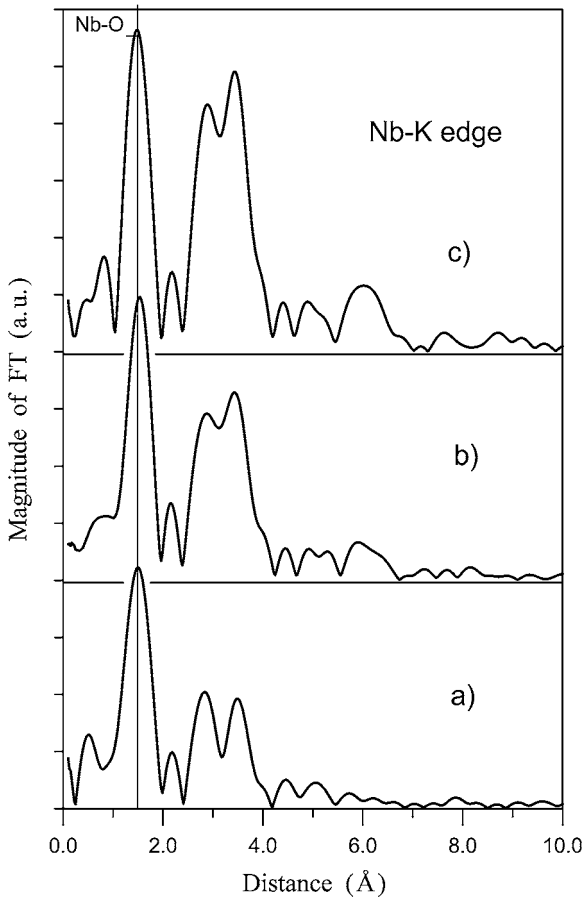

Fig. 2. Radial distribution function (RDF) curves describing Nb local surrounding of $SrCo_{0.7}Fe_{0.2}Nb_{0.1}O_{3-x}$ samples: a) $x \sim 0.5$; b) $x \sim 0.3$; c) $x \sim 0.1$.

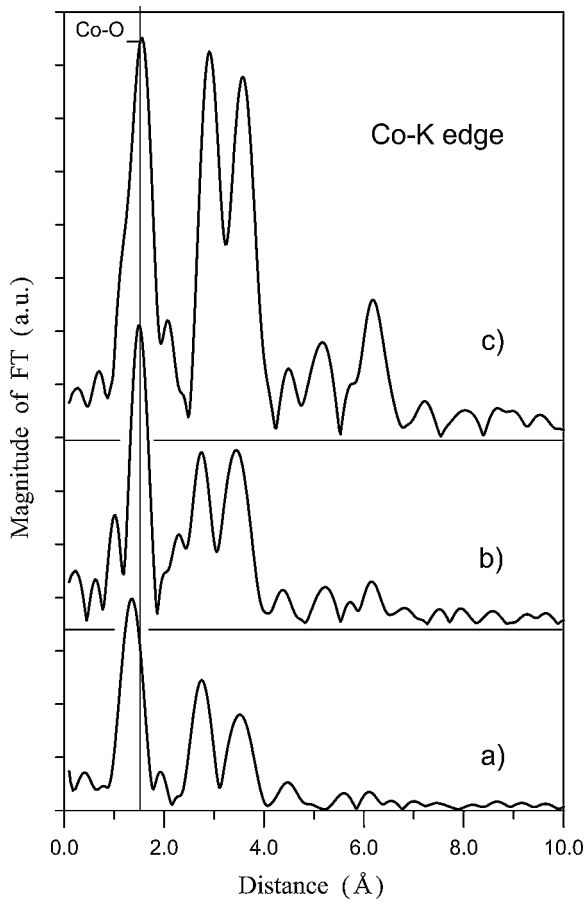

Fig. 3. Radial distribution function (RDF) curves describing Co local surrounding of $SrCo_{0.7}Fe_{0.2}Nb_{0.1}O_{3-x}$ samples: a) $x \sim 0.5$; b) $x \sim 0.3$; c) $x \sim 0.1$.

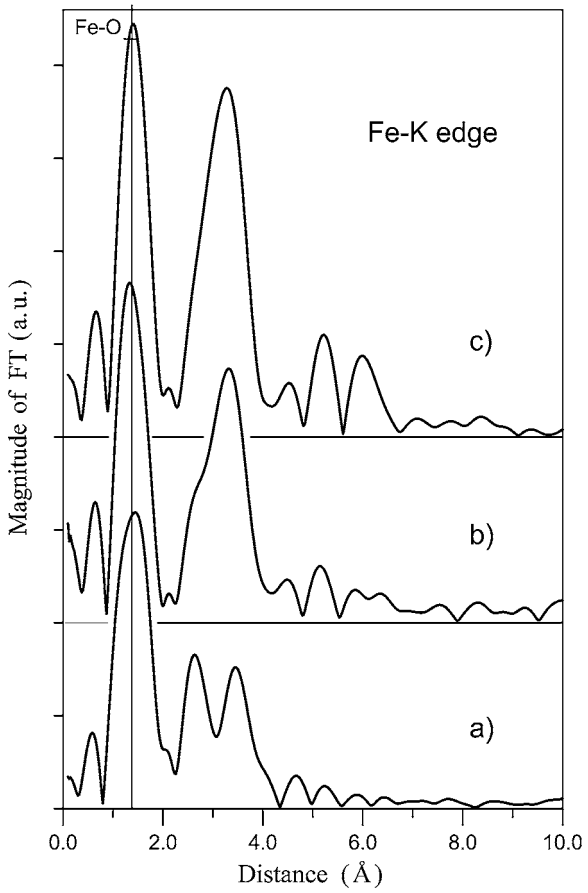

Fig. 4. Radial distribution function (RDF) curves describing Fe local surrounding of $SrCo_{0.7}Fe_{0.2}Nb_{0.1}O_{3-x}$ samples: a) $x \sim 0.5$; b) $x \sim 0.3$; c) $x \sim 0.1$.

along axis *a* significantly differs from that of the iron oxide. In EXAFS data (Fig. 1, Table I), this difference manifests itself as a decrease in the average interatomic distance Co-O by ∼0.1 Å. Whereas for the iron oxide, a transition to a brownmillerite structure does not affect average interactomic distances. For the cobalt sample, a great decrease in the effective coordination number of Co-O exceeds the probable decay value associated with a stoichiometry distortion and indicates large distortions in the cobalt environment with decreasing oxygen amount as compared to iron. Analysis of the changes in the interatomic distances and coordination numbers observed for the third coordination sphere permit one to arrive at the same conclusion. Therefore, though the iron and cobalt containing brownmillerite structures are similar in appearance, their local structures differ.

Additionally it should be noted that the sub-lattice of Co and Fe cations exhibits high symmetry. Some distortions are observed only in the oxygen sub-lattice and in the Me-Sr distances.

$SrCo_{0.7}Fe_{0.2}Nb_{0.1}O_{3-x}$ samples: XRD (Table V) suggests that all the synthesized samples (regardless of oxygen concentration) belong to the perovskite type and are crystallized into a cubic syngony. As oxygen concentration decreases, lattice parameters increase.

As noted above, all coordination numbers have relative values, which primarily evidence the degree of distortion of the local surrounding for given chemical element. According to the obtained data (Fig. 2, Table II), the niobium surrounding is highly symmetric and does not depend on the oxide stoichiometry. It is likely that the oxidation degree of niobium in all complexes is +5, the ion radius being small.

Table V. *XRD data for references and $SrCo_{0.7}Fe_{0.2}Nb_{0.1}O_{3-x}$ samples.*

	Reference samples								$SrCo_{0.7}Fe_{0.2}Nb_{0.1}O_{3-x}$		
	$SrCoO_{2.5}$		$SrFeO_{2.5}$		$SrCoO_3$		$SrFeO_3$		$x \sim 0.5$	$x \sim 0.3$	$x \sim 0.1$
	Brownmillerite (orth.)				Perovskite (cub.)				Perovskite (cub.)		
	Exper.	Lit. [7]	Exper.	Lit. [8]	Exper.	Lit. [9]	Exper.	Lit. [10]	Exper.		
a	5.477	5.456	5.664	5.671	3.824	3.840	3.855	3.855	3.926	3.886	3.856
b	15.746	15.664	15.553	15.590							
c	5.575	5.556	5.528	5.528							

The local surrounding of iron and cobalt radically differs (Fig. 3, 4; Tables III, IV). Thus, an increase in the oxygen concentration results in the increase in the iron coordination number only. For cobalt, changes in the effective coordination number are more complex. Since a change in the average coordination number is accompanied by an increase in the average interatomic distance Co-O. Within the limits of experimental error, distances Co-Co, Fe are constant. But the lattice parameter grows with oxygen removal. On studying the local distortions in cubic $KNbO_3$ [11–13], this observation was interpreted as a partial irregular shift of cations from their crystallographic positions and a turn of octahedrons being relative to each other, which is associated with a symmetry breakdown due to removal of some oxygen. Based on the above, one can assume that similar distortions are primarily associated with cobalt surrounding. Analysis of the EXAFS data suggest that local distortions accumulate with decreasing oxygen concentration on retention of macrosymmetry (long-range ordering). Thus, the introduced cations are not equivalent and the larger part of distortions is associated with cobalt. Indeed (Tables II–IV) a decrease in the oxygen concentration in the structure $SrCo_{0.7}Fe_{0.2}Nb_{0.1}O_{3-x}$ perovskites most strongly affects cobalt.

It is likely that iron and niobium are in the non-distorted octahedral at $(3 - x) = 2.5 - 3.0$, whereas cobalt can also occupy strongly distorted octahedral positions if oxygen is in deficiency. The cobalt local surrounding becomes more symmetric (more regular octahedral positions) with further decreasing oxygen deficiency.

It should be noted that the average distance Co-O for the modified perovskite in oxygen deficiency corresponds to that in $SrCoO_{2.5}$ having a brownmillerite structure.

On oxygen saturation the structure of all studied samples becomes more ordered, which manifests itself as appearance of new peaks in the region of large distances and a considerable rise in coordination numbers for the existing distances.

4. Conclusions

Using the EXAFS method to study modified perovskite-like $SrCo_{0.7}Fe_{0.2}Nb_{0.1}O_{3-x}$ system, it was shown that oxygen vacancies are mainly located near cobalt cation positions.

Acknowledgments

This research was supported by INTAS (00-00180), NATO (Ref. EST.CLG 979855), RFBR (03-03-32340a), RFBR (03-03-32192a), SB RAS Integ. Project No 42 and RAS Project (new materials) No 4.3.6 grants.

The authors also warmly thank Dr. S.V. Tsybulya and Dr. V.A. Ushakov (Boreskov Institute of Catalysis, Novosibirsk, Russia) for kindly presented XRD data and helpful discussions on the subject of the paper.

References

1. Bouwmeester, H. J. M. and Burggraaf, A. J., "Fundamentals of Inorganic membrane science and Technology" (Edited by A. J. Burggraaf and L. Cot) (Elsevier Science B. V., 1996) ch. 10.
2. Lee, T. H., Yang, Y. L., Jacobson, A. J., Abeles, B. and Zhou, M., Solid State Ionics **100**, 87 (1997).
3. Hendriksen, P. V., Larsen, P. H., Mogensen, M., Poulsen, F. W. and Wiik, K., Catalysis Today **56**, 283 (2000).
4. Nemudry, A. P., Koroleva, O. N., Pavlukhin, Yu. T., Podyacheva, O. Yu. and Ismagilov, Z. R., Izv. Ross. Akad. Nauk (seria Phys.) **67**, 952 (2003) (in Russian).
5. Kochubey, D. I., "EXAFS spectroscopy of catalysts" (Nauka, Novosibirsk 1992) (in Russian).
6. Binsted, N., Campbell, J. V., Gurman, S. J. and Stephenson, P. C., SERC Daresbury Laboratory, EXCURV92 code (1991).
7. Grenier, J. *et al.*, Mater. Res. Bull. **14**, 831 (1979).
8. Gallagher, *et al.*, J. Chem. Phys. **41**, 2429 (1964).
9. Shaplygin, I., Lazarev, V. and Russ, J., Inorg. Chem. (Engl. Transl.) **30**, 1828 (1985).
10. Takeda, Y., *et al.* Solid State Chem. **63**, 237 (1986).
11. Bugaev, L. A., Zhuchkov, K. N., Shuvaeva, V. A. and Rusakova, E. B., Japanese J. Appl. Phys. **38**, 215 (1999).
12. Bugaev, L. A., Shuvaeva, V. A., Zhuchkov, K. N., Rusakova, E. B. and Alekseenko, I. B., J. Synchrotron Rad. **6**, 299 (1999).
13. Bugaev, L. A., Shuvaeva, V. A., Zhuchkov, K. N., Rusakova, E. B. and Vedrinskii, R. V., J. Synchrotron Rad. **8**, 308 (2001).

Available online at www.sciencedirect.com
ScienceDirect
Catalysis Today 117 (2006) 525–535
CATALYSIS TODAY
www.elsevier.com/locate/cattod

High-temperature catalysts with a synergetic effect of Pd and manganese oxides

S.A. Yashnik, Z.R. Ismagilov *, V.V. Kuznetsov, V.V. Ushakov, V.A. Rogov, I.A. Ovsyannikova

Boreskov Institute of Catalysis, Pr. Akad. Lavrentieva 5, Novosibirsk 630090, Russia

Available online 28 August 2006

Abstract

A synergetic effect in the catalytic activity has been found after palladium introduction in Mn–Al–O systems. The magnitude of the synergetic effect depends on the types of the oxidic manganese species: oxide Mn_3O_4, spinel (Mn, Mg)[Mn, Al]$_2O_4$ or hexaaluminate (Mn, Mg)$LaAl_{11}O_{19}$. The synergetic effect of Pd and manganese-containing compounds is observed only if palladium is introduced to the low-temperature precursor of the manganese alumina spinel or manganese hexaaluminate. The synergetic effect is not observed when high-temperature samples with formed spinel or hexaaluminate phases are modified with Pd.

Keywords: Methane combustion; Bicomponent catalyst; Manganese oxides; Hexaaluminate; Manganese–alumina spinel; Palladium oxide; Synergetic effect

1. Introduction

Catalytic combustion of fuels is regarded as an attractive alternative to flame combustion. Catalytic combustion provides high combustion efficiency and low emission of air pollutions such as NO_x, CO, and unburned hydrocarbons [1–3]. At present, house hold appliances [4], catalytic boilers [5,6], gas turbines [2,7–12] and technical processes [4,6,13] have commercial potential for applications of catalytic combustion.

The catalytic materials must be active and stable in a wide temperature range from 500 to 1300 °C in order to ensure effective combustion of hydrocarbon fuel, including low-calorie fuel (or lean mixtures), in stable operation. At high temperatures, the catalysts are required to maintain a high surface area and catalytic activity, and to have high thermal shock resistance. On the other hand, the catalysts must have a low light-off temperature.

The existing catalysts for high-temperature combustion of hydrocarbon fuel may be divided into two categories: (1) catalysts based on noble metals, mostly Pd and Pt; (2) catalysts based on transition metal oxides, mostly, spinels, perovskites and hexaaluminates.

Among the catalysts of the first group, catalysts containing Pd are the most active in oxidation of methane [7] and unsaturated hydrocarbons [14]. Pd catalysts are more stable than Pt catalysts with respect to thermal sintering in the oxidizing environment. The upper temperature limit of their use is about 950–1000 °C [15,16]. However, the use of Pd at temperatures above 800 °C is limited due to PdO conversion to Pd metal at 750–800 °C, which has lower activity in oxidation reactions than PdO [17].

Among the catalysts of the second group, manganese oxides are the most promising material for synthesis of high-temperature catalysts due to high thermal stability of supported Mn oxides [18–20] and significant increase of the catalytic activity in deep oxidation of hydrocarbons, e.g. n-C_4H_{10}, benzene and cumene [18], observed after calcination at 900–1100 °C (called a thermal activation effect [18]). The thermal stability of manganese–alumina catalysts can be increased (up to 1300 °C) by doping with lanthanum, magnesium or cerium oxides [19,21], particularly, using disordered alumina for synthesis of the catalysts [21]. In this case, high-temperature Mn and Al compounds can be formed, e.g. spinels, perovskites and hexaaluminates of various compositions. This provides high thermal stability of manganese–alumina catalysts [19,21]

* Corresponding author. Tel.: +7 383 3306219; fax: +7 383 3397352.
E-mail addresses: zri@catalysis.ru, ZRI@catalysis.nsk.su (Z.R. Ismagilov).

0920-5861/$ – see front matter © 2006 Elsevier B.V. All rights reserved.
doi:10.1016/j.cattod.2006.06.036

and contributes to the overall activity of the catalysts [9,10]. In a number of studies it has been reported that partial substitution of the Al site in the hexaaluminate lattice by a Mn cation results in improvement of the oxidation activity without lowering the heat resistance [9,10,22]. Lanthanum–strontium–manganese and barium–manganese hexaaluminates has been recognized as some of the successful designs in hexaaluminate catalysts [9,10,12,22–25].

Considering of numerous publications on performance of Pd catalysts supported on pure alumina we conclude that potentialities of improving of thermal stability and combustion activity of this system (Pd/Al_2O_3) are mostly limited. During synthesis of high-temperature catalysts it is necessary to take into account that it is important to secure uniform distribution and high dispersity of the supported active component on the support to obtain materials with high reactive surface area at high temperatures. One of the technical solutions of this problem is synthesis of spinels and/or hexaaluminates having crystal lattices with strict positions of cations, e.g. Mn^{n+} ions. Manganese hexaaluminate having high thermal stability and sufficient specific surface area [9,10,23] can be used to support Pd and simultaneously contribute to the reactivity of the whole catalytic system. In addition, a synergetic effect is observed in hydrocarbon oxidation reactions, methane oxidation in particular [7,26–32], for most low-temperature catalytic systems containing a noble metal and a transition metal oxide [14,26–29]. This effect may be important for development of catalysts for high-temperature fuel combustion processes as well.

In this work we have studied the main physicochemical and catalytic properties of high-temperature catalysts containing Pd and/or manganese oxides in methane oxidation as a function of the type of the manganese-containing compound (MnO_x, $MnAl_2O_4$, $MnLaAl_{11}O_{19}$), palladium concentration (0.2–2 wt.%) and palladium deposition sequence. X-ray diffraction (XRD), X-ray microanalysis, and TPR have been used for characterization of the catalysts and understanding of the synergetic effect of Pd and manganese hexaaluminate.

2. Experimental

2.1. Alumina materials

Granulated alumina was prepared by hydrocarbon-ammonia moulding from pseudoboehmite aluminum, drying and calcination at 550 °C [33].

Granulated alumina modified by magnesium oxide (2.8 wt.%) was also used for hexaaluminate preparation. The modifying additive was introduced by immersion of ''raw'' granule of pseudoboehmite aluminum into magnesium nitrate solution followed by drying and calcination at 550 °C [33].

For both types of granulated aluminas, XRD phase composition was 85–90% of γ-Al_2O_3 and 10–15% of χ-Al_2O_3, the specific surface area was close to 170 m^2/g, and the total pore volume, 0.5 cm^3/g.

2.2. Catalyst preparation

2.2.1. Pd catalyst supported on ($\gamma + \chi$)-Al_2O_3

The Pd catalysts were prepared by wet impregnation of granulated ($\gamma + \chi$)-Al_2O_3 by chloropalladic acid solution, drying at 110 °C and annealing in air at 600, 900 and 1200 °C for 4 h. The Pd loading ranged from 0.25 to 2 wt.%. The specific surface areas of the samples calcined at 900 and 1200 °C were 90 and 12 m^2/g, respectively.

2.2.2. Manganese oxides catalysts supported on ($\gamma + \chi$)-Al_2O_3

Two series of supported manganese oxides catalysts were prepared.

The first series were manganese-containing catalysts supported on pure granulated ($\gamma + \chi$)-Al_2O_3. The catalysts were prepared by wet impregnation of granulated ($\gamma + \chi$)-Al_2O_3 with a manganese nitrate solution followed by drying at 110 °C. The catalysts were calcined at 500 and 900 °C or 1200 °C for 4 h. The manganese loading was 5 or 10 wt.% MnO_2. The type of manganese oxide: MnO_2, Mn_2O_3, Mn_3O_4 or $MnAl_2O_4$, was regulated by calcination of the air-dried catalysts at different temperatures. The specific surface areas of the samples calcined at 900 and 1200 °C were in the range of 85–90 and 3.8–5.5 m^2/g, respectively.

The second series were manganese-containing catalysts supported on granulated ($\gamma + \chi$)-Al_2O_3 modified by lanthanum and/or magnesium oxide. These catalysts contained $MnLaAl_{11}O_{19}$ or (Mg, Mn)$LaAl_{11}O_{19}$ hexaaluminates as the main active component.

The hexaaluminate catalysts of composition $MnLaAl_{11}O_{19}$ were prepared by successive wet impregnation of granulated ($\gamma + \chi$)-Al_2O_3 with lanthanum and manganese nitrate solutions followed by drying at 110 °C and calcination at 500 °C. The La_2O_3 loading was 5–18 wt.%, and the MnO_2 loading was 3–10 wt.%. For hexaaluminate formation the samples were calcined at 1200 °C for 4 h. The specific surface area was in the range of 12–14 m^2/g.

The hexaaluminate catalysts of composition (Mg, Mn) $LaAl_{11}O_{19}$ were prepared with using granulated ($\gamma + \chi$)-Al_2O_3 modified by MgO. The lanthanum oxide and manganese (as MnO_2) loadings introduced by wetness impregnation were 18 and 2–2.3 wt.%, respectively. The calcination temperature was 1200 °C. The specific surface area was equal to 14 m^2/g.

2.2.3. Supported PdMn oxide catalysts

Manganese–alumina catalysts prepared by methods described above were used for synthesis of binary PdMn catalysts. Manganese–alumina catalysts and manganese hexaaluminates were doped with palladium by impregnation of the low-temperature catalysts with chloropalladic acid of desired concentration followed by calcination at 600, 900 and 1200 °C. The Pd concentration in the catalysts was 0.25, 0.5, 1 and 2 wt.%.

Catalysts with Pd (0.5 wt.%) introduced after calcination of the manganese–alumina catalyst at 1200 °C were prepared for comparison.

The catalysts are denoted as xPd/yMnO$_2$/zLa$_2$O$_3$/Al$_2$O$_3$-T, where x, y and z are Pd, MnO$_2$ and La$_2$O$_3$ loadings (in wt.%), T is calcination temperature (in °C).

2.3. Physicochemical methods

The contents of Mn, La, Mg oxides and Pd were determined by atomic absorption spectroscopy with inductively coupled plasma (AAS-ICP), employing a BLYRD analyzer.

The XRD analysis of the samples was carried out using a HZG-4C (Freiberger Prazisionmechanik) diffractometer with monochromatic Cu Kα irradiation. The phase compositions were determined using diffraction patterns recorded in the 2θ range 10–70°. The diffraction patterns were identified using the JCPDS database [34].

Temperature-programmed reduction (TPR) experiments were carried out using 10% H_2 in Ar with a flow of 40 ml/min in a laboratory instrument equipped with a thermal conductivity detector. The temperature was raised from 25 to 900 °C with 10 °C/min rate. Before performing the TPR experiments, the samples were first pretreated in oxygen at 500 °C for 30 min and cooled to room temperature, then flushed with Ar flow. The weight of the samples was 100 mg and the particle size was 250–500 μm. Water produced during the TPR experiment was removed using a cold trap. Calibration for the hydrogen consumption was carried out by CuO reduction.

The distribution of Mn and Pd on the catalyst surface was studied using a MAP-3 microanalyzer. The samples were anchored in epoxy resin and polished. The probe diameter was 2 mm, the working voltage was 25 kV. Al Kα, Mn Kα, Pd Kα lines were analyzed.

Specific surface areas (S_{BET}, m^2/g) of the samples were determined using thermal desorption of argon.

2.4. Catalytic activity tests

The catalytic activity in methane oxidation was studied using a flow reactor in the temperature range of 200–700 °C at a space velocity of 1000 and 24,000 h^{-1}. The methane concentration in the feed was 1 vol.% in air. The granulated catalyst in amount of 1 cm^3 was used in the experiments. The catalytic activity was characterized by the temperature at which 50% methane conversion was achieved ($T_{50\%}$).

3. Results and discussion

To determine the synergetic effect of Pd and manganese oxides in deep oxidation of methane, three types of catalysts were prepared, and their catalytic and physicochemical properties were studied:

- Pd catalysts supported on (γ + χ)-Al$_2$O$_3$;
- Manganese–alumina catalysts containing MnO$_x$, MnAl$_2$O$_4$ or MnLaAl$_{11}$O$_{19}$ as the active component;
- Binary catalysts containing Pd and MnO$_x$, MnAl$_2$O$_4$ or MnLaAl$_{11}$O$_{19}$;

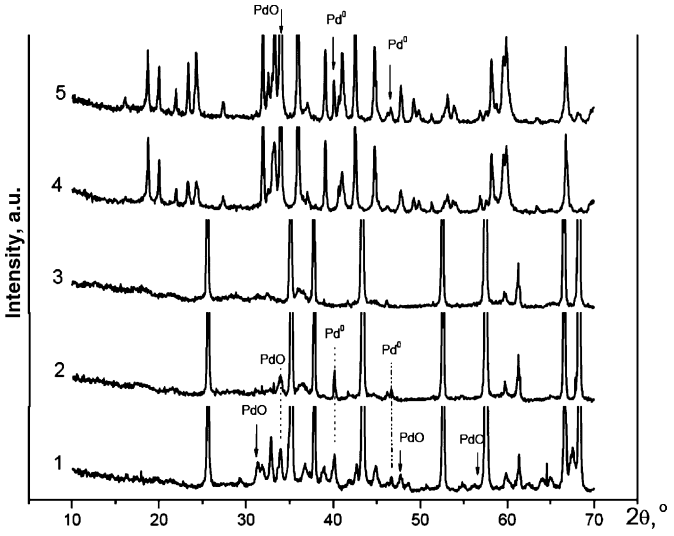

Fig. 1. XRD patterns of catalysts supported on alumina and calcined at 1200 °C for 4 h: 0.8Pd/Al$_2$O$_3$ (1), 0.8Pd/4.8MnO$_2$/Al$_2$O$_3$ (2), 4.8MnO$_2$/Al$_2$O$_3$ (3), 4.9MnO$_2$/2.8MgO–18La2O3/Al$_2$O$_3$ (4), and 1.5Pd/4.9MnO$_2$/2.8MgO–18La$_2$O$_3$/Al$_2$O$_3$ (5). Unmarked XRD peaks are α-Al$_2$O$_3$ on 1–3 curves and hexaaluminate on 4, 5 curves.

- Below we shall discuss the physicochemical and catalytic properties of these types of catalysts individually.

3.1. Catalytic properties of Pd catalysts supported on (γ + χ)-Al$_2$O$_3$

According to the XRD data, a well-crystallized PdO phase with large particle size (>30 nm) and Pd metal are present in the catalysts with Pd loading above 0.5 wt.% after calcination at 1200 °C (Fig. 1, curve 1). A wide hydrogen H_2-consumption peak at 80–200 °C corresponding to reduction of PdO particles is observed in the TPR spectrum of 0.8Pd/γ-Al$_2$O$_3$ catalyst calcined at 600 °C (Fig. 2, curve 1). The PdO particles are, most

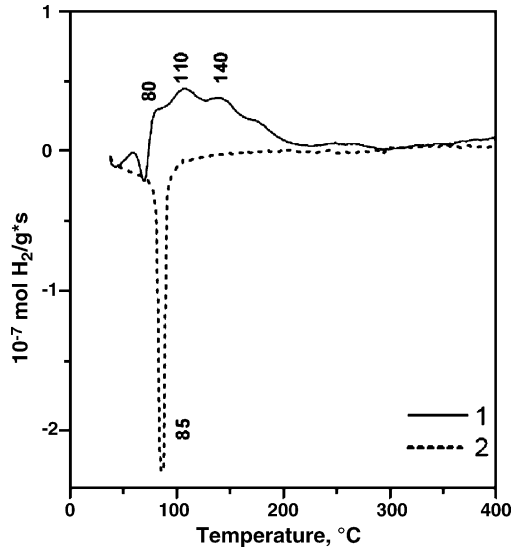

Fig. 2. TPR spectra of 0.8 Pd/Al$_2$O$_3$ catalyst calcined at 600 °C (1) and 1200 °C (2).

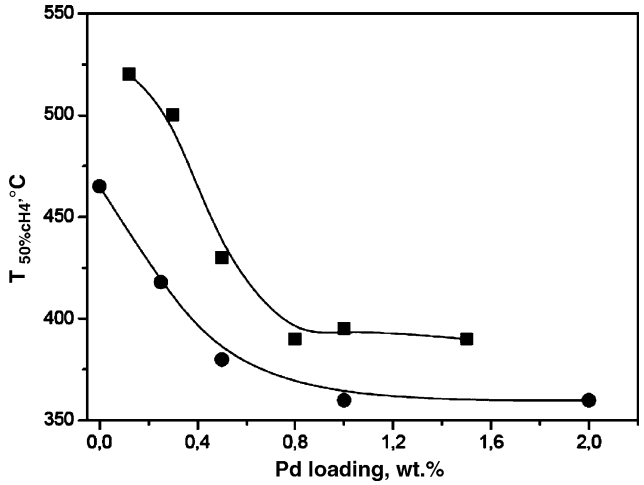

Fig. 3. Temperature of 50% methane conversion ($T_{50\%\,CH_4}$) on Pd catalysts supported on alumina (■) or $3MnO_2/2.8MgO–18La_2O_3/Al_2O_3$ (●) vs. Pd loading. The catalysts were calcined at 1200 °C for 4 h. Test conditions: 1 vol.% CH_4 in air, 1000 h^{-1}.

likely, observed in the TPR spectra of this catalyst calcined at 1200 °C as a week wide H_2-consumption peak in the temperature range of 200–300 °C (Fig. 2, curve 2). Also a hydrogen desorption peak at 78–86 °C is observed in the TPR spectra (Fig. 2, curve 2). Comparison of the TPR spectra of the catalysts calcined at 600 and 1200 °C suggests that the observed hydrogen desorption peak is due to the presence of Pd metal particles. This assumption is in good agreement with the results reported by Farrauto et.al. [17] and Lyubovsky co-workers [35] who observed irreversible PdO conversion to Pd during calcination of supported Pd/Al_2O_3 catalysts in air at 800–900 °C. PdO conversion to Pd is usually considered to be the cause of the methane oxidation activity decrease with the temperature increase [17]. However, it has been shown that the catalytic activity in methane oxidation grows after PdO conversion to Pd metal, especially at elevated temperatures [35].

The experimental data on the catalytic activity of Pd catalysts supported on γ-Al_2O_3 after high-temperature annealing at 1200 °C for 4 h are shown in Fig. 3 for different Pd concentrations (0.12–1.5 wt.%). One can see that the catalytic activity in methane oxidation grows when the Pd concentration increases from 0.12 to 0.8 wt.%. Meanwhile, the temperature of 50% methane conversion ($T_{50\%\,CH_4}$) decreases from 520 to 390 °C (Fig. 3). Note that the increase of the calcination temperature of $0.8Pd/\gamma$-Al_2O_3 catalyst from 600 to 1200 °C results in the increase of its catalytic activity in methane oxidation that is observed as an decrease of 50% methane conversion temperature from 430 to 390 °C.

3.2. Physicochemical and catalytic properties of manganese–alumina catalysts

Two series of manganese–alumina catalysts containing MnO_x, $MnAl_2O_4$, $MnLaAl_{11}O_{19}$ as the active component and their catalytic performance in methane oxidation will be discussed. The desired crystalline phase of manganese-containing compounds was obtained by varying the manganese concentration (3–10 wt.%), concentration of the modifying agents (MgO and La_2O_3) added to the alumina supports (5–21 wt.%) and the final calcination temperature.

3.2.1. Influence of the calcination temperature

Table 1 presents the phase compositions of two manganese–alumina catalysts supported on alumina as a function of the annealing temperature (the first series). The active component of the catalyst with 5 wt.% MnO_2 after calcination at 500 °C consists of highly dispersed MnO_2. The increase of the calcination temperature to 900 and 1200 °C results in successive phase transformation of MnO_2 to β-Mn_2O_3 and Mn_3O_4. The phase transformations of manganese oxides are made more complicated by the interaction of MnO_2 and β-Mn_2O_3 with alumina to form a solid solution of Mn^{3+} cations in γ-Al_2O_3 (a = 7.93–8.17 Å), which decomposes at 1200 °C to

Table 1
XRD composition and catalytic activity of the supported manganese–alumina catalysts calcined at different temperature

No.	Catalyst	Manganese loading, wt.% as MnO_2	Calcination temperature (°C)	XRD composition	S_{BET} (m^2/g)	Temperature of X% CH_4 conversion[a] (°C)	
						$T_{50\%\,CH_4}$	$T_{50\%\,CH_4}$
1	$5MnO_2/Al_2O_3$	5.4	500	γ*-Al_2O_3 (a ~ 7.910 Å); MnO_2 (D ~ 80 Å)	130	485	570
			900	α-Al_2O_3 + δ*-Al_2O_3; γ*-Al_2O_3 (a ~ 7.93–7.94 Å); β-Mn_3O_4	82	400	465
			1200	α-Al_2O_3; (Mn, Al)$[Al]_2O_4$ (a ~ 8.097 Å); (Mn, Al)$[Mn]_2O_4$ (a ~ 8.285 Å)	3.8	530	660
2	$10MnO_2/Al_2O_3$	9.45	500	γ*-Al_2O_3 (a ~ 7.910–8.115 Å); MnO_2 (D ~ 200 Å); β-Mn_2O_3 (D ~ 300 Å)	115	445	535
			900	α-Al_2O_3 + θ-Al_2O_3; γ*-Al_2O_3 (a ~ 7.93–8.17 Å); β-Mn_3O_4	75	420	525
			1200	α-Al_2O_3; (Mn, Al)$[Al]_2O_4$ (a ~ 8.078 Å); (Mn, Al)$[Mn]_2O_4$ (a ~ 8.27 Å)	3.0	575	700

γ*-Al_2O_3 and δ*-Al_2O_3 are solid solution of Mn^{3+} in structure of γ-Al_2O_3 and δ-Al_2O_3, respectively (Mn, Al)$[Mn]_2O_4$ are Mn_3O_4 spinel doped Al^{3+} cations or solid solution of Al^{3+} in structure of Mn_3O_4 spinel.

[a] Measured at 1000 h^{-1}, 1 vol.% CH_4 in air.

α-Al_2O_3 (Fig. 1, curve 3) and manganese-aluminum spinel (Mn, Al)$[Al]_2O_4$ (normal spinel, $a = 8.078$ Å). Note that Mn_3O_4 spinel, most likely, is doped with Al^{3+} cations (solid solution of Al^{3+} cations in spinel structure of Mn_3O_4) (Mn, Al)$[Mn]_2O_4$ as indicated by the lattice parameters ($a = 8.285$ Å). It is in a good agreement with [36]. The authors of [36] have observed a phase transformation of MnO_x/Al_2O_3 system starts at 950 °C with the formation of a metastable non-stoichiometric manganese–alumina cubic spinel and none-quilibrium solid solution of Mn^{3+} ions in the structure of γ-Al_2O_3, which decomposes to α-Al_2O_3 modified by Mn^{3+} ions and nanocrystalline β-Mn_3O_4 particles doped with Al^{3+} ions.

The increase of the manganese concentration in the catalyst to 10 wt.% leads to the formation of large quantities of well-crystallized oxide compounds with particle size ~20–30 nm. In addition to crystallized MnO_2 phase, the diffraction pattern contains peaks characteristic of β-Mn_2O_3 and a solid solution based on Al_3O_3 spinel structure with the lattice parameter a ~8.115 Å even after calcination at 500 °C. A calcination temperature increase results in the phase transformation of manganese oxides to Mn_3O_4 and perfection of the solid solution of Mn^{3+} in the Al_2O_3 structure with the formation of (Mn, Al)$[Al]_2O_4$ spinel.

Fig. 4 presents the TPR profiles for 5% MnO_2/Al_2O_3 catalyst annealed at various temperatures from 500 to 1300 °C. The chosen calcination temperature range may be divided into three regions where the catalytic activity is significantly different (Table 1). In the 500–800 °C calcination temperature range the catalysts shows the methane oxidation activity typical for oxide catalysts. The TPR spectra of the sample calcined at 500 °C (Fig. 4, curve 1) is characterized by three H_2-consumption peaks at 330, 400 and 445 °C, and H_2/Mn molar ratio equal to 0.85. The increase of the calcination temperature to 600–800 °C is accompanied by the disappearance of the peak at 330 °C, a slight shift of the peaks at higher temperatures to 445–485 °C (Fig. 4, curve 2) and a decrease of the H_2/Mn molar ratio to 0.54–0.58. Comparison of the TPR and XRD data indicates that in the low-temperature catalysts calcined at 500 °C manganese mostly exists as MnO_2. During the TPR experiment it is reduced first to Mn_2O_3 (330 °C), then to Mn_3O_4 (400 °C) and to MnO (445 °C). In the catalysts annealed at 600–800 °C manganese is stabilized as Mn_2O_3 with, most likely, larger particle size than in the catalysts calcined at 500 °C. These TPR profiles of low-temperature supported MnO_x catalysts are similar to those exhibited by bulk manganese oxides [37,38] and MnO_x crystallites on the alumina surface [14,38,39].

As shown previous publications [18,19,21,36], the increase of the calcination temperature of manganese–alumina catalysts from 500 to 900 °C results in an increase of their activity in methane [19,21], n-C_4H_{10} [18] and CO [36] oxidation. For instance, $T_{50\%\,CH_4}$ was about 400 and 485 °C, respectively, for 5% Mn/Al_2O_3 samples calcined at 900 and 500 °C [19]. According to the XRD data (Table 1) the active component of the former catalyst consists of Mn_3O_4 doped by Al^{3+} and solid solution of Mn^{3+} ions in the structure of γ-Al_2O_3, about 70–80% of all manganese atoms being in the Mn_3O_4 spinel. The sample calcined at 900 °C is characterized by a wide H_2-consumption peak in the low-temperature region of the TPR spectrum (150–500 °C, Fig. 4, curve 3), which splits into three peaks at 170, 265 and 410 °C when the calcination temperature is increased to 1000–1100 °C (Fig. 4, curve 4).

Further increase of the calcination temperature to 1200 and 1300 °C leads to a decrease of the catalytic activity (Table 1) and shift of the TPR peaks to higher temperatures (Fig. 4, curves 5 and 6), which indicates that the formed manganese-containing compounds are more difficult to reduce. The H_2/Mn molar ratio in the TPR spectra of the catalysts annealed at 1000–1300 °C was 0.45–0.42. Comparison of the TPR and XRD data shows that easily (170–270 °C) and difficultly (310–480 °C) reducible compounds correspond to Mn_3O_4

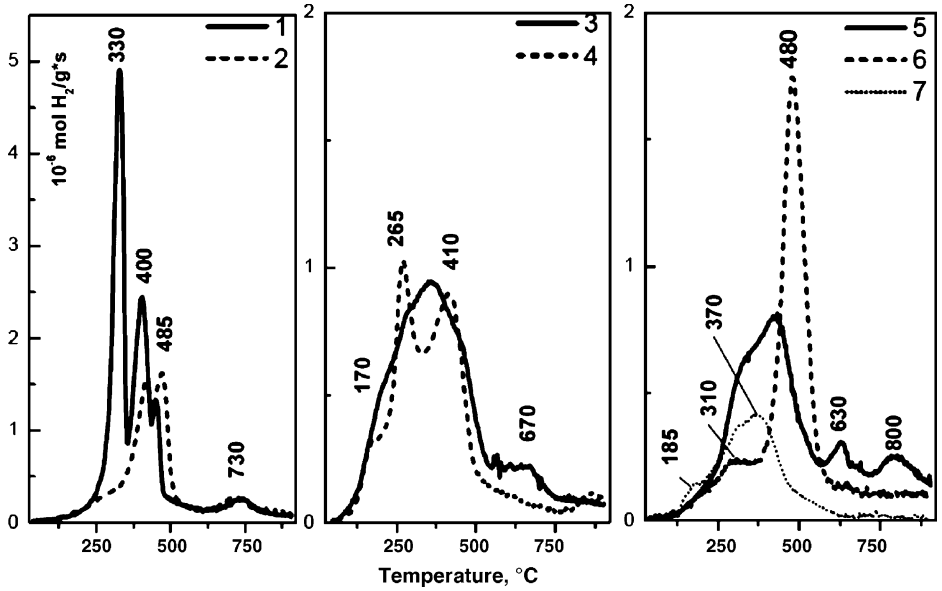

Fig. 4. TPR spectra of $5MnO_2/Al_2O_3$ catalyst calcined at 500 °C (1), 800 °C (2), 900 °C (3), 1100 °C (4), 1200 °C (5), and 1300 °C (6). TPR spectrum of catalysts with the structure of hexaaluminates (Mn, Mg)$LaAl_{11}O_{19}$ (7).

spinel doped with Al^{3+} cations and (Mn, Al)$[Al]_2O_4$ spinel doped with Mn^{3+} cations, respectively. Taking into account the data reported in [36], the TPR peak in the temperature range around 480 °C or higher might be also due to reduction of Mn^{3+} cations in α-Al_2O_3 structure. The analysis of the physico-chemical and catalytic properties of the samples annealed at 900–1100 and 1200–1300 °C leads to a conclusion that Mn_3O_4 spinel has higher catalytic activity. This conclusion agrees well with the results reported by Tsyrulnikov et al. [36]. It was shown in [36] that the formation of nanocrystalline particles of β-Mn_3O_4 phase doped with Al^{3+} ions during calcination of the MnO_x/Al_2O_3 system at 950 °C leads to a sharp increase of the activity in deep hydrocarbon oxidation reactions.

3.2.2. *Influence of the modifying agents*

Table 2 summarizes the crystalline phases identified by XRD for Mn catalysts supported on alumina modified by La and Mg oxide (the second series). α-Al_2O_3, hexaaluminate and spinel (Mg, Mn)Al_2O_4 are the main crystalline phase observed in the samples calcined at 1200 °C. Perovskite-type oxides, such as $LaMnO_3$ or $LaAlO_3$, were not detected. The data reported in Table 2 show that it is possible to change the ratio of the spinels and hexaaluminate formed in the catalyst after calcination at 1200 °C by varying the atomic (Mn + Mg)/La ratio. Manganese oxide introduced in the amount exceeding the stoichiometric (Mn + Mg)/La ratio is stabilized after the high-temperature annealing as (Mg, Mn)$[Al]_2O_4$ spinel. Its lattice parameter grows with the manganese concentration (Table 2).

When the sample with the La loading around 18–21 wt.% La_2O_3 and atomic ratio (Mn + Mg)/La equal to 1 was calcined at 1200 °C, the hexaaluminate phase was only one observed by XRD. These samples were characterized by a number of intensive XRD diffraction peaks at $2\theta = 32.0°$, 33.9°, 36°, 39.2°, 42.7°, 44.9°, 60.0°, and 67° (Fig. 1, curve 4). Hexaaluminates based on $LaAl_{11}O_{18}$, $MnLaAl_{11}O_{19}$ and $MgLaAl_{11}O_{19}$ are characterized in the JCPDS database by a practically the same set of diffraction peaks with similar intensities. Thus, the analysis of the XRD spectra indicates that high-temperature catalysts doped with magnesium appear to contain a hexaaluminates with different composition. As for manganese oxide, Mn_2O_3 is known to be transformed into Mn_3O_4 above ca. 1000 °C. The diffraction peak characteristic of Mn_3O_4 is at $2\theta = 36.1°$, 32.3° and 28.9°, numbers in parentheses are relative intensities. Although two intense peaks at 36.1° and 32.3° were superimposed on the peaks attributable to the hexaaluminate phase, the complete disappearance of the diffraction peak at 28.9° might mean that at these temperatures manganese oxide no longer exists in the form of Mn_3O_4. The lack of diffraction peaks typical for the spinel-type oxide ($2\theta = 30.8°$ and 64.2°), indicates that $MnAl_2O_4$ is not formed in this sample. Taking into account the fact that the crystallinity degree of hexaaluminate itself was poor, this suggests that supported manganese oxide reacts with alumina during calcination at high temperatures to form manganese-containing hexaaluminate at 1200 °C and above. Stabilization of rare earth elements, e.g. La^{3+} and/or Mg^{2+} cations, in a mixed solid solution based on the γ-Al_2O_3 structure in tetrahedral and octahedral positions, correspondingly, is known to limit substantially the diffusion of Al^{3+} ions leading to the formation of α-Al_2O_3 and result in the formation of hexaaluminates $MgLaAl_{11}O_{19}$ [40] and $La_2O_3{\cdot}11Al_2O_3$ [41] after calcination at high temperatures. A similar result was reported by Zhang et al. [42] who also observed the formation of La–β-Al_2O_3 phase doped at Mn^{2+} cation when the low-temperature sample with $La_2O_3{\cdot}19Al_2O_3$ composition was impregnated with manganese nitrate solution and calcined at 1000–1200 °C.

Table 2
XRD composition and catalytic activity of the supported manganese-lanthanum-alumina catalysts calcined at 1200 °C

No.	Catalyst	Chemical composition			XRD composition	S_{BET} (m^2/g)	Temperature of *X*% CH_4 conversion[a] (°C)	
		La_2O_3 (wt.%)	MnO_2 (wt.%)	(Mn + Mg)/La (at.%)			$T_{50\%\,CH_4}$	$T_{50\%\,CH_4}$
1	$3MnO_2/5La_2O_3/MgO–Al_2O_3$	5	3	3.5	α-Al_2O_3; (Mg, Mn)$[Al]_2O_4$, $a \sim 8.128$ Å; HAM[b], $d/n_{220} \sim 1.4004$ Å	9	470	560
2	$5MnO_2/5La_2O_3/MgO–Al_2O_3$	5	5	4.2	α-Al_2O_3; (Mg, Mn)$[Al]_2O_4$, $a \sim 8.128$ Å; HAM, $d/n_{220} \sim 1.4004$ Å	6	490	570
3	$7MnO_2/5La_2O_3/MgO–Al_2O_3$	5	7	5	α-Al_2O_3; (Mg, Mn)$[Al]_2O_4$, $a \sim 8{,}134$ Å; HAM, $d/n_{220} \sim 1.4004$ Å	14	520	600
4	$10MnO_2/5La_2O_3/MgO–Al_2O_3$	5	10	6.2	α-Al_2O_3; (Mg, Mn)$[Al]_2O_4$, $a \sim 8{,}166$ Å; HAM, $d/n_{220} \sim 1.4004$ Å	6	545	625
5	$5MnO_2/12La_2O_3/MgO–Al_2O_3$	12	5	1.7	α-Al_2O_3 (trace); (Mg, Mn)$[Al]_2O_4$, $a \sim 8.120$ Å; HAM, $d/n_{220} \sim 1.4004$ Å	9	480	570
6	$10MnO_2/12La_2O_3/MgO–Al_2O_3$	12	10	2.5	α-Al_2O_3 (trace); (Mn, Mg)$[Al]_2O_4$, $a \sim 8.171$ Å; (Mn, Al)[Mn, Al]$_2O_4$, $a \sim 8.276$ Å HAM, $d/n \sim 1.4011$ Å	7	520	600
7	$3.5MnO_2/18La_2O_3/MgO–Al_2O_3$	18	3.5	1.0	HAM, $d/n_{220} \sim 1.3993$ Å	14	460	560
8[c]	$3.5MnO_2/18La_2O_3/Al_2O_3$	18.9	10	1.0	HAM, $d/n_{220} \sim 1.4022$ Å	17	450	550

The granulated alumina modified by MgO (2.8 wt.%) were used for high-temperature catalyst preparation.
[a] Measured at 1000 h^{-1}, 1 vol.% CH_4 in air.
[b] HAM, $d/n_{220} \sim 1.4004$ Å is manganese hexaaluminate (Mg, Mn)$Al_{11}LaO_{19}$.
[c] Prepared on granulated alumina (without MgO addition).

The high-temperature samples (1200 °C) where manganese mostly exists as manganese hexaaluminate are characterized by a wide H_2-consumption peak with a maximum at 370 °C and H_2/Mn ratio in the range of 0.2–0.3 (Fig. 4, curve 7). It well known that Mn^{2+} cations in MnO are not reduced by hydrogen to metal until temperatures as high as 1700 °C [43]. Hence, it reasonable to assume that the H_2-consumption peak at 370 °C is due to Mn^{3+} cations doping the hexaaluminate structure.

Comparison of the catalytic activity of Mn–Al–O catalysts containing different high-temperature manganese compounds: (Mn, Mg)$[Al]_2O_4$ spinel and (Mn, Mg)$LaAl_{11}O_{19}$ hexaaluminate suggests that the formation of manganese hexaaluminate makes it possible to improve both the catalytic activity in methane oxidation and the thermal stability of the catalyst. For example, $T_{50\%\,CH_4}$ was equal to 530 °C (Table 1, no. 1) and 460 °C (Table 2, no. 7) for high-temperature (1200 °C) catalysts containing manganese as (Mn, Al)$[Al]_2O_4$ spinel and hexaaluminate, respectively. It should be noted that the catalytic activity of the samples based on $MnLaAl_{11}O_{19}$ (Table 2, no. 8) and (Mn, Mg)$LaAl_{11}O_{19}$ (Table 2, no. 7) hexaaluminates were identical at the same total concentration of the hexaaluminate phase in the catalyst, with $T_{50\%\,CH_4} = 450 - 460$ °C.

Thus, according to the XRD data (Table 2), it has been shown that is possible to stabilize different oxidic manganese species by varying the synthesis conditions of manganese–alumina catalysts: manganese oxide loading, modification of the alumina with La_2O_3 or/and MgO and calcination temperature. The nature of the manganese compounds MnO_2, Mn_2O_3, Mn_3O_4, (Mn, Mg)Al_2O_4 or (Mn, Mg)$Al_{11}O_{19}$ determines the catalytic activity of the manganese–alumina catalysts and the temperature range of their use. As it will be shown below, the type of the manganese compound has a significant effect on the appearance of a synergetic effect in the catalytic activity of Pd-containing manganese–alumina catalysts.

3.3. Physicochemical and catalytic properties of supported PdMn oxides catalysts

Fig. 1 presents the XRD patterns of high-temperature catalysts containing manganese oxides with Pd. XRD composition are summarized in Table 3. High-temperature annealing of manganese–alumina catalysts doped with Pd can result in the formation of three main oxidic manganese phases. The type of the resulting phase is determined by the manganese loading, composition of the modifying additives and calcination temperature. As in the case of one-component catalysts, Mn_3O_4 spinel doped with Al^{3+} cations (or solid solution of Al^{3+} cations in Mn_3O_4 structure) is formed after calcination at 900 °C (Table 3, no. 1). Crystallized phases of (Mn, Al)$[Al]_2O_4$ spinel (Table 3, no. 2) and manganese hexaaluminate (Table 3, no. 3) are observed after calcination at 1200 °C. The optimum method to obtain manganese hexaaluminate is to add manganese, lanthanum and magnesium oxides in the atomic ratio (Mn + Mg)/La ~1 to the granulated ($\gamma + \chi$)-Al_2O_3 (Fig. 1, curve 5). Thus, the palladium introduction to the low-temperature manganese–alumina catalysts does not affect the formation of high-temperature manganese compounds.

According to the XRD data presented in Fig. 1, curves 2 and 5, palladium exists in high-temperature binary catalysts as PdO particles ($2\theta = 33.9°$) and Pd metal ($2\theta = 40.15°$). The ratio of PdO and Pd phases depends on the calcination temperature of the binary catalyst. At the same palladium concentration in the catalysts, the concentration of palladium metal grows with the calcination temperature increase from 900 to 1200 °C in good agreement with the results reported by Lyubovsky co-workers [35]. At the same palladium concentration in the catalysts, the amounts of PdO and Pd observed by XRD after calcination at 1200 °C are smaller in manganese–alumina samples (Fig. 1, curve 2, 0.8Pd/5MnO_2/Al_2O_3-1200) than in alumina ones (Fig. 1, curve 1, 0.8Pd/Al_2O_3-1200). So, it appears that introduction of manganese cations to alumina improves the PdO stability to reduction to Pd metal. The suppression of PdO dissociation was first observed for NiO addition to Al_2O_3 support [44]. It was found that PdO supported on Al_2O_3 and mixed Al_2O_3–36NiO oxides was completely reduced to Pd metal at 800 and 860 °C, respectively [44].

For convenience during discussion of the results of TPR and catalytic experiments let us divide high-temperature binary Pd–Mn catalysts into three groups: spinel-type oxide Mn_3O_4,

Table 3
XRD composition and catalytic activity of the binary Pd–Mn catalysts calcined at 1200 °C

No.	Catalyst	Chemical composition (wt.%)			T_{calc}[a] (°C)	S_{BET} (m^2/g)	XRD composition	Temperature of X% CH_4 conversion[b] (°C)	
		La_2O_3	MnO_2	Pd				$T_{50\%\,CH_4}$	$T_{50\%\,CH_4}$
1	0.5Pd/5MnO_2/Al_2O_3	–	2.74	0.57	900	85	α-Al_2O_3 + δ*-Al_2O_3; γ*-Al_2O_3; β-Mn_3O_4	340	450
2	0.5Pd/5MnO_2/Al_2O_3	–	2.74	0.57	1200	5.4	α-Al_2O_3; (Mn, Al)$[Al]_2O_4$, $a \sim 8.060$ Å; PdO (>300 Å) and Pd	415	515
3	0.5Pd–$MnLaAl_{11}O_{19}$	La_2O_3, 18.9; MgO, 2.8	1.98	0.58	1200	14	$MnLaAl_{11}O_{19}$ ($d/n_{220} = 1.3993$ Å); PdO (>300 Å) and Pd	360	420
4	0.5Pd/$MnLaAl_{11}O_{19}$	La_2O_3, 18.9; MgO, 2.8	1.98	0.53	500	12	$MnLaAl_{11}O_{19}$ ($d/n_{220} = 1.3993$ Å); PdO (>500 Å)	400	480
5	Pd/(Mn, Al)$[Al]_2O_4$	MgO, 2.8	3.28	0.5	500	2.4	α-Al_2O_3; (Mn, Al)$[Al]_2O_4$, $a \sim 8.125$ Å; PdO (>500 Å)	480	590

[a] Final calcination temperature of binary Pd–Mn catalysts.
[b] Measured at 1000 h^{-1}, 1 vol.% CH_4 in air.

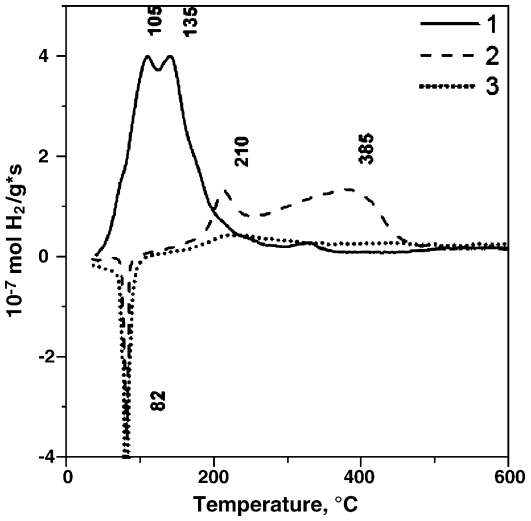

Fig. 5. TPR spectra of binary $0.5Pd/5MnO_2/Al_2O_3$ catalysts calcined at 500 °C (1) and 1200 °C (2). TPR spectrum of binary $1.5Pd/3MnO_2/2.8MgO–18La_2O_3/Al_2O_3$ catalysts with the structure of hexaaluminates (Mn, Mg)$LaAl_{11}O_{19}$ (3).

spinel-type oxide $MnAl_2O_4$, and hexaaluminate-type oxides $MnLaAl_{11}O_{19}$ and (Mn, Mg)$LaAl_{11}O_{19}$.

TPR profile of the binary Pd–Mn catalyst containing according to XRD spinel-type oxide Mn_3O_4 is presented in Fig. 5, curve 1. The TPR profile of binary Pd–Mn catalyst calcined at 900 °C only shows a H_2-consumption peak at around 105 °C with to reduction of PdO crystallites to Pd metal. The peak at 135 °C is due reduction of Mn^{3+} cation in Mn_3O_4 spinel to MnO. The weak peak at 330 °C should be ascribed to the reduction of large Mn_3O_4 particles to MnO or to the reduction of Mn^{3+} cations stabilized in the solid solution in the alumina structure.

TPR profiles of the binary Pd–Mn catalyst containing according to XRD spinel-type oxide $MnAl_2O_4$ and hexaaluminate-type oxide are presented in Fig. 5, curve 2 and curve 3, respectively. Independent of the type of the high-temperature manganese-containing compound, all binary Pd–Mn catalysts calcined at 1200 °C were characterized by H_2-desorption peak at 82 °C, related to Pd metal particles. Clear peaks at 170–265 °C observed in the TPR profile of binary Pd–Mn catalyst with spinel-type oxides (Fig. 5, curve 2) and manganese hexaaluminate (Fig. 5, curve 3) as the main active component are due to reduction of Mn^{3+} cation doping the structures of $MnAl_2O_4$ or α-Al_2O_3 and $MnLaAl_{11}O_{19}$. Note that for high-temperature binary Pd–Mn catalyst the H_2/Mn ratio varies in the range of 0.16–0.28, which is 3–10 times lower than for high-temperature Mn catalyst with similar phase composition.

So, the presence of Pd strongly affects the reduction profile of all catalysts containing different manganese oxides. The reduction temperature, the shape and the number of peaks are changed. Binary Pd–Mn catalysts containing spinel-type oxide Mn_3O_4 or manganese hexaaluminate are almost completely reduced at the temperature, at which the reduction of the samples consisting these Mn compounds alone is only starting. The TPR profile of binary Pd–Mn catalysts containing manganese–alumina spinel is also shifted to lower temperature. However, the shift is much smaller. The lower reduction temperature of MnO_x in the presence of Pd has been observed for binary Pd–Mn catalysts supported on Al_2O_3 and calcined at 800 °C [14], but has not been observed for the catalyst calcined at 350 °C [39]. The lower reduction temperature of MnO_x in the mixed samples is usually explained by two reasons [14]. Both require strong interaction between Pd and MnO_x. First, noble metals catalyze the reduction of MnO_x by hydrogen spill-over during the TPR experiment [14]. Second, the mobility of the lattice oxygen in MnO_x is increased [14].

Fig. 6A presents the data on the catalytic activity of high-temperature binary $0.5Pd/5MnO_2/Al_2O_3$ catalyst calcined at 900 °C. According to the XRD data, most of manganese in the manganese–alumina catalyst after calcination at 900 °C exists as spinel-type oxide Mn_3O_4 and a solid solution of Mn^{3+} in $(\gamma + \delta)$-Al_2O_3 and is reduced in hydrogen at 135–170 °C. The palladium introduction (0.5 wt.%) to the low-temperature $5MnO_2/Al_2O_3$ catalyst makes it possible to increase its activity in methane oxidation. At 1000 h^{-1} the temperature of 50% methane conversion was 340 °C, which is lower by 60–70 °C than those of single-component $0.5Pd/Al_2O_3$ and $5MnO_2/Al_2O_3$ (Table 1, no. 1) samples calcined at 900 °C. Note that the largest differences in the activity of binary and single-component catalysts were observed at low temperatures and long contact times.

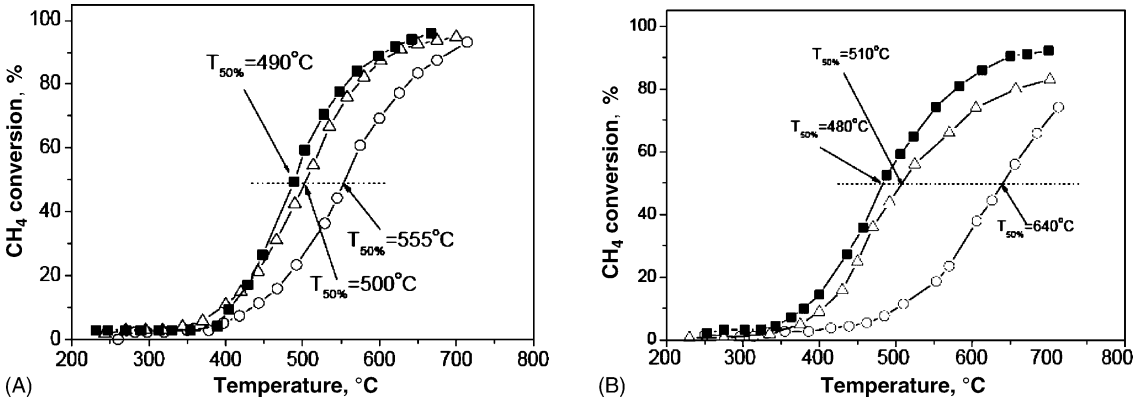

Fig. 6. Methane conversion over $5MnO_2/Al_2O_3$ (○), $0.5Pd/Al_2O_3$ (△) and $0.5Pd/5MnO_2/Al_2O_3$ (■) catalysts calcined at 900 °C (A) and at 1200 °C (B). Test condition: 1 vol.% CH_4 in air, 24,000 h^{-1}.

Fig. 6B shows the data on activity of high-temperature binary 0.5Pd/5MnO_2/Al_2O_3 catalyst calcined at 1200 °C. According to the XRD data, most manganese in the manganese–alumina catalyst calcined at 1200 °C is in the form of spinel-type oxide (Mn, Al)$[Al]_2O_4$ of variable composition, which is reduced in hydrogen at 300–450 °C. Palladium addition to the low-temperature 5MnO_2/Al_2O_3 catalyst followed by calcination at 1200 °C increases its methane oxidation activity. At 1000 h^{-1} the temperature of 50% methane conversion was 415 °C (Table 3, no. 2), which is lower by 115 °C than that of single-component 5MnO_2/Al_2O_3 sample (Table 1, no. 1) calcined at 1200 °C. However, the catalytic properties of binary Pd–Mn catalyst practically do not surpass those of 0.5Pd/Al_2O_3 catalyst calcined at 1200 °C.

The data on the catalytic activity of high-temperature binary Pd–Mn catalysts where the active manganese oxide is hexaaluminate are presented in Figs. 3 and 7. One can see that the addition of just 0.5 wt.% Pd to the catalysts based on hexaaluminate $MnLaAl_{11}O_{19}$ significantly decreases the 50% methane conversion temperature (Fig. 3). The data presented in Fig. 3 show that the increase of Pd concentration in binary Pd–Mn catalysts from 0.5 to 1–2 wt.% leads to an increase of the catalytic activity. Modification of manganese hexaaluminate with 1–2 wt.% Pd leads to the decrease of the 50% methane conversion temperature from 450–465 to 360 °C at 1000 h^{-1} and from 600 to 415 °C at 24,000 h^{-1} (Fig. 7).

Thus, we have shown that the nature of the manganese oxide—Mn_3O_4, (Mn, Mg)Al_2O_4 or (Mn, Mg)$Al_{11}O_{19}$ has a significant effect on the catalytic activity of high-temperature binary Pd–Mn catalysts. An increase of the catalytic activity after palladium addition to manganese–alumina catalysts is observed only for the catalysts where the main active component is Mn_3O_4 spinel or $MnLaAl_{11}O_{19}$ hexaaluminate.

The catalytic activity data show good correlation with the TPR data. As it has been discussed above, binary Pd–Mn catalysts containing spinel-type oxide Mn_3O_4 or manganese hexaaluminate are almost completely reduced at the temperature, at which the reduction of the sample of based only on Mn compounds is just starting. In our TPR experiments the decrease of the reduction temperature of oxidic manganese species is observed even for single-component Mn catalysts after calcination at 900–1100 °C. Similar changes of the TPR profile are also observed for high-temperature Mn catalysts modified by La_2O_3 where the main active component is hexaaluminate. The shift of the TPR profile to lower temperatures suggests that supported MnO_2 and Mn_2O_3 are dispersed during the high-temperature calcination. In our opinion, the high-temperature dispersion of manganese on the alumina provides for the interaction of Mn^{3+} and/or Mn^{4+} ions with the γ-Al_2O_3 structure to form solid solutions at the stage of low-temperature manganese oxides. Calcination at 900–1100 °C leads to decomposition of the solid solutions and formation of finely dispersed particles of Mn_3O_4 spinel and α-Al_2O_3 [11,29]. According to the XRD data and earlier results [36], some Mn^{3+} cations remain in the form of a solid solution of Mn^{3+} in the alumina structure (γ-, δ-, θ-, α-Al_2O_3) [36], as indicated by the increase of γ-Al_2O_3 lattice parameter to 7.93–8.15 Å (Table 1). It should be noted that the formation of nanoscale defective Mn_3O_4 particles is believed to cause thermal activation of Mn catalysts [36].

The TPR results show that the reduction rate of oxidic manganese species grows after Pd introduction, indicating strong interaction between Pd and the Mn oxides. In addition to the reasons suggested in [14,39], the lower reduction temperature of MnO_x in the binary Pd–Mn catalysts may be due to MnO_x dispersion in the Al_2O_3 structure during the Pd deposition stage. The MnO_x dispersion may result from its partial dissolution in the impregnating solution of Pd precursor (pH ~1). This leads to an increase of the concentration of Mn^{3+} cations stabilized in the alumina structure after calcination at 500 °C. Similar to single-component Mn catalysts [18,36], calcination of binary Pd–Mn catalysts at 900 °C results in decomposition of these solid solution and formation of Mn_3O_4 nanoparticles and high-temperature forms of Al_2O_3 modified by Mn^{3+} cations. Raising the temperature over 1200 °C leads to the formation of α-Al_2O_3, manganese–alumina spinel and/or hexaaluminate doped by Mn^{3+}. It should noted that while finely dispersed particles of manganese oxides MnO_2, Mn_2O_3 and Mn_3O_4 are easily dissolved in solutions with pH ~1, manganese extraction from the structure of high-temperature

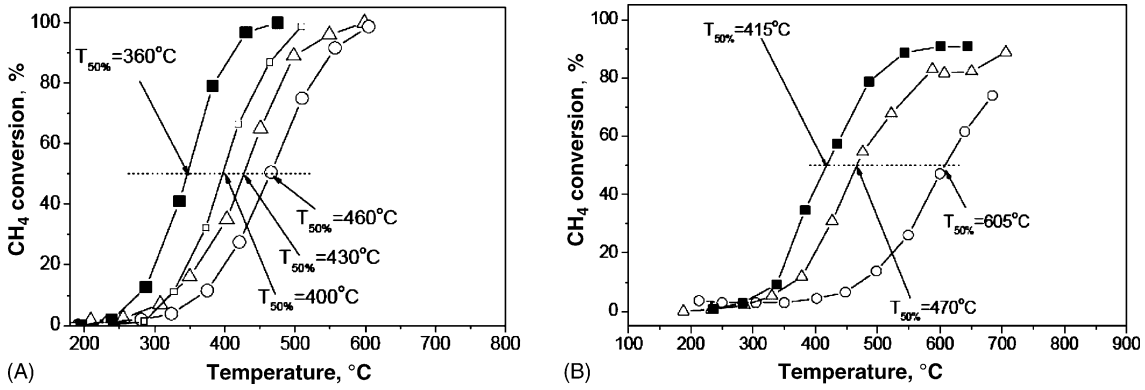

Fig. 7. Methane conversion over 3MnO_2/2.8MgO–18La_2O_3/Al_2O_3 (○), 1.5Pd/Al_2O_3 (△), and 1.5Pd/3MnO_2/2.8MgO–18La_2O_3/Al_2O_3 (■) catalysts calcined at 1200 °C. A sample with Pd deposited after the formation of hexaaluminate (□) is shown for comparison. The calculated concentration of (Mg, Mn)$LaAl_{11}O_{19}$ is 100 wt.%. Test conditions: (A) 1 vol.% CH_4 in air, 1000 h^{-1}, (B) 1 vol.% CH_4 in air, 24,000 h^{-1}.

compounds, e.g. $MnAl_2O_4$ or $MnLaAl_{11}O_{19}$, is possible only at elevated temperatures. In this case, the observation of the synergetic effect in the catalytic activity of binary Pd–Mn catalysts will depend not only on the nature of the manganese oxides, but also on the catalyst preparation procedure.

To check this hypothesis, we studied the catalytic activity of binary Pd–Mn samples modified with Pd after the formation of spinel (Table 3, no. 5) or hexaaluminate (Fig. 7A; Table 3, no. 4) phases. After the addition of 0.5 wt.% Pd in $5MnO_2/Al_2O_3$ catalyst calcined at 1200 °C and containing manganese–alumina spinel, $T_{50\%\,CH_4}$ was 480 °C, which is higher than for $0.5Pd/Al_2O_3$ catalyst (Fig. 3, 430 °C). The deposition of 0.5 wt.% Pd on the high-temperature sample containing the manganese hexaaluminate phase leads to an increase of the catalytic activity of the initial catalyst. However, the activity growth was much weaker than for modification of the low-temperature hexaaluminate precursors followed by the formation of hexaaluminate phase at 1200 °C. $T_{50\%\,CH_4}$ was 400 °C, which is lower by 60 °C than for the initial Mn–Al catalyst and by 30 °C than for $0.5Pd/Al_2O_3$. Indeed, the synergetic effect of Pd and manganese oxides is observed only if palladium is introduced at stage of the low-temperature precursor of the manganese–alumina spinel or manganese hexaaluminate. The synergetic effect is not observed when high-temperature samples with formed spinel or hexaaluminate phases are modified with Pd.

4. Conclusions

The possibility of stabilization of various oxidic manganese species by variation of the loadings of MnO_2 (3–11 wt.%), La_2O_3 (5–21 wt.%) and MgO (2–3 wt.%) in catalysts prepared on granulated $(\gamma + \chi)$-Al_2O_3 at calcination temperatures 900 and 1200 °C is demonstrated.

A strong synergetic effect in the catalytic activity in methane oxidation has been observed after introduction of 0.5–2 wt.% Pd to manganese–alumina catalysts stabilized in the form of Mn_3O_4 spinel doped with Al^{3+} cations or as hexaaluminate (Mn, Mg)$LaAl_{11}O_{19}$.

The synergetic effect of palladium and Mn_3O_4 or $MnLaAl_{11}O_{19}$ provides a low light-off temperature and high efficiency of the catalyst at high temperatures. The formation of high-temperature hexaaluminates $MnLaAl_{11}O_{19}$ and (Mn, Mg)$LaAl_{11}O_{19}$ improves the thermal stability of the catalyst, making it possible to increase the operation temperature of Pd catalysts up to 1000–1200 °C.

Acknowledgement

This work was supported by INTAS-00413, NWO-RFBR 047.015.012.

References

[1] G.K. Boreskov, E.A. Levitskii, Z.R. Ismagilov, Zh. Vses-go Khim. ob-va 29 (1984) 379.
[2] L.D. Pfefferle, W.C.L.D. Pfefferle, Catal. Rev. Sci. Eng. 29 (1987) 219.
[3] Z.R. Ismagilov, M.A. Kerzhentsev, Catal. Rev. Sci. Eng. 32 (1990) 51.
[4] V.N. Parmon, Z.R. Ismagilov, M.A. Kerzhentsev, in: J.M. Thomas, K.I. Zamaraev (Eds.), Perspectives in Catalysis, Chemistry for 21st Century Monograph, Blackwell Scientific Publication, Oxford, 1992, p. 337.
[5] Z.R. Ismagilov, V.G. Vasiliev, A.A. Kachesov, A.I. Falchevski, V.N. Antsiferov, Yu.V. Danchenko, S.A. Yashnik, in: Proceedings of the 5th International Workshop on Catalytic Combustion, Seoul, South Korea, April 29–May 1, (2002), p. 25.
[6] Z.R. Ismagilov, M.A. Kerzhentsev, V.A. Sazonov, L.T. Tsykoza, N.V. Shikina, V.V. Kuznetsov, V.A. Ushakov, S.V. Mishanin, N.G. Kozhukhar, G. Russo, O. Deutschmann, Korean J. Chem. Eng. 20 (2003) 461.
[7] M.F.M. Zwinkels, S.G. Jaras, P.G. Menon, T.A. Griffin, Catal. Rev. Sci. Eng. 35 (1993) 319.
[8] H. Sadamori, T. Tanioka, T. Matsuhisa, Catal. Today 26 (1995) 337.
[9] M. Machida, K. Eguchi, H. Arai, J. Catal. 103 (1987) 385.
[10] M. Machida, K. Eguchi, H. Arai, J. Catal. 120 (1989) 377.
[11] V.S. Babkin, Yu.M. Laevsky, Z.R. Ismagilov, in: R. Bennacer, A.A. Mohammad (Eds.), Proceedings of the 1st International Conference on Applications of Porous Media, APM2002, Jerba, Tunisia, (2002), p. 643.
[12] McCarty et al., Catalytic combustion process, US 6,015,285 (2000).
[13] Z.R. Ismagilov, V.V. Pushkarev, O.Yu. Podyacheva, N.A. Koryabkina, H. Veringa, Chem. Eng. J. 82 (2001) 355.
[14] M. Ferrandon, J. Carno, S. Jaras, E. Bjornbom, Appl. Catal. A 180 (1999) 141.
[15] J.J. Spivey, J.B. Butt, Catal. Today 11 (1992) 465.
[16] L.L. Hegedus, J.C. Summers, J.C. Schlatter, K. Baron, J. Catal. 56 (1979) 321.
[17] R.J. Farrauto, M.C. Hobson, T. Kennelly, E.M. Waterman, Appl. Catal. A 81 (1992) 227.
[18] P.G. Tsyrulnikov, V.S. Salnikov, V.A. Drozdov, S.A. Stuken, A.V. Bubnov, E.I. Grigorov, A.V. Kalinkin, V.I. Zaikovskii, Kinet. Katal. 32 (1991) 439.
[19] L.T. Tsykoza, Z.R. Ismagilov, V.A. Ushakov, Kinet. Katal. 44 (2003) 879.
[20] Z. Jaworska-Golas, W. Mista, J. Wrzyszcz, et al. Catal. Lett. 24 (1994) 133.
[21] L.T. Tsykoza, S.A. Yashnik, Z.R. Ismagilov, Russian Appl. (2002), 2185238.
[22] B.W.-L. Jang, R.M. Nelson, J.J. Spivey, M. Ocal, R. Oukaci, G. Marcelin, Catal. Today 47 (1999) 103–113.
[23] G. Groppi, C. Cristiani, P. Forzatti, J. Catal. 168 (1) (1997) 95.
[24] L.C. Yan, L.T. Thomson, Appl. Catal. A 171 (2) (1998) 219.
[25] P. Artizzu, Y. Brulle, F. Gaillard, N. Guilhaume, M. Primet, Catal. Today 54 (1) (1999) 181.
[26] J. Carno, M. Ferrandon, E. Bjornbom, S. Jaras, Appl. Catal. A 155 (1997) 265.
[27] M. Ferrandon, J. Carno, S. Jaras, E. Bjornbom, Appl. Catal. A 180 (1999) 153.
[28] B.E. Nieuwenhuys, J. Catal. 167 (1997) 305;
B.E. Nieuwenhuys, Adv. Catal. 44 (1999) 259.
[29] S.A. Yashnik, V.V. Kuznetsov, Z.R. Ismagilov, V.V. Ushakov, N.M. Danchenko, S.P. Denisov, Topics Catal. 30/31 (2004) 293.
[30] S. Koshi, M. Machida, K. Equchi, H. Arai, J. Catal. 142 (2) (1993) 655.
[31] E. Pocoroba, E. Magnus Johansson, S.G. Jaras, Catal. Today 59 (2000) 179.
[32] P. Artizzu-Duart, J.M. Millet, N. Guilhaume, E. Garbowski, Catal. Today 59 (2000) 163.
[33] Z.R. Ismagilov, R.A. Shkrabina, N.A. Koryabkina, Technol. Today (1990) 1506;
Z.R. Ismagilov, R.A. Shkrabina, N.A. Koryabkina, Catal. Today 47 (1999) 51.
[34] JCPDS X-ray crystallography database.
[35] A.K. Datye, J. Bravo, t.R. Nelson, P. Atanasova, M. Lyubovsky, L. Pfefferle, Appl. Catal. A 198 (2000) 179.
[36] P.G. Tsyrulnikov, S.V. Tsybulya, G.N. Kryukova, A.I. Boronin, S.V. Koscheev, T.G. Starostina, A.V. Bubnov, E.N. Kudrya, J. Mol. Catal. 179 (2002) 213.
[37] B.R. Strohmeier, D.M. Hercules, J. Phys. Chem. 88 (1984) 4922.
[38] F. Kapteijn, D. van Langeveld, J.A. Moulijn, A. Andreini, M.A. Vuurman, A.M. Turek, J. Jehng, I.E. Wachs, J. Catal. 150 (1994) 94.

[39] M.C. Alvarez-Galvan, V.A. de la Pena O'Shea, J.L.G. Fierro, P.L. Arias, Catal. Commun. 4 (2003) 223.
[40] R.A. Shkrabina, Z.R. Ismagilov, V.A. Ushakov, et al. Kinet. Katal. 38 (1997) 133.
[41] R.A. Shkrabina, Z.R. Ismagilov, V.A. Ushakov, et al. Kinet. Katal. 37 (1996) 116.
[42] H.M. Zhang, Y. Teraoka, N. Yamazoe, Appl. Catal. 41 (1988) 137–146.
[43] Dirk van de Kleut, On the preparation and properties of manganese oxide based combustion catalysts, Thesis, Utrecht, The Netherlands, 1989.
[44] H. Widjaja, K. Sekizawa, K. Eguchi, H. Arai, Catal. Today 47 (1999) 95.

Available online at www.sciencedirect.com
ScienceDirect
Catalysis Today 118 (2006) 151–157
CATALYSIS TODAY
www.elsevier.com/locate/cattod

Oxygen diffusion in nanostructured perovskites

I.L. Zhogin [a,*], A.P. Nemudry [a], P.V. Glyanenko [a], Yu.M. Kamenetsky [a], H.J.M. Bouwmeester [b], Z.R. Ismagilov [c]

[a] *Institute of Solid State Chemistry and Mechanochemistry, 630128 Novosibirsk, Russia*
[b] *Institute for Nanotechnology, University of Twente, The Netherlands*
[c] *Institute of Catalysis, 630090 Novosibirsk, Russia*

Available online 31 July 2006

Abstract

Nonstoichiometric perovskite-related oxides (e.g. ferrites and cobaltites, etc.) are characterized by fast oxygen transport at ambient temperatures, which relates to the microstructural texturing of these materials, consisting wholly of nanoscale microdomains.

We have developed a heterogeneous diffusion model to describe the kinetics of oxygen incorporation into nanostructured oxides. Nanodomain boundaries are assumed to be the high diffusivity paths for oxygen transport whereas diffusion into the ordered domains proceeds much slower. The model has been applied for qualitative evaluation of oxygen diffusion parameters from the data on wet electrochemical oxidation of nanostructured perovskite $SrCo_{0.5}Fe_{0.2}Ta_{0.3}O_{3-y}$ samples.

Using Laplace transform methods, an exact solution is found for a ramped step-wise potential, allowing fitting of the experimental data to theoretical curves (in Laplace transforms). A further model generalization is considered by introducing additional parameters for the size distribution of domains and particles.

Keywords: Heterogeneous oxygen diffusion; Nanostructured perovskites; Electrochemical oxidation

1. Introduction

Mixed ionic electronic conducting (MIEC) oxides, in particular perovskite related materials, possessing high oxygen mobility, are of interest for applications such as SOFC electrodes, sensors and membranes for oxygen separation and partial oxidation of hydrocarbons in catalytic membrane reactors [1]. It is evident that the basic knowledge on the mechanism of oxygen transport in perovskites is necessary for the development of these devices and for modelling of their functioning.

In order to describe oxygen transport properties usually homogeneous diffusion of oxygen ions through random distributed vacancies is suggested [1]. It should be mentioned, however, that MIEC perovskite-related oxides are grossly nonstoichiometric and doped materials which can be considered as homogeneous solid solutions with a high concentration of structural defects (oxygen vacancies, dopant ions, etc.) only at temperatures higher then point of order-disorder transition ($T > T_t$). At $T < T_t$ structural ordering is observed in these materials, either a total one with the formation of superstructures where the defects are assimilated as structural elements, or a partial one with the formation of stoichiometric microdomains separated by disordered interfaces (domain boundaries, extended defects, etc.). In the latter case, defects, e.g. oxygen vacancies, are redistributed inhomogeneously along the material: some of them are ordered inside the microdomains as structural elements, whereas the rest of the overstoichiometric defects are ejected to the vicinity of the interfaces where they have higher mobility. Such a situation has been described in the microdomain concept by J.C. Anderson [2] and was confirmed experimentally in the works of M.Á. Alario-Franco, J.-C. Grenier and P. Hagenmuller [3–5]; unmixing of nonstoichiometric and doped oxides with perovskite-related structures at $T < T_t$ results in the formation of coherently stacked microdomains of 5–50 nm in size and mobile oxygen ions situated in the vicinity of the microdomain boundaries.

Another reason for the intrinsic inhomogeneity of non-stoichiometric and doped MIEC perovskites relates to a strong tendency toward phase separation in systems with strongly

* Corresponding author. Tel.: +7 383 3394298.
E-mail addresses: zhogin@inp.nsk.su (I.L. Zhogin), nemudry@solid.nsk.su (A.P. Nemudry).

0920-5861/$ – see front matter © 2006 Elsevier B.V. All rights reserved.
doi:10.1016/j.cattod.2006.02.088

Nomenclature

$U(t)$	voltage pulse between the sample and reference electrodes (V)
t_0	time of linear growth of voltage pulse (s)
h	dimensionless parameter of the (step in) voltage pulse
$J(t)$	current passing through the electrochemical cell (A)
t	time measured after start of the voltage pulse (s)
p	parameter of Laplace transform (1/s)
$\hat{U}(p)$, $\hat{J}(p)$	Laplace transforms
$Q = \hat{J}(0)$	total charge serving as normalizing factor (C)
x	radial coordinate in a sphere (m)
R	radius of sample particles (m)
r	radius of nanodomains ($R \gg r$)
n_d	concentration of nanodomains (1/m^3)
v_1, v_2	volume fractions occupied by nanodomains and interfaces ($v_1 = 4\pi r^3 n_d/3, v_2 = 1 - v_1$)
D_1	coefficient of slow diffusion in nanodomain (m^2/s)
D_2	effective fast diffusivity (due to interfaces)
c_1, c_2	oxygen concentration in nanodomains and interfaces, respectively
$c_1 = \gamma c_2$	condition at boundary between nanodomain and interface (inter-domain region)
$\tau_1 = r^2/D_1$	first diffusion time (s)
$\tau_2 = R^2/D_2$	second diffusion time (for "fast" diffusion)
$\alpha = \gamma v_1/v_2$	dimensionless parameter of the model (α, τ_1, τ_2 form full set of fitting parameters)
$\kappa = \sqrt{p/D}$	useful parameter to write current transform (1/m)
$F(y)$, $f(y)$	functions of dimensionless argument used to write solution to the model of heterogeneous diffusion [$y = p\tau$, $f(y) = F(\sqrt{y})$]
$n = QM/mF$	charge transfer (e$^-$/formulae unit); here M is molecular weight of the sample, m weight of the sample, F Faraday constant
$n/2$	a number of intercalated oxygen ions per formulae unit
T_t	order-disorder transition temperature

correlated electrons. Electron conducting oxides with transition metals having different charges (for example, $Mn^{3/4+}$, $Co^{3/4+}$, $Cu^{2/3+}$, etc.) and magnetic states can break into a stable state made of nanoscale coexisting clusters because of complicated electron-phonon and magnetic interactions [6].

So, at $T < T_t$ MIEC oxides can be considered as nanostructured materials which are known to be able to show enhanced ionic transport properties owing to the high density of disordered interfaces [7]. In order to develop an adequate mathematical model describing oxygen transport at $T < T_t$, it is necessary to take into account heterogeneous character of oxygen diffusion in nanostructured perovskites.

Previously, as reported by Goldberg et al. [8,9], one of us proposed a model for oxygen diffusion in microdomain textured perovskites in which the domain boundaries are high diffusivity paths and changes in the oxygen stoichiometry in domains occurs due to a two-phase reaction. In the present work we continue modeling the oxygen transport in nanostructured materials having the channels for enhanced oxygen diffusion, however, unlike the previous papers, here we assume that oxidation of microdomains occurs as a result of one-phase reaction. To describe oxygen transport in such a system, we generalized the model of heterogeneous diffusion proposed by Bokshtein et al. [10] for description of diffusion processes in polycrystalline metals.

Since MIEC perovskites exhibit fast oxygen transport even at room temperature [11], the model was applied for the evaluation of oxygen diffusion parameters from the data on wet electrochemical oxidation of nanostructured perovskite $SrCo_{0.5}Fe_{0.2}Ta_{0.3}O_{3-y}$ samples in 1 M KOH at ambient temperatures. The choice of the material is because $SrCo_{0.5}Fe_{0.2}Ta_{0.3}O_{3-y}$ samples possess high oxygen transport properties and enhanced chemical stability in reducing environments and can be considered as promising membrane materials for partial oxidation of hydrocarbons [12].

Thus, the objectives of this work are: (1) the development of a mathematical model describing oxygen transport in nanostructured oxides in which the domain boundaries are the channels for enhanced oxygen diffusion, whereas oxygen penetration into domains occurs as a result of one-phase reaction; (2) its adaptation for the analysis of current transients under electrochemical oxidation of nanostructured materials; and (3) experimental verification with the samples of practical interest.

2. Experimental

The samples of $SrCo_{0.5}Fe_{0.2}Ta_{0.3}O_{3-y}$ nonstoichiometric perovskite were synthesized by solid-state reaction from the corresponding metal oxides and carbonates with preliminary homogenization of the starting materials in a planetary ball mill. A stoichiometric mixture of the powders was calcined at 900 °C, pressed in pellets, annealed in air at 1400 °C for 6 h and cooled in the furnace. Different oxygen stoichiometry of materials was achieved by (a) slow cooling in the furnace, (b) annealing at 950 °C in a quartz ampoule under dynamic vacuum ($P \sim 10^3$ Pa) and quenching of the sample in the ampoule to room temperature in water.

Phase analysis was performed by means of X-ray diffraction with DRON 3, whereas the oxygen content was determined by iodometric titration and thermogravimetry. Electron microscopy was applied for microstructural studies.

Electrochemical experiments were performed at room temperature by means of potentiostat/galvanostat PI-50-1 (three-electrode cell, 1 M KOH electrolyte, Hg/HgO reference electrode) with working electrodes of $SrCo_{0.5}Fe_{0.2}Ta_{0.3}O_{3-y}$ polycrystalline material (17–18 mg) pressed into Pt grids along with 1 wt.% of Teflon and 15–20 wt.% of acetylene black.

Chronopotentiometric investigation of the anode oxidation of $SrCo_{0.5}Fe_{0.2}Ta_{0.3}O_{3-y}$ in the galvanostatic mode combined with in situ X-ray diffraction was carried out to study the mechanism of phase transformations under the changes in the oxygen stoichiometry of the samples. For the kinetics studies (potentiostatic mode) the working electrode was placed in a cell at 25 °C and was maintained up to equilibrium potential U_0. At $t = 0$ a voltage pulse between the working electrode and reference electrode is applied. Re-equilibration through diffusion of oxygen into the working electrode material takes place. The rate of re-equilibration can be measured easily by monitoring the electric current passing through the cell. A more detailed description of electrochemical techniques can be found in refs. [13,14,11].

3. Theoretical model

Similar to the model of spheres filling a half-space (grains in a thick metal plate, see [10]), we consider a model in which the small spheres are inside large ones (nanodomains inside the perovskite powder particles). The simple geometry of our model allows us to derive an exact solution for the current passing through the cell using the Laplace transform method.

The inverse Laplace transformation to determine the original function is not possible in the analytical form (in analytical functions; this is the reason why one usually analyzes only the asymptotic current behavior at short and long times) [14]. Though there are computational methods to do the inverse Laplace transformations [15], they require intensive calculations (double Fourier transforms). Therefore, we have chosen another way to compare our experiment with the model. After we perform numerical Laplace transformation of the measured current function, $J_{exp}(t)$, (as well as potential function, if it is measured and is not given "analytically" with potentiostate) we adjust the experimental transform, $\hat{J}_{exp}(p)$, with model curves $\hat{J}_{th}(p)$ (which depend on the applied potential profile).

However, computer inversion of the Laplace transform may be useful for verifying the best approximation, or for the better choosing among several minima, if they occur.

A two-level model of spheres is used to describe the current passing through an electrochemical cell under potential of a chosen profile.

3.1. Diffusion in a spherical particle

The diffusion equation for a spherical particle, when the space derivatives (Laplacian) are reduced to differentiation over the radius, is written as follows:

$$\frac{\partial(x\,c)}{\partial t} = D\frac{\partial^2(x\,c)}{\partial x^2}. \tag{1}$$

here $c(t, x)$ is the concentration of the diffusing species, R the particle radius, and x the radial coordinate, $0 \le x \le R$. For initial and boundary conditions we have

$$c(t<0,x) = 0, \qquad c(t, x = R) = c_R(t).$$

Using the Laplace transform of $c(t, x)$

$$\hat{c}(p,x) \equiv \int_0^\infty c(t,x)e^{-pt}\,\mathrm{d}t$$

turns partial derivatives (1) into an ordinary differential equation

$$\frac{\partial^2(x\hat{c})}{\partial x^2} = \frac{p}{D}x\hat{c}. \tag{2}$$

Applying a boundary condition, $\hat{c}(p, R) = \hat{c}_R(p)$, one can easily find the exact solution to Eq. (2),

$$\hat{c}(p,x) = \hat{c}_R(p)\frac{\kappa R}{\sinh(\kappa R)}\frac{\sinh(\kappa x)}{\kappa x}, \quad \kappa = \sqrt{p/D}. \tag{3}$$

Diffusion current (and electric one, if diffusing component carriers charge q), passing through the whole particle boundary, may be expressed as follows:

$$J(t) = 4\pi q\int_0^R \frac{\partial c(t,x)}{\partial t}x^2\,\mathrm{d}x,$$

$$\hat{J}(p) = 4\pi q\frac{p\hat{c}_R(p)R}{\sinh(\kappa R)}\int_0^R \sinh(\kappa x)x\,\mathrm{d}x. \tag{4}$$

One may expect that the diffusion coefficient to be independent of the concentration, provided that the oxygen content in the perovskite lattice changes only slightly, e.g. $\Delta y < 0.1$. For this purpose the amplitude of potential pulse, U_A, applied to the cell, should be small enough. We assume that the access of oxygen ions to the particles is not limited and, hence, there is a linear dependence between concentration and the potential

$$\frac{c_R(t)}{c_A} = \frac{U(t)}{U_A}.$$

In our experiments we used the potential steps of the following form (see Fig. 6a):

$$\frac{U(t)}{U_A} = \begin{cases} 0, & t<0 \\ h+(1-h)t/t_0, & 0 \le t \le t_0; \\ 1, & t > t_0 \end{cases}$$

this gives the Laplace transform ($0 \le h \le 1$):

$$\frac{p\hat{c}_R(p)}{c_A} = h + (1-h)\frac{1-e^{-pt_0}}{pt_0}\left(\overset{p\to 0}{\longrightarrow}1\right). \tag{5}$$

Introducing the value $Q = \hat{J}(0) = 4\pi R^3 q c_A/3$ for a total charge passed through the cell, and using Eqs. (3)–(5) we obtain ($\tau = R^2/D$ is a characteristic diffusion time for a sphere of radius R; $\sqrt{p\tau} = \kappa R$)

$$\frac{\hat{J}(p)}{Q} = \frac{p\hat{c}_R(p)}{c_A}F(\sqrt{p\tau}), \tag{6}$$

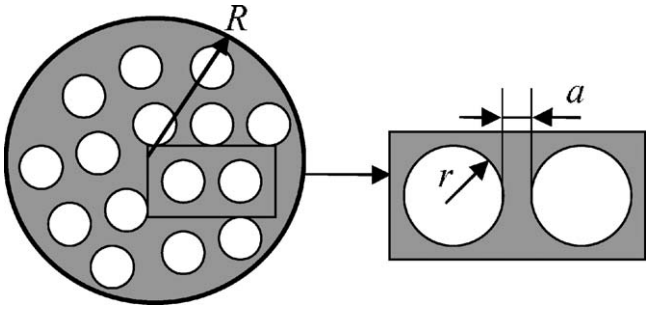

Fig. 1. Regions of slow (white) and fast (grey) diffusion.

where

$$F(y) \equiv \frac{3\coth(y)}{y} - \frac{3}{y^2}\left(\overset{y\to 0}{\longrightarrow} 1 - \frac{y^2}{15} + \cdots\right). \tag{7}$$

3.2. Heterogeneous diffusion model: spheres of two types

Let us imagine that the particles in the sample are heterogeneous (see Fig. 1) and contain domains of a typical size r, where the diffusion rate is small, D_1, and interfaces (regions neighboring with domains boundaries), where the diffusion rate is high, D_2. More exactly, let us consider D_2 as an effective diffusion coefficient for a porous particle, obtained, when all domains are removed, as if they are non-permeable for diffusion, i.e. $D_1 = 0$. This effective coefficient may change not only with temperature, but also with parameters related to the nanodomain structure, such as oxygen content, quenching rate, etc.

If diffusion coefficient D_1 is small but not equal to zero, then the diffusion equation should reflect oxygen incorporation inside the domains. One may assume that the concentration along the boundary of each domain is approximately the same (since transport to the boundary is fast) and proportional to the current local concentration:

$$c_{1r}(t) = \gamma c_2(x,t).$$

Therefore, we may write an effective diffusion equation in a heterogeneous particle instead of Eq. (1):

$$qv_2\left(\frac{\partial c_2}{\partial t} - D_2\frac{\partial^2(xc_2)}{x\partial x^2}\right) = -n_{\mathrm{d}}J_1(t,x).$$

Here n_{d} is the concentration of domains, J_1/q the diffusion current into domains, $v_1 = 4\pi r^3 n_{\mathrm{d}}/3$, $v_2 = 1 - v_1$ are volume fractions for regions of slow and fast diffusion, respectively. After the Laplace transformation we obtain (taking into account Eqs. (5) and (6)):

$$\frac{\partial^2(x\hat{c}_2)}{\partial x^2} = \frac{p}{D_2}x\hat{c}_2(1 + \alpha F(\sqrt{p\tau_1})), \tag{8}$$

where $\alpha = \gamma v_1/v_2$ is proportional to the ratio of above mentioned volume fractions (see Fig. 1).

As was mentioned in [10], the equilibrium concentrations (of diffusant) along the boundaries and inside the domains (i.e. grains in [10]) may not coincide. Therefore, the dimensionless parameter α may include not only geometry but also the concentration factor γ.

One may derive the final expression for the current using Eq. (8) (it is necessary to remember that the particle is heterogeneous):

$$\hat{J}(p) = 4\pi R^2 D_2 \left.\frac{\partial\hat{c}_2}{\partial x}\right|_{x=R} = Q\frac{p\hat{c}_{2R}(p)}{c_A} \times \frac{1+\alpha f(p\tau_1)}{1+\alpha} f(p\tau_2[1+\alpha f(p\tau_1)]). \tag{9}$$

Here notations $f(y) \equiv F(\sqrt{y})$, $\tau_1 \equiv r^2/D_1$, $\tau_2 \equiv R^2/D_2$ (see Eqs. (5)–(7)) are introduced.

3.3. Assembly of particles, particle size distribution

If powder particles are of different sizes, then the current expression (6) and expression (9) should be integrated with the function of volume (mass) distribution of particles, $M(R)$ (norm per unit):

$$\frac{\hat{J}(p)}{Q} = \frac{p\hat{c}_R(p)}{c_A}\int_0^\infty F(\kappa R)M(R)\,\mathrm{d}R.$$

If the 'relative' dispersion of the distribution,

$$\Delta_R = \frac{\langle(R-R_0)^2\rangle}{R_0^2}\,(R_0 = \langle R\rangle),$$

is small, we retain only the first correction term, changing functions in (9) or (6) as follows (prime means differentiation by argument):

$$F(\kappa R) \to F^*(\kappa R_0) = F(\kappa R_0) + \frac{1}{2}\kappa^2 R_0^2 F''(\kappa R_0)\Delta_R, \tag{10}$$

where

$$y^2F''(y) = 6\left(1 + \frac{y^2}{\sinh^2 y}\right)\left(1 + \frac{y}{\tanh y}\right) - \frac{24}{y^2}.$$

One may obtain this correction by e.g. integration with formal distribution (delta functions):

$$M(R) = \delta(R-R_0) + \frac{1}{2}\delta''(R-R_0)\Delta_R R_0^2,$$

which has proper first two moments. Saddle-point integration with the Gaussian distribution $M(R) \propto \exp(-(R/R_0-1)^2/2\Delta_R)$ gives the same result.

In a similar manner one may correct for the size dispersion of nanodomains, Δ_r, and dispersion of parameter α, Δ_α, as well.

4. Experimental results and computation

According to the X-ray diffraction data, $SrCo_{0.5}Fe_{0.2}Ta_{0.3}O_{3-y}$ samples obtained either by slow cooling or by quenching in vacuum are single-phase and have cubic perovskite structure

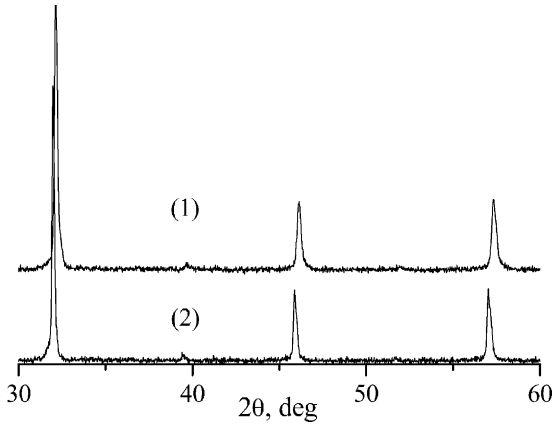

Fig. 2. Diffraction patterns of samples $SrCo_{0.5}Fe_{0.2}Ta_{0.3}O_{3-y}$: (1) as prepared, (2) after annealing in vacuum ($P \sim 10^3$ Pa) at 950 °C and quenching.

with the parameters 3.934 Å and 3.952 Å, respectively (Fig. 2). Iodometric titration showed that quenching of the samples in vacuum causes a decrease in oxygen content $(3 - y)$ from 2.92 to 2.70.

In spite of the fact that XRD suggests single-phase behavior, the HREM data show that the quenched samples possess a nanodomain texture (Fig. 3) with a typical domain size of about 10 nm. Such a situation is typical for the nanostructured materials with coherent/semicoherent stacking of domains: in terms of X-ray diffraction they behave as homogeneous single phases [2–5].

In order to determine the mechanism of oxidation of the nanostructured $SrCo_{0.5}Fe_{0.2}Ta_{0.3}O_{3-y}$ perovskite, we carried out chronopotentiometric measurements of the electrochemical anodic oxidation of the samples in the galvanostatic mode, combined with in situ X-ray diffraction studies. Measurements of the potential of the working (sample) electrode versus the charge that passed through the electrochemical cell ($n = JtM/mF$), which is connected through a simple relation with the amount of inserted oxygen $x = n/2$, provide evidence of phase transitions in the oxide under the changes of the oxygen stoichiometry. The character of phase transitions can be judged

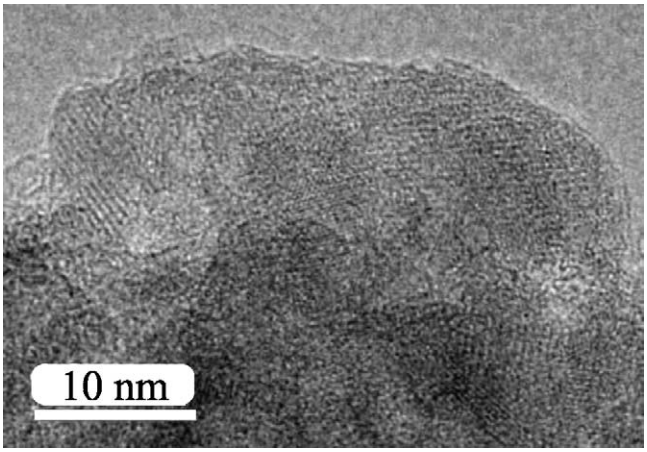

Fig. 3. High resolution image of $SrCo_{0.5}Fe_{0.2}Ta_{0.3}O_{2.7}$ sample possessing nanodomain texture.

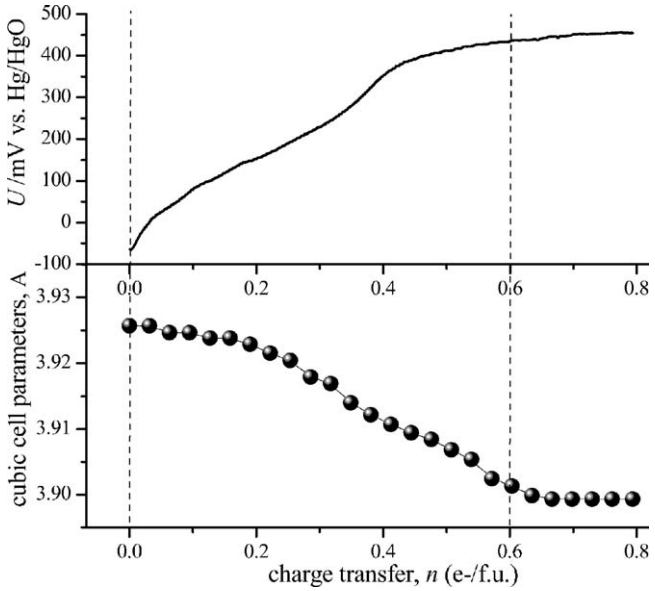

Fig. 4. In situ anodic oxidation of $SrCo_{0.5}Fe_{0.2}Ta_{0.3}O_{2.7+x}$: (a) potential U vs. charge transfer n, (b) change of unit-cell parameters with n, $n/2 = x$.

about from the shape of U—n curve and in situ X-ray diffraction data. Fig. 4 shows the results of chronopotentiometry and evaluation of the in situ XRD data.

Monotonous changes in the unit cell parameters and potential versus charge transfer provide evidence of one-phase mechanism of oxidation [11,16].

For kinetic studies, we used the powdered samples with particle size distribution shown in Fig. 5.

So, in the course of preliminary studies nanostructured $SrCo_{0.5}Fe_{0.2}Ta_{0.3}O_{2.7}$ perovskite samples were obtained, particle size distribution for powdered samples and the size of nanodomains were determined. It was shown that sample oxidation occurs as a result of one-phase reaction; the potential range within which the oxidation of the sample occurs was determined.

After that, kinetic studies of potentiostatic oxidation of $SrCo_{0.5}Fe_{0.2}Ta_{0.3}O_{2.7}$ perovskite were carried out according to

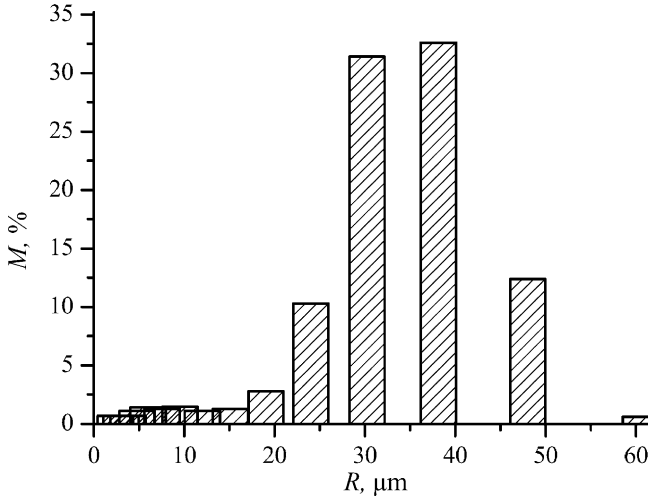

Fig. 5. Mass distribution of particles over size.

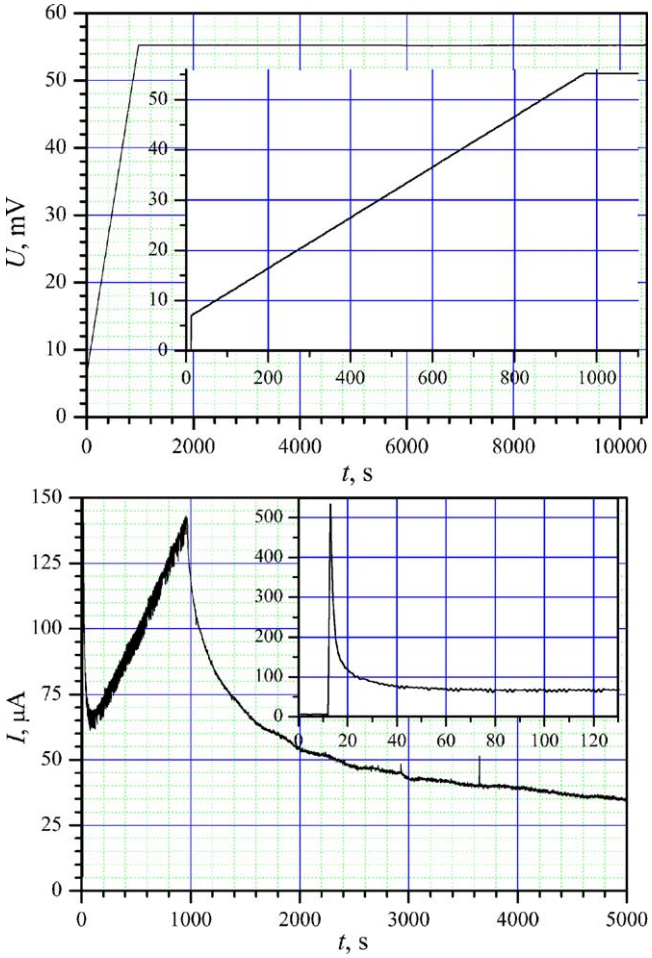

Fig. 6. Applied potential (a) and current transient (b) vs. time.

the procedure described in the Experimental section and in [11,13,14]; the analysis of current transients was also carried out (optimization of parameters τ_1, τ_2 and α) with the help of the Laplace transformation.

Fig. 6 shows $U(t)$ and $J_{exp}(t)$ functions versus time, obtained in one of experiments. The time of current measurement averaging was 1 s. This obstacle somewhat distorted the current plot at short times.

Computations were performed in MatLab. For the data, presented in Fig. 6, potential step parameters are the following (see Eqs. (5) and (9)):

$h = 7/55.25;\ t\_0 = 958;\ \%t\_0$ in seconds.

After $\hat{J}_{exp}(p)/Q$ was calculated (exponential slope at long times ($t > 3000$ s) was considered analytically), correction for the time of microammeter integration (1 s) was introduced:

$JeL = JeL. * p./(1 - \exp(-p));\ \%1$s.

Then optimization over three parameters entering the model function of current (Eq. (9)) was done.

Computing results are shown in Fig. 7, model parameters for theoretical curve (dotted line) being as follows:

$\tau_1 = 49$ s, $\tau_2 = 19 \times 10^3$ s, $\alpha = 4.8$.

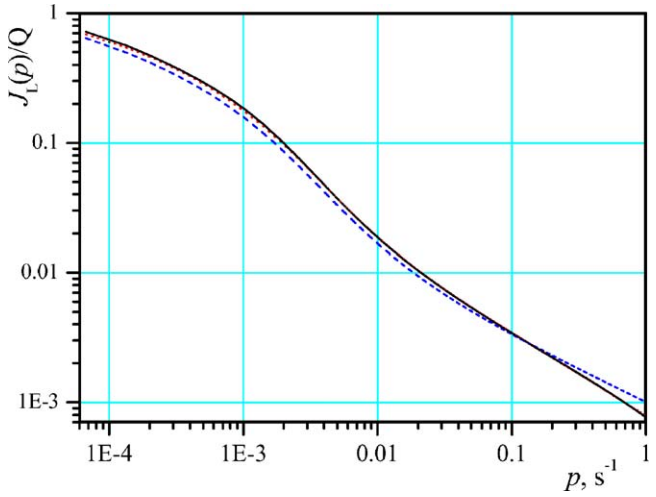

Fig. 7. Normalized Laplace transform of experimental data (solid; $Q = 0.44$ C) and fitting model curves for inhomogeneous (dot) and homogeneous (dash; $\alpha = 0$) model.

Using values $r \sim 10$ nm, $R = 32$ μm, one may estimate diffusion coefficients

$D_1 = 2 \times 10^{-13}$ cm^2/s, $D_2 = 5 \times 10^{-10}$cm^2/s.

Let us note that fitting by the homogeneous model gives essentially larger errors (see dashed curve in Fig. 7), and yields another value: $\tau_2 = 15 \times 10^4$ s.

5. Discussion and conclusions

In the present work we suggest a model describing oxygen transport in nanostructured materials having the channels for enhanced oxygen diffusion. Formally, we generalize the model of heterogeneous diffusion proposed by Bokshtein et al. [10] to describe diffusion processes in polycrystalline metals. Unlike the model of heterogeneous diffusion in which the grain spheres closely fill the semi-space, we consider another version of geometry: nanodomain spheres (r) form larger spheres which are the particles (radius R, $R \gg r$) of the oxide under investigation. So, the model proposed by Bokshtein et al. is a particular case of our model when the radius R tends to infinity. Changes in the geometry are due to the necessity of adapting of the model to the experimental conditions. For an express estimation of the oxygen transport properties of MIEC materials, we proposed using relatively simple techniques of wet electrochemistry. However, one should keep in mind that the model is valid within the temperature range ($T < T_t$) of existence of nanodomain texture. The question to what extent the wet electrochemical data correspond to the high-temperature data obtained under actual performance conditions is the subject of further investigations.

Using the Laplace method we have obtained an exact solution in transforms to our model. The inverse transition to the original is impossible in the analytical form; in such cases the consideration is usually limited to the analysis of the asymptotic behavior. Correspondingly, in the experiment one

analyzes either the initial region for short time or the region of long times (in comparison with the characteristic time of diffusion for this geometry) [13,14].

To analyze the electrochemical data (current transients), we realized a new approach allowing us to use the current transients as a whole: we carry out the numerical Laplace transform for the experimental current curve, then make the fitting procedure, compare the obtained transform with the analytical solutions of the model.

An important parameter of the model, along with the radius of domains r and radius of particles R, coefficients of fast (along domain boundaries, D_2) and slow diffusion (inside domains, D_1), is a dimensionless parameter α which has a sense of the ratio of fraction of inserted oxygen which finally (after equilibration) gets into the region of slow diffusion (domains) or into the region of fast diffusion (interfaces). According to our calculations, the part of new oxygen connected with highly conducting interfaces accounts for $100\%/(1 + \alpha) = 17\%$ of the all inserted oxygen.

With our developed model, we have shown that nanostructuring results in heterogeneous oxygen diffusion in domains and along the interfaces; the difference in diffusion coefficients may attain several orders of magnitude. The most important issue is that stationary flux of oxygen ions through nanostructured perovskite membranes at temperatures lower than the point of the order–disorder transition T_t is determined mostly by coefficient D_2. Since activation energy E_a, necessary for the oxygen ions migration along the domain boundaries (d.b.), may be essentially lower than that for the bulk (b.) diffusion, E_a(d.b.)$\sim$l/2 E_a(b.) [17], oxygen permeable membranes made of nanostructured oxides are able to provide several orders of magnitude higher oxygen fluxes at the working temperatures below the order–disorder transition point.

We shall further study the kinetics of nanostructured perovskites oxidation at various temperatures to determine the activation energy for oxygen ion migration along the interfaces and inside the domains and develop the method for measuring oxygen diffusion parameters in the nanostructured materials. Comparing the data obtained at low temperature by means of relatively simple wet electrochemical technique with the data related to oxygen permeability at high temperatures, we might define the mechanism of oxygen transport in nanodomain textured oxides, elucidate the factors determining the high values of oxygen fluxes in these materials and open the strategies to develop new oxygen-conducting materials operating at moderate temperature.

Acknowledgement

The work has been supported by RFBR-NWO (03-03-89005) and RFBR (05-03-32640, 05-03-08109) grants.

References

[1] H.J.M. Bouwmeester, A.J. Burggraaf, Dense ceramic membranes for oxygen separation, in: A.J. Burggraaf, L. Cot (Eds.), Fundamentals of Inorganic Membrane Science and Technology, Elsevier, Amsterdam, 1996, p. 435.
[2] J.S. Anderson, The thermodynamics and theory of nonstoichiometric compounds, in: A. Rabenau (Ed.), Problems of Nonstoichiometry, North-Holland Publ. Co., Amsterdam, 1970, p. 1.
[3] M.Á. Alario-Franco, J.M. Gonzalez-Calbet, M. Vallet-Regi, J.-C. Grenier, J. Solid State Chem. 49 (1983) 219.
[4] M. Vallet-Regi, J.M. Gonzalez-Calbet, J. Verde, M.Á. Alario-Franco, J. Solid State Chem. 57 (1985) 197.
[5] J.-C. Grenier, N. Ea, M. Pouchard, P. Hagenmuller, J. Solid State Chem. 58 (1985) 243.
[6] E. Dagotto, T. Hotta, A. Moreo, Phys. Rep. 344 (2001) 1–153.
[7] P. Heitjans, S. Indris, J. Phys.: Condens. Matter 15 (2003) R1257–R1289.
[8] E. Goldberg, A. Nemudry, V. Boldyrev, R. Schöllhorn, Solid State Ionics 110 (1998) 223.
[9] E. Goldberg, A. Nemudry, V. Boldyrev, R. Schöllhorn, Solid State Ionics 122 (1999) 17.
[10] B.S. Bokshtein, A.I. Magidson, I.L. Svetlov, Fizika Metallov i Metallovedenie 6 (1958) 1040, In Russian.
[11] A. Nemudry, E.L. Goldberg, M. Aguirre, M.Á. Alario-Franco, Solid State Sci. 4 (2002) 677.
[12] P. Glyanenko, A. Nemudry, Z.R. Ismagilov, H.J.M. Bouwmeester, Investigation of structure, phase transition and oxygen mobility in $SrCo_{0.8-x}Fe_{0.2}Ta_xO_{3-y}$ mixed conductors, 7-th ICCMR, 11–14 September 2005. Book of Abstracts, Cetraro, Italy, p. 241.
[13] S. Sunde, K. Nişancioğlu, T.M. Gür, J. Electrochem. Soc. 143 (11) (1996) 3497.
[14] C.J. Wen, C. Ho, B.A. Boukamp, I.D. Raistick, W. Weppner, R.A. Huggins, Int. Metals Rev. 5 (1981) 253.
[15] B. Hüpper, E. Pollak, A new method for numerical inversion of the Laplace transform, http://arXiv.org/physics/9807051.
[16] A. Nemudry, P. Rudolf, R. Schöllhorn, Chem. Mater. 8 (1996) 2232.
[17] P. Kofstad, High Temperature Corrosion, Elsevier, London, 1988, p. 558.

Catalysis Today 147 (2009) 270–274

Contents lists available at ScienceDirect

Catalysis Today

journal homepage: www.elsevier.com/locate/cattod

Properties of Nb-doped $SrCo_{0.8}Fe_{0.2}O_{3-d}$ perovskites in oxidizing and reducing environments

O.Yu. Podyacheva [a,*], Z.R. Ismagilov [a], A.N. Shmakov [a,b], M.G. Ivanov [a], A.N. Nadeev [a], S.V. Tsybulya [a,b], V.A. Rogov [a]

[a] Boreskov Institute of Catalysis, Novosibirsk 630090, Russia
[b] Novosibirsk State University, Novosibirsk 630090, Russia

ARTICLE INFO

Article history:
Available online 18 February 2009

Keywords:
Perovskite
Membrane
Oxygen non-stoichiometry
Partial oxidation of methane

ABSTRACT

The phase stability of $SrCo_{0.8}Fe_{0.2}O_{3-d}$ perovskite doped with niobium was studied by in situ high-temperature X-ray diffraction in the temperature range of 30–1000 °C and oxygen partial pressure 0.2–10^{-5} atm. The stability of the cubic perovskite structure in a wide range of oxygen partial pressures is the main advantage of $SrCo_{0.8-x}Fe_{0.2}Nb_xO_{3-d}$ (x = 0.1–0.3) system in comparison with $SrCo_{0.8}Fe_{0.2}O_{3-d}$. It is suggested that equilibrium of the thermal expansion with changes of the oxygen non-stoichiometry leading to the same lattice parameters in the oxidizing and reducing environments at the catalytic temperatures is a necessary requirement for stable operation of perovskite as an oxygen-conducting membrane. In the case of $SrCo_{0.8-x}Fe_{0.2}Nb_xO_{3-d}$ perovskite this condition is met at x = 0.2. This makes the $SrCo_{0.6}Fe_{0.2}Nb_{0.2}O_{3-d}$ composition promising for application as oxygen-conducting membrane.

1. Introduction

Dense oxygen-permeable membranes with mixed electronic–ionic conductivity based on perovskite-like oxides are of increasing interest during past years for novel separation of oxygen from air inside a reactor. Pure oxygen then can be used in different catalytic oxidation processes such as partial oxidation of methane [1–5] or ethane [6], oxidative coupling of methane [7,8], etc. During the process one side of the membrane where the air is fed contacts with atmosphere with high oxygen partial pressure. Meanwhile, the other side of the membrane where the catalytic reaction takes place is subjected to the environment with low oxygen pressure and the oxygen gradient across the membrane can reach extremely high values. Oxygen mobility in oxygen-conducting perovskites at elevated temperatures and the presence of an oxygen gradient across the membrane can result in its structural transformation, e.g. change of the oxygen non-stoichiometry or phase transformations. Consequently, to sustain stable catalytic oxidation process an oxygen-conducting membrane must possess structural stability under conditions with large oxygen gradients at the temperatures of the catalytic reaction.

The application of perovskite-type oxides as oxygen-conducting membranes was first demonstrated in 1985 [9], and $SrCo_{0.8}Fe_{0.2}O_{3-d}$ was shown to have the highest oxygen flux. This composition was later studied in detail by many researchers. It was found that at low oxygen pressures this material undergoes a perovskite–brownmillerite structural transformation and as a result destruction of the membrane during the process was observed [10,11]. To improve the stability of strontium cobaltite in a wide oxygen pressure range it was suggested to substitute the main cation in the initial structure by another cation. For example, a cycle of studies was devoted to $SrCo_{0.8}Fe_{0.2}O_{3-d}$ modification with barium [4,6,12]. It was shown that the barium introduction to the system improves the stability of the perovskite phase $Ba_{0.5}Sr_{0.5}Co_{0.8}Fe_{0.2}O_{3-d}$ at oxygen partial pressures range 1–10^{-5} atm [12]. However, a detailed study revealed that during operation the oxygen rich membrane side was subjected to segregation of Sr and Ba, whereas the oxygen lean side of the membrane was enriched with cobalt [4,6]. A significant change of the component ratio on different membrane sides during operation resulting in the membrane destruction was also observed for the material where strontium was partially substituted with lanthanum $La_{0.6}Sr_{0.4}Co_{0.2}Fe_{0.8}O_{3-d}$ [13]. Complete strontium substitution for other elements, e.g. Sm in $Sm_{0.4}Ba_{0.6}Fe_{0.8}Co_{0.2}O_{3-d}$, did not yield a stable composition. In this case the air side of the membrane was enriched with Ba and Co, whereas the catalytic side was enriched with Fe and depleted with Ba [14]. Other attempts to improve the stability of the $SrCo_{0.8}Fe_{0.2}O_{3-d}$ system included substitution of B-cation in

* Corresponding author at: Boreskov Institute of Catalysis, Environmental Catalysis, Prosp. Akad. Lavrentieva 5, Novosibirsk 630090, Russia.
Tel.: +7 383 3269 552; fax: +7 383 3306 219.
E-mail address: pod@catalysis.ru (O.Yu. Podyacheva).

0920-5861/$ – see front matter © 2009 Elsevier B.V. All rights reserved.
doi:10.1016/j.cattod.2009.01.017

perovskite, e.g. cobalt substitution for zirconium or cerium [15,16]. Such substitution led to improvement of the system stability in the reducing environment. Unfortunately, in this case the oxygen conductivity was much lower.

In this paper the physicochemical properties of strontium cobaltide $SrCo_{0.8}Fe_{0.2}O_{3-d}$ doped with niobium were investigated. We studied its structure, phase transformations in the oxidizing and reducing environments in the temperature range of 30–1000 °C and under conditions of partial methane oxidation. The choice of niobium as the modifying element was based on the two main factors. Niobium cations can stabilize the cubic structure after introduction into the perovskite lattice in wide range of oxygen non-stoichiometry $3 - d$ [17]. Also doping with niobium makes it possible to improve the reduction stability of system containing transition metals [18]. The structural stability of perovskites was studied by in situ high-temperature X-ray diffraction, which is successfully used for investigation of phase transformations as a function of temperature and gas phase [12,19].

2. Experimental

The $SrCo_{0.8-x}Fe_{0.2}Nb_xO_{3-d}$ (x = 0–0.3) samples were synthesized by ceramic method [17] using $SrCO_3$, Fe_2O_3, Co_3O_4 and Nb_2O_5 as precursors. Depending on the composition, the final calcination temperature was varied from 1100 to 1250 °C.

In situ high-temperature X-ray diffraction was carried out using a Bruker D8Advance diffractometer and an Anton Paar HTK-16 high temperature chamber in oxygen partial pressure window 0.2–10^{-5} atm. It was shown in [20] that major perovskite changes, i.e. chemical expansion, initially increases faster in this oxygen pressure window and then plateaus at lower oxygen pressure 10^{-5}–10^{-15}. A sample was deposited on the platinum heater plate and heated at 1 °C/s rate from 30 to 1000 °C in air or in vacuum (10^{-5} atm). The cooling rate was equal to 1 °C/s. When the desired temperature was reached, the sample was maintained at this temperature for 20 min followed by registration of diffraction pattern in 2θ range 20–70° with 0.05° step and 5 s accumulation at each point.

The microstructure of the samples was studied using a JEM 2010 transmission electron microscope with an attachment for elemental analysis.

Temperature-programmed reduction (TPR) was carried out in 10% H_2 in Ar mixture at 40 ml/min flow rate and 10 °C/min heating rate from ambient temperature to 900 °C.

To study the stability of perovskites in partial methane oxidation, the samples (0.5–1 mm fraction) were placed in a tubular reactor fed with the reaction mixture containing 70 vol.% Ar, 20 vol.% CH_4 and 10 vol.% O_2 at 50,000 h^{-1} flow rate. The composition of the reaction mixture and the products was analyzed by gas chromatography using a TCD detector.

3. Results

The chemical, phase and mechanical stability of the membrane in the oxidizing and reducing environments at temperatures of catalytic processes (700–1000 °C) is an important factor for choice of the optimal perovskite composition for application as an oxygen-conducting membrane. To evaluate these factors we studied the stability of $SrCo_{0.8-x}Fe_{0.2}Nb_xO_{3-d}$ (x = 0–0.3) samples during heating in the air and in vacuum up to the 1000 °C.

When $SrCo_{0.8}Fe_{0.2}O_{3-d}$ was heated in air from 30 to 1000 °C the perovskite structure was registered in the whole temperature range. The XRD pattern of the sample cooled from 1000 °C to ambient temperature practically matched that of the initial sample

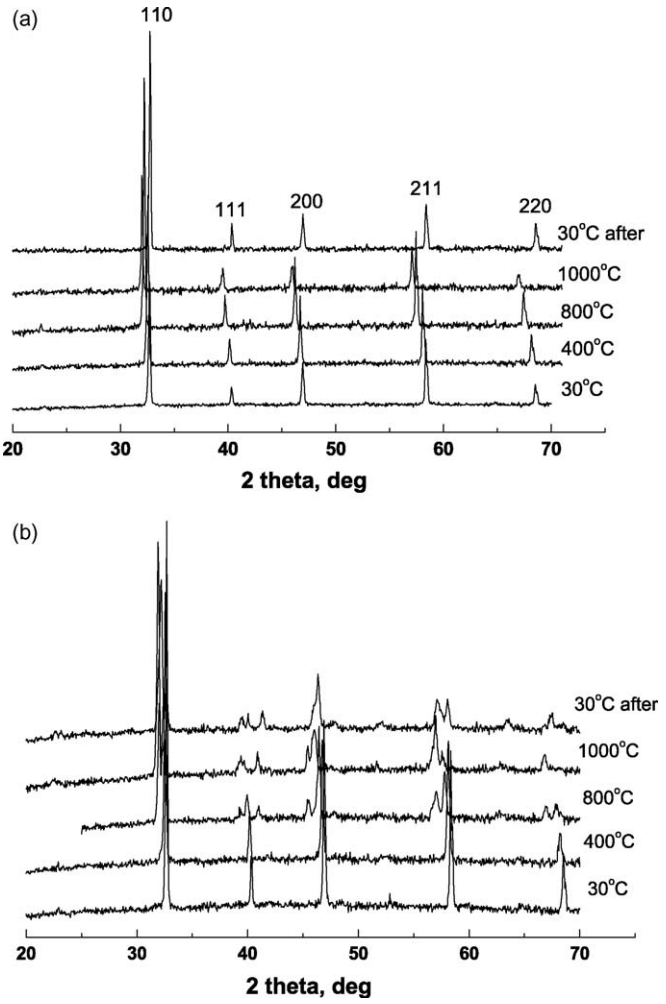

Fig. 1. XRD patterns of $SrCo_{0.8}Fe_{0.2}O_{3-d}$ recorded at different temperatures in air (a) and under vacuum (b).

(Fig. 1a). On the contrary, when the sample was heated under vacuum (Fig. 1b) a significant structural transformation was observed at 800 °C. This transformation resulted in the formation of a phase corresponding to brownmillerite structural type that was formed due to the ordering of oxygen vacancies. When the sample was cooled down under vacuum the brownmillerite structure with *Pnma* space group and lattice parameters a = 5603 Å, b = 15,776 Å, c = 5479 Å was preserved. These parameters are close to those of $Sr_2Fe_2O_5$ and $Sr_2Co_2O_5$ with brownmillerite structural type. The obtained results are in good agreement with the literature data showing that $SrCo_{0.8}Fe_{0.2}O_{3-d}$ perovskite is stable in the oxidizing atmosphere and is subjected to perovskite–brownmillerite structural transformation in the reducing environment [10–12].

The structure of $SrCo_{0.7}Fe_{0.2}Nb_{0.1}O_{3-d}$ sample looses stability during heating in air starting from 800 °C (Fig. 2a). The cubic structure of the initial perovskite with *Pm*3*m* symmetry is distorted resulting in the splitting of 1 1 0, 2 0 0 and 2 1 1 reflexes and change of their relative intensities. When the sample was heated under vacuum (Fig. 2b) the splitting of the individual reflexes at 800 °C was more evident. At 1000 °C all the observed reflexes were split. When the sample was cooled down under vacuum the structural distortion was preserved resulting in the reflex splitting untypical for the cubic phase. It is important to note that in the high temperature interval the lattice parameters in the air and in vacuum differed by 0.02 Å (Fig. 3a).

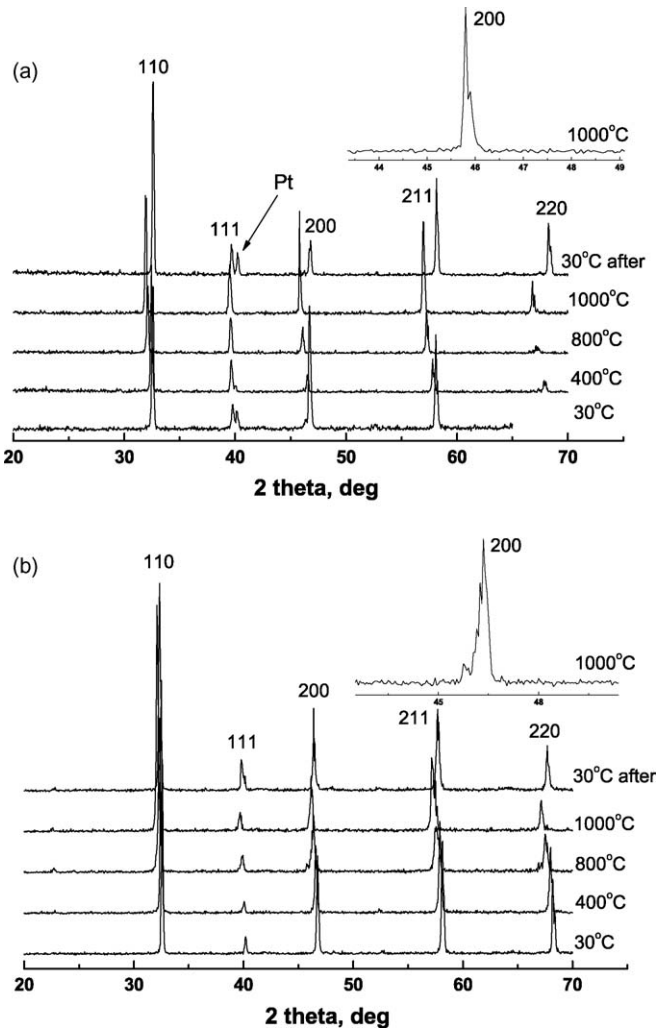

Fig. 2. XRD patterns of $SrCo_{0.7}Fe_{0.2}Nb_{0.1}O_{3-d}$ recorded at different temperatures in air (a) and under vacuum (b). The splitting of 2 0 0 reflex at 1000 °C is shown as an example.

The $SrCo_{0.6}Fe_{0.2}Nb_{0.2}O_{3-d}$ sample preserved the cubic perovskite structure in the whole temperature range studied both in the air and in vacuum (Fig. 4). This fact indicates that this system is very stable in the oxidizing and reducing environments. The changes observed during heating in the air were reversible, so that the lattice parameters before and after heating were identical. It is very important that the lattice parameters of this sample in the air and in vacuum at temperatures above 700 °C are the same within the experimental error (Fig. 3b).

The structure of $SrCo_{0.5}Fe_{0.2}Nb_{0.3}O_{3-d}$ sample was more stable with respect to temperature than that of $SrCo_{0.7}Fe_{0.2}Nb_{0.1}O_{3-d}$ but less stable than that of $SrCo_{0.6}Fe_{0.2}Nb_{0.2}O_{3-d}$ (Fig. 5). No peak splitting was observed during heating in air. Only their relative intensities at different temperatures changed, most likely, due to variation of the oxygen concentration in the sample. The changes observed during heating under vacuum were more significant. The splitting of the 2 2 0 peak was observed starting from 400 °C and the 2 0 0 peak was split starting from 800 °C. In the 800–1000 °C temperature range the lattice parameters in air and in vacuum differed by ~0.015 Å (Fig. 3c).

The niobium introduction into $SrCo_{0.8-x}Fe_{0.2}Nb_xO_{3-d}$ resulted in a continuous growth of the initial perovskite lattice parameter at room temperature in air from 3.871 Å at $x = 0$ to 3.920 Å at $x = 0.3$. For all three samples $SrCo_{0.8-x}Fe_{0.2}Nb_xO_{3-d}$ ($x = 0.1$–0.3) cooling in air returned the lattice parameters to the

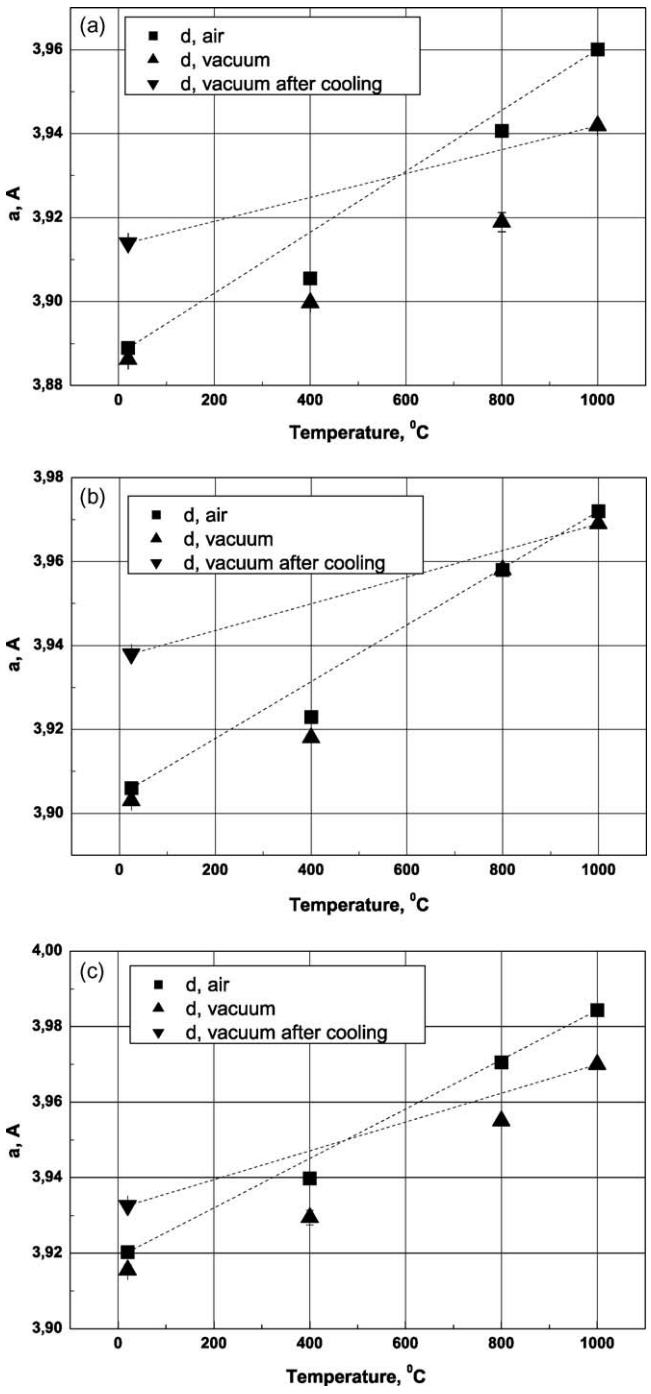

Fig. 3. Temperature dependence of the lattice parameters of $SrCo_{0.7}Fe_{0.2}Nb_{0.1}O_{3-d}$ (a), $SrCo_{0.6}Fe_{0.2}Nb_{0.2}O_{3-d}$ (b) and $SrCo_{0.5}Fe_{0.2}Nb_{0.3}O_{3-d}$ (c).

initial values. However, when the samples were cooled down in vacuum, their lattice parameters were increased by ~0.025, 0.035 and 0.013 Å, respectively (Fig. 3). The TEM with elemental analysis showed that initial composition of perovskite particle $SrCo_{0.6}Fe_{0.2}Nb_{0.2}O_{3-d}$ at the surface and in the bulk were identical Fe:Co:Sr:Nb = 11:25:53:11 (at.%). After the sample was heated under vacuum to 1000 °C and cooled down, the distribution of the elements across the particle did not change beyond the experimental error. Consequently, the observed increase of the sample lattice parameters after cooling under vacuum can be related only to changes in the perovskite oxygen non-stoichiometry. It is important that the perovskite–brownmillerite structural transformation observed for $SrCo_{0.8}Fe_{0.2}O_{3-d}$

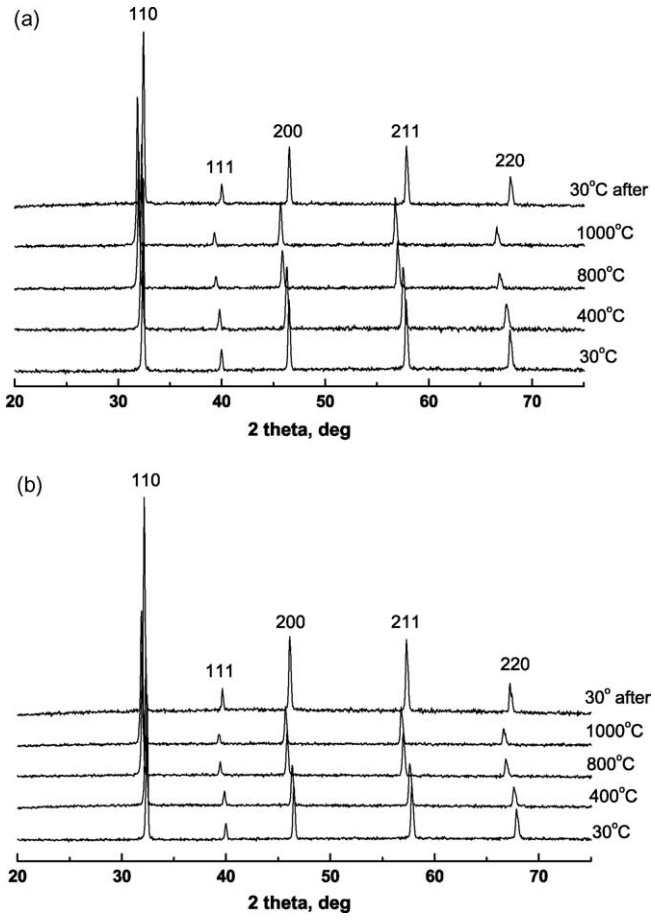

Fig. 4. XRD patterns of $SrCo_{0.6}Fe_{0.2}Nb_{0.2}O_{3-d}$ recorded at different temperatures in air (a) and under vacuum (b).

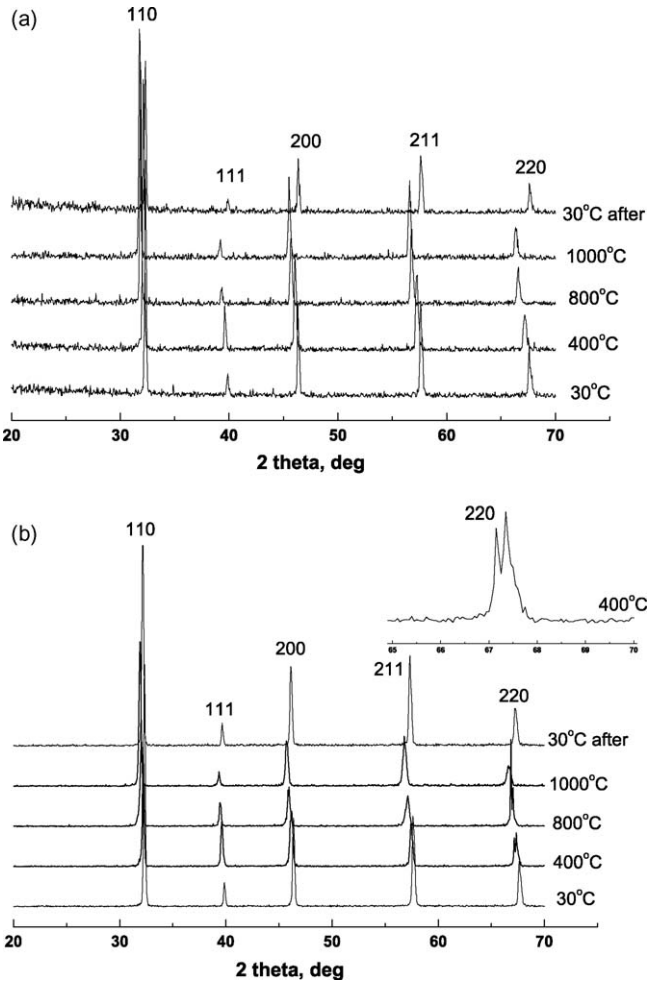

Fig. 5. XRD patterns of $SrCo_{0.5}Fe_{0.2}Nb_{0.3}O_{3-d}$ recorded at different temperatures in air (a) and under vacuum (b). The splitting of 2 2 0 reflex at 400 °C is shown as an example.

in reducing environment was not found for Nb-doped samples during heating under vacuum. This proves that Nb plays an important role in stabilization of the perovskite cubic structure.

The reduction stability of $SrCo_{0.8}Fe_{0.2}O_{3-d}$ and $SrCo_{0.6}Fe_{0.2}Nb_{0.2}O_{3-d}$ samples was also studied by TPR. The TPR profile of $SrCo_{0.8}Fe_{0.2}O_{3-d}$ has three major peaks at T_1 = 545 °C, T_2 = 634 °C, and T_3 = 751 °C (Fig. 6). Doping with niobium altered the TPR profile. The low-temperature peak shifted to lower temperatures by 35 °C and its relative area increased. The maximum positions of the other two peaks did not change whereas their relative peak areas decreased. The amounts of hydrogen consumed in the 25–900 °C temperature range were 0.00643 mol/g for $SrCo_{0.8}Fe_{0.2}O_{3-d}$ and 0.00428 mol/g for $SrCo_{0.6}Fe_{0.2}Nb_{0.2}O_{3-d}$. This indicates that the Nb-doped perovskite is more stable to reduction.

The investigation of $SrCo_{0.6}Fe_{0.2}Nb_{0.2}O_{3-d}$ sample in partial oxidation of methane showed that this sample was not active by itself. The methane conversion was 3.5%, with CO and H_2 selectivities equal to 40% and 30%, respectively. The phase composition of $SrCo_{0.6}Fe_{0.2}Nb_{0.2}O_{3-d}$ was preserved during the reaction but the perovskite lattice parameter increased by 0.019 Å. This proves that the oxygen non-stoichiometry was changed during reaction and is in agreement with the data obtained in the XRD chamber (Fig. 7).

4. Discussion

In this study the structural stability of Nb-doped $SrCo_{0.8}Fe_{0.2}O_{3-d}$ system in the oxidizing and reducing environments was studied by in situ high-temperature XRD. Its stability is an important factor determining the applicability of this material as an oxygen-conducting membrane. The main advantage of $SrCo_{0.8-x}Fe_{0.2}Nb_xO_{3-d}$ (x = 0.1–0.3) in comparison with $SrCo_{0.8}Fe_{0.2}O_{3-d}$ is the preservation of the perovskite cubic structure both in the oxidizing and reducing environments and, consequently, the absence of the perovskite–brownmillerite structural transformation.

The analysis of the perovskite lattice parameters in the oxidizing and reducing environments in the high temperature

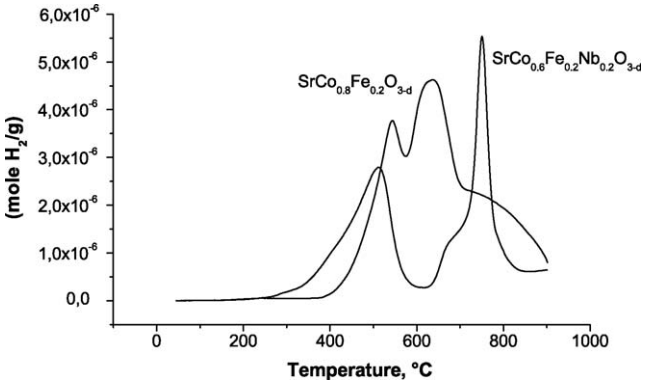

Fig. 6. TPR profiles of $SrCo_{0.8}Fe_{0.2}O_{3-d}$ and $SrCo_{0.6}Fe_{0.2}Nb_{0.2}O_{3-d}$.

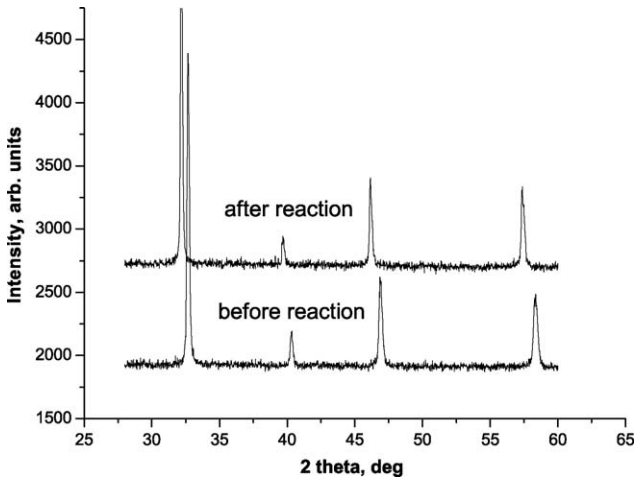

Fig. 7. XRD patterns of $SrCo_{0.6}Fe_{0.2}Nb_{0.2}O_{3-d}$ before and after methane partial oxidation reaction.

region ($T > 700$ °C) is crucial during the investigation of the structural and mechanical stability of the membrane material. The presented data indicate that the perovskite lattice parameters of all three samples depend on temperature in a non-linear way. The temperature dependence of the lattice parameters of the studied samples is determined by two processes: perovskite thermal expansion and change of the oxygen non-stoichiometry $3 - d$ due to the loss of a part of oxygen upon heating and reoxidation during cooling in the oxygen-containing environment. The conclusion on a significant dependence of the oxygen non-stoichiometry on the lattice parameter was made on the basis of our high-temperature experiments carried out under vacuum. When the sample was heated under vacuum to 1000 °C followed by cooling to room temperature, the perovskite lattice parameter was increased in comparison with the initial value by 0.025 Å for $x = 0.1$, 0.035 Å for $x = 0.2$ and 0.013 Å for $x = 0.3$. As transmission electron microscopy coupled by elemental analysis showed that the Fe:Co:Sr:Nb ratio in the cooled samples was constant, the lattice parameter growth can be attributed only to the change of the oxygen non-stoichiometry, namely, an increased concentration of oxygen vacancies. Indeed, it was measured by iodometric titration [21] that the oxygen concentration in the initial $SrCo_{0.6}Fe_{0.2}Nb_{0.2}O_{3-d}$ sample was 2.7 and it decreased after heating under vacuum to 2.6.

Two processes proceeding in perovskite system upon heating, i.e. loss of oxygen and thermal expansion, result in the lattice parameter growth. However, these processes are not completely independent because the change of the oxygen concentration in the sample seems accompanied by a significant decrease of the thermal expansion coefficient. Indeed, the straight lines connecting the values of the lattice parameters at room temperature and at 1000 °C for samples cooled under vacuum have substantially lower slope than the corresponding lines drawn for samples cooled in air (Fig. 3). Although the linear expansion law does not seem to hold in this case, this fact appears to indicate that the thermal expansion coefficient decreases when the concentration of oxygen vacancies increases.

Thus, the concentration of oxygen vacancies grows with temperature. This results in an increase of the lattice parameter but simultaneously decreases the thermal expansion coefficient. Therefore, it can be concluded that stable perovskite operation in the oxidizing and reducing environments requires equilibrium of these two processes, leading to the same lattice parameters in both environments in the temperature range of the catalytic process ($T > 700$ °C). The chemical composition of the samples is a regulated parameter that can be varied to achieve the desired result—equal lattice parameters in the oxidizing and reducing environments. The change of the chemical composition after introduction of Nb^{5+} cations with large charge appears to result in a change of the oxygen non-stoichiometry both at low and high temperatures, which eventually determines the lattice parameter. For samples $SrCo_{0.7}Fe_{0.2}Nb_{0.1}O_{3-d}$ and $SrCo_{0.5}Fe_{0.2}Nb_{0.3}O_{3-d}$ the differences of the lattice parameters at high temperatures are significant (0.02 and 0.015 Å, correspondingly). Consequently, they would lead to tensions during operation of these materials as membranes and would result in destruction under conditions with different oxygen partial pressure on the two sides of the membrane. On the contrary, the lattice parameters of $SrCo_{0.6}Fe_{0.2}Nb_{0.2}O_{3-d}$ are the same in the oxidizing and reducing environments. Hence, it is natural to expect that no mechanical tensions will appear during operation of a membrane with this chemical composition.

5. Conclusions

A series of samples $SrCo_{0.8}Fe_{0.2}O_{3-d}$, $SrCo_{0.7}Fe_{0.2}Nb_{0.1}O_{3-d}$, $SrCo_{0.6}Fe_{0.2}Nb_{0.2}O_{3-d}$, $SrCo_{0.5}Fe_{0.2}Nb_{0.3}O_{3-d}$ were studied by in situ high-temperature XRD in a wide oxygen partial pressure range ($0.2–10^{-5}$ atm). Perovskite with $SrCo_{0.6}Fe_{0.2}Nb_{0.2}O_{3-d}$ composition demonstrated the highest stability, apparently, due to equilibrium between the thermal expansion process and changes of the oxygen non-stoichiometry at temperatures above 700 °C. Consequently, perovskite with this composition is the most stable both from the phase composition and from the mechanical strength viewpoints. It preserves the ideal perovskite cubic structure and has about the same values of lattice parameters in air and under vacuum at high temperatures. The latter property makes $SrCo_{0.6}Fe_{0.2}Nb_{0.2}O_{3-d}$ perovskite the most promising among listed materials for further study. The final conclusion on possibility of the use of Nb-doped perovskites as oxygen-conducting membranes will be made based on the oxygen transport performance and stability of membrane during operation in real catalytic process, these experiments are in progress.

Acknowledgements

This work is a continuation of the NWO-RFBR project and authors thank Dr. H.J.M. Bouwmeester for fruitful discussions. The authors thank V.I. Zaikovskii for the TEM studies of the samples. This study was supported by the SB RAS Integration project No.82.

References

[1] U. Balachandran, J.T. Dusek, P.S. Maiya, B. Ma, R.L. Mieville, M.S. Kleefisch, C.A. Udovich, Catal. Today 36 (1997) 265.
[2] A.F. Sammells, M. Schwartz, R.A. Mackay, T.F. Barton, D.R. Peterson, Catal. Today 56 (2000) 325.
[3] H.J.M. Bouwmeester, Catal. Today 82 (2003) 141.
[4] Z. Shao, G. Xiong, H. Dong, W. Yang, L. Lin, Sep. Purif. Technol. 25 (2001) 97.
[5] A. Kleinert, A. Feldhoff, T. Schiestel, J. Caro, Catal. Today 118 (2006) 44.
[6] H. Wang, Y. Cong, W. Yang, J. Membr. Sci. 209 (2002) 143.
[7] Y. Lu, A.G. Dixon, W.R. Moser, Y.H. Ma, U. Balachandran, J. Membr. Sci. 170 (2000) 27.
[8] S. Haag, A.C. van Veen, C. Mirodatos, Catal. Today 127 (2007) 157.
[9] Y. Teraoka, H. Zhang, S. Furukawa, N. Yamazoe, Chem. Lett. (1985) 1743.
[10] L. Qiu, T.H. Lee, L.-M. Liu, Y.L. Yang, A.J. Jacobson, Solid State Ionics 76 (1995) 321.
[11] S. McIntosh, J.F. Vente, W.G. Haije, D.H.A. Blank, H.J.M. Bouwmeester, Solid State Ionics 177 (2006) 833.
[12] S. McIntosh, J.F. Vente, W.G. Haije, D.H.A. Blank, H.J.M. Bouwmeester, Solid State Ionics 177 (2006) 1737.
[13] W. Jin, S. Li, P. Huang, N. Xu, J. Shi, Y.S. Lin, J. Membr. Sci. 166 (2000) 13.
[14] M. Ikeguchi, T. Mimura, Y. Sekine, E. Kikuchi, M. Matsukata, Appl. Catal. A 290 (2005) 212.
[15] H. Lu, Y. Cong, W. Yang, Mater. Sci. Eng. B 141 (2007) 55.
[16] X. Zhu, Y. Cong, W. Yang, J. Membr. Sci. 283 (2006) 38.
[17] V.V. Kriventsov, D.I. Kochubey, Z.R. Ismagilov, O.Yu. Podyacheva, A.P. Nemudry, Phys. Scripta 115 (2005) 740.
[18] M. Ziolek, Catal. Today 78 (2003) 47.
[19] H. Wang, C. Tablet, W. Yang, J. Caro, Mater. Lett. 59 (2005) 3750.
[20] C. Park, A. Jacobson, Solid State Ionics 176 (2005) 2671.
[21] A. Nemudry, A. Rogachev, I. Gainutdinov, R. Schollhorn, J. Solid State Electrochem. 5 (2001) 450.

CHAPTER 10
Nanostructured Titanium Dioxide for Medicine and Biology

DOI 10.1070/RC2009v078n09ABEH004082

Synthesis and stabilization of nano-sized titanium dioxide

Z R Ismagilov, L T Tsykoza, N V Shikina, V F Zarytova, V V Zinoviev (deceased), S N Zagrebelnyi

Contents

Abstract. The published data on the preparation and the dispersion-structural properties of nano-sized TiO_2 are considered. Attention is focused on its sol–gel synthesis from different precursors. The possibilities for the purposeful control and stabilization of properties of TiO_2 nanopowders and sols are analyzed. Information on physicochemical methods used in studies of the particle size and the phase composition of nanodisperse TiO_2 is presented. The prospects of using nano-sized TiO_2 in medicine and nanobiotechnology are considered. The bibliography includes 95 references.

I. Introduction

Due to its unique properties, nano-sized titanium dioxide represents a promising research subject for various modern fields of science and technology, including microbiology, nanobiotechnology and fundamental medicine. Thus the most popular directions include the design of a new generation of drugs based on synthetic nanobioconstructs containing TiO_2 nanoparticles and aimed at curing cancer and viral or genetic diseases. The necessity of developing new approaches to fight against these diseases is associated with the limitations inherent in conventional methods of therapy and profilaxis. Thus for viral infections, the therapy efficacy tends to decrease due to permanent mutation of viruses.

Development of methods for the targeted impact on injured RNA and DNA molecules includes studies of the conjugates of oligonucleotides containing biologically active or photoreactive ligands targeted to a certain fragment of a nucleic acid.[1–3] Numerous oligonucleotides and their derivatives capable of an *in vitro* selective effect on nucleic acids were synthesized. The main problem of these studies was associated with the absence of reliable and efficient methods for the drug delivery to cells, because viruses are localized inside a cell and oligonucleotides fail to effectively penetrate there due to their high molecular weight and the hydrophobic nature of cell membranes. To solution of this problem, the methods of nanotechnology and nanobiotechnology oriented at employing nanoparticles as drug-loaded 'nanovectors' are engaged.[4] Thus oligonucleotides were immobilized on TiO_2 nanoparticles.[5] Covalently linked TiO_2–DNA nanocomposites were shown to possess the unique property of a light-inducible nucleic acid endonuclease.[6]

The first publication[7] on the use of titanium dioxide in microbiology for photoelectrochemical sterilization of microbial cells dates back to 1985; since that time, the number of studies devoted to the bactericidal effect of nanodisperse TiO_2 with respect to different pathogenic bacteria is being permanently increased.[8–17] Data on the efficient blood purification from residual viruses by filtering it through nanoceramic membranes or nanofibres containing nanostructured TiO_2 are documented.[18]

Recently, publications have appeared devoted to studies on the possibility of using TiO_2 in oncology.[19–22] This is associated with the quest for an alternative to two main methods of treating malignant tumours, *i.e.*, radio- and chemotherapy. For example, it was demonstrated[22] that the growth of the Ls-174-t culture of human colon carcinoma

Z R Ismagilov, L T Tsykoza, N V Shikina G K Boreskov Institute of Catalysis, Siberian Branch of the Russian Academy of Sciences, prosp. Akad. Lavrentieva 5, 630090 Novosibirsk, Russian Federation. Fax/tel. (7-383) 330 62 19, e-mail: zri@catalysis.ru (Z R Ismagilov), tel. (7-383) 326 95 38, e-mail: tsikoza@catalysis.ru (L T Tsykoza), tel. (7-383) 330 76 70, e-mail: shikina@catalysis.ru (N V Shikina)
V F Zarytova Institute of Chemical Biology and Fundamental Medicine, Siberian Branch of the Russian Academy of Sciences, prosp. Akad. Lavrentieva 8, 630090 Novosibirsk, Russian Federation. Fax (7-383) 333 36 77, tel. (7-383) 335 62 24, e-mail: zarytova@niboch.nsc.ru
V V Zinoviev State Research Centre of Virology and Biotechnology 'Vector', 630559 Koltsovo, Novosibirsk Region, Russian Federation. Fax (7-383) 336 74 09
S N Zagrebelnyi Novosibirsk State University, ul. Pirogova 2, 630090 Novosibirsk, Russian Federation. Fax (7-383) 330 22 42, tel. (7-383) 363 42 59, e-mail: grant@fen.nsu.ru

Received 28 May 2009
Uspekhi Khimii **78** (9) 942–955 (2009); translated by T Ya Safonova

Service code 4082
Last printed
28 october 11:28:32

cells can be suppressed by treating these cells with a dilute TiO_2 colloid solution followed by irradiation. The tumour cells were effectively killed *in vitro* by photoexcited TiO_2 nanoparticles. The survival ratio after 30-min irradiation decreased rapidly with the increase in TiO_2 concentration.

In Russia, studies devoted to the development of synthetic nanoconstructs involving TiO_2 particles for the targeted genome cleavage are of the innovating nature and largely represented by proceeding of conferences.[23–27] It was demonstrated[27] that nanocomposites built of titanium dioxide nanoparticles with immobilized polyamine-containing oligonucleotides interact with 30-mer [^{32}P]RNA and [^{32}P]DNA targets. It was shown that UV irradiation of complexes formed results in modification of the targets. Nanocomposites based on complexes of amorphous TiO_2–polylysine nanoparticles with oligonucleotides exhibited antiviral activity, which was especially pronounced under UV radiation carried out 2–3 h after infection. Obviously, the prerequisite for the use of TiO_2 in such constructs was its nanoscale size and colloidal state, which ensured the efficient penetration of nanostructures into cells.

The low cytotoxicity of TiO_2 nanoparticles was noted,[25,26] which, however, differed for different cell cultures and depended on the titanium dioxide phase composition. The low toxicity of TiO_2 nanoparticles was also demonstrated in another study[28] where a well-known *in vitro* procedure was used that assesses the organism response to dust from the induction of proinflammatory cytokines IL-6 and IL-8 generated by respiratory tract epithelium cells treated with relevant particles. It was shown that nanoparticles of commercial metal oxides including TiO_2 are not too toxic with respect to lung cells as compared with the environmental dust particles. It also followed from the results of this study that contrary to expectations, the metal oxide nanoparticles were not more toxic than micron-sized particles.

Nano-sized titanium dioxide finds wide application in other modern scientific and technological fields including photocatalysis, electrochemistry, optics, microelectronics, in the production of dyes, ceramics, cosmetics, gas sensors, inorganic membranes, dielectrics, in the synthesis of mesoporous film coatings, catalysts for environmental cleaning processes, *etc.*[29–44]

Thus, the synthesis and stabilization of nanodisperse forms of TiO_2 is a challenge for science and practice.

The most popular method of synthesis of disperse deposits of metal oxides including TiO_2 is their precipitation from the solutions of the corresponding salts with ammonia, alkalis and alkali-metal carbonates. Numerous studies have shown that the minimum size of primary particles is independent of the nature of the precipitating agent being equal to 45 ± 10 Å.[45] Depending on the synthesis conditions, the primary particles coalesce to form different-sized aggregates. The degree of aggregation depended on many factors and was controlled by the synthesis conditions. Varying the temperature, the synthesis time and pH of the medium allowed fabrication of titanium dioxide with different phase compositions, namely, amorphous TiO_2, anatase, brookite or rutile.

The present review summarizes studies on the synthesis of nano-sized titanium dioxide and the control and stabilization of the dispersed state, morphology and phase composition of TiO_2 nanoparticles and also discusses the prospects of their use in nanobiotechnology.

II. The effect of the synthesis conditions on the degree of dispersion, phase composition and properties of titanium dioxide

According to early studies,[45] hydrolysis of different titanium compounds (titanium alkoxides and inorganic salts, mainly, $TiCl_4$) in aqueous solutions with low pH (2–6) resulted in basic salts with variable compositions as the primary products. At higher pH, titanium dioxide hydrates, presumably, with the composition $TiO(OH)_2$ or $TiO_2 \cdot n\,H_2O$, where n depends on the ageing and drying conditions, form.

Freshly precipitated titatium(IV) dioxide hydrate exhibited high adsorbability with respect to both cations and anions; the content and the nature of impurities in TiO_2 depended on the pH of the medium and the nature of both the precipitating agent and the starting titanium compound.[45] According to the data from transmission electron microscopy (TEM), the TiO_2 gel represented spherical nonporous particles with the sizes 30–60 Å aggregated into chains and bunches. The gel specific surface (S) varied from 250 to 500 $m^2\ g^{-1}$ (Refs 45 and 46) and depended on the precipitation conditions and the presence of impurities (Fig. 1, 2).[45]

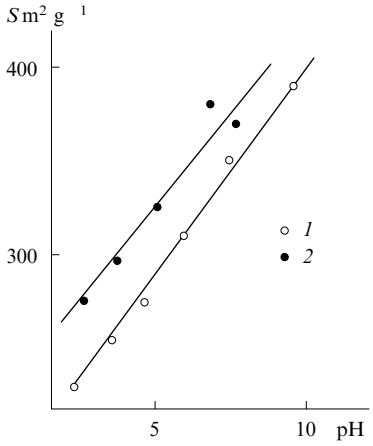

Figure 1. Dependence of the specific surface of titanium dioxide hydrate on the pH of the medium in the course of sedimentation at room temperature (*1*) and 70 °C (*2*).[45]

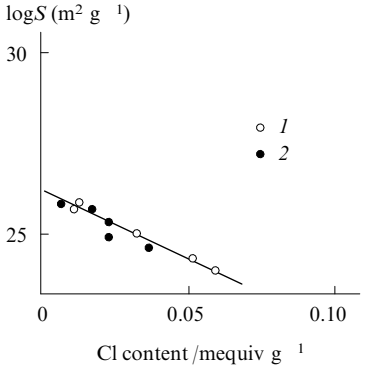

Figure 2. Dependence of the specific surface of titanium dioxide hydrate on the chloride ion content.[45]
(*1*) Sedimentation at room temperature, (*2*) at 70 °C.

The specific surface of titanium dioxide hydrate formed upon hydrolysis under hydrothermal conditions also depended substantially on the temperature and the duration of the process.[47] Strong effect of the initial concentration of $TiCl_4$, which determines the reaction medium acidity, on the degree of crystallinity of the hydrothermal hydrolysis product was obseved.[48]

A simple and accessible method of synthesizing pure and stable nano-sized TiO_2 (anatase) under mild hydrothermal conditions using $TiCl_4$ as the precursor was proposed.[49] Solvothermal hydrolysis of titanium ethoxide in anhydrous ethanol containing strictly definite amount of ultrapure water, carried out under mild conditions (< 200 °C, 2 h), also afforded pure ultradisperse nanocrystalline anatase with high specific surface (up to 250 $m^2\ g^{-1}$).[50]

Thermal treatment of gels of different titanium dioxide hydrates resulted in their crystallization to form anhydrous TiO_2. Depending on the calcination temperature, hydrated TiO_2 could be transformed into anatase, rutile or brookite, which was accompanied by changes in its specific surface and porous structure. Thus at temperatures below 600 °C, crystallization produced anatase with the virtually constant pore volume and specific surface.[51] For higher temperatures, the transition of anatase to rutile occurred with concomitant sharp decrease in both the pore volume and the specific surface (Fig. 3). Mineral impurities could also exert a strong effect on the polymorphous transition temperature. Numerous data have shown that besides the phase composition, the conditions of thermal treatment of TiO_2 gels determined other important performance characteristics of titanium dioxide, namely, its morphology and the particle size.

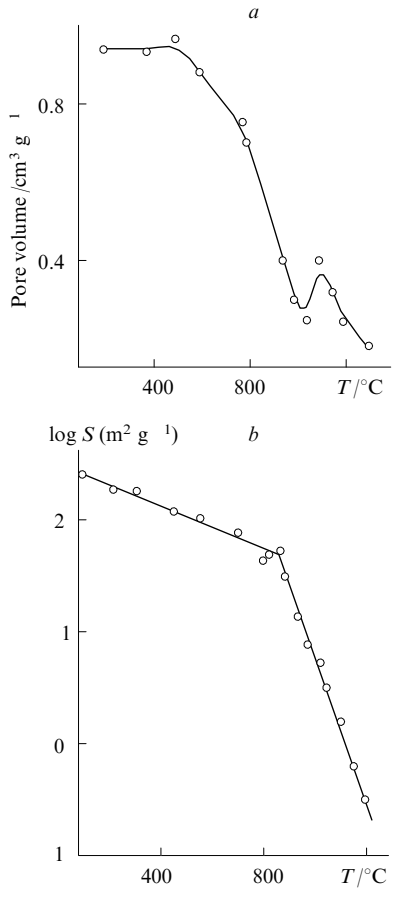

Figure 3. Changes in the porous structure (*a*) and the specific surface (*b*) of titanium dioxide in the calcination.[51]

The production of TiO_2 is carried out, most often, by the sulfate and chloride methods (from ilmenite and $TiCl_4$, respectively). Titanium tetrachloride can be processed according to three different schemes, namely, hydrothermal hydrolysis, vapour-phase hydrolysis and combustion in an oxygen flow. Recently, the sol–gel method that affords TiO_2 particles with desired structures and properties has gained in importance and, hence, has attracted attention from the viewpoint of development of nanotechnologies. Titanium alkoxides or titanium tetrachloride were used as the titanium-containing precursors in the sol–gel method.

In the following sections, the most significant results in the control over dispersion, morphology, phase composition and stability of nano-sized TiO_2 are considered.

III. Synthesis of nano-sized TiO_2 based on titanium alkoxides; product dispersion and phase composition

In the synthesis of TiO_2 from alkoxides, titanium tetraisopropoxide (from hereon, isopropoxide) and titanium tetrabutoxide (butoxide) are preferred.

Colloid solutions of TiO_2 with different particle sizes and stability were synthesized[52] from acetylacetone-modified $Ti(OPr^i)_4$ using organic solvents that differed in polarity and molar volume. According to data from X-ray phase analysis, irrespective of the nature of organic solvents used in the hydrolysis, all freshly prepared sols obtained both with or without acetylacetone contained amorphous TiO_2 that was transformed into the nanocrystalline anatase phase when heated to 450 °C. However, the use of solvents with small molar volumes and modification of the precursor with acetylacetone resulted in stabilization of the TiO_2 colloid solution, which actually was the principal result of the study cited above. An IR spectroscopic investigation suggested the formation of a chelate complex of titanium isopropoxide with acetylacetone (Fig. 4), which presumably slowed down the hydrolysis and condensation and, hence, decreased the degree of agglomeration of TiO_2 particles; the effect of solvent on the aggregate size (Fig. 5) was rationalized in terms of the Hansen solubility parameters. The Hansen solubility parameters found for TiO_2 samples prepared in different solvents in the presence of acetylacetone may be useful in the synthesis of stable colloidal TiO_2.

The data of the size of TiO_2 particles in colloid solutions and the degree of their aggregation in dry powders were obtained using light scattering, scanning electron microscopy (SEM) and TEM.[52]

Titanium isopropoxide, diethanolamine (DEA) and ethanol (3 : 1 : 20 by volume) were used[53] as the starting reagents in the fabrication of TiO_2 sols. The mixing order played an important role. Thus the introduction of EtOH before DEA led to very fast sedimentation of TiO_2 due to the high reactivity of the alkoxide in ethanol. Hence, first, half volume of ethanol was mixed with DEA and then titanium isopropoxide was added; the mixture was stirred for 30 min and the remaining amount of EtOH was added. The resulting mixture was vigorously stirred at room temperature. The obtained sol was stable for a week and then transformed into gel. A considerable increase in sol stability was observed with a decrease in its stirring time.

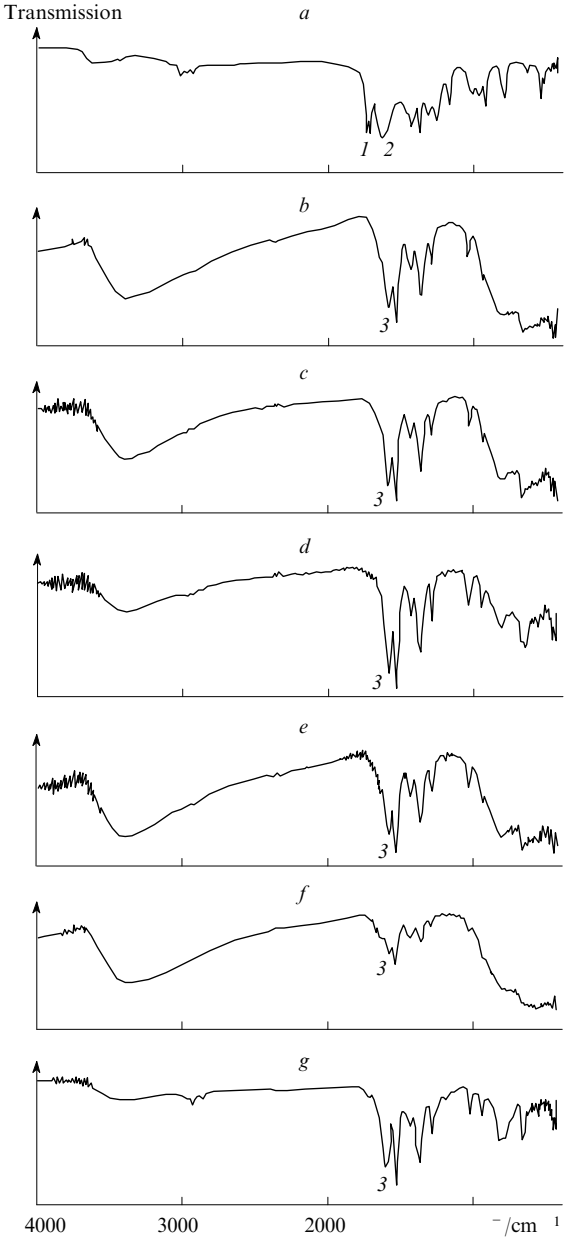

Figure 4. IR spectra of acetylacetone (*a*) and titanium dioxide sols prepared in the presence of acetylacetone in different organic solvents: THF (*b*), acetone (*c*), butanol (*d*), chloroform (*e*), toluene (*f*), hexane (*g*).[52]
(*1*) Peak of the C═O group of the keto form, (*2*) peak of the C═O group of the enol form, (*3*) peak of the C═O group of the chelate complex.

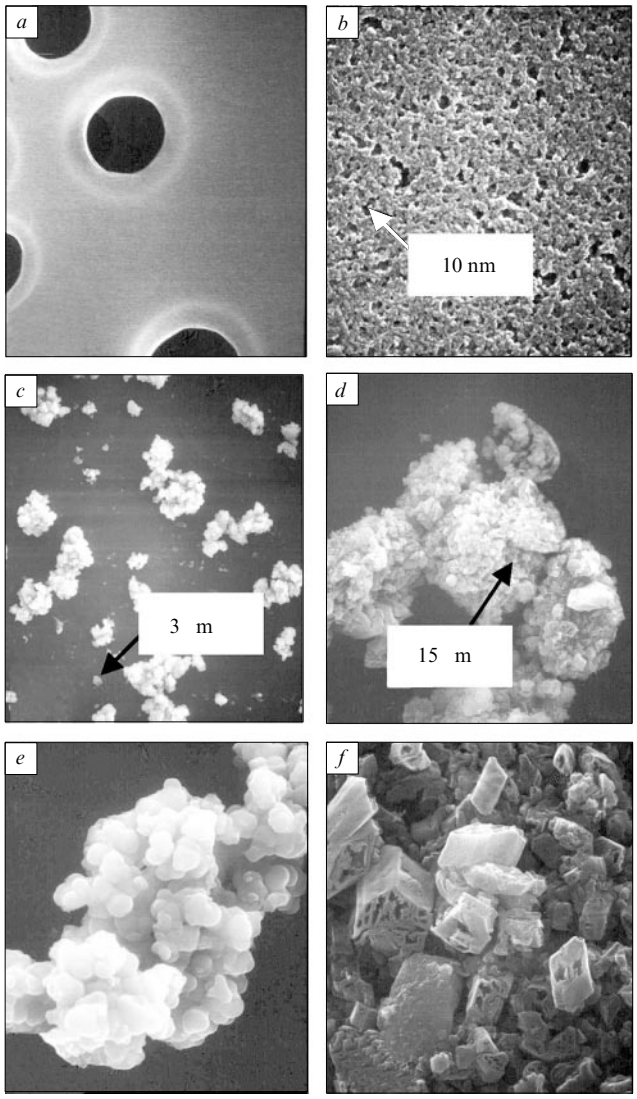

Figure 5. SEM microimages of titanium dioxide sols synthesized in the presence of acetylacetone in acetone (*a*), butanol (*b*), toluene (*c*, *e*) and hexane (*d*, *f*).[52]
Images (*e*) and (*f*) were obtained at larger magnification.

The sol stability also substantially increased under low humidity conditions. In the course of drying, the formation of a xerogel considerably 'shrinked' as compared with the starting gel was observed, the volume decreased five- to tenfold.

A pure anatase phase with particle sizes of 10–20 nm was prepared[54] by a very simple low-temperature (100 °C) procedure using only water as the medium and titanium isopropoxide as the precursor (without additives). The size, shape and phase composition of particles were studied by X-ray phase analysis and TEM.

Nanoparticles of TiO_2 obtained by hydrolysis of $Ti(OPr^i)_4$ at various pH were studied.[55] For the subsequent preparation of nanopowders with narrow size distribution, the final suspension was peptized. The effect of pH on the size and morphology of particles in nanopowders was evaluated. According to XRD, SEM and TEM data, the as-prepared powders entirely consisted of the anatase crystalline phase. Only the powder prepared in a strongly acidic solution contained fine spherical particles. It was shown that the anatase to rutile transformation occurred at temperatures below 600 °C.

In a different study,[56] the preparation of colloidal titania with the concentration of 0.9 mol litre ^{1} involved hydrolysis of titanium isopropoxide in a mixture of isopropyl alcohol with 2 M hydrochloric acid.

In yet another study,[57] the synthesis of nanostructural films involved the preparation of a TiO_2 sol by hydrolysis of titanium isopropoxide in a mixture of ethanol with hydrochloric acid (molar ratio $Ti(OPr^i)_4 : HCl : EtOH : H_2O = 1 : 1.1 : 10 : 10$), which was followed by the addition of an

aqueous methylcellulose (MC) solution. It was shown that an increase in the water content and the sol dilution retards gelation.

Calcination of a titanium dioxide sol afforded TiO_2 nanopowder to be used in the preparation of homogeneous suspensions for the purpose of producing films. The stability of TiO_2 suspensions was investigaed [57] by measuring the sedimentation rate. The anatase powder concentration in liquid was varied (5 mass % – 10 mass %) in the presence and in the absence of MC. It was shown that the sedimentation rate of the TiO_2 nanopowder sharply decreased in the presence of MC. For example, in 5% and 10% suspensions containing no MC, the sedimentation took 1 h and 30 min, respectively, whereas, in the presence of MC the 5% suspension remained stable for 3 days and the beginning of the settlement in 10% suspension began after 10 h. Thus, MC served as the dispersant. The SEM data pointed to a considerable increase in homogeneity and uniformity of TiO_2 films and their higher specific surface in the presence of MC (Fig. 6).

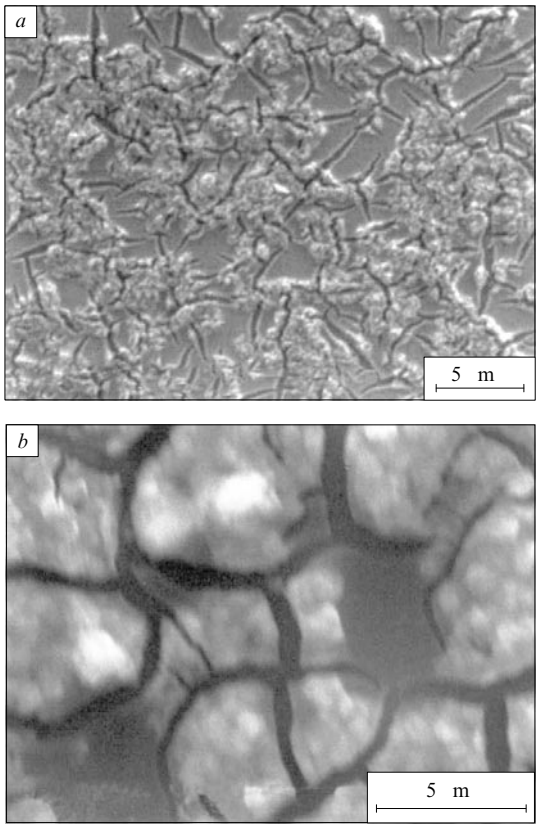

Figure 6. SEM microimages of TiO_2 films after thermal treatment at 500 °C of samples with addition of (*a*) and without methylcellulose (*b*).[57]

The synthesis of nano-sized TiO_2 by the sol – gel method on the basis of titanium isopropoxide was carried out in the presence of a peptide, poly-L-lysine (PLL), as an additive.[58] In this case, peptide served not only as the dispersant but also as the structure-determining additive: it was only in the presence of PLL that tubular TiO_2 particles were formed (Fig. 7 *a*). The particles retained their shape after calcination at 700 °C (Fig. 7 *b*). For a sample obtained in the absence of PLL, calcination at the same temperature led to

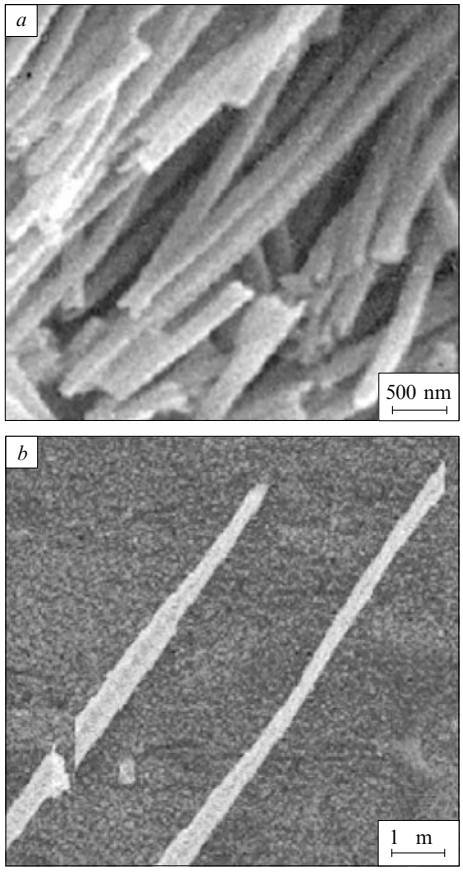

Figure 7. SEM microimages of TiO_2 syntheized in the presence of poly-L-lysine.[58]
(*a*) As-prepared sample, (*b*) sample after calcination at 700 °C.

titanium dioxide with irregular structure (Fig. 8). According to XRD data, titanium dioxide obtained in the presence of PLL and calcined at 700 °C represented anatase with a rutile admixture. In TEM microimages, nanoparticles with the anatase diffraction pattern looked as either coupled tubes with the diameter of 20 nm and the Y-shaped junction in the lower part or nanorods with the diameter from 10 to 25 nm. Materials based on nano-sized TiO_2 with the tubular structure can successfully be used in medicine, biotechnology, microelectronics, optics, *etc*.[58]

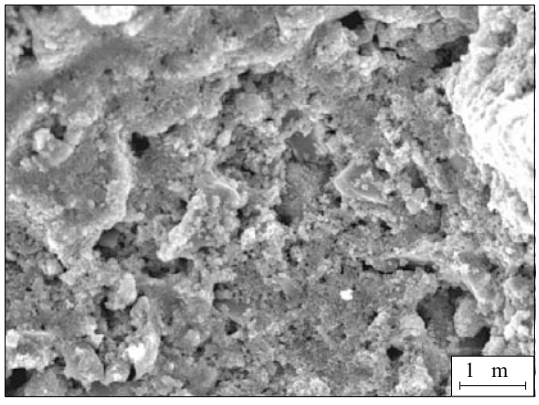

Figure 8. SEM microimage of a TiO_2 sample prepared without poly-L-lysine after calcination at 700 °C.[58]

Nano-sized mixed colloids with the composition PAA – TiO_2 [PAA is poly(acrylic acid)] were synthesized [59] by an *in situ* sol – gel method using titanium isopropoxide and a PAA solution in butanol. Depending on whether tutanium isopropoxide was added before or after the complete dissolution of PAA, the solid phase separation and gelation scenarios differed; however, after heating, stable colloidal solutions were formed in both cases. To confirm the presence of interactions between PAA and Ti, the PAA : isopropoxide : water molar ratio was varied. The formation of chelate complexes was reliably confirmed by IR spectroscopy. Differential scanning calorimetry (DSC) also demonstrated strong interaction between PAA and Ti, which confined the motion of PAA chains. Moreover, according to the data from thermogravimetric analysis (TGA), the thermal stability of PAA chelate was higher as compared with the free acid. On the whole, as followed from TEM results, the order in which reagents were mixed and the PAA : isopropoxide : water molar ratio substantially affected the size and the shape of PAA – TiO_2 hybrid aggregates and the degree of aggregation.[59]

Nanocrystalline TiO_2 was deposited from an ethanolic solution of titanium isopropoxide and hydrogen peroxide by refluxing at 80 °C for 2 days.[60] The resulting particles were filtered and dried at 100 °C. Elucidation of the role of subsequent treatment on the physicochemical and electrochemical properties of nanocrystalline TiO_2 was carried out using XRD and TEM of as-prepared powder, a sample calcined at 400 °C and a sample following sonication. According to the data from X-ray diffraction analysis, all samples represented the anatase phase. The TEM studies have shown that the dried sample consisted of uniform spherical particles measuring 5 nm. In the sample calcined at 400 °C, the particles retained their spherical shape but their size increased to 10 nm. The sample subjected to sonication for 5 h contained a considerable fraction of particles with the average diameter of 5 nm and the length of 20 nm.

Mesoporous titanium dioxide with bimodal pore size distribution was prepared [61] by sonication-assisted hydrolysis of titanium isopropoxide in EtOH : water with the molar ratio equal to 1:1 (sample R1) and 10:1 (sample R10) and also in pure water (sample R0). According to data from XRD, nanostructured xerogels formed after drying the hydrolysis products of R0, R1 and R10 at 100 °C represented an anatase and brookite mixture, pure anatase and the amorphous TiO_2 phase, respectively.

With the increase in calcination temperature, substantial changes in the qualitative and quantitative composition of the samples studied were observed (Fig. 9). Thus in R0 sample, the rutile phase appeared as soon as at 600 °C when the brookite phase was still present in a noticeable amount; at 700 °C, virtually all anatase was transformed to rutile. In R1 sample, small amount of brookite appeared at 400 °C but disappeared at 600 °C. This was accompanied by an increase in the anatase fraction, but the rutile admixture also appeared. At 700 °C, approximately half amount of anatase transformed to rutile. For amorphous xerogel R10, anatase nanocrystals appeared only at 373 °C and underwent no phase transitions up to 600 °C. Only at 700 °C, the transformation of anatase to rutile started.

Figure 10 shows that phase transitions in samples R0, R1 and R10 were accompanied by the increase in the size of TiO_2 particles, which was more pronounced at temperatures above 500 °C being associated with the rutile formation. All TiO_2 powders calcined at 400 – 600 °C were characterized by bimodal pore size distributions with maximum pore diameters at 2 – 4 and 16 – 24 nm. At 700 °C, all samples demonstrated monomodal pore size distribution as the result of destruction of fine pores.

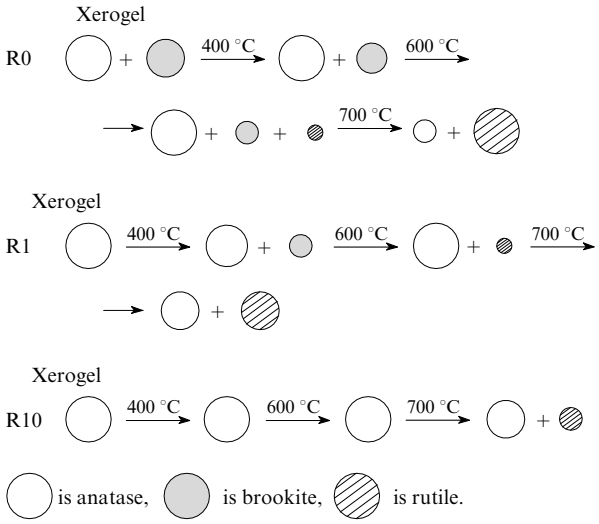

Figure 9. **Fig. 9**. Scheme of phase transformations in samples R0, R1 and R10 (see text) for different calcination temperatures.[61]
The content of individual phases is roughly proportional to the surface of the corresponding circle.

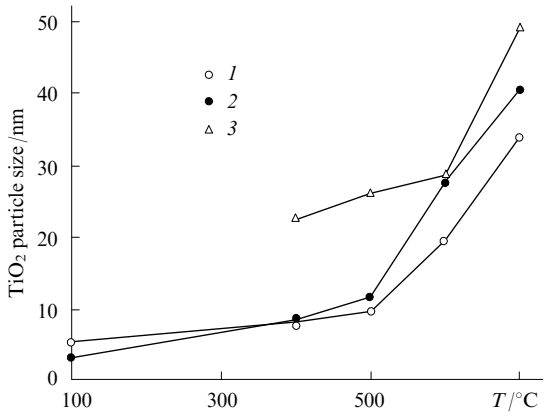

Figure 10. Average particle size of TiO_2 in R0 (*1*), R1 (*2*) and R10 (*3*) samples (see text) at different calcination temperatures.[61]

Pyrolysis of homogeneous TiO_2 gels prepared by hydrolysis of titanium isopropoxide pretreated with formic [62] or oxalic [63] acids with the aim of controlling the gelation process was studied. The amorphous titanium dioxide gel was characterized by FTIR spectroscopy, XRD and N_2 adsorption. Detection, qualitative analysis and identification of organic impurities in the TiO_2 gel and also the determination of the degree of their removal in the course of pyrolysis were carried out by TGA methods in combination with the gas chromatographic analysis and mass spectrometry.

Titanium isopropoxide was diluted with isopropyl alcohol in a flow of nitrogen; then, a carboxylic acid (formic or oxalic) was added with vigorous stirring, which was followed by dropwise addition of hydrochloric acid, which

served as the hydrolysis catalyst. This produced an emulsion that transformed into a uniform gel in 4 days.

The molar ratio $Ti(OPr^i)_4$: carboxylic acid : isopropyl alcohol : water : HCl = 1 : 1 : 20 : 1 : 0.0184 was found to be optimum.[62, 63] However, the physicochemical characteristics of TiO_2 samples synthesized in the presence of formic and oxalic acids[63, 64] substantially differed.

Thus according to N_2 adsorption isotherms, a mesoporous material was formed in the presence of HCOOH that was characterized by specific surface of 480 m^2 g^{-1} and the average pore diameter of 2.7 nm.[62] IR Spectroscopic studies showed that the sample contained Ti O Ti fragments, formate groups coordinated with titanium and non-hydrolyzed titanium isopropoxide. Absorption bands belonging to organic impurities in the TiO_2 gel completely disappeared upon heating the samples above 340 °C. According to data from XRD, the gel represented an amorphous product that crystallized at temperatures above 400 °C to form the anatase phase.

According to the data on N_2 adsorption, the sample formed in the presence of $(COOH)_2$ represented a macroporous material with specific surface of 18 m^2 g^{-1} and the average pore diameter of 24.4 nm.[63] IR Spectroscopic studies showed that titanium dioxide samples contained oxalate groups coordinated with titanium and also non-hydrolysed titanium isopropoxide. Absorption bands of organic impurities in the TiO_2 gel completely disappeared in samples heated above 550 °C. According to data from XRD, the original gel also represented an amorphous product (*cf.* Ref. 62), but the anatase crystallization occurred at temperatures above 550 °C.

As was shown by different physicochemical methods (XRD, IR spectroscopy, TGA, electron spectroscopy of diffuse reflectance (ESDR), ammonia thermoprogrammed desorption (TPD), adsorption methods),[64] the introduction of the sulfate ions into TiO_2 decreased the particle size, stabilized the anatase phase and increased both the specific surface and the pore volume (Table 1). The dependences of all parameters on the amount of sulfuric acid added in the impregnation had extrema. The sol–gel hydrolysis product of titanium isopropoxide in the presence of nitric acid was employed for the impregnation. After ageing, the sol formed was concentrated, dried, impregnated with sulfuric acid (0.5 mol $litre^{-1}$, 2–10 ml) and calcined.

Among modified methods for the preparation of nano-sized TiO_2, mention should be made of hydrolysis and condensation of titanium isopropoxide in anhydrous ethanol using a cellophane membrane that makes it possible to control the diffusion rate.[65] Hydrolysis combined with sonication is advantageous controlling the size of titanium dioxide nanoparticles.[66]

TiO_2 Nanoparticles of different shapes (spherical, cubic and hexagonal rods) and sizes (50–500 nm) were prepared from titanium butoxide as the precursor.[67] Hydrolysis of $Ti(OBu^n)_4$ was carried out in the presence of different surfactant compositions and concentrations. The prepared TiO_2 nanoparticles were studied for photocatalytic decomposition of Methyl Orange in fixed film batch reactors. It was shown that the shape is more important than the size: TiO_2 nanorods had higher photocatalytic activities than spherical and cubic TiO_2 nanoparticles.

The dependence of the morphology, the size and the crystal structure of nano-sized crystalline titanium dioxide on the hydrolysis conditions of titanium butoxide was studied in detail.[68] Hydrolysis of $Ti(OBu^n)_4$ was carried out at room temperature in inverse micellar systems formed by an aqueous solution of a mineral acid, cyclohexane and a surfactant Igepal® CO-520 [4-(n-C_9H_{19})$C_6H_4O(CH_2CH_2$. .O)$_4CH_2CH_2OH$]. The effect of the following hydrolysis conditions, such as concentration (c) and type of acid (hydrochloric, nitric, sulfuric or phosphoric), molar content of water [$w = H_2O$: surfactant and $h = H_2O$: $Ti(OBu^n)_4$], and hydrolysis time (t) on the formation, crystal phase, morphology, and size of the TiO_2 particles were investigated.

It was shown that the pH of the reaction medium had a significant effect on the crystal structure of the obtained TiO_2 nanoparticles. For example, according to TEM data, an amorphous product was formed when the hydrochloric acid concentration was below 2 mol $litre^{-1}$, all other conditions being equal. At the HCl concentration of 2 mol $litre^{-1}$, the resulting TiO_2 particles represented a mixture of anatase and rutile. The pure rutile phase was formed as the acid concentration reached 2.5 mol litre[71]. At still higher HCl concentration (to 4 mol $litre^{-1}$), the amorphous TiO_2 was formed again.

In the case of HCl at $c = 2.5$ mol $litre^{-1}$, $h = 28$, $t = 20$ days and $w = 3$, finely disperse shuttle-like TiO_2 nanoparticles with widths 35–40 nm and lengths 150–160 nm with the crystalline structure of rutile were formed. As the parameter w increased from 3 to 5, both the widths and the lengths of the particles increased slightly without changes in their morphology. For $w = 10$, the particles formed petal-shaped aggregates with retention of their crystalline structure. It is believed that the aqueous cores of inverse micelles served as microreactors for the hydrolysis of titanium butoxide. With the increase in parameter w, the number of these micelles increased, they had to coalesce; and thus, shuttle-like rutile nanoparticles from different micelles formed petal-like aggregates with the same crystal phase. However, the anatase phase appeared in aggregates for $w = 12$, probably because micelles were destroyed in the course of reaction with such a high water content.

For $c = 2.5$ mol $litre^{-1}$, $w = 8$, $t = 20$ days, the effect of parameter h was similar to the aforementioned effect of parameter w. For $h < 6$, *i.e.*, below the coordination number of Ti(IV) ions, the amount of water in micelle cores was insufficient for the complete hydrolysis of titanium butoxide. It this case, the crystallization slowed down and amorphous TiO_2 was formed. For $h > 10$, the amorphous product transformed into crystalline rutile. For $h = 10–20$, the nanoparticle size remained virtually unchanged; how-

Table 1. Adsorption characteristics of sulfated TiO_2.[64]

Sample[a]	Specific surface /m^2 g^{-1}	Pore volume /cm^3 g^{-1}	Particle size /nm	Rutile content (%)	Pore diameter /Å
T	35	0.09	12.71	46.6	103.4
ST2	91	0.21	9.62	0	95.0
ST4	98	0.18	8.62	0	74.1
ST6	79	0.12	7.48	0	58.1
ST8	57	0.11	11.05	0	78.4
ST10	48	0.10	11.74	18.3	85.5

[a] The following designations were used: T is the original TiO_2; ST2–ST10 are samples prepared by impregnation with 2, 4, 6, 8 and 10 ml, respectively, of sulfuric acid (0.5 mol $litre^{-1}$).

ever, for $h = 36$, flower-shaped aggregates were formed. High h values accelerated the butoxide hydrolysis and the crystalline TiO_2 particles formed were capable of aggregation both inside the aqueous cores of micelles and also in their environment.

As the hydrolysis time increased from 5 to 10 and 20 days all other conditions remaining standard (see above), the growth of particles with subsequent aggregation and morphological changes (Fig. 11) was observed.

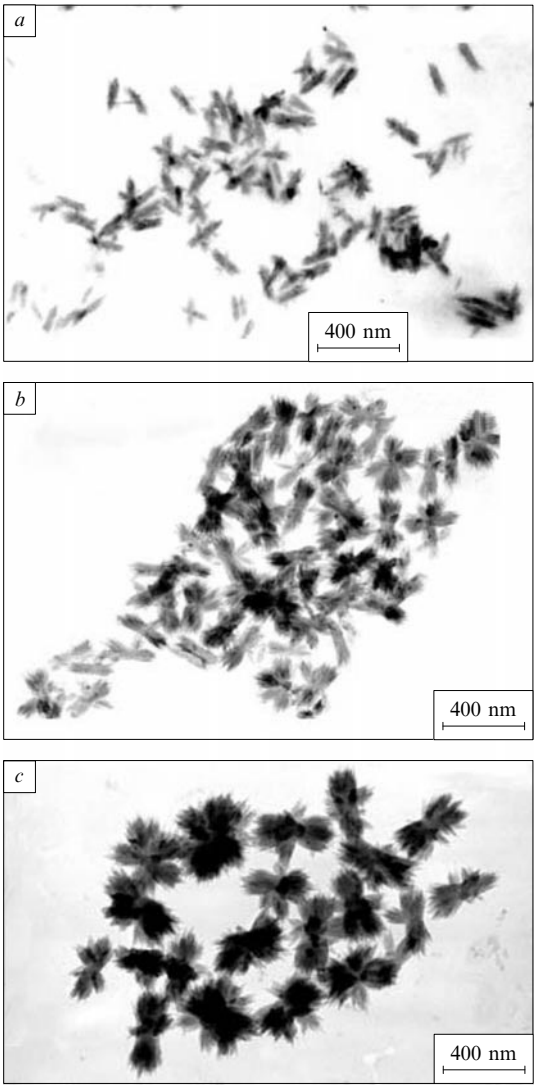

Figure 11. TEM microimages of TiO_2 particles formed upon hydrolysis of $Ti(OBu^n)_4$ under standard conditions for 5 (*a*), 10 (*b*) and 20 days (*c*).[68]

Hydrochloric, nitric, sulfuric and phosphoric acids used to adjust the pH of the medium were employed to examine the effect of the nature of acids.[68] The parameters w and h were taken to be 8 and 28, respectively, and the acid concentration was equivalent to 2.5 M HCl, all other things being the same. The nature of acid was found to substantially affect the crystalline phase composition, morphology and also the size of TiO_2 nanoparticles. Thus substitution of nitric acid for hydrochloric acid decreased the width of shuttle-like particles to 20–25 nm and their length to 120 nm. The use of sulfuric or phosphoric acids irrespectively of their concentration resulted in the formation of amorphous rather than crystalline spherical TiO_2, namely, uniform small spheres with diameter of 40 nm for sulfuric acid and coarse spheres with diameter of 240 nm for phosphoric acid (Fig. 12). Presumably, this can be associated with different affinity of the anions with respect to Ti(IV) ions in aqueous solutions (Cl^- and NO_3^- exhibited weak affinity, while SO_4^{2-} demonstrated strong affinity). The strong affinity of SO_4^{2-} for titanium inhibits the titanium dioxide rearrangement and, hence, the overall crystallization process. It thus follows[68] that phosphoric acid, like sulfuric acid, is the crystallization inhibitor.

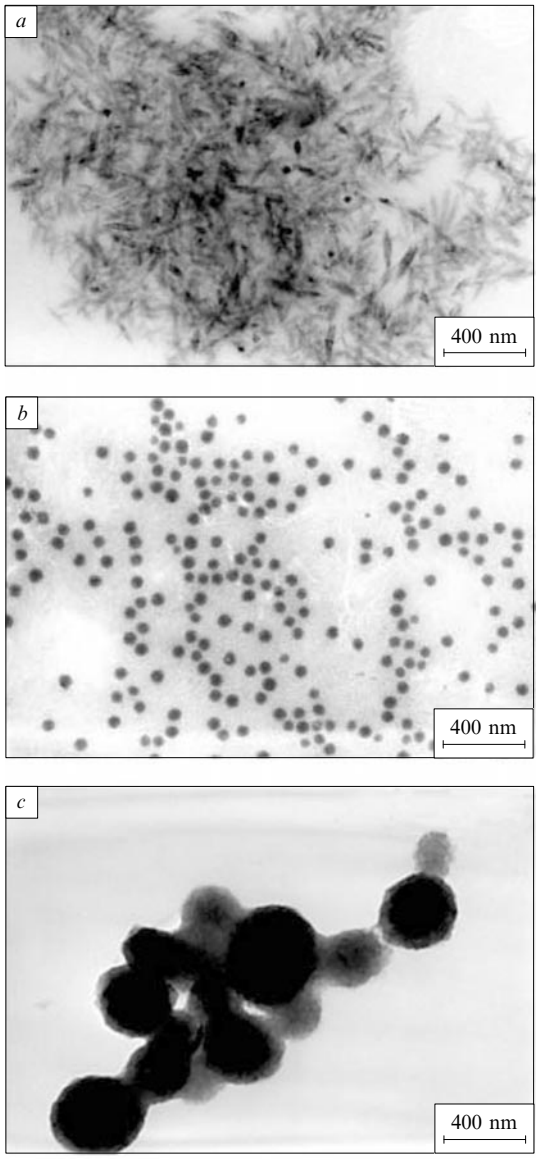

Figure 12. TEM microimages of TiO_2 particles formed upon hydrolysis of $Ti(OBu^n)_4$ in the presence of different mineral acids.[68]
(*a*) Nitric acid, (*b*) sulfuric acid, (*c*) phosphoric acid.

Acetic acid often used in the hydrolysis of titanium-containing precursors can also serve as an efficient stabilizer of the anatase phase in the calcination. Thus the hydrolysis of an acetic-acid solution of $Ti(OPr^i)_4$ with aqueous ammonia at pH 3–4 and 70 °C afforded a gel that showed an

anatase phase even at 1000 °C.[69] However, as the hydrolysis medium pH increased to 5, pure rutile was formed at 1000 °C, whereas at pH 6, anatase to rutile transformation is complete at 800 °C (Table 2), as for samples prepared by hydrolysis in the absence of acetic acid.

Table 2. Phase composition [a] of calcined TiO_2 samples as a function of the pH of acetic acid-containing solution of titanium isopropoxide during the hydrolysis.[69]

Calcination temperature /°C	Hydrolysis medium pH			
	3	4	5	6
1000	A + R	A + R	R	R
800	A + R (traces)	A + R (traces)	A + R	R
600	A	A	A	A
400	A	A	A	A

[a] Used designations: A is anatase, R is rutile.

Monodisperse non-aggregated nanoparticles of titanium dioxide were prepared [70] by hydrolysis of titanium butoxide at 60 °C in the presence of acetylacetone and *p*-toluenesulfonic acid. It was shown that a thorough choice of synthesis conditions that rule out gelation makes it possible to produce particles with the anatase structure and the average size of 1 – 5 nm. It was found [70] that the optimum conditions for synthesizing nanodisperse TiO_2 sols are as follows: the initial molar ratio (a) acetylacetone : metal 1 a 6; the molar ratio $h = H_2O : Ti$ 5 h 10 and the acidity of the medium expressed through the molar ratio $h^+ = H^+ : Ti$, 0 h^+ 0.8. In the mentioned variation ranges of parameters a, h and h^+, the titanium concentration in the sol could change from 0.5 to 1 mol litre $^{-1}$. Drying of a nanodisperse sol to form a xerosol could be accomplished by centrifugation, evaporation of solvent in vacuum at room temperature or by heating at 100 °C.

The prepared xerosol could be dispersed again without aggregation in a water – ethanol or ethanol solution. This afforded sufficiency concentrated sols (> 1 mol litre $^{-1}$ with respect to titanium) containing TiO_2 particles with the size of 1 – 5 nm, the same as in the original sol.[70] This was proved by the data from TEM and quasi-elastic light scattering. The use of other physicochemical research methods (XRD, IR spectroscopy, ^{13}C, ^{17}O and ^{1}H NMR, mass spectrometry, *etc.*) in studying TiO_2 nanoparticles has shown that particles were protected from aggregation by complexes with acetylacetone formed on their surface, which agreed with other results,[52] and also by a mixed organic-inorganic adsorption layer formed from acetylacetone, *p*-toluenesulfonic acid and water.

Nanodisperse (particle size 3.8 nm) pure anatase with the specific surface of 359.1 m^2 g $^{-1}$ was prepared based on the same precursor, *i.e.*, titanium butoxide.[71]

IV. Nano-sized TiO_2 synthesis based on $TiCl_4$; product dispersion and phase composition

Titanium tetrachloride belongs to the most widely used titanium dioxide precursors; it was employed in both the synthesis of substrates and catalysts by the precipitation method [72, 73] and preparation of nano-sized TiO_2 colloid solutions by the sol – gel method.

Thus a colloid solution of TiO_2 nanoparticles (40 – 60 Å), was prepared [74, 75] in an inert medium by dropwise addition of a $TiCl_4$ solution to cold water (pH 3.5 – 4.0). The temperature and the reactant mixing rate were regulated by an apparatus designed for automatic preparation of colloid systems.[76] The TiO_2 concentration (0.1 – 0.6 mol litre $^{-1}$) was determined from the concentration of the peroxide complex after dissolving the colloid in concentrated sulfuric acid by a known procedure.[77] The possibility of preparation of surface complexes of titanium dioxide colloid nanoparticles with cysteine to be used in photocatalysis was demonstrated.[74, 75]

Titanium dioxide was also synthesized [78] by thermal hydrolysis of $TiCl_4$ in a propanol – water mixture. The dependence of the precipitate morphology on the propanol : water volume ratio, the $TiCl_4$ concentration, temperature and the presence of a dispersant, namely, hydroxylpropylcellulose (HPC), was studied. It was shown that titanium dioxide prepared in a 3:1 (by volume) propanol : water mixture contained uniform-dispersed spherical particles. With the addition of HPC, the nanoparticle size distribution became narrower. The spherical shape of TiO_2 particles was independent of the $TiCl_4$ concentration, but their sizes increased with an increase in the suspension concentration. An increase in the synthesis temperature favoured the broader size distributions of particles. The effect of the liquid-phase temperature gradient on the morphology of TiO_2 particles was also noted. The morphology and size of titanium dioxide particles were studied by SEM and TEM methods; phase transitions were investigated by the XRD method.

In another study,[79] titanium dioxide was synthesized by the hydrolysis of $TiCl_4$ in a strongly acidic aqueous solution in the absence and in the presence of poly(ethylene glycol) PEG-1000 that served as the dispersant for controlling the shape and size of the TiO_2 particles. It was shown that in the absence of PEG-1000, uniform shuttle-shaped TiO_2 nanocrystals were formed and the degree of their aggregation increased with an increase in the acid content and a decrease in the $TiCl_4$ concentration. In the presence of PEG-1000, TiO_2 particles with sufficiently narrow size distributions were prepared, with the particle diameter decreasing with an increase in the PEG-1000 amount. The process was characterized by simplicity and a low cost and could be carried out in a continuous mode. The products were studied by the XRD and TEM methods.

In yet another study,[80] titanium dioxide sols were prepared by acid hydrolysis of $TiCl_4$ (pH of the medium was adjusted by addition of an ammonia solution), followed by peptization of precipitates with nitric acid. Stable titania sol (particle size 14 nm) was prepared at the molar ratio $H^+ : Ti = 0.5$ with vigorous stirring for 1 day at 70 °C (Table 3). It is remarkable that the activity of TiO_2 in photocatalytic reactions was largely determined by the degree of dispersion of TiO_2 rather than by the promoting effect of modifying additives (0.5% Pt or 10% of Si, Zr, W, Mo oxides) introduced into TiO_2 to increase its activity.

Nanosized TiO_2 powders prepared by controlled hydrolysis of $TiCl_4$ in aqueous solutions in the presence of small amounts of sulfate ions were studied [81] by TEM, high-resolution EM, XRD and electron diffraction; the specific surface was determined from adsorption isotherms using the Brunauer – Emmett – Teller (BET) equation. It was shown that the hydrolysis of $TiCl_4$ at 70 °C carried out in the presence of the sulfate ions produced a powder that con-

Table 3. TiO_2 sol particle size at different concentrations of HNO_3 (TiO_2 concentration 0.3125 mol litre $^{-1}$).[80]

H^+ : Ti (mol.)	Particle size /nm	Sol stability
0.08		precipitate was not peptized
0.2	102	stable
0.4	45	
0.5	14	
0.7	56	
1.0	96	
1.2		unstable

sisted of the pure anatase phase with the predominant particle size of 3.5 nm, which is much smaller than in powders prepared from titanium alkoxides. Moreover, the anatase–rutile phase transformation retarded. However, at the same hydrolysis temperature but in the absence of the sulfate ions, the product represented a mixture of anatase and rutile, the primary particle size in the rutile phase was 4.3 nm. Hydrolysis at 20 °C led to TiO_2 powders with the amorphous structure and high specific surfaces (500 m^2 g^{-1}). According to the electron spectroscopic data, the presence of the sulfate ions accelerated the anatase phase formation.

According to the literature data, from the practical viewpoint, TiO_2 in the form of anatase is often preferred to rutile. Optical and electrochemical properties of anatase and the third modification of titanium dioxide, *i.e.*, brookite, were compared and the conditions of synthesis of each phase by the sol–gel method were described.[82] It was demonstrated that the formation of one or another phase was determined by not only the pH of the solution, but also the molar ratio Cl : Ti, which was controlled in the interval 17–35 by the addition of NaCl. In addition, the simultaneously formed brookite and rutile phases were characterized by different degrees of dispersion and could easily be separated.

Studies by XRD and Raman spectroscopy[83] revealed traces of brookite in anatase in nano-sized TiO_2 samples prepared by precipitation from $TiCl_4$ at different pH. The average size of TiO_2 crystals after 2-h treatment at 450 °C was 7–9 nm. The lattice parameter *c* of anatase increased as the pH of the medium increased during the synthesis, while the volume fraction of the brookite phase increased with a decrease in pH. It was shown that the temperature range of anatase transformation to rutile shifted to low temperatures as the brookite volume fraction increased, *i.e.*, the brookite phase was to a certain extent responsible for the anatase transformation to rutile.

A simple method of synthesis of high purity brookite nanoparticles was described.[84] Hydrolysis of $TiCl_4$ was carried out in acidified isopropyl alcohol at ambient temperature and the peptization and crystallization of the gel formed occurred on refluxing. The data from SEM and TEM revealed the formation of spherical TiO_2 with the average size of 30 nm. The data from XRD confirmed the presence of the brookite crystalline structure. The degree of particle agglomeration could be predicted based on the amount of heat released during the hydrolysis of $TiCl_4$.

Ultradisperse TiO_2 samples with the structures of anatase, rutile and their mixture assayed for the photocatalytic degradation of phenol were synthesized[85,86] by hydrolysis of $TiCl_4$. The resulting product was studied by high resolution EM, XRD, BET and electron spectroscopy. In the catalytic process mentioned, the highest selectivity (very low concentrations of side products, namely, *p*-benzoquinone and hydroquinone) was observed for catalyst particles in the anatase phase measuring 4 nm, whereas rutile particles of the same size exhibited selectivity that differed insignificantly from that of coarse-grain rutile. Presumably, calcination was effective in increasing the activity of the TiO_2 catalyst because this favoured perfection of its crystal structure.

The addition of $(NH_4)_2SO_4$ and adjustment of the pH to 7 (with NH_4OH) resulted in anatase in the final stage; in the absence of ammonium sulfate, a mixture of anatase and rutile was formed. To prepare rutile, the same process was carried out without both ammonium sulfate and ammonium hydroxide. In each case, the hydrolysis product represented titanium dioxide hydrate ($TiO_2 \cdot n\,H_2O$), which was centrifuged off, dried and, if necessary, calcined.

Nanodisperse titanium dioxide was fabricated[87] by CO_2-laser-assisted pyrolysis of $TiCl_4$ in a gas–vapour mixture. The effect of synthesis conditions, namely, the laser power and the oxidant (air) delivery rate, on the structural characteristics of synthesized TiO_2 was studied. It was shown that moderate acceleration of the air delivery increased the degree of crystallinity, the grain size, and the rutile content.

V. Synthesis of TiO_2 based of miscellaneous titanium-containing precursors

Besides alkoxides and $TiCl_4$, yet another TiO_2 precursor used in the preparation of anatase nanocrystals, namely, ammonium dihydroxodilactatotitanate(IV) (ALT), deserves mention.[88] According to the available published data, this compound attracted attention as the starting material in the preparation of catalysts,[89] fabrication of electrodes for medicinal purposes[90] and production of UV-radiation-proof films on different surfaces.[91] In contrast to titanium alkoxides that are rapidly hydrolyzed, ALT is stable in neutral solutions at ambient temperatures and decomposes to form TiO_2 (anatase), NH_3 and sodium lactate only above 100 °C or in aqueous NaOH solutions. However, even under these conditions, ALT hydrolysizes more slowly; this makes it possible to synthesize nanocrystalline TiO_2 with predominantly oblate-shaped particles and a narrow size distribution; the latter is especially important for the synthesis of TiO_2 films.

Studies on ALT thermohydrolysis (up to 300 °C in hermetically sealed glass tubes or in a titanium autoclave has shown[88] that the size of formed anatase nanoparticles increased with the increase in the hydrolysis temperature (Fig. 13) and ALT concentration. Thus, it can be regulated by varying these parameters. In all the cases, extremely narrow particle size distributions were obtained. With the addition of ammonium lactate to the reaction mixture, the effects of ALT concentration and the reaction time on the size of TiO_2 particles became negligibly small, and the growth of particles stopped. This simple trick can be used for the interruption of the process to afford high yields of virtually uniform size anatase nanocrystals. The final product contains no admixtures (ions Cl^-, Na^+).

Nanocrystalline TiO_2 was prepared[92] using an unconventional method, namely, plasma synthesis from a titanium hydride TiH_2 powder.

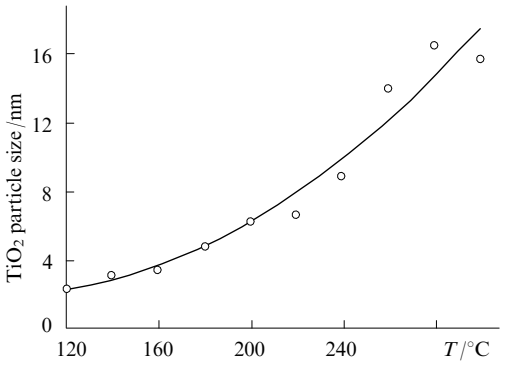

Figure 13. Dependence of the average TiO_2 particle size on the hydrolysis temperature.[88]
ALT Concentration in water is 0.415 mol litre $^{-1}$, duration of process is 24 h.

VI. Stabilization of the disperse state and phase composition of nano-sized TiO_2 sols

Despite the efficacy of using the sol–gel method for the synthesis of nanocrystalline TiO_2 sols, the pronounced trend of TiO_2 particles to aggregation during both the hydrolysis of a titanium-containing precursor and long-term storage of sols still remains the main problem of this method; aggregation is often accompanied by variations in the phase composition. The analysis of published data allowed the ways for solving this problem to be outlined.

Thus an acidic medium (pH = 1.8) and a low storage temperature (4 °C) favoured higher stability of TiO_2 colloid solutions.[22] Moreover, the stability of non-aqueous sols tended to increase under low humidity conditions.[53] The nature of solvent also affected the size and the stability of TiO_2 colloid particles.[52] On the whole, the majority of studies stressed that strict observance of the synthesis conditions (pH, temperature, precursor concentration) and also of the stoichiometric ratio of the reactants and the addition order is very important for the targeted synthesis of TiO_2 with desired properties.[53, 59, 68–70]

Stable nanodisperse TiO_2 sols can be prepared if organic disaggregating and stabilizing additives, namely, acetylacetone,[52, 70] diethanolamine,[53] polyacrylic acid,[59] methylcellulose,[57] hydroxypropylcellulose,[78] poly(ethylene glycol),[79] *etc.*, are introduced into the reaction mixture. Disaggregating additives operate through different mechanisms, namely, the inhibition of hydrolysis and condensation,[52, 53] which favoured the lower degree of aggregation of particles; the formation of surface organic-inorganic complexes with TiO_2 nanoparticles, which prevented aggregation;[52, 70] the shift of balance of attractive and repulsive forces as a result of which the sedimentation rate decreased.[57]

One of the most popullar methods of sol stabilization was the peptization of the hydrolysis product (after its centrifugation and rinsing with water) with nitric acid on vigorous stirring. The peptized precipitate was again centrifuged and dispersed in water.[80, 82]

In certain practical applications of nano-sized TiO_2, the stabilization of its phase composition was of no less importance than the definite size of nanoparticles. The amorphous TiO_2 phase was as a rule formed upon hydrolysis at 20 °C.[45, 81] The sol–gel method not only provided a possibility for regulation and reproduction of the ratio of TiO_2 crystal phases (anatase, rutile and brookite) in the final product, but also allowed preparation of each phase in its pure form. Like the control over the grain size of TiO_2, this was achieved[70] by accurate choice of the conditions of hydrolysis of titanium-containing precursors (pH, temperature, time, ratio of main components).[22, 68, 81, 82, 85, 93, 94]

Certain specific conditions for the formation of different TiO_2 phase compositions were mentioned. For example, the hydrolysis of $TiCl_4$ (Ref. 81) or titanium isopropoxide[64] in the presence of a small amount of the sulfate ions favoured the formation of the individual anatase phase, whereas in the absence of the sulfate ions, a mixture of anatase and rutile was formed under the same conditions.[64, 81] However, it was shown[68] that the strong affinity of SO_4^{2-} ions for titanium suppressed rearrangement of titanium dioxide and, hence, the overall crystallization process.

From the viewpoint of synthesizing pure anatase, it was of interest to use titanyl sulfate as the precursor. The substitution of an aqueous solution of $TiOSO_4$ (0.25 mol litre $^{-1}$) for the amorphous $TiO_2 \cdot n\,H_2O$ gel in the hydrothermal synthesis of nano-sized TiO_2 decreased the temperature of anatase formation from 250 to 150 °C, all other conditions being the same.[95] According to Table 4, this afforded highly disperse anatase with the particle size that increased with the increase in the temperature of hydrothermal treatment to 250 °C but nonetheless remained smaller than in anatase synthesized from amorphous TiO_2 gel. With the increase in the $TiOSO_4$ solution concentration to 0.44 mol litre $^{-1}$, the anatase particle size increased and the use of a $TiOSO_4$ solution in sulfuric acid (0.25 mol litre $^{-1}$) led to the appearance of the rutile phase at 250 °C. This is consistent with the data of Ref. 64 (see Table 1).

The synthesis of pure and stable nano-sized anatase was described[49, 50] (hydrothermal and solvothermal syntheses). Acetic acid added in the stage of hydrolysis strictly at pH 3–4 served as an efficient agent for stabilizing the anatase phase up to 1000 °C (see Table 2).[69]

As was mentioned above, non-standard titanium-containing precursors and synthesis conditions were sometimes used in the preparation of pure anatase and for controlling the quantitative ratio of anatase, rutile and brookite.[60, 65, 66, 88, 92]

Table 4. Grain size of nanocrystalline anatase prepared by hydrothermal synthesis from an amorphous $TiO_2 \cdot n\,H_2O$ gel and an aqueous $TiOSO_4$ solution.[95]

Precursor	Concentration /mol litre $^{-1}$	Synthesis conditions		Particle size[a] /nm		Specific surface[a] /m^2 g $^{-1}$
		T/°C	time	XRD	TEM	
Gel		250	10 min	27	35	60
$TiO_2 \cdot n\,H_2O$		250	6 x	28	38	
$TiOSO_4$	0.25	250	10 min	16	20	
in water		250	6 h	18	24	
		150	10 min	10	8	
		150	6 h	14	16	
	0.44	250	6 h	20	28	98
$TiOSO_4$	0.25	250	10 min	24	26	
in 1 M H_2SO_4		250	6 h	see[b]	22	

[a] These parameters were determined with the accuracy of ±10%.
[b] In this case, a mixture of anatase (85%) and rutile (15%) was formed; the particle size was 20 nm for anatase and 30 nm for rutile.

* * *

The material of the present review clearly demonstrated that the problem of synthesizing stable forms of nano-sized titanium dioxide is being successfully solved. Materials with desired structural and morphological characteristics were fabricated using either conventional methods by scrupulous selecting synthesis conditions or by new approaches (new reactants, unusual methods of treatment of the reaction mixtures, improved instrumental implementation). It can be assumed that the directions of further studies in this field will be determined by the requirements imposed by practical application of nano-sized TiO_2, first of all, in medicine. The first positive results in this field will undoubtedly attract attention of scientists and engineers and the quest for new applications of nano-sized TiO_2 will pose new problems for synthetic chemists.

This review was prepared with financial support by the Russian Foundation for Basic Research (Project No. 08-04-01045-a), the Siberian Branch of the Russian Academy of Sciences (Integration Project No. 61), Programmes of the Ministry for Education and Science of the Russian Federation 'Development of the Scientific Potential of the Higher School' (Project No. 2.1.1/5642).

References

1. D T Ros, G Spalluto, A S Boutorine, R V Bensasson, M Prato *Curr. Pharm. Des.* **7** 1781 (2001)
2. D G Knorre, V V Vlasov, V F Zarytova, A V Lebedev, O S Fedorova *Design and Targeted Reactions of Oligonucleotide Derivatives* (Boca Raton, FL: CRC Press, 1994)
3. D T Ros, G Spalluto, M Prato, T Saison-Behmoaras, A S Boutorine, B Cacciari *Curr. Med. Chem.* **12** 71 (2005)
4. M Ferrary *Curr. Opin. Chem. Biol.* **9** 343 (2005)
5. R Beutner, J Michael, A Förster, B Schwenzer, D Scharnweber *Biomaterials* **30** 2774 (2009)
6. T Paunesku, T Rajh, G Wiederrecht, J Maser, S Vogt, N Stojicevic, M Protic, B Lai, J Oryhon, M Thurnauer, G Woloschak *Nat. Mater.* **2** 343 (2003)
7. T Matsunaga, R Tomoda, T Nakajima, H Wake *FEMS Microbiol. Lett.* **29** 211 (1985)
8. B Kim, D Kim, D Cho, S Cho *Chemosphere* **52** 277 (2003)
9. N Suketa, T Sawase, H Kitaura, M Naito, K Baba, K Nakayama, A Wennerberg, M Atsuta *Clin. Implant Dent. Relat. Res.* **7** 105 (2005)
10. Y Lan, C Hu, X Hu, J Qu *Appl. Catal., B: Environ.* **73** 354 (2007)
11. L Zan, W Fa, T Peng, Z-K Gong *J. Photochem. Photobiol., B* **86** 165 (2007)
12. A-G Rincón, C Pulgarin *Appl. Catal., B: Environ.* **49** 99 (2004)
13. M F Dadjour, C Ogino, S Matsumura, N Shimizu *Biochem. Eng. J.* **25** 243 (2005)
14. P Hajkova, P Spatenka, J Horsky, I Horska, A Kolouch *Plasma Process. Polym.* **4** S397 (2007)
15. US P. 0071790 (2003)
16. US P. 02640 (2007)
17. Ch Göbbert, in *Handbook for Clearing/Decontamination of Surfaces* (Eds I Johansson, P Somasundaran) (Amsterdam: Elsevier, 2007) p. 813
18. Y Zhao, S Sugiyama, T Miller, X Miao *Exp. Rev. Med. Devices* **5** 395 (2008)
19. A Fujishima, R Cai, J Otsuki, K Hashimoto, K Itoh, T Yamashita, Y Kubota *Electrochim. Acta* **38** 153 (1993)
20. A Mills, S Hunte *J. Photochem. Photobiol., A* **108** 1 (1997)
21. A Fujishima, T Rao, D Tryk *J. Photochem. Photobiol., C* **1** 1 (2000)
22. A P Zhang, Y P Sun *World J. Gastroenterol.* **10** 3191 (2004)
23. V F Zarytova, A S Levina, M N Repkova, A S Ivanyi, Z R Ismagilov, N V Shikina, V V Zinovjev, E F Belanov, E G Malygin, S N Zagrebelnyi, S I Baiborodin, in *Materials of the 6th International Conference 'High Medical Technologies in XXI Century', Benidorm, Spain, 2007* p. 73
24. N V Shikina, Z R Ismagilov, F V Tuzikov, L T Tsikoza, V F Zarytova, V V Zinoviev, S N Zagrebelnyi, in *Tezisy Dokladov Vserossiiskoi Konferentsii s Mezhdunarodnym Uchastiem 'KATEK-2007', Sankt-Peterburg, 2007* (Abstracts of Reports of the All-Russian Conference with International Participation 'KATEK-2007', St Petersburg, 2007) p. 302
25. V Zinoviev, A Evdokimov, E Belanov, E Malygin, S Balachnin, O Serova, D Pletnev, V Zarytova, A Levina, M Repkova, Z Ismagilov, N Shikina, S Zagrebelnyi, S Baiborodin *Antiviral Res.* **78** A51 (2008)
26. V F Zarytova, A S Levina, M N Repkova, A S Pavlova, V V Zinov'ev, A A Evdokimov, E F Belanov, S M Balakhnin, E G Malygin, Z R Ismagilov, N V Shikina, S I Baiborodin, S N Zagrebelnyi, in *Materialy IV S'ezda Rossiiskogo Obshchestva Biokhimikov i Molekulyarnykh Biologov, Novosibirsk, 2008* (Proceedings of IVth Congress of Russian Society of Biochemists and Molecular Biologists, Novosibirsk, 2008) p. 315
27. V F Zarytova, V V Zinoviev, Z R Ismagilov, A S Levina, M N Repkova, N V Shikina, A A Evdokimov, E F Belanov, S M Balakhnin, O A Serova, S I Baiborodin, E G Malygin, S N Zagrebelnyi *Allergologiya i Immunologiya* **8** 235 (2007)
28. J M Veranth, E G Kaser, M M Veranth, M Koch, G S Yost *Part. Fibre Toxicol.* **4** (2) 1 (2007)
29. T Moritz, J Reiss, K Diesner, D Su, A Chemseddine *J. Phys. Chem. B* **101** 8052 (1997)
30. Y Wang, M Wu, W F Zhang *Electrochim. Acta* **53** 7863 (2008)
31. M R Hoffman, S T Martin, W Choi, D W Bahnemann *Chem. Rev.* **95** 69 (1995)
32. B Liu, L Wen, X Zhao *Sol. Energy Mater. Sol. Cells* **92** 1358 (2008)
33. J-M Giraudon, T B Nguyen, G Leclercq, S Siffert, J-F Lamonier, A Aboukaïs, A Vantomme, B-L Su *Catal. Today* **137** 379 (2008)
34. A Dey, S De, A De, S K De *Nanotechnology* **15** 1277 (2004)
35. S W Oh, S H Park, Y K Sun *J. Power Sources* **161** 1314 (2006)
36. H Zhou, L Liu, K Yin, S L Liu, G X Li *Electrochem. Commun.* **8** 1168 (2006)
37. R Wang, KHashimoto, A Fujishima *Nature (London)* **388** 431 (1997)
38. Y Qiao, S-J Bao, C M Li, X-Q Cui, Z-S Lu, J Guo *ACS Nano* **2** 113 (2008)
39. D M Antonelly *Microporous Mesoporous Mater.* **30** 315 (1999)
40. L Malfatti, P Falcaro, H Amenitsch, S Caramori, R Argazzi, C A Bignozzi, S Enzo, M Maggini, P Innocenzi *Microporous Mesoporous Mater.* **88** 304 (2006)
41. L T Tsykoza, N A Kulikovskaya, N K Zhulanov, Z R Ismagilov *React. Kinet. Catal. Lett.* **60** 323 (1997)
42. Z R Ismagilov, L T Tsikoza, R A Shkrabina, V A Sazonov, N V Shikina *Kinet. Katal.* **39** 607 (1998) [a]
43. Z R Ismagilov, R A Shkrabina, S A Yashnik, N V Shikina, I P Andrievskaya, S R Khairulin, V A Ushakov, J A Moulijn, I V Babich *Catal. Today* **69** 351 (2001)
44. J Le, Z Zhou, H Wang, G Li, Y Wu *Desalination* **212** 123 (2007)
45. V A Dzis'ko, A P Karnaukhov, D V Tarasova, in *Fiziko-khimicheskie Osnovy Sinteza Okisnykh Katalizatorov* (Physicochemistry Foundations of the Synthesis of Oxide Catalysts) (Novosibirsk: Nauka, 1978) p. 46
46. M R Harris, G Whitaker *J. Appl. Chem.* **13** 348 (1963)
47. V M Chertov, N T Okopnaya, I E Neimark *Dokl. Akad. Nauk SSSR* **209** 876 (1973) [b]
48. H Cheng, J Ma, Z Zhao, L Qi *Chem. Mater.* **7** 663 (1995)
49. A L Castro, M R Nunes, A P Carvalho, F M Costa, M H Florêncio *Solid State Sci.* **10** 602 (2008)

50. R K Wahi, Y Liu, J C Falkner, V L Colvin *J. Colloid Interface Sci.* **302** 530 (2006)
51. R C Asher, S J Gregg *J. Chem. Soc.* 5057 (1960)
52. H-J Chen, L Wang, W-Y Chiu *Mater. Chem. Phys.* **101** 12 (2007)
53. A Verma, S A Agnihotry *Electrochim. Acta* **52** 2701 (2007)
54. J Beusen, M K Van Bael, H Van den Rut, J D'Haen, J Mullens *J. Eur. Ceram. Soc.* **27** 4529 (2007)
55. S Mahshid, M Askari, M S Ghamsari *J. Mater. Process. Technol.* **189** 296 (2007)
56. A Fernandez, A Caballero, A R Gonzalez-Elipe, J-M Herrmann, H Dexpert, F Villain *J. Phys. Chem.* **99** 3303 (1995)
57. M H Habibi, M Nasr-Esfahani *Dyes Pigm.* **75** 714 (2007)
58. C A Martinez-Perez, P E Garcia-Casillas, H Camacho-Montes, H A Monreal-Romero, A Martinez-Villafane, J Chacon-Nava *J. Alloys Compd.* **434**–**435** 820 (2007)
59. H-J Chen, P-C Jian, J-H Chen, W Leeyih, W-Y Chiu *Ceram. Int.* **33** 643 (2007)
60. D H Kim, H W Ryu, J H Moon, J Kim *J. Power Sources* **163** 196 (2006)
61. J Yu, J C Yu, W Ho, M K-P Leung, B Cheng, G Zhang, X Zhao *Appl. Catal., A: General* **255** 309 (2003)
62. R Campostrini, M Ischia, L Palmisano *J. Therm. Anal. Calorim.* **71** 997 (2003)
63. R Campostrini, M Ischia, L Palmisano *J. Therm. Anal. Calorim.* **71** 1011 (2003)
64. K R Sunajadevi, S Sugunan *React. Kinet. Catal. Lett.* **82** 11 (2004)
65. N Wetchakun, S Phanichphant *Curr. Appl. Phys.* **8** 343 (2008)
66. D Neppolian, Q Wang, H Jung, H Choi *Ultrason. Sonochem.* **15** 649 (2008)
67. D Liao, B Liao *Int. J. Chem. Reactor Eng.* **5** A24 (2007)
68. D Zhang, L Qi, J Ma, H Cheng *J. Mater. Chem.* **12** 3677 (2002)
69. C Suresh, V Biju, P Mukundan, K G K Warrier *Polyhedron* **17** 3131 (1998)
70. E Scolan, C Sanchez *Chem. Mater.* **10** 3217 (1998)
71. L Mao, Q Li, H Dang, Zh Zhang *Mater. Res. Bull.* **40** 201 (2005)
72. I P Olen'kova, G A Zenkovets, D V Tarasova, I A Ovsyannikova *Izv. Sib. Otd. Akad. Nauk SSSR, Ser. Neorg. Mater.* **13** 383 (1977)
73. V Yu Gavrilov, G A Zenkovets *Kinet. Katal.* **31** 168 (1990) [a]
74. T Rajh, A E Ostafin, O I Micic, D M Tiede, M C Thurnauer *J. Phys. Chem.* **100** 4538 (1996)
75. T Rajh, O Poluektov, A A Dubinski, G Wiederrecht, M C Thurnauer, A D Trifunac *Chem. Phys. Lett.* **344** 31 (2001)
76. M C Thurnauer, L M Tiede, T Rajh *Acta Chem. Scand.* **51** 610 (1997)
77. R C Thompson *Inorg. Chem.* **23** 1794 (1984)
78. C-S Fang, Y-W Chen *Mater. Chem. Phys.* **78** 739 (2003)
79. R Chu, J Yan, S Lian, Y Wang, F Yan, D Chen *Solid State Commun.* **130** 789 (2004)
80. Y Zhang, G Xiong, N Yao, W Yang, X Fu *Catal. Today* **68** 89 (2001)
81. Q Zhang, L Gao, J Guo *J. Eur. Ceram. Soc.* **20** 2153 (2000)
82. M Koelsch, S Cassaignon, J F Guillemoles, J P Jolivet *Thin Solid Films* **403**–**404** 312 (2002)
83. Y Hu, H-L Tsai, C-L Huang *J. Eur. Ceram. Soc.* **23** 691 (2003)
84. B I Lee, X Wang, R Bhave, M Hu *Mater. Lett.* **60** 1179 (2006)
85. Q Zhang, L Gao, J Guo *Appl. Catal., B: Environ.* **26** 207 (2000)
86. Q Zhang, L Gao, J Guo *Nanostruct. Mater.* **11** 1293 (1999)
87. M Scarisoreanu, M R Alexandrescu, R Birjega, I Voicu, E Popovici, I Soare, L Gavrila-Florescu, O Cretu, G Prodan, V Ciupina, E Figgemeier *Appl. Surf. Sci.* **253** 7908 (2007)
88. H Möckel, M Giersig, F Willig *J. Mater. Chem.* **9** 3051 (1999)
89. A Hanprasopwattana, T Rieker, A G Sault, A K Datye *Catal. Lett.* **45** 165 (1997)
90. US P. 4692273 (1987)
91. S Baskaran, L Song, J Liu, Y I Chen, G L Graff *J. Am. Ceram. Soc.* **81** 401 (1998)
92. P V A Padmanabhan, K P Sreekumar, T K Thiyagarajan, R U Satpute, K Bhanumurthy, P Sengupta, G K Dey, K G K Warrier *Vacuum* **80** 1252 (2006)
93. S Qiu, S J Kalita *Mater. Sci. Eng., A* **435**–**436** 327 (2006)
94. N Venkatachalam, M Palanichamy, V Murugesan *Mater. Chem. Phys.* **104** 454 (2007)
95. Yu V Kolen'ko, A A Burukhin, B B Churagulov, N N Oleynikov *Mater. Lett.* **57** 1124 (2003)

[a] — *Kinet. Catal. (Engl. Transl.)*
[b] — *Dokl. Chem. (Engl. Transl.)*

ISSN 1995-0780, Nanotechnologies in Russia, 2009, Vol. 4, Nos. 9–10, pp. 732–735. © Pleiades Publishing, Ltd., 2009.
Original Russian Text © V.F. Zarytova, V.V.Zinov'ev, Z.R. Ismagilov, A.S. Levina, M.N. Repkova, N.V. Shikina, A.A. Evdokimov, E.F. Belanov, S.M. Balakhnin, O.A. Serova, S.I. Baiborodin, E.G. Malygin, S.N. Zagrebel'nyi, 2009, published in Rossiiskie nanotekhnologii, 2009, Vol. 4, Nos. 9–10.

ARTICLES

An Examination of the Ability of Titanium Dioxide Nanoparticles and Its Conjugates with Oligonucleotides to Penetrate into Eucariotis Cells

V. F. Zarytova[a], V. V. Zinov'ev[b], Z. R. Ismagilov[c], A. S. Levina[a], M. N. Repkova[a], N. V. Shikina[c], A. A. Evdokimov[b], E. F. Belanov[b], S. M. Balakhnin[b], O. A. Serova[b], S. I. Baiborodin[d], E. G. Malygin[b], and S. N. Zagrebel'nyi[d]

[a] *Institute of Chemical Biology and Fundamental Medicine, Siberian Branch, Russian Academy of Sciences, pr. Akademika Lavrent'eva 8, Novosibirsk, 630090 Russia*

[b] *The Vektor State Research Center of Virology and Biotechnology, Federal Service for Supervision in the Sphere of Protecting Consumer Rights and Human Wellbeing (Federal State Research Institution), ABK, korp. 12, Kol'tsovo, Novosibirsk oblast, 630559 Russia*

[c] *Institute of Catalysis, Siberian Branch, Russian Academy of Sciences, pr. Akademika Lavrent'eva 5, Novosibirsk, 630090 Russia*

[d] *State Educational Institution of Higher Professional Education, Novosibirsk State University Rosobrazovaniya, Russian Federation, ul. Pirogova 2, Novosibirsk, 630090 Russia*

* *e-mail: snz@post.nsu.ru*

Received July 24, 2008

Abstract—In this study we examine the possibility that TiO_2 nanoparticles and their conjugates can penetrate into cultivated cells without any special transfection procedures. Oligonucleotides and their derivates were conjugated with the TiO_2 nanoparticles, which were obtained as colloidal solutions at a concentration of TiO_2 0.3M by $TiCl_4$ hydrolysis. The electronic microscopy of various cell cultures (KCT, Vero, and MDCK) treated with nanoparticle solutions (20 μg/μl) showed that nanoparticles could enter the cells and accumulate in the vacuoles and phagosomes and form inclusions in cytoplasm. Thus, we demonstrated the penetration of TiO_2 nanoparticles and their oligonucleotide conjugates into intracellular space without any auxiliary operations. Most other researches used electroporation techniques for similar purposes [1, 2, 5].

DOI: 10.1134/S1995078009090158

INTRODUCTION

The threat that pathogenic virus agents pose to mankind has considerably increased in recent years. One reason for this growth is antibioticotherapy (a widespread method for treating bacterial infections), which is ineffective in treating viral diseases because of the principal difference in the duplication biology of bacteria and virus in the human organism. In addition, many of virus pathogens very changeable, which significantly decreases the efficiency of the vaccinal prevention of virus infections.

Viral genetic-material damage, particularly with antisense oligonucleotides, is one of the most promising strategies for antiviral therapy. However, delivering olygonucleotides directly into the injured cell is the biggest problem in this case.

Because of the rising interest in nanotechnologies in recent years, several methods for using nanoparticles of different nature—as a way to deliver drugs into cells—have appeared. Voloshchak et al. studied intracellular distribution in the eukaryotic cells of TiO_2 nanoparticles conjugated with specific oligonucleotides [1, 2]. As was determined during the experiments, these nanoconjugates interacted specifically with DNA localized in the cell nucleus and mitochondrion. The main method for the transformation of the cells was electroporation, which damages cell membranes. Unfortunately, this technology of delivering nanoparticles conjugated with bioactive substances into the damaged cells is not acceptable in clinical conditions. The authors specified that nanoparticles penetrate into the cells during incubation, but they didn't detail the conditions of the incubation.

In this work we examine how the TiO_2 nanoparticles and their conjugates with specific oligonucleotides penetrate into the eukaryotic cells in more detail.

MATERIALS AND METHODS

TiO_2 nanoparticles were obtained by $TiCl_4$ hydrolysis as a colloidal solution with a TiO_2 concentration of 0.3M and pH 6.7 [3]. For the immobilization of the oligonucleotides on the nanoparticles, TiO_2 solutions were diluted to 0.0125M (1–2 mg/ml).

X-ray analysis has indicated that titanium dioxide preparation is defined as a radioamorphous phase

state. It is probably a superfine brookite with D < 5 nm. Methods of small angle X-ray scattering (SARS) and atomic-force microscopy (AFM) were used to establish that the titanium dioxide in a colloidal solution is present in separated particles 3.5–5 nm in size and preserves the sol's dispersion degree for six months (during the study).

Conjugates of nanoparticles with the oligonucleotides and their derivatives were obtained by a similar procedure described previously [4].

Vero, KCT, MDCK, and MDBK cell lines were used for experiments. Cells were received from the cell culture collection at the Federal State Institute of Science, Scientific Research Center (FSIS SRC) VB Vektor, Rospotrebnadzor (Kol'tsovo, Novosibirsk oblast). Cells were cultivated in Igla DMEM media with 5% fetal bovine serum (FBS), penicillin (100 U/ml), and streptomycin (100 μg/ml).

SAMPLE PREPARATIONS AND MICROSCOPIC INVESTIGATION

For electronic microscopy, cells were incubated with nanoparticles for 24 h, then washed from media and fixed with 2.5% glutaraldehyde in a phosphate salt buffer (PBS) with pH 7.2 for 1 h on ice. Rest fixation was made in 1% osmium tetroxide in PBS with pH 7.2 for 1 h at room temperature. One they were dehydrated with ethanol, the cells were put on Araldite epoxy resin. Ultrathin sections were prepared on a Leica Ultracut UCT ultratome, then they were contrasted with uranyl acetate and plumbum citrate and analyzed using an LEO 910 (Zeiss) electronic microscope.

SAMPLE PREPARING FOR ANALYZING NANOPARTICLE PENETRATION INTO THE CELLS UNDER THE CONFOCAL MYCROSCOPY

Cells growing on cover slips were incubated with nanocomposites TiO_2-PL(Flu) and TiO_2-PL(Flu)-ON marked with a fluorescent label for 24 h.[1] Then cells were fixed with 0.4% formalin with 0.1% Triton X-100 (10 min) and treated with 0.5% Triton X-100 (10 min) and 2% formalin (10 min). Actin filaments were stained with a phalloidin-TRITC complex (red signal) to visualize the border of the cells. All the solutions were prepared on PBS, pH 7.2. The glasses with cells were put upside-down on the slide plates onto restricted media with antifade and DAPI. The samples were analyzed with a laser scanning microscope LSM 510 META (Zeiss). For label identification we used different laser wave lengths: 405 nm (for DAPI they were cellular nuclei), 488 nm (for nanocomposites they were marked with flouroscein), and 543 nm (for actin filaments they were marked with a phalloidin-TRITC complex). The thickness of optical sections was 0.3 mm.

Nanocomposites TiO_2-PL and TiO_2-PL-oligo were marked with a fluorescent label by treatment with FITC in 0.2 M $NaHCO_3$ solution for 1 h at 60°C with following washing off of excess FITC. In addition, we obtained nanocomposits with dopamine (TiO_2-DA-PL(Ac) and TiO_2-DA-PL(Ac)-oligo), because, according to the published data, DA increases the effects of nanoparticles under radiation [5]. TiO_2-nanoparticles (1 mg) were sequentially treated with glycidylisopropyl ether (100 μl) and then with 1 M DA solution. Samples with DA were brick-red color, which indicates the complex formation with charge transferring [6]. PL or PL-oligo were added to washed nanoparticles in the proportion TiO_2 : PL = 1 : 1000.

The cells growing on cover glasses were incubated for the whole day with TiO_2-PL(Flu) nanoparticles labeled by FITC; then they were fixed with 0.4% formalin with 0.1% Triton for 10 min, treated with 0.5% Triton X-100 for 10 min, and fixation was finished with 2% formalin for 10 min. All solutions were prepared in PBS, pH 7.2. The glasses with cells were put upside-down on the slide plates onto restricted media with antifade and DAPI. Samples were analyzed under an LSM 510 META laser scanning microscope (Zeiss). TiO_2-PL(Flu) nanocomposits were dyed green and localized in cytoplasm; cell nuclei were stained by DAPI (blue); and actin filaments were stained by actin-phalloidin-TRITC complex (red). The microscopic lens was ×100. Scan conditions were as follows: laser lines 405, 488, and 543; filters BP 420-480, BP 505-530, and LP 560. The thickness of the optical sections was 0.3 μm.

RESULTS AND DISCUSSION

Voloshchak et al. [2] obtained oligonucleotides conjugated with TiO_2 - nanoparticles and detected that these conjugates specifically interact with DNA when introduced into the cells, according to the complementary principles [2]. Nanoparticles with oligonucleotides, which are complementary to the gene sequence of the NADH-dehydrogenase's (ND2) second sub-particle on the mitochondrial genome, were detected in mitochondria, whereas conjugates with oligonucleotides, which are complementary to the gene fragment of 18S-rRNA, were localized in nuclei. These interesting findings allow us to suppose the complementary interaction between conjugated oligonucleotides and cell nucleic acids. The authors of [1, 2] used the electroporation technique to introduce conjugates into the cells.

In this study we examined the capability of the conjugates to penetrate the cells without the electropora-

[1] PL is polylysine; Flu is fluorescein; DA is dopamine; PL-ON is polylysine derivate of olygonucleotide; DAPI is 4',6-diamino-2-phenylindole dihydrochloride; TRITC is (tetrametylrodamin isothiocyanate) phalloidin (Sigma); and PBS is a phosphate salt buffer, pH 7.2, with density of 0.995 g/ml (Sigma).

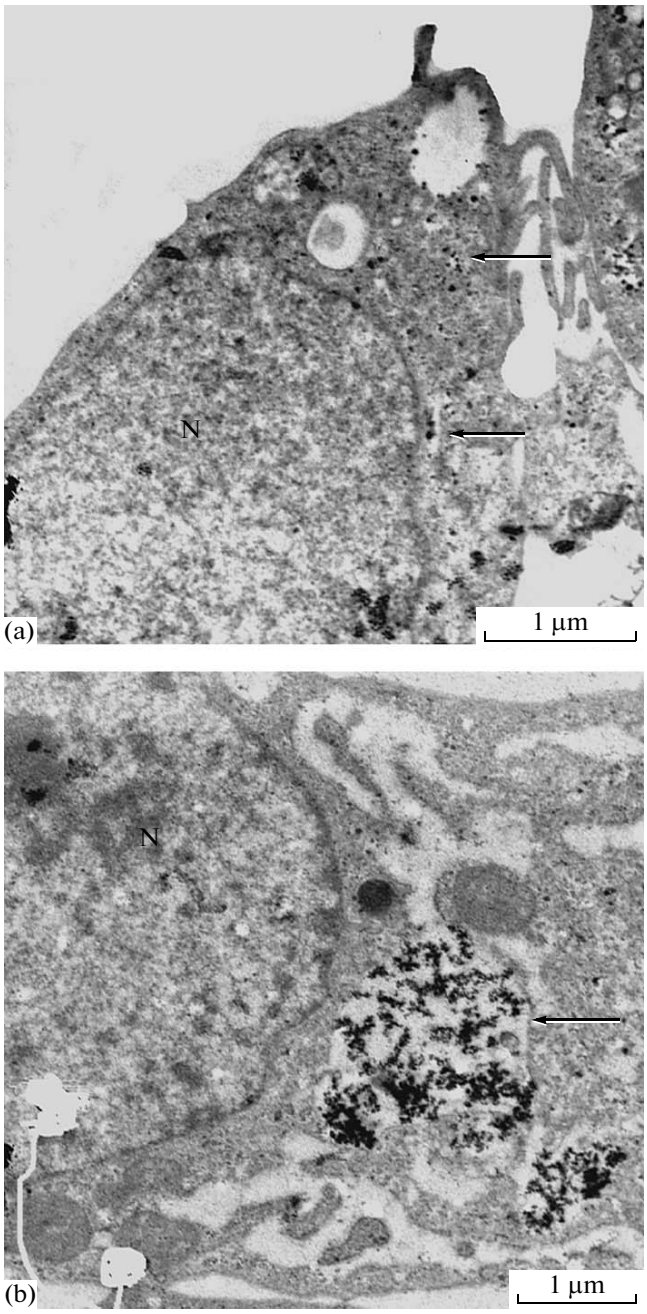

Fig. 1. Vero cells incubated with 20 μg/ml nanoparticles TiO_2, (a) treated with ultrasound and (b) not treated. N is the cell nuclei. Inclusions of nanoparticles in the cells are shown by arrows. Bar = 2 μm.

tion technique, because this method isn't available for the cells of an organism.

The electron microphotography of Vero cells incubated with TiO_2 nanoparticles are shown in Fig.1. The same pictures were made for KCT, MDCK, and MDBK cell cultures (data not shown).

The electron microscopy of different cell cultures (KCT, Vero, and MDCK) treated with 20 μg/μl showed that nanoparticles could enter the cells and accumulate in vacuoles and phagosomes and form inclusions in cytoplasm. Nanoparticles previously treated with ultrasound formed small inclusions or localized as separated particles and weren't detected in nuclei.

The penetration of nanoparticles into the cells were examined by confocal laser microscopy (Fig. 2). As you can see in Fig. 2, these data confirm the results of electron microscopy. Essentially, we didn't detect the oligonucleotides marked with fluoresceine and unbound to oligonucliotides in the cells (data not shown). Nanoparticles probably protect oligonucleotides from intracellular nucleases, which efficiently destroyed exposed oligonucleotides [7]. As was previously reported, Voloshchak et al. used the electroporation technique to introduce nanoparticles into the cells [1, 2]. Moreover, other researchers examined the penetrations of gold nanoparticles (which were conjugated with the anticancer drug herceptin) into the cells [8]. Herceptin is a humanized monoclonal antibody to receptor HER2/neu (erbB2), which is exposed on the cancer cells of the mammary gland. The authors demonstrated the dependency of the nanoparticles sizes and the penetrating efficiency of the conjugates. The optimal sizes of gold nanoparticles was from 40 to 50 nm. The authors supposed that, due to the binding of nanocojugates with their specific receptors, receptor mediated endocytosis occurs in this case. Herceptin binds to several specific receptors and formed clusters. Such multipoint binding is necessary to form a high affinity bond.

These findings are convincing, but we think that maybe this is possible only when the ligand, for instatnce herceptin, is a large protein molecule which binds ineffectively with smaller nanoparticles. In our case the sizes of ligand molecules are smaller (20–30 bp oligonucleotides) than the herceptin molecule, which facilitates the penetration of nanocojugates into the cells. Thus, we suggested that the optimal size of our nanoparticles may be smaller and the nanoconjugate's internalization occurs without interaction with a specific receptor.

Zhang and Sun examined the effects of TiO_2 nanoparticles on the rectal carcinoma LS 147-t cell line and found that cells treated with nanoparticles and UV radiation died [9]. The cells weren't exposed to any other special transfection procedures. The authors wondered whether nanoparticles accumulate on the surface of the cells or penetrate into the cells by endocytosis, but they didn't try to show the nanoparticles in the cells with direct methods.

Huojin et al. used nanodaimond to deliver doxorubicine antibiotic (apoptotic agent/stimulator) into the cells [10]. The authors detected that nanodaimonds penetrate into the cells without any special trasfection procedures. This evidence and our results allow us to suggest that using such a way to inject drugs into the cells is a general (not a specific) method.

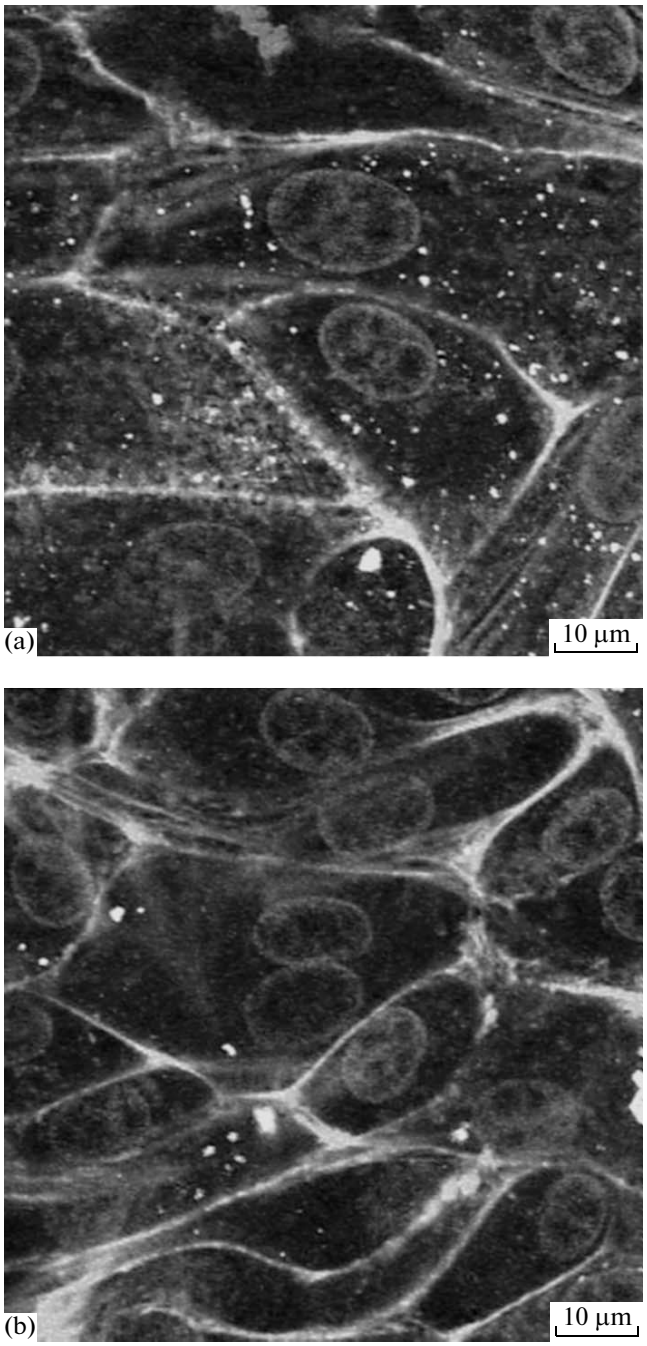

Fig. 2. Optic slice of KCT cells monolayer: (a) is the nanocomposite TiO_2-PL(Flu) localization and (b) is the nanocomposite TiO_2-PL(Photo, Flu)-ON localization. In the figure you can see the nanoparticles, labeled by fluoresceine, as bright signals in cytoplasm; nuclei (DAPI staining); and actin filaments (actin-phalloidin-TRITC complex staining). The microscopic lens is ×100. Scan conditions are as follows: laser lines 405, 488, and 543; filters BP 420-480, BP 505-530, and LP 560. The thickness of the optical sections was 0.3 μm.

Thus, in this study we detected the penetration of TiO_2-nanoparticles and their conjugates into the cultivated cells without any special transfection procedures; however, how they penetrate is not yet clear.

ACKNOWLEDGMENTS

This research was supported by the LIVING SYSTEM Federal Scientific and Technical Program within the framework of state contract no. 02.512.11.2081, by Developing the Scientific Potential of Higher Education, a departmental analytical program of the Ministry of Education and Science (Research) of the Russian Federation "Development of the Scientific Potential of the Higher School" (registration no. 2.1.1/5642), and by FRRF grant no. 08-04-01045-a.

REFERENCES

1. T. Paunesku, S. Vogt, B. Lai, J. Maser, N. Stojičević, K. T. Thurn, C. Osipo, H. Liu, D. Legnini, Z. Wang, Ch. Lee, and G. E. Woloschak, "Intracellular Distribution of TiO_2–DNA Oligonucleotide Nanoconjugates Directed to Nucleolus and Mitochondria Indicates Sequence Specificity," Nano Lett. **7** (3), 596–601 (2007).
2. R. J. Endres, T. Raunesku, S. Vogt, T. J. Meade and G. E. Woloschak, "DNA–TiO_2 Nanoconjugates Labeled with Magnetic Resonance Contrast Agents," J. Am. Chem. Soc. **129**, 15 760–15 761 (2007); http://pubs.acs.org
3. V. Yu. Gavrilov and G. A. Zenkovets, "Influence of Conditions Providing Precipitation of Titanium Dioxide Hydrogel on the Porous Xerogel Structure," Kinet. Katal. **31** (1), 168–173 (1990).
4. A. Levina, I. Pyshnaya, M. Repkova, V. Rar, and V. Zarytova, "Oligonucleotide Probes Containing Polylysine Residues for Fabrication of DNA Chips on Various Solid Surfaces," Biotechnol. J. **7**, 879–885 (2007).
5. T. Paunesku, T. Rajh, G. Wiederrecht, J. Maser, S. Vogt, N. Stojičević, M. Protič, B. Lai, J. Oryhon, M. Thurnauer, and G. Woloschak, "Biology of TiO_2–Oligonucleotide Nanocomposites," Nat. Mater. **2**, 343–346 (2003).
6. T. Rajh, L. X. Chen, K. Lukas, T. Liu, M. C. Thurnauer, and D. M. Tiede, "Surface Restructuring of Nanoparticles: An Efficient Route for Ligand–Metal Oxide Crosstalk," J. Phys. Chem. B **106**, 10 543–10 552 (2002).
7. F. Plenat, N. Klein-Monhoven, B. Marie, J. M. Vignaud, and A. Duprez, "Cell and Tissue Distribution of Synthetic Oligonucleotides in Healthy and Tumor-Bearing Nude Mice: An Autoradiographic, Immunohistological, and Direct Fluorescence Microscopy Study," Am. J. Pathol. **147** (1), 124–135 (1995).
8. W. Jiang, B. Y. S. Kim, J. T. Rutka, and W. C. W. Chan, "Nanoparticle-Mediated Cellular Response Is Size-Dependent," Nat. Nanotechnol. **3**, 145–150 (2008).
9. Zhang Ai-Ping and Sun Yan-Ping, "Photocatalytic Killing Effect of TiO_2 Nanoparticles on Ls-174-t Human Colon Carcinoma Cells," World J. Gastroenterol. **10** (21), 3191–3193 (2004).
10. H. Houjin, E. Pierstorff, E. Osawa, and D. Ho, "Active Nanodiamond Hydrogels for Chemotherapeutic Delivery," Nano Lett. **7** (11), 3305–3314 (2007).

ISSN 1995-0780, Nanotechnologies in Russia, 2010, Vol. 5, Nos. 5–6, pp. 417–420. © Pleiades Publishing, Ltd., 2010.
Original Russian Text © N.A. Mazurkova, Yu.E. Spitsyna, N.V. Shikina, Z.R. Ismagilov, S.N. Zagrebel'nyi, E.I. Ryabchikova, 2010, published in Rossiiskie nanotekhnologii, 2010, Vol. 5, Nos. 5–6.

ARTICLES

Interaction of Titanium Dioxide Nanoparticles with Influenza Virus

N. A. Mazurkova[a, b], Yu. E. Spitsyna[a, d], N. V. Shikina[c], Z. R. Ismagilov[c], S. N. Zagrebel'nyi[a], and E. I. Ryabchikova[a, d]

[a] *Novosibirsk State University, ul. Pirogova 2, Novosibirsk, 630090 Russia*

[b] *Vector State Scientific Center for Virology and Biotechnology, r.p. Kol'tsovo, Novosibirsk oblast, 630559 Russia*

[c] *Boreskov Institute of Catalysis, Siberian Branch, Russian Academy of Sciences, pr. Akademika Lavrent'eva 5, Novosibirsk, 630090 Russia*

[d] *Institute of Chemical Biology and Fundamental Medicine, Siberian Branch, Russian Academy of Sciences, pr. Akademika Lavrent'eva 8, Novosibirsk, 630090 Russia*

e-mail: snz@post.nsu.ru

Received January 24, 2010; in final form February 10, 2010

Abstract—Titanium dioxide (TiO_2) in a suspension or absorbed on a film possesses bactericidal and virucidal properties caused by photocatalytic reactions. Our electron microscopic examinations showed that titanium dioxide nanoparticles destroyed the influenza virus after 30 min incubation. Virological studies revealed the inactivation of the influenza virus by TiO_2, depending on the concentration of nanoparticles and the incubation period. The inactivation effect was observed when the incubation was performed in darkness, unlike the TiO_2 suspension. We propose that the virus-inactivation properties of TiO_2 are mainly based on the direct contact between nanoparticles and virus particles.

DOI: 10.1134/S1995078010050174

INTRODUCTION

Searching for substances and ways to inactivate pathogenic microorganisms that are safe for humans and the environment is an important for providing for the health and epidemic safety of the population. Sunlight and its ultraviolet component are powerful natural disinfectants. Titanium dioxide has photocatalytic properties and produces active oxygen-containing radicals under ultraviolet irradiation [1–3]. Bactericidal and virucidal features of titanium dioxide (TiO_2) in a suspension form or layered onto a film are described in many works where the destruction of viruses and bacteria under ultraviolet irradiation was presented [3–5]. Published investigations on the effect of a TiO_2 nanoform onto microorganisms are rare; the destruction of particles of the surface hepatitis B antigen (HBsAg) as a result of photocatalytic reaction developed on the surface of TiO_2 nanoparticles (anatase) under the action of UV and sunlight was shown [6]. The task of the present work is to study the effect of TiO_2 nanoparticles on the influenza virus.

EXPERIMENTAL METHODS

Preparations of Titanium Dioxide

TiO_2 nanoparticles (TiO_2-1) were obtained by the hydrolysis of $TiCl_4$ in a form of colloid solution (pH = 6.7) containing 2.5 wt % TiO_2 and less than 0.05 wt % of Na and Cl [7]. Titanium dioxide powder (TiO_2-2) was obtained by the exiccation of a colloid solution of TiO_2-1 in air with its subsequent calcination at 700°C for 3 h. The size of the nanoparticles (TiO_2-1) was about 4–10 nm according to electron microscopy data, with the predominance of particles being 4–5 nm in size; powder particles (TiO_2-2) were 500 nm and larger.

To perform virologic and ultrastructural investigations, suspensions of TiO_2-1 and TiO_2-2 preparations with a concentration of 7 mg/ml were used. The smallest nanoparticle concentration (0.2 mg/ml) was determined in preliminary experiments using the visible destruction of influenza virus particles according to electron microscopy data (the data are not presented). To evaluate the level that nanoparticles influence virions, large concentrations (10-fold and 35-fold, 2 and 7 mg/ml, respectively) were used. Concentrations larger than 7 mg/ml were not used due to the toxic action it caused to the MDCK cell culture used for assessing the amount of living virus.

Influenza Virus

An A/Aichi/2/68(H3N2) virus strain grown on chicken embryos in a suspension form (virus–allantois liquid) with an infection titer of 9.5 lg TCD_{50}/ml was used to prepare working dilutions.

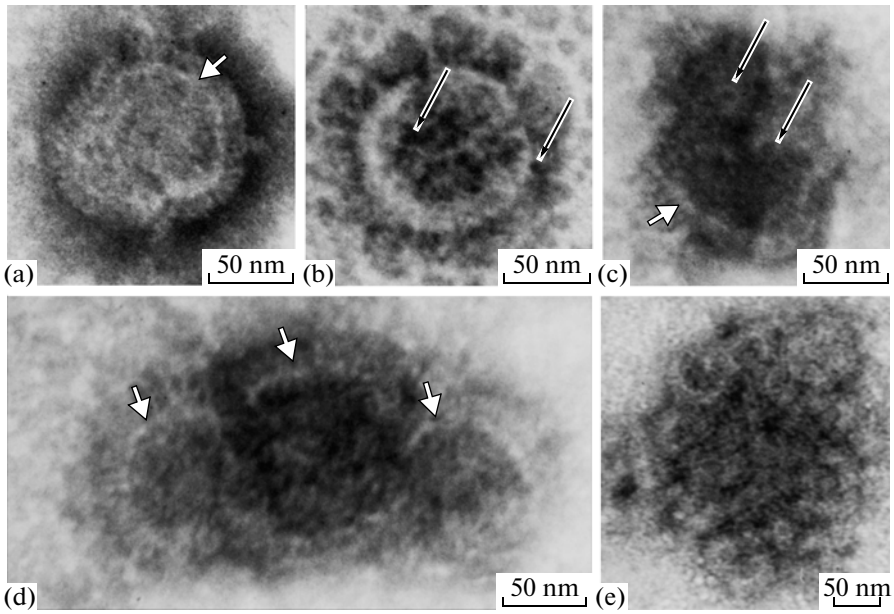

Fig. 1. Interaction between TiO_2-1 nanoparticles and particles of the A/Aichi/2/68 influenza virus (H3N2). White arrow indicates the virus envelope; black arrow indicates the nanoparticles: (a) intact influenza virus particle, (b) glued surface spinules and the adherence of particles onto virion surface (15 min of incubation), (c) the destruction of the virion envelope, and (d, e) the aggregation of virus particles entering the contrasting stain into the virion (3 and 5 h of incubation). Negative contrasting with phosphotungstic acid.

Inactivation of Influenza Virus with TiO_2 Preparations

Equal volumes of the suspension of influenza virus and TiO_2 preparations (500 μl) were mixed and incubated at room temperature for 0.5, 1, 5, 14, and 24 h in wells with a 2 cm diameter of the shielded plastic plate. The incubation was performed in the dark or under irradiation by a fluorescent lamp (40-W power) located at a distance of 160 cm or with an ultraviolet-light source (30-W power) located at a distance of 25 cm.

The biological activity of the influenza virus treated with TiO_2 nanoparticles

Concentration of TiO_2-1 nanoparticles (mg/ml)	Concentration of influenza virus (log TCD_{50}/ml)	Time of incubation of TiO_2-1 nanoparticles with influenza virus (h)	Virus production in MDCK cell culture (log TCD_{50}/ml)
0.2	9.5	0.5	7.5 ± 0.03 ($n = 3$)
		1.0	$5.5 \pm 0.03^{\bullet}$ ($n = 3$)
		5.0	$4.5 \pm 0.03^{\clubsuit}$ ($n = 3$)
2	9.5	0.5	4.5 ± 0.06* ($n = 3$)
		1.0	$4.5 \pm 0.08^{\blacksquare}$ ($n = 3$)
		5.0	$3.0 \pm 0.29^{\heartsuit}$ ($n = 3$)
Absence (control)	9.5	0.5	8.5 ± 0.29* ($n = 3$)
		1.0	$8.5 \pm 0.06^{\bullet\blacksquare}$ ($n = 3$)
		5.0	$8.5 \pm 0.58^{\clubsuit\heartsuit}$ ($n = 3$)
0.2	6.5	5	3.5 ± 0.29 ($n = 3$)
		14	2.5 ± 0.29 ($n = 3$)
		24	$0^{\diamondsuit}$ ($n = 3$)
2	6.5	5	2.5 ± 0.29 ($n = 3$)
		14	$0^{\spadesuit}$ ($n = 3$)
		24	$0^{\clubsuit}$ ($n = 3$)
7 mg/ml	6.5	5	$0.5 \pm 0.29^{\circ}$ ($n = 3$)
		14	$0^{\blacklozenge}$ ($n = 3$)
		24	$0^{\blacktriangleleft}$ ($n = 3$)
Absence (control)	6.5	5	$3.5 \pm 0.29^{\circ}$ ($n = 3$)
		14	$3.5 \pm 0.58^{\spadesuit\blacklozenge}$ ($n = 3$)
		24	$2.5 \pm 0.29^{\diamondsuit\clubsuit\blacktriangleleft}$ ($n = 3$)

Notes: *, °, •, ■, ♠, ♦, ♣, ♥, ♢, ♫, ◄—credible differences between two values.

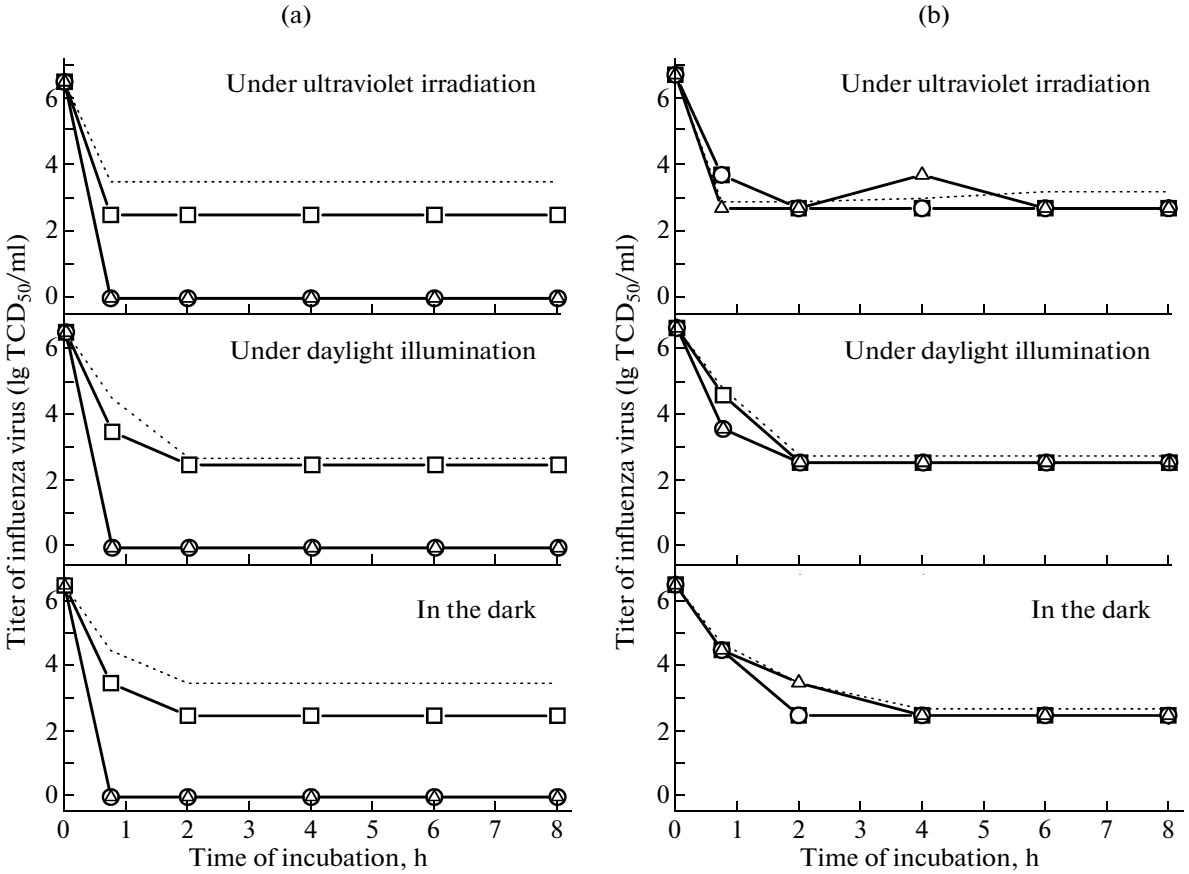

Fig. 2. Biological activity of influenza virus treated with nanoparticles and TiO_2 suspension (logTCD_{50}/ml): (a) TiO_2-1 sample and (b) TiO_2-2 sample. Concentration of TiO_2: (□) 0.2 mg/ml, (○) 2 mg/ml, and (△) 7 mg/ml. The dotted line shows the control influenza virus (without treatment with titanium dioxide).

Detection of the Infectious Activity of Influenza Virus

Tenfold dilutions of the TiO_2-mix preparation and virus suspension were prepared; then each dilution was introduced into separate well with MDCK cell culture and incubated at 37°C for 20 h. The production of the infectious influenza virus was assessed in a reaction of hemagglutination with 1% chicken erythrocytes [8]. Samples of the virus suspension incubated similarly to a mix with TiO_2 were used as controls. All experiments were performed in triplicate.

An electron microscopy investigation of the interaction between TiO_2-1 and the influenza virus was done using the method of negative staining. A mix of the nanoparticle suspension with a concentration of 2 mg/ml and an influenza virus suspension with a particle concentration of 10^9/ml was incubated at room temperature for 0, 1, 2, 3, and 5 h. A drop of the mix was coated onto a copper network with formvar support and incubated for 30 s; then the excess of liquid was eliminated with a filter paper and the networks were incubated in a drop of phosphotungstic acid for 30 s. The preparations were studied using a JEM 1400 electron transmission microscope (Jeol, Japan) at an accelerating voltage of 80 kV.

RESULTS AND DISCUSSION

The direct action of TiO_2-1 nanoparticles on the influenza virus was studied using an electron microscope; 15–20 units of each network were browsed. Virus particles mixed with TiO_2-1 nanoparticles are destroyed (Fig. 1). After 15 min of incubation, nanoparticles adhered onto the external surface of the virus envelope, surface spinules of the virus were glued together, and the envelope was broken. After 30 min, the degree of destruction was increased; the virus envelope was fragmented; a contrasting substance was penetrated into the virus vesicle and the aggregation of the virus particles was detected. After 1–5 h of incubation, virus particles were destroyed; their fragments associated with nanoparticles were found on networks. It should be noted that, at all stages of incubation, there were separate virus particles that still had their normal structures and did not contact the nanoparticles.

The inactivating effect of TiO_2-1 nanoparticles, which depends on the incubation time, concentration

of the virus, and concentration of nanoparticles, was revealed during an investigation of TiO_2-1 action on the virus vitality under daylight illumination (table).

To reveal the mechanisms of the inactivating effect of the TiO_2 nanoform, a comparative investigation of TiO_2-1 and TiO_2-2 action on the influenza virus was performed in the dark, in ultraviolet irradiation, and during daylight illumination (Fig. 2).

The obtained results show that TiO_2-1 nanoparticles express inactivation action on influenza virus regardless of the presence of daylight illumination or ultraviolet illumination; this is probably not connected with photocatalytic effects described previously for TiO_2 suspensions [1–3]. It is very likely that virus inactivation occurs due to the destruction of the virus envelope by nanoparticles, which results in the destruction and disintegration of the virion entirely. The envelope of influenza virus particles is a lipoprotein membrane, and it has a structure similar to the biological membranes of eukaryotic cells [9]. The ability of TiO_2 nanoparticles to enter virus particles that was revealed in our work may suggest the necessity of a detailed investigation of this process, since it may be used for the delivery of biologically active compounds associated with nanoparticles to a cell. From the other side, membrane destruction by nanoparticles may result in cell death, which should be kept in mind during the development of preparations on their base. The inactivating action of TiO_2 nanoparticles toward the influenza virus may be used for the development of new compounds and ways for disinfections to inactivate the influenza virus.

ACKNOWLEDGMENTS

This work was supported by the Federal Purposive Program "Living Systems," Governmental Contracts nos. 02.512.11.2081 and 02.512.11.2038, as well as by the departmental analytical program of the Ministry of Education and Science of the Russian Federation "Development of the Scientific Potential of Higher Education" (Registration no. 2.1.1/5642) and by RFBR (grant no. 08-04-01045-a).

REFERENCES

1. J. C. Ireland, P. Klostermann, E. W. Rice, and R. A. Clark, Appl. Environ. Microbiol. **59** (5), 1668 (1993).
2. E. J. Wolfrum, J. Huang, D. M. Blake, P. C. Maness, Z. Huang, and W. A. Jacoby, Environ. Sci. Technol. **36** (1), 3412 (2002).
3. M. Cho, H. Chung, W. Choi, and J. Yoon, Appl. Environ. Microbiol. **71** (1), 270 (2005).
4. X. Sang, T. G. Phan, S. Sugihara, F. Yagyu, S. Okitsu, N. Maneekarn, W. E. Müller, and H. Ushijima, Clin. Lab. (Heidelberg) **53** (7–8), 413 (2007).
5. J. E. Lee, K. D. Zoh, and G. P. Ko, Appl. Environ. Microbiol. **74** (7), 2111 (2008).
6. L. Zan, W. Fa, T. Peng, and Z. J. Grong, Photochem. Photobiol., B **86** (1), 165 (2007).
7. V. F. Zarytova, V. V. Zinov'ev, Z. R. Ismagilov, A. S. Levina, M. N. Repkova, N. V. Shikina, A. A. Evdokimov, E. F. Belanov, S. M. Balakhnin, O. A. Serova, S. I. Baiborodin, E. G. Malygin, and S. N. Zagrebel'nyi, Ross. Nanotekhnol. **4** (9–10), 115–118 (2009) [Nanotechnol. Russ. **4** (9–10), 732–735 (2009)].
8. *Virology: A Practical Approach*, Ed. by B. W. J. Mahy (Oxford University Press, Oxford, 1985; Mir, Moscow, 1988).
9. D. P. Nayak, R. A. Balogun, H. Yamada, Z. H. Zhou, and S. Barman, Virus Res. **143** (2), 147 (2009).